APPLICATION OF 2¼Cr-1Mo STEEL FOR THICK-WALL PRESSURE VESSELS

Sangdahl/Semchyshen, *editors*

ASTM STP 755

APPLICATION OF $2^1/_4$Cr-1Mo STEEL FOR THICK-WALL PRESSURE VESSELS

A symposium
sponsored by
Metal Properties Council
AMERICAN SOCIETY FOR
TESTING AND MATERIALS
Denver, Colo., 19–20 May 1980

ASTM SPECIAL TECHNICAL PUBLICATION 755
G. S. Sangdahl, Chicago Bridge & Iron
Company, and M. Semchyshen, Climax
Molybdenum Company, editors

ASTM Publication Code Number (PCN)
04-755000-02

AMERICAN SOCIETY FOR TESTING AND MATERIALS
1916 Race Street, Philadelphia, Pa. 19103

Library of Congress Catalog Card Number: 81-67407

NOTE

Printed in Baltimore, Md.
January 1982

Foreword

The Symposium on Application of $2\frac{1}{4}$Cr-1Mo Steel for Thick-Wall Pressure Vessels, sponsored by the Metal Properties Council, was held in Denver, Colorado, on 19-20 May 1980. G. S. Sangdahl, Chicago Bridge & Iron Company, and M. Semchyshen, Climax Molybdenum Company, served as symposium chairmen and also edited this publication.

Related ASTM Publications

Toughness of Ferritic Stainless Steels, STP 706 (1980), $32.50, 04-706000-02

Evaluations of the Elevated Temperature Tensile and Creep Rupture Properties of 12 to 27 Percent Chromium Steels, DS 59 (1980), $24.00, 05-059000-40

Properties of Austenitic Stainless Steels and Their Weld Metals (Influence of Slight Chemistry Variations), STP 679 (1979), $13.50, 04-679000-02

Rail Steels—Developments, Processing, and Use, STP 644 (1978), $45.00, 04-644000-01

Structures, Constitution, and General Characteristics of Wrought Ferritic Stainless Steels, STP 619 (1976), $7.50, 04-619000-02

Bearing Steels: The Rating of Nonmetallic Inclusion, STP 575 (1975), $22.25, 04-575000-02

A Note of Appreciation to Reviewers

This publication is made possible by the authors and, also, the unheralded efforts of the reviewers. This is a body of technical experts whose dedication, sacrifice of time and effort, and collective wisdom in reviewing the papers must be acknowledged. The quality level of ASTM publications is a direct function of their respected opinions. On behalf of ASTM we acknowledge with appreciation their contribution.

ASTM Committee on Publications

Editorial Staff

Jane B. Wheeler, *Managing Editor*
Helen M. Hoersch, *Senior Associate Editor*
Helen P. Mahy, *Senior Assistant Editor*
Allan S. Kleinberg, *Assistant Editor*
Virginia M. Barishek, *Assistant Editor*

Contents

Overview of Properties of 2¼Cr-1Mo Plates and Castings

Design Considerations in Application of 2¼Cr-1Mo Steel at Elevated Temperatures

Processing and Properties of 2¼Cr-1Mo Steel for Thick-Wall Pressure Vessels

FABRICATION, WELDING, AND CLADDING OF HEAVY-GAGE 2¼Cr-1Mo STEEL FOR PRESSURE VESSEL APPLICATIONS

STUDIES OF HEAT TREATING AND TEMPER EMBRITTLEMENT OF 2¼Cr-1Mo STEEL

SUMMARY

Introduction

The symposium on which this volume is based derived from an activity of Subcommittee 1 on Engineering Properties of Boiler and Pressure Vessel Materials (Dr. M. Semchyshen, chairman) of the Metal Properties Council (MPC). This work was started in response to industry's stating to MPC the need for more information about the properties of 2¼Cr-1Mo steel in heavy sections. The principal driving forces are the considerable benefits which may be realized. A Task Group was formed under G. S. Sangdahl to investigate this subject and, if need be, to develop a program to provide the necessary data. The symposium was a key stage in the development of the program. This volume now serves to provide the state-of-the-art basis for future activities.

MPC now has three subgroups working under Mr. Sangdahl's task group. These are Mechanical Properties, led by Dr. R. A. Swift; Fabrication and Inspection, led by A. G. Imgram; and Environmental Effects, led by A. R. Ciuffreda. Participation by industry in these subgroups and the task group has been outstanding. As a result, there is better understanding of the capabilities of chromium-molybdenum steels, wider interest in this important subject, and a sharper focus on future activities.

Some thoughts on these activities have been provided by the subgroup chairmen:

Mechanical Properties (R. A. Swift, chairman)—This symposium was held to have public discussions of the properties of heavy-gage 2¼Cr-1Mo steel and potential problems that may occur during fabrication and operation of pressure vessels. The sessions were well attended, attesting to the great interest in this subject. Authors came from France, Mexico, Switzerland, and the United States, and represented plate and casting manufacturers, forging and vessel fabricators, private research laboratories, and universities. The presentations ranged from research on new modifications to 2¼Cr-1Mo to fabrication and inspection of heavy-wall vessels.

It was interesting to note the varied points of view expressed by the authors. The major differences of opinion were in the areas of microstructure and silicon control. Several authors presented data showing that fully bainitic structures could be obtained at the centerline of 500-mm-gage plates or forgings without the addition of hardenability improvers such as vanadium or boron. Others, equally convincing, showed that proeutectoid ferrite forms in plates as light as 260 mm. This topic, needless to say, was a priority discussion at the panel session which followed.

The second area of controversy was the need for silicon control as a means of improving the resistance to temper embrittlement. Again, equally convincing data were presented on both sides of the argument. In addition, factors such as the possible loss in elevated temperature strength and resistance to tempering that low silicon (<0.10 percent) might have on 2¼Cr-1Mo steel were addressed. This also was hotly discussed in the panel session.

The symposium was a very refreshing experience to all concerned. There was a great deal of information on topics such as welding and fabrication, casting, forging, plate production, and material properties. The greatest contribution of this session, however, is that the conflicting data presented will be subject to intense scrutiny. It is hoped that test programs will be initiated to clear up these areas. In the final analysis, the producers and users of 2¼Cr-1Mo steel will profit more from this than from a session in which all participants agree.

These informative papers will aid one in weighing all the factors affecting material properties and future specifications. Finally, new ideas for research may also be generated as a result of these papers.

Fabrication and Inspection (A. G. Imgram, chairman)—It is envisioned that very large reactor vessels, weighing as much as 3000 to 4000 tons, will be required for the most economic commercialization of coal liquefaction processes. The field fabrication techniques described by J. E. Bonta of Chicago Bridge & Iron will be a very important factor for obtaining these large vessels. It appears that shop fabrication will be impractical because of the considerable difficulty of transportation and erection. However, plant operators must be assured of the same high integrity for safe operation as obtained with shop fabrication.

Higher speed welding processes, such as electroslag discussed by G. R. Edwards of Colorado School of Mines and electron beam detailed by W. J. Farrell of Sciaky and C. M. Weber of Babcock & Wilcox, offer considerable potential for increasing the efficiency of large vessel fabrication. Reduced welding time will reduce the cost of vessels fabricated in a shop. Rapid fabrication will be very important if the vessels are fabricated in the field in order not to obstruct other construction at the plant site. The high-temperature strength of weldments produced by newly developed welding processes must be verified before they can be used for vessel fabrication.

Research for low-alloy steel pressure vessel technology is currently being concentrated upon the requirements for coal liquefaction and gasification processing. It should be recognized that the resulting advancements in technology will also significantly benefit high-temperature/high-pressure petroleum refining processes.

Environmental Effects (A. R. Ciuffreda, chairman)—Hydrogen attack of steels has traditionally been avoided by application of the empirical Nelson curves during the material selection process. Nelson curves describing the acceptable limits of temperature and pressure for each class of steel are periodically revised if experience reveals the occurrence of potentially destructive methane bubbles following hydrogen service. The Nelson curves have served industry well; however, the next generation of vessels is pushing them to their extreme limits into a range in which there is little support for the suitability of even 2¼Cr-1Mo steel, one of the alloys most resistant to fissuring by methane formation.

Surprisingly little is understood about the effects of hydrogen on the carbides present in these alloys. In addition, carbides change during welding, heat treatment, and exposure in service. The papers in this symposium indicate there are important environmental effects, but they are not well understood. Programs to systematically examine the effects of hydrogen on carbides are needed. Long-term creep-rupture tests should be performed at realistic stress levels for times to 20 000 h or beyond. Current MPC studies involving exposure of 2¼Cr-1Mo and 3Cr-1Mo steels for times beyond 8000 h demonstrate the value of the long-time, low-stress approach.

There may be benefits of stainless steel clad or overlayed layers in retarding hydrogen degradation. Work needs to be done to establish under what conditions a measure of protection against hydrogen degradation can be reliably obtained.

The symposium committee extends acknowledgments to the authors and reviewers of the papers presented and to the ASTM staff for their help in conducting the symposium. Particular thanks are due Martin Prager of the Metal Properties Council for his tireless efforts in the organization of the symposium.

G. S. Sangdahl

Senior Metallurgical Consultant, Chicago Bridge & Iron Company, Oak Brook, Ill. 60521; symposium co-chairman and co-editor

M. Semchyshen

Vice-President, Metallurgical Development, Climax Molybdenum Company, Ann Arbor, Mich. 48106; symposium co-chairman and co-editor

Overview of Properties of 2¼Cr-1Mo Plates and Castings

T. E. Scott[1]

Pressure Vessels for Coal Liquefaction—An Overview

REFERENCE: Scott, T. E., **"Pressure Vessels for Coal Liquefaction—An Overview,"** *Application of 2¼Cr-1Mo Steel for Thick-Wall Pressure Vessels, ASTM STP 755,* G. S. Sangdahl and M. Semchyshen, Eds., American Society for Testing and Materials, 1982, pp. 7-25.

ABSTRACT: The existing world economic and political climate has intensified the need for a domestic source of liquid fuels. With dwindling crude oil reserves the need for alternative sources of liquid fuels has become pressing. Coal-derived liquids can be an important substitute for crude oil. A key component of process plants designed to liquefy coals is the "reactor". Coal liquefaction pressure vessels (reactors) for anticipated commercial operations are large by conventional standards. They must maintain a high level of reliability for lifetimes from 20 to 30 years while operating at temperatures near 425°C (800°F) and while containing a variety of sulfurous species and hydrogen at pressures up to about 28 MPa (4000 psi). This paper attempts to emphasize the role of reactors in the coal liquefaction process and to point out potential life-limiting aspects that must be considered in the design, construction, and operation of these large, thick-walled pressure vessels.

KEY WORDS: pressure vessels, coal liquefaction, coal conversion, materials, 2¼Cr-1Mo steel, corrosion, hydrogen attack, weld overlay, temper embrittlement

The Arab embargo on oil in 1973 and dwindling domestic petroleum resources have served to emphasize the need for an alternative to crude oil for liquid fuel and petrochemical feed stocks. Coal liquefaction provides an attractive alternative.

Coal liquefaction is not a contemporary concept; its beginnings can be traced back 120 years. Germany fueled its military machines with synthetic fuels derived from coal during World War II, and South Africa has been operating a commercial coal liquefaction plant (Sasol I) since 1953. Sasol I is an indirect liquefaction process requiring an intermediate gas-production stage

---

[1] Senior Technical Supervisor, Alcoa Technical Center, Alcoa Center, Pa. 15069; formerly Professor and Metallurgy and Ceramics Program Director, Ames Laboratory, Iowa State University, Ames, Iowa 50011.

before liquid fuels can be made. The viability of coal-derived liquids as an alternative to petroleum is largely a question of economics. In the United States, direct liquefaction appears more competitive, economically, than indirect liquefaction. Consequently, most of the second-generation processes being developed are in the direct liquefaction category called hydroliquefaction. These include (*1*) direct, noncatalytic processes such as SRC-I, SRC-II, and UOP extraction; (*2*) direct, catalytic processes such as H-Coal and Conoco Zinc Halide Hydrocracking; and (*3*) indirect, donor solvent processes such as the Exxon Donor Solvent (EDS) process.

Four of these hydroliquefaction processes in advanced stages of development are SRC-I, SRC-II, EDS, and H-Coal. These processes form the basis of this paper. Figure 1 is a block flow diagram indicating the general components of all four advanced liquefaction processes. For the SRC-I process a product solidification step should be added following the solvent separation stage. For the purposes of this paper, attention is focussed on the Reactor-Dissolver and the Gas Separation stages which involve the critical pressure

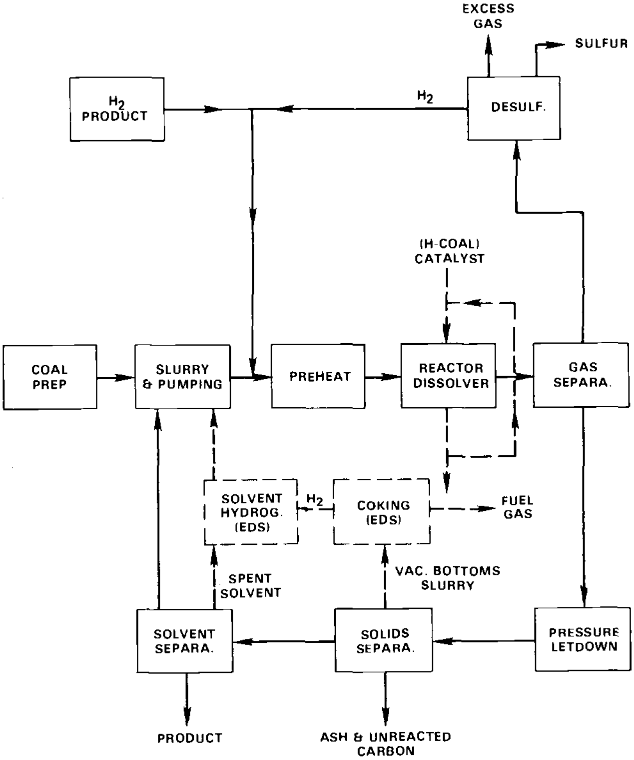

FIG. 1—*Generic block flow diagram for advanced hydroliquefaction processes.*

vessels. A materials-oriented discussion of the overall liquefaction process may be found in an earlier paper [*1*].[2]

The fundamental process of making syncrudes from coal is that of increasing the hydrogen to carbon (H/C) ratio. Hydrocarbons of interest have H/C ratios ranging from something less than one for coals to that of methane, namely, four. Between these extremes are crude oil, gasoline, and fuel oil with respective H/C values of 1.5, 1.8, and 1.9. It is clear, then, that to make liquid fuels from coal, a means must be found to increase its hydrogen level. Consequently, the more advanced U.S. liquefaction processes involve a chemical transfer of hydrogen from a donor solvent. Rehydrogenation of the solvent donors requires catalysis by one means or another. It is essentially the variation in schemes used to rehydrogenate the solvent that distinguishes the hydroliquefaction processes being developed. During liquefaction, temperatures are maintained somewhat below 499°C (930°F) [usually ~445°C (~825°F)] to avoid thermal cracking of liquid-size molecules because this increases the gas yield and the hydrogen consumption (methane consumes four hydrogens per carbon). Economics demands that hydrogen consumption be kept as low as liquefaction permits because the cost penalty for hydrogen production is high. During liquefaction, oxygen is removed from the coal by reacting with hydrogen to form H_2O and some of the sulfur is removed as H_2S. Nitrogen, which is in the organic rings, apparently can only be reacted to NH_3 in the presence of a catalyst; otherwise it concentrates in the char or heavy-liquid product. The primary liquefaction reactions occur in the "dissolver" or "reactor-dissolver". All other phases of a coal liquefaction process scheme are either for the preparation of the dissolver components or for separating the products generated in the dissolver.

Role of Pressure Vessels in Coal Liquefaction and Pilot-Plant Experiences

The "heart" of all advanced hydroliquefaction processes for coal conversion is the "dissolver" or reactor vessel. While partial dissolution of coal takes place in preheaters, the function of the reactor is to provide the mixture of coal slurry and high-pressure hydrogen sufficient residence time to permit the dissolution reactions to approach completion. Although the coal dissolution reactions are complex and ill understood, it is believed that thermal cracking of coal molecules is accompanied by stabilization of the lighter molecules by hydrogen donated by the solvent. Hydrogenation of the solvent requires a catalyst. The EDS process provides a separate solvent hydrogenation step into the process, while the H-Coal process adds catalyst to the dissolver and the SRC processes rely on minerals (ash) in the coal to catalyze solvent hydrogenation in the dissolver. Pressure, temperature, and residence time in

---

[2] The italic numbers in brackets refer to the list of references appended to this paper.

the dissolver depend on the type of coal, the catalyst, and the end-product desired.

Another critical vessel in advanced hydroliquefaction processes is the high-temperature—high-pressure flash drum. This vessel, which receives the effluent from the dissolver, serves as a gas-liquid separator. It keeps the effluent slurry at sufficiently high temperatures and pressures to maintain its fluidity and to prevent repolymerization before the more volatile components have been separated adequately. Downstream from the high-pressure flash drum, in both the overheads and bottoms (slurry) streams, are additional pressure vessels that can employ lower-grade steel shells because the operating conditions of temperature and pressure are less severe. Typical operating conditions and some structural characteristics of the reactor vessel and high-pressure flash drum are shown in Figs. 2 and 3, respectively. The operating conditions shown in these figures include the ranges for all advanced liquefaction processes. Structural characteristics are based on the SRC-Ft. Lewis pilot plant; except for size, they are expected to be similar in other pilot plants and commercial-size plants.

Operating experience with coal hydroliquefaction plants has been limited

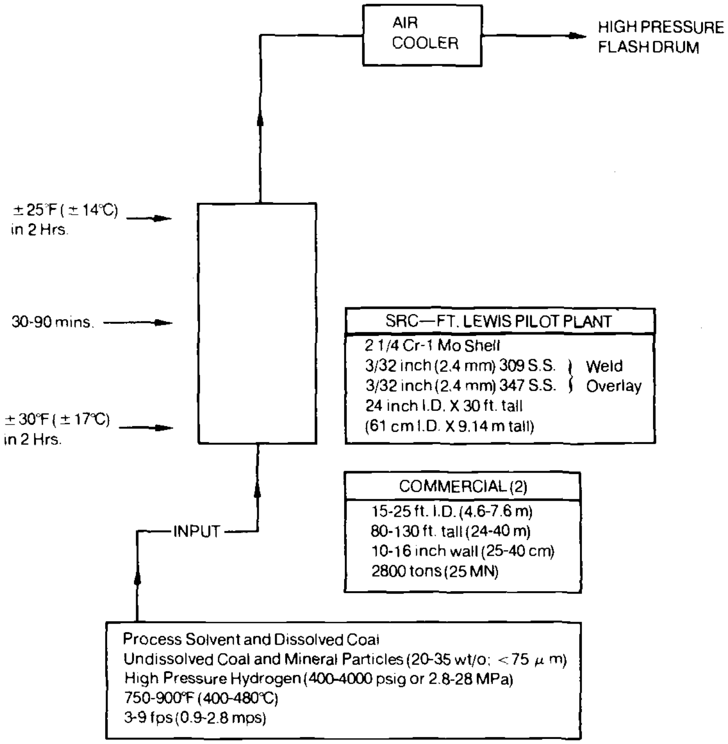

FIG. 2—*Reactor vessel conditions and characteristics.*

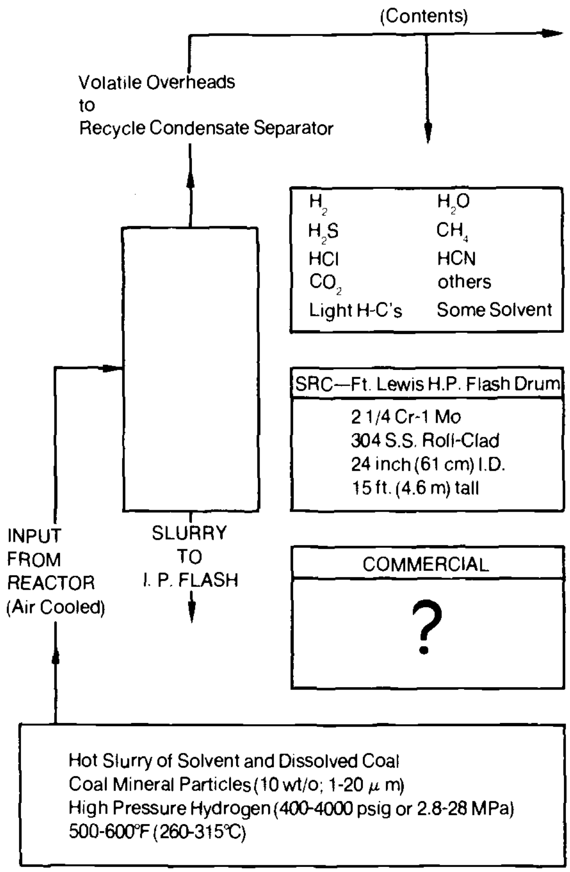

FIG. 3—*High-pressure flash drum (gas-liquid separator) conditions and characteristics.*

to pilot plant (SRC process) and smaller scale units. Rather serious problems have been encountered with pumps and let-down valves (erosion) and fractionation columns (corrosion); however, no operation-limiting problems have occurred in the reactors or high-pressure flash drums. Cracks have been noted in the stainless steel overlay near the bottom of the SRC-Ft. Lewis reactor vessel but they, apparently, have not penetrated to the underlying shell material (2¼Cr-1Mo steel) [*2*]. It is believed that the small-size vessel made weld overlaying difficult and the cracks were probably a result of unsatisfactory welding. Other minor degradations include general corrosion of the 347 stainless steel overlay and the formation of a feathery carbide structure which suggests that carbon penetrated into the stainless overlay. The high-pressure flash drum exhibited transgranular (probably chloride) and intergranular (probably polythionic) cracking of the 304 stainless steel cladding. Neither type of crack had penetrated to the 2¼Cr-1Mo shell. In one instance, substantial base metal (2¼Cr-1Mo) was lost to corrosion under a cracked breather ring. These observations were made during routine examination and were not the cause of a shutdown. Nevertheless, it must be recognized that operating time of pilot plants has been short compared with the operating lives commercial plants will have to survive for coal liquefaction to be economically feasible. It would be unwise to assume, at this time, that the reasonably satisfactory experience with the key pressure vessels is an indication there will be no problems with commercial-size pressure vessels for this application.

Since economics mitigates against numerous process streams when residence times are long, such as the 30 to 90 min required in reactor vessels, there is a strong motivation to use single streams with large vessels. Reactor vessels having diameters on the order of 4.6 to 7.6 m (15 to 25 ft) and heights ranging from 24 to 40 m (80 to 130 ft) with wall thicknesses of 25 to 40 cm (10 to 16 in.) are being considered [*3,4*]. Forced plant shutdown for extensive repair or replacement of one of these vessels would require months or years at immense cost. For example, it is estimated that unscheduled downtime of a petroleum refinery pressure vessel considerably smaller than those anticipated for commercial hydroliquefaction of coal can cost in excess of $50 000 *per hour* [*5*]. Clearly, reliability of the reactor vessel and high-pressure flash drum must be assured if coal hydroliquefaction is to become a significant liquid fuel alternative to petroleum. This means that every effort must be made to anticipate potential pressure vessel materials problems and to conduct well-conceived evaluations of each anticipated problem.

Applicability of Refinery Experience to Coal Liquefaction

In the absence of a long-term experience base in coal liquefaction processing, valuable guidance can be obtained from refinery processing experiences. For a perspective on the relevance of experience with materials in refinery processes, a brief description of some factors which parallel those in coal liquefaction processes is in order.

As shown in Fig. 2, the operating conditions for coal liquefaction reactor pressure vessels include temperatures ranging from 399 to 482°C (750 to 900°F) and pressures in the range of 6.9 to 28 MPa (1000 to 4000 psi). Table 1 reveals that several petroleum refining process pressure vessels approach these conditions, especially the hydrocrackers [*6*]. Many petroleum processing materials problems stem from sulfur in the crude, and it is anticipated that such problems would appear in coal processing. Sulfur concentrations in crude oils from major sources in the world are given in Table 2 [*7*]. Generally the sulfur content is less than one percent, but concentrations of sulfur in the range of 2 to about 5 weight percent exist. By comparison, run-of-the-mine Illinois No. 6 seam coal contains more than 10 weight percent sulfur. On the other hand, Pennsylvania anthracites generally have less than

TABLE 1—*Operating conditions for petroleum refining pressure vessels* [6].

	Temperature Range		Pressure Range	
Operation	°C	(°F)	MPa	(psi)
Catalytic cracking	449 to 565	(840 to 1050)	0.05 to 3.1	(7 to 450)
Hydrocracking	205 to 482	(400 to 900)	0.7 to 28	(100 to 4000)
Catalytic reforming	427 to 538	(800 to 1000)	0.35 to 5.2	(50 to 750)
Hydrogen treating	205 to 427	(400 to 800)	0.1 to 10	(15 to 1500)

TABLE 2—*Crude oil sulfur analyses* [7].

Source	Sulfur (wt %)
Africa: Algona, Egypt, Gabon, Libya, Nigeria	most 0 to 0.5
Middle East: Iran, Iraq, Kuwait, Saudi Arabia	most 1 to 3
Indonesia	most 0 to 0.5
Europe	most 0 to 1
Canada	most 0.1 to 0.55 some 3.38
Mexico	range 0.06 to 5.38 most 1.75
South America	most above 2
United States:	range 0.02 to 3.25
Colorado, Florida, Louisiana, Montana, Oklahoma, New Mexico, Utah, Pennsylvania	below 1
Texas	0.05 to 2.40
Wyoming	0.1 to 3.25

one weight percent sulfur [*8*]. In view of the sulfur concentrations cited above, coal liquefaction processing pressure vessels may be subjected to more exaggerated sulfur-based degradations than their counterparts in crude refining. Furthermore, it has been suggested that coal liquefaction process streams will contain NH_3, COS, and particulate matter, components not generally found in crude refining [*9*]. In summary, there is much similarity between coal liquefaction and refining processing conditions, but the differences should alert us that refinery experience may not be adequate for coal liquefaction materials considerations.

Potential Pressure Vessel Problems

Abrasion

The term abrasion encompasses gouging, grinding (high stress abrasion), erosion (low stress abrasion), erosion-corrosion, and erosion-cavitation. Virtually all of these forms of abrasion occur in the overall coal liquefaction process. However, no form of abrasion has been reported for the critical pressure vessels. If abrasion occurs in the reactor vessel or high-pressure flash drum it probably will be of the erosion or erosion-corrosion type because the fluid velocity in these components will be low [about 0.9 to 2.7 m/s (3 to 9 ft/s)]. Although the total solids loading of the slurry that enters the preheater prior to entering the reactor vessel is expected to be 20 to 35 weight percent, the solid content will be reduced substantially by dissolution of the coal in the preheater. In the reactor vessel, the solids loading will be about 10 to 15 weight percent and consist of coal minerals and some undissolved coal. Typically, the coal minerals will consist of inorganic sulfides and oxides such as Na_2O, K_2O, CaO, MgO, Fe_2O_3,TiO_2, P_2O_5, SiO_2, Al_2O_3, and SO_3 [*10*].

No basis exists for the prediction of long-term erosion or erosion-corrosion effects in the pressure vessels of concern. Thermocouple wells or other intrusion of the vessel wall where turbulent conditions could occur are the most susceptible sites for erosion in the pressure vessels. Several models or theories of erosion have been proposed [*11-19*] but none seems capable of predicting erosion behavior in the regime of particle types and sizes (1 to 75 μm) and fluid velocities (0.9 to 2.7 mps) pertinent to coal liquefaction pressure vessels. Furthermore, most experimental studies have employed fluid or particle velocities about 50 times greater than expected in the reactor vessel. Abrasion-resistant coatings, if they can be applied in the field, might be a realistic preventative for large pressure vessel walls.

Corrosion

Organic sulfur compounds are the primary cause of corrosion during sour crude processing. This form of corrosion occurs at temperatures generally in the range of 288 to 454°C (550 to 850°F) with the maximum rate of attack occurring near 370°C (700°F) [*5*]. Attack of steels in H_2S-H_2 mixtures occurs at temperatures above 370°C (700°F). Corrosion by organic sulfur compounds and by H_2S-H_2 is adequately resisted by austenitic stainless steels and a few other alloys with high chromium content. Consequently, petroleum processing pressure vessels are internally clad with stainless steel to prevent corrosion caused by the presence of sulfur. However, even these steels have been observed to corrode at a rate greater than 0.254 mm/year (10 mils/year) at 427°C (800°F) when the partial pressure of H_2S exceeds 0.07 MPa (10 psi) [*9*]. For the higher sulfur coals, the partial pressure of H_2S may be sufficiently high to cause excessive wastage of a stainless steel cladding or overlay in coal liquefaction pressure vessels operating at high total pressures.

Naphthenic acid is a potentially strong corrodent of stainless steels [*20*]. It is most active between 221 to 399°C (430 and 750°F), but it is not corrosive in the vapor state. Consequently, it is most troublesome if it can vaporize and concentrate by condensation. Therefore high pressures such as those existing during coal liquefaction reactor operation, might be expected to mitigate naphthenic corrosion. A particularly troublesome aspect of this form of corrosion is the fact that it does not form protective films because the corrosion products are soluble in hydrocarbons.

Chloride and polythionic acid stress corrosion cracking (SCC) of stainless steel cladding have occurred, as mentioned earlier, in coal liquefaction pilot plant pressure vessels. However, these two forms of SCC are most likely to occur during shutdown. Chloride SCC generally is most prevalent below the dewpoint of water, and polythionic acid SCC, an intergranular process requiring the steel to be sensitized, is formed by the interaction of sulfidic scale, moisture, and oxygen at ambient temperatures [*21*]. Interestingly, 347 stainless steel weld overlay metal has never exhibited polythionic acid SCC, even under conditions where the acid should have formed. This behavior has been attributed to the rapid cooling of the weld metal as it is laid down [*22*].

Conditions existing in a coal liquefaction reactor vessel present the potential (carbon potential and temperatures above 400°C) for dusting and carburization or both [*21*]. However, sulfur tends to reduce the tendency for these phenomena to occur.

In addition to the known or potential corrodents just cited, there are many other possible species in coal liquefaction pressure vessels that may cause corrosion. Several of these are listed in Table 3; there may be more. A major deterrent to predictability, or even laboratory evaluation, of corrosion in the coal liquefaction reactor vessel is the absence of chemical analyses under operating conditions of pressure and temperature.

Cladding Integrity

Since the main function of the stainless steel overlay or cladding (Figs. 2 and 3) is to protect the less corrosion resistant steel used for the structural

TABLE 3—*Possible reactor vessel chemical species.*

H_2	ammonium polysulfides
H_2S	ammonium thiocyanates
H_2O	aliphatic mercaptans
HCN	aromatic mercaptans
HCl	naphthenic mercaptans
NH_3	aliphatic sulfides
CH_4	aromatic sulfides
CO_2	cyclic sulfides
CO	aliphatic disulfides
COS	aromatic disulfides
S	polysulfides
Cl	naphthenic acid
NH_4Cl	polythionic acid
NH_4CN	sulfuric acid
NH_4HS	sulfurous acid
$(NH_4)_2S$	hydrocarbons
$(NH_4)_2CO_3$	coal minerals

shell of the reactor or the high-pressure flash drum, it is important to anticipate phenomena that might compromise the cladding integrity during a 20 to 30 year operating life. Several degrading phenomena are listed in Table 4. Most of them require no comment; however, the cladding adherence and hydrogen embrittlement require amplification. Hydrogen embrittlement of 347 stainless steel weld metal has been noted and attributed to embrittlement of the sigma phase transformed from delta-ferrite in the weld metal [*23,24*]. Cracking due to this embrittlement would only occur during cooldown because the brittleness is not significant at operating temperatures. Loss of adherence of 347 stainless steel weld overlay has been reported by Japanese investigators [*25,26*]. De-bonding occurred subsequent to air cooling from 24 h, high-pressure hydrogen exposures. Frequently, several hours elapsed after air cooling before de-bonding was revealed by ultrasonic nondestructive evaluation (NDE). Temperature-pressure exposure conditions that led to de-bonding are shown in Fig. 4. Perhaps other weld overlay alloys and improved overlay techniques should be considered.

TABLE 4—*Potential causes of cladding degradation.*

Microstructural or phase changes including sensitization
- embrittlement (for example, σ or χ phases)
- loss of corrosion resistance

Low-cycle fatigue cracking (thermally induced)
- fatigue cracks into base metal

Composition changes due to environment
- carburization and subsequent sensitization

Loss of adherence

Hydrogen embrittlement of the weld overlay
- during shutdown

Corrosion

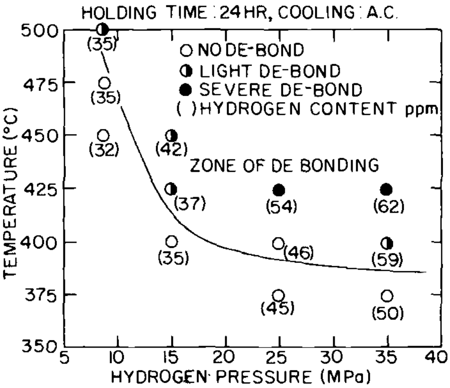

FIG. 4—*Pressure-temperature boundary for overlay de-bonding of 347 stainless steel* [25].

Pressure Vessel Shell Reliability

Since pressure vessels for hydrotreating and similar processes in the petroleum refining industry are designed to the ASME Boiler and Pressure Vessel (Unfired) Code (Section VIII, either Division 1 or Division 2), it is expected that this will be the applicable code for coal liquefaction pressure vessels. Division 2 is more stringent in its design and inspection requirements than Division 1, but Division 1 has a lower allowable stress. It has been suggested [*4*] that the criticality of these high-hydrogen pressure vessels would necessitate the use of Division 1 allowable stress while applying Division 2 requirements to fabrication for adequate reliability. However, the large size of these vessels imposes certain difficulties that must be overcome in order to meet the Code requirements. For example, heat treating thick sections (0.3 m) to achieve required properties at quarter thickness will demand water quenching rather than air cooling. Furthermore, it has been indicated [*27*] that the Charpy V-notch toughness requirement of Section VIII of the Code may not be adequate for 0.3 to 0.4 m (12 to 16 in.) thick sections which would allow critical crack sizes to be attained in materials that meet the 14 to 27 J (10 to 20 ft · lb) requirement at ambient temperature. Even when the as-constructed toughness requirements are met, time-dependent processes acting over the 20 to 30 year operating lifetime of one of these pressure vessels can degrade the material properties and seriously compromise the toughness and strength. Several potential degrading phenomena are listed in Table 5; there may be others.

TABLE 5—*Potential pressure vessel shell problems.*

Microstructure and phase stability
- strength
- toughness
- H_2 attack

Temper embrittlement (shutdown)
- toughness
- H_2 embrittlement

Hydrogen embrittlement (shutdown)
- sulfide stress cracking
- toughness
- slow crack growth

Environment-assisted crack growth
- toughness
- flow localization
- fatigue crack growth rate

Corrosion

Hydrogen attack
- strength and creep-resistance
- toughness

Field Fabrication and Heat Treatment

The complexity of field fabrication by welding and associated Code-required stress-relief treatment has already been stated succinctly [*4*]. Table 6 illustrates the incredible time it would take to fabricate large coal liquefaction pressure vessels and emphasizes the gains to be made if welding techniques such as narrow-gap, electroslag, or electron-beam can be developed. Additional gains would accrue if heat treatments or alloys can develop sufficient strength in small section thicknesses. For stress relief after welding 2¼Cr-1Mo (P5 grade) steel, the Code requires heating uniformly to a minimum of 677°C (1250°F), holding for 140 s per millimetre of thickness (1 h/in.) for the first 127 mm (5 in.) and 35 s per each additional millimetre (15 min/in.), then cooling uniformly. This procedure may have to be repeated several times during fabrication and erection of a large vessel [*4*]. Such treatments might reduce the strength of 2¼Cr-1Mo to below Code specifications.

Inspection

Field inspection of thick-wall vessels presents additional difficulties because the ASME Code demands pressure vessel shell welds to be radiographed. To accomplish this in the field would be a herculean task. An alternative would be to develop NDE technology to the level of sophistication needed to quantitatively characterize flaws in three dimensions. This would avoid the problems associated with the construction of a field-based linear accelerator for radiography. In fact, there are several aspects of pressure vessel reliability that could benefit greatly by advances in NDE capability. The potential exists for monitoring (continuously by permanently mounted ultrasonic transducers if necessary) changes in the structure of materials, integrity of cladding or overlay, residual stresses, porosity, and weldments. Development of noncontact transducers (EMAT) would alleviate the problems of NDE at hot walls. Clearly, there is much incentive for advancing the technology of NDE.

TABLE 6—*Pressure vessel weldments* [4].[a]

Welding Procedure	Vertical (Person-Hours)	Girth
Conventional submerged-arc	2880	8640 (63 000)[b]
Electroslag	864	. . .
Narrow gap	. . .	5760
Electron beam	117	240

[a] Based on 4.9 m (16 ft) inside diameter by 39.6 m (130 ft) high by 0.4 m (16 in.) thick wall or 119 m (390 ft) of vertical seams for plate-formed rings and 16 girth seams.

[b] Girth welds if sections in vertical position; manual submerged-arc welding.

Temper Embrittlement

Although not a problem at operating temperatures, temper embrittlement results in an upward shift in the ductile-brittle transition temperature and, sometimes, a reduction in the upper-shelf toughness of ferritic steels. Consequently, failures due to temper embrittlement may occur during shutdown. Mechanistically, this phenomenon is caused by segregation of certain impurity elements to grain boundaries when ferritic steel is held in, or slowly cooled through, a critical temperature range that encompasses the liquefaction reactor operating temperatures. It is an insidious problem in the sense that several years of operating time can pass before the degree of embrittlement becomes critical. The propensity of a steel to temper embrittlement can be minimized by controlling impurities and specific alloy elements that act synergistically with impurities to promote grain boundary segregation [*28*]. One of the purposes of the molybdenum in 2¼Cr-1Mo steel is to suppress temper embrittlement. Apparently molybdenum scavenges phosphorous and prevents it from segregating to grain boundaries, whereas chromium promotes the phosphorous segregation [*29*]. However, because of its greater stability, molybdenum-rich M_2C precipitates at the expense of chromium-rich M_7C_3. This change in carbide species removes molybdenum from solution where it scavenges phosphorous and increases the availability of chromium, thus altering the resistance of the alloy to temper embrittlement. It is evident that heat treatment and welding can alter the types of carbides present and hence the resistance to temper embrittlement.

Hydrogen Embrittlement

Hydrogen embrittlement is a well-documented phenomenon. It is characterized by slow strain-rate enhanced embrittlement that is most severe near ambient temperature. Sulfide stress cracking, a petroleum industry term, is a hydrogen embrittlement phenomenon in which the source of hydrogen is H_2S. Industry combats hydrogen embrittlement by controlling the hardness or strength level of the structural steels. Typically, hardness is kept below a Rockwell C of 20 to 22, and the yield strength is generally specified to be less than 552 MPa (80 000 psi). In this respect care must be taken with weldments where postweld cooling rates can induce locally hard regions with increased hydrogen embrittlement susceptibility. In terms of the pressure vessel, hydrogen embrittlement is a potential problem only when the vessel is cooled to ambient temperature. Whether or not the cladding is breached, hydrogen will diffuse into the structural steel at the pressure and temperature of operation. Solubility of hydrogen in ferritic steel decreases sharply with decreasing temperature and pressure (Fig. 5*a*). Depending on the cooling rate during shutdown relative to the diffusion rate of hydrogen out of the steel, more or less hydrogen will be effectively quenched into the steel at ambient temperature. Furthermore, fracture toughness decreases with increas-

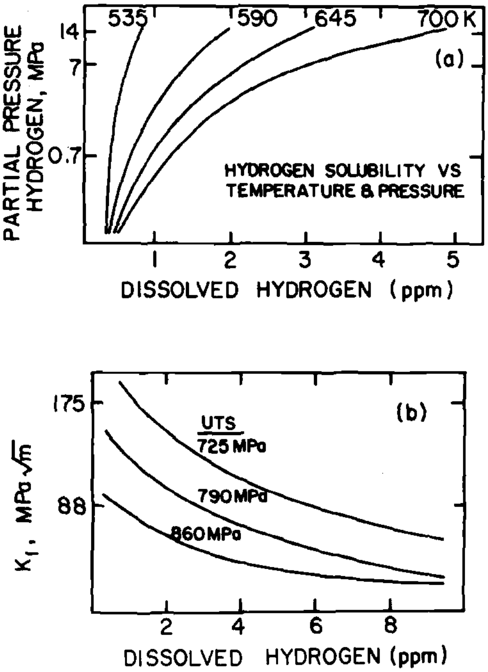

FIG. 5—*Dissolved hydrogen concentration* (a) *as a function of pressure and temperature (labeled on curves) and* (b) *its effect on fracture toughness of 2¼Cr-1Mo steel of various tensile strengths (labeled on curves)* [30].

ing concentration of dissolved hydrogen (Fig. 5*b*) [*30*]. To avoid delayed cracking, the cooling rate should be controlled during shutdown to enable hydrogen outgassing to occur before ambient temperature is reached. Thick-section pressure vessels, especially with a sound stainless steel cladding (lower hydrogen diffusivity), will require extended cooling times to avoid "quenching in" more hydrogen than is compatible with the fracture toughness required by design. Such procedures are costly in terms of lost productivity. A better alternative would be an improved low-cost steel. The cost benefits to be derived from the development of a low-cost steel with higher hardness (R"C" > 25 to 30) and higher strength [yield strength 862 MPa (125 ksi)], but sufficient toughness to tolerate the presence of residual hydrogen would be enormous.

Environmental-assisted crack growth, in fracture mechanics terminology, is the reduction of the critical stress intensity (K_{IC}) by the environment. Although many gases or liquids are possible crack growth assisters, the effective component is frequently hydrogen. The phenomenon of hydrogen-assisted crack growth or external hydrogen embrittlement is most commonly observed at near-ambient temperatures, but it can appear at elevated temperatures. It is important to design hydrogen-containing pressure vessels so that the stress intensity does not exceed the critical stress intensity for the operating hydrogen service conditions. However, many factors involved are yet to be defined, quantified, or both.

Hydrogen Attack (HA)

This may be the most obvious potential materials problem associated with hydroliquefaction processes. Petroleum refinery engineers, who are keenly aware of HA, circumvent the degradation it causes by employing Nelson curves [*31*] for materials selection or for defining operating limits. These experience-based curves (Fig. 6) have served a very useful function in the petroleum and petrochemical industries. However, they entail several uncertainties:

1. The position of the curves changes with experience, always downward. For example, recent Russian work [*32,33*] lowered the Nelson curve for plain carbon steel. While the change was only about 25°C (45°F) on the temperature scale, the corresponding pressure decreased by about 5.5 MPa (800 psi) (Fig. 7).
2. They do not represent weld metal or heat-affected zone (HAZ) behavior. It has been shown [*34*] that 0.5Mo steels (with carbon greater than 0.20 percent) experienced HA in the HAZ at temperatures about 39°C (70°F) below the appropriate Nelson curve.
3. Potential effects of other gaseous components are not identifiable or accountable from the Nelson curves. For example, no HA of 1020 steel was found at temperatures 259°C (460°F) above and pressures of 2.1 MPa (300 psi) above the Nelson curve when 10 percent H_2S was added to H_2 [*35*]. This is a positive observation but not well understood. Other species might have negative effects.
4. Methane blisters have been noted by Merrick and McGuire [*36*] at conditions well below the Nelson curves. The phenomenon they described is close enough to HA that the adequacy of the curves is questionable.
5. Nelson curves are based on experience with steels used in accordance with earlier design codes that specified annealed material. The curves may not represent the behavior of quenched, or normalized, and tempered steels selected for higher stress applications; thus, they may not be sufficiently conservative for ASME Section VIII, Division 2 structures. Moreover, there are no data points for 2¼Cr-1Mo steel in any heat-treated condition.
6. Effects of impurities, inclusions, and manufacturing processes (for example, cold work) are not accounted for or predictable from the curves.
7. Conditions under which HA will occur in new steels cannot be predicted from the Nelson curves.

All these points, and possibly others, indicate that a mechanistic understanding of HA is needed. Otherwise hydrogen-service designers will remain

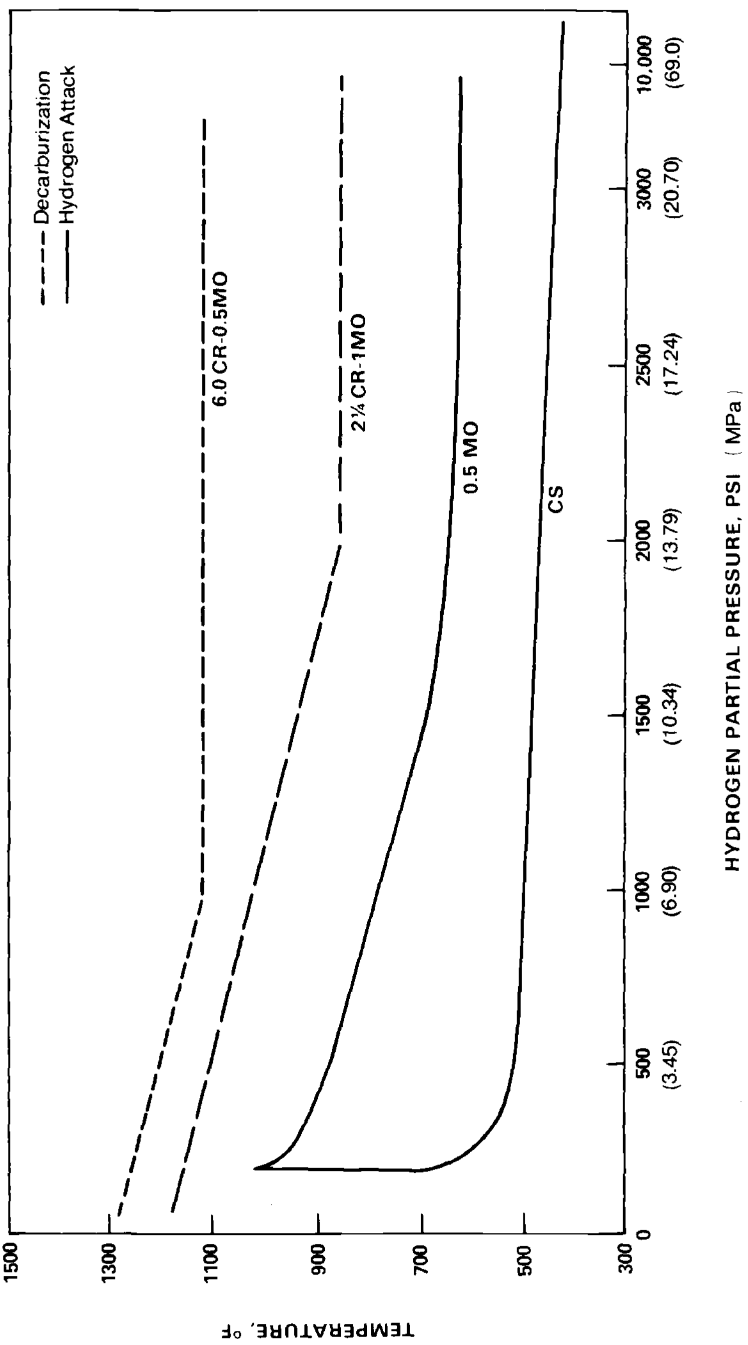

FIG. 6—*Partial set of Nelson curves.*

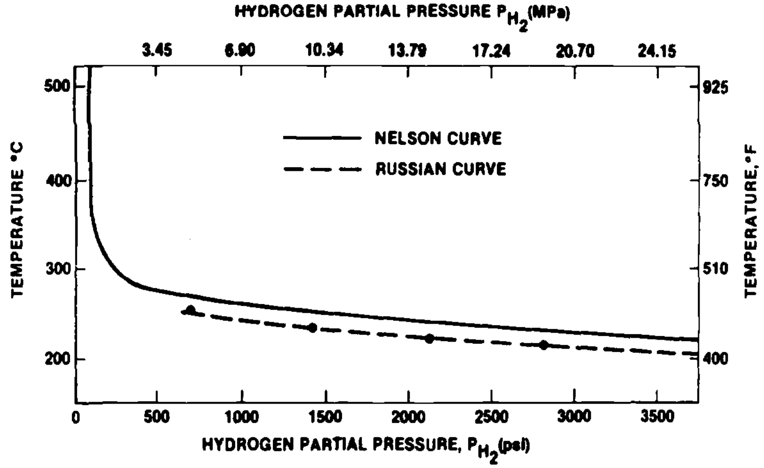

FIG. 7—*Russian modification of Nelson curve* [33].

committed to older types of steel and, by implication, to overdesign in terms of materials, dimensions, or both. Or, they will be forced to limit process conditions. Such design constraints increase the initial cost of pressure vessels. If they choose not to overdesign, the reliability of the vessel is jeopardized. Recent progress to develop mechanistic models of HA is encouraging [*33,37-41*].

Acknowledgments

The author acknowledges with gratitude the continued support of the U.S. Department of Energy, Assistant Secretary for Fossil Energy, Office of Advanced Research and Technology, WPAS-AA-K-10-10, and the Division of Energy Research, Office of Basic Energy Sciences, WPAS-KC-02-01.

References

[*1*] Scott, T. E. in *Fourth Annual Conference on Materials for Coal Conversion and Utilization*, U.S. Department of Energy Report CONF 791014, 9-11 Oct. 1979, pp. K1-K59.

[*2*] PAMCO, "Solvent Refined Coal (SRC) Process," Quarterly Technical Progress Report, 1 April-30 June 1978, Report No. FE/496-157, U.S. Department of Energy, May 1979.

[*3*] Lochmann, W. in *Fourth Annual Conference on Materials for Coal Conversion and Utilization*, U.S. Department of Energy Report CONF 791014, 9-11 Oct. 1979, pp. 1-31.

[*4*] Dempsey, P. E. and Tunnell, G., "The Challenges of Gigantic Pressure Vessels," paper presented to the American Welding Society at Colorado School of Mines, Stearns-Roger Engineering Corporation, 27 April 1979.

[*5*] Bauman, T. C., *Journal of Metals*, Vol. 12, Aug. 1977, pp. 8-11.

[*6*] *Petroleum Processing Handbook*, W. F. Bland and R. L. Davidson, Eds., McGraw-Hill, New York, 1967.

[*7*] Thompson, C. J., Shelton, E. M., and Coleman, H. J., *Hydrocarbon Processing*, Vol. 55, Feb. 1976, pp. 73-76.

[*8*] Nowacki, P., *Coal Liquefaction Processes*, Noyes Data Corporation, Chemical Technology Review No. 131, Park Ridge, N.J., 1979.
[*9*] Ciuffreda, A. R. and Krystow, P. E. in *Materials Problems and Research Opportunities in Coal Conversion—Vol. II*, Report No. CR-402, based on an NSF-OCR sponsored workshop coordinated by R. Staehle, Ohio State University, Columbus, Ohio, April 1974, pp. 469-479.
[*10*] Lewis, H. E., Weber, W. H., Usnick, G. B., Hollenack, W. R., and Hooks, H. W., "Solvent Refined Coal Pilot Plant at Wilsonville, Alabama," Annual Report for 1977, Report No. FE-2270-31, prepared for U.S. Department of Energy by Catalytic Inc., Wilsonville, Ala., May 1978.
[*11*] Finnie, I., Wolak, J., and Kabil, Y., *Journal of Metals*, Vol. 2, 1967, p. 682.
[*12*] Finnie, I., *Wear*, Vol. 3, 1960, p. 87.
[*13*] Finnie, I., *Wear*, Vol. 19, 1972, p. 81.
[*14*] Finnie, I. and McFadden, D. H., *Wear*, Vol. 48, 1978, p. 181.
[*15*] Bitter, J. G. A., *Wear*, Vol. 6, 1963, pp. 5, 169.
[*16*] Hutchings, I. M., Winter, R. E., and Field, J. E., *Proceedings of the Royal Society*, London, Vol. A348, 1976, p. 379.
[*17*] Winter, R. E. and Hutchings, I. M., *Wear*, Vol. 29, 1975, p. 181.
[*18*] Winter, R. E. and Hutchings, I. M., *Wear*, Vol. 34, 1975, p. 141.
[*19*] Mamoun, M. M., "Materials Science Division Coal Technology," Quarterly Reports for Jan.-March 1975 and April-June 1975; Argonne National Laboratory Reports ANL-75-XX-2 and ANL-75-XX-3, Argonne, Ill.
[*20*] Gutzeit, J., *Materials Performance*, Oct. 1977, p. 24.
[*21*] Wolfe, L. H., *Materials Performance*, April 1978, p. 38.
[*22*] Lendvai-Lintner, E., *Materials Performance*, March 1979, p. 9.
[*23*] Johnson, E. W. and Hudak, S. J., "WRC Bulletin No. 240," Aug. 1978.
[*24*] Watanabe, J., Ohnishi, K., Murai, M., and Chiba, R., *NACE Corrosion-77*, Paper No. 104, 1977.
[*25*] Watanabe, J., private communication, June 1979.
[*26*] Ikeuchi, M., Nonaka, K., and Maruyama, T., *Tetsu-To-Hagane*, Vol. 62, 1976, p. 5232.
[*27*] Canonico, D. A., Robinson, G. C., and Martin, W. R. "Pressure Vessels for Coal Conversion Systems," Report No. ORNL/TM-5685, Oak Ridge National Laboratory, Oak Ridge, Tenn., Sept. 1978.
[*28*] Murakami, Y., Watanabe, J., and Mima, S., "Heavy Section Cr-Mo Steel for Hydrogenation Service," paper presented at the 17th C.I.M. Annual Conference of Metallurgists, Montreal, Canada, 27-31 August 1978, The Japan Steel Works, Ltd., Report No. PV-78-8-234.
[*29*] Yu, J. and McMahon, C. J., *Metallurgical Transactions*, Vol. 11A, 1980, pp. 277-289.
[*30*] Thomas, J. W. and Klechka, E. W. in *Effect of Hydrogen on Behavior of Materials*, A. W. Thompson and I. M. Bernstein, Eds., Metallurgical Society of the American Institute of Mechanical Engineers, 1976, p. 542.
[*31*] Anonymous, "Steels for Hydrogen Service at Elevated Temperatures and Pressures in Petroleum Refineries and Petrochemical Plants," American Petroleum Institute Publication No. 941, Second Ed., June 1977.
[*32*] Arkakov, Y. I., Grebashkova, I. D., and Dubovski, V. V., *Zashchita Metallov*, Vol. 5, No. 1, 1969, p. 70.
[*33*] Odette, G. R., Vagarali, S., and Oldfield, W., "Analysis of Hydrogen Attack on Pressure Vessel Steels," Quarterly Progress Report No. 3 to DOE-FE, 13 Jan.-1 May 1979, University of California, Santa Barbara, Calif., 15 May 1979.
[*34*] Bailey, N., *Welding Institute Research Bulletin No. 18*, 1977, pp. 2, 33.
[*35*] Eliezer, D. and Nelson, H. G., *Corrosion*, Vol. 35, No. 1, 1979, p. 17.
[*36*] Merrick, R. D. and McGuire, C. J., "Methane Blistering of Equipment in High Temperature Hydrogen Service," in *NACE Corrosion-79*, Paper No. 30.
[*37*] Shih, H. M. and Johnson, H. H., *Scripta Metallurgica*, Vol. 11, 1977, p. 151.
[*38*] Raj, R., Shih, H. M., and Johnson, H. H., *Scripta Metallurgica*, Vol. 11, 1977, p. 839.
[*39*] Saques, A., Okray-Hall, B., and Wiedersich, H., *Scripta Metallurgica*, Vol. 12, 1978, p. 319.
[*40*] Shewmon, P., *Metallurgical Transactions*, Vol. 74A, 1976, p. 279.
[*41*] Sundararajan, G. and Shewmon, P., *Metallurgical Transactions*, Vol. 11A, 1980, p. 509.

DISCUSSION

P. E. Dempsey[1] (*written discussion*)—Professor Scott referenced work done by the Japanese P.V. Committee, wherein stainless steel overlay on 2¼Cr-1Mo backing had delaminated in laboratory tests. These tests were performed by heating and holding a sample in hydrogen at very high pressure and then removing and air cooling. This is intended to call attention to the fact that such a test does not even approach actual pressure vessel performance for the following reasons:

(*1*) The sample is subject to hydrogen saturation from all sides. It can enter from the carbon steel side. There is no escape route. In service, the hydrogen must pass through the overlay at a mobility rate much slower than its escape rate through the carbon steel. Therefore the concentration of hydrogen at the interface is an order of magnitude lower than the Japanese test indicates.

(*2*) The rate of cooling in the coal liquefaction heavy-wall pressure vessels is nowhere near the cooling rate that was used. Thus the hydrogen would have more time to escape in real service cooldown.

This discussion is very important to the technology because it borders on a proposed test which this author has planned as chairman of a performance task group on the subject. It is the object of the proposed work to test the reported conditions under conditions that are much more closely related to service conditions.

T. E. Scott (*author's closure*)—Mr. Dempsey's comments are correct. The writer was only pointing out, however, that delamination of stainless steel overlay from the 2¼Cr-1Mo backing was a reality under appropriate conditions. Moreover, any voids at the backing/overlay interface would trap hydrogen and negate his relative diffusion rate argument. Also, the cooler outer zones of the 2¼Cr-1Mo backing would reduce the hydrogen escape rate. Finally, large blisters or delaminations of stainless steel overlay in an operating refinery pressure vessel were reported at this symposium. Consequently, although Mr. Dempsey's criticisms are valid, delamination has occurred under service conditions.

---

[1] Stearns-Roger Engineering Corporation, Denver, Colo. 80217.

H. C. Lueling,[1] *Karl Achtelik,*[2] *and J. M. Motz*[3]

Internal Properties of 2¼Cr-1Mo Cast Steel for Heavy Castings

REFERENCE: Lueling, H. C., Achtelik, Karl, and Motz, J. M., "**Internal Properties of 2¼Cr-1Mo Cast Steel for Heavy Castings,**" *Application of 2¼Cr-1Mo Steel for Thick-Wall Pressure Vessels, ASTM STP 755,* G. S. Sangdahl and M. Semchyshen, Eds., 1982, pp. 26-45.

ABSTRACT: This paper describes research on 2¼Cr-1Mo steel using a heavy test block [weight approximately 4540 kg (10 000 lb)] having wall thicknesses of 15, 30, and 50 cm (6, 12, and 20 in.) (solidification moduli of 5.5, 9.5, and 13.1 cm, respectively).

The relation of solidification and secondary structures (surface, transition, and center area) versus mechanical properties after normalizing and tempering as well as in the quenched and tempered condition were studied. ISO-V-notch energy between −60 and +100°C (−76° and 212°F) at surface and center areas of the three wall thicknesses was determined.

Results of fracture toughness K_{1c} (ASTM E 399) and crack-opening displacement (COD) (ASK-AN-220, 1976) are given. Furthermore, results of fatigue crack growth tests using specimens from the 30-cm (12-in.) casting in the oil-quenched and tempered condition are given.

KEY WORDS: 2¼Cr-1Mo cast steel, heat treatment, microstructure, mechanical properties, fracture toughness, fatigue, fatigue crack growth rate

This paper deals with the application of 2¼Cr-1Mo steel castings with heavy cross sections. The applicable documents in the United States are ASTM Specifications for Martensitic Stainless Steel and Alloy Steel Castings for Pressure-Containing Parts Suitable for High-Temperature Service (A 217-80, Grade WC9), for Heavy-Walled Carbon and Low-Alloy Steel Castings for Steam Turbines (A 356-77, Grade 10), and for Ferritic and Martensitic Steel Castings for Pressure-Containing and Other Applications for Low-Temperature Service (A 757-79, Grades D1Q1, D1Q2, and D1Q3). Table 1 shows chemical composition, tolerable residual elements, and tensile requirements. For the impact properties some regulations are given in the ASME Boiler and Pressure Vessel Code in Section I (Power Boilers), Section IV (Heating

---

[1] Dipl.-Ing., George Fischer Limited, Schaffhausen, Switzerland.
[2] Dipl.-Ing., Stahlwerke Bochum AG, Bochum, Germany.
[3] Dr.-Ing., Thyssen Giesserei AG, Mulheim/Ruhr, Germany.

TABLE 1—*ANSI/ASTM standard specifications for 2¼Cr-1Mo cast steels.*

ANSI/ASTM Specification	Chemical Requirements, maximum %								Residual Elements, maximum %				
	C	Mn	P	S	Si	Ni	Cr	Mo	Cu	Ni	W	V	Total Content, maximum
A 217 Grade WC9	0.18	0.40 0.70	0.04	0.045	0.60	...	2.00 2.75	0.90 1.20	0.50	0.50	0.10	...	1.00
A 356 Grade 10	0.20	0.80	0.035	0.030	0.60	...	2.00 2.75	0.90 1.20	...	...	...	...	...
A 757 Grade D1Q1	0.20	0.40 0.80	0.025	0.025	0.60	...	2.0 2.75	0.90 1.20	0.50	0.50	0.10	0.03	1.00

ANSI/ASTM Specification	Tensile Requirements, minimum values				Impact ISO-V-Notch Energy Value, J
	Tensile MPa	Yield MPa	Elongation (50 mm), %	Reduction of Area, %	
A 217 Grade WC9	485 to 655	275	20	35	see ASME Boiler and Pressure Vessel Code, Section IV
A 356 Grade 10	585	380	20.0	35	see ASME Boiler and Pressure Vessel Code, Sections I and VIII
A 757 Grade D1Q1	585 to 795	380	20	35	subject to agreement between manufacturer and purchaser
D1Q2	655 to 860	515	18	35	
D1Q3	725 to 930	585	15	30	

Boilers), and Section VIII (Pressure Vessels). Further requirements are subject to agreement between manufacturer and purchaser.

There are indications that the application of this alloy has been limited by the unavailability of adequate data. Specifically there was a lack of data describing the internal properties of heavy castings with wall thicknesses in excess of 25.4 cm (10 in.).

Some data on forged or rolled steel types with wall thicknesses exceeding 100 mm are available. Kalwa and Schnabel [*1*][4] give some properties of pipe parts up to a section size of 150 mm (0.12 percent carbon). After heat treatment at 960°C, air cooling, and tempering at 760°C, the highest toughness values could be observed within wall thicknesses of less than 100 mm. In greater sections increasing amounts of ferrite had a harmful influence on the toughness properties. Marandet and Sanz [*2*] investigated steel plates (0.11 to 0.14 percent carbon) with wall thicknesses of 110 and 170 mm. The standard heat treatment consisted of an annealing at 925°C with a subsequent water quench. The tempering treatment was varied between 600 and 700°C in steps of 20 degrees centigrade. The results of tensile tests, V-notched bar impact tests, and compact tensile tests (fracture toughness) were discussed. Increasing tempering temperature up to 640°C raised the fracture toughness of the steel. Tempering at higher temperatures had an insignificant influence on the results. A close relationship could be found between the temperatures of the 28-J impact values and the 3160 N $\text{mm}^{-3/2}$ values (100 $\text{MPa} \cdot \text{m}^{0.5}$) for K_{Ic}.

When dealing with 2¼Cr-1Mo cast steel, three investigations should be considered. Haines [*3*] approved this steel with about 0.18 percent carbon for use as castings within Section III (Nuclear Vessels) of the ASME Boiler and Pressure Vessel Code. He used cast plates with 200 and 560 mm wall thicknesses and after two different heat treatments, normalizing at 930°C or water quenching from 930°C and subsequent tempering at 700°C, tensile and Charpy-V-notch specimens were taken out of the different zones of the plate castings and tested. He recommended a vacuum-degassing treatment of the melt, and concluded that the cast steel then met the requirements of the Code.

A further investigation of fracture toughness of cast 2¼Cr-1Mo steel was performed by Bamford [*4*] with 50- and 100-mm compact tension test specimens. Achtelik and Motz [*5*] summarized the internal properties of different cast steel grades, including 2¼Cr-1Mo steel in the quenched and tempered condition of wall thicknesses above 100 mm (4 in.).

History of the Investigation

Research started in 1972 with the investigation of the internal properties of quenched and tempered cast test blocks of great section thicknesses. This co-

---

[4] The italic numbers in brackets refer to the list of references appended to this paper.

operative project of four German and two Swiss steel foundries was coordinated by the German Foundrymen Association (VDG = Verein Deutscher Giessereifachleute, Düsseldorf). Ten different steel grades commonly used in Europe differently heat treated were investigated. The work was finished in 1977 with the completion of the SEW Standard Specification "Stahl-Eisen-Werkstoffblatt No. 515" designated "Quenched and Tempered Cast Steel for Castings of Wall Thicknesses above 100 mm."

The procedure applied for the production of the test blocks, the heat treatment, the sampling of the test bars, and the testing methods were preserved for the present work. Additionally, core samples were also taken out of actual heavy-walled production castings and tested in order to complete the information about the properties.

Experimental Conditions

Production of the Test Block

The steel was melted in a basic-lined arc furnace. After meltdown, the minimum carbon content was kept higher than 0.65 percent in order to guarantee a sufficiently intense boiling period. After the refining period the deoxidation was performed by the addition of calcium-silicon and aluminum. Depending on the nitrogen content of the melt, more or less aluminum was added. The specified composition and the results of the chemical analysis from the test block itself are given in Table 2.

With a pouring temperature of about 1550°C the steel was cast into a resin-bonded sand mold. The dimensions of the test block, weighing approximately 2800 kg, are given in Fig. 1. The block consists of three steps, with 150, 300, and 500 mm cross sections. The dimensions of the sections have

TABLE 2—*Specification and chemical composition of the casting.*

	Chemical Composition							
	C, %	Si, %	Mn, %	P, %	S, %	Cr, %	Mo, %	Ni, %
Minimum	0.15	0.30	0.60	...	...	2.00	0.90	...
Maximum	0.22	0.50	1.00	0.025	0.015	2.50	1.10	0.4
Heat 6165-4	0.18	0.48	0.63	0.004	0.007	2.25	1.02	0.13

	Residual Elements						
	Cu, %	Sn, %	As, %	Al, %	N, %	Sb, %	V, %
Maximum	0.25	0.025	0.025	...	...	...	...
Heat 6165-4	0.12	0.025	0.026	0.033	...	0.004	0.01

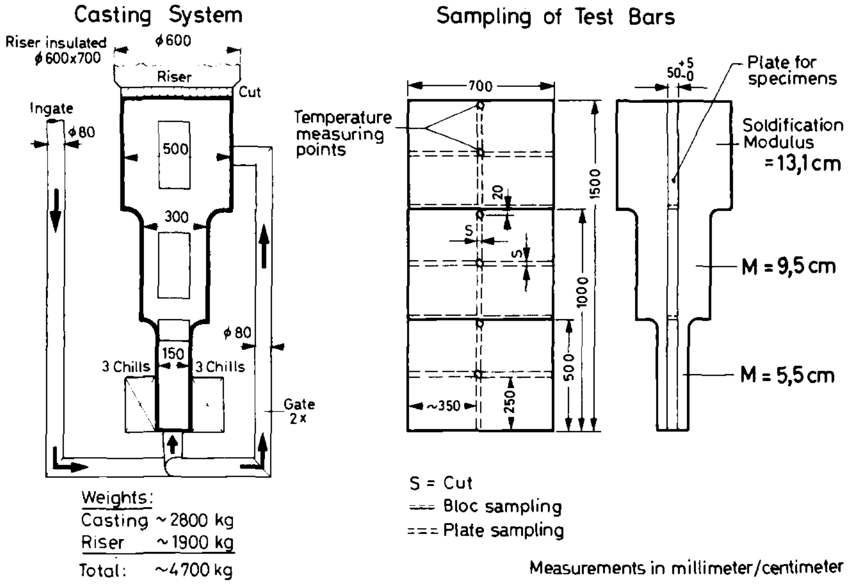

FIG. 1—*Test block.*

been chosen to cover those solidification moduli that are encountered in all heavy-walled production castings. The overall weight, including the insulated riser, is nearly 5000 kg. The first heat treatment of the test block was an annealing treatment at 920°C with subsequent furnace cooling. After that treatment the riser was burned off.

By a carefully performed nondestructive examination, such as ultrasonic and radiographic testing, the integrity of the three test block thicknesses was proved to be satisfactory.

Heat Treatment and Sampling

The three sections of the block were cut off. Each part was annealed at 920°C for 12 h and oil quenched. This hardening procedure was registered by introduced thermocouples. One was inserted into the center, the other was placed 20 mm deep under the surface near the edge. In this manner the cooling rate range could be determined for each section.

Subsequently the wall sections were tempered at 650°C and furnace cooled. A center plate taken out of the three sections (Fig. 1) was cut off and divided into two parts. One half was further divided. One of these parts was again tempered for 4 h at 680°C and furnace cooled (investigation of retention of hardness and improvement of elongation and impact ISO-V at 20°C by 30°C higher tempering). The second half-part of the center plate was used for air cooling and tempering. Because of the reduced mass compared with the original test block dimensions, the cooling rate was simulated. The test specimens were again annealed at 920°C for 4 h and cooled under controlled conditions in a special heating-cooling equipment. Between the range of 800 and 200°C the cooling rates were kept constant:

section thickness, mm	150	300	500
simulated cooling rate in air, °C/min	4.2	2.4	1.8

The plates were then tempered for 4 h at 650°C.

After normalizing, the different types of test bars were taken out of the plates (Fig. 2). Three different zones were distinguished. From the surface and from the center zone tensile and ISO-V-notch test specimens were machined. Additionally, the center was the position for rotating-bending fatigue test bars. From the transition zone of the 300 and 500 mm sections only tensile test bars were machined. In this investigation the definition of the transition zone did not agree with the *T*/4 regulation that is given as an ASME recommendation. But the position at face-sides of plate was fixed in agreement with the determination of the macrostructure at the cut surface. Additionally, samples for a metallographic inspection were taken from all positions.

The remaining pieces of the 300-mm-section compact tension test bars (CT2, CT3, and CT4) were taken in such a manner that the position in the test block was near the middle, close to the center plate from which the tensile and impact test specimens had been cut off.

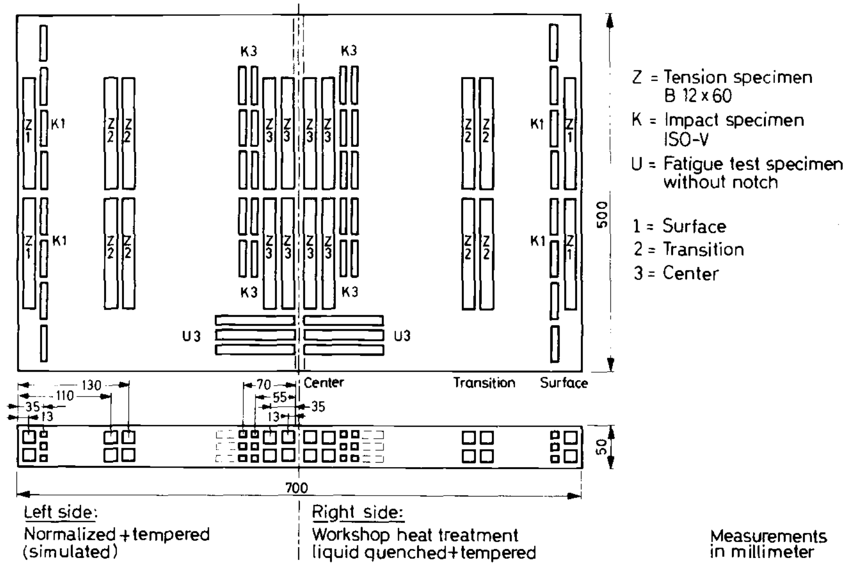

FIG. 2—*Order of removal of test specimens.*

Results

Microstructure

After the heat treatments the microstructures were determined in the surface region and in the center of the different section plates. Only ferrite and bainite could be observed (Table 3). There was a close relationship between the cooling conditions and the microstructure (Fig. 3).

After oil quenching the 150- and 300-mm sections the lower-bainite was the predominant matrix. With lower cooling velocity this structure was more and more replaced by upper-bainite and ferrite. The transformation behavior of the cast 2¼Cr-1Mo steel itself is one subject of a paper by Trautwein et al.[5] Microsegregation could be observed especially in the center of the plates after the normal nital etching procedure (Fig. 4).

Tensile Properties

After heat treatment the tensile properties were determined in the different zones of the three sections. Usually four test specimens (10 mm diameter) had been pulled for one value. The average results are given in Fig. 5.

Close relationships could be observed between the microstructure and the tensile properties. If lower-bainite was the structure before tempering, a tensile strength of approximately 800 N/mm^2 and a yield strength of approximately 600 N/mm^2 could be measured. This was, for instance, a typical result after oil quenching and 650°C tempering treatment in the smaller sec-

TABLE 3—*Survey on microstructure in walls of 150, 300, and 500 mm after heat treatment (secondary structures) (2¼Cr-1Mo cast steel, Heat 6165-4).*

Liquid Quenched and Tempered				
150 mm	300 mm		500 mm	
Center	Surface	Center	Surface	Center
Bainite	Bainite	Bainite 10% Ferrite	Bainite 10% Ferrite	Bainite 20% Ferrite
Normalized and Tempered				
150 mm	300 mm		500 mm	
Center	Surface	Center	Surface	Center
Bainite 20% Ferrite	...	Bainite 40% Ferrite	...	Bainite 40% Ferrite

---

[5] This publication, pp. 189-207.

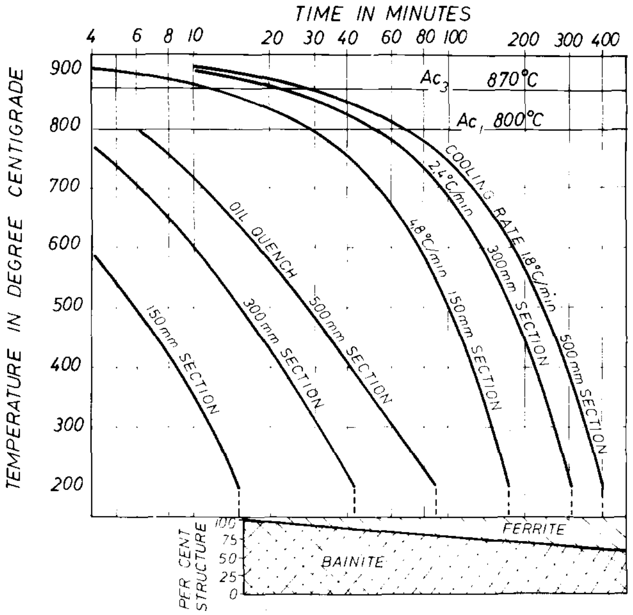

FIG. 3—*Cooling rates of the section centers and microstructure.*

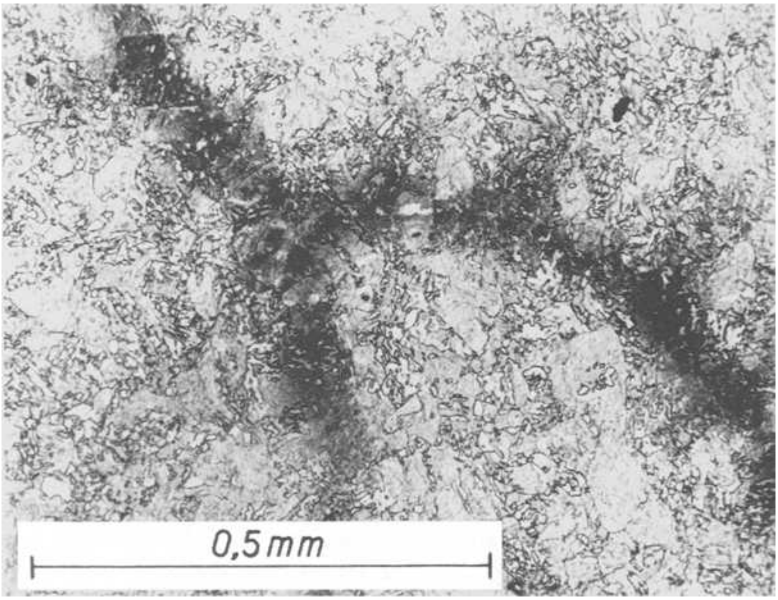

FIG. 4—*Microsegregation in the center of the 150-mm section (nital etched).*

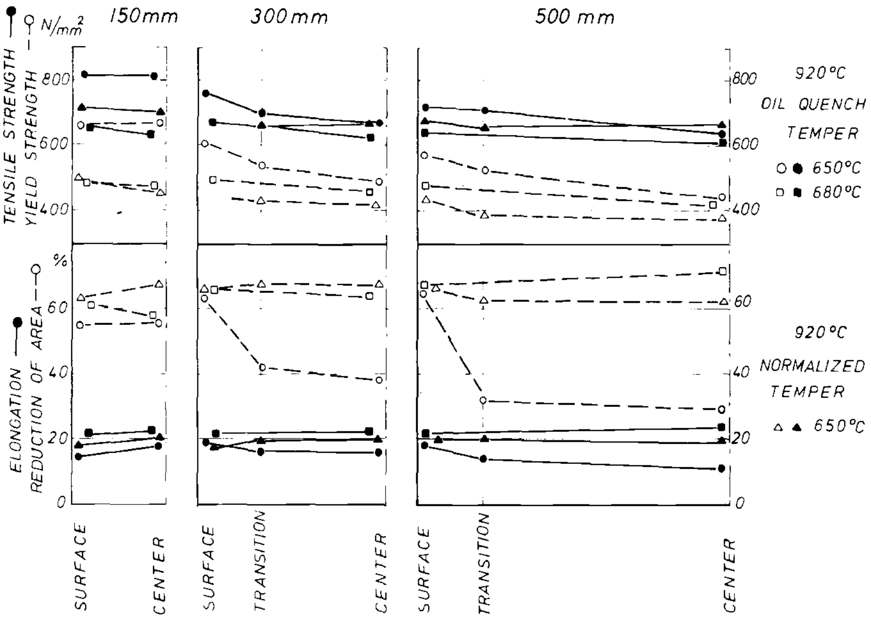

FIG. 5—*Tensile properties of 2¼Cr-1Mo cast steel.*

tions. Upper-bainite with increasing amounts of ferrite led to lower strength values.

The higher tempering temperature of 680°C lowers the tensile strength and causes an equalizing of all tensile and yield values. This effect was nearly independent from the quenched structure before the tempering treatment. The results were similar to those obtained by normalizing and tempering treatment at 650°C.

The data summary (Fig. 5) shows that rather uniform high-strength values are obtained independently of section size. The tensile strength value decreased only slightly to the center but less than the yield strength. Each section size when properly processed will exhibit a specific microstructure.

In the case of medium or lower strength, nearly no influence of the position and the section thickness on the ductility could be measured. But the elongation and particularly the reduction of area had a marked decrease from the surface to the center after oil quenching and 650°C tempering. The reason seemed to be in the inhomogeneity of the structure in the specimens. Dendrites with lower alloy content transformed presumably into softer upper-bainite and ferrite. The segregated interdendritic zones formed a lower-bainitic matrix of a higher hardness. During the tensile tests the elongation started in the dendritic zones. In these micro-areas the strain was hindered by the harder regions. The result was a nonuniform distribution of strain that especially limited the reduction of areas. After equalizing the properties either by the higher tempering temperature or by the normalizing treatment this effect was eliminated and constant ductility values could be observed.

The improvement of the 30°C higher tempering on the elongation are evident. The differences are given in Table 4. Particularly in the center of the greater sections the ductility values increased approximately 40 to 110 percent.

Impact Properties

The results of the impact investigation on ISO-V-notched test bars are summarized in Fig. 6. The range covers the test temperatures from −60 to +60°C. Figure 6 is split into three diagrams each for the different section thicknesses. Within each diagram are distinguished the surface area (open signs) and the center (full signs) and each different heat treatment (different signs).

TABLE 4—*Improvement of elongation and impact ISO-V at 20°C by 30°C higher tempering (2¼Cr-1Mo cast steel: Heat 6165-4; cross sections of 150, 300, and 500 mm).*

	Oil Quenching 150 mm Wall Thickness			
Tempering Temperature, °C	Surface		Center	
	Elongation %	ISO-V at 20°C	Elongation %	ISO-V at 20°C
650	15	44	17	37
680	21	65	22.5	39
Δ30	6	19	5.5	2
Improvement %	40	43	32	5

	Oil Quenching 300 mm Wall Thickness			
Tempering Temperature, °C	Surface		Center	
	Elongation %	ISO-V at 20°C	Elongation %	ISO-V at 20°C
650	19	47	16	99
680	22	137	22	128
Δ30	3	90	6	29
Improvement %	16	190	37	29

	Oil Quenching 500 mm Wall Thickness			
Tempering Temperature, °C	Surface		Center	
	Elongation %	ISO-V at 20°C	Elongation %	ISO-V at 20°C
650	18	61	11	76
680	21.5	125	23.5	105
Δ30	3.5	64	12.5	29
Improvement %	20	105	113	38

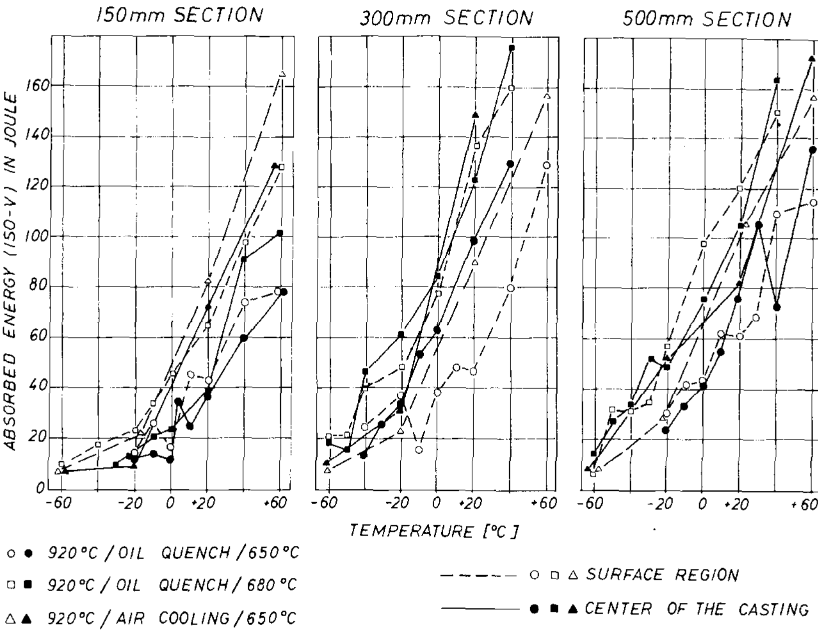

FIG. 6—*Impact properties of 2¼Cr-1Mo cast steel with large section thickness.*

The lowest impact-temperature curves were obtained from the 150-mm section and the surface area of the 300-mm plate after the oil-quench and tempering treatment at 650°C. There is a good correlation with the high tensile properties, as mentioned before. The tempering at 680°C was followed by a clear increase of the absorbed energy at all temperatures (Table 4). When the values between surface and center were compared, no significant differences could be observed if the level of the tensile strength and the microstructure were equal and the center region was correctly fed. Consequently the opinion is not valid that the impact properties in the center of heavy castings are generally lower than those of the surface region.

The normalizing treatment caused the steepest impact-temperature curves. This means that at room temperature high-energy values could be obtained, but with decreasing temperatures the loss of toughness is greater. This fact can easily be explained by comparing the transition temperature curves, where it is defined that the transition is equal to an absorbed energy level of 27 J. Table 5 presents this transition temperature for all conditions. The results of the oil-quenched and at 650°C tempered 300- and 500-mm sections are of special interest because the tensile test results showed a sharp drop of the reduction of area and the elongation (Fig. 6) with increasing distance from the surface. The comparable impact-temperature curves give no indication of any embrittlement. Indeed it can be supposed that the interdendritic hardened zones of the microsegregation can limit the tensile ductility

TABLE 5—*Impact transition temperatures of 2¼Cr-1Mo cast steel.*[a]

	Heat Treatment at 920°C					
	Oil Quench				Simulated Air Cooling	
	Tempering at				Tempering at 650°C	
	650°C		680°C			
Section, mm	Surface, °C	Center, °C	Surface, °C	Center, °C	Surface, °C	Center, °C
150	+4	+4	−15	+4	−13	+2
300	−5	−32	−47	−43	−18	−20
500	−25	−15	−53	−50	−25	−40

[a] The transition temperature is equal to ISO-V = 27 J.

values. But during impact load the tough and softer dendrites may act as crack arrestors. In steel castings no close relationship between the reduction of area and the impact energy values seems to exist (Fig. 7). A more comprehensive investigation of this subject is presented by Trautwein et al.[5]

Properties of Actual Production Castings Determined with Core Sampling

Table 6 shows the mechanical properties determined in core samples taken from wall thicknesses from 180 to 340 mm in comparison with properties of attached test coupons with cross sections of 80 by 80 mm. The castings with weights ranging from 18 000 to 23 000 kg were heat treated as follows: 950°C quenched in oil and tempered at 700°C with a subsequent furnace cooling. These data were gathered by the Kraftwerk Union AG, Mülheim (Germany). They illustrate clearly the close correlation between the test block and actual production casting data.

Fracture Toughness

The compact tension test bars were tested in accordance with ASTM E 399 (since discontinued; available from the American Welding Society). Additionally some further procedures were applied during the investigation. The crack-opening displacement (COD) was measured by four strain gages inserted into the notch. The beginning of stable crack growth was determined by acoustic emission.

If no valid K_{1c}-result could be determined because either the size of the test bar was too small or the testing temperature was too high, then, besides COD, a P_{ae}-value was measured by acoustic emission. This result was registered beside that of the P_Q-load.

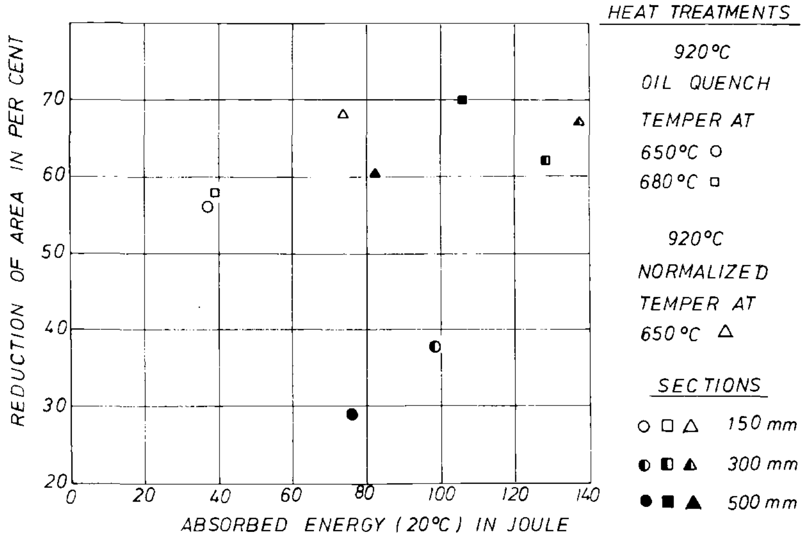

FIG. 7—*No close correlation between reduction of area and impact in the center of steel castings.*

The investigation was performed in the temperature range between −60 and +50°C (Table 7). It was completed by values that were received from cast-on-samples of heavy castings. The heat treatment of these parts consisted of an oil quench from 950°C and a tempering treatment at 720°C. The testing was performed at temperatures lower than −40°C (information given from Kraftwerk Union AG, Erlangen/Germany). The results are presented in Fig. 8.

Up to about −60°C linear elastic behavior was registrated. At higher temperatures the crack growth was increasingly elastoplastic. This can be proved by the COD results (Fig. 9). Increasing plastic deformation at the tip of the notch could be correlated with higher temperatures. Observing the fracture surfaces of the test bars these results can be clarified (Fig. 10). At −59°C, only at the starting zone near the notch and at the end of the crack can greater deformations be observed. At 0°C, two thirds of the fracture area is already ductile, and at 50°C an overall ductility is evident.

Fatigue Tests

The fatigue performance in the center sections of the three wall thicknesses has been determined by rotating-bending test bars with constant amplitude, test frequency 100 Hz, stress ratio $R = -1$, and with a run-out of 10×10^6 cycles at room temperature in air (testing machine RAPID 1). The test specimens had a diameter of 6.74 mm (normalized and tempered) and for the oil-quenched and tempered conditions additionally a cylindrical length of 24 mm.

TABLE 6—*Comparison of mechanical properties between cast-on and core-sampled test specimens taken out of heavy castings with weights between 18 000 and 23 000 kg of 2¼Cr-1Mo cast steel.*

Attached Test Coupon[a]					Core Sample[b]					
Yield Strength (0.2% offset), N/mm^2	Tensile Strength, N/mm^2	Elongation ($L_o = 5d$), %	Reduction of Area, %	Impact ISO-V-Notch at 20°C, J	Yield Strength (0.2% offset), N/mm^2	Tensile Strength, N/mm^2	Elongation ($L_o = 5d$), %	Reduction of Area, %	Impact ISO-V-Notch at 20°C, J	Wall Thickness, mm
452	622	23	58	69/89	413	586	23	56	68, 71	245
					419	593	23	53	63, 71	245
479	634	25	66	106	446	625	21	64	59, 81	245
					456	618	21	53	70, 73	245
427	617	26	62	58	422	610	23	66	65, 67	340
					438	603	23	62	94, 52	340
414	575	26	67	54	393	569	25	62	68, 79	240
					400	576	25	64	74, 69	240
					378	561	24	62	61	180
479	651	22	62	121	503	659	21	63	85, 64	315
					493	655	21	64	86, 71	315

[a] Cross section of attached test coupons is 80 by 80 mm.

[b] Diameter of core samples is 70 mm.

TABLE 7—*Results of tests with samples ≥ CT3 that gave no valid* K_{Ic}*-value [2¼Cr-1Mo cast steel: wall thickness 30 cm (12 in.)].*[a]

Temperature, °C	Type of Sample[b]	Wall Thickness, mm	P_Q/P_{max}	K_Q, N mm$^{-3/2}$	$K_{Q(ae)}$, N mm$^{-3/2}$	COD, mm	K_C (COD), N mm$^{-3/2}$
−59	CT3	300	1.0	3090	3090	0.09	4270
−1	CT3	300	0.70	3530	4370	0.22	5490
0	CT4	300	0.77	4080	5300	0.18	4950
+22	CT4	300	0.67	4270	6380	0.32	6620
+50	CT3	300	0.52	3480	6030	0.49	6670
+51	CT4	300	0.50	3460	6920	0.61	7460

[a] Carried out by Sulzer Brothers Ltd., Winterthur, Switzerland.

[b] Sample CT3 has a sample thickness of 75 mm; Sample CT4 has a sample thickness of 100 mm.

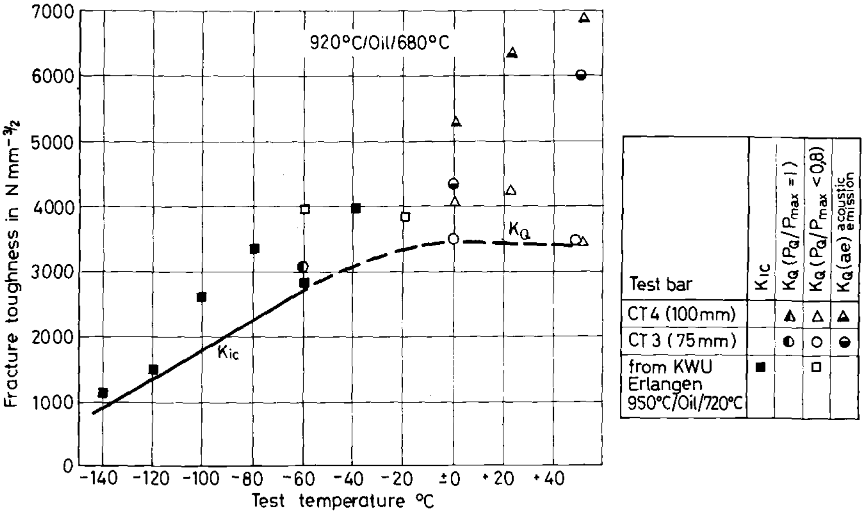

FIG. 8—*Fracture toughness of 2¼Cr-1Mo cast steel of 30 cm (12 in.) wall thickness.*

The evaluation (Fig. 11) shows a systematic correlation of the endurance limit in the three wall thicknesses with decreasing bending stresses. In the most thoroughly investigated quenched and 680°C tempered condition, between the 300 and 500 mm section, considerably increased scatter could be observed.

The verification of the fracture surfaces of the rotating-bending test bars confirmed that the fatigue failures usually started from one or several small microshrinkage voids. There seems to be a close relationship between the portion of the microporosity and the development of the solidification of the different wall thicknesses.

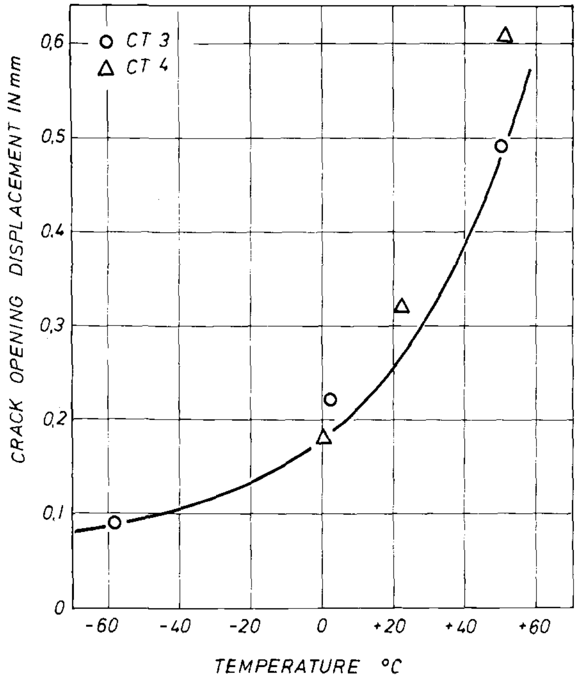

FIG. 9—*Crack-opening displacement (COD) of the 2¼Cr-1Mo cast steel in the 300-mm section.*

Fatigue Crack Growth Rate

Two compact tension test bars (CT2) were machined from the 300-mm-section center that was 920°C oil quenched and tempered at 680°C. The load range between 3000 and 33 000 N was cyclic alternated with a frequency of approximately 150 Hz. At room temperature the crack growth was measured. Figure 12 presents the relationship between the stress-intensity factor range and the crack growth rate. According to the approximation given by Paris and Erdogan [*6*]:

$$da/dN = C(\Delta K)^m$$

the two constants can be calculated.

With the factors $m = 2.95$ and $C = 1.58 \cdot 10^{-13}$ (ΔK in N mm$^{-3/2}$) the results are in good agreement with comparable cast or forged steels.

Discussion

Some further items of general interest should be briefly mentioned and discussed:

1. The somewhat higher carbon content (0.18 percent) of the cast steel proved to be useful in large sections in order to delay the precipitation of prebainitic ferrite during slower cooling rates. Moreover, this ferrite has a fine-grain structure that increases ductility.
2. The macrostructure tested over the entire center plate (Baumann-Print) shows visually in all three wall sections neither inhomogeneities nor macrosegregation. Microsegregation can affect the reduction of area and the elongation values.
3. The quench and 680°C temper treatment seems to be more suitable than normalizing and tempering for the properties within heavy castings.
4. To ensure high values of the reduction of area ($Z \geq 50$ percent) in the center of the castings, the heat treatment should be performed so that no great differences of strength can occur between dendrites and interdendritic zones of microsegregation.
5. Owing to the existence of some micropores in the center regions, the scatter of the fatigue test results is somewhat greater than that of wrought steel.

Conclusion

The properties determined in the large test block and in actual heavy-walled castings hardened and subsequently tempered at 680°/700°C are in agreement with the standard specification summarized in Table 1. Only the higher strength grades D1Q2 and D1Q3 (ASTM A 757) should be excluded here. They were not the subject of this investigation. There is a good correlation with the results given by Haines [*3*]. However, his conclusion that a vacuum degassing of the melt should be applied is incorrect. The use of modern melting and foundry techniques is sufficient to obtain the required results. It is well known that the larger the contoured cross section in a design, the smaller will be the wrought effect to the originally cast structure.

The results of all measured internal properties show in general a high degree of reproducibility in the different section thicknesses if the cooling rates after austenitizing at 920°C can be kept in narrow limits.

Summarizing critically the internal properties of 2¼Cr-1Mo cast steel the following facts seem to be remarkable for quenched and tempered condition. For heavy cross sections, the normalized and tempered condition is not recommended.

Tensile Strength/Yield Strength—There is only a slight decrease in tensile strength between surfaces and center in all three section sizes. A similar characteristic can be noted for the yield strength.

Elongation/Reduction of Area—If tempered at 680°C practically no loss of elongation and reduction of area can be found between surface and center even in the 300 and 500 mm wall. A tempering temperature of at least 680°C

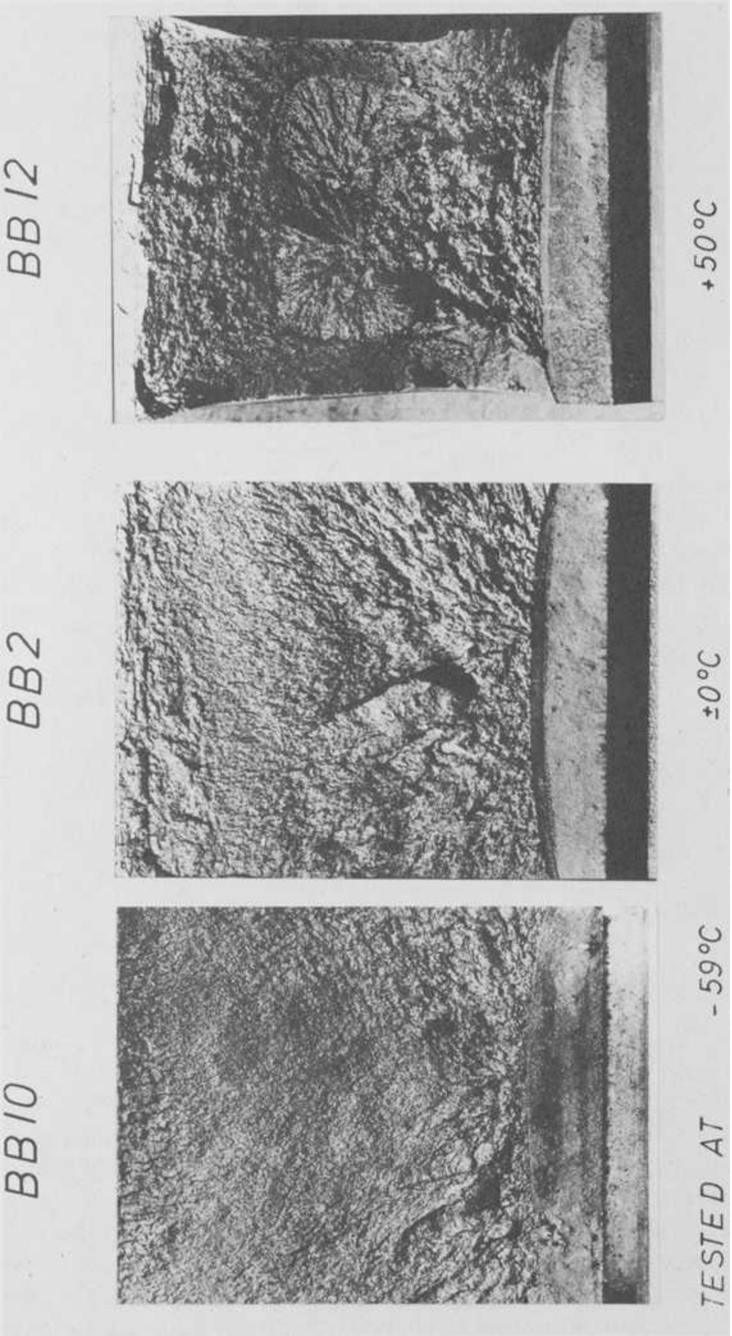

FIG. 10—*Fracture surfaces of 2¼Cr-1Mo cast steel (CT test bars; heat treatment 920°C/oil/680°C).*

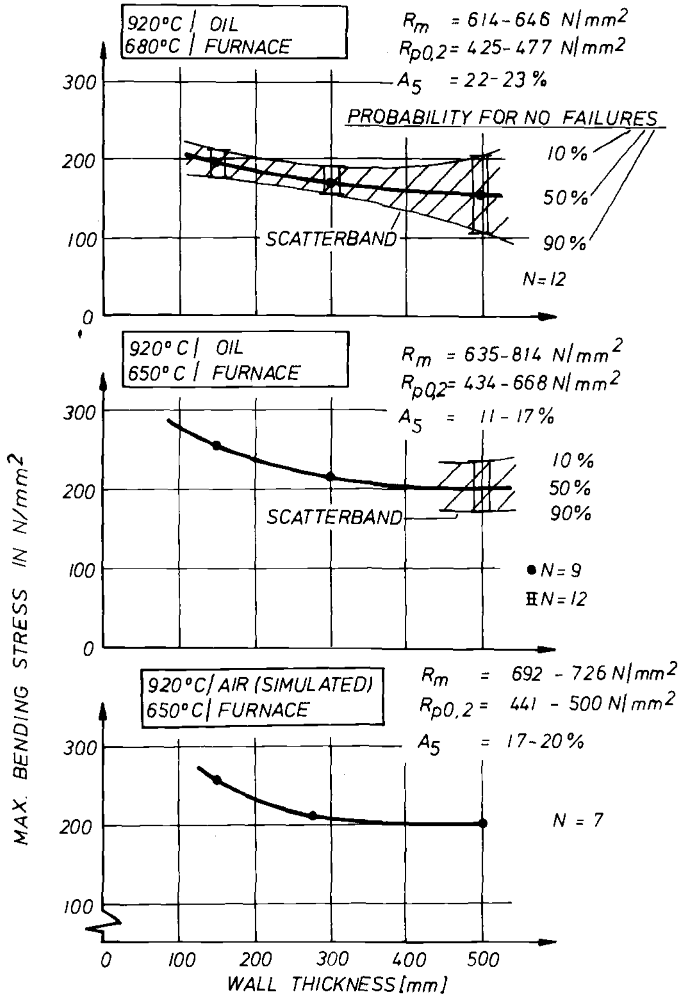

FIG. 11—*Fatigue test under rotating bending loads (scatterband) versus wall thickness.*

should be considered a minimum for 2¼Cr-1Mo cast steel to meet the ASTM requirements.

Impact Properties versus Temperature—In the oil-quenched and tempered (680°C) condition a rather small scatterband can be noted between surface and center in all three wall thicknesses. The difference of tempering temperature between 650 and 680°C on the impact-V-notch energy is remarkable. The reasons for the generally lower impact values in the 150-mm wall compared with the 300- and 500-mm walls are explained by Trautwein et al.[5] Generally, after oil-quench and 680/700°C tempering ISO-V impact values of more than 40 J at room temperature can be achieved within heavy castings.

Test bar		Test temperature	P_{max}	P_{min}	Frequency	$R_{p0,2}$
No.	Size		N	N	Hz	N/mm²
○ BB 26	CT 2	20°	33000	3000	140	667
□ BB 27	CT 2	20°	33000	3000	155	755

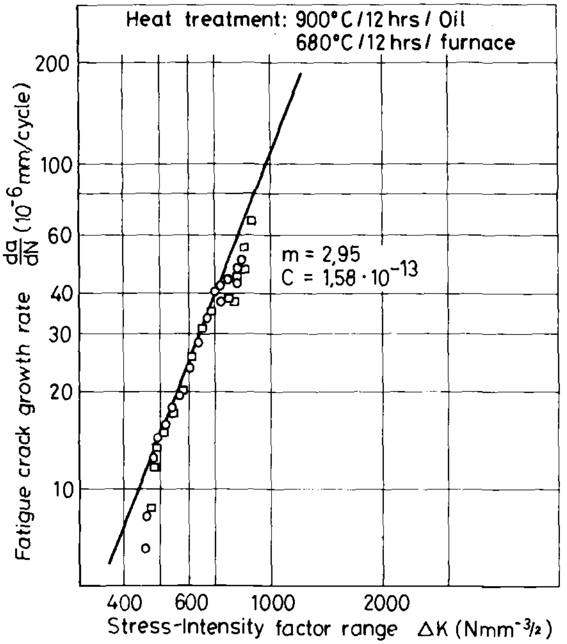

FIG. 12—*Fatigue crack growth rate of 2¼Cr-1Mo cast steel of 30 cm (12 in.) wall thickness (dynamic stresses).*

Fatigue Performance—A close relationship exists between the endurance limit and the tensile strength. The ratio is about 0.30.

Fracture Toughness/Fatigue Crack Growth Rate—The fracture toughness behavior of cast steel is comparable with that of wrought steel. The same statement can be made for the crack propagation rate under cyclic load.

References

[1] Kalwa, G. and Schnabel, E., *VGB-Kraftwerkstechn.* Vol. 58, No. 8, 1978, pp. 604-613.

[2] Marandet, B. and Sanz, G., *Circular Information Techniques*, Vol. 33, 1976, pp. 2231-2266.

[3] Haines, D. R., "Report of General Electric Foundry Department," 2 Oct. 1967.

[4] Bamford, W. H., paper presented at CSNI/NCR Meeting on Elastic-Plastic-Fracture, San Francisco, 25 June 1976.

[5] Achtelik, K. and Motz, J. M., *VDI-Z*, Vol. 120, No. 17, 1978, pp. 775-789; *Giesserei 65*, Vol. 18, 1978, pp. 475-486.

[6] Paris, P. and Erdogan, F., *Journal of Basic Engineering*, Vol. 85, 1963, p. 528.

Design Considerations in Application of $2^1/_4$Cr-1Mo Steel at Elevated Temperatures

S. Suresh,[1] *G. F. Zamiski,*[1] *and R. O. Ritchie*[1]

Fatigue Crack Propagation Behavior of 2¼Cr-1Mo Steels for Thick-Wall Pressure Vessels

---

REFERENCE: Suresh, S., Zamiski, G. F., and Ritchie, R. O., **"Fatigue Crack Propagation Behavior of 2¼Cr-1Mo Steels for Thick-Wall Pressure Vessels,"** *Application of 2¼Cr-1Mo Steel for Thick-Wall Pressure Vessels, ASTM STP 755,* G. S. Sangdahl and M. Semchyshen, Eds., American Society for Testing and Materials, 1982, pp. 49–67.

ABSTRACT: The fatigue crack propagation behavior of a series of thick-section [20.3 cm (8 in.)] 2¼Cr-1Mo steels has been investigated in environments of gaseous hydrogen and ambient temperature air over a wide range of growth rates from near-threshold levels (10^{-11} m/cycle) to 10^{-4} m/cycle, as part of a program to characterize potential materials for coal gasification pressure vessel applications. Normalized bainitic-ferritic microstructures (ASTM A 387, Class 2, Grade 22) have been compared with quenched and tempered fully bainitic (ASTM A 542, Class 3) and fully martensitic (ASTM A 542, Class 2) microstructures, representing a range of yield strengths from 290 to 769 MPa. Although growth rates above 10^{-9} m/cycle are largely unaffected by microstructure and strength level, at near-threshold growth rates there is a marked deterioration in crack propagation resistance with increasing strength which becomes accentuated for tests in hydrogen environments. Further, the influence of gaseous hydrogen on fatigue crack propagation rates is found to be particularly severe at stress intensities far below K_{Iscc}, the threshold for hydrogen-assisted growth under sustained loading. At near-threshold levels ("true corrosion fatigue" regime) the presence of hydrogen gas enhances growth rates by up to two orders of magnitude compared with air, without a significant change in fracture mechanism. At higher growth rates ("apparent stress-corrosion fatigue" regime), a second acceleration in growth rates (up to 20 times compared with air) due to hydrogen is observed above a critical $K_{\max}$-value, which is both sensitive to frequency and load ratio and is associated with a predominately intergranular fracture mode. The characteristics of these distinct regimes of hydrogen-assisted fatigue crack propagation in 2¼Cr-1Mo steels are discussed in the light of the potential use of these steels for coal conversion pressure vessel construction.

KEY WORDS: fatigue (materials), crack propagation, near-threshold, load ratio, microstructure, hydrogen embrittlement, stress corrosion, fracture, intergranular, transgranular, crack closure

The present uncertainty in oil supplies to this country has spurred renewed interest in coal as a viable major energy source. Although the technology for

---

[1] Graduate Research Assistant, Graduate Research Assistant, and Associate Professor, respectively, Department of Mechanical Engineering, Massachusetts Institute of Technology, Cambridge, Mass. 02139. Professor Ritchie is currently with the Department of Materials Science and Mineral Engineering, University of California, Berkeley, Calif. 94720.

extensive utilization of this coal is rapidly emerging, materials-related problems cause us to persist in the search for less-expensive materials capable of improved performance in the presence of mechanically and chemically hostile environments [*1,2*].[2] Coal conversion processes require, for example, massive welded steel pressure vessels, as large as 60 m high, 6 m in diameter, with 300 to 400 mm wall thicknesses, to operate continuously, economically, and above all safely at high pressures (up to 20 MPa) and temperatures (450 to 1000°C) in the presence of erosion-producing solid particles and chemically aggressive atmospheres including H_2O, H_2, H_2S, etc. [*2*]. The vessel wall, although insulated from the reaction processes by a refractory lining and an additional stainless steel weld overlay, may be expected to be in contact with these gas mixtures at operating temperatures up to 450°C [*1*].

Material requirements for the pressure vessel include homogeneous, tough, weldable steels having yield strengths in excess of 350 MPa, with good resistance to creep, fatigue, and environmental degradation (that is, hydrogen embrittlement and hydrogen attack). Prime candidates for this application are the 2¼Cr-1Mo low-alloy steels. Considerable effort has been directed towards characterizing the fabrication and mechanical and environmental properties of 2¼Cr-1Mo steels (as evidenced by the papers in this volume), and background information on the use of such steels in thick sections is available from hydrocarbon processes, and fossil energy and nuclear technologies. However, one area which has received relatively little attention is the fatigue crack growth of small incipient flaws at growth rates less than 10^{-6} mm/cycle, approaching the so-called alternating threshold stress intensity, ΔK_0, below which cracks remain dormant or propagate at experimentally undetectable rates. In coal conversion service, such growth may arise from high-cycle, low-amplitude stresses generated from small pressure and temperature fluctuations ("operational transients") which are expected to occur during "steady state" operation as a result of real variations in coal feed rate, "clusters" of pulverized coal, combustion instabilities, and pressure fluctuations in feed and discharge lines for gases.

The object of the present work is to study the near-threshold fatigue crack growth behavior of several thick-section 2¼Cr-1Mo steels, with yield strengths ranging from 290 to 769 MPa (42 to 112 ksi), in environments of moist air and dry gaseous hydrogen. Influences of load ratio, strength level, microstructure, and environment on near-threshold growth rates and threshold ΔK_0-values are investigated, and the role of hydrogen in accelerating crack propagation is specifically examined.

Materials and Experimental Procedures

Three heats of 2¼Cr-1Mo steels were obtained: (*1*.) a 184-mm-thick plate of normalized and tempered ASTM Specification for Pressure Vessel Plates,

---

[2] The italic numbers in brackets refer to the list of references appended to this paper.

Alloy Steel, Chromium-Molybdenum (A 387-79b), Class 2, Grade 22, (*2*) a 175-mm-thick plate of quenched and tempered ASTM Specification for Pressure Vessel Plates, Alloy Steel, Quenched and Tempered Chromium-Molybdenum (A 542-79), Class 3, and (*3*) a 25-mm-thick plate of quenched and tempered ASTM A 542, Class 2. These steels are hereafter referred to as SA387, SA542-3, and SA542-2, respectively. Chemical composition, heat treatment, and as-received mechanical properties are listed in Tables 1 to 3.

Owing to differences in cooling rates following austenitization, microstructures and properties in the thick-section plates varied with through-thickness position (Table 4). In normalized SA387, samples cut from surface layers showed yield strengths of 390 MPa, with a bainitic microstructure (approximate grain size 40 μm) containing roughly 10 percent free polygonal ferrite. At midthickness (½-T), however, yield strengths decreased to 290 MPa, consistent with an increase in proportion of ferrite in the microstructure to almost 40 percent (Fig. 1*a*). Microstructures and properties in quenched and tempered SA542-3 varied only marginally with thickness, the structure being predominately bainitic (less than 3 percent ferrite at midthickness) with a yield strength of 485 to 500 MPa (Fig. 1*b*). Microstructures in the 25-mm-thick plate of SA542-2 were fully martensitic with an as-received yield strength of 769 MPa (Fig. 1*c*).

Fatigue crack propagation tests were performed with 12.7-mm-thick compact test pieces (*T-L* orientation) using servo-hydraulic testing machines operating under load control at 50 Hz frequency (sine wave) with load ratios ($R = K_{\min}/K_{\max}$) between 0.05 and 0.80. Tests were conducted at ambient temperature in environments of moist air (30 percent relative humidity) and dehumidified gaseous hydrogen (138 kPa pressure). Crack growth monitoring was achieved using d-c electrical potential techniques capable of detecting changes in crack length on the order of 0.01 mm [*3*]. Near-threshold growth rates (below 10^{-6} mm/cycle) were measured under both load-shedding (decreasing stress intensity) and increasing stress-intensity conditions, with the threshold ΔK_0 defined in terms of a maximum growth rate of 10^{-8} mm/cycle. Higher growth rates above 10^{-6} mm/cycle were measured at constant load amplitude. Full experimental details have been described elsewhere [*4-8*].

Results

Effect of Load Ratio

The variation in fatigue crack propagation rate, *da/dN*, with alternating stress intensity, ΔK, for ½-*T* samples of normalized SA387 as a function of load ratio, *R*, is shown in Figs. 2 and 3 for environments of moist air and dry hydrogen gas, respectively. Whereas growth rates above 10^{-5} mm/cycle are

TABLE 1—*Base-plate chemistries of 2¼Cr-1Mo steels investigated.*

Steel	C	Mn	Si	Ni	Cr	Mo	Cu	P	S	Heat	Specified Heat Treatment (as-received)
SA387 Class 2 Grade 22	0.12	0.42	0.25	0.14	2.48	1.06	0.16	0.013	0.020	Lukens Heat #3596	normalized and tempered
SA542 Class 3	0.12	0.45	0.21	0.11	2.28	1.05	0.12	0.014	0.015	Lukens Heat #3707	quenched and tempered
SA542 Class 2	0.14	0.44	0.22	0.61	2.28	0.92	. . .	0.010	0.020	Lukens Heat #C7158	quenched and tempered

TABLE 2—*As-received heat treatments of 2¼Cr-1Mo steels.*

SA387 Class 2, Grade 22 Steel (section thickness 184 mm)		
Normalize	5½ h at 954°C	accelerated fan air cool
Temper	8 h at 691°C	
Stress relieve	15 h at 593°C	
	22 h at 649°C	
	18 h at 691°C	
SA542 Class 3 Steel (section thickness 175 mm)		
Austenitize	5½ h at 954°C	water quench
Temper	8 h at 663°C	
Stress relieve	15 h at 593°C	
	22 h at 649°C	
	18 h at 663°C	
SA542 Class 2 Steel (section thickness 25 mm)		
Austenitize	1 h at 900 to 927°C	water quench
Temper	1½ h at 638°C	water quench

relatively unaffected by either load ratio or environment,[3] at near-threshold levels growth rates become strongly sensitive to load ratio, and are increased by up to an order of magnitude with increase in R from 0.05 to 0.80. The variation of threshold stress intensity, ΔK_0, with load ratio (Fig. 4) indicates that ΔK_0-values are decreased markedly with increasing R up to a critical load ratio, whereupon the value of ΔK_0 remains constant. Similar increases in near-threshold growth rates (and reduced ΔK_0-values) with increasing load ratio are seen in the higher strength quenched and tempered 2¼Cr-1Mo steels, as shown in Fig. 5 for fully bainitic SA542-3 and in Fig. 6 for fully martensitic SA542-2. Fractographically, fatigue surfaces consisted of a fine-scale transgranular mode with evidence of intergranular facets (Fig. 7). The proportion of intergranular facets was negligible close to ΔK_0, rising typically to approximately 40 percent at around a K_{max}-value of 20 MPa$\sqrt{m}$, before being reduced to zero above a K_{max}-value of 30 MPa$\sqrt{m}$.[4]

Effect of Gaseous Hydrogen

In both SA387 (Figs. 2 and 3) and SA542-3 (Fig. 5), the presence of dry hydrogen gas can be seen to have little effect on growth rates above 10^{-5} mm/cycle, yet results at near-threshold levels show a marked deterioration in crack growth resistance. Compared with behavior in air, growth rates are enhanced by up to two orders of magnitude, and threshold ΔK_0-values decrease by as much as 32 percent. The effect, however, is surprisingly confined

---

[3] At lower frequencies (<5 Hz), marked hydrogen-assisted growth can occur above 10^{-5}mm/cycle, and correspondingly strong effects of both load ratio and environment are observed in these steels [*7-11*].

[4] Extensive measurements on SA387 tested *in air* indicated that the proportion of intergranular facets was solely a function of K_{max} [*5*].

TABLE 3—*Mechanical properties of as-received 2¼Cr-1Mo steels at ambient temperature (mean values).*

Steel	Yield Strength, MPa	Tensile Strength, MPa	Elongation, %	Reduction in Area, %	Charpy Impact Energy, J	K_{Ic},[a] MPa$\sqrt{m}$	K_{Iscc},[b] MPa$\sqrt{m}$
SA387 Class 2 Grade 22	345 ± 57	528 ± 33	29[c]	76	165 ± 23	286	>60
SA542 Class 3	496 ± 7	610 ± 17	25[c]	77	197 ± 18	295	>85
SA542 Class 2	769	838	17 to 21[d]	51 to 70	. . .	. . .	>80

[a] Computed from J_{Ic}-measurements.

[b] For dehumidified gaseous hydrogen at 138 kPa pressure.

[c] For 45-mm gage length.

[d] For 50-mm gage length.

TABLE 4—*Threshold* ΔK_0*-data for SA387 and SA542 steels in moist air at* R = *0.05.*

Steel	Condition	Grain Size, μm	Microstructure	Yield Strength, MPa	Tensile Strength, MPa	ΔK_0, MPa$\sqrt{m}$	Cyclic CTOD,[a] μm	Maximum CTOD,[a] μm
SA542 Class 2	as-received	40	100% martensite	769	838	7.1	0.08	0.17
SA542 Class 3	surface	70	100% bainite	500	610	7.4	0.13	0.28
SA542 Class 3	¼-*T*	65	100% bainite	500	625	7.4	0.13	0.28
SA542 Class 3	½-*T*	60	97% bainite 3% ferrite	485	590	7.7	0.14	0.32
SA387 Class 2 Grade 22	surface	44	90% bainite 10% ferrite	390	550	8.3	0.21	0.46
SA387 Class 2 Grade 22	¼-*T*	40	87% bainite 13% ferrite	340	520	8.6	0.25	0.56
SA387 Class 2 Grade 22	½-*T*	36	63% bainite 37% ferrite	290	500	9.0	0.33	0.72

[a] Crack-tip opening displacement computed at threshold.

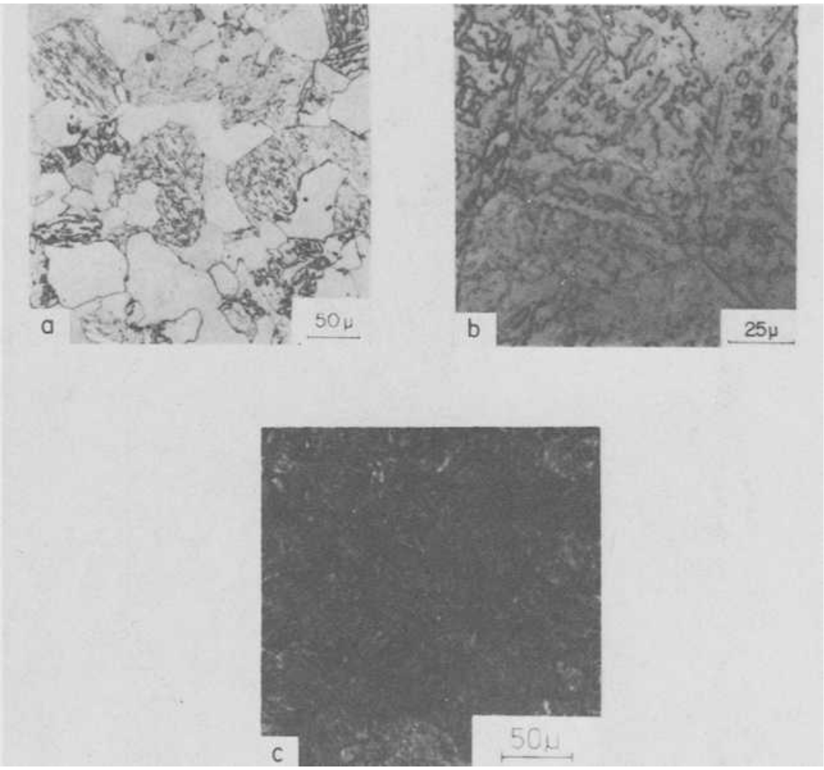

FIG. 1—*Microstructures of as-received 2¼Cr-1Mo steels (½-*T *sections) showing* (a) *duplex bainitic-ferritic structure in SA387,* (b) *fully bainitic structure in SA542 Class 3, and* (c) *fully martensitic structure in SA542 Class 2 (2 percent nital etch).*

to low load ratios (for example, Figs. 4 and 5), behavior above $R = 0.5$ being essentially similar in both air and hydrogen. Microscopically, fracture modes at near-threshold levels were identical for both environments, being predominately transgranular in nature (Figs. 7*a* and 7*d*). There was no evidence of a characteristic fracture mode for hydrogen-assisted growth below 10^{-6} mm/cycle, although above 10^{-5} mm/cycle, for load ratios exceeding 0.3 (at 50 Hz) where a small hydrogen-assisted contribution to growth is evident (Fig. 3), fracture surfaces in hydrogen became predominately intergranular (Figs. 7*c* and 7*d*).

Effect of Microstructure and Strength Level

A comparison between near-threshold crack growth behavior in SA387, SA542-3, and SA542-2 steels tested in moist air at $R = 0.05$ and at 0.75 to 0.80 is shown in Fig. 6. It is apparent that an increase in strength level (that

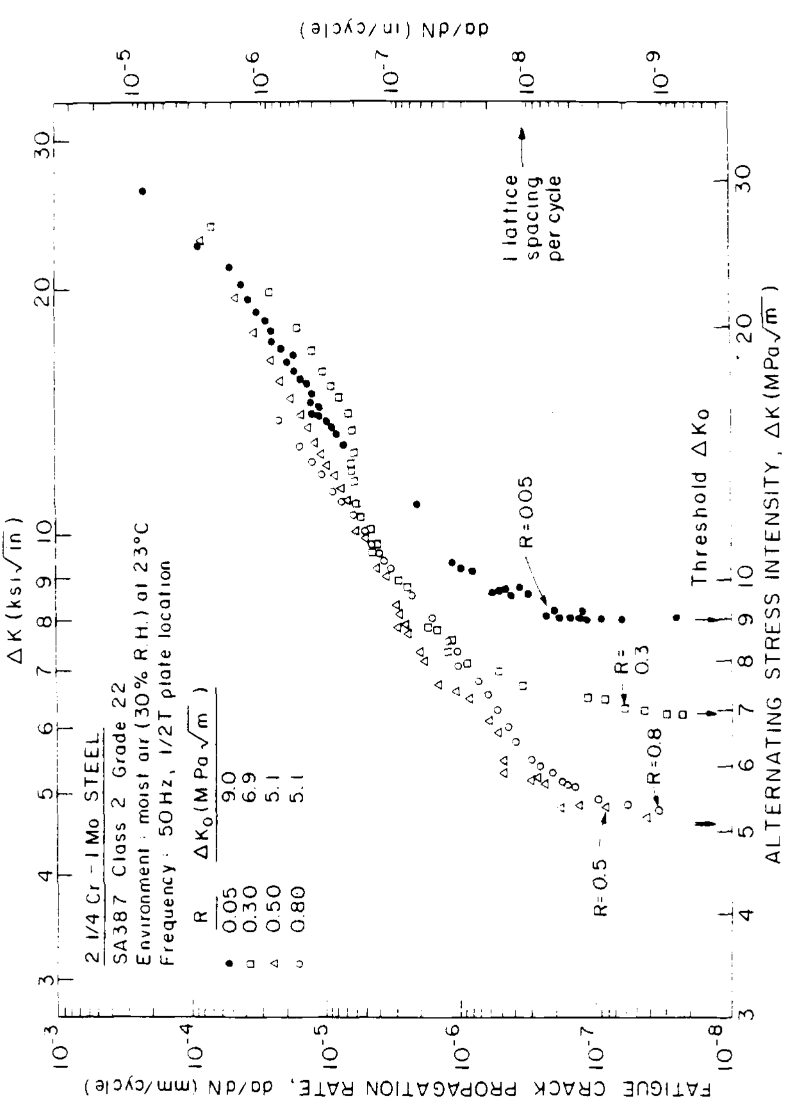

FIG. 2—*Variation of fatigue crack propagation rates, da/dN, with stress intensity, ΔK, in SA387 steel tested at 50 Hz in moist air as a function of load ratio, R.*

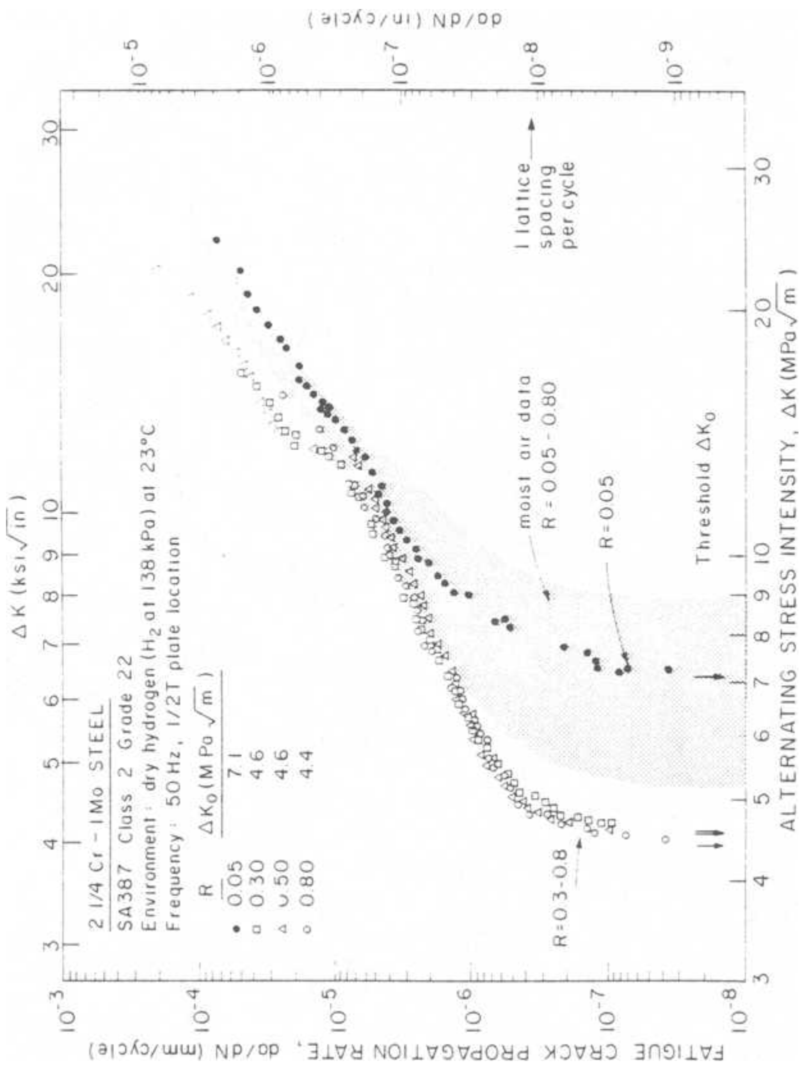

FIG. 3—*Variation of fatigue crack propagation rates,* da/dN, *with alternating stress intensity,* ΔK, *in SA387 steel tested at 50 Hz in dehumidified gaseous hydrogen as a function of load ratio,* R. *Hatched area represents moist air data from Fig. 2.*

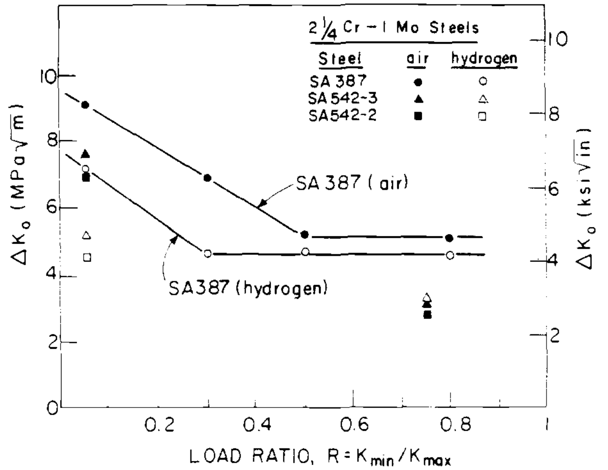

FIG. 4—*Variation of threshold stress intensities,* ΔK_0, *with load ratio,* R, *for 2¼Cr-1Mo steels tested at 50 Hz in air and hydrogen gas.*

is, a yield strength increase from 290 to 769 MPa) results in faster near-threshold crack propagation rates and a reduction in ΔK_0-values from 9.0 to 7.1 MPa$\sqrt{m}$ (at $R = 0.05$). This implies that lower strength ferritic-bainitic microstructures offer better resistance to near-threshold crack growth than fully bainitic and fully martensitic structures in 2¼Cr-1Mo steel (Table 4). This is supported by the general trend of data in the literature, as shown in Fig. 8 for steels ranging in strength from 200 to 1800 MPa, compiled from results listed in Refs *12* to *14*. Not only is there an overall trend of increasing thresholds with decreasing strength, but at given strength levels, bainitic structures are generally superior to martensitic structures and, with few exceptions, ferritic and pearlitic structures appear superior to primarily bainitic structures.

Discussion

The present work has shown that near-threshold fatigue crack propagation in a range of 2¼Cr-1Mo steels is strongly sensitive to load ratio and strength level, with the greatest resistance to near-threshold growth occurring at low load ratios with lower strength bainitic-ferritic microstructures. In addition, for steels generally regarded as being relatively immune to hydrogen embrittlement based on their high K_{Iscc}-thresholds for hydrogen-induced failure under sustained loading, significant accelerations in growth rates by up to two orders of magnitude are apparent for crack propagation in dry gaseous hydrogen at stress intensities far below K_{Iscc}. In the current study, where a frequency of 50 Hz was used, the principal regime of hydrogen-assisted growth is clearly below 10^{-6} mm/cycle. Parallel studies in these steels [*7-9*]

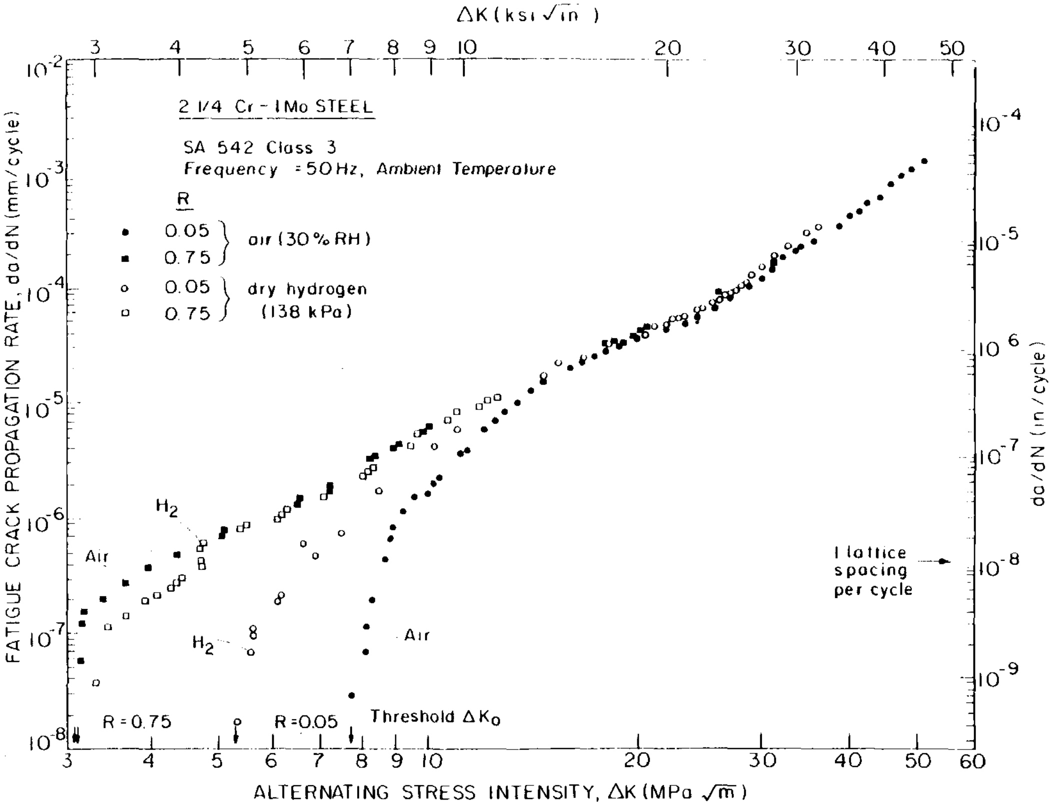

FIG. 5—*Variation of fatigue crack propagation rates,* da/dN, *with alternating stress intensity,* ΔK, *for SA542 Class 3 steel, showing marked influence of hydrogen on near-threshold growth rates only at low load ratios.*

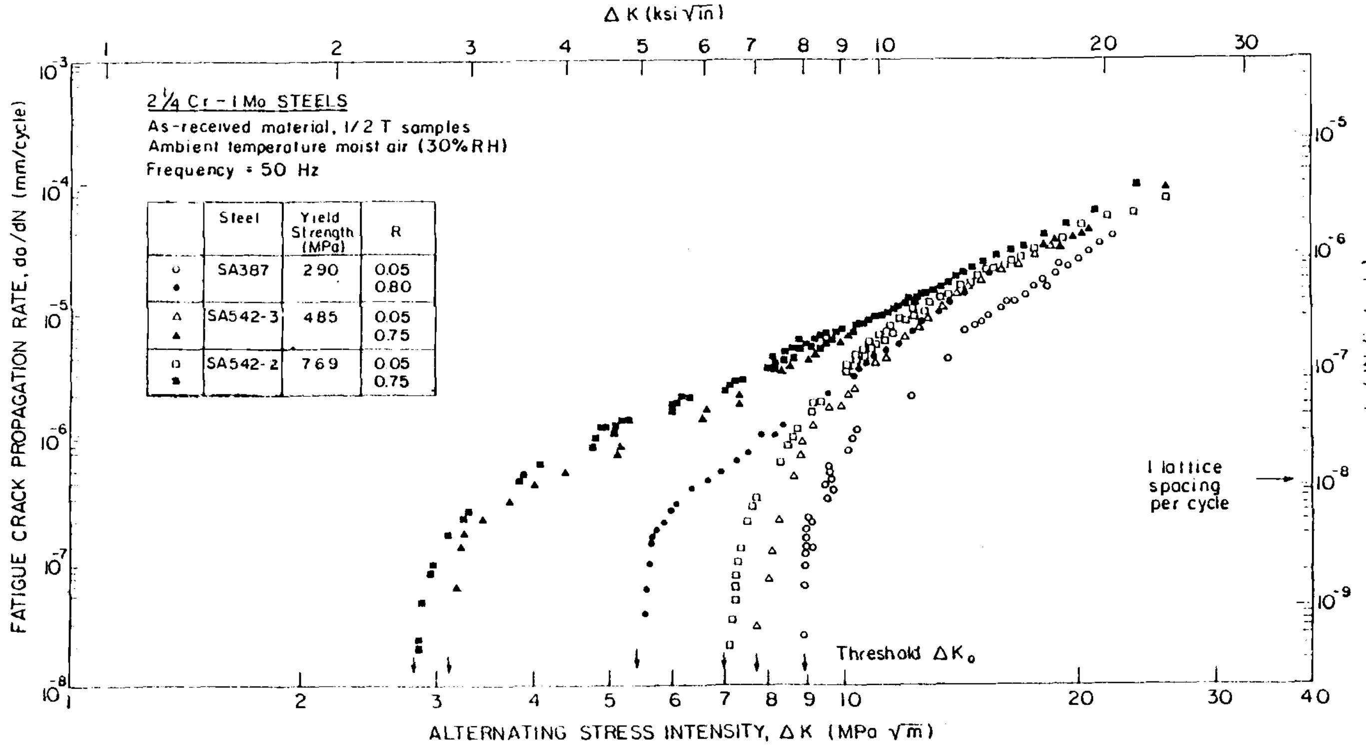

FIG. 6—*Variation of fatigue crack propagation rates,* da/dN, *with alternating stress intensity,* ΔK, *for 2¼Cr-1Mo steels tested at 50 Hz in moist air at low* (R = *0.05) and high* (R = *0.75 to 0.80) load ratios.*

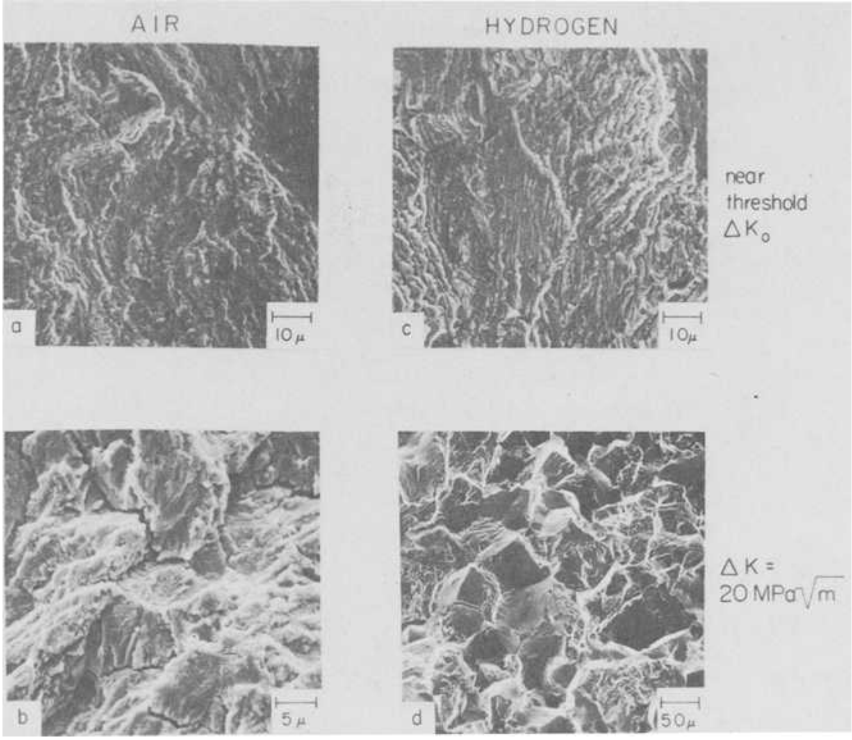

FIG. 7—*Mechanisms of fatigue crack propagation in 2¼Cr-1Mo steels tested at 50 Hz in air and hydrogen at* R = *0.3, showing* (a) *and* (c) *near-threshold surfaces in SA387, and* (b) *and* (d) *surfaces in SA542-3 where crack growth rates are greater than* 10^{-5} *mm/cycle.*

at lower frequencies down to 0.5 Hz, however, have shown the existence of a second regime, typically above 10^{-5} mm/cycle, where abrupt accelerations in growth rates (by up to 40 times) can occur above a critical $K_{\max}$-value in hydrogen gas relative to air. Unlike behavior at near-threshold levels, such hydrogen-assisted growth generally involves a fracture mode transition to predominantly intergranular fracture (for example, Fig. 7*d*) and is strongly sensitive to frequency [*8, 9*]. At 50 Hz, the effect is small and only seen above a load ratio of 0.3, as shown for SA387 above 10^{-5} mm/cycle (Fig. 3). Extensive kinetic studies by Wei and co-workers [*9*] have revealed that rate-limiting steps for such hydrogen-assisted growth may be the chemi-sorption of hydrogen at the crack tip, and the effect has been generally attributed to hydrogen embrittlement mechanisms.[5]

At near-threshold levels in steels, however, hydrogen embrittlement

---

[5] Although precise mechanisms of hydrogen embrittlement are unknown, particularly in lower strength steels, we imply here mechanisms by which hydrogen can enter the iron lattice and lead to a degradation in resistance to fracture.

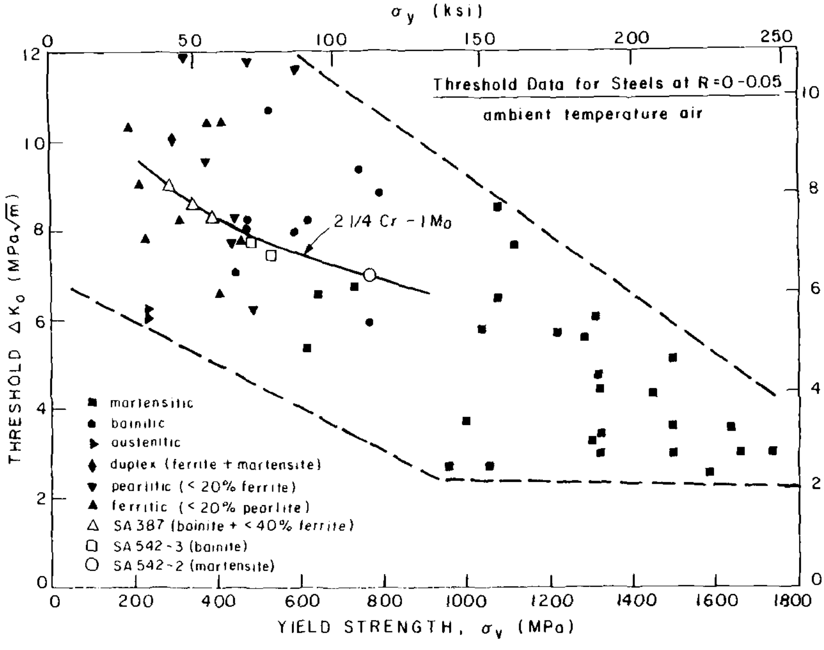

FIG. 8—*Variation of threshold* ΔK_0 *values at* R = *0 to 0.05 with yield strength for a wide range of steels* [12-14] *showing present data for* 2¼Cr-1Mo *pressure vessel steels.*

mechanisms have recently been questioned as the explanation for the accelerating influence of hydrogen [*6,8,15*]. This is because enhancements in growth rates due to hydrogen below 10^{-6} mm/cycle are seen to predominate only at low load ratios and in lower strength steels. Tests on high strength 300-M and NiCrMoV steels, which are extremely susceptible to hydrogen embrittlement, have shown near-threshold growth rates and ΔK_0-values to be relatively unchanged in air and hydrogen [*8,15*]. Accordingly, a new model for environmental effects near threshold has been proposed based on the concept of "oxide-induced crack closure" [*6,8,15*]. According to this model, near-threshold growth rates are enhanced in dry hydrogen gas because of an absence of moisture compared with air. Moist atmospheres result in the formation of oxide films at the crack tip, which are thickened at low load ratios by "fretting oxidation" [*6,15,16*], that is, a continual breaking and re-forming of the oxide scale behind the crack tip due to the "smashing" together of crack surfaces as a result of plasticity-induced crack closure.[6] Such oxide debris, which is much less predominant in dry hydrogen atmospheres or at high load ratios (where there is no plasticity-induced closure), can result in higher closure loads and a corresponding reduction in

---

[6] Here we refer to crack closure generated as a result of residual plastic deformation left in the wake of the crack, as originally described by Elber [*17*].

the effective ΔK at the crack tip. This effect can be appreciated by realizing that oxide films, which are clearly visible as corrosion bands on near-threshold fracture surfaces [*6,8,12,16*], are typically several submicrons thick[7] in near-threshold cracks where near-tip cyclic crack opening displacements (ΔCTOD) would be expected to be of the same size scale (Table 4).

The role of hydrogen in accelerating near-threshold crack growth rates (and reducing ΔK_0) in low strength steels with respect to moist air can thus be interpreted in terms of reduced oxide-induced crack closure, consistent with oxide debris observations [*6*], that the effect on ΔK_0 is most pronounced at low load ratios (Figs. 4 and 5) and that there is no characteristic hydrogen fracture mode (Fig. 7). The influence of load ratio on threshold values (Fig. 4) also follows from such closure concepts [*6.18*], since above a critical load ratio, where the crack is fully open during the complete loading cycle, no further change in ΔK_0 would be expected with increase in R. The fact that this critical load ratio is lower in hydrogen compared with air (Fig. 4) is indicative of lower closure loads in the drier environment [*6*]. Finally, the reduction in threshold ΔK_0-values with increasing material strength (Fig. 6) and the lack of an effect of hydrogen in ultra high-strength steels [*8,15*] may also be consistent with this model, since plasticity-induced crack closure would be expected to be reduced in higher strength materials and, further, fretting damage from oxide debris would be somewhat less severe on the harder fracture surface.

Verification that the role of hydrogen on near-threshold crack growth is not primarily associated with hydrogen embrittlement mechanisms was provided by testing SA387 in dry argon gas [*6*]. The results indicate that argon *accelerates* near-threshold growth rates relative to moist air with a corresponding reduction in ΔK_0 (Fig. 9). The fact that dry argon behaves like dry hydrogen is clearly inconsistent with any hydrogen embrittlement mechanism, yet is totally in accord with concepts of oxide-induced closure. This latter experiment emphasizes the fact that inert gas and high vacuum environments may be very different "reference environments" for near-threshold fatigue crack growth. Generally, threshold ΔK_0-values measured *in vacuo* are higher compared with those measured in air [*14,19,20*], a result which may be more a consequence of mechanisms such as crack tip rewelding, rather than the elimination of environmentally assisted growth.

In summary, marked influences of load ratio, strength level, and environment have been presented for near-threshold fatigue crack propagation in 2¼Cr-1Mo steels, and have been rationalized in terms of a new model based on oxide-induced crack closure. It is difficult, however, to further predict in the light of such concepts the effect of multicomponent gaseous atmospheres,

---

[7] Auger measurements using Ar^+ sputtering indicate that the oxide film thickness at 5×10^{-8} mm/cycle (moist air, $R = 0.05$) in SA387 is about 30 times thicker (~ 0.2 μm) than at 10^{-5} mm/cycle [*6*].

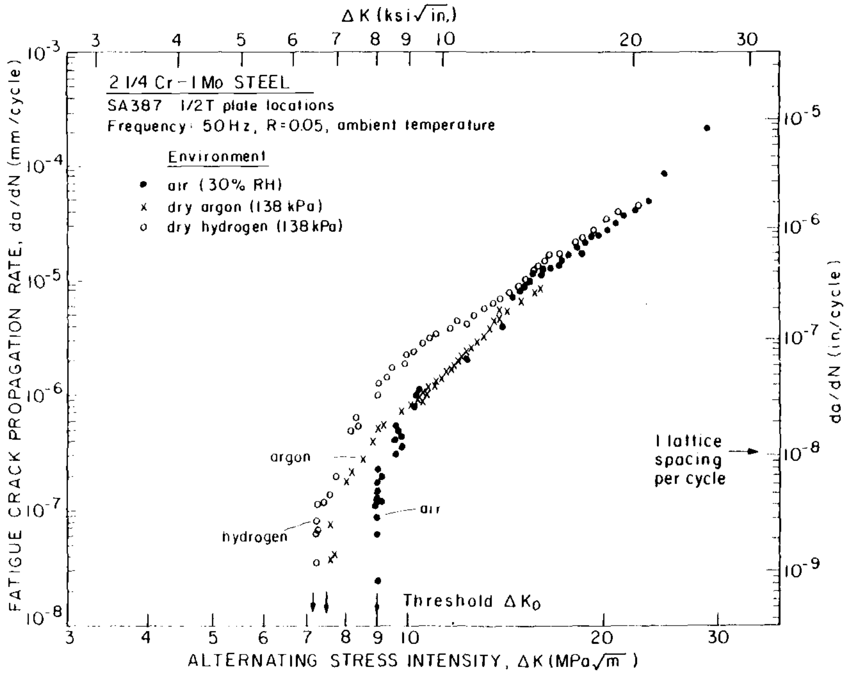

FIG. 9—*Fatigue crack propagation data for SA387 steel tested at* R = *0.05 (50 Hz) in ambient temperature moist air, dry gaseous hydrogen, and dry gaseous argon.*

especially those typical of coal conversion processes. Suffice it to say it is to be expected that in the same way that traces of oxygen may retard "true" hydrogen embrittlement by selective adsorption at the crack tip to prevent hydrogen entry [*21*], traces of moisture may similarly retard near-threshold crack growth in hydrogen, but in this case by oxide formation to promote increased closure loads which in turn lowers effective stress intensities experienced at the crack tip.

Conclusions

Based on a study of the characteristics of near-threshold fatigue crack propagation in a range of 2¼Cr-1Mo steels, namely bainitic/ferritic normalized SA387, bainitic quenched and tempered SA542-3, and martensitic quenched and tempered SA542-2, tested at 50 Hz in moist air and dehumidified gaseous hydrogen, the following general conclusions can be made:

1. Increases in load ratio, *R*, from 0.05 to 0.75-0.80, while having little influence on growth rate behavior above 10^{-5} mm/cycle, led to significant increases in near-threshold growth rates below 10^{-6} mm/cycle. Threshold

ΔK_0-values were reduced with increasing load ratio up to a critical R-value, whereupon they remained constant with further increase in R.

2. Near-threshold fatigue crack propagation was found to be markedly enhanced in dry hydrogen compared with moist air; enhancements in growth rates up to 100 times and reductions in ΔK_0-values by up to 32 percent were observed. The influence of hydrogen was most pronounced at low load ratios, involved no apparent change in fracture mechanism, and was seen to decrease with increasing growth rates below 10^{-5} mm/cycle.
3. Near-threshold fatigue crack growth resistance was found to be improved with decreasing strength level. Lowest crack propagation rates and highest ΔK_0-values were observed in the lower strength bainitic-ferritic microstructures.
4. The influence of environment on near-threshold crack growth behavior is ascribed to a mechanism involving oxide-induced crack closure. According to this model, near-threshold growth rates are accelerated in hydrogen compared with air because less oxide debris is created on crack surfaces, thereby reducing closure loads.
5. Concepts of oxide-induced closure are consistent with observed effects of load ratio, strength level, fracture morphology, and environment on near-threshold behavior, and further are in accord with observations that dry gaseous argon *enhances* near-threshold crack growth rates in SA387 compared with air.

Acknowledgments

This work was supported by the U.S. Department of Energy under contracts with the Divisions of Fossil Energy Research and Basic Energy Sciences. The authors wish to thank Drs. S. J. Dapkunas and S. M. Wolf for helpful discussions as program monitors, C. M. Moss and C. White for experimental assistance, and Drs. J. D. Landes, D. E. McCabe, and R. P. Wei for supplying the steel plate.

References

[1] Lochmann, W. in *Proceedings*, Fourth Annual Conference on Materials for Coal Conversion and Utilization, Gaithersburg, Md., Oct. 1979, U.S. Department of Energy, Washington, D.C., 1979, pp. 1-31.

[2] Scott, T. in *Proceedings*, Fourth Annual Conference on Materials for Coal Conversion and Utilization, Gaithersburg, Md., Oct. 1979, U.S. Department of Energy, Washington, D.C., 1979, pp. K1-K59.

[3] Ritchie, R. O., "Crack Growth Monitoring: Some Considerations on the Electrical Potential Method," Department of Metallurgy and Materials Science Technical Report, Cambridge University, Jan. 1972.

[4] Ritchie, R. O., *Journal of Engineering Materials and Technology, Transactions of ASME*, Series H, Vol. 99, No. 3, July 1977, pp. 195-204.

[5] Moss, C. M., "Near-Threshold Fatigue Crack Propagation in Pressure Vessel Steels," S.M. thesis, Massachusetts Institute of Technology, Cambridge, Mass., Sept. 1979.

[6] Ritchie, R. O., Moss, C. M., and Suresh, S., *Journal of Engineering Materials and Technology, Transactions of ASME*, Series H, Vol. 102, 1980, pp. 293-299.

[7] Suresh, S., Moss, C. M., and Ritchie, R. O., *Transactions of the Japan Institute of Metals*, Vol. 21, 1980, pp. 481-484.

[8] Ritchie, R. O., Suresh, S., and Toplosky, J., "Influences of Gaseous Environment on Low-Growth Rate Fatigue Crack Propagation in Steels," MIT Fatigue and Plasticity Laboratory Report No. FPL/R/80/1030, Massachusetts Institute of Technology, Cambridge, Mass., Jan. 1980.

[9] Brazill, R. L., Simmons, G. W., and Wei, R. P., *Journal of Engineering Materials and Technology, Transactions of ASME*, Series H, Vol. 101, No. 3, July 1979, pp. 199-204.

[10] Nelson, H. G. in *Proceedings*, Second International Conference on Mechanical Behavior of Materials, Boston, Aug. 1976, American Society for Metals, 1976, pp. 690-694.

[11] Nelson, H. G. in *Effect of Hydrogen on Behavior of Materials*, A. W. Thompson and I. M. Bernstein, Eds., The Metallurgical Society of AIME, 1976, pp. 602-611.

[12] Ritchie, R. O., *International Metals Reviews*, Vol. 20, 1979, pp. 205-230.

[13] Vosikovsky, O., *Engineering Fracture Mechanics*, Vol. 11, No. 3, 1979, pp. 595-602.

[14] Lindley, T. C. and Richards, C. E., "Fatigue Crack Growth at Low Stresses in Steels," Central Electricity Generating Board Laboratory Note No. RD/L/N 135/78, Aug. 1978 (Central Electricity Research Laboratories, Leatherland, U.K.).

[15] Stewart, A. T., *Engineering Fracture Mechanics*, Vol. 13, 1980, pp. 463-478.

[16] Benoit, D., Namdar-Tixier, R., and Tixier, R., *Materials Science and Engineering*, Vol. 45, 1980, pp. 1-7.

[17] Elber, W. in *Damage Tolerance in Aircraft Structures, ASTM STP 486*, American Society for Testing and Materials, 1971, pp. 230-262.

[18] Schmidt, R. A. and Paris, P. C. in *Progress in Flaw Growth and Fracture Toughness Testing, ASTM STP 536*, American Society for Testing and Materials, 1973, pp. 79-94.

[19] Cooke, R. J., Irving, P. E., Booth, G. S., and Beevers, G. J., *Engineering Fracture Mechanics*, Vol. 7, No. 1, March 1975, pp. 69-77.

[20] Irving, P. E. and Kurzfeld, A., *Metal Science*, Vol. 12, No. 11, Nov. 1978, pp. 495-502.

[21] Simmons, G. W., Pao, P. S., and Wei, R. P., *Metallurgical Transactions A*, Vol. 9A, No. 8, Aug. 1978, pp. 1147-1158.

J. D. Landes[1] *and D. E. McCabe*[1]

Design Properties for Steels Used in Coal Conversion Vessels

REFERENCE: Landes, J. D. and McCabe, D. E., "**Design Properties for Steels Used in Coal Conversion Vessels,**" *Application of 2¼Cr-1Mo Steel for Thick-Wall Pressure Vessels, ASTM STP 755.* G. S. Sangdahl and M. Semchyshen, Eds., American Society for Testing and Materials, 1982, pp. 68-92.

ABSTRACT: A fracture-mechanics related approach was used to evaluate the performance of 2¼Cr-1Mo in simulated coal conversion environments. Two heats of ASTM A 387 and ASTM A 542 were prepared in the form of commercially produced weldments on 178-mm (7-in.)-thick plate. Base metal, weld metal, and heat-affected zone (HAZ) were investigated. In addition, a simulation of Type 347 stainless steel weld overlay was prepared.

The sensitivity to environmentally enhanced crack growth was evaluated by rising load test for exposure in 6 percent H_2S-Balance H_2. The temperature range covered was from room temperature to 727 K (850°F), and pressures were from 5.5 to 24.1 MPa (800 to 3500 psi). Fixed-displacement wedge-loaded specimens were exposed in 100 percent H_2 at 24.1 MPa for six months.

Results indicate that 2¼Cr-1Mo in all metallurgical conditions will be sensitive to environmental cracking in 6 percent H_2S-Balance H_2 at room temperature. At 588 K (600°F) effects due to 6 percent H_2S-Balance H_2 are minimal, but at 727 K significant environmentally assisted plasticity develops.

Fixed-displacement specimens in high-pressure hydrogen were found to have severely degraded postexposure toughness. The mechanism of degradation is believed to be hydrogen-assisted cracking. It also was found that highly preloaded and cracked specimens of 2¼Cr-1Mo will develop creep at temperatures as low as 727 K.

KEY WORDS: coal conversion, pressure vessels, chromium-molybdenum steels, environment, hydrogen, hydrogen sulfide, liquefaction, fracture, testing, plasticity

Coal conversion processes currently envisioned for converting coal to more useful forms of energy use various sizes and types of steel pressure vessels that operate at high pressures and temperatures. Continuous, safe, and reliable performance of these vessels is vital to the successful development of commercial operations. The basic problem is not only high pressures and

---

[1] Advisory Engineer and Senior Engineer, respectively, Westinghouse R&D Center, Pittsburgh, Pa. 15235.

temperatures, but also hostile aggressive hydrogen-containing environments. These environments, in conjunction with the high pressures and temperatures, could have pronounced detrimental effects on vessel materials, causing cracks to initiate and propagate, ultimately resulting in a structural failure. In addition, it is possible that the structural integrity of the pressure vessels will suffer from some form of material toughness degradation that is dependent on time, temperature, pressure, and environment.

A fracture-mechanics approach to design can be used to quantify these deteriorations and thus improve reliability and to reduce unscheduled equipment outages. Since fracture mechanics will almost certainly come to dominate pressure-vessel design in the future, the dependence of subcritical crack growth upon stress, flaw dimensions, temperature, gas composition, gas pressure, and time have to be determined. Therefore a fracture-mechanics approach was taken in this program which represents a first attempt to apply this technology to study high temperature and pressure effects on pressure vessel grade steels.

One objective of this program was to develop the testing procedures and background data needed to evaluate quantitatively the structural reliability of pressure vessels for coal conversion systems. Because this was a first attempt to develop data of this type, emphasis was placed on obtaining an overview of the types of behavior which may be important for pressure vessel evaluation rather than developing detailed information in any one area. Another objective was to identify any problem areas that might be of concern in the design and operation of coal conversion pressure vessels. Once identified these problem areas could be studied more completely in future programs. The environments used consisted mainly of a mixture of H_2 and H_2S gases. Pressures of up to 24.1 MPa (3500 psi) and temperatures up to 727 K (850°F) were used. Typical combinations were 10.3 MPa (1500 psi) pressure at 689 K (600°F) simulating vessel wall conditions for coal gasification processing, and 24.1 MPa at 727 K simulating coal liquefaction vessel wall conditions that are directly exposed to the reaction process, and protected only by Type 347 stainless steel welded on cladding.

Materials

Two grades of 2¼Cr-1Mo steel were chosen for testing: a normalized and tempered ASTM Specification for Pressure Vessel Plates, Alloy Steel, Chromium-Molybdenum (A 387-79b) Class 2, Grade 22 steel, and a quenched and tempered ASTM Specification for Pressure Vessel Plates, Alloy Steel, Quenched and Tempered Chromium-Molybdenum (A 542-79) Class 3 steel. These steels were supplied as submerged arc weldments of approximately 178 mm (7 in.) thickness. Pressure vessels for coal liquefaction processes are to be clad with Type 347 stainless steel, and a weldment was also prepared on ASTM A 387 plate to simulate this cladding material.

The plates were manufactured by Lukens Steel Company, and weldments were prepared by Chicago Bridge & Iron Company (CB&I), a major producer of welded pressure vessels. Five heats were used to fabricate all of the test pieces; two heats for the ASTM A 387 normalized and tempered weldment (Heat Nos. 3324 and 3596), two heats for the ASTM A 542 quenched and tempered weldment (Heat Nos. 7868 and 3707), and one heat of ASTM A 387 as vessel body material for the Type 347 stainless steel overlay (Heat No. 4040). All weldments were made in accordance with CB&I commercial welding practice. The ASTM A 387 weldment was made with Linde 124 flux and ASTM A 542 with Linde 0091 flux. The Type 347 stainless steel overlay was fabricated using a special geometry to allow for the preparation of fracture mechanics type specimens. The first pass of the overlay was a columbium-modified Type 309 stainless steel, and when diluted by the 2¼Cr-1Mo substrate during welding gives the aim composition for Type 347 stainless steel. Subsequent passes were made with Type 347 stainless steel filler wire. A section of the ASTM A 387 weld metal was subjected to a deliberate temper embrittling treatment. This was done so that the crack growth behavior of temper embrittled (T.E.) weld metal due to coal conversion environments could be compared with in air temper embrittlement effects.

Material characterization included tensile properties (Table 1, Section A), chemistries reported by Lukens Steel Company (Section B), and fracture toughness from a Charpy V transition temperature standpoint as well as fracture-mechanics, J_{Ic}-tests (Section C).

Facilities

Measurement requirements on fracture-mechanics type specimens are precise, and applied load versus specimen displacement should be measured accurately to stringent precision not common in ordinary mechanical testing. Conducting such tests under high-temperature and high-pressure conditions presents a special challenge, and a great deal of effort was put into the design and development of a test system, the heart of which is shown in Fig. 1.

The special feature making this test chamber unique is that there are no friction seals on the measuring devices which are located outside the chamber, namely, the load cell and the Linear Variable Differential Transducer (LVDT) that measures extended front face displacement. The load cell is made an integral part of the chamber pressure system and pressure effects are electronically zeroed out.

The environment used most in the present project was 6 percent H_2S–Balance H_2, and because the 2¼Cr-1Mo and chamber walls had a high affinity to react with H_2S, the concentration was expected to rapidly diminish with time. Therefore the gas had to be supplied on a flowing basis.

A scheme to produce 6 percent H_2S-H_2 on a continuous basis was devised as illustrated in Fig. 2. A commercial autoclave was used as a mixing

TABLE 1—*Properties of 2¼Cr-1Mo materials selected for the present study.*

Section A—Tensile and Impact Properties

		Tensile Properties			Room Temperature Charpy V Impact		
Heat No.	Grade	Yield Strength, MPa	Tensile Strength, MPa	% Elongation at 44 mm	Test Temperature, K	Impact Energy, J	Fract./Appear., % Brittle
3596	A 387	313	521	30.1	298	165	16
Weld	A 387	440	589	57.7[a]	298	115	14
7868	A 542	495	608	23.6	298	176	0
Weld	A 542	559	696	50.2[a]	298	58	54
Temper-Embrittlement Weld	A 387	...	...	...	298	29	90
347 stainless		596	807	41.4[a]	339	77	0

Section B—Base Plate Chemistries

Grade	Heat No.	C	Mn	P	S	Cu	Si	Ni	Cr	Mo
A 387	3596	0.12	0.42	0.013	0.020	0.16	0.25	0.14	2.48	1.06
A 542	7868	0.12	0.47	0.010	0.017	0.12	0.22	0.22	2.26	0.99
	ASTM Specification for 2¼Cr-1Mo Steel, A 387 and A 542									
	minimum	...	0.27	...	...	...	...	...	1.88	0.85
	maximum	0.15	0.63	0.035	0.035	...	0.50	...	2.62	1.15

Section C—Toughness Evaluation Summary

Material	Heat	J_{Ic}, kJ/m^2	K_{Ic}, MPa$\sqrt{m}$	Upper-Shelf CVN, J	FATT
387	3596	560	340	183	294 K (70°F)
A 387 WM		210	208	117	275 K (35°F)
A 387 WM-T.E.		420	295	127	344 K (160°F)
A 387 HAZ		350	269	171	...
347 stainless		140	170	77	...
A 542	7868	440	302	180	244 K (−20°F)

[a] 6.4 mm gage length.

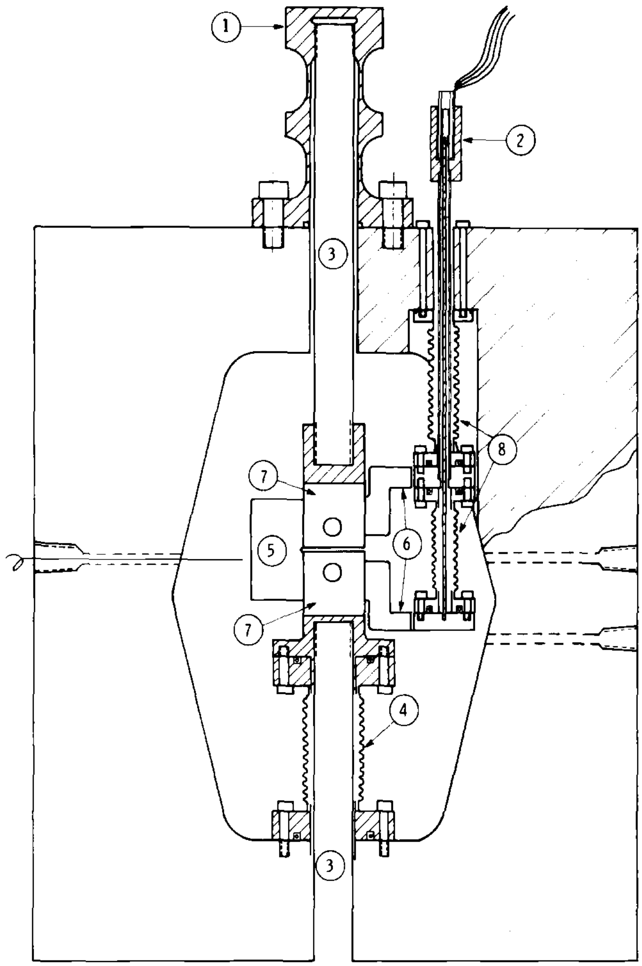

1 Load cell
2 LVDT
3 Connecting rods
4 Bellows
5 Specimen
6 Extension arms for displacement measurements
7 Specimen loading clevisis
8 LVDT bellows

FIG. 1—*Sectioned view of high-pressure dynamic loading chamber.*

chamber. The liquid layer of H_2S produces a partial pressure of H_2S gas which is controlled by regulating the temperature of the liquid. High-pressure hydrogen gas is added such that the gas mix will be 6 percent H_2S by volume. This gas source is then tapped at a controlled rate using a pressure regulator.

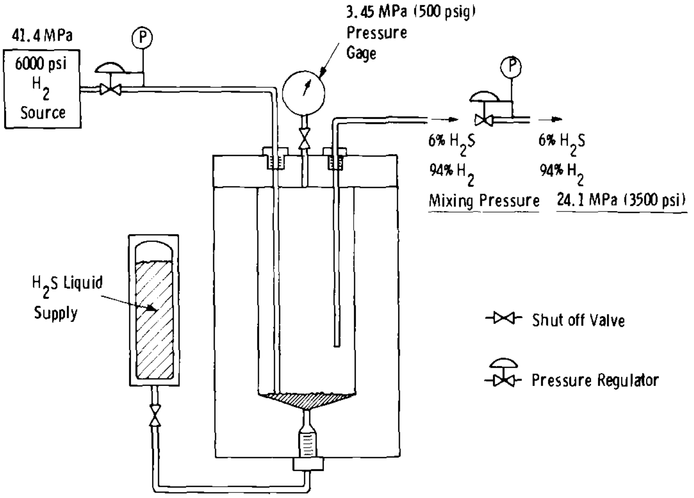

FIG. 2—*Schematic of an autoclave system for generating 6 percent H_2S-94 percent H_2 gas mixture on a continuously flowing system.*

Rising-Load Tests

Rising-load tests are used to identify the onset of environmentally enhanced crack growth [*1*].[2] For ultra high-strength materials this corresponds to K_{Iscc}, but for 2¼Cr-1Mo steel the method can only be justified for ranking the severity of material-environment combinations. In the present project, the objective was to cover the range of environment versus material conditions of greatest interest and to identify the most critical for more detailed study. Emphasis was placed on testing ASTM A 387 because it is considered the primary candidate material for coal liquefaction vessels.

The compact specimen shown in Fig. 3 is loaded under displacement control at a rate such that the load increases about 67 N (15 lb) per minute. This corresponds to a $\dot{K}_{\mathrm{I}}$-rate of 0.11 MN/m$^{3/2}$ per minute.

In the rising-load method, a baseline load-displacement record is developed to characterize the material under nonaggressive conditions (Fig. 4*a*). When an identical specimen is loaded at the same rate in environment, a deviation from the baseline behavior indicates the onset of environmentally assisted crack growth. The load at first deviation, P_{Iscc}, can be used to estimate K_{Iscc}. If the environmental attack mechanism is weak, first deviation may be difficult to determine. This in particular can be a problem if initial specimen dimensions are not identical (specifically initial crack size) or if there is substantial plastic deformation prior to onset of deviation (Fig. 4*b*).

A modified analysis procedure was introduced in the present program to

---

[2] The italic numbers in brackets refer to the list of references appended to this paper.

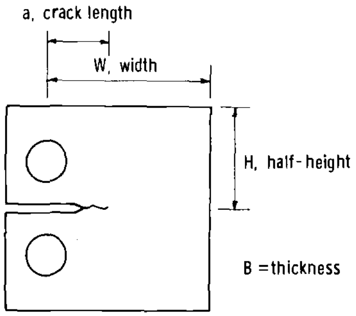

FIG. 3—*Compact specimen geometry employed in rising-load tests* (H/W = *0.6;* B/W = *0.5;* a_0/W = *0.5*).

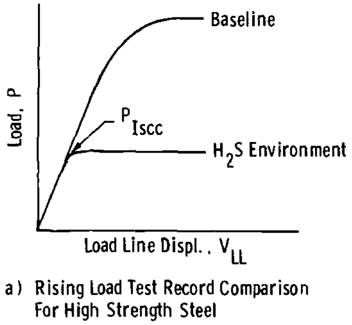

a) Rising Load Test Record Comparison For High Strength Steel

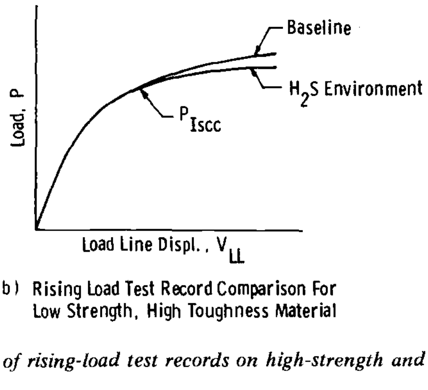

b) Rising Load Test Record Comparison For Low Strength, High Toughness Material

FIG. 4—*Schematic of rising-load test records on high-strength and low-strength steels.*

add versatility to test record comparisons. Every test record has an initial linear-elastic portion, the slope of which is related to the displacement measurement location and initial crack size (Fig. 5*a*). For any load above the linear elastic level, displacement will have an elastic component, V_e, and a nonlinear component ΔV due to plastic deformation or possibly mixed

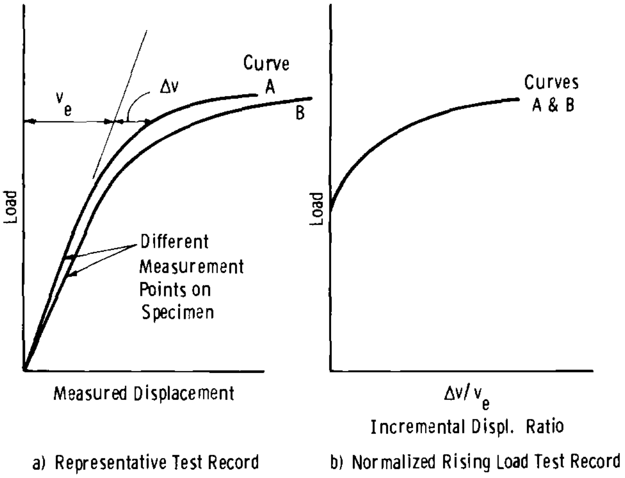

FIG. 5—*Schematic of test record normalization for rising-load tests.*

plastic deformation and crack growth. If the ΔV is normalized by V_e, as in Fig. 5*b*, elastic displacement contributions are eliminated and test record comparisons are made more sensitive for showing plasticity development and crack growth.

As a result of this, three categories of test record have been identified (Fig. 6). For ultra high-strength materials, deviation is from linear-elastic behavior as before, and load P_{Iscc} is used to estimate K_{Iscc} (Fig. 6*a*). For ductile materials in the category of 2¼Cr-1Mo and for room temperature testing in 6 percent H_2S-Balance H_2, onset of crack growth at P_{Iscc} occurs after substantial plasticity (Fig. 6*b*). A plasticity corrected K_{Iscc}-value can be determined. However, this cannot be correctly defined as a design-usable K_{Iscc} without supporting evidence from tests of another type [*2*]. For tests at high temperature in 6 percent H_2S-Balance H_2, early deviation from baseline be-

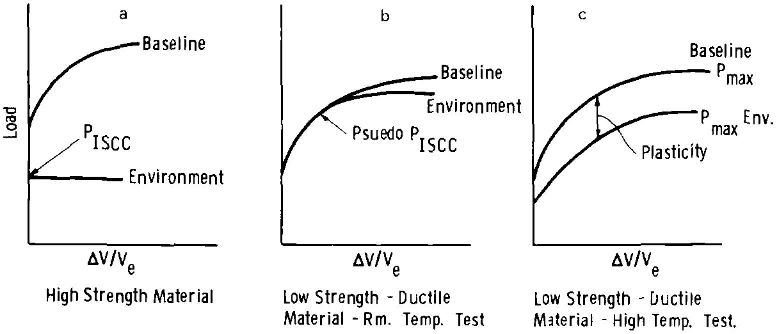

FIG. 6—*Three categories of rising-load records.*

havior was seen which was not associated with crack growth (Fig. 6*c*). Deviation was due to early plasticity development, and a $K_{\rm Iscc}$-determination at first deviation is of doubtful use as an evaluation criterion. For these cases, there usually was very little crack growth to maximum load (identified from a post-test fracture surface examination), and the ratio of maximum loads, comparing environment with baseline, provided a specimen geometry dependent criterion for ranking material-environment sensitivities. The type of test record in Fig. 6*c* might also be caused by environmentally induced crack growth. In this case, however, it was positively identified as environmentally induced plasticity from a post-test fracture surface examination which confirmed that there was essentially no crack growth.

Rising-Load Test Results

Tests conducted at room temperature in 6 percent H_2S-Balance H_2 showed that 2¼Cr-1Mo exhibits environmentally assisted crack growth. A representative test record is shown in Fig. 7, and Table 2 lists the $K_{\rm Iscc}$-values calculated. Again, the $K_{\rm Iscc}$-values reported here could be nonconservative compared with $K_{\rm Iscc}$ from long-time testing. Nevertheless, these nonconservative $K_{\rm Iscc}$-values are generally on the order of ¼ to ⅓ of the room temperature toughness capability of these materials as measured by $J_{\rm Ic}$ in air. Environmental pressures between 5.6 and 24.1 MPa were only of secondary influence, giving slightly decreased $K_{\rm Iscc}$ with increased pressure.

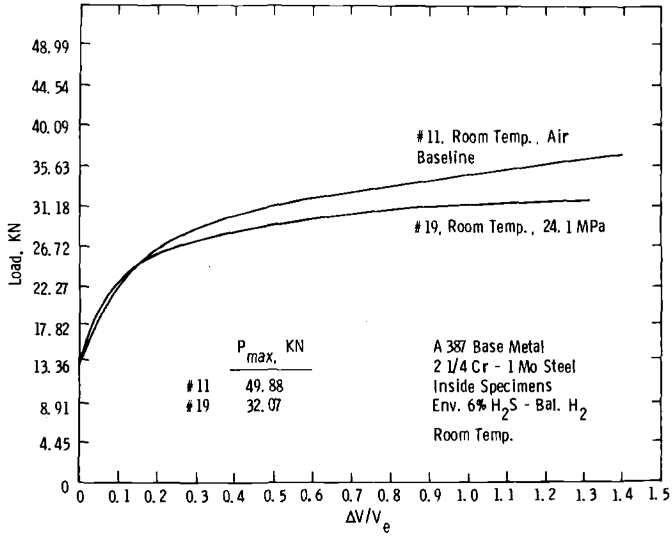

FIG. 7—*Rising-load test record for ASTM A 387 base metal, inside-slab centerline position, room temperature.*

TABLE 2—K_{Ic} *from* J_{Ic} *and* K_{Iscc} *by rising load for ASTM A 387 and ASTM A 542 base metal (BM), weld metal (WM), and heat-affected zone (HAZ) room temperature in 6 percent* H_2S*-Balance* H_2.

	Pressure		K_{Iscc}		K_{Ic} from J_{Ic}	
Material	MPa	(psi)	MPa$\sqrt{m}$	(ksi$\sqrt{in.}$)	MPa$\sqrt{m}$	(ksi$\sqrt{in.}$)
A 387 BM	10.3	(1500)	83.8	(76.2)	286	(260)
A 387 BM	24.1	(3500)	76.9	(69.9)	286	(260)
A 387 WM	24.1	(3500)	68.1	(61.9)	307	(279)
A 387 HAZ	24.1	(3500)	45.8	(41.6)	297	(270)
A 387 WM[a]	24.1	(3500)	48.2	(43.8)	...	...
A 542 BM	5.5	(800)	96.8	(88.0)	295	(268)
A 542 BM	10.3	(1500)	98.0	(89.1)	295	(268)
A 542 BM	24.1	(3500)	67.9	(61.7)	295	(268)
A 542 WM	24.1	(3500)	77.0	(70.0)	...	...

[a] Temper embrittled.

Table 3 presents a summary of the results of tests conducted at 588 K (600°F). In general, it can be stated that the performance of 2¼Cr-1Mo in all metallurgical conditions is near that of baseline behavior at 588 K in benign environment, namely, air. In other words, the aggressive attack of 6 percent H_2S-Balance H_2 environment seen at room temperature is for all intents and purposes eliminated at 588 K. An exception was for ASTM A 542 weld metal, which retained a propensity for environmentally assisted cracking (Fig. 8). Also, a metallurgical condition peculiar to the midthickness of ASTM A 387 base material showed the first evidence of hydrogen-assisted plasticity (Fig. 9). The evidence was weak and was manifest only in early deviation from baseline load versus displacement behavior. There was no accompanying enhanced crack growth or loss of maximum load carrying capability of the specimens.

Rising-load tests conducted at 727 K are summarized in Table 4, and a typical test record is shown in Fig. 10. Again there was very little crack growth to maximum load, and the evidence of hydrogen-assisted plasticity was manifest as both early deviation from baseline behavior and a loss in maximum load carrying capability on the specimen. Virtually all the 2¼Cr-1Mo conditions displayed this environmentally assisted plasticity, and the summation of these effects is shown in Fig. 11 in the 727 K grouping. Here the maximum load in environment is compared with baseline maximum load. At 727 K, there is relatively minor crack growth and the loss in strength is due principally to enhanced plasticity effects. At 588 K, all materials appear to perform satisfactorily, with the exception of ASTM A 542 weld metal which displayed the crack growth shown in Fig. 8. Reduced load bearing capability of the room temperature specimens was due strictly to the environmentally enhanced crack growth.

A further interesting observation was that many specimens which dis-

TABLE 3—*Rising-load tests at 588 K (600°F), 6 percent H_2S-Balance H_2.*

Material	Position O/I[a]	Pressure, MPa	K_{Iscc}/H_2 Plastic	P_{max}, kN		Post-Test Information			
				Baseline	Test	P_{max}, kN[b]	D/B[c]	Δa_p, mm[d]	δ_{total}, mm[e]
A 387	O	5.5	no effect	48.23	46.32	50.11	D	0	3.56
A 387	I	5.5	H_2 plasticity	45.88	43.20	11.14	B	0	3.91
A 387	O	10.5	no effect	48.23	45.65	48.99	B	0.38	...
A 387	I	24.1	H_2 plasticity	45.88	41.87	10.69	B	0.38	3.84
A 387 WM		10.5	no effect	61.02	57.01	61.91	D	1.65	3.30
A 387 HAZ		10.5	no effect	...	56.12	58.79	D	0	3.66
A 387 WM-T.E.		10.5	no effect	61.02	58.35	49.00	B	1.27	3.25
A 387 WM-T.E.		24.1	slight H_2 plasticity	61.02	51.89	53.45	B	0.71	3.81
A 542	O	5.5	no effect	67.70	64.14	66.81	D	1.14	2.69
A 542	O	24.1	slight H_2 plasticity	67.70	55.23	59.68	D	1.52	3.81
A 542 WM		10.5	$K_{Iscc} = 189$ MN/m$^{3/2}$	73.04	52.56	52.33	B	4.06	1.60
A 542 HAZ		10.5		...	61.69	66.81	D	1.90	3.05

[a] O = outside of slab centerline; I = inside near slab centerline.

[b] Maximum load in breaking open at room temperature.

[c] Ductile versus brittle cracking mode.

[d] Physical crack growth in rising-load test.

[e] Total displacement, δ, at LVDT in rising-load test.

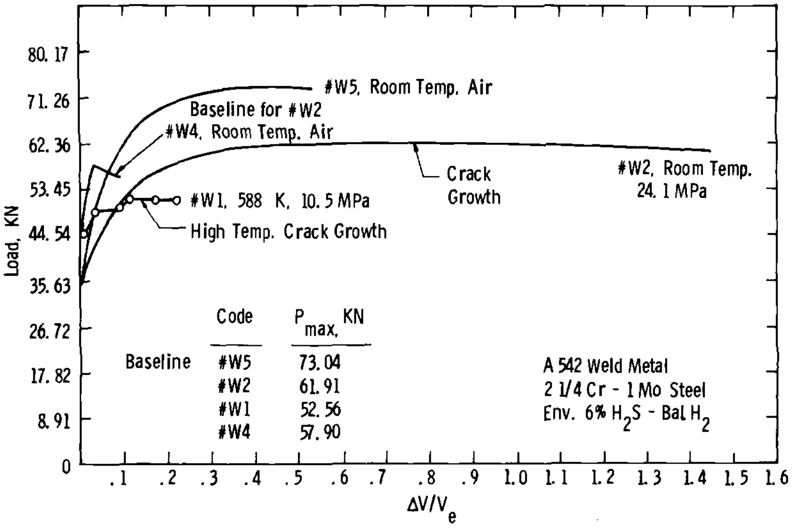

FIG. 8—*Rising-load test records for ASTM A 542 weld metal.*

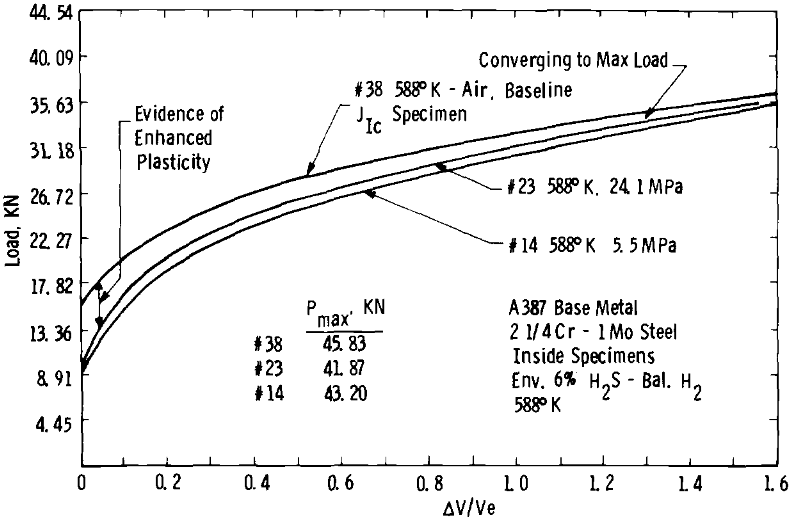

FIG. 9—*Rising-load test record for ASTM A 387 base metal, inside-slab centerline position, 588 K.*

played H_2-assisted plasticity in rising-load tests broke brittlely in post-test opening of specimens at room temperature. In fact the worst case was for the 588 K rising-load specimens of ASTM A 387 base metal which showed marginal hydrogen-assisted plasticity. Room temperature brittle fracture occurred at $K_1 = 18$ MPa$\sqrt{m}$. The baseline behavior of almost all of these materials was ductile in room-temperature tests.

TABLE 4—*Rising-load tests at 727 K (850°F), 6 percent H_2S-Balance H_2.*

Material	Position O/I[a]	Pressure, MPa	K_{Iscc}/H_2 Plasticity	P_{max}, kN		Post-Test Information			
				Baseline	Test	P_{max}, kN[b]	D/B[c]	Δa_p, mm[d]	δ_{total}, mm[e]
A 387	I	5.5	H_2 plasticity	41.18	31.18	39.20	B	1.40	3.45
A 387	I	10.5	H_2 plasticity	41.18	30.73	42.76	B	1.40	3.81
A 387	O	24.1	H_2 plasticity	45.97	33.63	44.54	D	0.25	3.81
A 387 WM		24.1	H_2 plasticity	57.01	42.53	51.66	D	0.51	3.86
A 387 WM-T.E.		10.5	H_2 plasticity	58.35	41.87	52.56	D/B	0.89	3.81
A 387 WM-T.E.		20.7	H_2 plasticity	58.35	40.35	57.90	D	1.38	3.81
A 387 HAZ		24.1	H_2 plasticity	...	28.95	13.36	B	2.18	3.81
A 542	O	10.5	H_2 plasticity	59.68	46.82	...	D	1.14	3.81

[a] O = outside of slab centerline; I = inside near slab centerline.

[b] Maximum load in breaking open at room temperature.

[c] *Ductile versus brittle cracking mode.*

[d] Physical crack growth in rising-load test.

[e] Total displacement, δ, at LVDT in rising-load test.

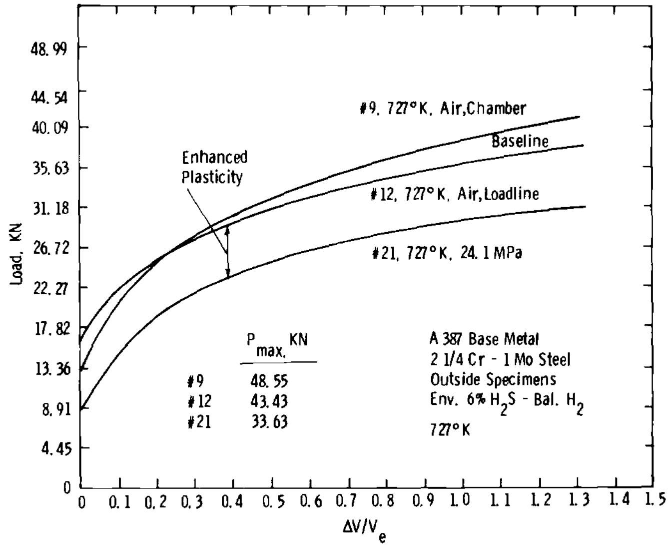

FIG. 10—*Rising-load test record for ASTM A 387 base metal, outside centerline of slab, 727 K.*

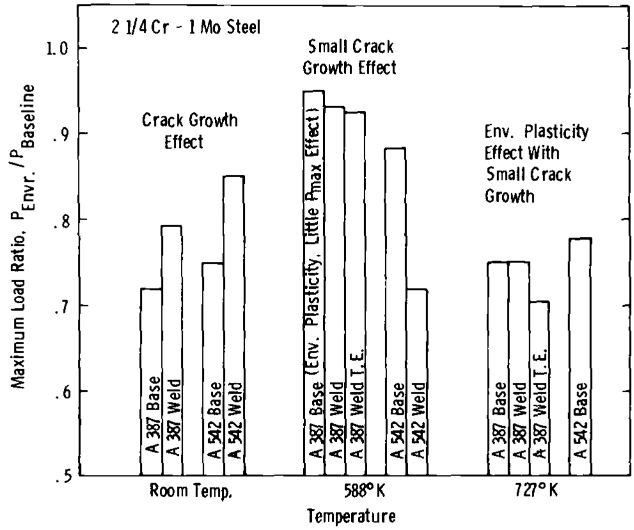

FIG. 11—*Ratio of maximum load in environment to baseline for various temperature and material conditions.*

Two rising-load tests were conducted in 100 percent hydrogen at 10.5 MPa and 588 K using ASTM A 387 and A 542 base metal specimens. The results showed no effects due to the high-pressure hydrogen environment. The test on ASTM A 387 was not particularly typical, but the overall result in both cases clearly indicated that there was no effect of significance compared with the behavior with 6 percent H_2S. However, the 588 K test temperature chosen did not produce strong effects even with 6 percent H_2S environment; thus it cannot be concluded that 100 percent hydrogen will not affect the material behavior; only that the 100 percent hydrogen severity was not markedly stronger than that of 6 percent H_2S-Balance H_2.

The specimen construction for testing the simulation of weld overlay material is shown in Fig. 12. The aim was to have the material to be tested embedded in ASTM A 387 vessel wall material. The machined notch in the CT specimen projects to 6.3 mm (0.25 in.) from the bottom of the weldment, and a 2.5 mm (0.10 in.) fatigue precrack would leave 3.8 mm (0.15 in.) of overlay material to be tested.

Rising-load records from tests at 727 K are presented in Fig. 13. Room-temperature baseline maximum load is 37.4 kN, which is reduced to 30.45 kN at 727 K, and this is essentially a reflection of the loss in high-temperature strength. This difference, of course, is dominated by the ASTM A 387 host material. Judging from the closeness of all the rising-load records, there was no detectable effect of 727 K and 6 percent H_2S-H_2 environment on the crack growth behavior of Type 347 stainless steel. The size of the weld ligament dimensions involved is tabulated in Fig. 13.

Fixed-Displacement Test Method

This experimental method is designed to allow environmentally enhanced crack growth under decreasing K_I until crack arrest at K_{Iscc} (Fig. 14); and this procedure is regarded as the more accurate method of determining K_{Iscc} [*3*]. The specimen is loaded to a relatively high initial K_I using the split-pin wedge shown. The time needed to cause crack growth incubation is a func-

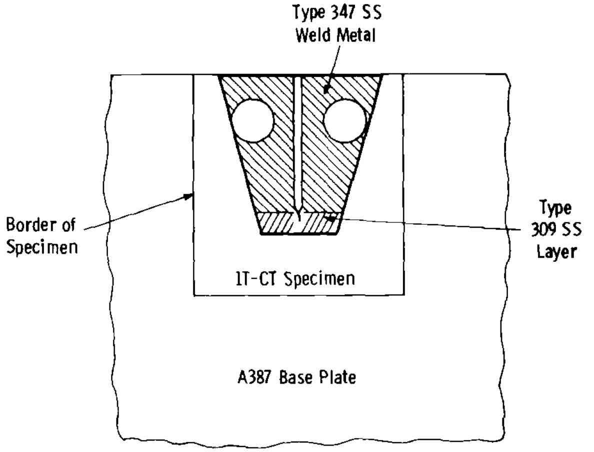

FIG. 12—*Specimen location for 1T-CT in Type 347 stainless steel overlay.*

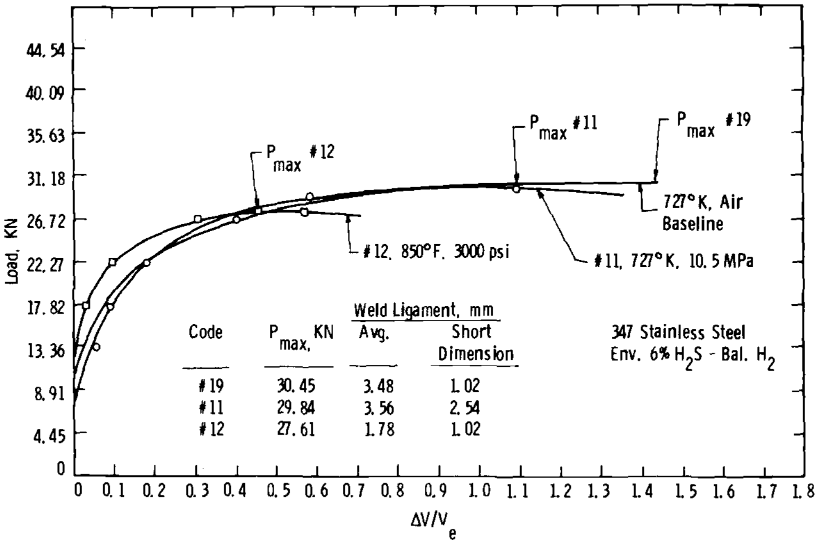

FIG. 13—*Rising-load test records for Type 347 stainless steel overlay (727 K).*

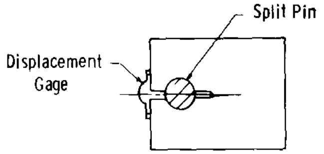

WOL specimen modified for use as a stress corrosion susceptibility test specimen

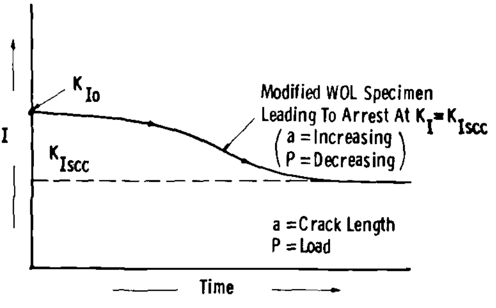

FIG. 14—*Modified WOL specimen behavior.*

tion of environment aggressiveness and initial K_I. These tests were made in 100 percent H_2 at 24.1 MPa and 727 K (850°F), and since the severity of the high-temperature environment was not known beforehand, the specimens were preloaded to a large displacement, to approximately the J_{Ic}-level. J_{Ic} is defined as the point at which there is onset of stable crack growth in fracture mechanics type specimens when they are tested in air. Exposure time was for six months (4000 h) at room temperature and pressure. This temperature-pressure combination is almost exactly on the limiting condition for decarburization damage of 2¼Cr-1Mo as indicated by the Nelson curve (Fig. 15) [*4*]. After exposure, visual evidence of crack growth was checked by examining the specimen surfaces. The specimens were then unloaded by removing the split-pin wedges and measuring unloading displacement. Next they were reloaded in tension grips and the load corresponding to unloading displacement noted, indicating the postexposure wedge load. In the process, full reload load-displacement measurements were made to near complete fracture of the specimens, even though the objective was only to reveal the extent of environmentally enhanced crack propagation. The additional information obtained because of this proved to be the observation of principal value.

Fixed-Displacement Test Results

Virtually all specimens were found to be totally unloaded after exposure. Measurement of postexposure pin diameters indicated that the set point on displacements had been maintained and that the unloading was due to creep deformation, ostensibly at the specimen crack tips. Postexposure examination for crack growth indicated that ASTM A 387 WM, A 542 BM, A 542 WM, and A 542 HAZ developed environmental crack growth in 727 K - 24.1 MPa H_2. Crack advance in these cases was on the order of 1 mm (0.04 in.), but K_{Iscc} could not be determined because load at crack arrest was not known. Figure 16 illustrates typical preexposure and postexposure loading test

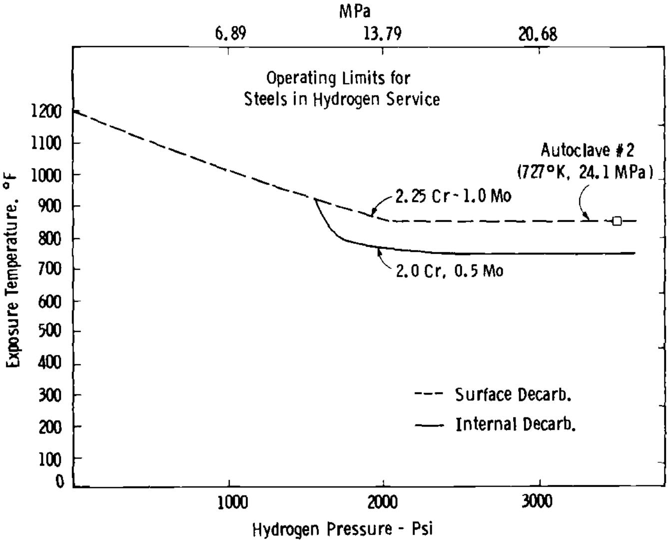

FIG. 15—*Autoclave exposure positions on the Nelson curve.*

records. The postexposure maximum loads were always much less than the preload levels set by the wedges, often less than ½ this value (Table 5). If the material were undamaged, the reload would return to the preload set point level. The reason for the loss in load-carrying capability was loss in material toughness.

The easy crack propagation mode in postexposure opening of exposed ASTM A 387 and A 542 K_{Iscc}-specimens was fully intergranular. Figure 17 is a fractograph of ASTM A 387. The introduction of fast loading for final ligament separation resulted in a change in fracture mode to dimpled rupture (Fig. 18). This suggests that the toughness loss was due to retained hydrogen.

A further point of interest was that the specimens had been out of the exposure chamber for several weeks prior to the final opening. This represents time enough for more than 50 percent of the entrapped hydrogen to escape.

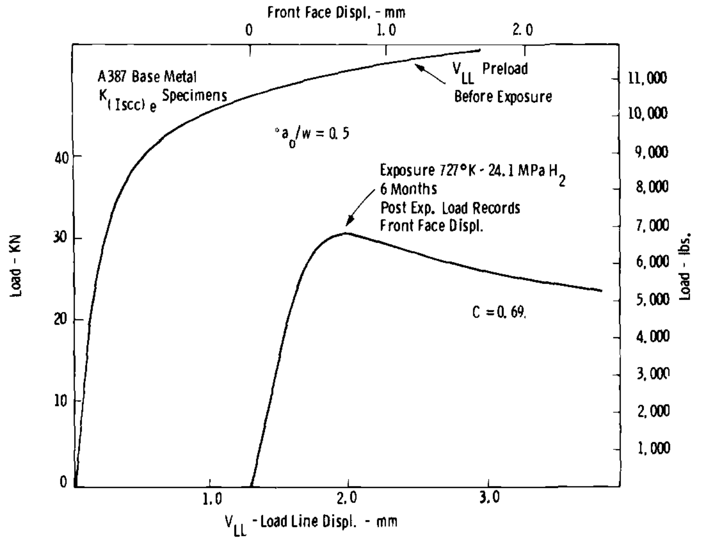

FIG. 16—*Preload and postexposure test records for ASTM A 387.*

TABLE 5—*Test load before and after 727 K (850°F)-H_2 exposure.*

Material	Preload, kN (kips)	Room Temperature Postexposure Load, kN (kips)
A 387 BM	51.2 (11.5)	30.3 (6.8)
A 387 WM	61.4 (13.8)	34.7 (7.8)
A 387 HAZ	56.1 (12.6)	14.7 (3.3)
A 387 WM-T.E.	53.0 (11.9)	32.5 (7.3)
A 542 BM	65.0 (14.6)	19.6 (4.4)
A 542 WM	57.0 (12.8)	7.6/20.5 (1.7/4.6)
A 542 HAZ	72.1 (16.2)	21.4 (4.8)

FIG. 17—*Easy crack propagation surface on ASTM A 387 after 727 K-24.1 MPa H_2 exposure; room temperature; SEM X500.*

However, this estimation was arrived at using an assumption that the hydrogen was diffusing through a normal undistorted microstructure.

The six months' exposure in the autoclave at 727 K — 24.1 MPa H_2 did not show an unusually severe effect from the microstructure standpoint. Surface decarburization was slightly less than 1 mm, and the bainitic carbide platelets at midthickness were substantially retained (Figs. 19 and 20). However, carbon extraction replicas indicated a slight buildup of grain boundary carbides.

Summary of Findings

Rising-Load Tests

All metallurgical conditions of ASTM A 387 and A 542 base metals and weldments suffered environmentally enhanced cracking in 6 percent H_2S-H_2

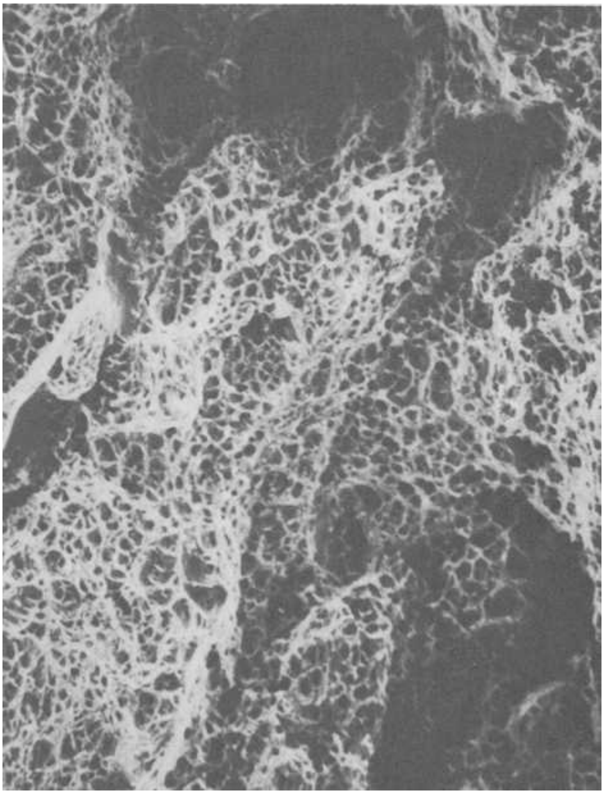

FIG. 18—*Fast fracture surface on ASTM A 387 after 727 K-24.1 MPa H_2 exposure; room temperature; SEM X300.*

at room temperature. Initiation of crack growth occurs at K_I-levels approximately between ¼ to ⅓ of the material baseline toughness.

For rising-load tests at 588 K the propensity for environmental cracking is substantially diminished in almost all materials. However, the metallurgical condition peculiar to the ASTM A 387 centerline material of base plate (inside specimens) developed some evidence of hydrogen-assisted plasticity. An ASTM A 542 weld metal material in 10.5 MPa 6 percent H_2S-H_2 displayed environmental cracking; this was the only classical case of rising-load crack growth behavior observed at elevated temperatures.

For tests at 727 K, all metallurgical conditions, base metals, weld metals, and heat-affected zones displayed marked evidence of hydrogen-assisted plasticity. Crack growth increased marginally over that at 588 K. An interesting aspect is that many of the specimens that showed this hydrogen-assisted plasticity in rising-load tests failed in a brittle manner in post-test opening of the specimens at room temperature. This is a result of either a

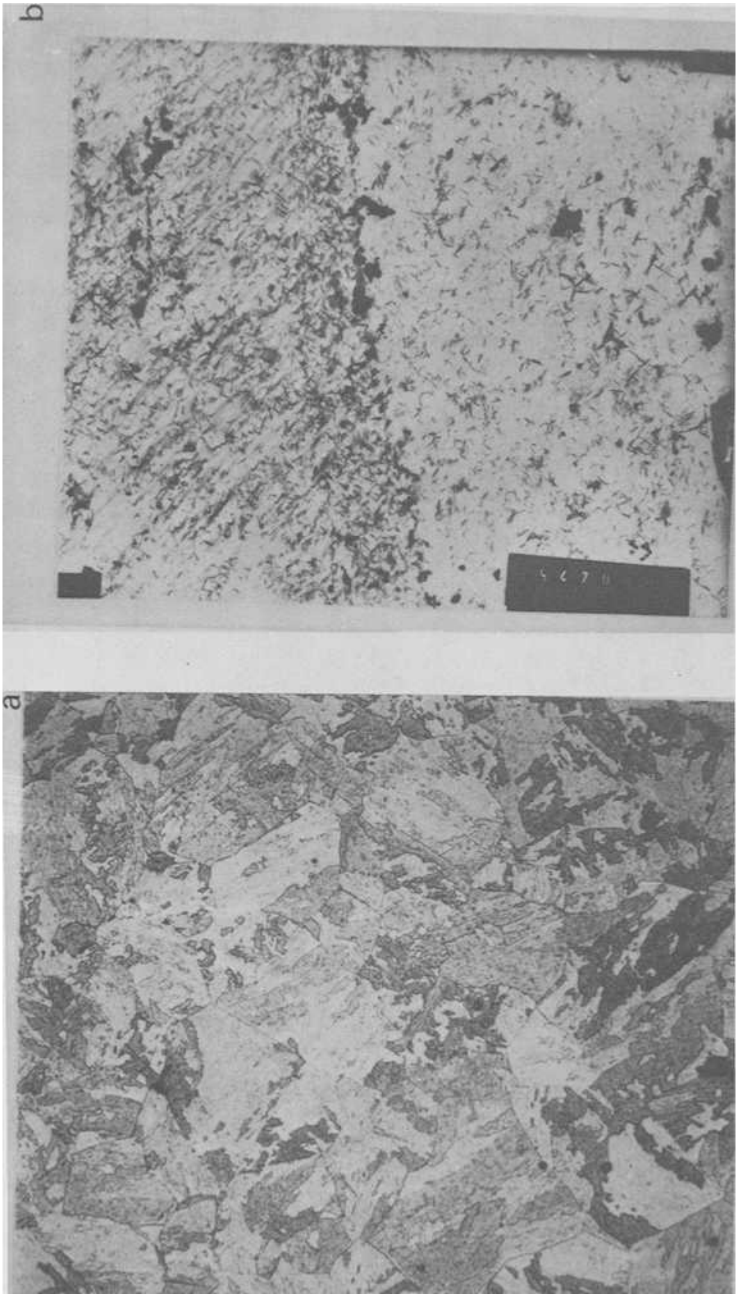

FIG. 19—(a) *ASTM A 542 as-received micrograph, Vilella's etch, X200.* (b) *ASTM A 542 as-received carbon extraction replica, X5800.*

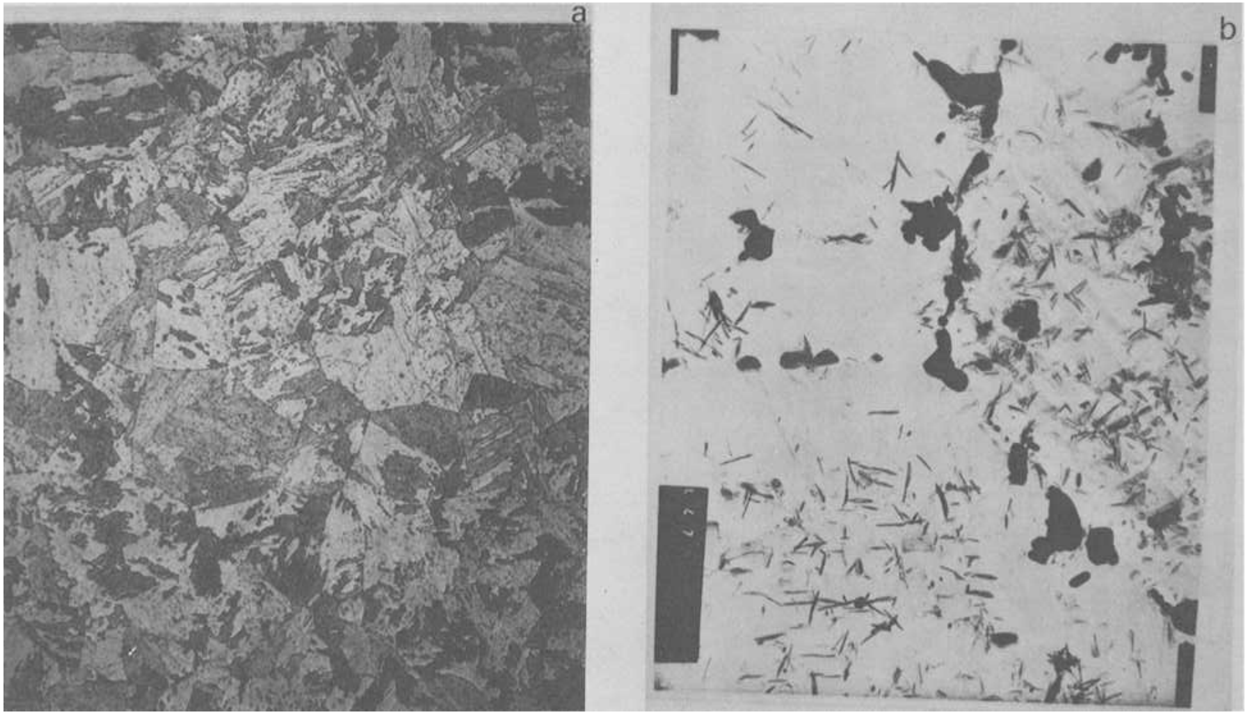

FIG. 20—(a) *ASTM A 542 after 727 K-24.1 MPa* H_2 *exposure, 6 months, Vilella's etch, X200.* (b) *ASTM A 542 after 727 K-24.1 MPa* H_2 *exposure, 6 months, extraction replica, X21 000.*

transition temperature shift or the effect of residual hydrogen retained in the specimen after cooldown.

The tests on a simulation of Type 347 stainless steel overlay material indicated that there was no detectable effect of environment on this material at the simulated service temperature of 727 K.

Single rising-load tests on ASTM A 387 and A 542 base metals at 588 K and in 100 percent hydrogen showed no detectable response to the environment. This condition was expected to be more severe than the 6 percent H_2S environment because a sulfide layer that builds up on the specimen surface is reputed to impede hydrogen entry into the specimen. However, the 588 K temperature was marginal for most of these materials, and possibly an effect could have developed if the tests had been made at 727 K. In any event, 100 percent hydrogen did not appear to have a more severe effect than 6 percent H_2S-Balance H_2 environment.

Pressure of environment has not been focused on for comparisons in this report because the effects observed have been dominated by the more important variable of test temperature. However, increased pressure between 5.5 MPa and 24.1 MPa caused only slightly increased sensitivity to cracking, plasticity, or both.

Fixed-Displacement Tests

Long-term exposures of 2¼Cr-1Mo at 727 K using severely loaded fracture mechanics type specimens demonstrated the material to be creep sensitive. Conditions of ASTM A 387, A 542, and their weldments developed creep at the crack tips, and all K_{Iscc}-specimens with displacement controlled loading were found to have been virtually unloaded at the end of six months' exposure.

Examination of specimens after six months' exposure in 24.1 MPa H_2 at 727 K showed partial evidence of environmentally enhanced crack growth. The materials having slightly higher strengths, such as ASTM A 387 weld metal and ASTM A 542 base metal, weld metal, and heat-affected zone, showed about 1 mm crack growth. Materials that did not respond were ASTM A 387 base metal, ASTM A 387 heat-affected zone, and Type 347 stainless steel. K_{Iscc}-levels could not be associated with these observations, because all specimens went through gradual unloading during the six months' exposure period due to creep.

Full postexposure load-displacement records were made on all specimens, and the toughness of virtually all materials was greatly reduced as indicated by a loss in load-carrying capability. Generally almost all specimens showed a drop of 40 percent or more. The major reason for loss in toughness was easy crack propagation. The fracture mode was identified as intergranular. Microstructural evaluation indicated no substantial change in carbide morphology, but there was a slight buildup of grain boundary carbides. Fast fracture was induced in the final stages of separation and the mode changed to dimpled rupture, indicative of a hydrogen-embrittlement mechanism.

Conclusions

1. 2¼Cr-1Mo will suffer environmentally enhanced crack growth in 6 percent H_2S-Balance H_2 environment at room temperature. This applies to all metallurgical conditions investigated in this project. The usable toughness level of the materials in terms of K_I is reduced by a factor of at least three.
2. Environmentally enhanced plasticity was identified in 6 percent H_2S-Balance H_2. This was observed to a very limited extent at 588 K for a metallurgical condition peculiar to midslab thickness of ASTM A 387 base metal. At 727 K all metallurgical conditions displayed environmentally assisted plasticity.
3. The preloaded fracture mechanics specimens developed crack-tip creep at 727 K. The higher strength conditions for 2¼Cr-1Mo developed a minor amount of environmental cracking in 24.1 MPa H_2 at this temperature. After six months' exposure, the room temperature toughness of all metallurgical conditions was severely reduced. The mechanism of damage is believed to be retained hydrogen, which gives the property of easy crack propagation. The mode of fracture was identified as intergranular.
4. The information given in this report is condensed from several topical reports [*5,6*] prepared on various phases of a somewhat larger-scale project than indicated here. Other phases of study not included here were degradation of fracture toughness [*7*], creep under sustained load [*6*], and fatigue crack growth rate studies [*8*].

Acknowledgments

This project was conducted under the sponsorship of the Electrical Power Research Institute under contract RP627. Dr. R. Richman originated this project and was the EPRI project manager for most of the period of the project. He has been followed by Dr. R. Viswanathan who has seen the project through to completion. We would like to acknowledge the many helpful contributors of Drs. E. Johnson and B. Shaw of Westinghouse R&D Center. Mr. F. Gradich of the Structural Behavior of Materials Laboratory at Westinghouse R&D Center assumed the principal role of preparing the testing equipment and conducting these tests. Many others at the Westinghouse R&D Center, too numerous to mention, have made significant contributions at one time or another.

References

[*1*] McIntyre, P. and Priest, A. H., "Accelerated Test Technique for the Determination of K_{Iscc} in Steels," privately transmitted British Steel Corporation report, 1972.

[2] Wei, R. P., Novak, S. R., and Williams, D. P., "Some Important Considerations in the Development of Stress-Corrosion Cracking Test Methods," in *Proceedings*, 33rd AGARD Structures and Materials Panel Meeting, Brussels, Belgium, Oct. 1971.

[3] Novak, S. R., "A Fracture Mechanics Analysis of the Kinetics of Stress-Corrosion Crack Growth in a High Strength 12Ni-5Cr-3Mo Maraging Steel," thesis for Doctor of Philosophy degree, University of Pittsburgh, Pittsburgh, Pa., 1977.

[4] "Steels for Hydrogen Service at Elevated Temperatures and Pressures in Petroleum Refineries and Petrochemical Plants," API Publication 941, 2nd ed., June 1977.

[5] McCabe, D. E. and Landes, J. D., "Design Properties of Steels for Coal Conversion Vessels-Topical Report on Rising Load Tests," EPRI Report on RP627, Aug. 1979.

[6] McCabe, D. E. and Landes, J. D., "Design Properties of Steels for Coal Conversion Vessels-Topical Report on Long-Term Testing," EPRI Report on RP627, Feb. 1980.

[7] Landes, J. D. and McCabe, D. E., "Design Properties of Steels for Coal Conversion Vessels-Topical Report on Fracture Toughness," EPRI Report on RP627, Dec. 1979.

[8] McCabe, D. E. and Landes, J. D., "Design Properties of Steels for Coal Conversion Vessels-Topical Report on Fatigue Cracking," EPRI Report on RP627, Feb. 1980.

J. Wanagel,[1] *T. Hakkarainen,*[1] *and Che-Yu Li*[1]

Hydrogen Attack in Thick-Section 2¼Cr-1Mo Steels at Elevated Temperatures

---

REFERENCE: Wanagel, J., Hakkarainen, T., and Li, Che-Yu, **"Hydrogen Attack in Thick-Section 2¼Cr-1Mo Steels at Elevated Temperatures,"** *Application of 2¼Cr-1Mo Steel for Thick-Wall Pressure Vessels, ASTM STP 755,* G. S. Sangdahl and M. Semchyshen, Eds., American Society for Testing and Materials, 1982, pp. 93-108.

ABSTRACT: Changes in microstructure and mechanical properties of a 2¼Cr-1Mo steel under the influence of hydrogen attack at elevated temperatures were investigated. Evidence of methane bubble formation at grain boundary carbides was established by direct transmission electron microscope (TEM) and scanning electron microscope (SEM) observations. The stress-to-rupture life was found to be significantly reduced for hydrogen-exposed specimens. A new approach for data correlation in the form of Nelson curves as a function of stress is proposed.

KEY WORDS: chromium-molybdenum steels, hydrogen embrittlement, creep properties, microstructure, electron microscopy

This paper reports an investigation of the nucleation and growth of methane bubbles in a thick-section 2¼Cr-1Mo steel under high-pressure hydrogen at elevated temperatures. The effects of applied stress during hydrogen attack are also explored.

2¼Cr-1Mo steels have been identified as potential structural materials for coal conversion plants [*1*].[2] Existing experiences of utilizing these materials for hydrogen service at elevated temperatures are summarized in the form of Nelson curves [*2*]. Additional information on hydrogen attack in these materials is reviewed in Ref *3*.

When a carbon-containing material is exposed to high-pressure hydrogen at elevated temperatures, methane bubbles are known to nucleate and grow at the grain boundary [*4*]. Nelson curves [*2*] indicate no direct evidence of methane bubble formation in 2¼Cr-1Mo steels resulting from hydrogen ex-

---

[1] Department of Materials Science and Engineering, Cornell University, Ithaca, N.Y. 14853.

[2] The italic numbers in brackets refer to the list of references appended to this paper.

posure alone. We have recently reported transmission electron microscope (TEM) observations of methane bubbles in a 2¼Cr-1Mo steel produced by hydrogen attack in the absence of applied stress [*5*].

Grain boundary cavitation at elevated temperatures is also known to accompany creep deformation at low stresses [*6,7*]. The nucleation of creep cavities under stress in the absence of high-pressure hydrogen is believed to result from the tensile stress concentration at grain boundary steps and corners and at second-phase particles in the grain boundary. The stress concentration is produced by deformation incompatibility between the grain matrix and grain boundary when grain boundary sliding occurs.

Under the influence of high-pressure hydrogen and at stress and temperature conditions conducive to creep cavitation the co-existence of methane pressure and tensile stress concentration is expected to accelerate cavity nucleation at the grain boundary. This combined effect has been demonstrated by results of creep rupture tests in a hydrogen atmosphere [*3*]. These results show that steels which are relatively immune to hydrogen attack in the unloaded condition rupture rapidly under the combined effect of stress and hydrogen.

The rate of creep cavity nucleation and growth in the absence of a hydrogen environment has been reported to vary with stress in a complex manner [*6,7*]. The combined effect of stress and high-pressure hydrogen has not been fully investigated. It would be useful if stress were added as a third variable to the Nelson curve type of data correlation. Thus we would have a family of temperature-hydrogen pressure curves, each curve representing a different stress. The temperature-hydrogen pressure boundaries for safe hydrogen service can therefore be defined depending on the stress level (including residual stresses). A purpose of the work reported herein is to develop theoretical and experimental capabilities that can be used to obtain information for the aforementioned application.

We shall first describe the experimental techniques used in this work, and then report some of our experimental results and discuss their significance.

Experimental Techniques and Apparatus

Materials

All specimens were fabricated from the material of the surface region of a 305-mm (12-in.)-thick plate of ASTM Specification for Pressure Vessel Plates, Alloy Steel, Chromium-Molybdenum (A 387) (normalized and tempered) steel provided through the courtesy of J. A. Gulya and R. A. Swift of Lukens Steel (Heat No. B3085). This thick-section material has a microstructure of mixed bainite and proeutectoid ferrite. Specific conditions of heat treatment, properties, and composition are given in Table 1.

TABLE 1—*Properties of 2¼Cr-1Mo normalized and tempered 12-in.-thick steel plate (Lukens Steel Heat B3085; ASTM A 387, Grade 22).*

Lukens Analyses [*16*]	C	Mn	P	S	Si	Ni	Cr	Mo	Al
Ladle	0.13	0.52	0.010	0.010	0.23	0.18	2.23	0.95	0.021

Heat Treatment

austenitized 913°C (1675°F), 12 h, air cool + tempered 691°C (1275°F), 12 h, air cool

Mechanical Properties

Lukens Data [*16*]	Yield Strength, MPa (ksi)	Tensile Strength, MPa (ksi)	Reduction of Area, %	Elongation, %
Transverse	293 (42.4)	534 (77.4)	64.3	24.3
(centergage)	286 (41.4)	527 (76.4)	64.8	27.1
(Average)	289.5 (41.9)	530.5 (76.9)	64.6	25.7

Hydrogen-Charging Equipment and Conditions

Hydrogen charging of specimens in the absence of applied stress was performed in a stainless steel chamber placed in a standard tube furnace [*8*]. This equipment was designed to operate at temperatures up to 600°C and hydrogen pressures up to 13.8 MPa (2000 psi).

Hydrogen charging of specimens under applied stress was performed in a creep apparatus enclosed in a high-pressure hydrogen chamber. A schematic of this setup is shown in Fig. 1. The components of this unit were also constructed of stainless steel for resistance to hydrogen attack (further details can be found in Ref *9*). The latter equipment was also designed to operate at temperatures up to 600°C and hydrogen pressures up to 13.8 MPa (2000 psi).

Creep and Creep-to-Rupture Tests

Creep tests in air were performed in a conventional creep stand consisting of a furnace, a dead-weight loading system, and a displacement transducer for measuring the creep strain [*10*].

Round tension test specimens with a gage length of 19 mm and a gage diameter of 1.8 mm were used for these tests and for the hydrogen-charging experiments mentioned previously.

Metallographic Examinations

The transmission electron microscopy was performed with a JEM-100B electron microscope at a 100-kV acceleration voltage. The specimens were

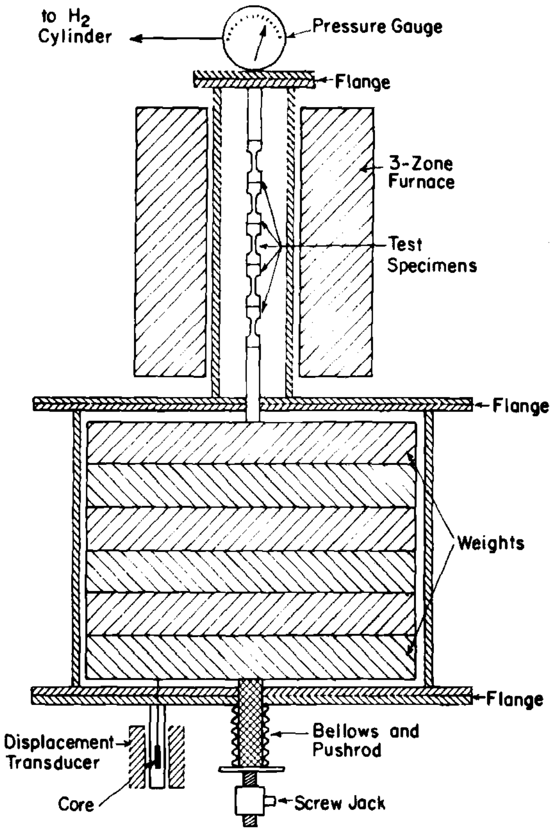

FIG. 1—*Schematic diagram of a creep apparatus enclosed in a hydrogen pressure chamber used for hydrogen charging under applied stress.*

prepared by JET-electropolishing techniques at −35°C in a 30 percent HNO_3 + methanol solution and a 14V polishing potential. More detailed descriptions of the TEM techniques can be found in Refs *5* and *11*.

A JEOL-733 SuperProbe scanning electron microscope (SEM) was used for cavity observation. A creep growth treatment after the hydrogen exposure was found to be necessary to grow the methane bubbles by a mechanism of stress-induced mass transport to a size large enough to be observed in a scanning microscope. The creep growth treatment was performed at 600°C under 110 MPa stress for a period of several days. Most of the SEM observations were made on sectioned, polished, and lightly etched surfaces (15 s in 2 percent Nital). Some of the specimens were fractured at −196°C to reveal grain boundary surfaces for direct cavity observations. It was necessary to use matched fracture surfaces to distinguish the actual cavities from the carbide pull-outs.

Results

Transmission Electron Microscopy Results

Figure 2 shows a typical transmission electron photomicrograph of methane bubbles formed on grain boundary carbide particles. The carbide particle shown has been identified by electron diffraction to be of the Fe_2MoC type. The exposure conditions were 20 days at 600°C under a hydrogen pressure of 13.8 MPa. Methane bubbles were not observed to form on higher carbides in the grain boundary of the same specimen. Additional information on this TEM work can be found in Ref 5. It is believed that these results represent the first direct observation of methane bubbles in 2¼Cr-1Mo steels after hydrogen exposure.

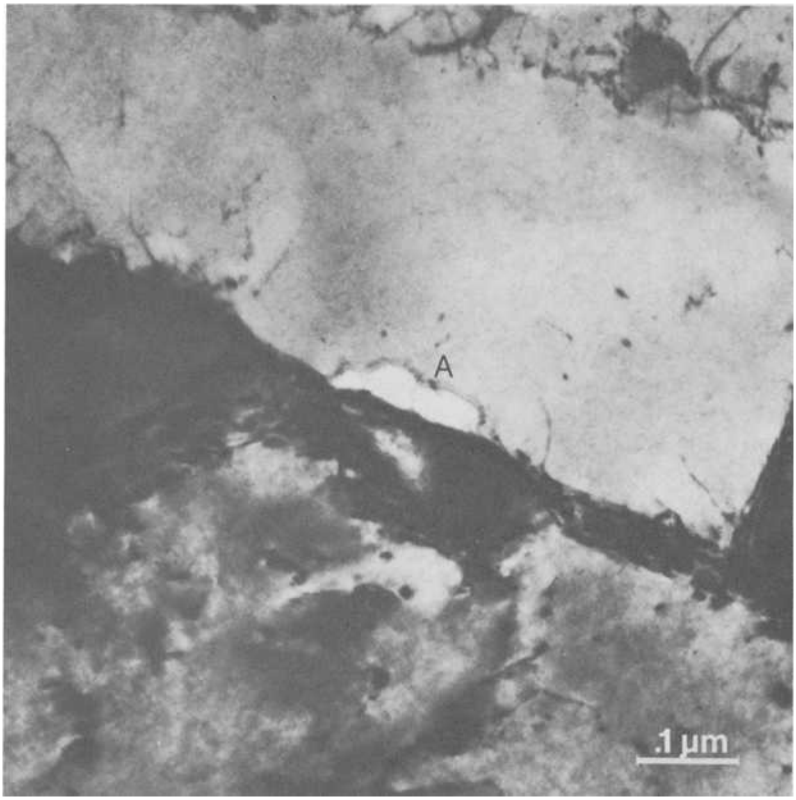

FIG. 2—*Transmission electron micrograph showing methane bubbles* (A) *on a grain boundary carbide surface. Hydrogen exposure: 20 days under 13.8 MPa pressure at 600°C.*

Scanning Electron Microscopy Results

TEM examination does not provide an efficient method for a quantitative determination of the rate of nucleation and growth of methane bubbles. In this work we have relied on SEM observations for this purpose. Figure 3 shows two typical scanning electron photomicrographs obtained on polished and etched sections. The specimen was hydrogen exposed for 20 days at 600°C and a hydrogen pressure of 13.8 MPa, and followed by a creep growth period of 7 days at 600°C under a stress of 110 MPa in air. These photomicrographs clearly revealed grain boundary cavities. The cavities were observed to concentrate on grain boundaries which are normal or near normal to the applied stress axis. According to current theories of stress-induced cavity growth [*6*], maximum growth rate should occur at grain boundaries normal to the applied stress axis.

It should be noted that methane bubble nucleation resulting from hydrogen attack alone should occur at the same rate at all grain boundaries. The creep growth treatment, however, favors cavities at grain boundaries normal and nearly normal to the applied stress axis. The number density of grain boundary cavities in specimens after the creep growth treatment can be estimated from photomicrographs such as those shown in Fig. 3. If this number density is used to calculate the rate of nucleation, the rate obtained will be lower than the actual rate for the aforementioned reason. A geometrical correction will have to be made. It should also be noted that several methane bubbles were observed by TEM to form on a carbide particle. After creep growth these bubbles will coalesce and appear as a single cavity in SEM observations. Another correction will be needed to estimate the number density of methane bubbles prior to the creep growth treatment.

SEM observations of grain boundary cavities were also made on intergranularly fractured surfaces. A variety of approaches have been tried in an effort to produce intergranular fracture in 2¼Cr-1Mo steel specimens [*9*]. Presently we are able to produce intergranular fracture on about 20 percent of the fractured surface. The SEM photographs shown in Fig. 4 represent typical intergranularly fractured surfaces produced by fracture of a notched specimen at liquid nitrogen temperature. The history of the specimen was the same as that for Fig. 3. The identification of cavities require matched fracture surfaces as shown in these figures. We have compared the number density of cavities determined from polished and etched sections and from intergranularly fractured surfaces. The agreement was within experimental scatter.

Effect of Hydrogen Exposure on Creep-to-Rupture Properties

Figure 5 shows strain versus time data obtained at 600°C on specimens with and without hydrogen exposure. The hydrogen-treatment conditions

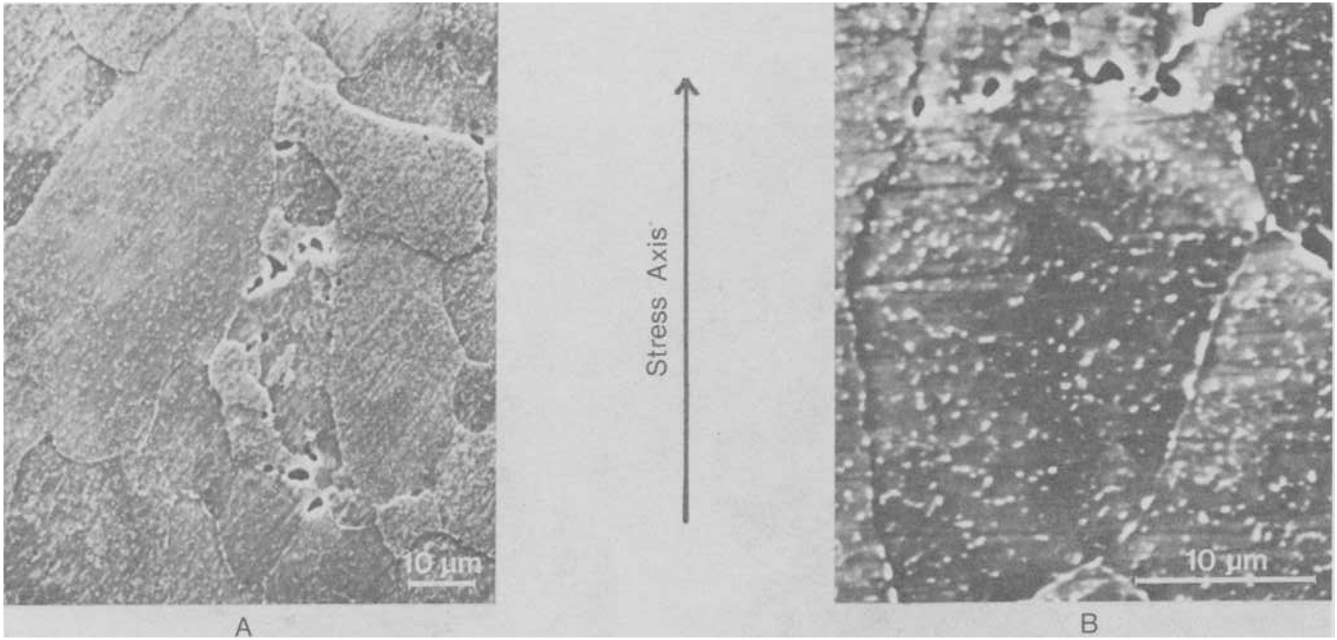

FIG. 3—(a) *SEM photomicrograph of a polished and etched specimen with prior hydrogen exposure and creep growth treatment showing a distribution of grain boundary cavities.* (b) *SEM photomicrograph in a different region than Fig.* 3a *showing cavities located at grain boundaries normal to the applied stress axis.*

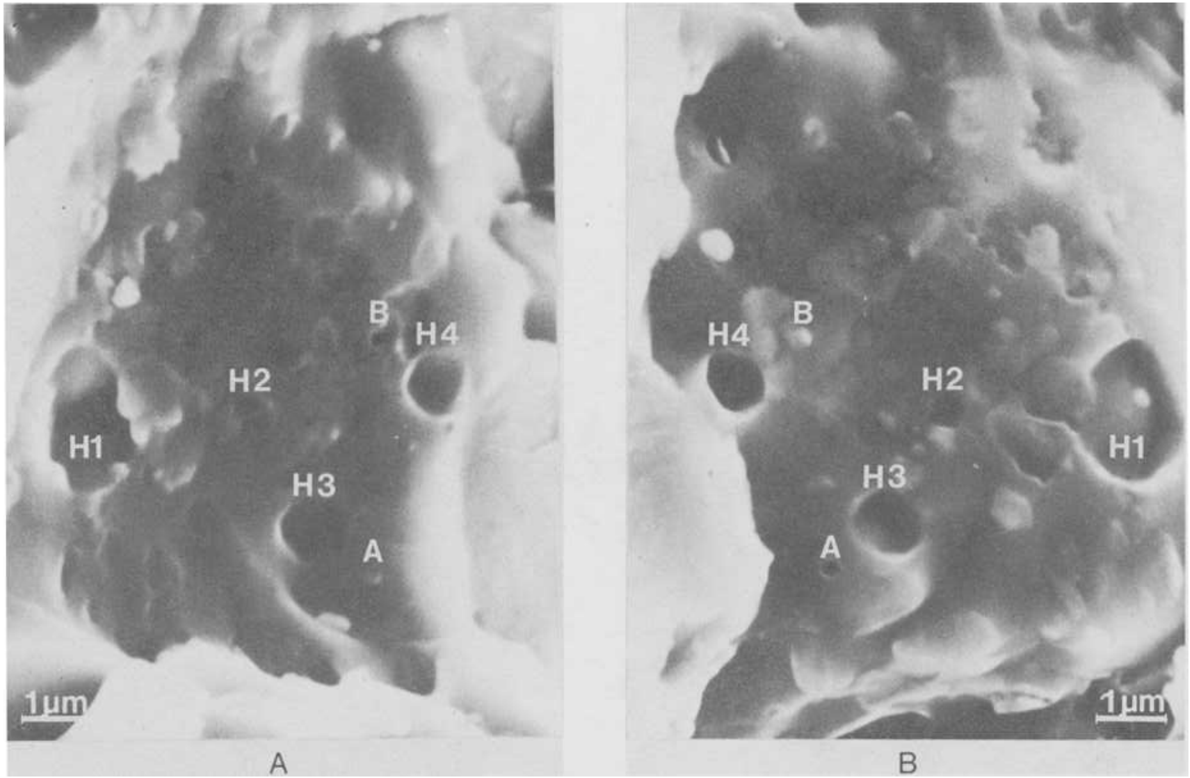

FIG. 4—*Matching fracture surfaces of specimens fractured at −196°C showing holes (cavities) on both sides (H1, H2, H3, and H4) and carbide pull-outs (A and B). Hydrogen exposure under 13.8 MPa pressure at 600°C for 20 days, followed by creep growth treatment under 88 MPa applied stress at 600°C in air for 16 days.*

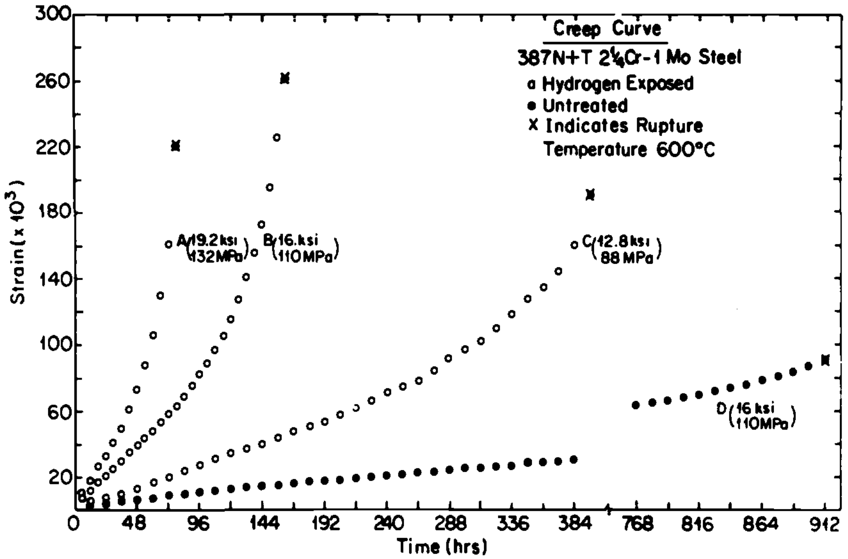

FIG. 5—*Creep curves of ASTM A 387 (normalized and tempered) steel comparing specimens with prior hydrogen exposure to an untreated specimen.*

were 20 days at 600°C under a pressure of 13.8 MPa. The hydrogen-exposed specimens were creep tested at three different stresses (Fig. 5). It is seen from these data that the creep-to-rupture life of hydrogen-exposed specimens was significantly lower than that of the unexposed specimens. This reduction probably reflected the time or creep strain required to nucleate creep cavities, since the hydrogen-exposed specimens already contained grain boundary cavities produced by the methane reaction. The specimens with prior hydrogen exposure failed at shorter times as the applied stress was increased. This stress dependence corresponds essentially to the stress dependence of stress-induced cavity growth [*6*].

The literature stress-to-rupture data of 2¼Cr-1Mo steels without prior hydrogen exposure in the form of a stress versus logarithmic stress-to-rupture life plot are reproduced in Fig. 6 [*12*]. It is seen that at higher temperatures and lower stresses the data show a steeper slope which is usually associated with failure governed by the nucleation and growth of creep cavities [*13*]. The stress-to-rupture data (Fig. 5) obtained in the present work are also plotted in the same figure. The data of specimens with prior hydrogen exposure also showed a steeper slope compared with those of specimens without prior hydrogen exposure. These results support the aforementioned conclusion that the stress-to-rupture life of the hydrogen-exposed specimens is controlled by cavity growth.

The creep-to-rupture data obtained under the combined effect of stress

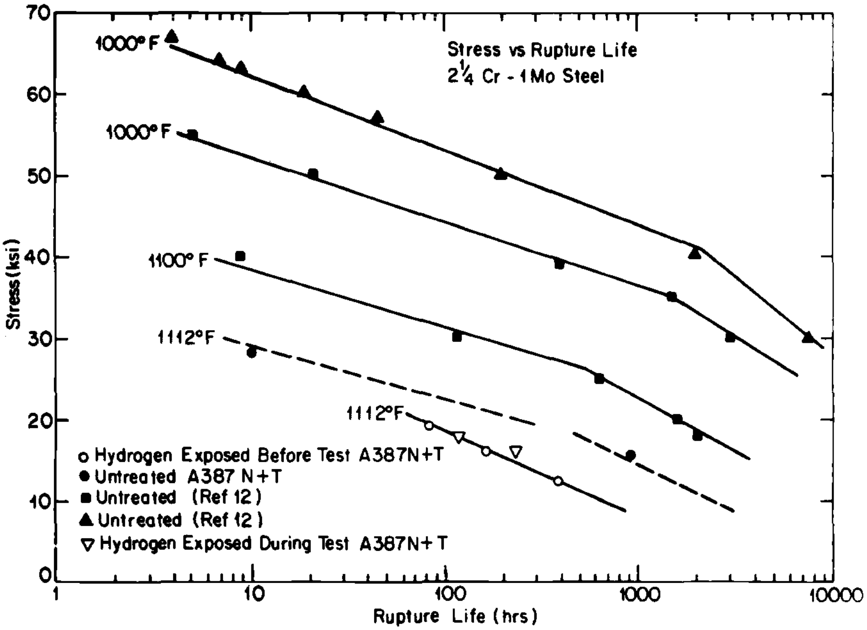

FIG. 6—*Stress-to-rupture data for ASTM A 387 (normalized and tempered) and other 2¼Cr-1Mo steels.*

and high-pressure hydrogen are also shown in Fig. 6. These experiments were performed at 600°C and a hydrogen pressure of 13.8 MPa as a function of stress. The observed reduction in stress-to-rupture life can be attributed to the effect of stress-enhanced cavity nucleation (discussed further in the next section).

Rate of Cavity Nucleation

According to current macroscopic concepts of nucleation, the size of the critical nucleus and the magnitude of the free-energy barrier of nucleation are roughly determined by the ratio of a surface tension term and the internal methane pressure [*4,14*]. These parameters are related to the rate of nucleation and the incubation time. For steels of high chromium content, the stability of the carbides could be such that the time required to build up the internal methane pressure in a bubble of critical size can be expected to be a significant portion of the incubation time observed during hydrogen attack.

In the presence of an applied stress, depending on the magnitude of the applied stress, grain boundary sliding will occur and cause deformation incompatibility at grain boundary steps and second-phase particles. This deformation incompatibility can produce large tensile stresses at these sites which will enhance the rate of bubble or cavity nucleation [*8*]. Under these circumstances, the size of the critical nucleus will be determined roughly by the ratio of a surface tension term and the sum of the internal methane pressure and the hydrostatic component of the tensile stresses. An applied stress can be expected to significantly reduce the size of the critical nucleus through the tensile stresses produced by deformation incompatibility, and thus increase the probability of methane bubble nucleation.

Typical nucleation data without the influence of applied stress in the form of a grain boundary cavity density versus hydrogen exposure time plot are shown in Fig. 7. The period during which cavity density remained unchanged gives a measure of the incubation time; this is approximately 20 days for hydrogen exposure at 580°C under a hydrogen pressure of 13.8 MPa. The cavity density found during the incubation period resulted from the creep growth treatment discussed previously for SEM observation and was not produced by hydrogen attack. The portion of the data which shows an increase in the cavity density with exposure time gives a rate of cavity nucleation of 5×10^{-4}/day μm^2 (6×10^3/s m^2). We have also found that the rate of nucleation, as well as the incubation time, varies significantly with tem-

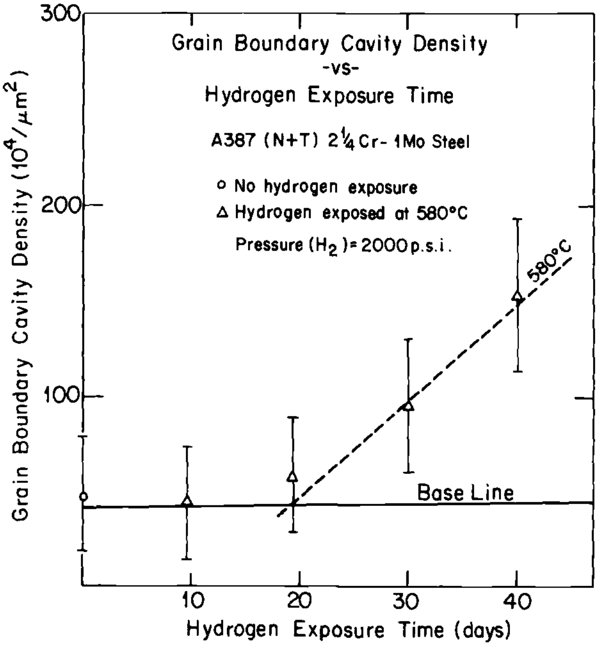

FIG. 7—*Observed grain boundary cavity density as a function of hydrogen exposure time (without coalescence correction).*

perature; for example, at 510°C under the same hydrogen pressure the incubation time was found to increase to more than 40 days.

As expected from theoretical considerations described previously, the effect of applied stress on the rate of nucleation has been found to be significant. The SEM photomicrographs shown in Figs. 8*a*, 8*b*, and 8*c* were obtained from polished and etched sections of three different specimens. Specimen 8*a* has been creep tested in air at 600°C for 38 days under a stress of 110 MPa (16 ksi). Specimen 8*b* was given a hydrogen exposure of 20 days at 600°C under a hydrogen pressure of 13.8 MPa (2000 psi), and followed by a creep growth treatment of 7 days in air at 600°C and under a stress of 110 MPa (16 ksi). Specimen 8*c* was creep tested in a hydrogen environment at 600°C for 10 days under a stress of 110 MPa (16 ksi) and a hydrogen pressure of 13.8 MPa (2000 psi). The average number density of grain boundary cavities in those specimens was found to be $5 \times 10^{-3}/\mu m^2$, $16 \times 10^{-3}/\mu m^2$, and $38 \times 10^{-3}/\mu m^2$ for Specimens 8*a*, 8*b*, and 8*c*, respectively. The large increase in the number density of grain boundary cavities in Specimen 8*c* demonstrates clearly the combined effect of applied stress and high-pressure hydrogen on cavity nucleation.

Rate of Cavity Growth

For practical interests, a coal conversion plant will be operated under conditions (temperature and hydrogen pressure) where the rate of bubble growth in 2¼Cr-1Mo steels under the influence of internal methane pressure would ordinarily be extremely small. However, the hydrogen environment could be sufficient with the aid of an applied stress to nucleate grain boundary bubbles or cavities which will grow under the influence of an applied stress resulting in accumulated damage.

A discussion of stress-induced cavity growth is given in Ref *6*. It involves a mechanism similar to that for Herring-Naborro Creep, except that in the present instance the component of the applied stress normal to the grain boundary is the driving force, and the cavity surface and the grain boundary are the source and sink for atoms, respectively.

We can estimate the rate of cavity growth directly from cavity size, measured as a function of time under stress from SEM photomicrographs such as those in Fig. 4.

We can also estimate the rate of cavity growth based on the number density of cavities (Fig. 2) and the creep-to-rupture life (Fig. 6). The rate of change of the cross-sectional area of grain boundary cavities resulting from a stress-induced mechanism should remain constant as a function of time [*6*]. We assume that rupture will occur when the cavities grow to a certain size comparable to their average spacing (center to center) which can be calculated from the number density of the cavities. For the case of Sample B in Figs. 5 and 6, the average cavity spacing on the grain surface is calculated

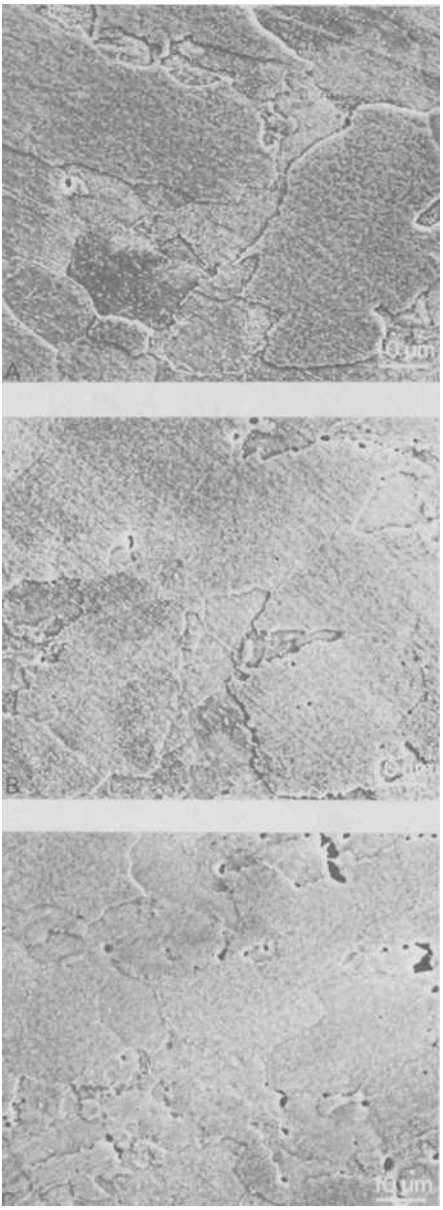

FIG. 8—*SEM photomicrographs showing the effect of applied stress on cavity nucleation.* (a) *Specimen creep tested in air at 600°C, 110 MPa stress for 38 days:* (b) *Specimen with a prior hydrogen exposure (600°C, 13.8 MPa, hydrogen for 20 days), and then creep tested at 600°C, 110 MPa stress for 7 days;* (c) *Specimen creep tested in a hydrogen environment (13.8 MPa hydrogen, 600°C, 110 MPa stress for 10 days).*

to be 7 μm. If it is assumed that the cavity must grow to a diameter of half the average cavity spacing for rupture to occur, the cavity growth rate dA/dt can be estimated to be 1.7×10^{-5} μm²/s, where A is the cavity cross-sectional area and t is time. Values of cavity growth rate calculated based on the same assumption are plotted versus applied stress in Fig. 9 for hydrogen-exposed specimens A, B, and C in Fig. 5.

It is seen from Fig. 9 that the cavity growth rate, in agreement with reported results, depends on the applied stress in a nonlinear fashion [*6*]. The significance of this type of stress dependence has been discussed in detail in a previous report of this laboratory [*6*]. The nonlinear dependence can be attributed to grain boundary sliding which produces stress concentration at grain corners. This nonlinear stress dependence suggests the need for extensive work to obtain cavity growth data for the purpose of data correlation and extrapolation.

Discussion

The normalized and tempered, 305-mm-section, ASTM A 387 2¼Cr-1Mo steel investigated in this work is being considered for applications in coal conversion plants. In addition to materials damage in the form of nucleation and growth of grain boundary cavities reported here, surface decarburization

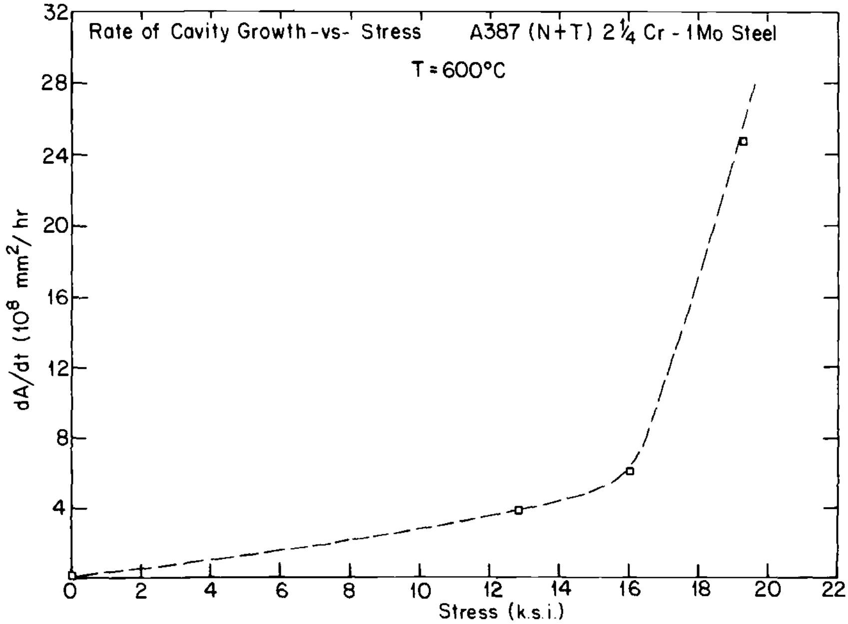

FIG. 9—*Grain boundary cavity growth rate versus stress showing a nonlinear stress dependence.*

of appreciable depth was also observed. Some of the results of decarburization and related microstructural changes are described in Refs *11* and *14*. It is clear from the results obtained that extensive work is required in order to fully characterize the effect of hydrogen attack in this material.

The results obtained in this work also demonstrated clearly the role of stress in hydrogen attack. The importance of applied stress has been recognized in Ref *3*. It should be noted that thermal stresses and residual stresses can have the same effect as applied stresses.

We have shown that the rate of cavity nucleation is significantly enhanced by an applied stress. Once nucleated, these grain boundary cavities can grow under stress and lead to earlier failure. The relationship between stress-enhanced cavity nucleation and between stress-induced cavity growth and grain boundary sliding will depend on the magnitude of stress in a complex manner. This is because the extent of grain boundary sliding in a material is a sensitive function of temperature and stress [*6, 7, 15*]. Additional experimental information covering a wide range of creep and creep-fatigue conditions in hydrogen environments is required in order to quantitatively determine the role of stress in hydrogen attack.

As experimental data become available, we propose to add stress as the third variable in the Nelson curve type of data correlation. A schematic representation of this type of construction is shown in Fig. 10. It is believed that there is a range of stress which produces the ductility minimum in creep-

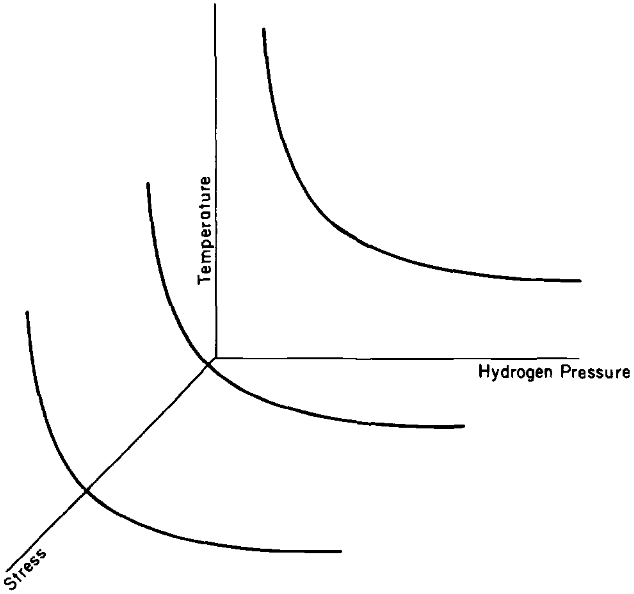

FIG. 10—*Schematic representation of Nelson curves with stress added as a third variable.*

to-rupture tests and over which the effect of grain boundary sliding is important and the effect of stress will be maximized in hydrogen attack. We believe that this type of data correlation should help to reduce some of the uncertainties presently involved in structural design for hydrogen services at elevated temperatures.

Acknowledgments

This work was supported by the Department of Energy through Contract No. ET-78-S-01-3299.

References

[*1*] Lochman, W. I., *Metallurgical Transactions A*, Vol. 9A, 1978, p. 115.

[*2*] "Steel for Hydrogen Service at Elevated Temperatures and Pressures in Petroleum Refineries and Petrochemical Plants," Publication 941, American Petroleum Institute, 1977.

[*3*] "Temper Embrittlement and Hydrogen Embrittlement in Pressure Vessel Steels," Japan Pressure Vessel Research Committee Report No. 2, Iron and Steel Institute of Japan, May 1979.

[*4*] Shewmon, P. G., *Metallurgical Transactions A*, Vol. 7A, 1976, p. 279.

[*5*] Hakkarainen, T. J., Wanagel, J., and Li, C.-Y., *Metallurgical Transactions A*, Vol. 11A, 1980, p. 2035.

[*6*] Mancuso, J. F. and Li, C.-Y., *Metallurgical Transactions A*, Vol. 10A, 1979, p. 1719.

[*7*] Cane, B. J., *Metal Science*, Vol. 13, 1979, p. 287.

[*8*] Allen, R. E., Jansen, R. J., Rosenthal, P. C., and Vitovec, F. H., *Proceedings of the American Petroleum Institute*, Vol. 42, 1962, p. 452.

[*9*] Li, C.-Y., "Hydrogen Attack in Cr-Mo Steels at Elevated Temperatures," DOE Contract No. ET-78-S-01-3299, Quarterly Report No. 2, 1979.

[*10*] Mancuso, J. F., "Grain Boundary Cavity Growth Under Applied Stress and Internal Pressure," Ph.D. thesis, Cornell University, Ithaca, N.Y., 1977.

[*11*] Li, C.-Y., "Hydrogen Attack in Cr-Mo Steels at Elevated Temperatures," DOE Contract No. ET-78-S-01-3299, Quarterly Report No. 3, 1979.

[*12*] Gulya, J. A. and Marshall, E. G., *Hydrocarbon Processing*, Vol. 49, 1979, p. 91.

[*13*] Garofalo, F., *Fundamentals of Creep and Creep Rupture in Metals*, MacMillan, New York, 1965.

[*14*] Li, C.-Y., "Hydrogen Attack in Cr-Mo Steels at Elevated Temperatures," DOE Contract No. ET-78-S-01-3299, Quarterly Report No. 4, 1979.

[*15*] Huang, F. H., Yamada, H., and Li, C.-Y., "Characterization of Materials for Service at Elevated Temperatures," Series MPC-7, American Society of Mechanical Engineers, 1978, p. 83.

[*16*] Gulya, J. A., Lukens Steel, private communication.

Tusit Weerasooriya[1]

Fatigue Crack Propagation in the Heat-Affected Zone of 2¼Cr-1Mo Steel and ERNiCr-3 Weldments

---

REFERENCE: Weerasooriya, Tusit, **"Fatigue Crack Propagation in the Heat-Affected Zone of 2¼Cr-1Mo Steel and ERNiCr-3 Weldments,"** *Application of 2¼Cr-1Mo Steel for Thick-Wall Pressure Vessels, ASTM STP 755,* G. S. Sangdahl and M. Semchyshen, Eds., American Society for Testing and Materials, 1982, pp. 109–126.

ABSTRACT: The fatigue crack growth rate at 510°C in the heat-affected zone (HAZ) of a 2¼Cr-1Mo steel weldment was examined as a function of frequency and stress-intensity factor. The weldment was made of isothermally annealed 2¼Cr-1Mo steel base metal and ERNiCr-3 weld metal. Fatigue crack growth rate data for thermally aged HAZ material lie between the two scatter bands of data for the base metal and ERNiCr-3 filler metal at 510°C. Prior thermal aging up to 2000 h at 566°C does not substantially change the fatigue crack growth rate of HAZ material at 510°C. Fatigue crack growth rate of HAZ material increases with decreasing frequency at 510°C and stress ratio of 0.05 for 20 $\text{MPa}\sqrt{\text{m}} < \Delta K < 35\ \text{MPa}\sqrt{\text{m}}$.

KEY WORDS: crack propagation affected zone, frequency dependence, thermally aged material, low alloy steel, press vessels

Some components of proposed Breeder Reactor and High-Temperature Gas-Cooled Reactor (HTGR) steam generators may be made of annealed 2¼Cr-1Mo steel. Fabrication procedures require that these components be connected by weld joints to piping components made of austenitic stainless steel. A diagram of a cross section of a proposed transition joint between 2¼Cr-1Mo low-alloy steel (ferritic) and Type 316 stainless steel (austenitic) is shown in Fig. 1. A typical design temperature for this joint is 520°C *[1–3]*.[2] Weld filler metals are ERNiCr-3 (67 min Ni-18 to 22Cr-2.5 to 3.5Mn-3Fe-2.5Nb + Ta-0.75Ti-0.1C-0.5Si-0.5Cu) and Type 16-8-2 stainless steel

---

[1] Associate Research Engineer, Aerospace Mechanics Division, University of Dayton Research Institute, Dayton, Ohio 45469.

[2] The italic numbers in brackets refer to the list of references appended to this paper.

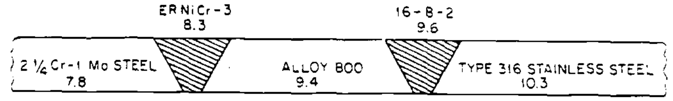

FIG. 1—*Cross section of a transition joint between 2¼Cr-1Mo steel and Type 316 stainless steel. Mean coefficients of expansion from 22 to 538°C are noted below each material in SI units.*

(Fe-16Cr-8Ni-2Mo). Alloy 800H is added in between as shown in Fig. 1 so that the coefficient of thermal expansion of the whole transition joint will gradually change across the weld joint, allowing the joint to withstand static and dynamic thermal stresses.

Transition joints between 2¼Cr-1Mo ferritic steel and Types 316 and 304 stainless steel have been subjected to elevated temperatures for many years in commercial fossil-fired power plants. Although these have generally performed satisfactorily, a number have recently failed in service after approximately 100 000 h. Consequently, these joints are now being studied.

Of the few failures reported, most occurred in the ferritic region (2¼Cr-1Mo steel) parallel and adjacent to the fusion line, which is the heat-affected zone (HAZ) (Fig. 2). The following factors are possible causes of the

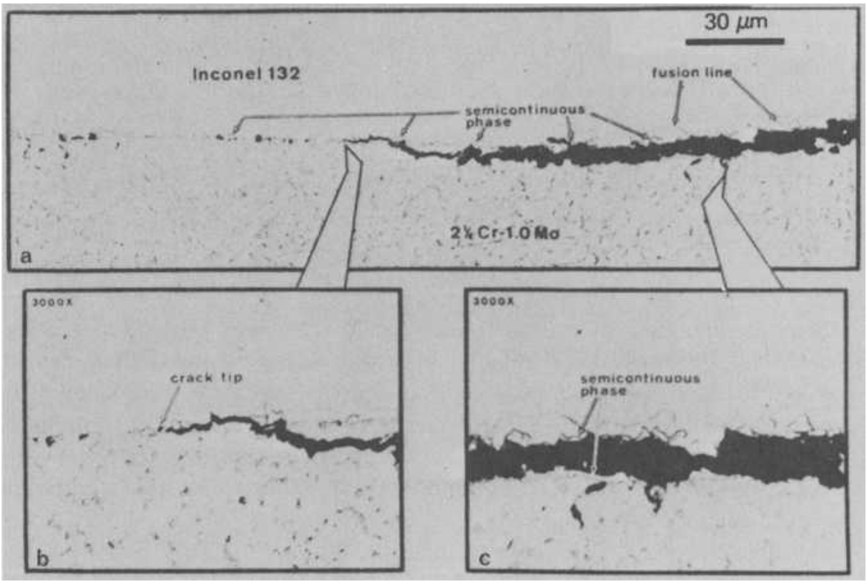

FIG. 2—*Failed transition joint and crack propagation. The crack is propagating primarily in a semicontinuous phase in 2¼Cr-1Mo very close to the fusion line. The relationship of the route of the crack tip and this phase is apparent in* (a) *and* (b). *Further evidence of the crack following this phase is shown in* (a) *and* (c) *with the phase being split and on both sides of the fracture* [4].

failures: (*1*) high thermal stresses resulting from differences in thermal expansion coefficients, (*2*) preferential stress oxidation at the interface, and (*3*) metallurgical changes in the HAZ (for example, accelerated fatigue and creep in the HAZ, which has been weakened by carbon migration into the weld) [*2,4*]. The use of nickel-base filler metal greatly reduces both the carbon migration from the ferritic metal and the drastic change in thermal expansion coefficients.

Although it is believed that the operating temperatures of the breeder system will be low enough to have no adverse effects on the HAZ in 2¼Cr-1Mo steel, the possibility of damaging mechanisms over the 30 years of design life cannot be totally excluded. Hence fatigue crack growth rates in the HAZ of 2¼Cr-1Mo steel were studied after various aging times. This paper shows both the effect of frequency on the fatigue crack growth rates in the HAZ of thermally unaged welds and the results of tests conducted to study the effect of thermal aging up to 2000 h at 566°C. Presently, additional material is being aged at 566°C for 10 000, 20 000, and 30 000 h for subsequent crack propagation tests. This temperature was chosen for thermal aging because it is typical of the working temperature for this type of welded joints in reactor structures.

Material Characterization

Specimens were fabricated from 2¼Cr-1Mo steel and ERNiCr-3 and 2¼Cr-1Mo steel weldments. The 19-mm-thick 2¼Cr-1Mo steel plates used to fabricate weldments have the properties shown in Table 1.

Figure 3 shows the microstructure of an unaged weldment; the HAZ (Fig. 4*a*) consists of a tempered bainite structure, and the base metal (Fig. 4*b*) is primarily proeutectoid ferritic grains with some bainite (dark areas).

Welds in 19-mm-thick plate were fabricated by the automatic gas tungsten arc (GTA) process with hot wire filler additions of ERNiCr-3 weld metal. A square-groove butt joint was used with a 25-mm root opening and a backing strip for these welds. This geometry resulted in a uniform fusion line and an HAZ perpendicular to the plate surface.

The weldments were radiographed, and no flaws were detected. Before

TABLE 1—*Properties of 2¼Cr-1Mo steel.*

Heat treatment	Austenitize at 915°C for 1 h, cool to 710°C at 83°C/h, hold at 710°C for 2 h, and cool to room temperature less than 360°C/h
Ultimate tensile strength, MPa	572
Yield strength, MPa	372
Elongation in 51 mm (2 in.), %	27.0
Reduction in area, %	50.5

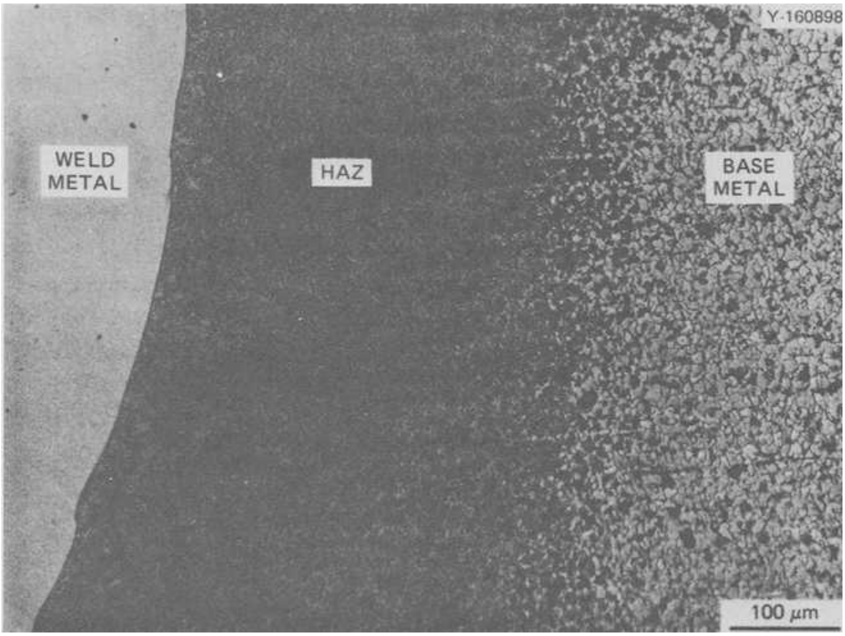

FIG. 3—*Microstructure of unaged weldment.*

machining the specimens, the weldments were given a 1-h stress relief at 732°C.

Some of the specimens were thermally aged for 2000 h at 566°C in argon before testing.

Experimental Procedure

Standard [ASTM Method for Constant-Load-Amplitude Fatigue Crack Growth Rates above 10^{-8} m/Cycle (E 647-78 T)] compact tension (CT) specimens of the dimensions shown in Fig. 5 were used for fatigue crack growth tests ($W = 50$ mm; $B = 12.5$ mm). The machined notch was located in the HAZ in 2¼Cr-1Mo steel and was parallel to the fusion line (Fig. 6). The base metal is oriented so that the rolling direction is perpendicular to the crack growth plane.

These specimens were precracked in air at room temperature or at 510°C with a MTS closed-loop servohydraulic testing machine. Precracking was conducted with a sinusoidal wave form and was finished with a value for K_{max} (maximum stress intensity), which is less than the initial K_{max}-value for the tests.

All tests were conducted on an MTS closed-loop servohydraulic machine

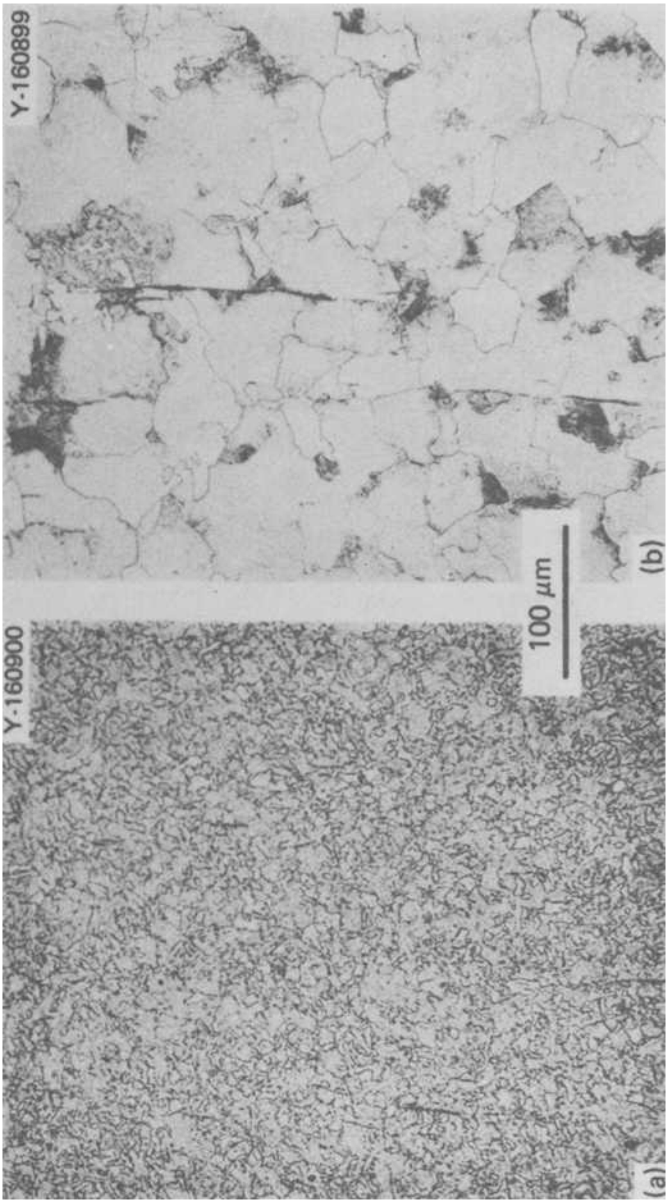

FIG. 4—*Microstructural details of the unaged weldment (etchant is 2 percent Nital).* (a) *HAZ;* (b) *Base metal.*

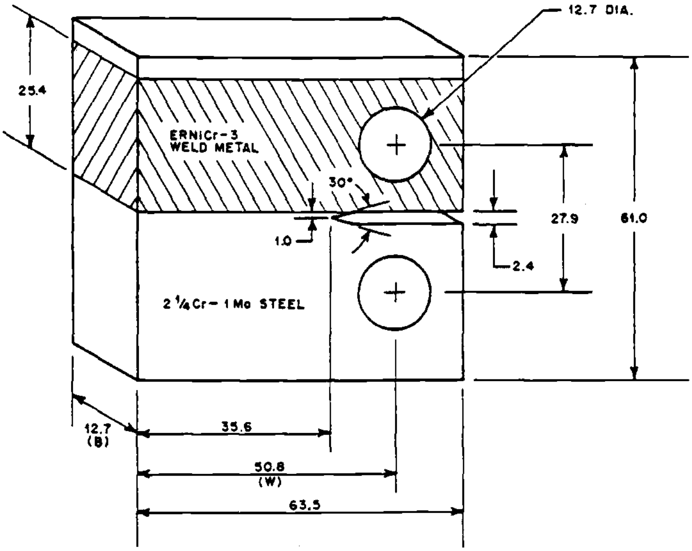

FIG. 5—*Details of a CT specimen used in crack growth studies (dimensions in millimetres).*

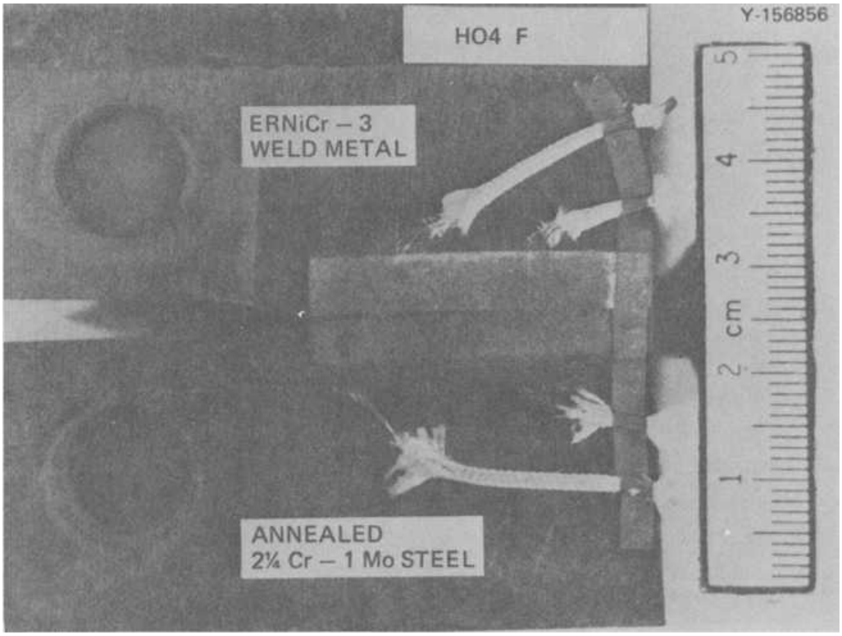

FIG. 6—*Specimen tested at 510°C. Crack is confined to the HAZ.*

employing a triangular wave form. The tests were conducted in air with a ratio of minimum to maximum stress intensity (R) of 0.05 (in accordance with ASTM E 647, unless stated otherwise). The testing temperature was 510°C. Specimens were heated by induction, and the temperature distribution of the zone of crack growth was controlled to within ±1°C. Temperature was measured with several thermocouples, which were spot welded to the specimen. Variation of temperature along the path of the crack was less than 10°C.

Crack length was measured optically at periodic intervals of cycles with the help of a traveling microscope. Induction heating permitted the continuous monitoring of the crack tip.

Crack growth rate was computed by fitting a continuous cubic spline curve to the average crack length data.

Elastic properties of the base metal and the weld metal were assumed to be the same in the computation of stress intensities (difference in elastic moduli is less than 3 percent). The stress-intensity expression used to calculate ΔK is as follows:

$$\Delta K = \frac{\Delta P}{B\sqrt{W}}\left[29.6\left(\frac{a}{W}\right)^{0.5} - 18.5\left(\frac{a}{W}\right)^{1.5} + 655.7\left(\frac{a}{W}\right)^{2.5} - 1017\left(\frac{a}{W}\right)^{3.5} + 638.9\left(\frac{a}{W}\right)^{4.5}\right] \quad (1)$$

where

ΔP = cyclic load range (that is, $P_{\max} - P_{\min}$),
a = crack length,
B = specimen thickness, and
W = specimen width.

$$\frac{da}{dN} = A\Delta K^{n} \quad (2)$$

where

da/dN = crack growth rate in mm/cycle, and
ΔK = stress intensity in MPa$\sqrt{\text{m}}$

for each plot.

A program of testing was undertaken to find the effect of frequency on thermally unaged and aged HAZ material at 510°C. Tests were conducted in air at frequencies of 0.067, 0.67, and 6.7 Hz for thermally unaged HAZ material. Tests were also conducted at 0.67 Hz and 510°C for HAZ material that was thermally aged for 2000 h in order to study the effect of thermal aging on fatigue crack growth rate (FCGR).

Results and Discussion

Figures 7 to 11 show plots of *da/dN* versus ΔK for the tests conducted. Figure 8 compares the crack growth rate of the HAZ with that of 2¼Cr-1Mo steel base metal [5] and ERNiCr-3 weld metal at a temperature of 510°C and a frequency of 0.67 Hz. The fatigue crack growth rate of the HAZ material is not unusual compared with that of either 2¼Cr-1Mo steel base metal or ERNiCr-3 weld metal. For lower ranges of stress intensities, fatigue crack growth rate data for HAZ material are similar to that for ERNiCr-3 weld metal. For higher stress intensities, fatigue crack growth rate data for the HAZ approach that for 2¼Cr-1Mo steel base metal.

The effect of frequency on the fatigue crack growth rate of HAZ material is shown in Fig. 12. Decreasing frequency increases the fatigue crack growth rate of HAZ material at a temperature of 510°C. Environmental attack at the crack tip is believed to be the reasons for observed higher crack growth rates at lower frequencies. The lower the frequency, the longer the exposure of the crack tip to high-temperature oxidation. The relative effect of frequency on crack growth rate decreases at higher crack growth rates (higher ΔK) and the following explanation may be the reason for this observation. Independent of frequency, higher FCGRs (high ΔK) continually expose new (virgin) material to the atmosphere. Before any measurable degradation has occurred to the exposed material, the crack will advance out of the region of the exposed material into new material. In this case, the effect of environment, and hence the effect of frequency on FCGR diminishes.

The difference between crack growth rates of HAZ material for frequencies between 0.067 and 0.67 Hz is appreciable compared with that for frequencies between 0.67 and 6.7 Hz. The frequency effect on fatigue crack growth rate seems to disappear as the frequency approaches 6.7 Hz.

The crack growth rates of base metal were always observed to be higher than those of HAZ material for the frequencies studied. Comprehensive residual stresses at the HAZ material (even after 1 h of stress relief at 732°C there may be some residual stresses present) and the metallurgical difference of the two materials may be speculated as the reason for the aforementioned effect.

Figures 10 and 11 show the crack growth rate of the HAZ material which was thermally aged at 566°C for 2000 h. For lower ΔK-values, thermally aged material has a higher crack growth rate than unaged HAZ material; but for higher ΔK-values, unaged material has a higher growth rate (Fig. 11). This trend is also true for the base metal [*6*]. Figures 10 and 11 also show the fatigue crack growth rate curve for thermally aged (482 or 538°C for 10 000 h) 2¼Cr-1Mo steel [*7*]. Thermally aged base material (482 or 538°C for 10 000 h) has a higher crack growth rate than thermally aged HAZ material (566°C for 2000 h).

Figure 13 shows the microstructure of an aged weldment. The HAZ (Fig.

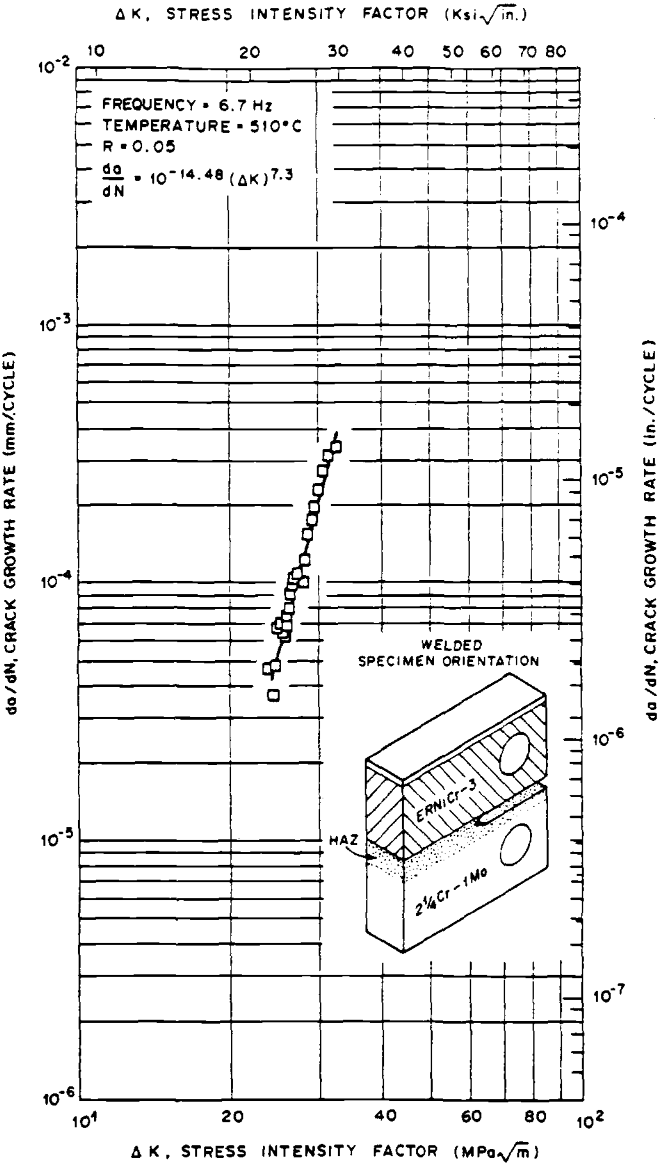

FIG. 7—*FCGR at the HAZ for a frequency of 6.7 Hz in air.*

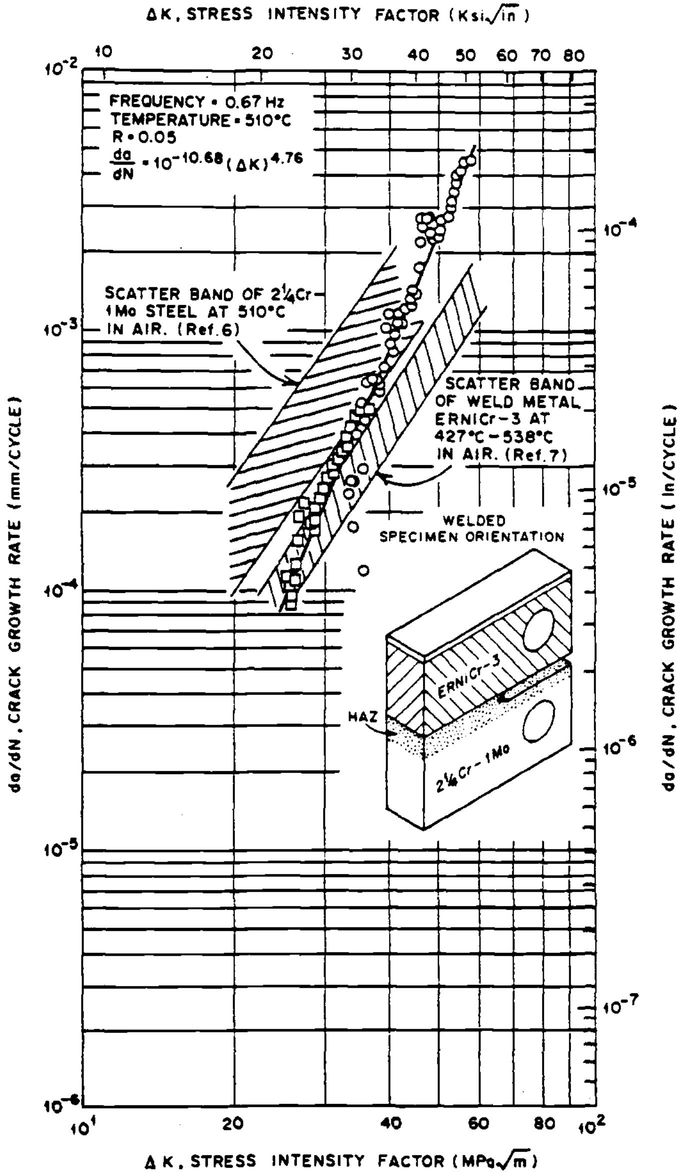

FIG. 8—*Comparison of fatigue crack growth rates for 2¼Cr-1Mo steel, HAZ, and ERNiCr-3 weld metal in air. Data points* □ *and* ○ *indicate crack growth rates of HAZ material.*

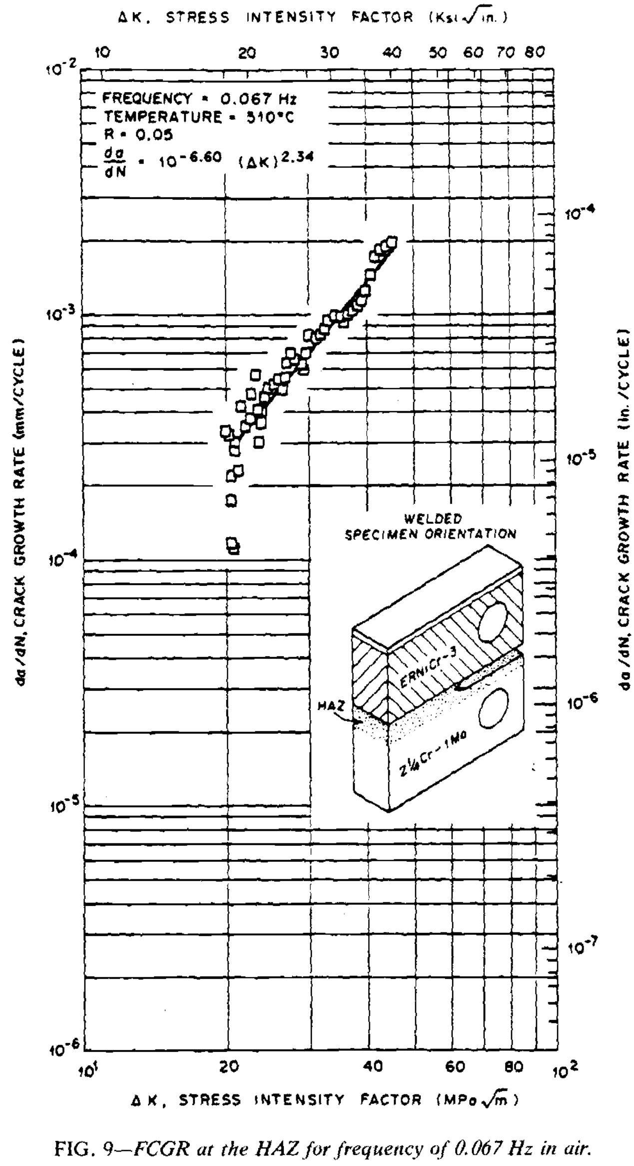

FIG. 9—*FCGR at the HAZ for frequency of 0.067 Hz in air.*

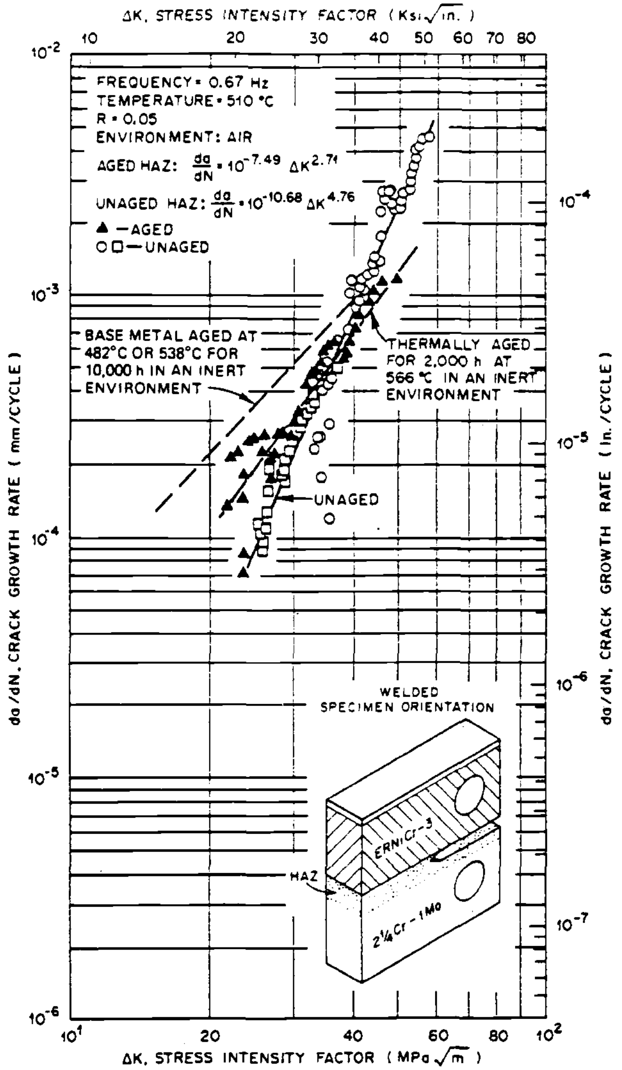

FIG. 10—*FCGR of thermally aged HAZ material at 566°C for 2000 h compared with the unaged material at 510°C and 0.67 Hz. FCGR of annealed and aged 2¼Cr-1Mo steel at 482 or 583°C for 10 000 h is higher than the FCGR HAZ material aged at 566°C (base metal data obtained from Ref 7).*

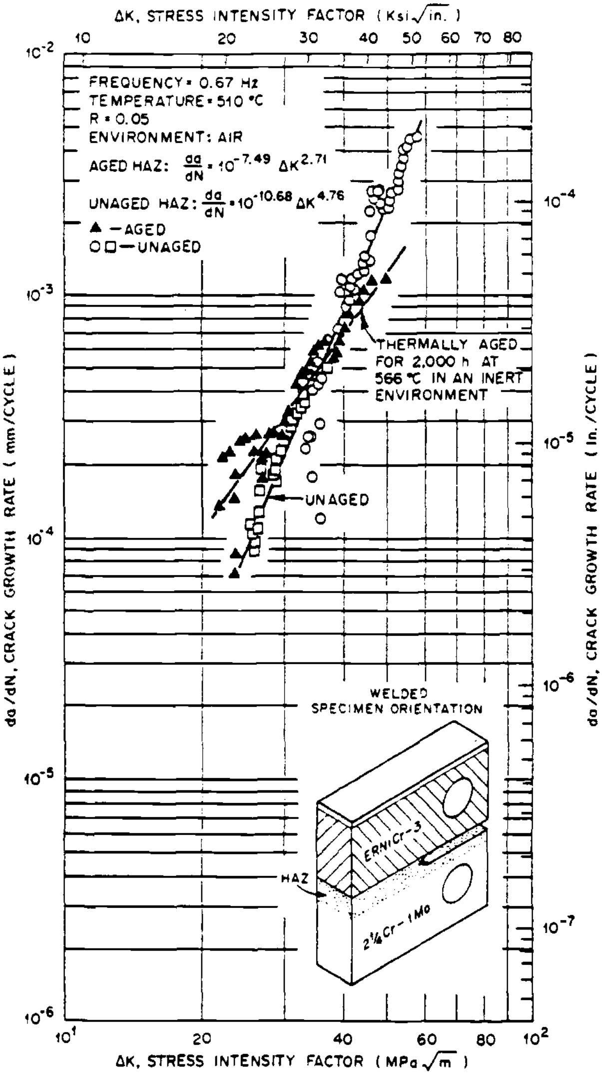

FIG. 11—*Comparison of FCGR data for aged and unaged HAZ material (same as Fig. 10 except base metal comparison omitted for clarity).*

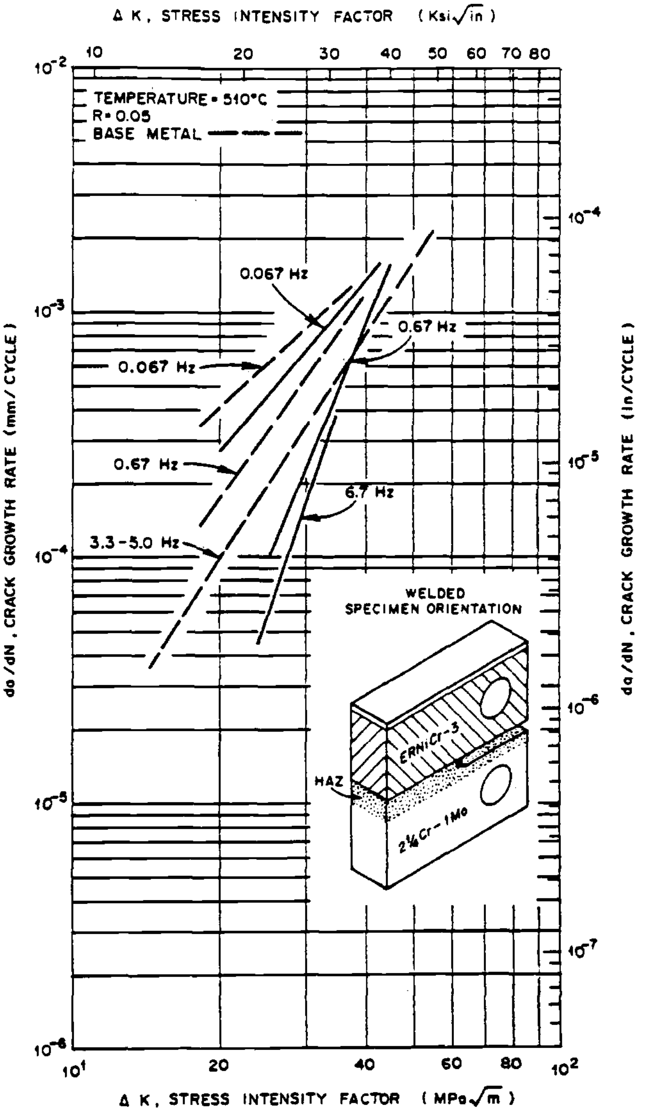

FIG. 12—*Effect of frequency on FCGR in HAZ in air. Crack growth rate of base metal at the corresponding frequency is always higher (base metal data obtained from Ref 7).*

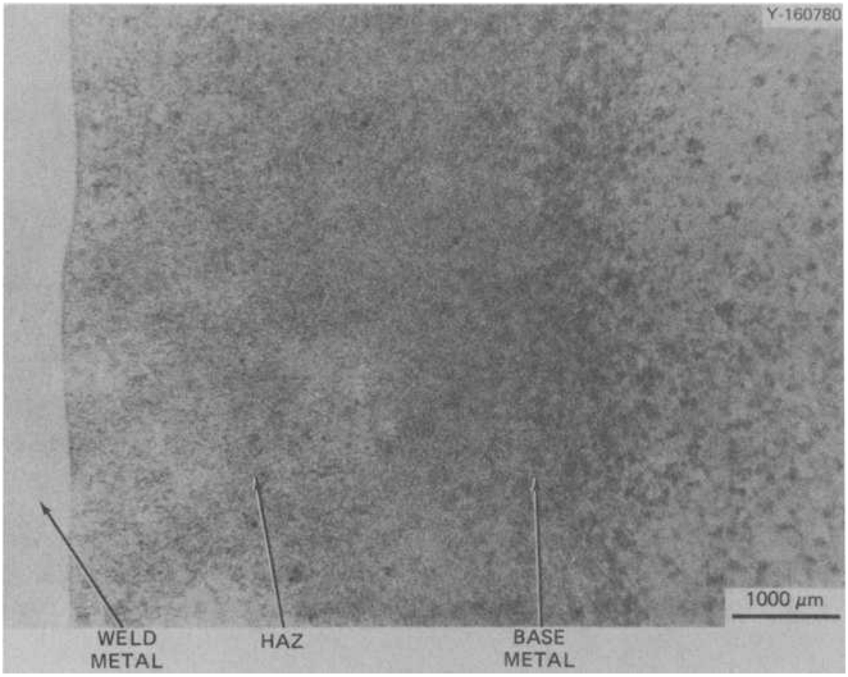

FIG. 13—*Microstructure of thermally aged weldment.*

14*a*) and base metal (Fig. 14*b*) microstructures of aged (2000 h at 566°C) material do not differ detectably from those of the unaged material shown in Fig. 4.

Figure 15 shows a typical microstructure of specimens tested. In all tests conducted, cracks grew within the HAZ. Figure 16 shows a typical fracture surface of the specimens tested. Striations are clearly visible, and the crack growth was transgranular. Mode of microfracture was the same for both thermally unaged and aged HAZ material at all tested frequencies and ΔK-levels.

Conclusions

The following conclusions are drawn for the fatigue crack growth rate of HAZ material of 2¼Cr-1Mo steel and ERNiCr-3 weldments:

1. Fatigue crack growth rate of HAZ material increases with decreasing frequency at 510°C, and $R = 0.05$ for $20\ \mathrm{MPa}\sqrt{\mathrm{m}} < \Delta K < 35\ \mathrm{MPa}\sqrt{\mathrm{m}}$.

2. Fatigue crack growth rate of HAZ material lies between the scatter bands fatigue crack growth rates of 2¼Cr-1Mo steel base metal and ERNiCr-3 weld metal at 510°C and 0.67 Hz.

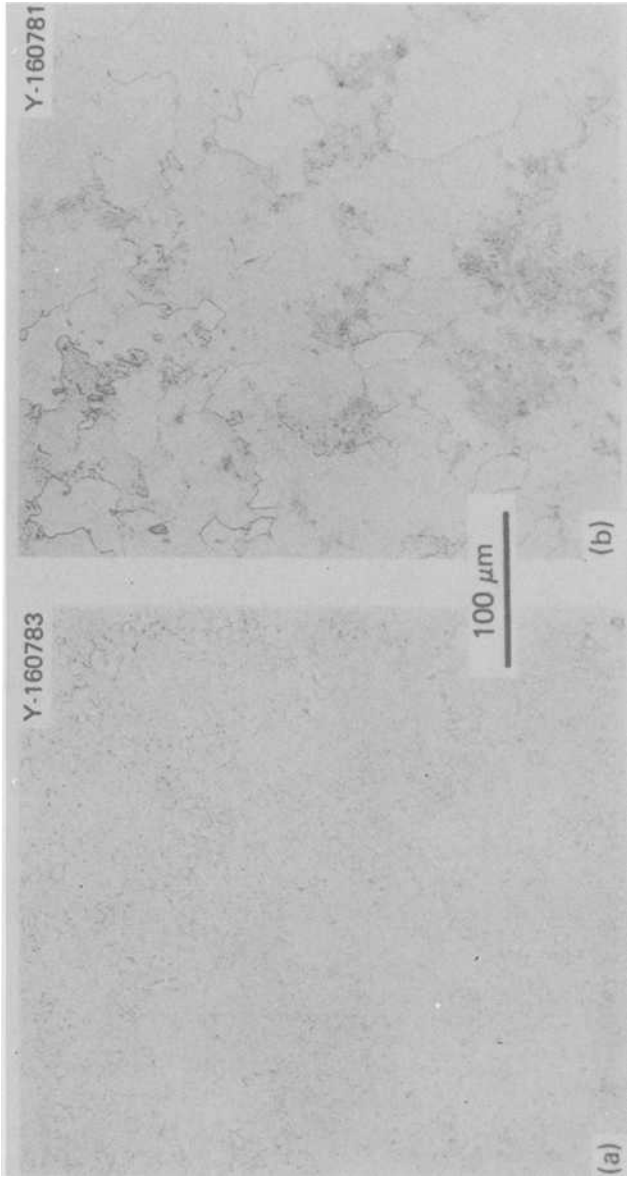

FIG. 14—*Microstructure of thermally aged weldment at 566°C for 2000 h (etchant is 2 percent Nital). (a) HAZ; (b) Base metal.*

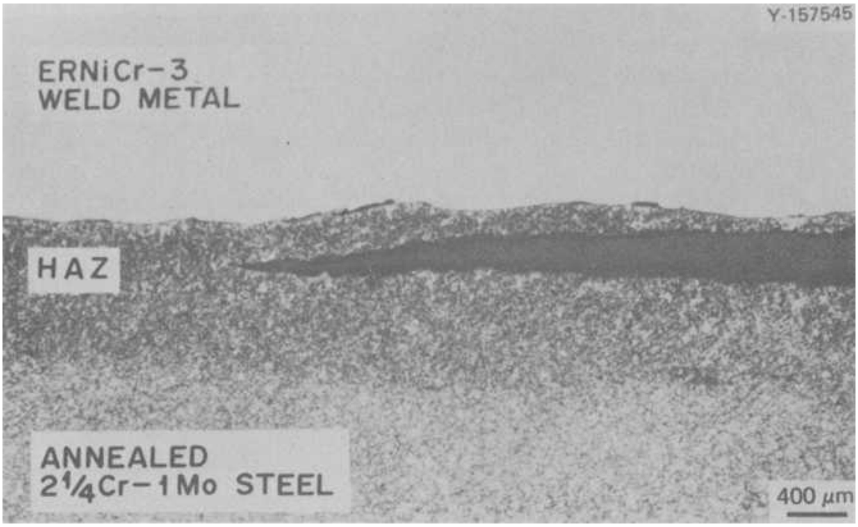

FIG. 15—*Specimen with crack tip (etchant is 2 percent Nital).*

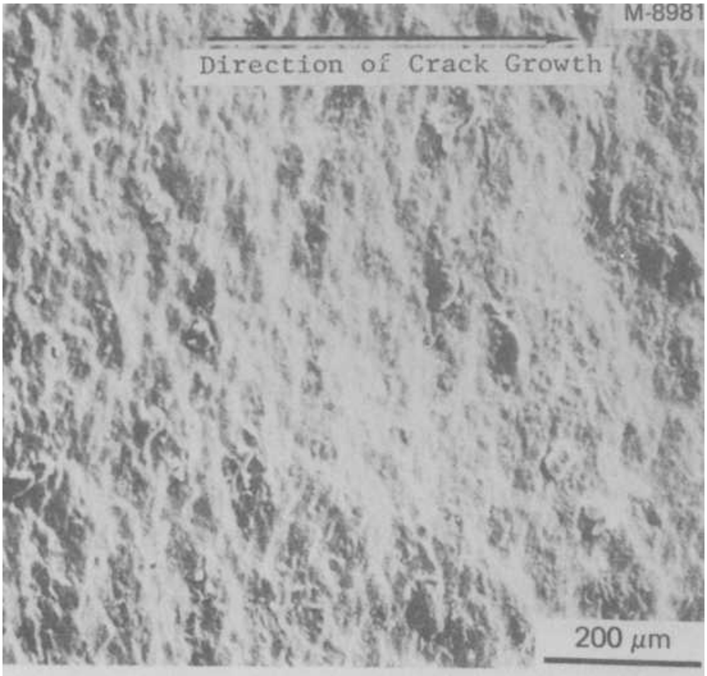

FIG. 16—*Typical fracture surface.*

3. Fatigue crack growth rate of base metal is always higher than that of the HAZ material for the frequencies studied.

4. The fatigue crack growth rate of thermally aged (2000 h at 566°C) HAZ material is slightly higher compared with that of unaged HAZ material at lower stress intensities; but for high stress intensities the fatigue crack growth rate of unaged HAZ material is slightly higher than the fatigue crack growth rate of aged HAZ material.

Acknowledgments

This work was conducted while the author was at Oak Ridge National Laboratory. He is happy to acknowledge the help given to him by his colleagues J. P. Strizak and C. R. Brinkman. The welds were prepared by J. F. King. This research was sponsored by the Department of Energy under contract with Union Carbide Corporation.

References

[*1*] Dalcher, A. W. and Yang, T. M., "High-Temperature Elastic Analysis of Dissimilar Metal Welded Pipe Joints," in *Proceedings of the Second International Conference on Mechanical Behavior of Materials,* 16-20 Aug. 1976, Boston, American Society for Metals, 1976, pp. 1978-1983.

[*2*] King, J. F., "Behavior and Properties of Welded Transition Joints Between Austenitic Steels and Ferritic Steels—A Literature Review," ORNL/TM-5163, Nov. 1975.

[*3*] King, J. F., Sullivan, M. D., and Slaughter, G. M., *Welding Journal,* Vol. 56, No. 11, Nov. 1977, pp. 354-s-358-s.

[*4*] Gray, R. J., King, J. F., Leitnaker, J. M., and Slaughter, G. M., "Examination of a Failed Transition Weld Joint and the Associated Base Metal," ORNL-5223, Jan. 1977.

[*5*] Corwin, W. R., "Subcritical Crack Growth Studies," Mechanical Properties Test Data for Structural Materials Quarterly Progress Report, ORNL-5287, 30 April 1977, pp. 337-341.

[*6*] James, L. A., "Fatigue Crack Growth Behavior in Dissimilar Metal Weldments," HEDL-TME 76-93, March 1977.

[*7*] Corwin, W. R., Booker, M. K., Booker, B. L. P., and Brinkman, C. R., "Fatigue Crack Propagation in 2¼Cr-1Mo Steel," ORNL-5355, Feb. 1978.

Processing and Properties of 2¼Cr-1Mo Steel for Thick-Wall Pressure Vessels

T. Ishiguro,[1] *Y. Murakami,*[2] *K. Ohnishi,*[1] *and J. Watanabe*[1]

A 2¼Cr-1Mo Pressure Vessel Steel with Improved Creep Rupture Strength

---

REFERENCE: Ishiguro, T., Murakami, Y., Ohnishi, K., and Watanabe, J., **"A 2¼Cr-1Mo Pressure Vessel Steel with Improved Creep Rupture Strength,"** *Application of 2¼Cr-1Mo Steel for Thick-Wall Pressure Vessels, ASTM STP 755,* G. S. Sangdahl and M. Semchyshen, Eds., American Society for Testing and Materials, 1982, pp. 129–147.

ABSTRACT: In the ASME Boiler and Pressure Vessel Code, Sec. VIII, Div. 1, design allowable stress-intensity values are influenced by the creep rupture strength at temperatures higher than 450°C. Pressure vessels for such high-temperature service inevitably tend to be thickwalled unless a steel with high creep strength is used. In the case of a coal liquefaction reactor, for instance, a possible wall thickness would be approximately 300 mm or even greater with the use of conventional 2¼Cr-1Mo steel (SA336 F22).

The objective of the present work was to develop a heavy-section 2¼Cr-1Mo steel with better creep strength by conducting a set of experiments with regard to the effect of microalloying elements. The best composition to obtain improved creep-rupture properties was found to be low Si-0.10C-2¼Cr-1Mo-¼V-Ti-B. With this composition, remarkable reduction in temper embrittlement susceptibility was also achieved. Other properties, such as weldability, low temperature toughness, and hydrogen embrittlement resistance, were similar to those of conventional 2¼Cr-1Mo steel.

KEY WORDS: creep rupture strength, microalloying, hardenability, microstructure, temper embrittlement, hydrogen assisted cracking, design stress intensity value, weld heat affected zone, base metal

Heavy-wall 2¼Cr-1Mo steel has been used for many hydrogenation reactors, and its properties have been studied extensively with regard to various aspects of the performance requirement for a pressure vessel steel of this kind [*1*-*4*].[3] The need for even heavier 2¼Cr-1Mo steel is anticipated in light of a steadily increasing trend of more aggravating operational conditions of these pressure vessels—a good example being coal liquefaction reactors [*5*-*8*].

In the ASME Boiler and Pressure Vessel Code, Sec. VIII, Div. 1, the design stress-intensity value for 2¼Cr-1Mo steel sharply decreases at about 450°C, since for temperatures higher than 450°C the design stress is influenced by

---

[1] Material Research Laboratory, The Japan Steel Works, Ltd., Muroran, Japan.
[2] Research Laboratory, Muroran Plant, The Japan Steel Works, Ltd., Muroran, Japan.
[3] The italic numbers in brackets refer to the list of references appended to this paper.

the creep rupture strength. This is one reason that reactors tend to be heavy walled when designed for such high temperature.

On the other hand, encouraged by an even stronger need for a steel with higher creep strength, studies to improve the creep strength of 2¼Cr-1Mo steel have been carried out [*9,10*]. The present study involves the microalloying of 2¼Cr-1Mo steel to increase creep strength, and a set of experiments with the steels of the best composition to evaluate their performance in the atmosphere of hydrogenation reactors.

The most difficult task in alloying the steel is achieving better creep properties without deteriorating other mechanical properties; for example, the achievement of high creep strength often results in unsatisfactory impact toughness.

The best composition found in the present study to improve creep strength of 2¼Cr-1Mo steel is low Si-2¼Cr-1Mo-¼V-Ti-B. The following properties were considered: creep rupture strength, impact toughness, weld heat-affected zone (HAZ) properties, susceptibility to temper embrittlement, hydrogen-assisted cracking, and stress relief cracking.

High creep rupture strength and ductility are essential for pressure vessel steels such as those dealt with in this paper for the reason given earlier. However, past experience with creep failure indicates that the creep properties of weld HAZ are even more critical [*11*].

Impact toughness, when considered in connection with temper embrittlement, is of course a major concern with regard to the brittle fracture of the reactors. Here again the weld HAZ receives keen attention as well as the base metal.

Hydrogen damage—namely, hydrogen attack and hydrogen-assisted cracking—is another element of in-service deterioration to consider when selecting a steel for hydrogenation reactors. Carbide precipitation plays an important role in hydrogen damage. Stable carbides like vanadium carbide and titanium carbide are known to be beneficial in terms of hydrogen-attack resistance, but may enhance hydrogen-assisted cracking in view of the high strength achieved by such carbides.

Last, but not least, is the resistance to weld cracking. 2¼Cr-1Mo steel is sensitive to cold cracking caused by dissolved hydrogen and to stress relief cracking associated with creep relaxation during stress relief treatment. When alloyed with strong carbide formers like vanadium, the latter is a serious concern in the fabrication of the pressure vessels.

Procedure

Materials

Vanadium, molybdenum, niobium, titanium, and boron were added in various combinations to low Si-2¼Cr-1Mo steel to obtain a wide, systematic variation of chemical composition (Table 1). The low silicon content was chosen for its favorable effect on temper embrittlement [12]. Carbon content was reduced to alleviate the deterioration of stress relief cracking resistance due to the addition of vanadium in conjunction with the grain refining effect of titanium and niobium.

The test heats were melted in a 50-kg vacuum-induction furnace, hot forged into 50-mm-thick, 180-mm-wide, 500-mm-long plates, austenitized at 950°C for 5 h followed by programmed cooling to simulate the quarter-thickness location of 200-mm-thick water-quenched plates, and then tempered at 690°C for 20 h.

Experimental Procedure

Tension and Charpy impact tests were conducted at ambient temperature. Hot tension tests were conducted at temperatures up to 650°C. Creep rupture tests were carried out at 500°C and 550°C with smooth round bar specimens. Rupture time at 482°C (900°F) for a stress level of 196 MPa (20 kgf/mm^2) was then estimated by interpolation using Larson-Miller's parametric method. Micrographs were taken to assess the hardenability with attention given to proeutectoid ferrite in the microstructure.

Stress relief cracking test utilized *y*-slit restraint cracking test specimens. The detailed procedure is described elsewhere in the literature [13]. The weld was made with a heat input of 20 000 J/cm at a preheat temperature of 200 to 250°C. The welded specimen was stress relieved at 650°C for 5 h following the dehydrogenation treatment at 350°C, saw cut at five different locations, ground, and macro-etched for the observation of cracks.

Results

Test results are summarized in Table 1. Tensile strength, impact test, and creep rupture test data were obtained for the simulated 200-mm-thick plates. Stress relief cracking susceptibility and hardenability were judged based on the result of the stress relief cracking test and the microstructural change upon cooling at a rate of water-quenched, up to 400-mm-thick plate, respectively. Heat N1, for example, shows fairly high strength, but its hardenability was judged to be insufficient because it produced proeutectoid ferrite when simulated for 400-mm-thick plate. Creep rupture time generally varied with tensile strength. Creep strength appeared to increase to a significant extent when more than 0.2 percent vanadium was added. Hardenability was not sufficient to produce homogeneous martensitic or bainitic structure unless the addition of boron was incorporated. Thus the best micro-alloying to achieve high creep strength with no loss in other properties was found to be the modification with ¼V-Ti-B.

TABLE 1—*Summary of alloy composition and test results.*

Material No.	Tensile Strength		FATT,[a] °C	Rupture Time at[b] 482°C and 196 MPa, h	SR Cracking Susceptibility	Hardenability
	$\sigma_{0.2}$, MPa	σ_{TS}, MPA				
VB1 0.10C-0.10V-0.02Ti-0.002B	426	547	−48	1.2×10^4	resistant	sufficient
VB2 0.10C-0.10V-0.02Ti-0.006B	408	534	−33	. . .	resistant	sufficient
VB3 0.10C-0.10V-0.02Ti-0.010B	419	545	−33	1.5×10^4	resistant	sufficient
VB4 0.10C-0.30V-0.02Ti-0.002B	548	653	0	4.8×10^6	resistant	sufficient
VB5 0.15C-0.10V-0.02Ti-0.002B	442	576	−53	1.1×10^4	resistant	sufficient
VB6 0.10C-0.20V-0.02Ti-0.002B	524	616	−17	4.9×10^5	resistant	sufficient
VN1 0.10C-0.03Nb	466	576	−44	. . .	resistant	insufficient
VN2 0.10C-0.10V-0.03Nb	484	591	−60	5.1×10^4	resistant	insufficient
VN3 0.10C-0.20V-0.03Nb	528	627	−50	. . .	resistant	insufficient
VN4 0.10C-0.30V-0.03Nb	566	667	−61	2.2×10^5	resistant	insufficient
VN5 0.10C-1.50Mo-0.03Nb	490	612	−62	. . .	resistant	insufficient
VN6 0.10C-1.50Mo-0.10V-0.03Nb	486	612	−65	1.8×10^4	resistant	insufficient
VN7 0.10C-1.50Mo-0.20V-0.03Nb	477	599	−65	. . .	resistant	insufficient
VN8 0.10C-1.50Mo-0.30V-0.03Nb	515	627	−50	1.4×10^5	resistant	insufficient
VN9 0.10C-2.00Mo-0.10V-0.03Nb	461	610	−53	1.2×10^4	resistant	insufficient
N 1 0.15C-0.10Nb	477	592	−45	2.9×10^4	resistant	insufficient
N 2 0.15C-0.20Nb	481	596	−55	. . .	resistant	insufficient
N 3 0.15C-0.30Nb	449	571	−35	1.8×10^4	resistant	insufficient
N 4 0.10C-0.10Nb-0.02Ti-0.002B	423	541	−16	. . .	resistant	sufficient
N 5 0.10C-0.20Nb-0.02Ti-0.002B	423	544	−10	1.4×10^4	resistant	sufficient
N 6 0.10C-0.30Nb-0.02Ti-0.002B	417	536	+28	. . .	resistant	sufficient

[a] Fracture appearance transition temperature in V-notch Charpy test.
[b] Interpolated value using Larson-Miller's parametric method.

Materials

From the results of the micro-alloying tests, the best heats were VB4 and VB6. More detailed study was conducted with these two heats to learn their performance as a steel for hydrogenation reactors. An additional two heats were made to study the influence of impurities on temper embrittlement susceptibility. The chemical composition of the steels studied is shown in Table 2.

The steels were heat treated to simulate the quarter-thickness location of 100 to 400-mm-thick, water-quenched plates following the cooling curves shown in Fig. 1. The austenitizing temperature was 950°C unless otherwise stated. The steels were then tempered at 690°C for 20 h as a standard tempering condition, but tempering time was varied to study its effect in some cases. A special heat treatment was given with a weld thermal cycle simulator to simulate the weld HAZ made with a heat input of 20 000 J/cm (Fig. 2). The simulated HAZ was then postweld heat treated at 690°C for 20 h. In order to study the temper embrittlement susceptibility, an acceleration treatment known as step cooling (Fig. 3) was also conducted for Heats VB7 and VB8, with higher impurity levels.

Experiments

Continuous cooling transformation (CCT) diagrams were constructed in a dilatometric study using a Format-F. Specimens for dilatometry were subjected to metallographic observation. Mechanical tests were conducted as described previously in this paper.

Stress relief cracking tests were conducted with the use of 40-mm-thick plates that were restrained by frames (Fig. 4). The test plates were submerged arc welded (Fig. 4) with a heat input of 39 000 J/cm, common in shop fabrication. The test plates were then stress relief treated at 690°C for 20 h and sectioned for observation. A sulfide stress cracking test was conducted with notched round bar specimens in a solution containing 500 ppm hydrogen sulfide and 0.5 percent acetic acid under an applied stress of maximum 1100 MPa.

Hardenability

Figure 5 shows CCT diagrams of Heat VB4 and a commercial 2¼Cr-1Mo steel with the same carbon content. Austenite to ferrite transformation was suppressed considerably in Heat VB4 compared with the 2¼Cr-1Mo steel. This was believed to be caused mostly by the addition of a small amount of boron. Microstructural changes of Heat VB4 with cooling rate are shown in

TABLE 2—*Chemical composition of modified 2¼Cr-1Mo steels studied (in weight percent).*

Sample No.	C	Si	Mn	P	S	Ni	Cr	Mo	V	Ti	B	Al	Sn	As	Sb	N
VB4	0.10	0.02	0.51	0.005	0.005	0.10	2.20	0.94	0.30	0.022	0.0023	0.008	0.005	0.005	0.0004	0.0088
VB6	0.10	0.02	0.54	0.009	0.007	0.11	2.30	0.97	0.21	0.022	0.0022	0.010	0.005	0.005	0.0004	0.0094
VB7	0.10	0.02	0.53	0.018	0.007	0.10	2.24	1.00	0.20	0.021	0.0020	0.009	0.018	0.005	0.0004	0.0088
VB8	0.10	0.02	0.51	0.027	0.007	0.10	2.15	0.94	0.19	0.023	0.0024	0.009	0.035	0.005	0.0004	0.0095

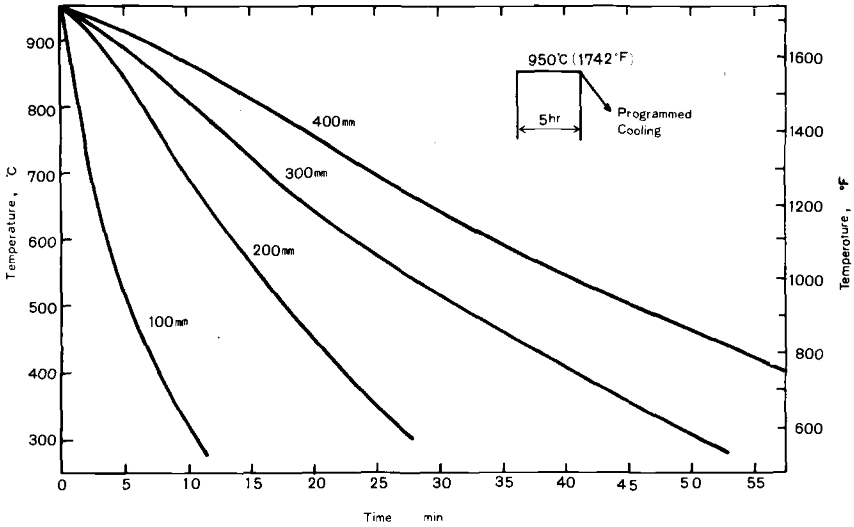

FIG. 1—*Cooling curves used to simulate the quarter-thickness location of 100- to 400-mm-thick, water-quenched plates.*

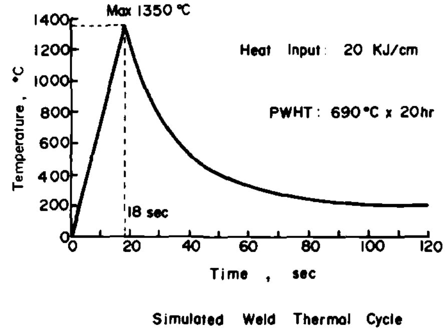

FIG. 2—*Thermal cycle for simulating HAZ made with a heat input of 20 000 J/cm.*

Fig. 6. The microstructure consisted of martensite or bainite or a mixture of the two at a cooling rate as slow as 10°C/min, as already indicated in Fig. 5.

Figure 7 shows the microstructure of Heat VB6 that was heat treated to simulate the quarter-thickness location of 100- to 400-mm-thick, quenched and tempered plates. The microstructure was bainitic for every thickness, as expected from the CCT diagram. Table 3 summarizes the results of tension and impact tests for the VB6 steel. Tensile properties remained much the same regardless of the thickness, whereas impact transition temperature (FATT) increased slightly over the wide range of plate thickness.

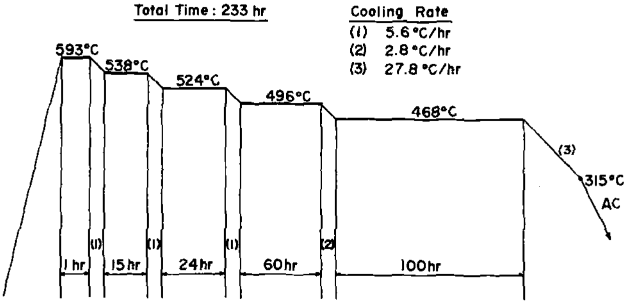

FIG. 3—*Heat treatment program to accelerate temper embrittlement.*

Welding Process : SAW (AWS F92-EG-G)

Current : 590 A

Voltage : 31 V

Traveling Speed : 280 mm / min

Pre-heating Temperature : 250 °C

Interpass Temperature : 200-250 °C

PWHT : 690 °C x 20hr

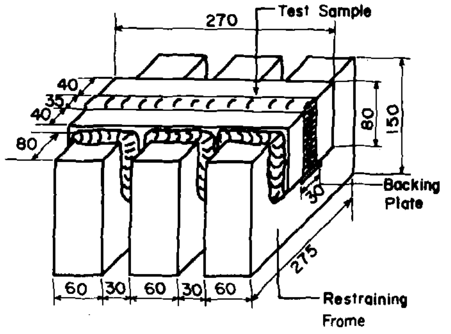

(Note) 3passes per layer totaling 20 passes

FIG. 4—*Stress relief cracking test specimen and test conditions.*

Effect of Heat Treatment

The effect of austenitizing temperature on the tensile and impact properties of Heat VB6 is shown in Table 4. A higher austenitizing temperature resulted in higher yield and tensile strengths and a higher impact transition temperature. This was attributed to larger amounts of vanadium in solution, at higher austenitizing temperature, available for subsequent precipitation. Austenitizing at 950°C was thought appropriate in view of the balance of strength and toughness.

	C	Si	Mn	P	S	Cr	Mo	V	Ti	B	Austenitizing Temperature
$2^1\!/\!_4$Cr-1Mo-V-Ti-B	.10	.02	.51	.005	.005	2.20	.94	.30	.022	.0023	950°C (1742°F)
$2^1\!/\!_4$Cr-1Mo	.10	.34	.48	.017	.013	2.16	.96	–	–	–	920°C (1688°F)

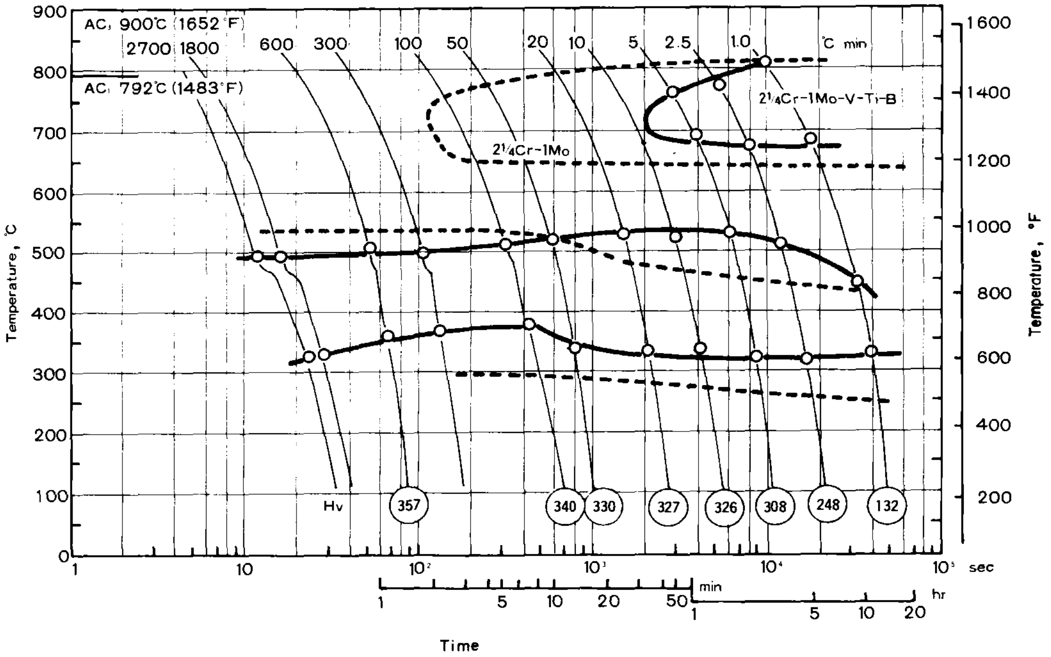

FIG. 5—*Continuous cooling transformation diagrams of a $2^1\!/\!_4$Cr-1Mo steel and low Si-$2^1\!/\!_4$Cr-1Mo-$^1\!/\!_4$V-Ti-B steel.*

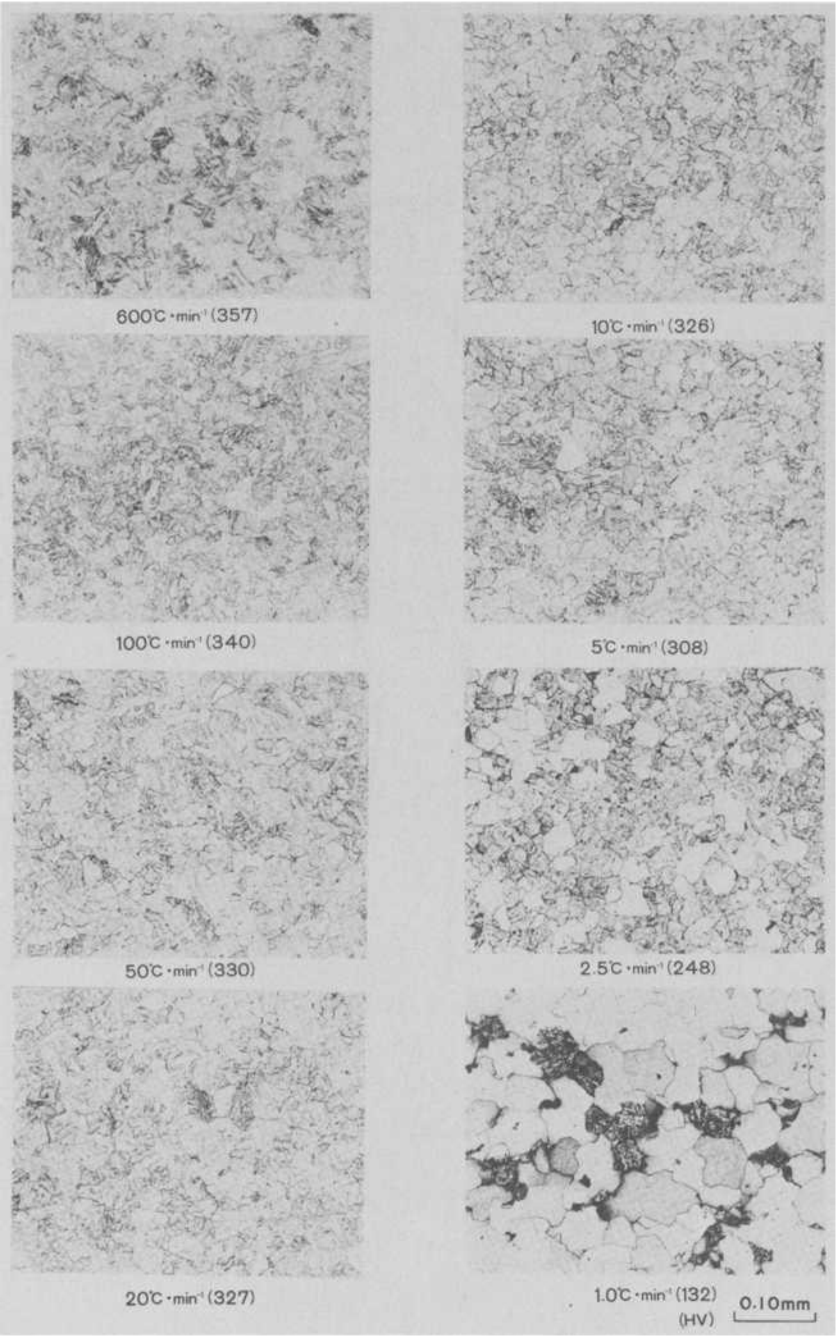

600°C·min^{-1} (357)

10°C·min^{-1} (326)

100°C·min^{-1} (340)

5°C·min^{-1} (308)

50°C·min^{-1} (330)

2.5°C·min^{-1} (248)

20°C·min^{-1} (327)

1.0°C·min^{-1} (132)
(HV)

FIG. 6—*Microstructure of low Si-2¼Cr-1Mo-¼V-Ti-B steel as a function of cooling rate.*

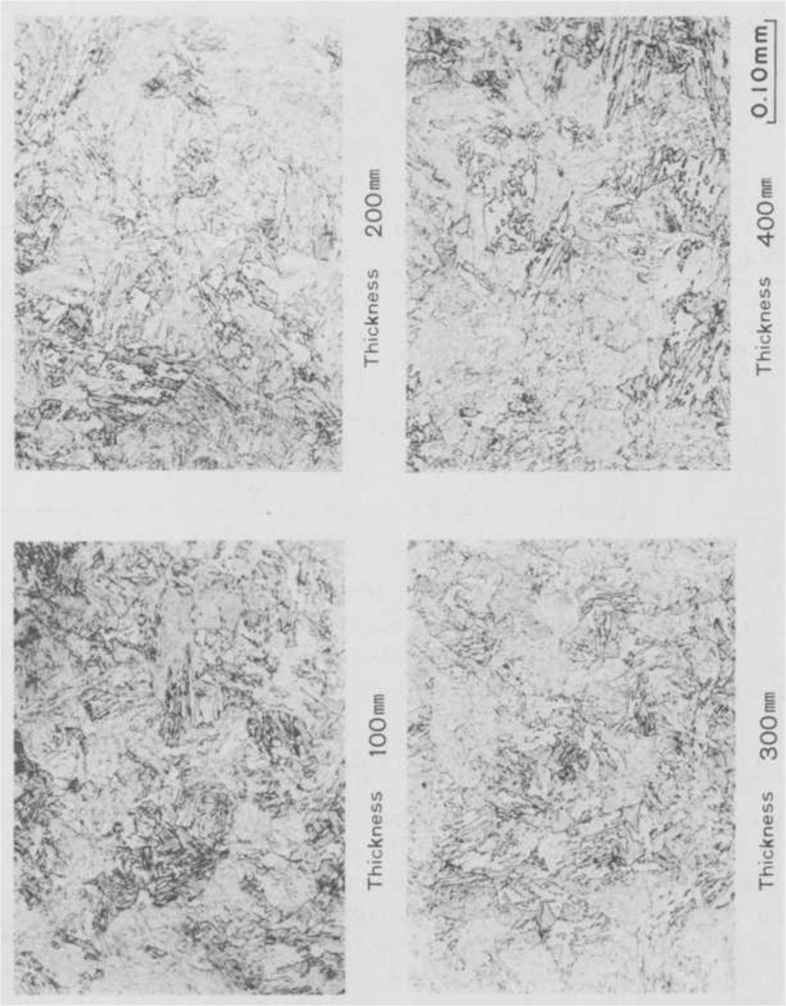

FIG. 7—*Microstructure of Heat VB6 simulating 100- to 400-mm thick, quenched and tempered plate.*

TABLE 3—*Results of tension and impact tests for Heat VB6 simulating 100- to 400-mm-thick, water-quenched and tempered plates.*

	Tension Test Results				
Thickness, mm	0.2% Proof Stress, MPa	Ultimate Tensile Strength, MPa	Elongation, %	Reduction of Area, %	FATT, °C
100	529	625	26.5	80.4	−31
200	524	616	26.1	80.0	−17
300	535	622	25.4	80.2	−14
400	520	617	26.5	82.3	− 7

TABLE 4—*Results of tension and impact tests as a function of austenitizing temperature for Heat VB6 simulating 200-mm-thick, water-quenched and tempered plates.*

	Tension Test Results				
Austenitizing Temperature, °C	0.2% Proof Stress, MPa	Ultimate Tensile Strength, MPa	Elongation, %	Reduction of Area, %	FATT, °C
920	490	589	25.8	80.1	−20
950	524	616	26.1	80.0	−17
980	557	637	24.7	78.3	−6

Table 5 shows the effect of tempering time. Yield and tensile strength and impact transition temperature all decreased monotonically with increase of tempering time up to 50 h. It should be noted that stress relief embrittlement, often observed in low-alloy steels, did not take place in Heat VB6.

Elevated Temperature Properties

The results of hot tension tests and creep rupture tests conducted on Heats VB6 and VB4 for a simulated quarter-thickness location for a 200-mm-thick, quenched and tempered plate are shown in Figs. 8 and 9.

Heat VB6 was superior in its room temperature and hot tensile properties to conventional 2¼Cr-1Mo steels (SA336 F22) that received heat treatments practically identical to that of Heat VB6. The vanadium bearing 2¼Cr-1Mo steels showed excellent creep rupture strength, approximately 50 percent greater than the average creep rupture strength of conventional 2¼Cr-1Mo steels (SA336 F22). The reason for the superior creep rupture strength of the modified steel probably is a combination of higher room temperature strength and alloy additions. The precipitation of V_4C_3 and TiC seems to play an important role in this regard because these stable carbides tend to raise creep rupture strength even for the same room temperature strength. Creep rup-

TABLE 5—*Effect of tempering time on mechanical properties of Heat VB6 simulating 200-mm-thick, quenched and tempered plates.*

Tempering Condition	Tension Test Results				FATT, °C
	0.2% Proof Stress, MPa	Ultimate Tensile Strength, MPa	Elongation, %	Reduction of Area, %	
690°C for 5 h	632	706	25.4	79.2	+32
690°C for 10 h	594	673	24.6	79.5	0
690°C for 20 h	524	616	26.1	80.0	−17
690°C for 50 h	468	564	27.0	80.7	−24

ture ductility was as good as conventional 2¼Cr-1Mo steels, which resulted from the excellent resistance to grain boundary microcracking.

Susceptibility to Temper Embrittlement

Three 0.2V-Ti-B steels with different phosphorus and tin contents were Charpy tested before and after the step cooling treatment described earlier. These steels showed surprisingly small shifts in transition temperature even in the presence of large amounts of the impurity elements, thus indicating extremely low susceptibility to temper embrittlement (Table 6). Such results

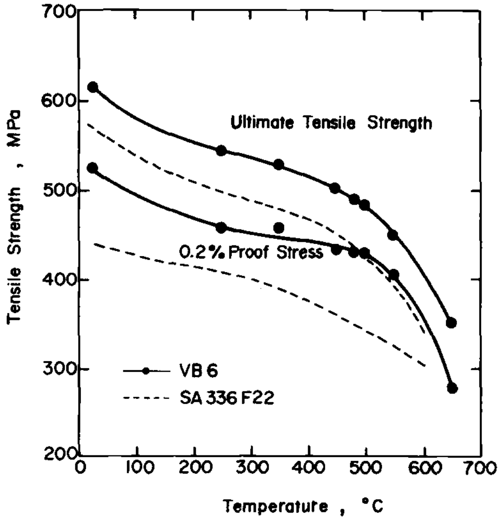

FIG. 8—*Hot tensile properties of Heat VB6 compared with 2¼Cr-1Mo steel similarly heat treated.*

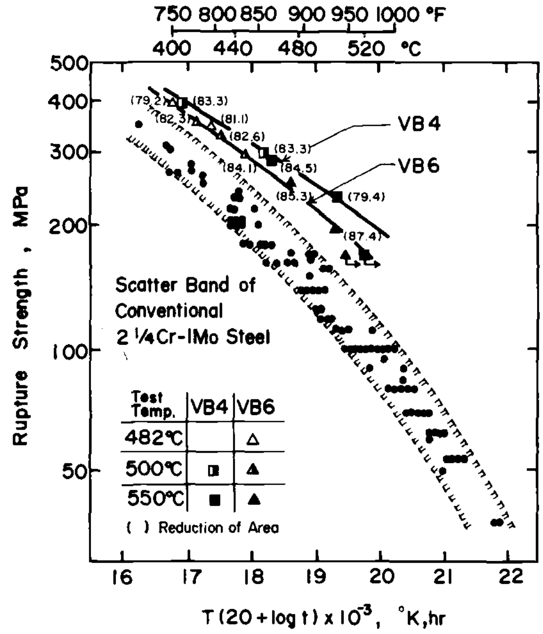

FIG. 9—*Creep rupture strength of ¼V-Ti-B modified steels and conventional 2¼Cr-1Mo steels (temperature in kelvin, time in hours).*

TABLE 6—*Results of Charpy impact test before and after step cooling.*

Sample No.	FATT,[a] °C		vTr40,[b] °C		vEu.s.,[c] J	
	Before	After	Before	After	Before	After
VB6	−17	−23	−30	−36	274	272
VB7	+2	+5	−13	−18	274	272
VB8	+2	+10	−8	−4	269	269

[a] Transition temperature at shear fracture of 50 percent.
[b] Transition temperature at absorbed energy of 40 ft·lb.
[c] Absorbed energy at upper shelf temperature.

were attributed partly to the low silicon content [*12*] and partly to titanium and boron present in the steels [*14*].

Properties of Weld Heat-Affected Zone (HAZ)

The results of tension and impact tests of the simulated weld HAZ (Table 7) indicate that, compared with the base metal properties already shown in Table 3, the HAZ is superior in its tensile and impact properties to the base metal, especially in impact toughness.

TABLE 7—*Mechanical properties of simulated weld HAZ for Heats VB4 and VB6.*

	Tension Test Results				
Sample No.	0.2% Proof Stress, MPa	Ultimate Tensile Strength, MPa	Elongation, %	Reduction of Area, %	FATT, °C
VB4	604	693	25.0	82.6	−79
VB6	562	662	24.5	81.8	−80

Figure 10 demonstrates the creep rupture strength and ductility of simulated weld heat-affected zones for Heat VB4 and a commercial 2¼Cr-1Mo steel. The creep rupture ductility of the Heat VB4 HAZ was as high as the 2¼Cr-1Mo HAZ despite the considerable difference in rupture strength. The rupture strength of the simulated HAZ was virtually identical to that of the base metal.

Stress Relief Cracking and Hydrogen-Assisted Cracking

Figure 11 shows the cross section of the restraint cracking test specimen shown in Fig. 4 and the microstructure of the weld HAZ. No stress relief cracks were observed, probably because of the reduced carbon content and a microstructure which was well refined for the most part by the small amount of titanium present in Heat VB4.

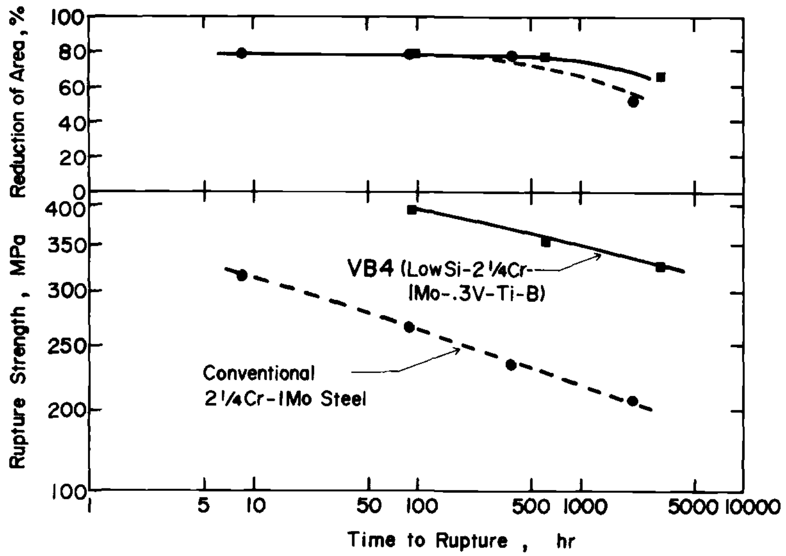

FIG. 10—*Comparison of creep rupture properties between simulated Heat VB4 and a commercial 2¼Cr-1Mo steel.*

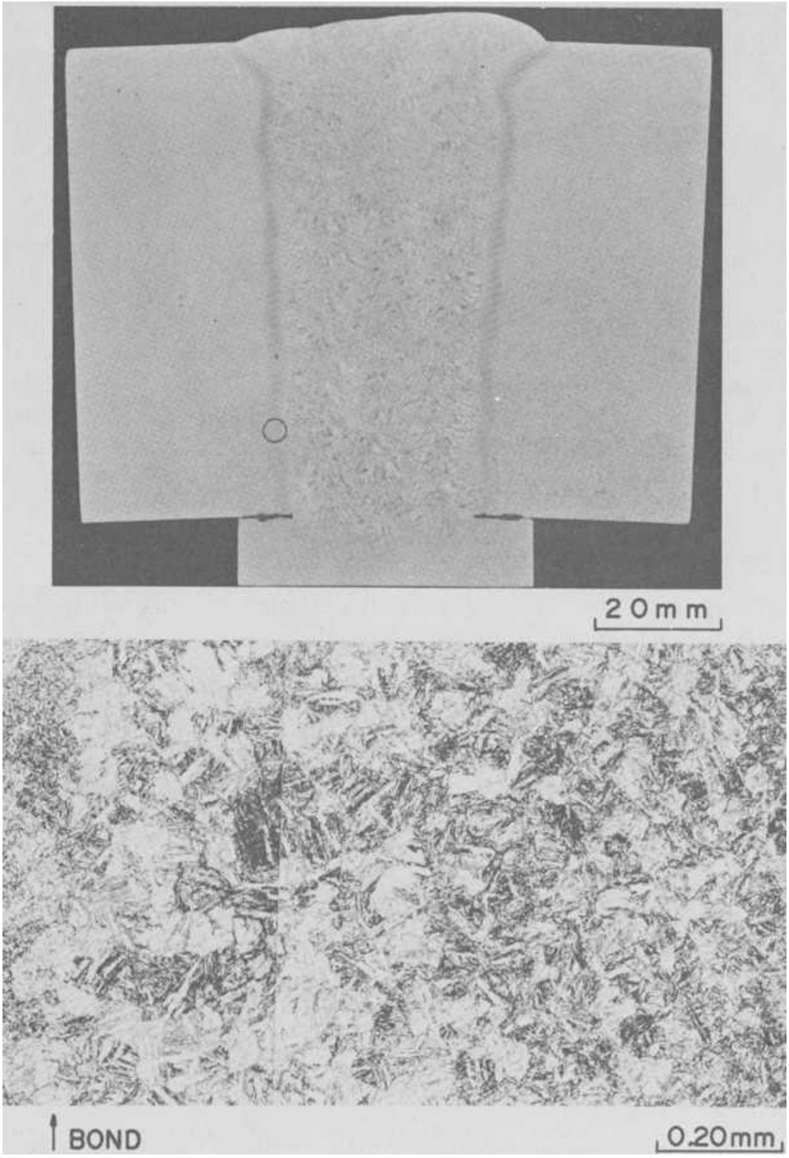

FIG. 11—*Cross section of stress relief cracking test specimen and microstructure of HAZ.*

The results of sulfide stress cracking tests conducted on the simulated heat-affected zones of Heat VB4 and a commercial 2¼Cr-1Mo steel are shown in Fig. 12. Greater resistance of Heat VB4 to hydrogen-assisted cracking was apparent.

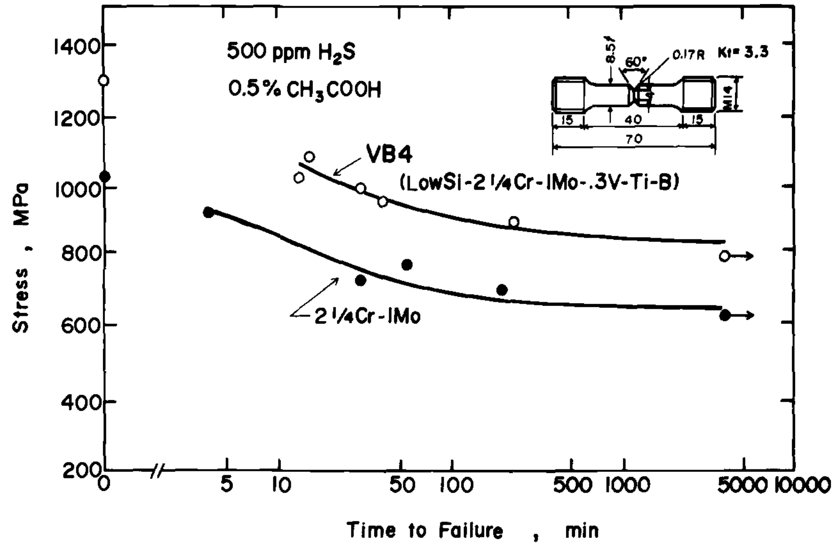

FIG. 12—*Results of sulfide stress cracking test for Heat VB4 and a conventional 2¼Cr-1Mo steel.*

Design Stress-Intensity Value

In the ASME Boiler and Pressure Vessel Code, Sec. VIII, Div. 1, the design stress-intensity value is established as the least of either one fourth of tensile strength at temperature or eight tenths of 10^5-h minimum rupture strength for many steels. In the case of 2¼Cr-1Mo steel the rupture strength determines the design stress at temperatures above approximately 450°C. In view of its high tensile strength and high creep rupture strength, the design stress for the ¼V-Ti-B bearing 2¼Cr-1Mo steel could be raised to a significant degree over the present design stress for 2¼Cr-1Mo steel. For the firm establishment of the design stress-intensity value, a substantial amount of work needs to be done to accumulate hot tensile and creep rupture data of this steel.

Summary and Conclusions

Low Si-0.10C-2¼Cr-1Mo-¼V-Ti-B steel has emerged from the study of microalloying 2¼Cr-1Mo steel. The modified 2¼Cr-1Mo steel possesses high hardenability (sufficient to produce bainitic structure at a thickness up to 400 mm) and excellent creep rupture strength. When considered as a steel for high-temperature hydrogenation reactors, there are some point's to be mentioned concerning its performance in the atmosphere of those reactors.

The creep rupture ductility of weld HAZ generally tends to be low compared with the base metal. The modified 2¼Cr-1Mo steel shows excellent creep rupture ductility in the HAZ despite its high creep rupture strength. This is an advantage in view of the past experience with creep cracking that took place in the HAZ [*11*].

As for the temper embrittlement susceptibility, low silicon 2¼Cr-1Mo steel shows markedly high resistance to temper embrittlement in both the base metal and the HAZ [*12,15*]. The modified steel contains titanium and boron in addition to the reduced silicon content, and therefore its resistance is considered better than that of 2¼Cr-1Mo steel.

Hydrogen attack is another material degradation that takes place in pressure vessels such as hydrogenation reactors. The modified steel contains a fair amount of vanadium and titanium, which results in the formation of carbides more stable than chromium carbide. Thus the steel is considered more resistant to hydrogen attack than 2¼Cr-1Mo steel.

The last point to mention is hydrogen-assisted cracking, which is a concern when a reactor wall containing residual hydrogen is cooled below a critical temperature. Strength has been considered a good measure for the susceptibility to hydrogen-assisted cracking. Strength of the modified steel is, compared with 2¼Cr-1Mo steel, significantly higher in both the base metal and the HAZ, and to a greater degree in the latter. However, the results of sulfide stress cracking tests proved that the steel is resistant to hydrogen-assisted cracking even in the HAZ. Thus it is reasonable to conclude that the modified steel is more resistant than 2¼Cr-1Mo steel.

The following conclusions can be drawn from the results obtained in the present study:

1. The creep rupture strength of the modified steel was improved compared with conventional 2¼Cr-1Mo (SA336 F22) steel.
2. The addition of a small amount of boron resulted in increased hardenability, thereby producing homogeneous bainitic structure in 400-mm-thick, water-quenched plates.
3. Considerable increase in resistance to temper embrittlement was achieved by the reduction of silicon content and the addition of titanium and boron.
4. The modified steel exhibited sufficiently high resistance to hydrogen-assisted cracking compared with 2¼Cr-1Mo steel.
5. In view of its high tensile strength and high creep rupture strength, the design stress-intensity value for the modified 2¼Cr-1Mo steel could be raised to a significant degree over the present design stress for SA336 F22 steel.

Acknowledgments

The authors wish to express their sincere appreciation to Masao Kashihara, director of the Steel Product and Fabrication Division of Japan

Steel Works, for his encouragement in conducting the present work, and to Tetsuo Nara, director of the R&D Division of the Japan Steel Works, for permission to publish this paper.

References

[1] Watanabe, J., Murakami, Y., Iwadate, T., and Mima, S., "A Fracture Safe Analysis of Pressure Vessel Made of $2^{1}/_{4}$Cr-1Mo Steels," Paper No. 126, Corrosion/76, International Corrosion Forum, Houston, 22-26 March 1976.

[2] Watanabe, J., Ohnishi, K., Murakami, M., and Chiba, R., "On the Cracks in Stainless Steel Internal Attachment Welds for High Temperature, High Pressure Hydrogen Services," Paper No. 104, Corrosion/77, International Corrosion Forum, San Francisco, 14-18 March 1977.

[3] Nelson, G. A., "Action of Hydrogen on Steel at High Temperatures and Pressures," Welding Research Council Bulletin No. 145, Oct. 1969.

[4] Weck, R., "Brittle Fracture of a Thick Walled Pressure Vessel," British Welding Research Association Bulletin No. 7, June 1966.

[5] Hicklin, W. L., "The Construction of Coal Conversion Vessels," presented at the Clean Fuels from Coal Conference, Institute of Gas Technology, 22-27 June 1975.

[6] Lacy, J. J., "Overview of Coal Liquefaction in the U.S. Department of Energy," ASME Publication 79-PVP-45, American Society of Mechanical Engineers, 1979.

[7] Canonico, D. A., "Assessment of Materials Technology for Gasifier and Reaction Pressure Vessels and Piping for Second Generation Commercial Coal Conversion Systems," ORNL-5238, Oak Ridge National Laboratory, Aug. 1978.

[8] Lochman, W. J., *Metallurgical Transactions*, Vol. 9A, Feb. 1978, pp. 175-181.

[9] Tanoosaki, K., *Tetsu-To-Hagane*, Vol. 57, No. 2, 1971, pp. 169-187.

[10] Klueh, R. L., *Metallurgical Transactions*, Vol. 9A, No. 11, Nov. 1978, pp. 1591-1598.

[11] Watanabe, J. and Chiba, R., *Journal of the Japan Welding Society*, Vol. 48, No. 3, March 1979, pp. 167-176.

[12] Murakami, Y., Watanabe, J., and Mima, S., "Heavy Section Cr-Mo Steels for Hydrogenation Services," presented at the 17th C.I.M. Annual Conference of Metallurgists, Montreal, 27-31 Aug. 1978.

[13] JIS Hand Book, Welding, Z3158-1966, "Method of Y-Groove Cracking Test," edited and published by the Japan Standards Association, 1979.

[14] Kanazawa, S., Otoguro, Y., Hashimoto, K., Sato, M., Takeda, T., and Horitani, T., *Tetsu-To-Hagane*, Vol. 63, No. 11 S761, Sept. 1977, p. 345.

[15] Murakami, Y., Nitta, Y., Nomura, T., and Nakajo, Y., Reprint of the National Meeting of the Japan Welding Society, No. 25, 1979, pp. 40-43.

J. A. Berthet,[1] *R. Blondeau,*[2] *D. Catelin,*[3] *A. Cheviet,*[1] *and J. H. Roux*[4]

Data Obtained on Industrial Production Plates 150 to 500 mm (6 to 20 in.) Thick in Chromium-Molybdenum Steel

REFERENCE: Berthet, J. A., Blondeau, R., Catelin, D., Cheviet, A., and Roux, J. H., **"Data Obtained on Industrial Production Plates 150 to 500 mm (6 to 20 in.) Thick in Chromium-Molybdenum Steel,"** *Application of 2¼Cr-1Mo Steel for Thick-Wall Pressure Vessels, ASTM STP 755,* G. S. Sangdahl and M. Semchyshen, Eds., American Society for Testing and Materials, 1982, pp. 148-165.

ABSTRACT: The construction of large petrochemical reactors working at elevated temperature in a hydrogen environment necessitates the use of 2¼Cr-1Mo (ASTM A 387, Grade 22, Class 2) steel with increasingly thicker plates. With this in mind, the aim of this paper is to present information on plates from 150 to 500 mm (6 to 20 in.) thick. After describing the production process, the following points are discussed: (*1*) reproducibility of analysis on different heats, (*2*) homogeneity of the composition and material properties in a heavy plate, (*3*) analysis of the development of the metallurgical properties in relation to the thickness and heat treatment, (*4*) examples of industrial production plates up to 500 mm (20 in.) thick, and (*5*) influence of low residual element contents with regard to resistance to temper embrittlement associated with long-duration service at elevated temperature.

KEY WORDS: chromium-molybdenum steels, temper embrittlement, tempering parameter, mechanical properties, residual elements, cleanliness, homogeneity, reproducibility

Several petrochemical processes—hydrocracking, hydrodesulfurization, coal liquefaction—need 2¼Cr-1Mo steel for the construction of large reactors working at elevated temperature in the presence of hydrogen. To improve the process, the present trend is to increase the size of these units; thus the need for large diameter [>4000 mm (13 ft)] and heavy weight (>1000

---

[1] Creusot-Loire, division Creusot-Marrel, Rive-de-Gier, France.
[2] Creusot-Loire, laboratoire, Le Creusot, France.
[3] Creusot-Loire, division Creusot-Marrel, Le Creusot, France.
[4] Creusot-Loire, division Creusot-Marrel, Paris, France.

ton) vessels is developing. This entails the use of increasingly thicker material [greater than 300 mm (12 in.)]. The metallurgical problems involved in the realization of high quality in products which are so thick must be understood and controlled. This 2¼Cr-1Mo steel has been manufactured in heavy plates up to 500 mm (20 in.) thick. The aim of this paper, after a description of the production process, is to show that these extra-thick products meet all the major quality requirements for the construction of large petrochemical reactors.

Heavy-Plate Production

Steel Mill Production

The steel is produced in an electric furnace and vacuum treated; this treatment comprises complete degassing and precise chemical composition adjustment by means of the introduction of elements under vacuum. The system offers two major advantages: (*1*) precise analysis, and (*2*) reproducibility of heats in the production of plates for the same reactor. This is an essential element of quality.

Analyses obtained on 420 heats are presented in Fig. 1. The histograms take account of thicknesses from 100 to 500 mm (4 to 20 in.). The aim in carbon and manganese content is a function of the thickness and heat treatment condition. In fact, several histograms are combined together. With regard to chromium and molybdenum content, the aim is at the same figure: 1 percent for molybdenum, average value of 420 heats is 0.995; 2.25 percent for chromium, average value of 420 heats is 2.244. Furthermore, impurity levels are very low. For instance, the average sulfur content on 420 heats is 0.007 percent, and the average phosphorus content is 0.009 percent. The following values can be guaranteed for the most severe specifications: $S \leq 0.005$ and $P \leq 0.009$.

Semiflat ingot molds are bottom poured. In this way, excellent chemical homogeneity within the same plate can be achieved. This is shown in Fig. 2 as regards carbon content, for which the results of 45 analyses on a plate [6530 by 3480 by 285 mm (257 by 137 by 11 in.) weighing 50 tons] are given.

Rolling

Ingot transformation is carried out by different routes chosen mainly with regard to the thickness of the final product. The techniques used could range from normal hot rolling to preforging before hot rolling. The advantages have been described elsewhere [*1*].[5] Use of preforging allows production of very heavy thick plates [500 mm (20 in.) or more] with the same soundness as

---

[5] The italic numbers in brackets refer to the list of references appended to this paper.

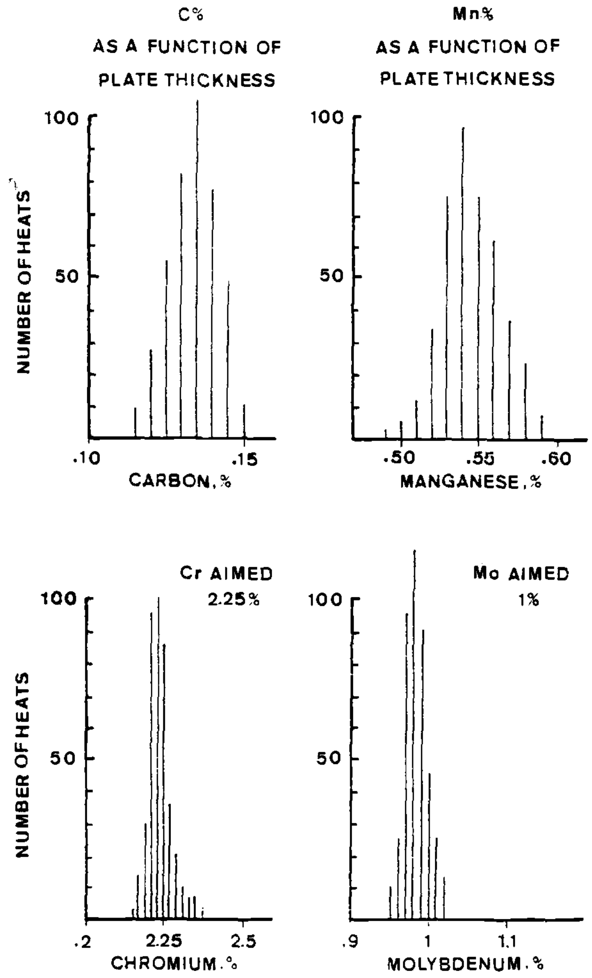

FIG. 1—*Histograms of 420 heats of 2¼Cr-1Mo steel.*

that which could be obtained on a thinner plate. Plates with unit weights up to 80 tons have been produced.

Heat Treatment

Plates can be heat treated at the steel mill or at the fabricator's shop (after forming).

Plates Delivered Heat Treated—Plates are austenitized at about 900 to 950°C (1650 to 1750°F), followed by accelerated cooling by means of water immersion. Plates are vertically immersed, which gives excellent homogene-

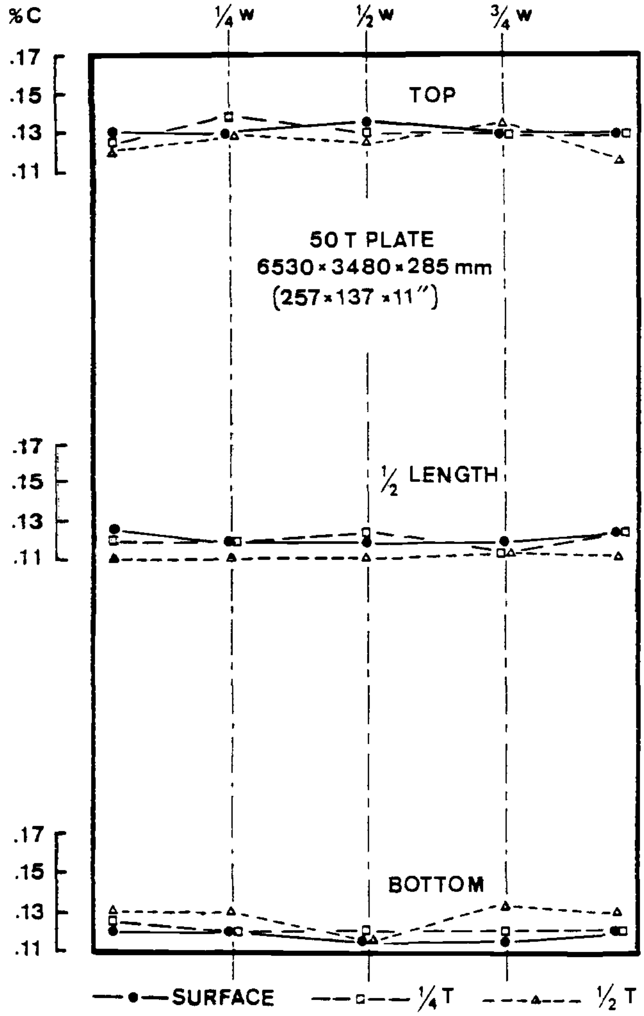

FIG. 2—*Histogram of carbon content in a 50-ton plate.*

ity of cooling rate between the two faces of the plate. A good knowledge of the kinetics of cooling obtained in the thickness of the plate is indispensable to ensure the right aim in chemical elements.

A great number of recordings of cooling rates have been carried out on plates up to 700 mm (28 in.) thick. Examples are reported in Fig. 3 for 200, 300, and 427 mm (8, 12, and 17 in.) thick plates. After cooling, a tempering treatment is carried out in order to improve workability of the plate on the shop floor. Generally this is carried out at about 650°C (1200°F). Indeed, the summation of tempering and stress-relieving treatments carried out at high

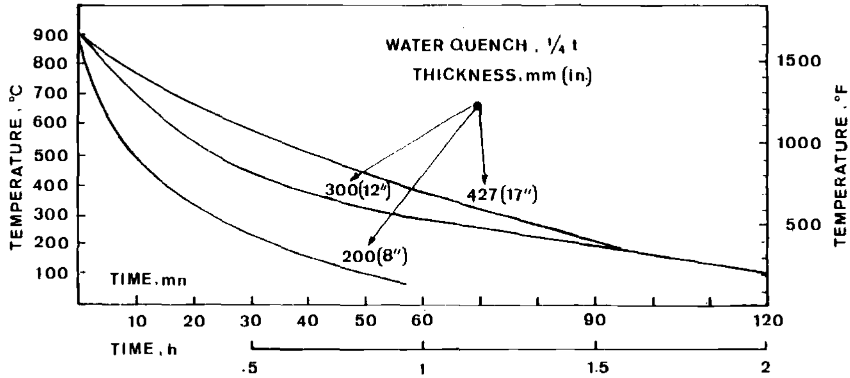

FIG. 3—*Examples of cooling curves of water-quenched heavy plates.*

temperature can be unfavorable for certain properties, as we will see later. Thus it is necessary to limit the tempering temperature.

The stress-relieving treatments to be carried out later at the fabricator's are simulated on test coupons.

Plates Delivered As Rolled (Stress Relieved)—This is the most frequent case for those heavy thicknesses which need to be hot formed; the austenitizing heat treatment is carried out in the fabricator's shop.

Complete cycles, including heating and cooling rates, are simulated at the steel plant. Sophisticated means allow precise simulation of cooling rates and cycles are carried out on plates using Data Trak, for instance.

Product Quality

Users seek the following properties:

1. Those which enable design of pressure vessels; these consist mainly of tensile and creep properties.
2. Those which improve workability; these essentially concern problems of weldability.
3. Those ensuring the stability of the material in service; for example, those giving assurance against a possible embrittlement in service.

Metal Properties Enabling the Design of Pressure Vessels

These are basically tensile and creep properties.

Tensile Properties—The attainment of mechanical properties on plates is mainly related to obtaining a structure consisting mainly of bainite, following the austenitizing heat treatment. It is therefore necessary to limit ferrite content to a minimum.

Figure 4 shows the development of transformation curves for different chemical analyses. If we take a 300-mm (12-in.)-thick plate, for example, with regard to cooling rates given in Fig. 3, it appears that only one chemical composition gives a structure free of ferrite—that is, Heat 4. This heat, however, is outside ASTM Specification for Pressure Vessel Plates, Alloy Steel, Chromium-Molybdenum (A 387-79b) limits of manganese content, namely, 0.74.

All of the industrial chemistries produced in accordance with ASTM A 387 necessarily show a certain amount of ferrite unless certain other additions have been made, in which case it would be necessary to give assurances regarding weldability (a steel outside ASTM A 387 limits being difficult to weld [*2*]), in addition to the proof of good subsequent behavior in service from a general point of view.

However, it is necessary to insist on two points:

1. It is possible to minimize ferrite content by taking advantage of the homogeneity of analyses between heats and for the same production order,

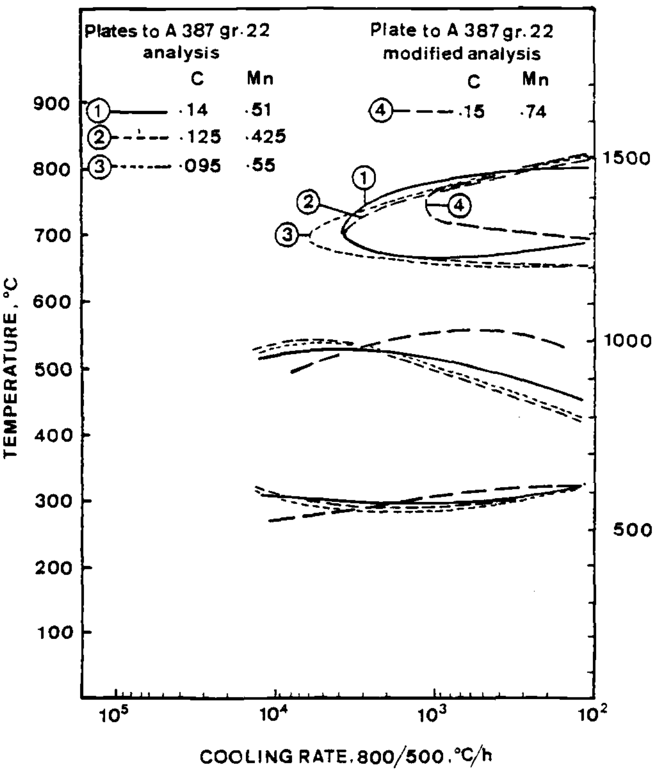

FIG. 4—*CCT diagrams with different plate analyses.*

and by at the same time having a chemistry aimed at the maximum permitted by ASTM A 387 for heavy-gage plates.

2. With constant parameter of tempering and stress-relieving treatments, the same tensile properties will be obtained by the same structure without resorting to the use of hardening elements. Let us take then the case of a 500-mm (20-in.)-thick plate with accelerated cooling and a 80-mm (3-in.)-thick plate with air cooling. If each has the same tensile properties, they each will have the same structure. A question is thus posed: Is it possible to obtain good mechanical properties on an industrial product 500-mm (20-in.)-thick and weighing 50 or even 80 tons?

The development of yield and tensile strength properties at ¼ thickness is given in Fig. 5 for two plates 200 and 500 mm (8 and 20 in.) thick, each having the same chemical composition in accordance with ASTM requirements. We have represented these characteristics in relation to a time/temperature parameter P,[6] including tempering and simulated stress-relieving treatments. These curves show that, for the same treatment, the drop in yield strength between 200 and 500 mm (8 and 20 in.) is in the range of 80 MPa (12 ksi) and in the range of 60 MPa (9 ksi) for tensile strength. In this case, for the given chemical composition on the coupon (carbon = 0.137 percent), ASTM minimum requirements are met.

Mechanical Properties at Elevated Temperature—The evolution of the ratios YS_T/YS_{RT} and TS_T/TS_{RT} as a function of temperature is given in Fig. 6 between 20 and 525°C [room temperature (RT) and 975°F] for plates up to 500 mm (20 in.) thick. In spite of the wide range of thickness considered, the scatter band of the UTS ratio is relatively narrow, although wider for the yield ratio. For these two ratios, the values obtained on the plates fall perfectly within the range of results published by ASTM [*3*].

Effect on Impact Properties—Figure 7 shows for the two plates with the same chemical composition the evolution of impact properties at −40°C (¼ thickness; transverse direction) as a function of the tempering parameter. Impact properties have the best level for a 650 to 690°C (1200 to 1275°F) stress-relief treatment for 20 h, while there is a drop in values for higher stress-relieving treatments.

Creep Properties—A great number of long-duration creep tests (up to 20 000 h) have been carried out in a wide range of temperatures and for dif-

---

[6]
$$\frac{1}{P} = \frac{1}{T} - \frac{R}{\Delta H} \ln t$$

where

T = temperature, K,
R = gas constant, and
ΔH = tempering activity energy = 100 kcal/mol.

From *Heat Treatment 76*, published by the Metal Society, United Kingdom.

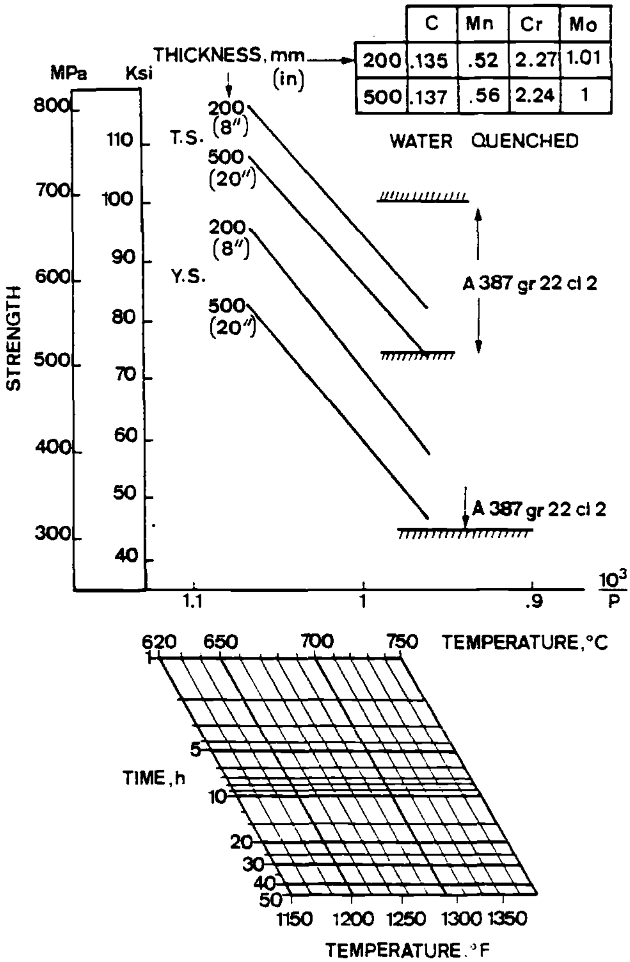

	C	Mn	Cr	Mo
200	.135	.52	2.27	1.01
500	.137	.56	2.24	1

FIG. 5—*Evolution of tensile properties in relation to tempering condition.*

ferent levels of tensile properties at room temperature. The stress rupture results are reported as a function of the time/temperature parameter in Fig. 8.

Examples of Industrial Production Plates—After showing the influence of the composition, thickness, and heat treatment parameters on the evolution of mechanical properties, it is necessary to give some examples of characteristics obtained on very thick plates. Tables 1, 2, and 3 give product analysis for several samples of plates, the heat treatments carried out, and tensile and impact properties. Analyses show in particular the very high level of cleanliness (very low sulfur, phosphorus, and tin contents) which give high impact values at low temperature (see also Fig. 9). Note the high upper shelf.

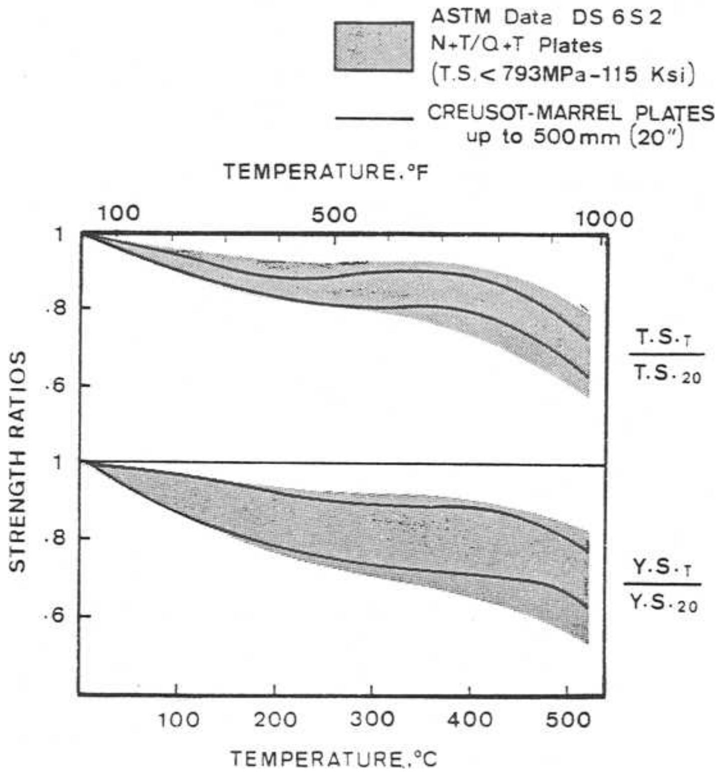

FIG. 6—*Evolution of strength ratios in relation to temperature.*

It is the proof of the cleanliness of the steel. The tensile properties in all cases conform with ASTM A 387 whatever the thickness.

Properties Improving the Workability

Essentially all aspects affect weldability. It is therefore primarily a question of analysis: highly precise analysis must be aimed at to obtain the uniform characteristics required after all the heat treatments imposed (as we have discussed earlier). Homogeneity of analysis within the plate itself (see Fig. 2) and homogeneity between heats makes it possible to limit the drawbacks due to chemical composition. Indeed, the maximum authorized by ASTM A 387 is not exceeded because it is possible to improve the homogeneity which removes the lowest points. Welding procedures therefore do not need to be varied to compensate for composition variations.

It is also a question of cleanliness of the steel; a low level of inclusions is

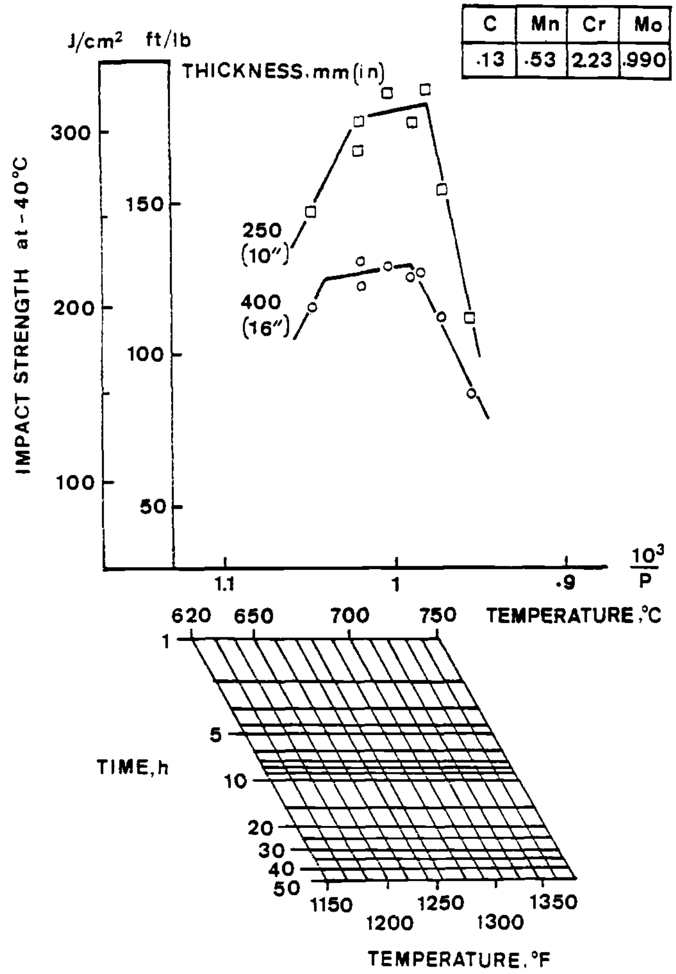

FIG. 7—*Evolution of impact strength in relation to tempering condition.*

necessary to offer all of the necessary guarantees against lamellar tearing, in particular. Tensile properties in the through-thickness direction are an excellent means, which is measurable, to appreciate the level of cleanliness. Good tensile properties are obtained in the three directions [see the example given in Table 4 for a 400-mm (16-in.)-thick plate]. In this example, the degree of homogeneity and isotropy which it is possible to obtain may be noted. A last point to take into account regards ultrasonic characteristics. A high level of ultrasonic quality is the result of great cleanliness of the steel and excellent soundness. Plates must be inspected on 100 percent of the sur-

TABLE 1—*Examples of analyses of production plates in 2¼Cr-1Mo steel.*

Thickness, mm (in.)	C	Mn	Si	Ni	Cr	Mo	Cu	Al	S	P	Sn	As	Sb
154 (6)	0.13	0.54	0.40	0.17	2.32	1.00	0.095	0.021	0.005	0.009	0.006	0.036	0.001^7
178 (7)	0.15	0.52	0.24	0.26	2.24	1.02	0.15	0.023	0.004	0.008	0.014	0.034	0.001^8
200 (8)	0.135	0.57	0.22	0.13	2.31	0.95	0.079	0.023	0.003	0.008	0.006	0.022	0.002
275 (11)	0.125	0.57	0.255	0.17	2.21	0.95	0.09	0.022	0.002	0.007	0.007	0.024	0.002
400 (16)	0.136	0.53	0.257	0.16	2.18	0.96	0.058	0.022	0.005	0.006	0.005	0.017	0.001^8
500 (20)	0.15	0.514	0.289	0.15	2.34	1.04	0.056	0.022	0.006	0.007	0.006	0.018	0.001^7

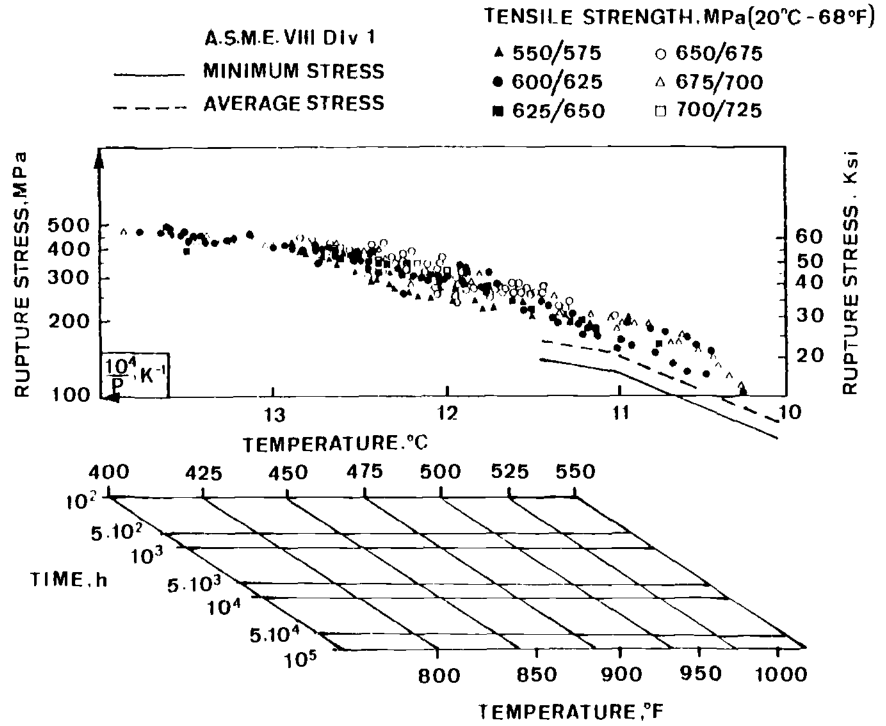

FIG. 8—*Creep results on heavy plates in 2¼Cr-1Mo steel.*

TABLE 2—*Heat treatment and tensile properties of industrial production plates.*

Top End - Transverse - ¼*t*				Test at 20°C (68°F)	
Thickness, mm (in.)	Quenching (W.Q.)	Tempering (A.C.)	PWHT[a]	Yield Strength, MPa (ksi)	Tensile Strength, MPa (ksi)
154 (6)	925°C 6 h (1700°F)	650°C 4 h (1200°F)	700°C 12 h (1290°F)	423 (61.3)	580 (84)
178 (7)	940°C 8.5 h (1725°F)	700°C 7.6 h (1290°F)	690°C 14 h (1275°F)	451 (65.5)	598 (86.8)
200 (8)	925°C 6 h (1700°F)	720°C 4 h (1330°F)	690°C 24 h (1275°F)	401 (58.2)	554 (80.4)
275 (11)	925°C 9.5 h (1700°F)	635°C 7.5 h (1175°F)	690°C 13 h (1275°F)	435 (63.2)	620 (90)
400 (16)	925°C 9 h (1700°F)	680°C 8 h (1255°F)	690°C 23 h (1275°F)	398 (57.8)	542 (78.7)
500 (20)	925°C 11 h (1700°F)	680°C 8 h (1255°F)	690°C 18 h (1275°F)	423 (61.4)	583 (84.6)

[a] Cooling rate: 50°C (90°F)/h for 154 to 275 mm (6 to 11 in.) plates; 20°C (36°F)/h for 400 to 500 mm (16 to 20 in.) plates.

TABLE 3—*Data on impact properties on production plates.*

Thickness, mm (in.)	FATT, °C (°F) Ref.[a]	FATT, °C (°F) S.C.[b]	ΔFATT °C (°F), (S.C.) − (Ref.)	T (40 ft·lb) 67.5 J/cm^2, °C (°F) Ref.	T (40 ft·lb) 67.5 J/cm^2, °C (°F) S.C.	ΔT 40 ft·lb (67.5 J/cm^2), °C (°F), (S.C.) − (Ref.)	(Mn + Si)-(P + Sn) × 10^4 [c]	$\bar{X}$[d]
154 (6)	−15 (10)	−0 (30)	15 (20)	−75 (−105)	65 (−80)	10 (25)	140	15.9
178 (7)	−15 (0)	−10 (10)	5 (10)	−70 (−95)	−50 (−60)	20 (35)	168	17.9
200 (8)	−25 (−15)	−25 (−15)	0 (0)	−75 (−100)	−70 (−90)	5 (10)	110.6	11.4
275 (11)	−45 (−50)	−30 (−20)	15 (30)	−80 (−115)	−80 (−110)	0 (5)	115.5	13.2
400 (16)	−15 (5)	+5 (40)	20 (35)	−65 (−90)	−50 (−60)	15 (30)	86.6	10.6
500 (20)	0 (30)	+15 (60)	15 (30)	−40 (−40)	−30 (−20)	10 (15)	104.4	11.9

[a] Ref.: WQ + T + PWHT.

[b] S.C.: Ref. + step cooled.

[c] Elements in percent.

[d] $\bar{X} = 10P + 5Sb + 4Sn + As/100$; elements in 10^{-4} percent.

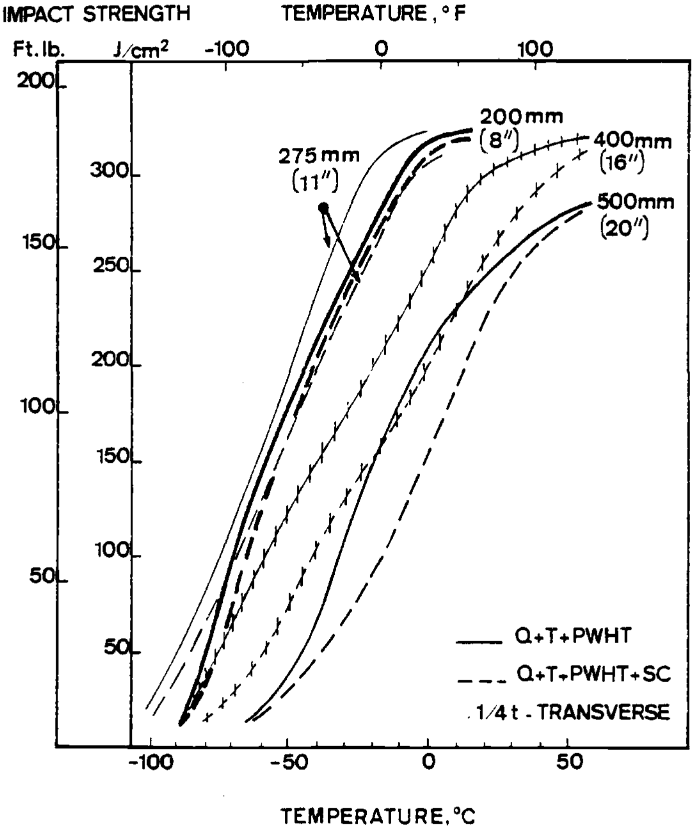

FIG. 9—*Examples of Charpy transition curves on production plates.*

face, and the most severe ultrasonic criteria must be met—for example, ASTM Specification for Straight-Beam Ultrasonic Examination of Plain and Clad Steel Plates for Special Applications (A 578-80) supplementary requirements. This is very important for the fabricator, for instance, during nondestructive testing of welded zones.

Properties Regarding the Security of the Installation In Service

A very important aspect is the risk of embrittlement of the material during the life of the vessel. It is generally accepted that the susceptibility to this reversible embrittlement may be measured by simulation of step-cooling treatment. We have compared the representation of this treatment with a long holding time at a service temperature by means of tests carried out on a 154-mm (6-in.)-thick plate.

TABLE 4—*Homogeneity of mechanical properties in a 400-mm (16-in.) thick plate.*

C	Mn	Si	Ni	Cr	Mo	Cu	Al	S	P	Sn	As	Sb
0.135	0.53	0.24	0.10	2.23	0.99	0.08	0.022	0.003	0.007	0.007	0.028	0.002

Location	Direction	Yield Strength, MPa (ksi)	Tensile Strength, MPa (ksi)	Elongation, %	Reduction of Area, %	FATT, °C (°F)	T 40 ft·lb (67.5 J/cm^2), °C (°F)
¼ t Top end	longitudinal	395 (57.5)	560 (81.2)	27	76	+5 (+40)	−40 (−40)
	transverse	374 (54.2)	550 (79.7)	27	75	+10 (+50)	−40 (−40)
	through thickness	369 (53.5)	544 (79)	25	74	+15 (+60)	−30 (−20)
½ t Top end	longitudinal	387 (56)	560 (81.2)	22	72	+15 (+60)	−25 (−15)
	transverse	365 (53)	551 (79.7)	26	75	+15 (+60)	−30 (−20)
	through thickness	399 (58)	556 (80.7)	20	68	+20 (+70)	−25 (−15)

Heat treatment at 925°C (1700°F) for 10 h, WQ at 650°C (1200°F) for 12 h, AC at 690°C (1275°F) for 23 h, cooling 20°C/h (36°F/h)

Tests have been carried out after the following cycles:

Reference	925°C (1700°F), 6 h, WQ + 620°C (1150°F), 6h, AC + 700°C (1290°F), 12 h, cooling at 50°C/h (90°F/h)
Step cooling	Two different cycles were compared (see Table 5)
Long-duration treatment	427°C (800°F), 17 500 h

Impact curves (Fig. 10) show that the two step-cooling cycles give identical results and that embrittlement is at least the same or even more than after long holding times at the test temperature 427°C (800°F).

A great number of plates have been subjected to this step-cooling cycle. Results corresponding to the plates discussed previously are given in Table 3. The impact levels obtained are consistently very good when we consider the development of the FATT criteria or T 67.5 J/cm^2 (T 40 ft·lb) between 0 and 20°C (0 and 35°F). This can be related to the very high level of cleanliness, which is expressed by the very low values in the factor $\bar{X}$ [*4*] and the factor (Mn + Si) (P + Sn) × 10^4.

In particular, it would appear that very low phosphorus and tin contents are an essential condition of high toughness after embrittlement treatments [*5,6*].

Embrittlement tests were also carried out on multipass weld joints of thick plates welded by the submerged arc process. For instance, Fig. 11 gives im-

TABLE 5—*Step-cooling treatments A and B.*

A	heating up to 593°C (1100°F), holding time 1 h cooling 5.6°C/h (10°F/h) down to 538°C (1000°F), holding time 15 h cooling 5.6°C/h (10°F/h) down to 524°C (975°F), holding time 24 h cooling 5.6°C/h (10°F/h) down to 496°C (925°F), holding time 60 h cooling 5.6°C/h (10°F/h) down to 468°C (875°F), holding time 125 h cooling 2.8°C/h (5°F/h) down to 316°C (600°F), then air cooling
B	heating up to 593°C (1100°F), holding time 1 h cooling 5.6°C/h (10°F/h) down to 538°C (1000°F), holding time 5 h cooling 5.6°C/h (10°F/h) down to 524°C (975°F), holding time 10 h cooling 5.6°C/h (10°F/h) down to 496°C (925°F), holding time 50 h cooling 5.6°C/h (10°F/h) down to 468°C (875°F), holding time 75 h cooling 5.6°C/h (10°F/h) down to 454°C (850°F), holding time 100 h cooling 5.6°C/h (10°F/h) down to 399°C (750°F), holding time 100 h cooling 2.8°C/h (5°F/h) down to 316°C (600°F), then air cooling

C	Mn	Si	Ni	Cr	Mo	Cu	S	P	Sn	As	Sb
.14	.56	.38	.13	2.26	.99	.11	.004	.008	.008	.033	.002

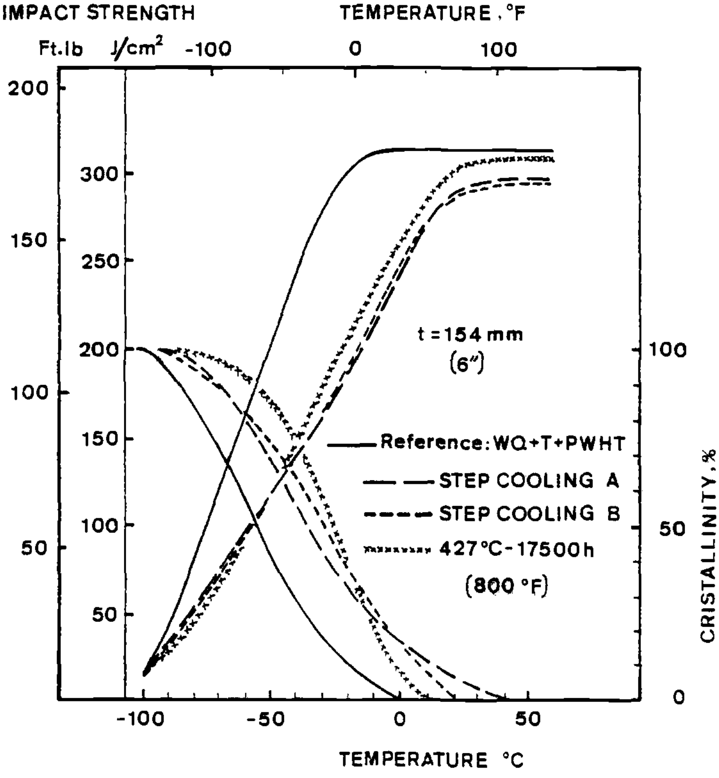

FIG. 10—*Comparison of results obtained with different embrittlement treatments.*

C	Mn	Si	Ni	Cr	Mo	Cu	Al	S	P	Sn	As	Sb
.12	.51	.305	.26	2.17	.995	.14	.025	.004	.007	.014	.035	.002

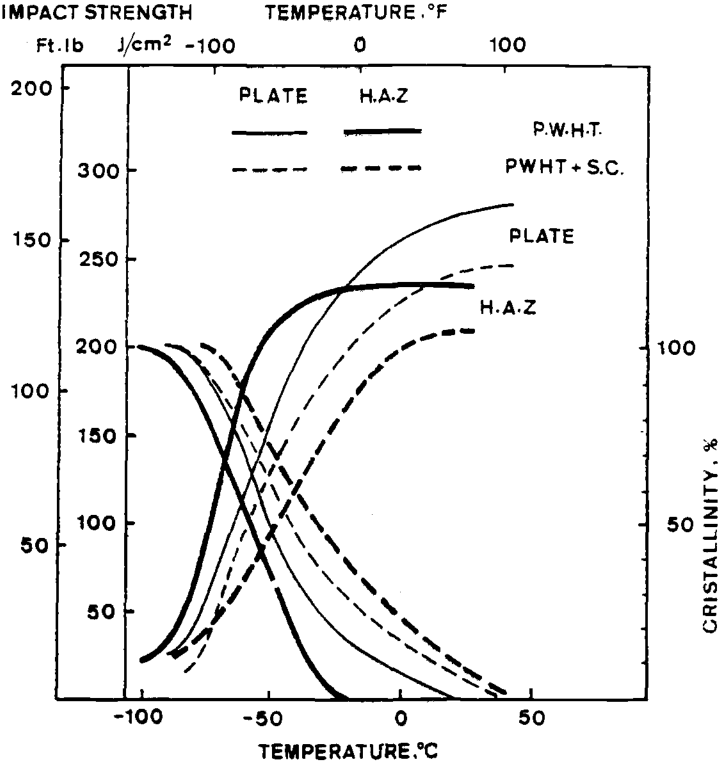

FIG. 11—*Comparison of embrittlement results on plate and in HAZ.*

pact curves obtained on a joint in 150-mm (6-in.)-thick plate with a weld energy of 23 kJ/cm.

The harder structure obtained in the heat-affected zone (HAZ) gives higher impact properties after stress-relieving treatment than in the base plate, but at the same time a larger shift after embrittling heat treatment. Both, however, present high values at low temperatures: *T* 67.5 J/cm² (*T* 40 ft·lb) = 70°C (−94°F).

Conclusions

This review of production and properties obtained on heavy thick plates in 2¼Cr-1Mo steel shows that:

1. It is possible to obtain a high and reproducible level of plate quality by a production process controlled at every stage.

2. Extensive metallurgical knowledge of this type of steel is necessary to meet the requirements of ASTM A 387, Grade 22, Class 2, by precise adjustment of the chemical composition adapted specially to subsequent heat treatment, and this for plates up to about 500 mm (20 in.).

3. The specifically adapted chemical composition and the high level of cleanliness give excellent impact values after a step-cooling treatment. Impact values obtained in the HAZ of welds in thick plates are also very high.

To conclude, it appears that very thick plates [up to 500 mm (20 in.)] in 2¼Cr-1Mo steel can be produced for the construction of large pressure vessels for the petrochemical industry.

References

[1] Cheviet, A. and Roux, J. H., "Heavy Gauge Plates for Nuclear Application," *Matériaux et Techniques*, Special Issue on "Special Steels and Nuclear Energy," No. 9-10, Sept./Oct. 1977.

[2] Creusot-Marrel internal study.

[3] Smith, G. V., "Supplemental Report on the Elevated-Temperature Properties of Chromium-Molybdenum Steels (An Evaluation of 2¼Cr-1Mo Steel)," ASTM Data Series Publication D.S. 6S2, 1971.

[4] Bruscato, R., "Temper Embrittlement and Creep Embrittlement of 2¼Cr-1Mo Shielded Metal Arc Weld Deposits," Welding Research Council Supplement, April 1970, p. 1480.

[5] Palmier, M., Comon, J., and Dollet, J., "Stabilité en Service d'Aciers Faiblement Alliés pour Emplois à Chaud Sous Contrainte," *Revue de Métallurgie*, Nov. 1972, p. 737.

[6] McMahon, C. J., Jr., "Temper Embrittlement Studies in 2¼Cr-1Mo Steel," API Refining Department, 42nd Meeting on Corrosion, May 1977, Chicago, Ill.

R. A. Swift[1]

Effects of Composition and Heat Treatment on the Mechanical Properties of 300-mm-Gage 2¼Cr-1Mo Steel Plate

---

REFERENCE: Swift, R. A., **"Effects of Composition and Heat Treatment on the Mechanical Properties of 300-mm-Gage 2¼Cr-1Mo Steel Plate,"** *Application of 2¼Cr-1Mo Steel for Thick-Wall Pressure Vessels, ASTM STP 755*, G. S. Sangdahl and M. Semchyshen, Eds., American Society for Testing and Materials, 1982, pp. 166–188.

ABSTRACT: The operating conditions of coal liquefaction and petrochemical pressure vessels require heavy-gage 2¼Cr-1Mo steel for which only limited data exist. A program was initiated to determine the effects of heat treatment and composition on the tensile and impact properties of 260- to 300-mm-thick 2¼Cr-1Mo steel. This work is the result of that study.

Commercial heats were produced with a variety of modifications in melting practice to obtain different levels of silicon, sulfur, phosphorus, and tin, and to modify the shapes of inclusions. Plates were rolled from large ingots, heat treated, and tested. Testing included room-temperature and elevated-temperature tension tests, and Charpy V-notch (CVN) tests for base condition toughness and for measuring the resistance to temper embrittlement.

Data are presented to show that low sulfur and a fine-grain size are important for improving base-notch toughness, and silicon, manganese, and phosphorus control are necessary to improve the resistance to temper embrittlement. Also, it is necessary to accelerate cool after austenitizing to achieve acceptable toughness levels and SA387-22 Class 2 properties.

KEY WORDS: heavy gage, notch toughness, chromium-molybdenum steels, residual elements

Chromium-molybdenum steels have been used in pressure vessels and boiler steam pipes since the 1930s. Although initially used in the annealed condition, normalizing and tempering, and quenching and tempering were introduced to enhance their mechanical properties. In the 1960s and early

---

[1] Supervisor, Product Research and Development, Lukens Steel Company, Coatesville, Pa. 19320.

1970s, research and development was aimed at increasing the strength of the steel [*1-3*][2] and at studying the factors affecting elevated temperature ductility [*3-5*]. It soon became evident that notch toughness is an important material property that could be adversely affected by heat treatment and exposure to elevated temperatures. Several review papers on the subject [*6-9*] and research on various embrittling phenomena [*4,10-13*] have shown the need to consider toughness in specifying a material.

Presently, there is much interest in 2¼Cr-1Mo steel in gages over 250 mm (10 in.) for coal liquefaction and high-pressure petrochemical vessels. Designs are to SA387-22 Class 2 properties, and users are demanding excellent notch toughness with some assurance of resistance to temper embrittlement (TE).

The traditional guarantee for notch toughness was quarterline, transverse Charpy V-notch (CVN) toughness of 54 J at 10°C (see Table 1 for conversion factors). This is being replaced by 54 J at −7°C. The most obvious means to improve notch toughness are to reduce sulfur, use sulfide shape control, heat treat to provide a tempered bainite microstructure, and use grain refiners to get a fine-grain size. A less obvious way to improve toughness is reportedly reducing the silicon content [*14*]. While each of these four factors has an effect on notch toughness, all but sulfur are reported to have an effect on resistance to TE [*14,15*]. Temper embrittlement is measured by testing the notch toughness of the material before and after a slow cooling cycle from 595 to 315°C. The shift in an energy transition temperature, usually the 54-J transition, is the measure of embrittlement. An indicator of resistance to TE is the Watanabe number or J^*-factor [*10*]. This number is defined by the equation:

$$J^* = (\%\text{Mn} + \%\text{Si}) \times (\%\text{P} + \%\text{Sn}) \times 10^4 \qquad (1)$$

and is reported to indicate resistance to TE when $J^* \leq 200$.

Experimental work performed on 91 and 136 tonne heats of SA387-22 with a variety of composition modifications with respect to silicon and sulfur is reviewed. Plate gages are 264 and 305 mm. Both air-cooled and accelerated-cooled plates have been tested. The strength and toughness are presented and discussed in relation to the aforementioned factors.

TABLE 1—*Conversion factors.*

1 ton = 1.103 tonne
1 in. = 25.4 mm
1 ksi = 6.89 MPa
°F = 9/5 °C + 32
1 ft·lb = 1.36 J

---

[2] The italic numbers in brackets refer to the list of references appended to this paper.

Material

All materials used in this study were obtained from full-size production heats. Several heats were produced using conventional commercial electric furnace and vacuum degassing practices. Others were produced with fine-grain practice, low sulfur, and/or low silicon. Table 2 lists the general characteristics of each heat and Table 3 lists their compositions.

Heats 2, 4, and 7 are the heats produced by conventional practices. They were bottom poured into 711 by 1575 mm cross-section molds. The only difference between the three heats is that Heat 2 was aluminum treated for grain-size control. Heat 1 was produced to 0.10 silicon maxima without aluminum deoxidation to ensure a coarse grain size. Only enough aluminum was used to permit treatment with a combination of calcium carbide (CaC_2) and calcium silicon (CaSi) powders for deoxidation and not for desulfurization or sulfide shape control. After degassing, the heat was teemed into 711 by 1575 mm molds. The remaining heats were double slag, electric furnace melted, aluminum deoxidized, calcium treated for desulfurization and inclusion shape modification, vacuum degassed, and teemed into 1016 by 2794 mm molds.

All ingots were rolled using standard heating and rolling practices. The plates were heat treated in car bottom furnaces using the treatments listed in Table 4. After tempering, test coupons, 76 by 230 mm by gage, were cut from top and bottom locations of the original ingot, stress relieved, and step cooled in laboratory furnaces. Minimum testing included transverse tension tests of the quarterline (QL) and transverse CVN transition temperature determinations of the centerline (CL). Additional testing was performed as shown in the data for individual plates.

Quantitative metallography was performed on the CL of each plate in each heat treated condition to determine the fraction proeutectoid ferrite ($\%\alpha$) and both the ferrite (α) and austenite (γ) grain sizes.

TABLE 2—*Types of melting practices.*

Heat	Type of Practice
1	low Si, conventional S, coarse grain
2	high Si, conventional S, fine grain
3	low Si, low S, fine grain, shape control
4	high Si, conventional S, coarse grain
5	high Si, low S, fine grain, shape control
6	high Si, low S, fine grain, shape control
7	high Si, conventional S, coarse grain
8	low Si, low S, fine grain, shape control

TABLE 3—*Compositions.*

Heat	C	Mn	Cr	Mo	Si	Cu	Ni	S	P	Sn	Al	J^*[a]
1	0.13	0.33	2.34	0.99	0.05	0.15	0.12	0.020	0.012	0.008	0.004	76
2	0.13	0.52	2.23	0.95	0.23	0.17	0.18	0.021	0.011	0.012	0.031	172
3	0.12	0.35	2.28	0.98	0.05	0.22	0.25	0.010	0.012	0.024	0.025	144
4	0.13	0.48	2.13	1.00	0.21	0.10	0.08	0.023	0.011	0.006	0.003	117
5	0.13	0.44	2.00	1.00	0.21	0.19	0.18	0.005	0.011	0.009	0.042	130
6	0.13	0.42	2.25	0.99	0.23	0.16	0.11	0.007	0.011	0.029	0.043	260
7	0.10	0.48	2.39	0.95	0.21	0.18	0.23	0.023	0.012	0.012	0.003	166
8	0.13	0.36	2.28	1.00	0.08	0.12	0.10	0.010	0.010	0.004	0.022	62
ASTM A 387-22	0.15 max	0.30-0.60	2.00-2.50	0.90-1.10	0.50 max	. . .	. . .	0.035 max	0.035 max	. . .	. . .	. . .

[a] $J^* = (Mn + Si)(P + Sn) \times 10^4$.

TABLE 4—*Heat treatments.*

Heat 1	900°C/12-AC-690°C/12-AC (1650°F/12-AC-1275°F/12-AC)	LMP[a] = 20.30 LMP = 36.55
Heat 2	900°C/12-WQ-690°C/12-WQ (1650°F/12-WQ-1275°F/12-AC)	LMP = 20.30 LMP = 36.55
Heat 3	900°C/12-WQ-690°C/12-WQ-690°C/36-FC (1650°F/12-WQ-1275°F/12-WQ-1275°F/36-FC)	LMP = 20.88 LMP = 37.56
Heat 4	955°C/12-WQ-655°C/6-WQ (1750°F/12-WQ-1225°F/6-WQ)	LMP = 19.49 LMP = 34.99
Heat 5	955°C/12-WQ-655°C/6-WQ-690°C/24-FC (1750°F/12-WQ-1225°F/6-WQ-1275°F/24-FC)	LMP = 20.62 LMP = 37.12
Heat 6	955°C/10-WQ-655°C/5-WQ (1750°F/10-WQ-1225°F/5-WQ)	LMP = 19.42 LMP = 34.86
Heat 7	955°C/10-WQ-655°C/5-WQ-690°C/24-FC (1750°F/10-WQ-1225°F/5-WQ-1275°F/24-FC)	LMP = 20.61 LMP = 37.11

Step-Cooling Cycle

595°C(1100°F) - hold 1 h - FC to 540°C(1000°F) - hold 15 h - FC to 525°C(975°F) - hold 24 h - FC to 495°C(925°F) - hold 60 h - FC to 470°C(875°F) - hold 100 h - FC to 315°C(600°F) - AC

[a] LMP = T°R (20 + $\log_{10} t$).

Data and Discussion

Metallography

Since microstructure is a critical factor in determining the toughness of a material, quantitative metallography was performed on the CL of each plate in the as-tempered condition. The microstructures of the air-cooled plates were measured for α grain size and those of the accelerated-cooled plates for prior γ and α grain sizes. The fraction α was obtained by standard lineal analysis. Grain sizes were calculated by

$$\text{GS} = 6.65 \log \quad \psi = 12.64 \tag{2}$$

where

$$\psi = \frac{\text{number of grain boundary intercepts}}{\text{total line length}}$$

The data in Table 5 summarize the quantitative metallography. Also included is the carbon equivalent (CE) calculated by

$$\text{CE} = \text{C} + \frac{\text{Mn}}{6} + \frac{\text{Cr} + \text{Mo}}{5} + \frac{\text{Cu} + \text{Ni}}{15} \tag{3}$$

TABLE 5—*Quantitative metallographic data.*

Heat	CE[a]	D_I[b]	Heat Treatment	%α	α Grain Size	γ Grain Size
1	0.869	7.94	NT	66	6.2	6.2
			QT	8.7		5.1
2	0.872	8.53	NT	57	8.9	8.3
			QT	35	8.7	7.7
3	0.862	6.68	QT	48	8.0	7.9
4	0.848	9.04	NT	72	6.4	7.5
			QT	5.6		5.1
5	0.828	7.04	QT	28	8.7	8.0
6	0.866	7.82	QT	14	8.9	8.2
7	0.875	8.98	NT	63	6.4	6.5
			QT	32	7.6	5.4
8	0.873	6.91	QT	16	9.4	7.9

[a] CE = Carbon equivalent.
[b] D_I = Ideal diameter.

and the ideal diameter (D_I) calculated from standard tables [*16*]. Representative micrographs are shown in Figs. 1 and 2.

The microstructures resulting from air cooling and tempering (NT) are a mixture of α and upper bainite (Fig. 1). Both coarse-grain (Figs. 1*a* and 1*b*) and fine-grain (Fig. 1*c*) plates are shown. The plates have 66, 72, and 57 percent α respectively. The coarse-grain plates have comparable α and γ grain sizes, ranging from 6.2 to 6.4 for α and 6.2 to 7.5 for γ. The fine-grain plate has an 8.9 α grain size and 8.3 γ grain size.

Microstructures obtained by accelerated cooling and tempered (QT) are a mixture of α and lower bainite (Fig. 2). The fraction α for all QT plates ranges from 5.6 to 48 percent. The coarse-grain plates have γ grain sizes of 5.1 to 5.4. The fine-grain heats have γ grain sizes from 7.7 to 8.2 and α grain sizes from 8.0 to 9.4.

The data in Table 6 indicate there may be a dependence of %α on CE and D_I. A regression analysis, however, showed less than a 50 percent correlation with either of these empirical measures of hardenability. This lack of correlation with commercial plates given commercial heat treatments is common because the calculations for CE and D_I do not consider all variables.

Room-Temperature Tensile Data

Tension tests were performed on material in the NT, QT, and QT plus stress relieved (QT + SR) conditions. The NT plates were tested for transverse and longitudinal properties at the surface (S), QL, and CL loca-

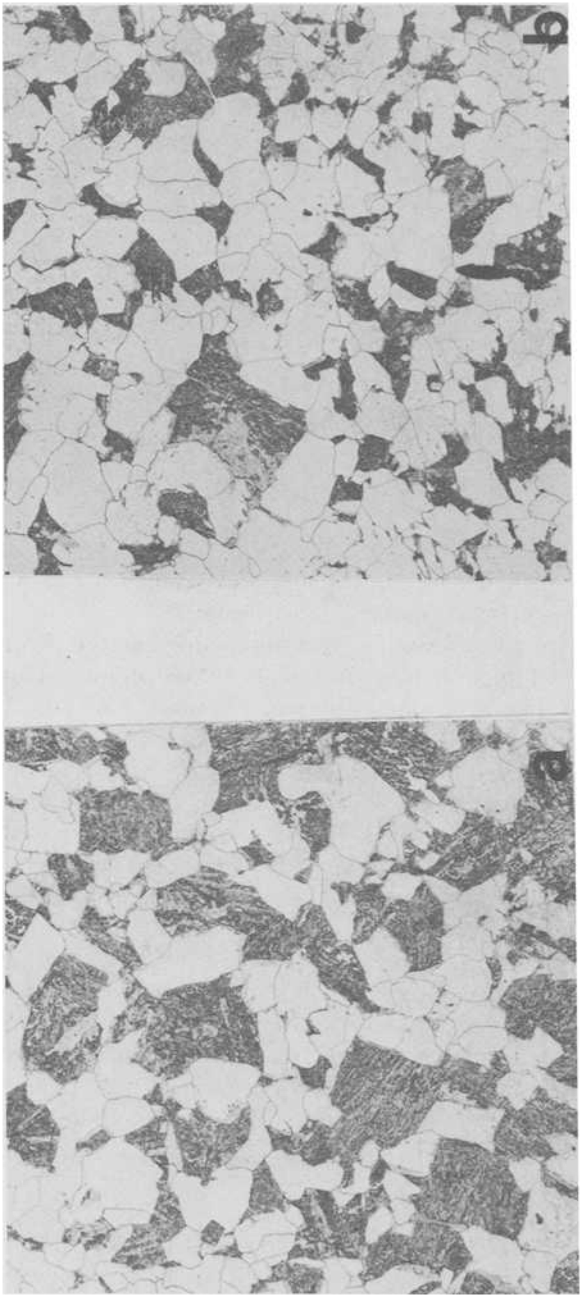
b
a

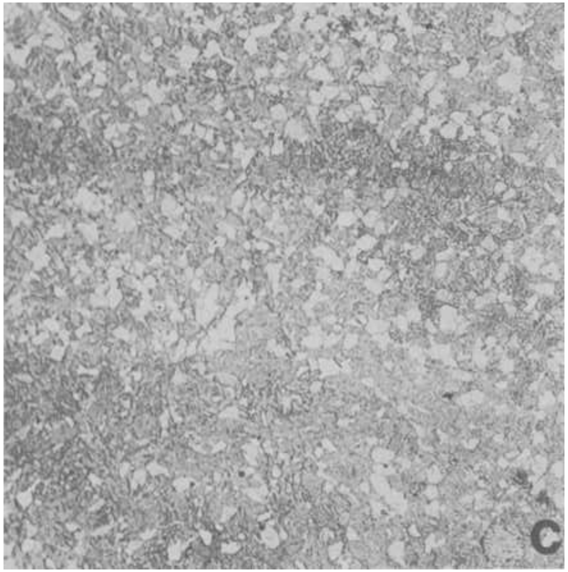

FIG. 1—*Optical micrographs of the centerline of 300-mm NT plates. Nital etch. X100.* (a) *Plate 1. Low silicon, coarse grain.* (b) *Plate 4. High silicon, coarse grain.* (c) *Plate 2. High silicon, fine grain.*

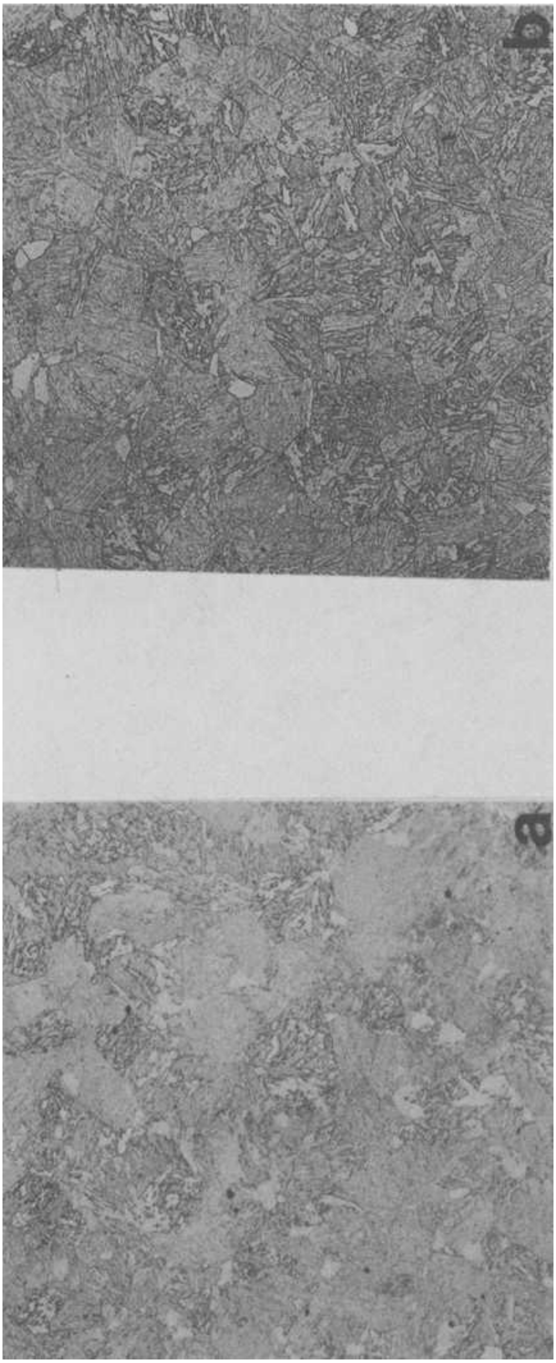
b
a

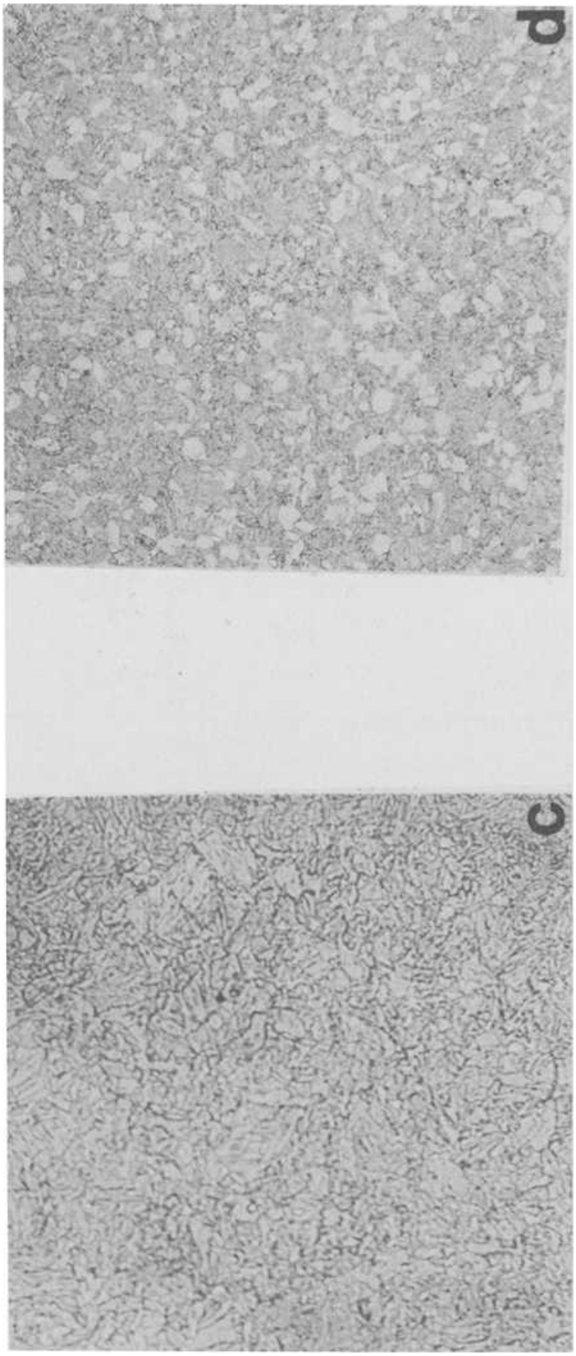

FIG. 2—*Optical micrographs of the centerline of 300-mm QT plates. Nital etch. X100.* (a) *Plate 1. Low silicon, coarse grain.* (b) *Plate 4. High silicon, coarse grain.* (c) *Plate 3. Low silicon, fine grain.* (d) *Plate 2. High silicon, fine grain.*

TABLE 6—*Tensile data for air-cooled plates.*

Heat	Gage, mm (in.)	Location	Orientation	YS, MPa (ksi)	UTS, MPa (ksi)	%E in 50 mm (2 in.)	%RA
1	305 (12)	S	T	336 (48.8)	548 (79.5)	24	67.0
		Q	T	325 (47.1)	523 (75.9)	26	68.5
		C	T	336 (48.7)	546 (79.2)	24	66.5
2	305 (12)	S	T	313 (45.5)	538 (78.1)	26	64.5
			L	336 (48.7)	533 (77.4)	28	73.5
		Q	T	296 (43.0)	527 (76.5)	24	48.6
			L	278 (40.4)	517 (75.0)	28	72.2
		C	T	338 (49.0)	520 (75.5)	24	60.4
			L	345 (50.1)	532 (77.2)	25	63.2
4	305 (12)	S	T	333 (48.3)	558 (81.0)	24	67.0
			L	332 (48.2)	555 (80.5)	25	68.8
		Q	T	287 (41.7)	525 (76.2)	23	53.1
			L	316 (45.9)	546 (79.3)	25	64.9
		C	T	300 (43.5)	535 (77.7)	18	38.3
			L	306 (44.4)	543 (78.8)	22	48.2
7	305 (12)	S	T	328 (47.6)	524 (76.0)	26	67.9
			L	341 (49.5)	532 (77.2)	27	74.3
		Q	T	274 (39.8)	494 (71.7)	26	61.9
			L	291 (42.3)	508 (73.8)	27	71.2
		C	T	271 (39.3)	488 (70.8)	24	47.0
			L	302 (43.9)	485 (70.4)	26	64.4
ASTM A 387-22 Class 1 Heat Treatment: HT1				205 (30)	415 to 585 (60 to 85)	18	45

tions. Transverse tests at the S, QL, and CL locations were made on the QT plates. Only the QL of QT + SR plates was tested.

All NT plates meet the requirements of SA387-22 Class 1 at S, QL, and CL. With the exception of Plate 7, the transverse yield strength (YS) and tensile strength (UTS) are fairly consistent through the gage. The large mass of the plates slows the cooling rate at the surface sufficiently to keep its strength relatively low. Plate 7, having only 0.10 percent carbon, appears to have the lowest hardenability and shows decreasing strength through the gage.

Accelerated cooling results in higher strength levels than obtained with the NT treatment. The difference in strength between S and QL or CL is more pronounced (Table 7). This is due to the "skin" effect; that is, S cools much faster than either QL or CL and therefore has a higher strength. Generally, the differences between QL and CL are minimal. Since the heat treatments are designed to provide specified properties after a subsequent postweld heat treatment (PWHT), QT plates may exhibit strength levels above specification (Plate 6) or ductility below specification (Plates 3 and 5).

Stress relieving causes an approximate 100 MPa drop in both YS and UTS and increases in percent elongation (%E) and percent reduction in area

TABLE 7—*Tensile data for accelerated-cooled plates.*

Heat	Heat Treatment	Gage, mm (in.)	Location	Orien-tation	YS, MPa (ksi)	UTS, MPa (ksi)	%E in 50 mm (2 in.)	%RA
1	2	305 (12)	S	T	538 (78.1)	644 (93.4)	20	67.7
			Q	T	506 (73.5)	630 (91.5)	20	67.0
			C	T	506 (73.5)	654 (94.9)	20	64.1
3	2	305 (12)	Q	T	485 (70.4)	614 (89.1)	16	37.6
			C	T	492 (71.4)	617 (89.6)	16	36.1
4	2	305 (12)	S	T	522 (75.1)	649 (94.2)	23	67.6
			Q	T	480 (69.7)	629 (91.3)	22	62.7
			C	T	485 (70.5)	623 (90.4)	17	39.2
5	6	264 (10⅜)	Q	T	544 (78.9)	668 (97.0)	16	52.7
6	6	264 (10⅜)	Q	T	603 (87.5)	744 (108)	ND[a]	ND
7	2	305 (12)	S	T	491 (71.3)	621 (90.0)	22	71.0
			Q	T	462 (67.1)	600 (87.1)	21	58.6
			C	T	396 (57.5)	548 (79.6)	21	46.3
8	6	264 (10⅜)	Q	T	558 (81.1)	654 (96.4)	20	65.6
ASTM A 387-22 Class 2					310 (45)	515 to 690 (75 to 100)	18	45

[a] ND = Not determined.

(%RA) (Table 8). While no plate fails to meet the required ductility, the decrease in strength has caused Plate 7 to fail to meet the UTS requirement. As with the large strength gradient noted previously, the low strength is probably due to the low carbon content of the plate (0.10 percent).

A regression analysis has shown that molybdenum, silicon, and manganese explain 91 percent of the YS and UTS data. Molybdenum and silicon have positive effects; manganese has a negative effect. D_I is more significant than CE but not as significant as the individual elements listed above. Grain size and $\%\alpha$ are insignificant factors within the scope of this study.

Elevated-Temperature Tensile Data

The data in Tables 9 and 10 summarize the results of elevated temperature tension tests of NT and QT + SR plates. The elevated temperature YS and UTS are also expressed as a fraction of the room temperature YS (RTYS) and UTS (RTUTS). The data are plotted in Figs. 3 to 8.

The NT plates show either a YS plateau or maximum in the temperature range of 370 to 480°C (Fig. 3). This is more evident when YS is expressed as the fraction RTYS (Fig. 4). Plate 7 shows a decrease in YS between the two coarse-grain heats. The UTS follows the same general trends as YS except that the maxima in UTS are not as pronounced. When expressed as fraction RTUTS, the trends are more evident (Fig. 4). Ductility, both %E and %RA, have slight minima in the temperature range of 316 to 482°C (Fig. 5). All data are within experimental scatter, and there are no apparent grain size effects. Also, the NT plates meet the design stresses for SA387-22 Class 1.

The data in Table 10 and Figs. 6 to 8 are for both the QT (Plate 4) and QT + SR (Plate 3) conditions. The tensile data (Fig. 6) show that the QT plate appears to lose strength rapidly with increasing temperature above 317°C. The QT + SR plate, on the other hand, appears to have a relatively constant strength up to 482°C. Above approximately 528°C, YS and UTS

TABLE 8—*Tensile data for the quarterline of stress-relieved accelerated-cooled plates.*

Heat	Heat Treatment	Gage, mm (in.)	YS, MPa (ksi)	UTS. MPa (ksi)	%E in 50 mm (2 in.)	%RA
1	3	305 (12)	403 (58.5)	540 (78.3)	24	70.8
2	3	305 (12)	379 (55.0)	534 (77.7)	24	62.6
3	5	305 (12)	379 (55.1)	543 (78.8)	26	72.9
4	3	305 (12)	395 (57.3)	541 (78.5)	22	64.7
5	7	264 (10⅜)	474 (68.8)	598 (86.8)	24	67.7
6	7	264 (10⅜)	462 (67.0)	606 (87.9)	24	74.4
7	3	305 (12)	378 (54.9)	512 (74.3)	28	65.9
8	7	264 (10⅜)	430 (62.4)	557 (80.8)	25	76.8
ASTM A 387-22 Class 2			310 (45)	515 to 690 (75 to 100)	18	45

TABLE 9—*Elevated temperature data for air-cooled plates.*

Heat	Temperature, °C (°F)	YS, MPa (ksi)	Fraction RTYS	UTS, MPa (ksi)	Fraction RTUTS	%E in 50 mm (2 in.)	%RA
2	21 (70)	298 (43.3)	. . .	528 (76.6)	. . .	24	40.4
	316 (600)	246 (35.8)	0.826	425 (61.7)	0.805	21	59.9
	371 (700)	258 (37.5)	0.866	433 (62.8)	0.820	19	55.8
	427 (800)	252 (36.6)	0.846	424 (61.6)	0.803	21	57.6
	482 (900)	243 (35.2)	0.815	404 (58.7)	0.765	21	60.2
	538 (1000)	219 (31.8)	0.735	342 (49.7)	0.648	26	67.5
	593 (1100)	198 (27.4)	0.664	261 (37.9)	0.494	36	82.0
4	21 (70)	296 (43.0)	. . .	524 (76.0)	. . .	26	60.0
	316 (600)	264 (38.3)	0.892	447 (64.9)	0.853	20	59.0
	371 (700)	265 (38.5)	0.895	457 (66.4)	0.872	19	58.9
	427 (800)	291 (42.3)	0.983	446 (64.8)	0.851	21	64.3
	482 (900)	254 (36.9)	0.858	413 (59.9)	0.788	21	66.3
	538 (1000)	257 (37.3)	0.868	370 (53.7)	0.706	24	73.6
	593 (1100)	220 (32.0)	0.743	286 (41.5)	0.546	33	82.6
7	21 (70)	283 (41.0)	. . .	509 (73.8)	. . .	27	67.1
	316 (600)	233 (33.8)	0.823	379 (55.0)	0.745	25	63.5
	371 (700)	212 (30.7)	0.749	392 (56.8)	0.770	21	60.0
	427 (800)	210 (30.5)	0.742	398 (57.7)	0.782	21	60.6
	482 (900)	220 (31.9)	0.777	380 (55.1)	0.747	23	62.6
	538 (1000)	207 (30.0)	0.731	333 (49.1)	0.664	24	69.4
	593 (1100)	185 (26.9)	0.654	253 (36.7)	0.497	37	82.7
Heat Treatment: HT 1							
ASME allowable stresses for SA387 Grade 22 Class 1	21 (70)	207 (30)		413 (60)			
	316 (600)	207 (30)		413 (60)			
	371 (700)	207 (30)		413 (60)			
	427 (800)	207 (30)		413 (60)			
	482 (900)	179 (26)		358 (52)			
	538 (1000)	103 (15)		207 (30)			

TABLE 10—*Elevated temperature data for accelerated cooled plates.*

Heat	Heat Treatment	Temperature, °C (°F)	YS, MPa (ksi)	Fraction RTYS	UTS, MPa (ksi)	Fraction RTUTS	%E in 50 mm (2 in.)	%RA
3	5	21 (70)	380 (55.1)	. . .	544 (78.9)	. . .	26	72.9
		316 (600)	369 (53.5)	0.971	493 (71.6)	0.906	20	70.4
		371 (700)	345 (50.0)	0.908	486 (70.6)	0.893	21	66.0
		427 (800)	338 (49.1)	0.889	464 (67.3)	0.853	21	68.8
		482 (900)	328 (47.6)	0.863	420 (60.9)	0.772	22	71.9
		528 (1000)	311 (45.2)	0.818	362 (52.5)	0.665	25	79.8
		593 (1100)	271 (39.4)	0.713	292 (42.4)	0.537	30	87.4
4	2	21 (70)	476 (69.1)	. . .	630 (91.4)	. . .	23	62.4
		316 (600)	444 (64.4)	0.933	576 (83.6)	0.914	18	62.7
		371 (700)	446 (64.8)	0.937	586 (85.0)	0.930	16	55.8
		427 (800)	428 (62.2)	0.899	542 (78.6)	0.860	17	64.1
		482 (900)	402 (58.3)	0.845	490 (71.1)	0.778	17	66.9
		593 (1100)	331 (48.1)	0.695	349 (50.7)	0.554	25	82.6
		649 (1200)	267 (38.7)	0.561	282 (40.9)	0.448	28	84.2
		704 (1300)	192 (27.9)	0.403	209 (30.4)	0.332	31	87.8
ASME allowable stresses for SA387 Grade 22 Class 2		21 (70)	310 (45)		517 (75)			
		316 (600)	234 (34)		469 (68)			
		371 (700)	227 (33)		455 (66)			
		427 (800)	220 (32)		441 (64)			
		482 (900)	207 (30)		413 (60)			

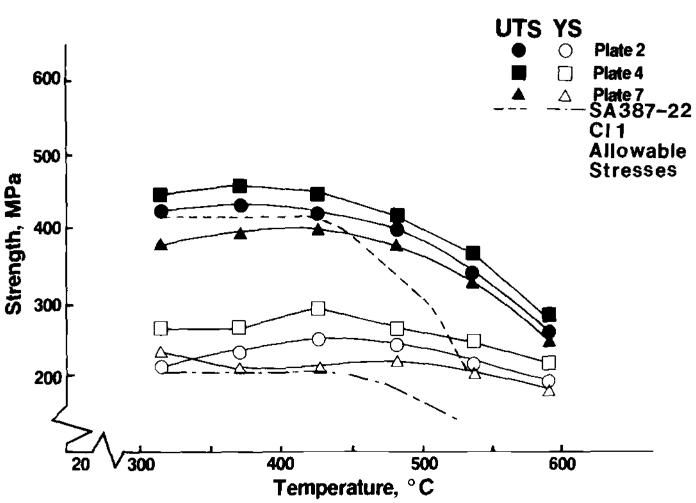

FIG. 3—*Elevated temperature yield and tensile strengths of NT plates.*

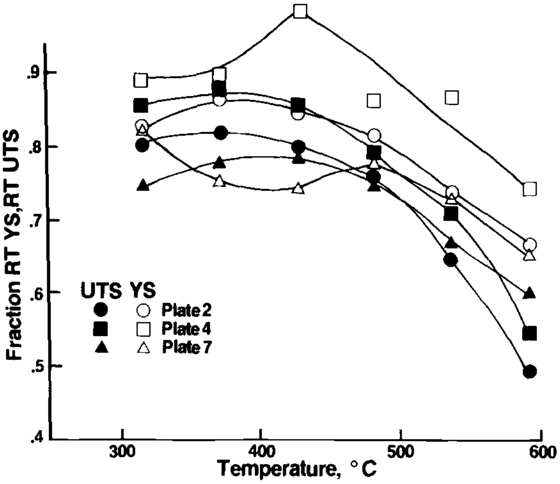

FIG. 4—*Elevated temperature yield and tensile strengths of NT plates as a fraction of room temperature strengths.*

appear to be independent of stress relieving. Expressing YS and UTS as the fraction of RT strength (Fig. 7) shows that both plates lose strength at a relatively constant rate above 400°C. The difference in initial strengths explains the apparent trends in Fig. 6. The ductility minima in Fig. 8 are more pronounced than those for the NT condition (Fig. 5). Although the fine-grain

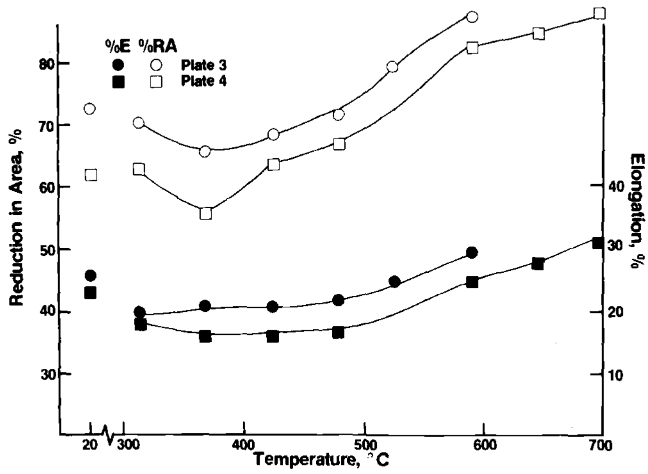

FIG. 5—*Elevated temperature ductility of NT plates.*

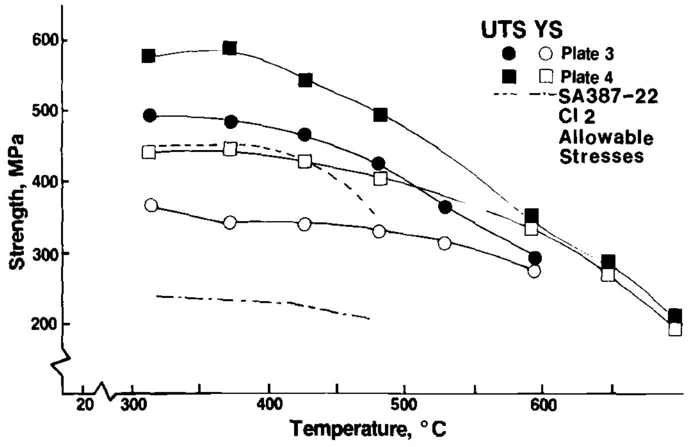

FIG. 6—*Elevated temperature yield and tensile strengths of Plate 4 (QT) and Plate 3 (QT + SR).*

plate (Plate 3) has higher ductility than the coarse-grain plate (Plate 4), it is not known if this is a grain size effect or a strength effect. It is probably a combination of both. Comparing the experimental data with the ASME design stresses for SA387-22 Class 2 shows that the QT and QT + SR exceed the allowables.

It is evident that the range of compositions tested herein will comfortably meet SA387-22 Class 2 in gages to 305 mm (12 in.) when QT + SR and SA387-22 Class 1 properties when NT. Also, the elevated temperature tensile

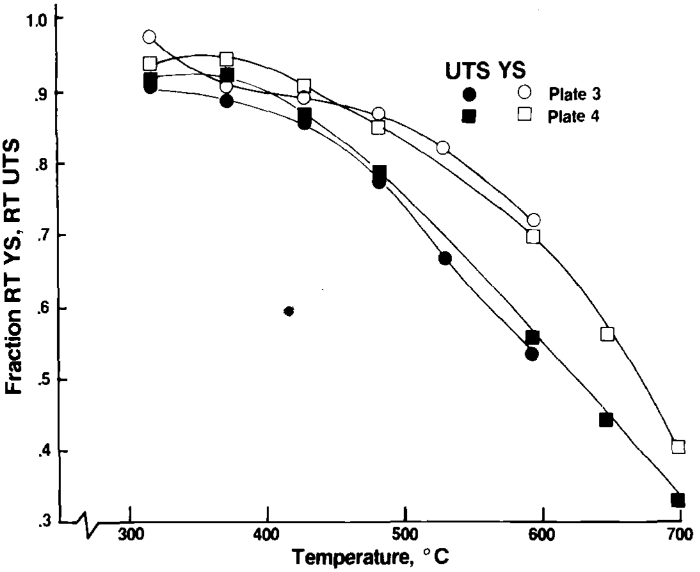

FIG. 7—*Elevated temperature yield and tensile strength of Plate 4 (QT) and Plate 3 (QT + SR) as a fraction of room temperature strengths.*

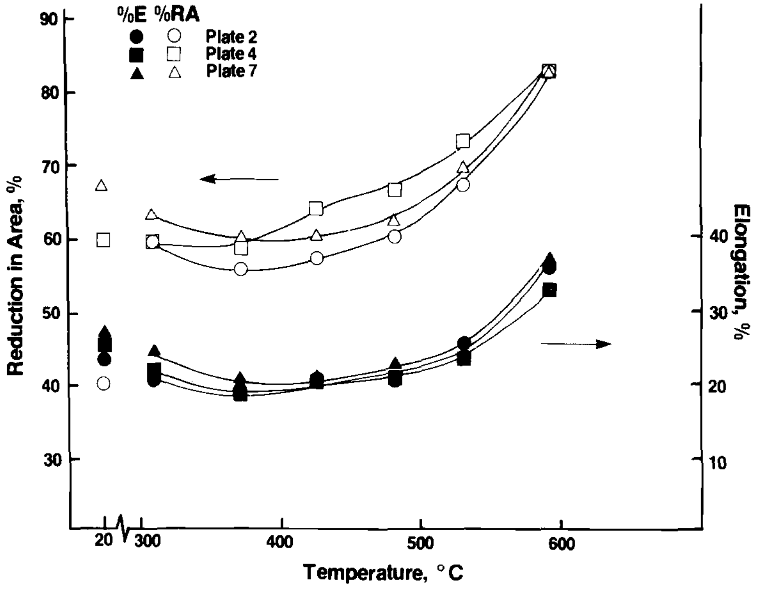

FIG. 8—*Elevated temperature ductility of Plate 4 (QT) and Plate 3 (QT + SR).*

properties are comparable for both the coarse-grain and the fine-grain plates.

Notch Toughness

Charpy V-notch impact data for the NT plates are given in Table 11. The measure of toughness is TT_{54}. Both as-tempered and step-cooled data, as well as the upper shelf energy (E_{us}) are given. Plate 2, the fine-grain plate, has the best as-tempered toughness with a TT_{54} of −4°C and an E_{us} of 122 J at the quarterline. This plate also has the highest *J**-factor (177) and shows the greatest shift in TT_{54} (ΔTT_{54}) after step cooling (see Table 4 for step-cooling cycle). Plate 1 has a *J**-factor of 76 and zero ΔTT_{54}. No E_{us} could be determined for Plate 3 since the highest test temperature was 52°C and the CVN curve was still in the transition region.

The QT and QT + SR toughness data are given in Table 12. The as-tempered toughness for all plates is superior to that of the NT plates. This is due to the much tougher microstructure obtained by accelerated cooling. Accelerated cooling is the only possible way to obtain SA387-22 Class 2 properties in these heavy gages without the use of vanadium or titanium as deoxidants [with high (0.05 or greater) residuals to increase hardenability] or boron as a grain refiner and hardenability agent.

The stress-relieved (SR) and step-cooled (SC) conditions are of most interest. For this reason, not all plates were tested for TT_{54} in the as-tempered condition. Tests were conducted as low as −34°C to determine whether or not TT_{54} was below that temperature. Full transition curves were generated only for the SR and SC conditions.

TABLE 11—*Transverse 54 J transition data for air-cooled plates.*

Heat	Location	$TT_{54}1$, °C (°F)	$TT_{54}3$, °C (°F)	ΔTT_{54}, °C (°F)	E_{us}, J (ft·lb)
1	Q	21 (70)	21 (70)	0 (0)	95 (70)
	C	16 (60)	...	...	82 (65)
2	Q	−4 (25)	16 (60)	20 (35)	122 (90)
	C	−4 (25)	...	...	95 (70)
4	Q	38 (100)	52 (125)	14 (25)	ND
	C	21 (70)	...	...	ND
7	Q	10 (50)	16 (60)	6 (10)	88 (65)
	C	16 (60)	...	...	75 (55)

Heat Treatment: HT 1
$TT_{54}1$: 54 J (40 ft·lb) transition temperature after tempering.
$TT_{54}3$: 54 J (40 ft·lb) transition temperature after step cooling.
ΔTT_{54}: $TT_{54}3 - TT_{54}1$
E_{us}: upper shelf energy after tempering
ND: not determined

TABLE 12—*Transverse 54 J transition data for accelerated-cooled plates.*

Heat	Heat Treatment	Location	$TT_{54}1$, °C (°F)	$TT_{54}2$, °C (°F)	$TT_{54}3$, °C (°F)	ΔTT_{54}, °C (°F)	E_{us}, J (ft·lb)[a]
1	2,3	Q	−51 (−60)	−46 (−50)	−40 (−40)	11 (20)*	122 (90)
		C	−34 (−30)	...	...	...	116 (85)
2	2,3	Q	−18 (0)	−32 (−25)	10 (50)	28 (50)*	102 (75)
		C	−18 (0)	...	...	...	102 (75)
3	4,5	Q	−48 (−55)	−57 (−70)	−71 (−95)	−14 (−25)+	204 (150)
		C	−46 (−50)	−51 (−60)	−46 (−50)	5 (10)+	150 (110)
4	2,3	Q	−26 (−15)	−18 (0)	2 (35)	28 (50)*	122 (90)
		C	4 (40)	...	...	...	102 (75)
5	6,7	Q	< −34 (< −30)	−74 (−95)	−57 (−70)	14 (20)+	204 (150)
		C	< −34 (< −30)	−71 (−95)	−34 (−30)	37 (65)+	204 (150)
6	6,7	Q	< −34 (< −30)	−107 (−160)	−65 (−85)	42 (75)+	241 (180)
		C	< −34 (< −30)	−62 (−80)	−29 (−20)	33 (60)+	174 (130)
7	2,3	Q	−15 (5)	−34 (−30)	2 (35)	17 (30)*	109 (80)
		C	−12 (10)	...	...	...	109 (80)
8	6,7	Q	< −34 (< −30)	−86 (−120)	−79 (−110)	5 (10)+	207 (155)
		C	< −34 (< −30)	−57 (−70)	−57 (−70)	0 (0)+	204 (150)

$TT_{54}1$: 54 J (40 ft·lb) transition temperature (TT) for base condition
$TT_{54}2$: 54 J (40 ft·lb) TT after stress relief
$TT_{54}3$: 54 J (40 ft·lb) TT after step cooling
ΔTT_{54}: * $TT_{54}3 - TT_{54}1$
+ $TT_{54}3 - TT_{54}2$

[a] Upper shelf energy after stress relieving.

The data in Table 12 show that grain size and sulfur level are critical factors in determining TT_{54} in the QT + SR condition. Silicon level does not seem to have a significant effect. In fact, a regression analysis shows that sulfur, γ grain size, chromium, and YS are the most significant factors.

The step-cooled data show positive or zero shifts in TT_{54} (ΔTT_{54}) for all plates and locations tested, except for QL of Plate 3 which has a −14°C ΔTT_{54}. This behavior is not unusual when the susceptibility to TE is low. The most severe embrittlement is shown by CL of Plate 6 with a ΔTT_{54} of 42°C. All other plates and locations have shifts between these two values.

Using the available QL data, an attempt to determine the significance of the J^*-factor on toughness was made. A correlation coefficient of 0.10 was obtained for the step-cooled TT_{54} as a function of the J^*-factor. The ΔTT_{54}, however, has a correlation coefficient of 0.59. When the CL data are added, the correlation of J^* with the step-cooled TT_{54} is 0.19 and with ΔTT_{54} is 0.60. The analysis also showed that silicon, carbon, manganese, and phosphorus are significant elements in determining ΔTT_{54}. Figure 9 is a graph of ΔTT_{54} versus J^*, and shows the trends even though there is considerable scatter.

Analysis of Data and Conclusions

As stated previously, cursory attempts at quantifying the effects of composition on strength and toughness were made. Due to the limited range in composition and small population size, it was not possible to be rigorous. Some significant findings, however, did come out of the data.

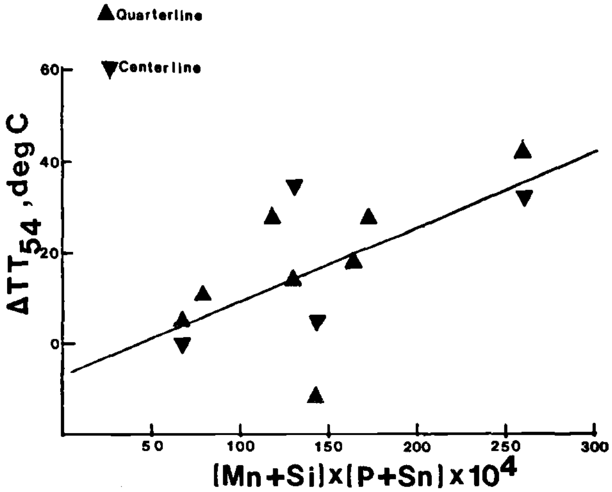

FIG. 9—ΔTT_{54} *as a function of* $(Mn + Si) \times (P + SN) \times 10^4$ *for both quarterline and centerline locations.*

Strength

Within the limits of this study, molybdenum, silicon, and manganese are the elements with the most significant effect on YS and UTS. Carbon is not significant since it has a narrow range and all but one data point is 0.12 to 0.13 percent. The usual hardenability factors do not adequately predict strength although D_I is better than CE.

Toughness

Sulfur level is the most significant factor in determining TT_{54}. γ grain size, chromium, and YS are also significant in TT_{54}. The ΔTT_{54} is affected most by silicon, carbon, manganese, and phosphorus, and there is a fair correlation of ΔTT_{54} with the J^*-factor. Other factors such as α grain size and strength affect notch toughness but did not appear to be significant in this study. This may be due to sample size and inherent variability that only a larger sample size will clarify.

Microstructure

The ideal diameter and carbon equivalent are equally significant in determining $\%\alpha$ but neither is 50 percent significant.

It should be realized that the levels of toughness reported in this study may not be the guarantee limits, nor should they be expected in every plate. Individual suppliers have different methods of producing their materials. That plus inherent heat-to-heat variations may cause levels of toughness lower than those reported herein.

References

[1] Mandich, L. I., Fogleman, E. L., and Gulya, J. A., "Elevated Temperature Properties of Heavy Gauge Cr-Mo Steel Plated," *Symposium on Heat Treated Steels for Elevated Temperature Service*, American Society for Mechanical Engineers, 1966.

[2] Carpenter, O. R. and Emmanuel, G. N., "The Use of Quenched and Tempered 2¼Cr-1Mo Steel for Fabrication of Advanced Design Pressure Vessels," *Symposium of Heat Treated Steels for Elevated Temperature Service*, American Society for Mechanical Engineers, 1966.

[3] Swift, R. A., "The Mechanism of Creep Embrittlement in 2¼Cr-1Mo Steel," *2¼ Chromium-1 Molybdenum Steel in Pressure Vessels and Piping*, American Society for Mechanical Engineers, 1971.

[4] Swift, R. A., "A Study of the Embrittlement of 2¼Cr-1Mo Steel Weld Metal," Ph.D. thesis, Drexel University, Philadelphia, Pa., 1974.

[5] Bruscato, Robert, "High Temperature Embrittlement Phenomena of 2¼Cr-1Mo Weldments," ASME Publication 71-Pet-19, American Society for Mechanical Engineers, 1971.

[6] McMahon, C. J., Jr., in *Temper Embrittlement in Steel, American Society of Testing and Materials, ASTM STP 407*, American Society for Testing and Materials, 1968, pp. 127-169.

[7] Emmer, L. G., Pense, A. W., and Stludt, R. D., "A Phenomenological Study of the

Susceptibility to Temper Embrittlement of 2.25Cr-1Mo," Report to the Pressure Vessel Research Committee, Lehigh University, Bethlehem, Pa., 1971.

[*8*] Swift, R. A. and Rogers, H. C., "A Critical Review of Weld Metal Embrittlement," *Welding Journal*, Vol. 50, No. 8, Welding Research Supplement, 1971, pp. 357s-373s.

[*9*] Jaffe, L. D. and Buffum, D. C., *Transactions of American Society for Metals, ASM 42*, 1950, pp. 604-618.

[*10*] Watanabe, J., Shindo, Y., Murakami, Y., Adachi, T., and Ajiki, S., *29th Annual PMEC of the ASME*, Dallas, Sept. 1974, pp. 15-18.

[*11*] Simmers, A. M., "Temper Embrittlement Susceptibility of Several Low Alloy Steels and Their Weld Metals," Lukens Steel Company RDR 69-20, Sept. 1969.

[*12*] Bruscato, Robert, *Welding Journal*, Vol. 49, No. 4, Welding Research Supplement, 1970, pp. 148s-156s.

[*13*] *Chrome Moly Steel in 1976*, MPC-4, American Society of Mechanical Engineers, 1976.

[*14*] McMahon, C. J., Jr., and Murza, J. C., *Journal of Engineering Materials and Technology*, ASME, Vol. 102, Oct. 1980, pp. 369-375.

[*15*] Capus, J. M., *Journal of the Iron and Steel Institute*, Vol. 200, No. 11, Nov. 1962, pp. 922-927.

[*16*] "Alloying Elements and Their Effects on Hardenability," Republic Steel Corporation, 1973.

A. Trautwein,[1] *H. Mayer,*[2] *W. Gysel,*[1] *and B. Walser*[2]

Structure and Mechanical Properties of 2¼Cr-1Mo Cast Steel for Pressure Components with Wall Thicknesses up to 500 mm

---

REFERENCE: Trautwein, A., Mayer, H., Gysel, W., and Walser, B., "**Structure and Mechanical Properties of 2¼Cr-1Mo Cast Steel for Pressure Components with Wall Thicknesses up to 500 mm,**" *Application of 2¼Cr-1Mo Steel for Thick-Wall Pressure Vessels, ASTM STP 755,* G. S. Sangdahl and M. Semchyshen, Eds., American Society for Testing and Materials, 1982, pp. 189-207.

ABSTRACT: 2¼Cr-1Mo steel is uniquely suited for heavy-walled steel castings because of its outstanding quenching and tempering characteristics, good impact properties, and ease of processing. This steel has been recently accepted in numerous specifications, for example, ASTM A 217, ASTM A 356, and DIN 17245. This contribution should be viewed in conjunction with the paper "Internal Properties of 2¼Cr-1Mo Cast Steel for Heavy Castings" by H. C. Lueling, Karl Achtelik, and J. M. Motz, in this publication. The present paper makes a contribution to the relatively sparse documentation regarding the core properties of large cast sections. The primary topic is the determination of the relation between primary and secondary structures and the toughness characteristics or transition temperatures. This is accomplished by comparing the test results on specimens taken from different casting sections with the results of separately heat-treated samples from the same casting using the actual cooling curves. In addition, continuous cooling diagrams and typical microstructures for selected casting sections were determined to demonstrate the segregation effect. This work was augmented with Pellini and FATT 50 percent testing together with elevated-temperature tension tests. Extended weld procedure investigations with matching electrodes were conducted on plates of 100 mm thickness. All results confirm that 2¼Cr-1Mo cast steel when oil quenched and tempered will show very homogeneous strength and toughness characteristics in wall thicknesses up to 500 mm (20 in.). The properties of weld joints made with matching electrodes are also uniform. This material performance makes this steel particularly well suited for heavy-walled components subjected to pressure.

KEY WORDS: 2¼Cr-1Mo cast steel, thick walled casting, heat treatment, internal properties, NDT temperature, impact transition, microstructure, CCT diagram, high temperature tensile properties, welding qualification

[1] Dipl.-Ing. and Ingenieur SIA, respectively, George Fischer Ltd., Schaffhausen, Switzerland.
[2] Dr.-Ing. and Dr. SC. techn., respectively, Sulzer Brothers Ltd., Winterthur, Switzerland.

Creep testing of 2¼Cr-1Mo cast steel began in Switzerland in the early 1960s. Initially, the carbon content was limited to the range of 0.10 to 0.15 percent, corresponding to the 0.10 to 0.15 percent carbon content of 2¼Cr-1Mo forging steel. However, the creep tests showed that increasing the carbon range to 0.15 to 0.20 percent provided a definite improvement in the creep properties without any significant effect on the good weldability of this material.[3] In the meantime, this steel has been included in all of the important European standards concerning creep resisting cast steel. It soon became evident that this cast steel has excellent hardenability due to its relatively high alloy content. This hardenability guarantees uniform properties over the entire cross section of thick-walled castings. Thus, besides being used as a creep-resisting steel, 2¼Cr-1Mo cast steel is increasingly being considered for thick-walled parts requiring a quenched and tempered structure. Also, it is thought that the best properties are attained for this steel when subjected to a liquid quench. The earlier development of 2¼Cr-1Mo cast steel concentrated on optimizing the chemical composition and heat treatment. As a further development, the Swiss Working Group for Creep Resisting Steels (see Note at end of this paper) is presently focusing its efforts on investigating the creep behavior within large cross sections of the base material as well as the creep properties of the weld joints and the weld metal.

Until recently, little was known about creep properties of 2¼Cr-1Mo cast steel. The Working Group investigations of this material, which will be reported here, had the following goals: (*1*) to produce a test block, according to exact production specifications, with various wall thickness up to 500 mm, (*2*) to extensively test the properties of the base material in the various cross sections of the test block, (*3*) to establish a well-documented welding procedure qualification, and (*4*) to run extensive creep tests on material from the test block and the welded test plate.

At present, the creep tests have not run long enough to provide a detailed report, but all of the other investigations have been completed. This report should be viewed in connection with the paper by Lueling et al.[4]

Test Material

The investigations utilized a standardized test block with a weight of 2800 kg in the as-cast condition. The chemical analysis is given in Table 1 and conforms with ASTM Specification for Martensitic Stainless Steel and Alloy Steel Castings for Pressure-Containing Parts Suitable for High-Temperature Service (A 217-80, Grade WC9) and DIN 17245/GS-18CrMo910 standard specifications for creep resisting steel. The test block consisted of three sec-

---

[3] Gysel, W., "Thick-Walled Castings for Welded Components" (in German), *Konstruieren und Giessen*, Vol. 4, Okt. 1980, VDI Verlag, Duesseldorf.

[4] This publication, pp. 26-45.

TABLE 1—*Specification, chemical analysis, and test results on cast specimen.*

Specification and Heat Treatment			Mechanical Properties (Range or Minimum)				
Specification	Grade	Heat Treatment	Tensile Strength, MPa	Yield Strength, MPa	Elongation in 2 in., %	Reduction of Area, %	Impact Energy (CVN/ISOV), J
ASTM A 217	WC 9	NT 675 C	485 655	275	20	35	. . .
DIN 17245	6S-18CrMo910	QT 680 C	590 740	400	18	. . .	40
Testblock 2¼Cr-1Mo Heat 6F 49 335		QT 700 C			Results		
Test bar cast on:[a]							
Sector 150 mm			612	451	26	70	. . .
Sector 300 mm			622	469	26	72	. . .
Sector 500 mm			612	460	26	70	. . .

		Chemical Composition (Range or Minimum or Actual)							
Specification	Grade	C	Mn	P	S	Si	Ni	Cr	Mo
ASTM A 217	WC 9	0.18	0.40 to 0.70	0.04	0.045	0.60	0.50	2.00 to 2.75	0.90 to 1.20
DIN 17245	GS-18CrMo910	0.15 to 0.20	0.50 to 0.80	0.03	0.025	0.30 to 0.60	. . .	2.00 to 2.50	0.90 to 1.10
Testblock 2¼Cr-1Mo Heat GF 49 335		0.18	0.57	0.013	0.007	0.34	0.08	2.34	0.93
Weld electrode 2¼Cr-1Mo Deposit analysis		0.13	0.88	0.018	0.013	0.35	0.03	2.41	0.91

[a] Dimensions: 100 by 120 by 500 mm.

tions (in the figures called sectors) with wall thicknesses of 150, 300, and 500 mm. The initial heat treatment of the test block is given in Table 2. The temperature distribution during heat treatment was measured by means of six thermocouples. Each section contained a thermocouple exactly in the middle of the section and one 20 mm below the surface. The measured cooling curves after oil quenching are shown in Fig. 1. The material properties,

TABLE 2—*Heat treatment and cooling simulation.*

Heat Treatment A	
2¼Cr-1Mo test block; Heat GF 49335	
Soft Annealing	730°C/20 h/furnace
Quenching	940°C/20 h/oil
Tempering	700°C/12 h/furnace
Cooling Simulation B	
Test specimen from 150-mm sector; center	
Hardening	940°C/8 h/cooling simulated
Tempering	700°C/8 h/furnace
Cooling Simulation C	
Test specimen from bar 100 by 120 by 500 mm cast on 500-mm sector	
Hardening	940°C/1 h/cooling simulated
Tempering	700°C/4 h/furnace

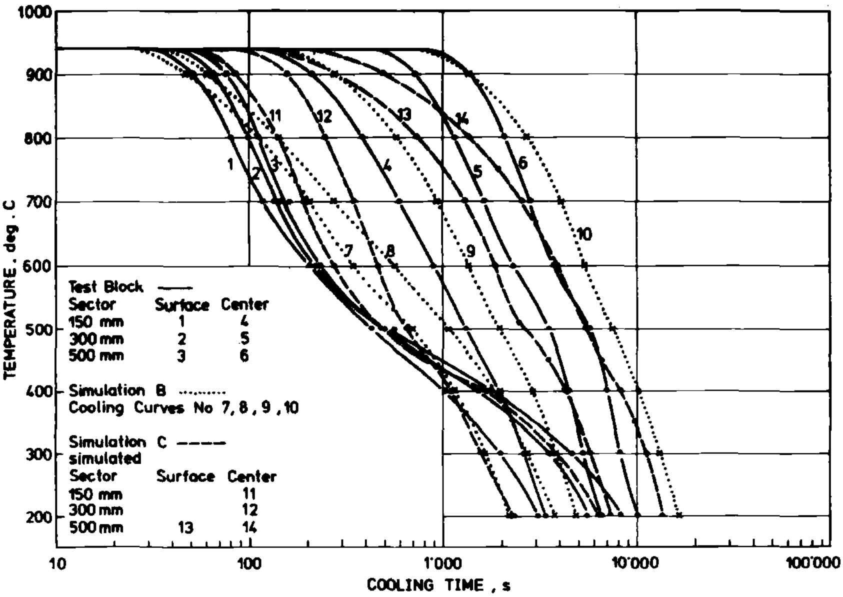

FIG. 1—*Measured cooling curves.*

after this initial heat treatment, were obtained from 100 by 120 by 500 mm coupons cast onto each section of the test block. The results are also given in Table 1.

Test Procedure

Figure 2 shows how the test block was cut up. After the heat treatment, a plate was taken from the center region and the surface region of each section. This allowed the material properties to be determined as a function of the wall thickness and of the position within the test block. In addition, a 100-mm plate was cut from the 150-mm section and used for a welding

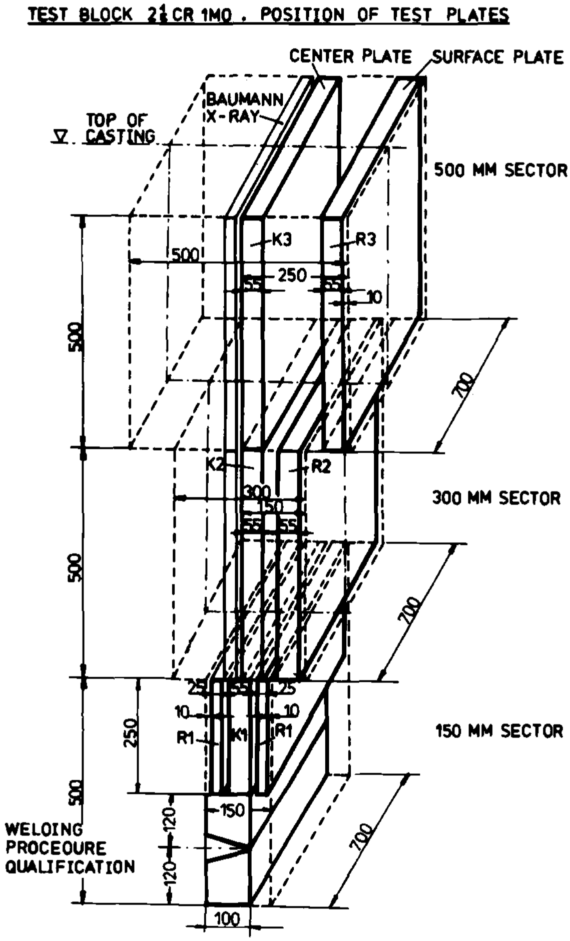

FIG. 2—*Cutup of the test block.*

qualification test. A 10-mm-thick plate, used for investigation of the solidification characteristics of the block cross section, was taken from the center region of the test block.

The integrity of the test block had been proved by Baumann sulfur prints and radiographic testing. Figure 3 shows how the individual test plates were cut up into test specimens for the various material property tests. The test specimens were systematically numbered so that an exact relationship between the test results and the position of each specimen within the test block could be obtained.

Results

Macrostructure of the Test Block

The test blocks were cast by a well-proven method. The macrostructure of the entire block cross section was investigated, but neither the sulfur print nor the radiographic testing indicated any important segregation effects or other macrostructural defects.

Transformation Characteristics

Figure 4 shows the CCT diagram, measured under continuous cooling conditions, for test specimens from the surface and center of the 500-mm section and from the coupon from this section. The position of the test specimen within the block had remarkably little influence on the transformation behavior. The most distinct feature is the small shift of the ferrite region to shorter times for center specimens compared with coupon specimens. However, the upper and lower bainite regions and the martensite transformation temperature were not significantly influenced. These results show that the as cast macrostructure has only a small influence on the transformation behavior of 2¼Cr-1Mo cast steel.

Examination of the microstructures of the various specimens for each of three typical cooling rates (II, VI, and IX), as shown in Fig. 5, confirms this. These microstructures are practically identical. The ferrite content, however, increases with increasingly slower cooling rate for all specimens. This is in agreement with the CCT diagram. With very slow cooling, an unfavorable pearlite-ferrite structure occurs. This structure has inferior notch toughness. Thus very thick cross sections need to be liquid quenched or forced-air quenched in order to prevent such a microstructure.

Mechanical Properties at Room Temperature

Figure 6 shows that the wall thickness has very little influence on the mechanical properties at room temperature. The difference between

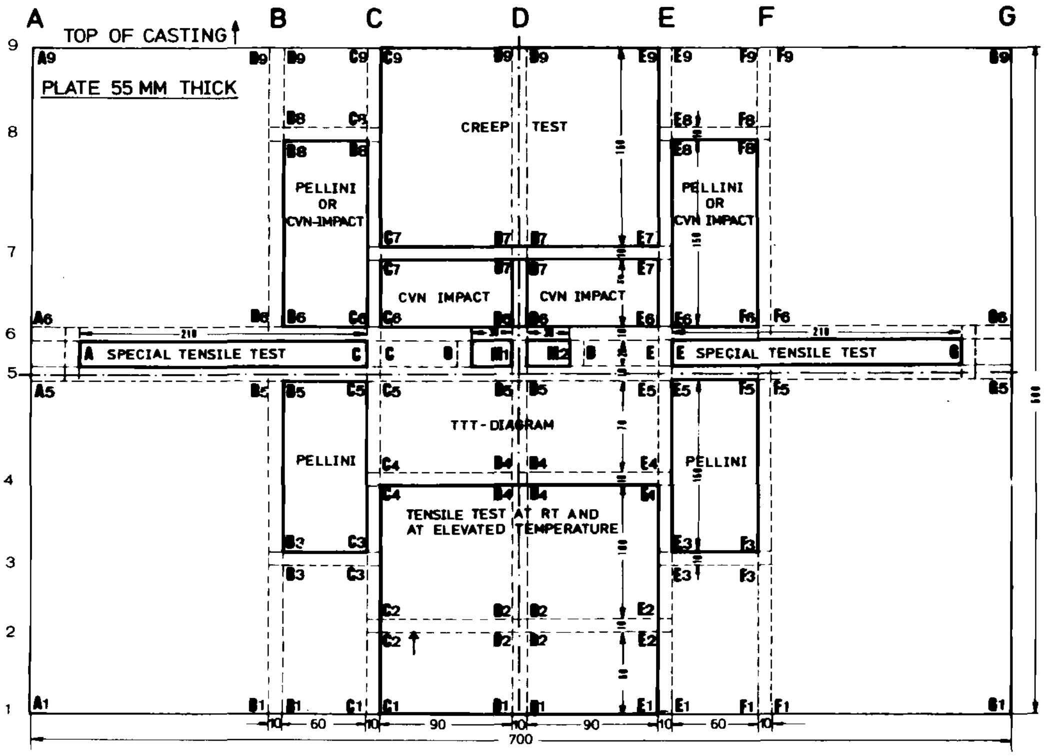

FIG. 3—*Cutup of individual test plates into test specimens.*

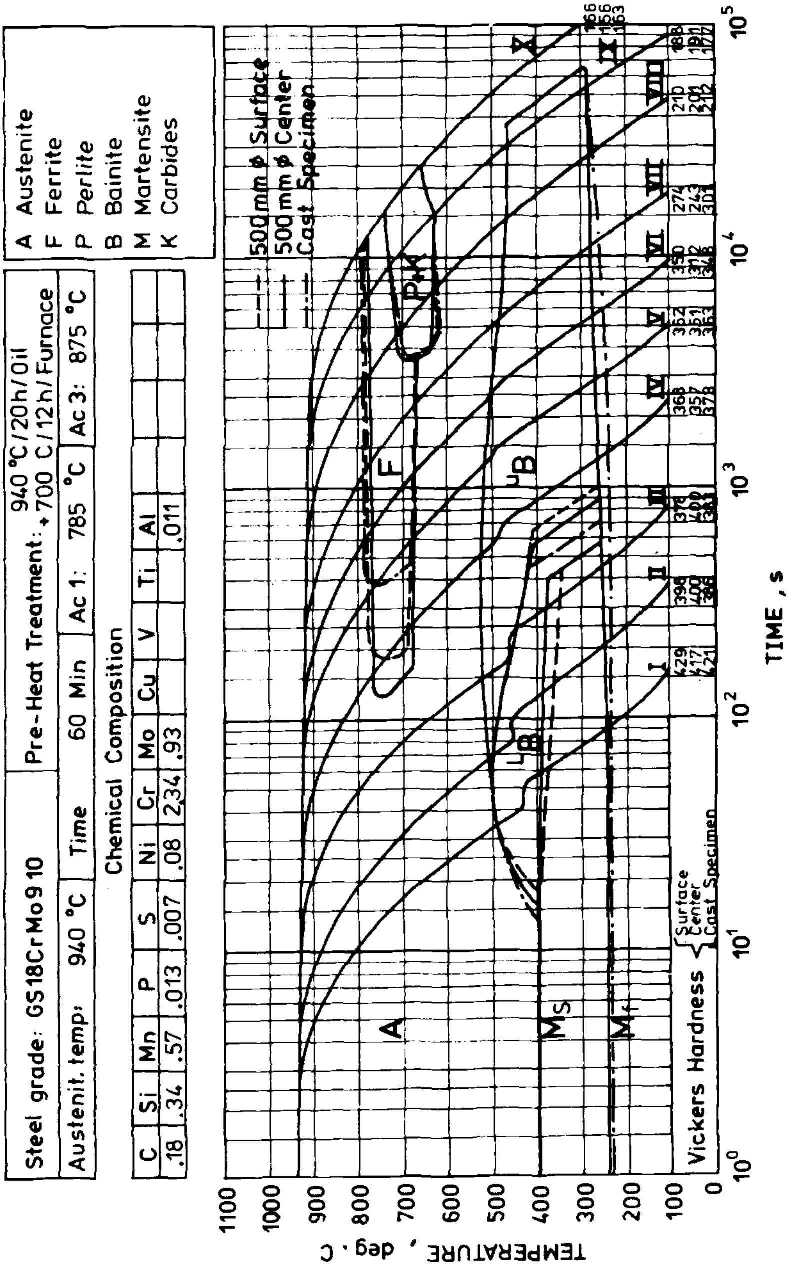

FIG. 4—*Effect of primary structure on the CCT diagram (continuous cooling).*

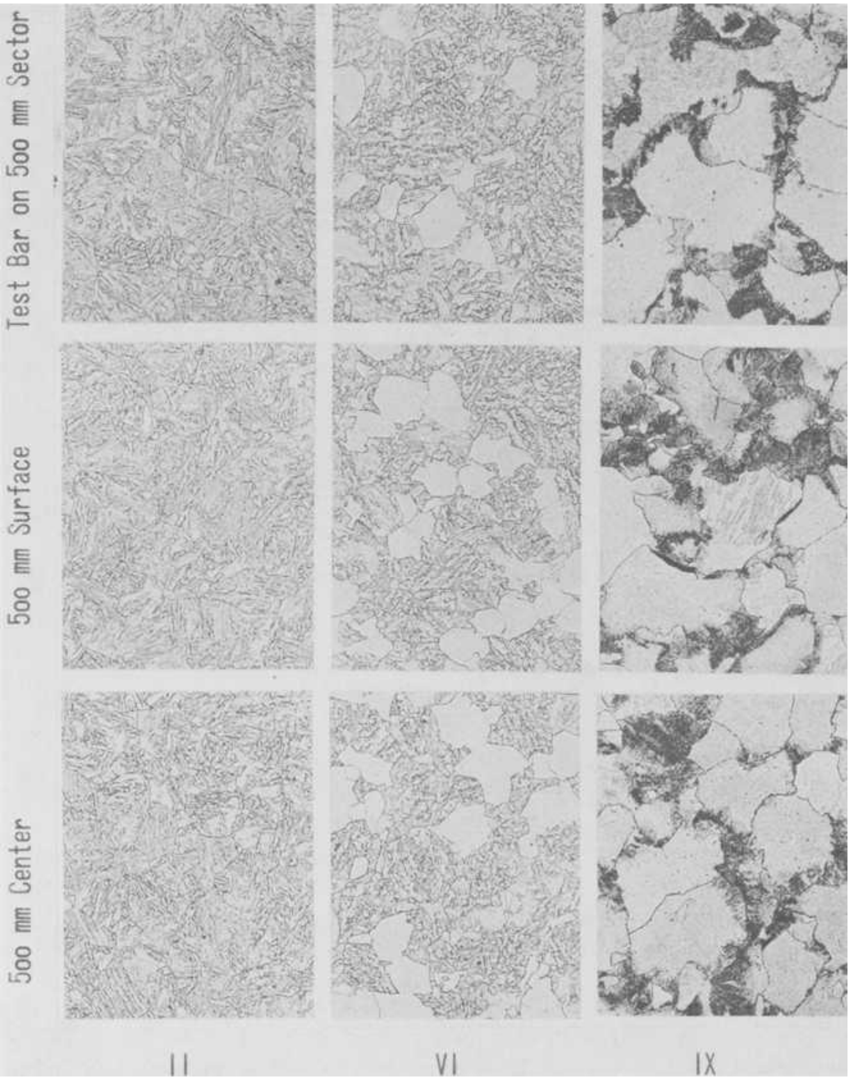

FIG. 5—*Microstructure of various specimens for three typical cooling rates of CCT diagram.*

specimens from the surface and from the center is very small. (The notch toughness, as will be discussed later, varies to a greater extent.) The tensile strength data show that even for very thick cross sections, such as 500 mm, an excellent uniformity of the microstructure is achieved when the casting undergoes an oil quenching. The tensile values of the coupon specimens for the various test block section thicknesses, as given in Fig. 6, are only slightly

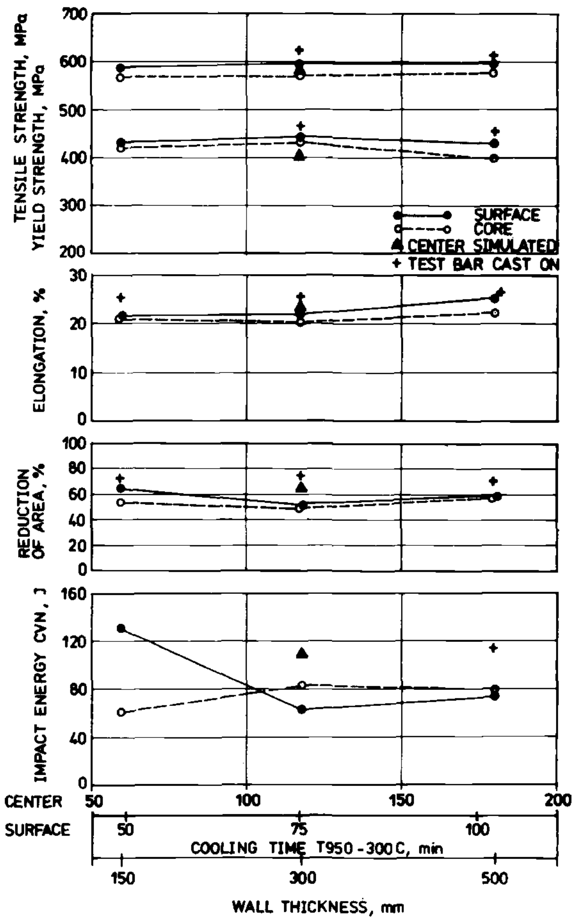

FIG. 6—*Effect of wall thickness on the mechanical properties at room temperature.*

higher than the values for the actual section specimens. Therefore the properties of the 100 by 120 by 300 mm coupons give a true indication of the mechanical properties of the test block. For further supporting data, specimens from the coupon of the 500-mm section were given a heat treatment that simulated the cooling conditions of the center of the 300-mm section. This heat treatment was as follows: 940°C/1 h/simulated cooling + 700°C/4 h/furnace. The results of this simulated heat treatment (C), given in Fig. 6, show that the original values are well reproduced by the simulated treatment.

Ductile to Brittle Transition of Charpy V-Notch (CVN) Impact Tests

Test Block with Original Heat Treatment (A)—The results of the CVN impact tests are given in Fig. 7. The transition temperatures for an impact energy of 68 J plus the measured lateral expansion and the shear fracture are summarized in Table 3. For a 68-J impact energy, the transition temperatures lie in the range of −20 to 25°C. The lower shelf occurred at −60°C, and the upper shelf, in all cases, above 60°C. In contrast to the tension test

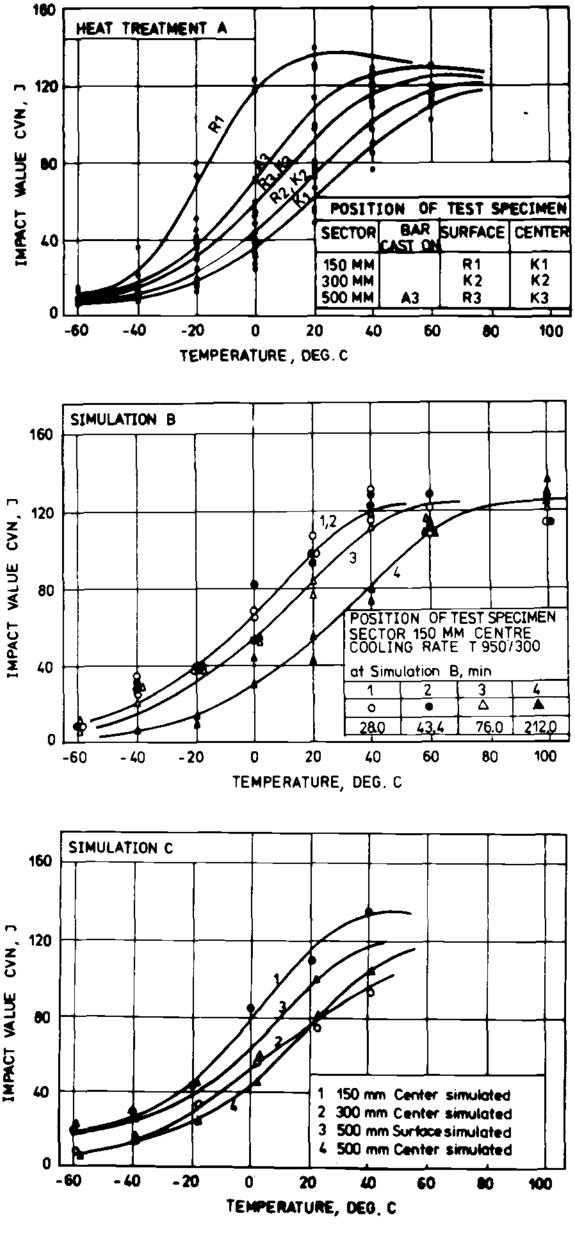

FIG. 7—*Results of CVN impact tests.*

TABLE 3—*Results of impact and Pellini tests.*

Test Specimen			Heat Treatment Type	Cooling Time (950 to 300°C), min	Transition Temperature, °C	Percent Shear at 68-J CVN, %	Lateral Expansion, mm	NDT Temperature, °C
Sector	Position	Type						
150 mm	surface	R 1	A	49.0	−20	50	1.00	. . .
	center	K 1		59.2	+25	60	1.08	. . .
300 mm	surface	R 2		76.7	+16	55	1.30	. . .
	center	K 2		117.2	+16	55	1.30	−0
500 mm	surface	R 3		107.2	+7	60	1.14	−0
	center	K 3		180.0	+7	60	1.14	−5
150 mm simulated	center	B 1	A + B	24.0	+3	70	0.99	. . .
		B 2		43.4	+3	70	1.12	. . .
		B 3		76.0	+10	70	0.95	. . .
		B 4		212.0	+32	60	1.02	. . .
Test bar cast on sector 500 mm		A 3	A	. . .	−2	55	0.96	. . .
Test bar A 3 simulated to			A + C					
150 mm	center			26.7	−6			
300 mm	center			93.3	+14			
Surface 500 mm simulated to								
500 mm	surface			65.0	+15			
Center 500 mm simulated to								
500 mm	center			205.0	+3			

results, the position within the test block of the impact test specimens from the 150-mm section has a notable influence on the CVN transition curves. For the 300 and 500 mm sections, there is no significant difference between the surface and center curves. However, the surface of the 150-mm section shows the best impact behavior while the center of the 150-mm section shows the worst impact behavior of all the test specimens. This behavior is not surprising, since it was previously noted in other investigations.[4]

Test Specimens with Simulated Heat Treatments—For certain test specimens the heat treatment of the test block was simulated by controlling the cooling rate, after the heating cycle, to correspond to that of the test block core. Two points are to be noted: (*1*) the position, within the test block, of the specimens chosen for the simulation, and (*2*) the double hardening of these specimens in contrast to the single hardening of the original test block material.

Figure 8 shows that the microstructure of the specimens with simulated cooling is practically identical to the original test block microstructure. There was similar good agreement for the notched impact transition behavior of the 300 and 500 mm sections, but the behavior of the 150-mm section center could not be reproduced with simulated cooling. Examination of the microstructure of the 150-mm-section center showed the cause of the reduced notched impact toughness to be a special form of bainite, approximately the transition stage between upper and lower bainite, in the absence of eutectoid ferrite. It was not possible to reproduce this microstructure by simulated cooling because simulation requires a second quench and temper stage. This could well be the reason for the better notch toughness exhibited by the simulated cooled specimens of the 150-mm section compared with the original material of this section.

Nil-Ductility-Transition (NDT) Temperature

Eight specimens from each section were used to determine the Nil-Ductility-Transition (NDT) temperature for the 300 and 500 mm sections. The NDT temperature was found to lie between 0°C and −5°C. This agrees well with the notch toughness results.

High-Temperature Tensile Strength Tests up to 550°C

These tests were made on specimens from the surface and center regions of the 500-mm section. The results are shown in Fig. 9. Within the tested temperature range, the yield point decreases nearly linearly by approximately 100 MPa. The surface and center show exactly the same behavior. Above approximately 400°C, the elongation initially drops and then increases together with a greater decrease in the tensile strength. These results agree with the well-known behavior of other low-alloy creep-resisting steels.

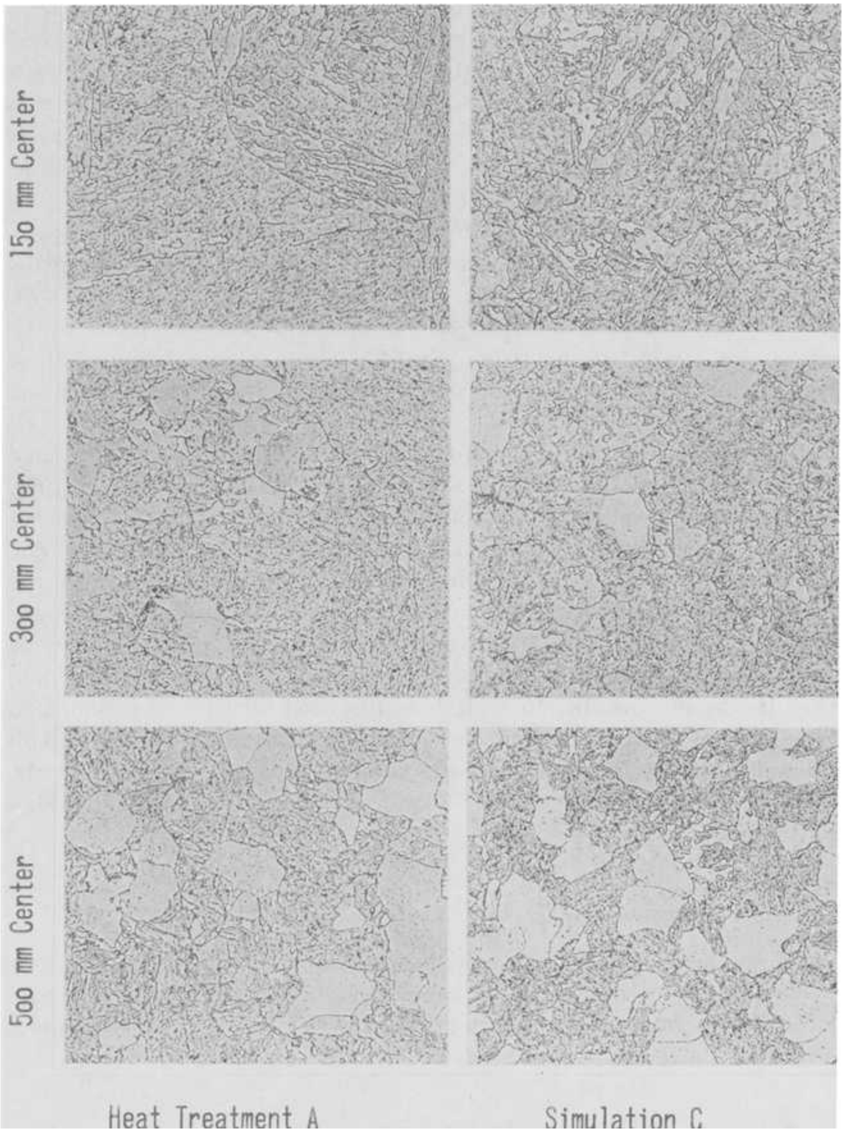

FIG. 8—*Microstructure of the test block and simulated specimens.*

Creep Tests

Extensive creep tests comprise the main part of the present investigations. The influence of wall thickness is being tested in the temperature range of 500 to 600°C; among other items, specimens from the center of the in-

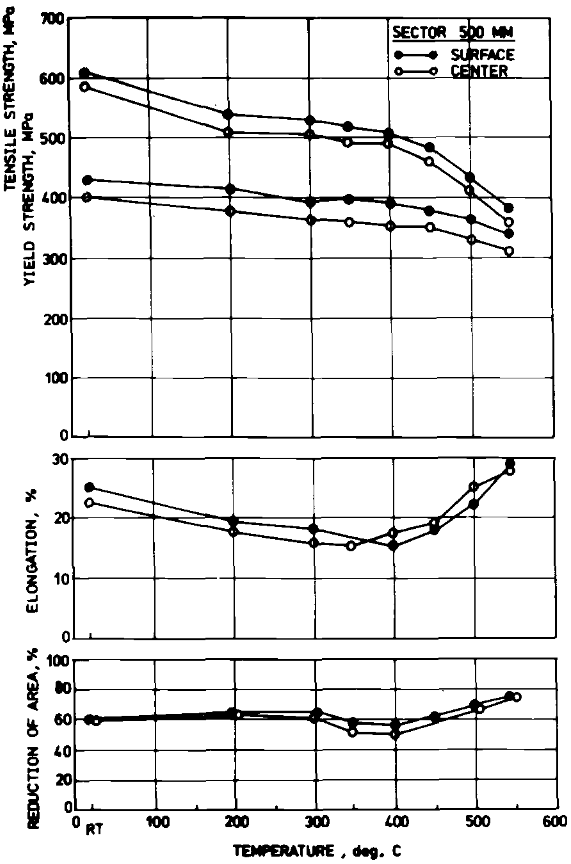

FIG. 9—*High-temperature tensile properties.*

dividual sections are being investigated. Furthermore, the creep properties of the weld material and the weld joints will be proved. The creep tests were begun in mid 1979. A detailed report of the results will be published at a later date.

Weld Procedure Qualification

For the weld procedure qualification tests, two 125 by 100 by 700 mm plates were taken from the 150-mm section and welded together as described in Table 4. An electrode of the same 2¼Cr-1Mo analysis but with a lower carbon content, 0.13 percent, was used. This lower carbon weld metal corresponds to normal European practice whereby, after welding, only a stress relief anneal is done. In addition to the classical weld procedure qualification test, many specimens from the weld and the heat-affected zone are being

TABLE 4—*Welding conditions.*

WELDING PROCESS: SMAW TYPE: MANUAL

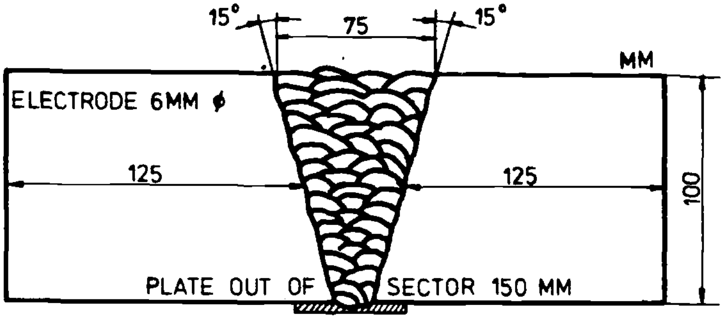

BASE METAL: Test block 2¼ Cr 1 Mo

Material Spec.: DIN 17 245
Type or Grade : GS-18 Cr Mo 910
P No to P No : 5 to 5
Thickness : 100 mm

FILLER METAL : 2¼ Cr 1 Mo

Weld Metal A No : 4
Filler Metal F No : 4
Size of Electrode : 6 mm Ø
SFA Specification : 5.5
AWS Classifikation : Similar 9018-B3
Elektrode Trade Name: OEN 117 (CH)

POSITION

Position of Groove : 1 G

PREHEAT

Preheat Temperature : 200 deg. C*
Interpass Temperature:240-360 deg.C*

POSTWELD HEAT TREATMENT

Temperature : 680 deg. C
Time : 13 h
Cooling : furnace

ELECTRICAL CHARACTERISTICS

Current : DC/=
Polarity : Elektrode (+)
Amps. 270±8* Volts: 26±2*

TECHNIQUE

Travel Speed :5.1 ± 0.5 cm/min
Bead :Weave bead
Oscillation :4x Electrode core Ø
Pass :Multipass
Number of Electr.:Single
Melting Capacity
of one Electrode:95 ± 5 g
Heat Input :83 ± 17 kJ/cm

* measured

TYPE OF TESTS: Bend Tests, Tensile Tests, Toughness Tests
Hardness Test, Chemical Analysis
Creep Rupture Tests at 450 and 550 deg. C
for Deposited Weld Metal and Weld Joints

creep tested at 500 to 550°C and, in some cases, at 600°C. Fracture times of up to 50 000 h are expected. Figure 10 shows how the welded test plate was cut up into test specimens. By choosing an electrode diameter of 6 mm and with a suitable oscillation, a very high heat input of 80 kJ/cm was purposely applied in order to impose a high stress on the base material. The weld procedure qualification test results are given in Table 5. There is a certain dif-

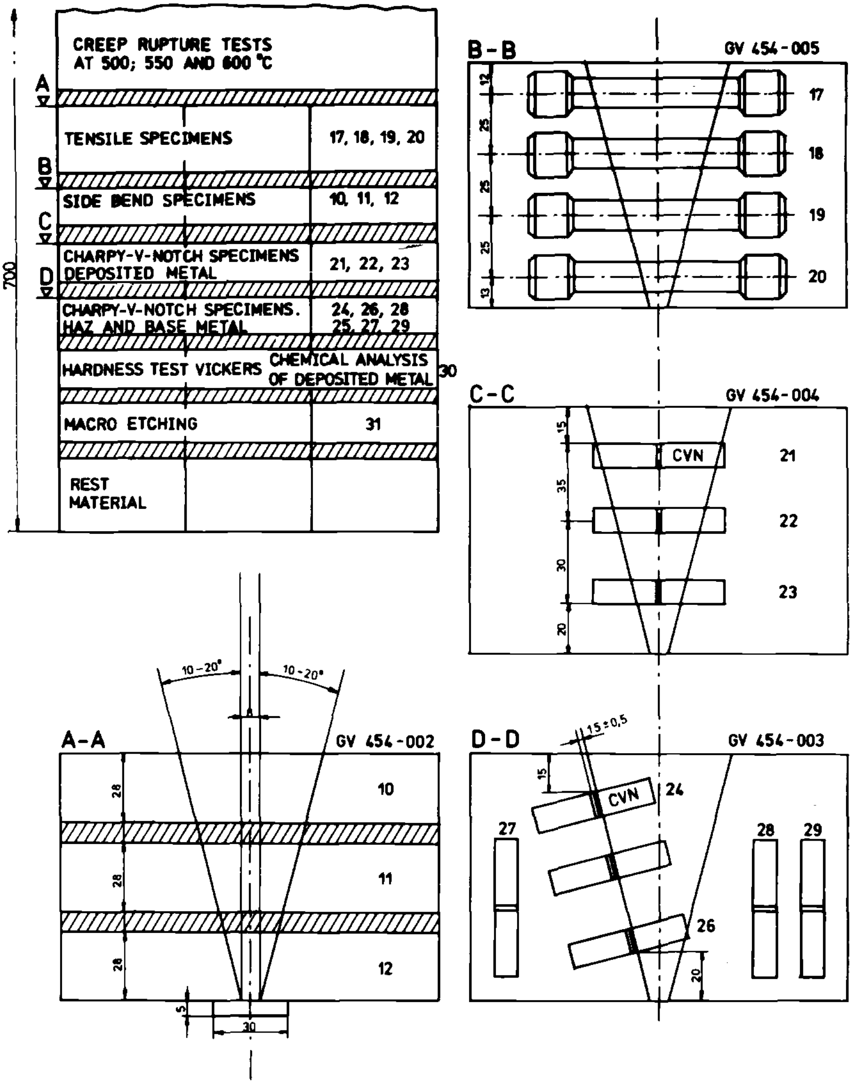

FIG. 10—*Cutup of the welded test plate.*

ference in strength and hardness between the tempered weld metal and the tempered base material. This difference can not be completely equalized by tempering. It was smaller for the lower carbon electrodes of approximately 0.05 percent carbon that were used in the past. The 0.10 to 0.15 percent carbon electrodes used today are a compromise necessary for the greatly improved creep behavior of the weld.

TABLE 5—*Results of weld procedure qualification.*

1. GUIDED BEND TESTS (Type QW-462-2a)

Specimen No:	Position	Results	Acceptance
10	top pass	no defect	acceptable in accordance with QW-163
11	between	no defect	
12	root pass	2 defect 1.5 mm fusion line	

2. TENSILE TESTS (QW-462.1 (d), Type a)

Specimen No:	Position	Tensile Strength MPA	Yield Strength MPA	Elong. in 2" %	Red. Area %	Location of Fracture
13	top pass	687	575	21	75	Dep.weld.met.
14	between	631	515	20.4	76	HAZ
15		610	417	15	77	Base metal
16	root pass	596	391	18	71	Base metal

3. TOUGHNESS TESTS CVN (ASME II A SA-370 Type A)

Specimen No:	Position	Notch Type	Notch Location	Impact Value J	Perc. Shear %	Lateral Expans. mm
21	top pass	V-Notch	Dep.weld metal	108	90	1.4
22	between			101	90	1.5
23	root pass			119	90	1.4
24	top pass	V-Notch	HAZ	162	100	2.2
25	between			164	100	2.1
26	root pass			124	90	1.7
27		V-Notch	base metal	104	70	1.4
28				131	80	1.7
29				138	80	1.8

4. VICKERS HARDNESS TEST (on between-beads)

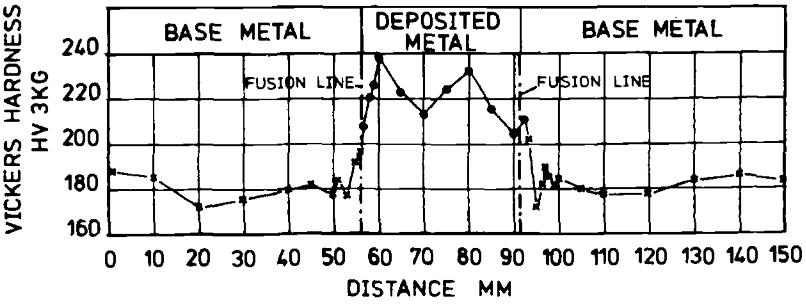

Conclusions

The results show that for cross sections up to 500 mm, 2¼Cr-1Mo cast steel has very uniform properties when liquid quenched and adequately tempered. These property values, in general, are only slightly less than the values for specimens taken from coupons cast onto the sections. This is due to the excellent hardenability of this steel plus the insignificant effect of the as-cast macrostructure on the CCT diagram. Within a relatively wide cooling range, neither the macrostructure nor the decreased cooling rate in large sections has a significant influence on the heat-treated microstructure. The prerequisite for this, however, is that the cooling rate, after the hardening, is fast enough. A liquid quench seems necessary. The measured notch toughness transition curves show the good impact toughness of this steel with a NDT of about 0°C. All these factors, together with the good high temperature strength up to 550°C, indicate that this steel is suitable for thick-walled castings at room temperature and at higher temperatures. The good weldability of 2¼Cr-1Mo cast steel, using an electrode of similar composition, is confirmed by the test results.

Note

This paper is a contribution by the Swiss Working Group for Creep Resisting Steels (George Fischer Ltd., Schaffhausen; Sulzer Brothers Ltd., Winterthur; Brown Boveri Ltd., Baden; Escher Wyss Ltd., Zurich; Von Roll, Gerlafingen).

M. Kohno,[1] *M. Makioka,*[2] *S. Kinoshita,*[2] *and A. Suzuki*[1]

Mechanical Properties of Vacuum Carbon-Deoxidized Thick-Wall 2¼Cr-1Mo Steel Forging

---

REFERENCE: Kohno, M., Makioka, M., Kinoshita, S., and Suzuki, A., "**Mechanical Properties of Vacuum Carbon-Deoxidized Thick-Wall 2¼Cr-1Mo Steel Forging,**" *Application of 2¼Cr-1Mo Steel for Thick-Wall Pressure Vessels, ASTM STP 755,* G. S. Sangdahl and M. Semchyshen, Eds., American Society for Testing and Materials, 1982, pp. 208–227.

ABSTRACT: The effect of postweld heat treatment on the susceptibility to temper embrittlement of 2¼Cr-1Mo steel forgings which have various silicon contents has been investigated. Then, to verify the validity of low-silicon 2¼Cr-1Mo steel for an actual forging, the mechanical properties and the susceptibility to temper embrittlement of a 296-mm (11.7-in.)-thick forged ring made from a 100-ton ingot with silicon content reduced to below 0.10 percent by the vacuum carbon deoxidation (VCD) process have been tested. The results are as follows: (*1*) the through-thickness mechanical properties of the forging meet the requirements of ASME SA-336, F22; (*2*) silicon content has no significant effect on the creep-rupture strength at least to 15 000 h at 550°C (1022°F) and 600°C (1112°F); and (*3*) the susceptibility to embrittlement is very low, as the shift in 50 percent fracture appearance transition temperature is 14°C (25°F) for step cooling and 22°C (40°F) for isothermal treatment at 475°C (887°F) for 5000 h.

KEY WORDS: 2¼Cr-1Mo steel, mechanical property, temper embrittlement, creep strength, postweld heat treatment, silicon, vacuum carbon deoxidation process

Temper embrittlement is of particular importance for 2¼Cr-1Mo steels used in pressure vessels operating in the temperature range of 350 to 550°C (662 to 1022°F). It is well known that the reduction of silicon content decreases the susceptibility to temper embrittlement [*1–4*].[3]

The ASME Code requires a prolonged holding time for postweld heat treatment (PWHT) of thick-wall steel forgings for pressure vessels; consequently, the tempering parameter $[P]$ increases where $[P] = T \cdot (20 + \log t) \times 10^{-3}$

---

[1] Senior Researcher and Manager, respectively, Takasago Plant, Kobe Steel, Ltd., Hyogo-ken, Japan.

[2] Assistant Manager, Takasago Plant, Kobe Steel, Ltd., Hyogo-ken, Japan.

[3] The italic numbers in brackets refer to the list of references appended to this paper.

where T is tempering or PWHT temperature, K, and t is tempering or PWHT time, h.

Therefore, as a first step, the effect of PWHT on the susceptibility to temper embrittlement of 2¼Cr-1Mo steels with various silicon contents was investigated. As a second step, to verify the validity of low silicon 2¼Cr-1Mo steel for an actual forging, the mechanical properties and the susceptibility to temper embrittlement of a 296-mm (11.7-in.)-thick shell ring forged from a 100-ton ingot with reduced silicon content reduced to below 0.10 percent by the vacuum carbon-deoxidation process were investigated.

Influence of Post Weld Heat Treatment and Silicon Content on Susceptibility to Temper Embrittlement

The chemical composition of 2¼Cr-1Mo steels used in the present study are shown in Table 1. The test materials were 25-mm (1.0-in.)-thick plates forged from 100-kg ingots. After austenitizing at 940°C (1724°F), each plate was cooled at an average cooling rate of 58°C/min (104°F/min), corresponding to the cooling rate at the quarter thickness of a 200-mm (7.9-in.)-thick steel forging when water quenched. Tempering and PWHT under various conditions were then carried out in which the tempering parameter was in the range of 19.1 to 20.7. Heat treatment conditions are summarized in Table 2. After heat treatment, test materials were subjected to the step-cooling treatment described in Fig. 1. The propensity to embrittlement was measured mainly in terms of the shift in the fracture appearance transition temperature (vTrs) observed in the Charpy V-notch impact test.

Figure 2 shows the vTrs before and after the step-cooling treatment, and Fig. 3 shows the shift in vTrs due to step-cooling embrittlement (ΔvTrs-sc). The vTrs of unembrittling steels with higher silicon contents, such as 0.22, 0.34, and 0.57 percent, decreases steadily with increasing temper parameter. In unembrittling lower silicon steels, however, vTrs reaches a minimum at some temper parameter while the increasing silicon content increases the temper parameter at which vTrs touches bottom. After step-cooling treatment, on the other hand, vTrs in higher silicon steels peaks at a temper pa-

TABLE 1—*Chemical composition of test materials.*

Steel	C	Si	Mn	P	S	Cr	Mo	Sn	Sb	As	$\bar{X}$[a]
A	0.16	0.05	0.50	0.012	0.010	2.17	1.04	0.005	0.0040	0.006	16.6
B	0.13	0.10	0.45	0.008	0.010	2.39	1.06	0.006	0.0140	0.008	18.2
C	0.15	0.22	0.61	0.011	0.012	2.43	1.00	0.005	0.0043	0.005	15.7
D	0.13	0.34	0.47	0.008	0.010	2.34	0.96	0.004	0.0110	0.007	15.8
E	0.14	0.57	0.49	0.009	0.012	2.43	1.03	0.007	0.0120	0.010	18.8

[a] $\bar{X}$ = (10P + 5Sb + 4Sn + As, ppm)/100.

TABLE 2—*Heat treatment conditions of test materials.*

Hardening	940°C×3hr, CR:58°C/min
↓ Tempering	630°C×3hr AC (P)=18.5
↓ PWHT	620°C×20hr FC (P)=19.1
	660°C×20hr FC (P)=19.9
	700°C×20hr FC (P)=20.7
↓ Step cooling	$(P)=T(20+\log t)\times 10^{-3}$ T: tempering or PWHT temperature K t: tempering or PWHT time Hr

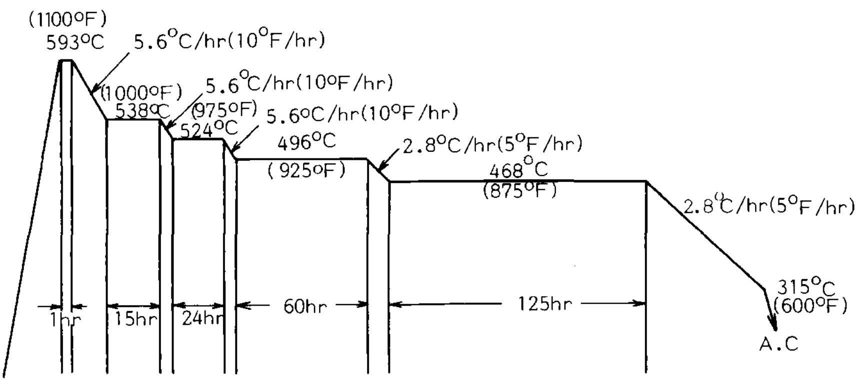

FIG. 1—*Step-cooling cycle.*

rameter which increases with increasing silicon content of the steel, although vTrs in lower silicon steel shows a steady decrease with the increase of temper parameter. Consequently, the silicon content does not greatly affect ΔvTrs-sc at a smaller temper parameter, as shown in Fig. 3. This is also shown in Fig. 4. In general, the temper parameter applied to 2¼Cr-1Mo steel forgings with over 200 mm (8 in.) thickness is approximately 20.5 to 20.75 because the PWHT is carried out at a high temperature for a long time. Therefore reducing the silicon content proves to reduce the susceptibility to temper embrittlement induced by extended service of thick-wall 2¼Cr-1Mo steel forgings at elevated temperatures.

Figure 5 indicates the relationship between ΔvTrs-sc and tensile strength. Silicon content has a marked influence on the susceptibility to temper em-

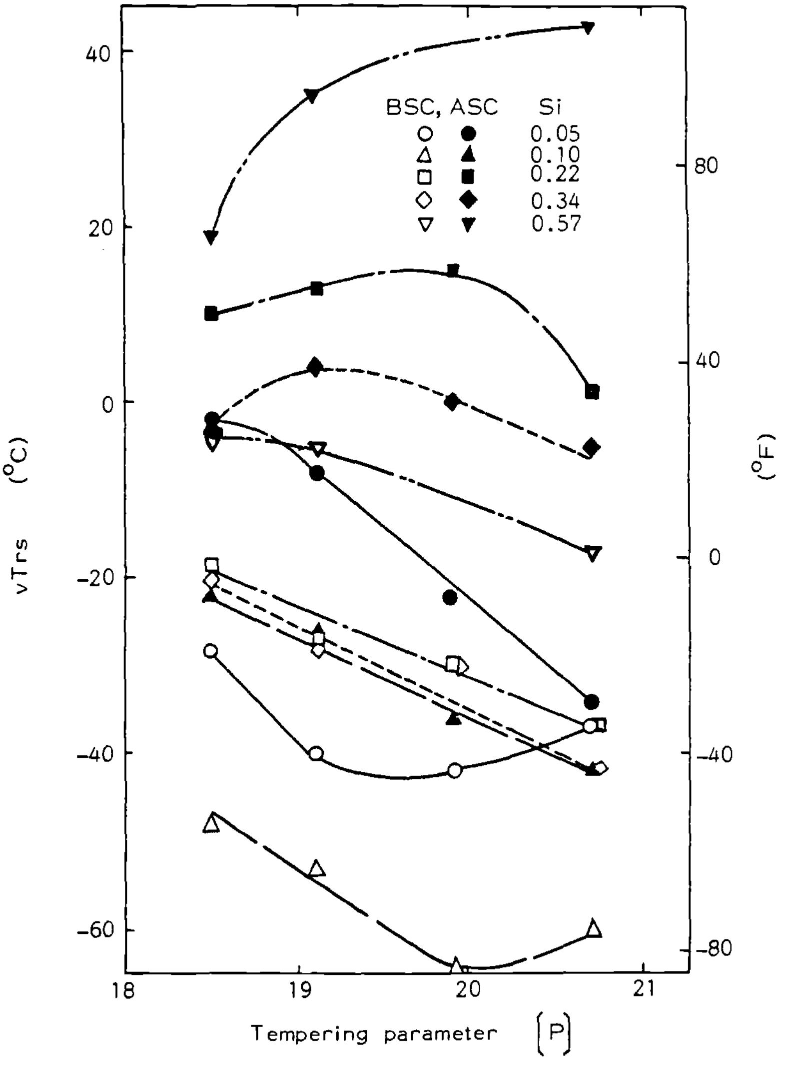

FIG. 2—*vTrs before and after step-cooling treatment of 2¼Cr-1Mo steels with various silicon content.*

brittlement of medium-strength steels such as ASME SA-182 F22 and ASME SA-336 F22, but less influence on higher-strength steels of over 75 kgf/mm^2 (105 ksi) tensile strength such as ASME SA-542, Class 1 and Class 2.

It is found from Fig. 5 that a decrease in strength results in increasing susceptibility to temper embrittlement for high-silicon steels, but the inverse is

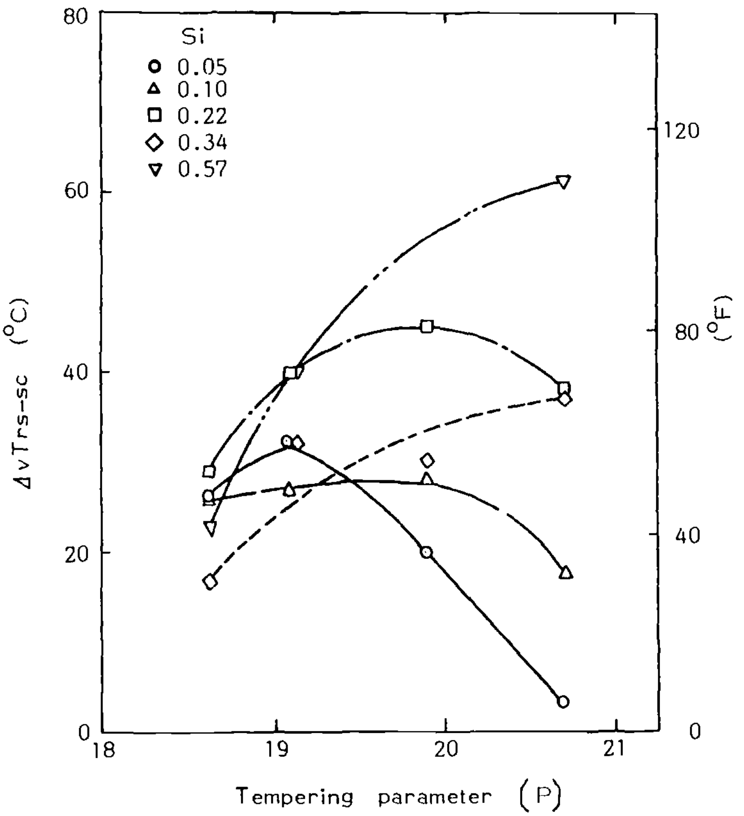

FIG. 3—*Effect of PWHT on temper embrittlement in 2¼Cr-1Mo steels with various silicon content.*

observed for low-silicon steels. Concerning the effect of strength on the susceptibility to temper embrittlement of 2¼Cr-1Mo steel, Swift et al [5] and Clauser et al [6] reported that the loss in notch toughness after step-cooling treatment is greater in low-strength steels than high-strength steels, but Kinoshita and Katsumata [7] reported inverse results. This inconsistency can be explained by the result in Fig. 5, which indicates that the strength dependence of the susceptibility to temper embrittlement for the steels examined decreased at higher values of tensile strength.

Auger microprobe analysis of phosphorus segregating on the grain boundaries was performed to study the role of silicon to the susceptibility to temper embrittlement. Table 3 summarizes results, including results of intergranular fracture measurement on fractured V-notch Charpy specimens and the shift of the transition temperature due to step cooling. No segregation of tin and arsenic and little of antimony were detected. It is very interesting that

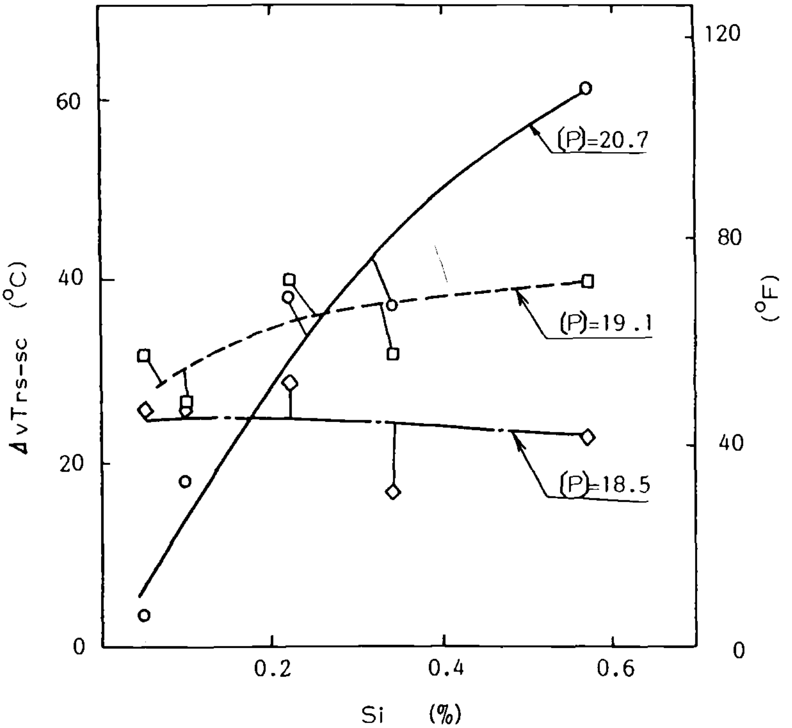

FIG. 4—*Effect of silicon content on temper embrittlement in 2¼Cr-1Mo steels.*

peak height ratios of P to Fe do not vary with silicon content in spite of extreme variations of impact transition temperature and intergranular fracture facets with silicon content. Thus, the shift of transition temperature does not relate with phosphorus concentration on grain boundaries but with the amount of intergranular fracture, which seems to support the suggestion of Yu and McMahon [*8*].

Effect of Chemical Composition on the Susceptibility to Temper Embrittlement

The effect of chemical composition on the susceptibility to temper embrittlement of 2¼Cr-1Mo steels with an applied tempering parameter of 20.60 to 20.75 has been investigated. Multiple regression analyses were performed with regression equations between ΔvTrs-sc and chemical composition as shown in Table 4 obtained. It has been found that the effect of silicon content is greater than that of other alloying elements in these equations.

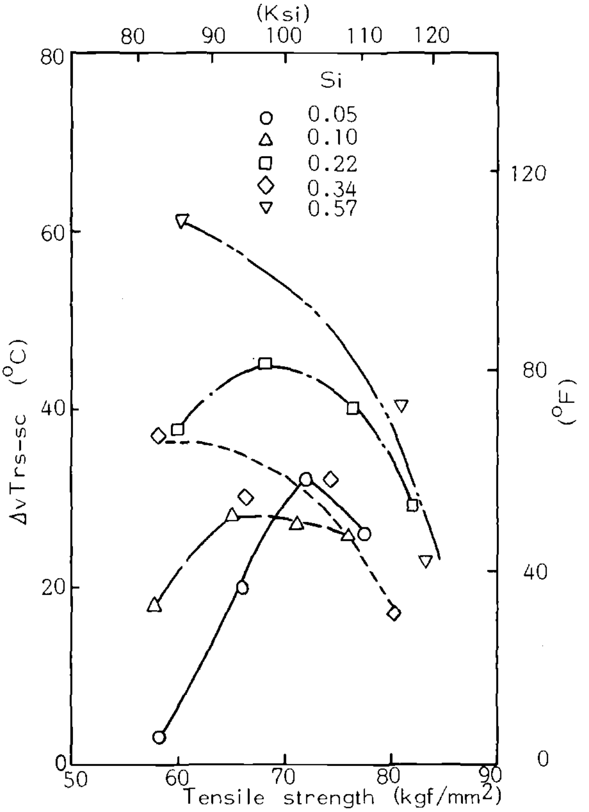

FIG. 5—*Relation between temper embrittlement and tensile strength of 2¼Cr-1Mo steels with various silicon content.*

Correlation in the two equations at the top of Table 4 is well known, while the three equations at the bottom were obtained in the present study for 2¼Cr-1Mo steel. As can be seen, consideration of the small quantity of nickel and copper in 2¼Cr-1Mo steel results in better correlation, but (2Si + Mn)$\bar{X}$ was used as the temper-embrittling factor here for convenience since correlation coefficients in the two equations at the bottom of Table 4 do not make much difference.

The correlation between ΔvTrs-sc and the embrittling factor (2Si + Mn)$\bar{X}$ is shown in Fig. 6, where vTr40 is the 54 J (40 ft·lb) transition temperature and ΔvTr40-sc is the shift in vTr40 by step-cooling treatment. The critical value of (2Si + Mn)$\bar{X}$ for the Chevron Research Company (CRC) criterion [vTr40 + 1.5 ΔvTr40-sc $\leq$ 38°C (100°F)], which is often used for commercial purposes, is about 17. The step-cooling treatment is utilized to determine

TABLE 3—*Analysis of temper embrittlement.*[a]

Si content, %	Tempering Parameter $[P] \times 10^{-3}$	ΔvTrs-sc, °C (°F)	Intergranular Fracture,[b] %	Auger Peak Height Ratio, P120/Fe703 × 100, %
0.10	19.9	28 (50.4)	15	8.4
0.22	19.1	40 (72)	55	8.0
	19.9	45 (81)	60	8.2
0.57	19.1	40 (72)	85	10.7
	20.7	61 (109.8)	90	7.7

[a] Auger analysis conditions:

Incident beam energy	5 keV	Election multiplier voltage	1 keV
Incident beam size	0.75 μ	Sensitivity	20×
Primary beam current	2.0 μA	Vacuum	~5 × 10^{-9} torr
Modulation voltage	6 eV		

[b] Fractured *in situ*.

TABLE 4—*Regression equations between temper embrittlement and various embrittling factors in 2¼Cr-1Mo steel.*

Regression Equation	Correlation Coefficient
$\Delta vTrs\text{-}sc = 3.10(Si + Mn)\bar{X} - 10.7$	0.82
$\Delta vTrs\text{-}sc = 3.36(Si + Mn)(P + Sn)/100 - 10.7$	0.80
$\Delta vTrs\text{-}sc = 2.05(2Si + Mn)\bar{X} - 5.6$	0.84
$\Delta vTrs\text{-}sc = (4.39Si + 1.40Mn + 2.28Ni)\bar{X} - 6.4$	0.86
$\Delta vTrs\text{-}sc = (4.22Si + 1.28Mn + 2.39Ni + 2.81Cu)\bar{X} - 7.1$	0.87

[a] Si, Mn, Ni, Cu: %; P + Sn: ppm; $\bar{X} = (10P + 5Sb + 4Sn + As, \text{ppm})/100$.

the relative susceptibility of a material to temper embrittlement, although it will not give quantitative evaluation for an actual service period. Thus an isothermal embrittlement treatment of 2¼Cr-1Mo steel was carried out at 475°C (887°F) for 1000 to 5000 h. Figure 7 gives the isothermal embrittlement at 475°C (887°F) for three 2¼Cr-1Mo steels. Embrittlement appears to increase rapidly up to 3000 h, then levels off with a further increase of aging time up to 5000 h. Step-cooling embrittlement is found to be comparable with isothermal embrittlement at 475°C (887°F) for 800 to 1800 h.

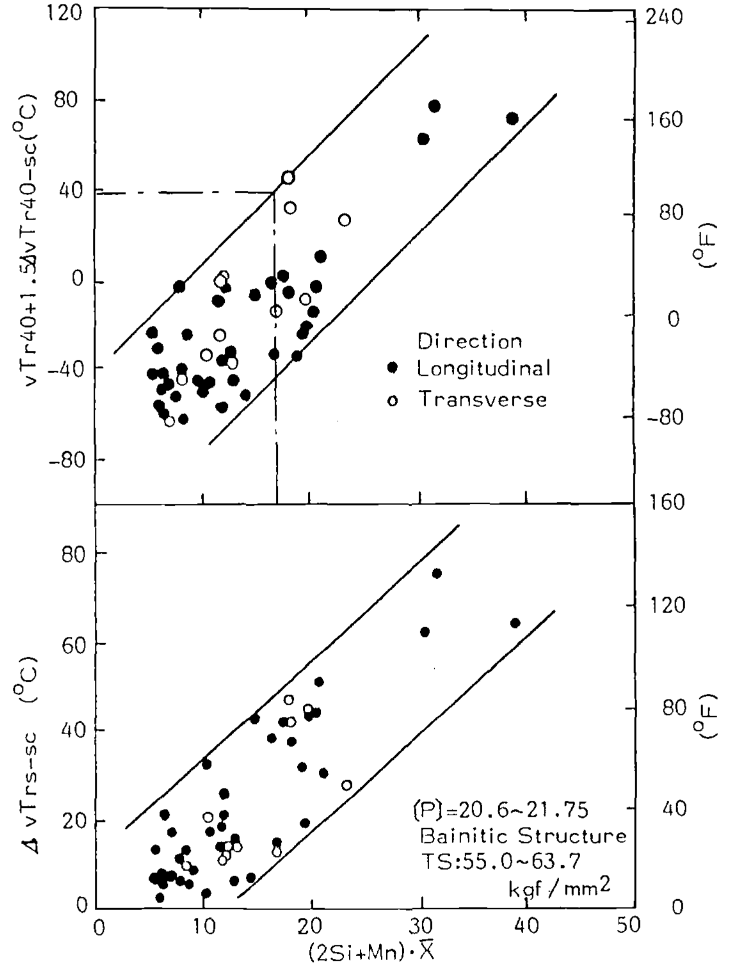

FIG. 6—*Correlation between temper embrittlement by step-cooling treatment and embrittling factor in 2¼Cr-1Mo steels.*

Figure 8 shows the relationship between the shift in vTrs by isothermal embrittlement at 475°C (887°F) for 5000 h (ΔvTrs-475) and ΔvTrs-sc. A strong correlation is observed between the extent of isothermal embrittlement and step-cooling embrittlement. Consequently, vTr40 after isothermal embrittlement at 475°C (887°F) for 5000 h can be estimated from step-cooling embrittlement (Fig. 9). If vTr40 + 1.5 ΔvTr40-sc is controlled below 38°C (100°F), vTr40 after isothermal embrittlement at 475°C (887°F) for 5000 h is also below 38°C (100°F). Figure 10 shows the relation between ΔvTrs-475 and

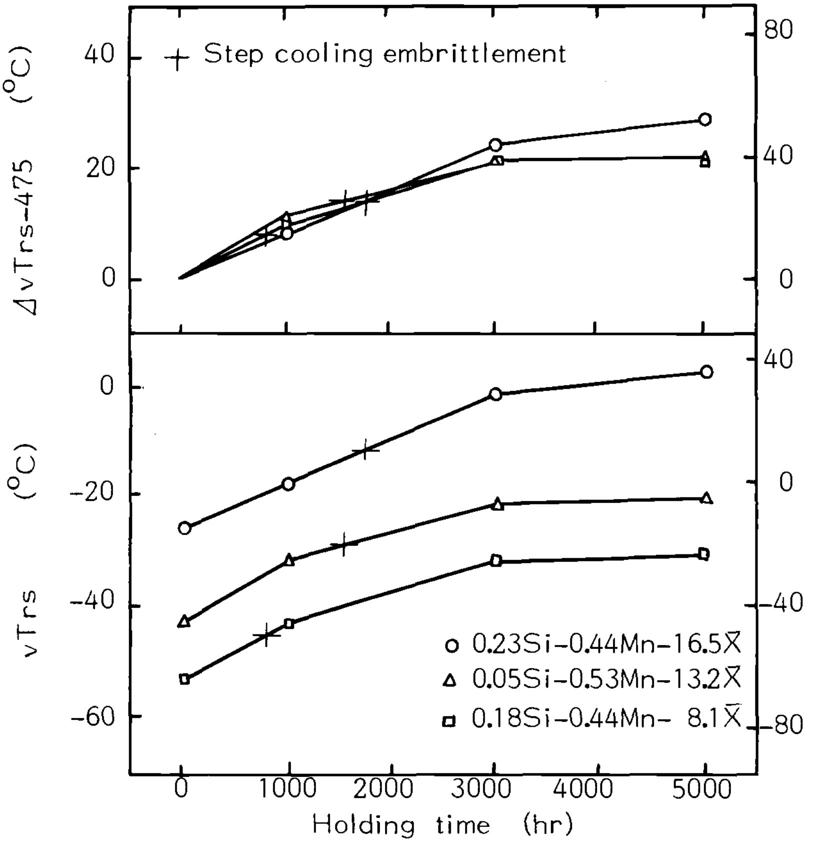

FIG. 7—*Change in vTrs of 2¼Cr-1Mo steels by isothermal embrittlement at 475°C.*

embrittling factor (2Si + Mn)$\bar{X}$. There also seems to be a strong correlation, the same as in step-cooling embrittlement.

Mechanical Properties of 296-mm (11.7-in.)-Thick Low-Silicon 2¼Cr-1Mo Steel Forging

The outline of the manufacturing process for 2¼Cr-1Mo steel forged ring used in this study is shown in Table 5. A vacuum carbon-deoxidized 100-ton ingot was forged to a shell ring. The forged ring was water quenched and tempered after rough machining to 296 mm (11.7 in.) thickness and 3544 mm (139.5 in.) outer diameter. The mechanical properties of the forging were investigated using the test coupons taken from top and bottom prolongations.

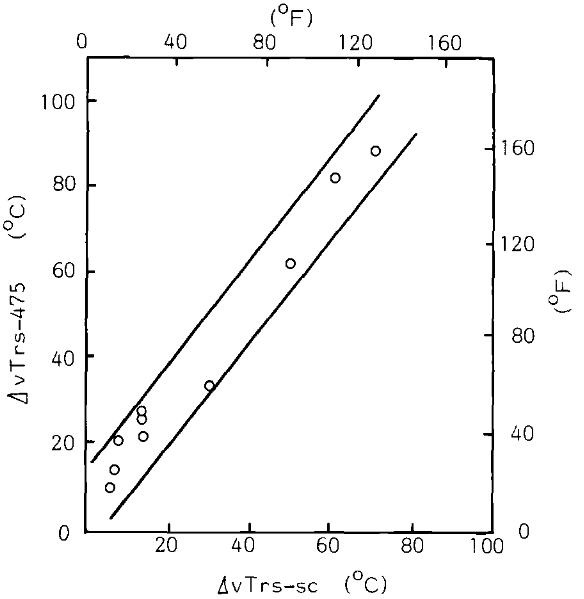

FIG. 8—*Relation between shift in vTrs of 2¼Cr-1Mo steels by isothermal treatment at 475°C and step-cooling treatment.*

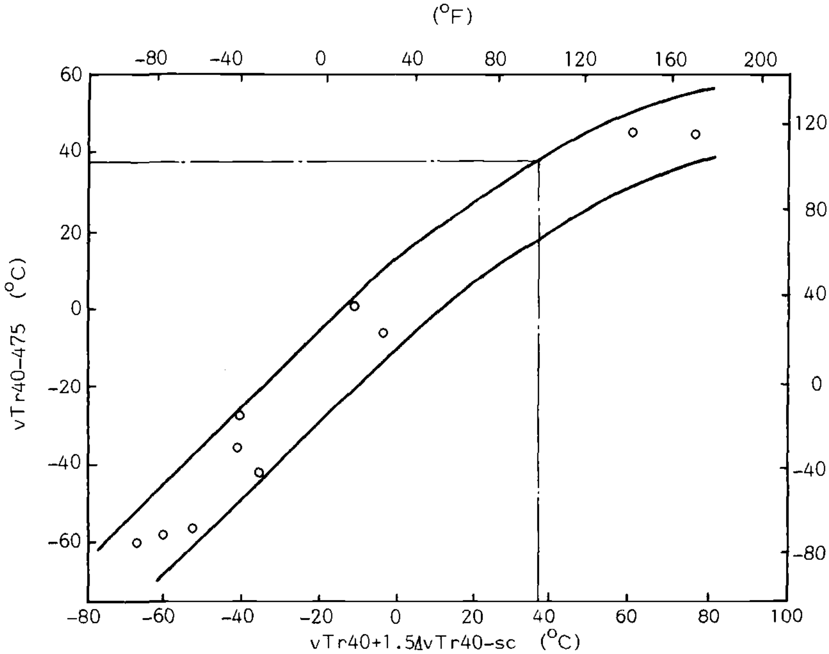

FIG. 9—*Relation between vTr40 after isothermal embrittlement at 475°C and vTr40 + 1.5 ΔvTr40-sc of 2¼Cr-1Mo steel.*

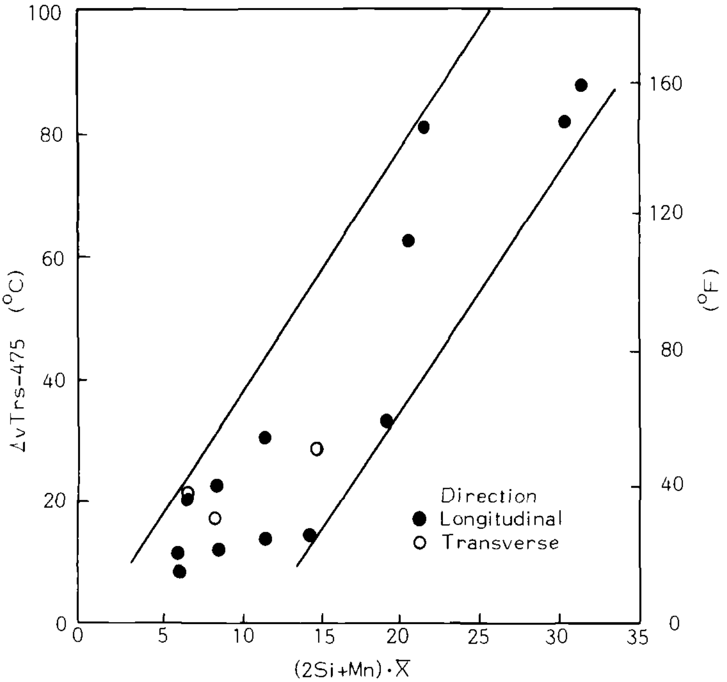

FIG. 10—*Correlation between temper embrittlement by isothermal treatment at 475°C and embrittlement factor in 2¼Cr-1Mo steels.*

Table 6 shows the check analysis of the forged ring. The variation of each element from top to bottom is minimum. The silicon content is reduced to 0.04 to 0.07 percent.

Tensile properties of the forged ring are shown in Fig. 11. Tensile properties are within the range of specification requirements of ASME SA-336, F22 after PWHT of 695°C (1283°F) for 20 h F.C. ([*P*] = 20.68); no significant difference in properties were found through the thickness. Tensile and yield strength at elevated temperatures are shown in Fig. 12. For steel subjected to PWHT to a tempering parameter below about 20.7, the tensile strength in the range of 400 to 500°C (752 to 932°F) is more than three times the maximum allowable stress specified by the ASME, Section VIII, Division 2.

Charpy Code, impact properties and nil-ductility transition temperature (T_{NDT}) of the forged ring are shown in Fig. 13. This forging has sufficiently high toughness at any location.

Creep rupture tests of the forging were conducted at 550°C (1022°F) and 600°C (1112°F) up to 15 000 h; results are shown in Figs. 14 and 15 compared with steel of ordinary silicon content. There is no difference in creep rupture strength between low and ordinary silicon steel, and the data are

TABLE 5—*Manufacturing process of low-silicon 2¼Cr-1Mo steel forged ring.*

<table>
<tr><td>Melting
Ingot Making</td><td>1 Melting Furnace:100 ton Basic Electric Furnace
2 Ingot Making :Top Degassing+Vacuum Casting
(Vacuum Carbon Deoxidation) – 100 ton Ingot
3 Ladle Analysis
<table>
<tr><td>C</td><td>Si</td><td>Mn</td><td>P</td><td>S</td><td>Cr</td><td>Mo</td></tr>
<tr><td>0.14</td><td>0.04</td><td>0.50</td><td>0.011</td><td>0.015</td><td>2.40</td><td>1.04</td></tr>
</table></td></tr>
<tr><td>Forging</td><td>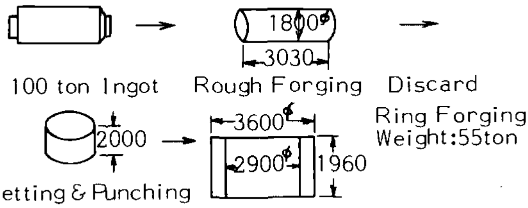
</td></tr>
<tr><td>Annealing</td><td>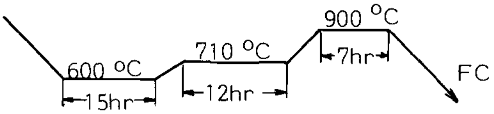
</td></tr>
<tr><td>Rough Machining</td><td>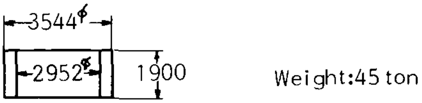
</td></tr>
<tr><td>Welding of Thermal Buffer</td><td>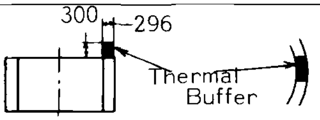
</td></tr>
<tr><td>Heat Treatment</td><td>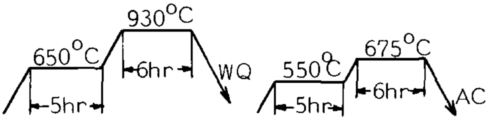
</td></tr>
</table>

located in the middle of scatter band for ASTM creep rupture data for 2¼Cr-1Mo steel [9].

To evaluate the susceptibility to temper embrittlement of a forged ring, step-cooling and isothermal treatments at 475°C (887°F) were carried out. Changes in impact properties by the embrittling treatment are shown in Tables 7 and 8. With the shift in vTrs being 10 to 14°C (18 to 25°F) for step-cooling treatment and 17 to 22°C (31 to 40°F) for isothermal treatment at 475°C (887°F) for 5000 h, the susceptibility to temper embrittlement was found to be very low.

As a result of this investigation, it is confirmed that a thick-wall 2¼Cr-1Mo steel forged ring made from a 100-ton ingot with the silicon content reduced

TABLE 6—*Chemical analysis of low-silicon 2¼Cr-1Mo steel forged ring.*

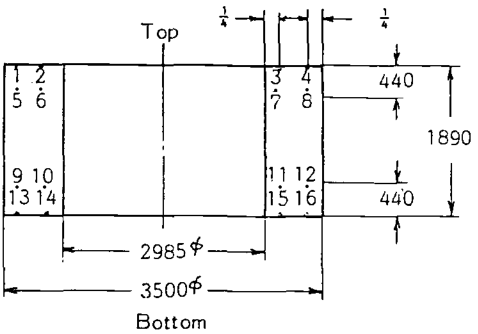

Location	Chemical Analysis (%)									
	C	Si	Mn	P	S	Cu	Ni	Cr	Mo	Al
1	.14	.05	.52	.009	.014	.03	.15	2.38	1.06	.001
2	.15	.05	.53	.009	.014	.03	.16	2.39	1.05	.002
3	.15	.05	.53	.010	.015	.03	.17	2.41	1.06	.002
4	.14	.05	.54	.009	.013	.03	.16	2.39	1.07	.001
5*	.14	.04	.52	.009	.013	.03	.16	2.40	1.04	.001
6	.15	.04	.54	.010	.015	.03	.16	2.41	1.10	.002
7	.15	.05	.51	.010	.015	.03	.17	2.39	1.08	.001
8	.14	.04	.52	.009	.013	.03	.17	2.39	1.06	.002
9	.14	.07	.52	.008	.012	.03	.16	2.36	1.03	.001
10	.13	.06	.50	.007	.011	.03	.15	2.30	.98	.001
11	.13	.05	.52	.008	.012	.03	.15	2.36	1.03	.001
12	.14	.05	.52	.008	.013	.03	.15	2.36	1.03	.001
13	.14	.06	.52	.009	.013	.03	.15	2.37	1.04	.001
14	.12	.07	.49	.007	.010	.03	.14	2.29	.98	.003
15	.12	.05	.50	.007	.010	.03	.15	2.30	.99	.003
16	.14	.06	.52	.009	.013	.03	.16	2.35	1.06	.002
Ladle	.14	.04	.50	.011	.015	.04	.17	2.40	1.04	.003
A336F22 Spec.	≦.15	≦.50	.30 .60	≦.030	≦.030	—	—	2.00 2.50	.90 1.10	—

*Sn=0.004 As=0.005 Sb=0.0041
$\overline{X}$=(10P+5Sn+4Sb+As,ppm)/100=13.2

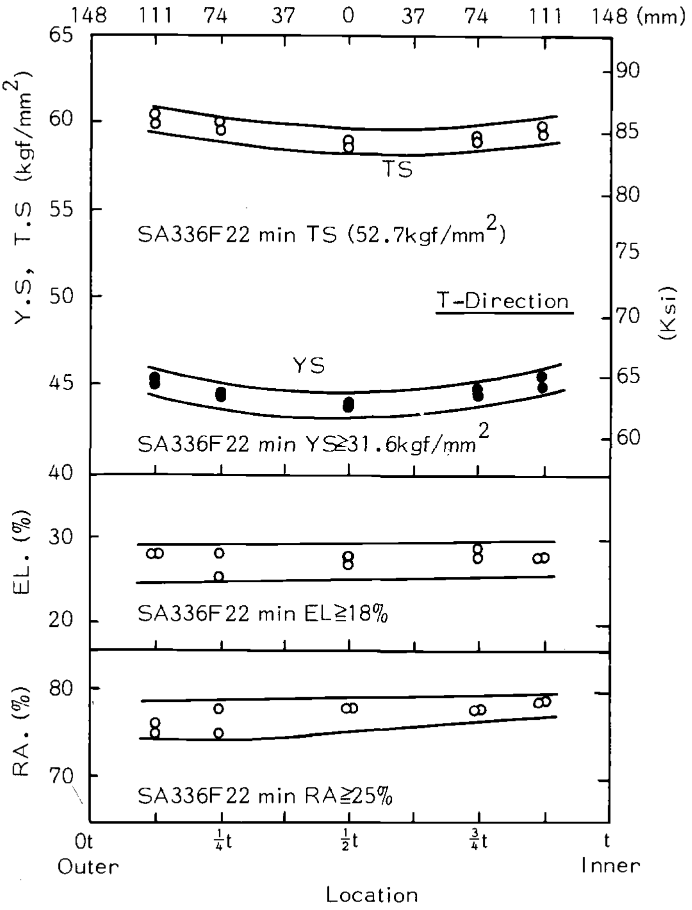

FIG. 11—*Tensile properties at various locations in thickness of low-silicon 2¼Cr-1Mo steel forged ring after PWHT.*

below 0.10 percent by the VCD process has mechanical properties which satisfy the specification requirements of ASME SA-336, F22, and also has good resistance to temper embrittlement.

Conclusions

From the results of the present investigation, the following conclusions have been obtained:

1. The effect of silicon content on the susceptibility to temper embrittlement is greater for the higher temper parameter required for thick-wall 2¼Cr-1Mo steel forgings.

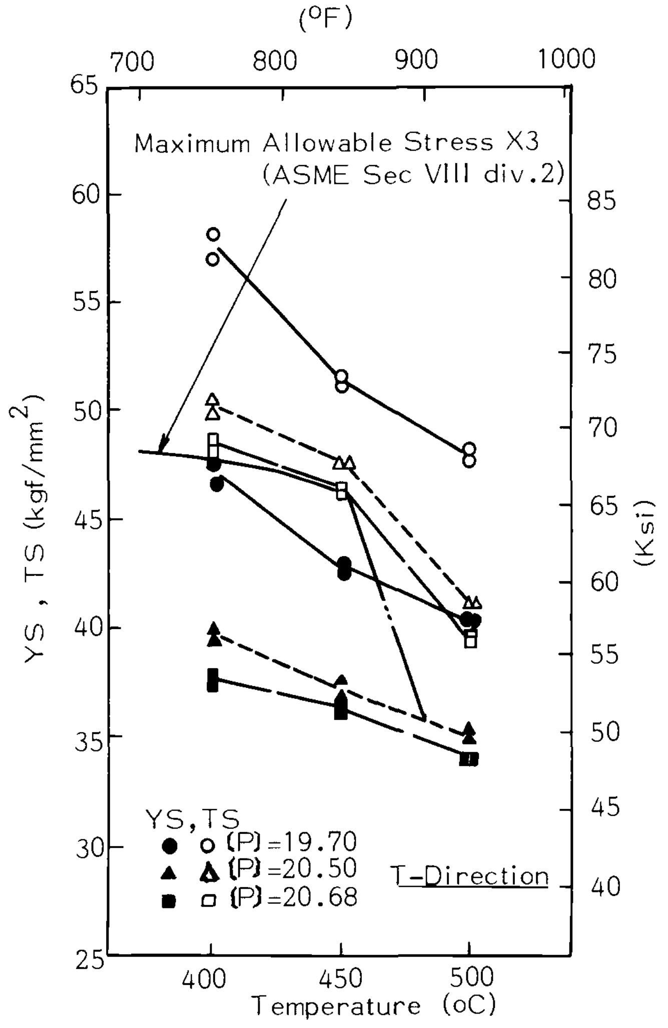

FIG. 12—*Yield and tensile strength at elevated temperature of low-silicon 2¼Cr-1Mo steel shell ring after PWHT.*

2. The reduction of silicon content does not affect the phosphorus concentration on grain boundaries, but the quantity of grain boundaries which can be fractured is reduced.

3. An embrittling factor defined as (2Si + Mn, %)$\bar{X}$, where $\bar{X}$ = (10P + 5Sb + 4Sn + As, ppm)/100, provided a good indication of the susceptibility to temper embrittlement of a thick-wall 2¼Cr-1Mo steel forging in step-cooling and in isothermal embrittlements at 475°C (887°F).

4. The reduction of silicon content did not affect the creep rupture strength

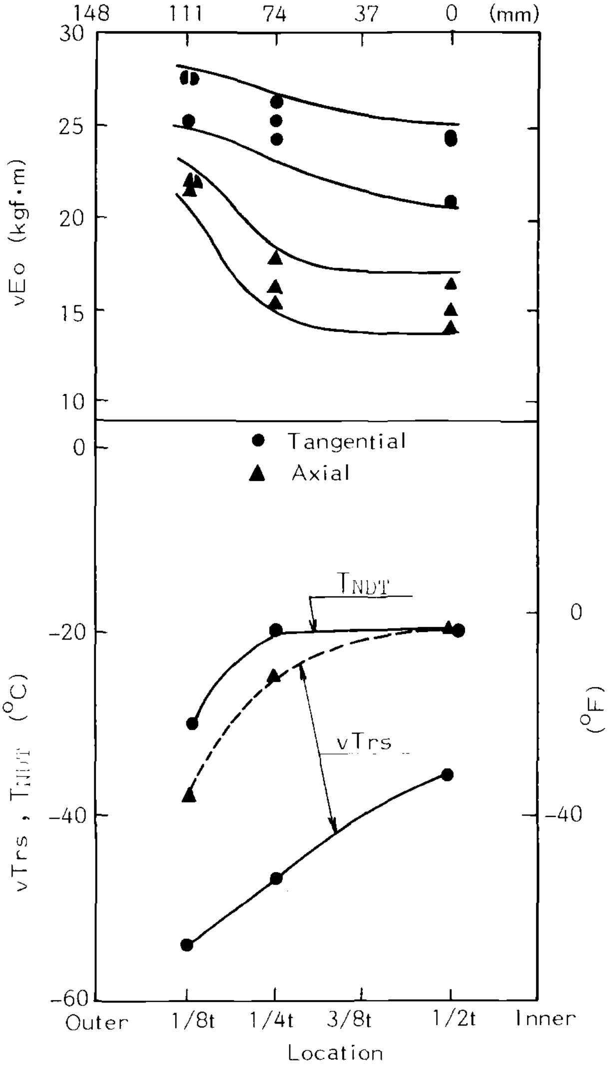

FIG. 13—*Notch toughness at various locations in thickness of low-silicon 2¼Cr-1Mo steel forged ring after PWHT.*

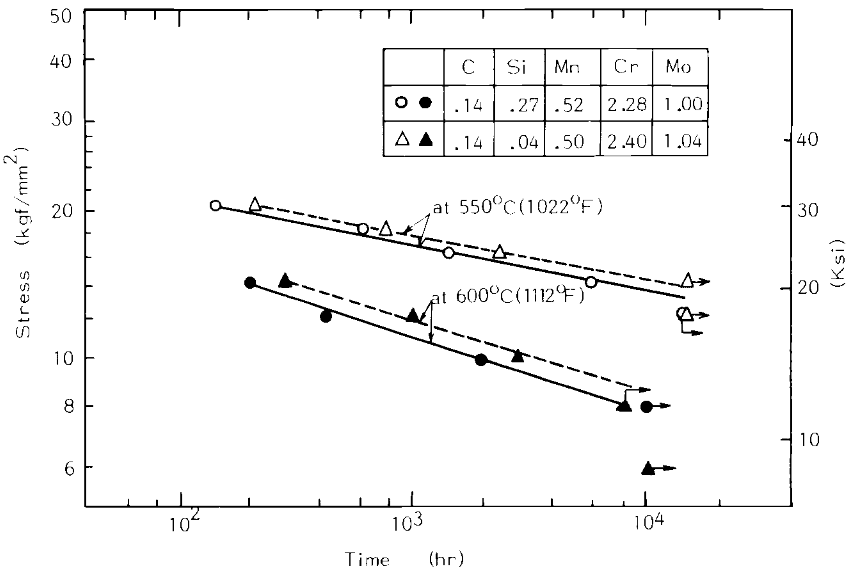

FIG. 14—*Creep rupture strength of low-silicon 2¼Cr-1Mo steel forged ring.*

TABLE 7—*Change in impact properties of low-silicon 2¼Cr-1Mo steel forged ring by step-cooling embrittlement.*

Location	Direction	vTrs, °C (°F) BSC[a]	vTrs, °C (°F) ASC[b]	ΔvTrs, °C (°F)	vTr40, °C (°F) BSC	vTr40, °C (°F) ASC	ΔvTr40, °C (°F)	vTr40 + 1.5 ΔvTr40, °C (°F)
¼ *t*	tangential	−43 (−45)	−29 (−20)	14 (25)	−63 (−81)	−48 (−54)	15 (27)	−40.5 (−41)
	axial	−30 (−22)	−20 (−4)	10 (18)	−59 (−74)	−49 (−56)	10 (18)	−44 (−47)

[a] BSC: Before step cooling; ΔvTrs: shift in vTrs.
[b] ASC: After step cooling; ΔvTr40: shift in vTr40. PWHT: 695°C for 20 h F.C.

of 2¼Cr-1Mo steel. Thus thick-wall 2¼Cr-1Mo steel forgings with reduced silicon content below 0.10 percent by vacuum carbon-deoxidization process showed excellent mechanical properties and good resistance to temper embrittlement.

We conclude that low-silicon 2¼Cr-1Mo steel is extremely suitable for thick-wall pressure vessel material, especially for pressure vessels operating in the temperature range of 350 to 550°C (662 to 1022°F).

TABLE 8—*Change in impact properties of low silicon 2¼Cr-1Mo steel forged ring by isothermal embrittlement at 475°C.*

		vTrs, °C (°F)				vTr40, °C (°F)			
Location	Direction	0 h	1000 h	3000 h	5000 h	0 h	1000 h	3000 h	5000 h
¼ *t*	tangential	−43 (−45)	−32 (−26)	−21 (−6)	−21 (−6)	−63 (−81)	−52 (−62)	−42 (−44)	−36 (−33)
	axial	−30 (−22)	−24 (−11)	−13 (9)	−13 (9)	−59 (−74)	−49 (−56)	−39 (−38)	−34 (−29)

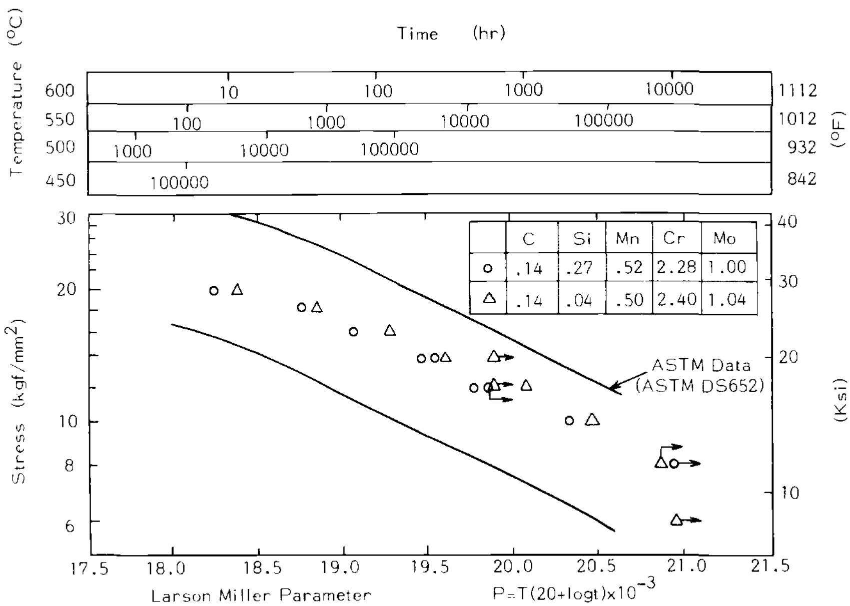

FIG. 15—*Relation between rupture stress and Larson-Miller parameter of low-silicon 2¼Cr-1Mo steel forged ring.*

References

[1] Bruscato, R., *Welding Journal*, Vol. 49, 1970, p. 148S.

[2] Miyano, K., *Journal of the High Pressure Institute of Japan*, Vol. 12, 1974, p. 23.

[3] Wade, T., "Climax Molybdenum Company Progress Report," Report No. 32-74-03, 1975.

[4] Makioka, M. and Kohno, M., *Kobe Steel Engineering Reports*, Vol. 26, 1976, p. 24.

[5] Swift, R. A. and Gulya, J. A., *Welding Journal*, Vol. 52, 1973, p. 57S.

[6] Clauser, C. B. et al, *37th Midyear Meeting of the American Petroleum Institute*, Print No. 52-72, May 11, 1972.

[7] Kinoshita, S. and Katsumata, M., *Reports of Materials Research Committee*, Iron and Steel Institute, London, 1976, p. 95.

[8] Yu, J. and McMahon, C. J., Jr., *Metallurgical Transactions A*, Vol. 11A, 1980, p. 291.

[9] Smith, G. V., "Supplemental Report on the Elevated-Temperature Properties of Chromium-Molybdenum Steels," ASTM Data Series Publication DS 652, American Society for Testing and Materials, 1971.

R. J. Kar[1] *and J. A. Todd*[2]

Alloy Modification of Thick-Section 2¼Cr-1Mo Steel

REFERENCE: Kar, R. J. and Todd, J. A., **"Alloy Modification of Thick-Section 2¼Cr-1Mo Steel,"** *Application of 2¼Cr-1Mo Steel for Thick-Wall Pressure Vessels, ASTM STP 755*. G. S. Sangdahl and M. Semchyshen, Eds., American Society for Testing and Materials, 1982, pp. 228-252.

ABSTRACT: The manufacture of large-scale pressure vessels required for coal gasification and liquefaction systems requires a steel technology capable of producing plates up to 400 mm (16 in.) thick with good combinations of strength, fracture toughness, resistance to hydrogenous environments, weldability in the field, and resistance to temper embrittlement. A research program was initiated with the object of optimizing microstructure and mechanical properties of thick-section 2¼Cr-1Mo steels through compositional modifications. It was found that minor additions of nickel and manganese led to improved mechanical properties in simulated slow-cooled thick plates through the presence of optimum microstructural constituents.

As an extension to this program, the temper-embrittlement susceptibility, hydrogen-attack resistance, weldability, fracture toughness, and elevated temperature properties of the modified alloys are now being compared with those of commercial SA 387 steel. A summary of results obtained to date is presented.

KEY WORDS: 2¼Cr-1Mo steel, thick section applications, microstructure, mechanical properties, impact toughness, temper embrittlement, hydrogen attack, weldability, alloy design, nickel-manganese modifications

The vessels required for coal gasification and liquefaction systems will, for economic reasons, be the largest pressure vessels ever constructed in the United States; for example, recent figures suggest vessel dimensions of 61 m (200 ft) in height and 6.1 m (20 ft) in diameter [*1*].[3] They will contain hydrogen at elevated temperatures and pressures of 20 700 to 27 580 kPa (3000 to 4000 psi) [*2*], and therefore wall thicknesses of at least 300 mm (12 in.) and possibly 400 mm (16 in.) will be required for the support structure. In addi-

---

[1] Senior Metallurgist, Anamet Laboratories, Inc., Berkeley, Calif. 94710.

[2] Research Engineer, Department of Materials Science and Mineral Engineering, University of California, Berkeley, Calif. 94720.

[3] The italic numbers in brackets refer to the list of references appended to this paper.

tion, because it will not be possible to shop fabricate the entire vessel due to size and transportation difficulties, field fabrication techniques must also be developed. The steel selected by designers for these vessels is 2¼Cr-1Mo steel, which is widely used in the petrochemical industry because of its good elevated temperature properties [*3*] and its resistance to hydrogen environments [*4*]. However, the large wall thicknesses and the pressure/temperature regimes of the proposed systems will go considerably beyond present experience and indicate that the following metallurgical problems must be carefully considered.

Hardenability—During spray quenching from the austenitizing temperature, a uniform martensitic or lower bainitic microstructure is desired for optimum mechanical properties on subsequent tempering. However, the slow cooling rates occurring within the interiors of thick plates can lead to mixed ferritic/bainitic microstructures in a wide region of the plate [*5-8*], with a consequent deterioration in mechanical properties.

Hydrogen-Attack Resistance—Elevated temperature/pressure hydrogen can react with carbon in interstitial solid solution resulting in initial decarburization, followed by destabilization of the carbides and the formation of methane bubbles at grain boundaries [*9*]. Marked deterioration in strength and toughness is observed at this stage. Stable carbide compositions, morphologies, and distributions are required to reduce this problem.

Temper Embrittlement Susceptibility—Reversible temper embrittlement occurs when trace impurities such as phosphorus and tin segregate to prior austenite grain boundaries either on slow cooling from the austenitizing temperature or on prolonged exposure to temperatures in the range of 350 to 550°C [*10*]. Phosphorus is known to be a potent embrittling element in 2¼Cr-1Mo steels [*10,11*].

Elevated Temperature Properties—Good creep strength and fracture properties may be required up to temperatures of 750°C in these vessels.

Weldability—The high deposition rate welding processes required for field fabrication of 400-mm (16-in.)-thick vessels may result in a wide range of metallurgical and inspection problems. Of particular interest to this program are the heat-affected zone microstructures produced in thick-section welds.

The object of this research program was to optimize the microstructures and associated mechanical properties in thick-section 2¼Cr-1Mo steel through compositional modifications. Minor alloy additions of manganese and nickel were selected because these elements are known to enhance the hardenability of low-alloy steels [*7*], and improved combinations of strength and impact toughness were obtained. Recent research programs [*12,13*] have been initiated to determine whether the additions of manganese and nickel affect the temper embrittlement susceptibility of 2¼Cr-1Mo steel and whether this phenomenon can be eliminated by the addition of rare-earth elements. An assessment of the hydrogen-attack behavior and the weldability of the alloy modifications is currently in progress.

Materials

The 2¼Cr-1Mo steels used in this investigation were supplied by Lukens Steel Company, Coatesville, Pennsylvania, in the form of 68-kg (150-lb) heats which had been air induction melted. The ingots were then upset forged and cross rolled into 30-mm (1¼-in.) plates from which test specimens were cut. The alloy compositions of the heats used are given in Table 1. Additional remelts were made by ESCO, Portland, Oregon, for the temper embrittlement study; these compositions are given in Table 2.

Experimental Procedure

In view of the limited quantity of material available to the program, simulation heat treatments were developed to produce microstructures representative of thick-section steel plates. Cooling rates corresponding to those of the quarter-thickness locations of 150 to 300 mm (6 to 12 in.) plates were supplied courtesy of Lukens Steel Company, accurately reproduced in the laboratory, and used to program an induction furnace. The validity of such techniques has been discussed elsewhere [*7*].

[It should be noted that the cooling rates used in this investigation were conservative compared with actual commercial practice capability. This can be seen in Fig. 1, which compares the cooling rates used in this program with data from pressure vessel fabricators supplied courtesy of G. S. Sangdahl, Chicago Bridge and Iron Co. It would therefore appear that rates slower than 10°C/min (20°F/min) used in this study are actually representative of commercial 300 to 400 mm (12 to 16 in.) plate.]

After simulated cooling, specimen blanks were tempered in neutral salt pots to time-tempering parameters of 34.1 and 36.2 (4 h at 650°C and 700°C) and then finished to size using appropriate flood-cooling techniques.

The mechanical properties evaluated in the work included room temperature tension tests and impact properties using Charpy V-notch impact specimens (L-T orientation). These tests were performed in accordance with ASTM Methods of Tension Testing of Metallic Materials (E 8-79a) and Methods for Notched Bar Impact Testing of Metallic Materials [E 23-72 (1978)], respectively.

Microstructural examination was carried out using optical metallography and transmission electron microscopy. In addition, fractured Charpy specimens were examined with an AMR 1000 scanning electron microscope.

Results and Discussion

The results obtained in the investigation can be classified into the following sections:

1. Comparison between the mechanical properties of modified and base 2¼Cr-1Mo steels.

TABLE 1—*Compositions of chromium-molybdenum steels investigated.*[a]

Type	Ingot No.	C	Mn	Ni	Cr	Mo	Si	P	S	V	Al
Base	B542	0.15	0.42	0.10	2.18	0.91	0.30	0.015	0.009	. . .	0.019
Base + 1Mn	B543	0.15	1.50	0.13	2.25	0.96	0.33	0.012	0.007	. . .	0.021
Base + 0.5Mn + 0.5Ni	B547	0.16	0.92	0.51	2.27	1.03	0.28	0.013	0.008	. . .	0.021
Base + 0.5Mn + 0.5Ni(GR)[b]	B548	0.16	0.92	0.50	2.25	1.03	0.28	0.013	0.008	0.022	0.035
Base + 0.5Mn + 1.0Ni	B550	0.16	0.95	1.02	2.29	1.02	0.29	0.014	0.007	. . .	0.014
Base + 0.5Mn + 1.0Ni + 0.7Cr	B551	0.15	0.94	0.97	2.96	0.98	0.28	0.010	0.008	. . .	0.014

[a] All alloy additions are weight percent.

[b] GR = grain refined with 0.02 percent vanadium and 0.01 percent aluminum.

TABLE 2—*Temper embrittlement study.*

	C	Al	Cr	Cu	Mn	Mo	Ni	P	Si	S	Sn	La	Ce
Remelt	0.10	0.14	2.78	0.10	0.69	1.02	0.46	0.014	0.35	0.016	0.009	0.01	0.01
Remelt + misch metal	0.13	0.06	2.50	0.10	0.44	1.04	0.32	0.013	0.12	0.011	0.008	0.03	0.13

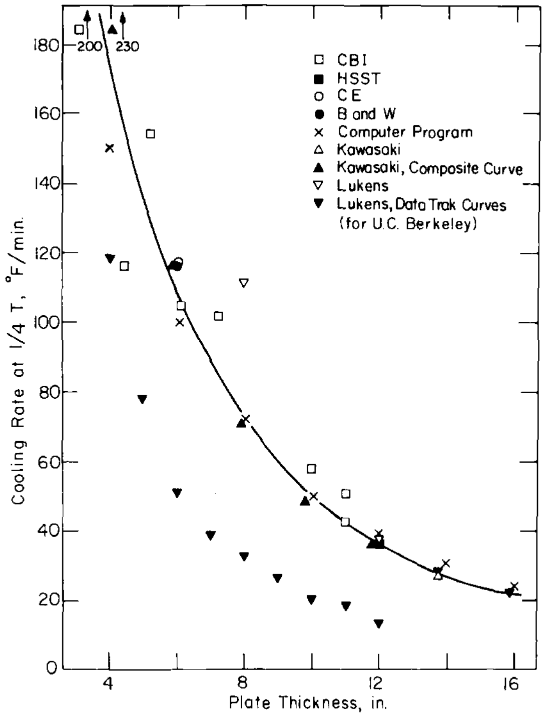

FIG. 1—*Comparison between cooling rate data supplied to program by Lukens and data from commercial pressure vessel fabricators* (Courtesy G. S. Sangdahl, Chicago Bridge and Iron).

2. Correlation between the microstructures of both the modified alloys and base 2¼Cr-1Mo steels with their observed mechanical properties.
3. Reversible temper embrittlement studies of 2¼Cr-1Mo steel and two of its nickel-manganese modifications.
4. The effects of rare-earth additions on the temper embrittlement susceptibility of 2¼Cr-1Mo steel.
5. An overview of the current research programs investigating the hydrogen-attack resistance and the weldability of the modified alloys.

Nickel and Manganese Modifications of 2¼Cr-1Mo Steel

The slow cooling that occurs on spray quenching 200- to 300-mm-thick plates of 2¼Cr-1Mo steel results in the formation of a second phase in the microstructure which is commonly referred to as polygonal, free, or proeutectoid ferrite [*14*]. The associated degradation in tensile properties with increasing polygonal ferrite content has led to applications where design stresses are low and strength is not an important parameter [*15*].

The approach in this research program was to increase the hardenability of thick-plate 2¼Cr-1Mo steel by minor compositional modification. Alloy additions of nickel and manganese were selected because they are known to retard the kinetics of the proeutectoid ferrite reaction in simple iron-carbon systems [*16,17*], and research by Kar [*7*] has shown that these elements are also effective in 2¼Cr-1Mo steels. The compositions of the modifications investigated in this program are given in Table 1.

Preliminary studies of the transformation kinetics of the modified alloys were carried out using high-speed dilatometry. It was found that additions of 1 weight percent manganese and/or nickel were sufficient to completely suppress the formation of free ferrite. The continuous-cooling transformation diagram for the 2¼Cr-1Mo alloy modified with 0.5%Mn + 0.5%Ni (referred to as Base + 0.5Mn + 0.5Ni) is shown in Fig. 2. It was found that even for the slowest cooling rate (rate 8 = 2.8°C/min) no polygonal ferrite was observed.

Figures *3a* and *3b* are optical microstructures of 2¼Cr-1Mo steel and the 1Mn modified steel cooled at 7°C/min. It can be seen that whereas the base alloy has about 40 percent polygonal ferrite in the structure, none was detected in the modified alloy.

The mechanical properties of the modified alloys were evaluated after simulated heat treatments corresponding to a cooling rate of 7°C/min and tempering to two different Larson-Miller time tempering parameters (TTP) of 34.1 and 36.2. The tensile properties are given in Tables 3 and 4, and the impact properties are shown in Figs. 4 and 5.

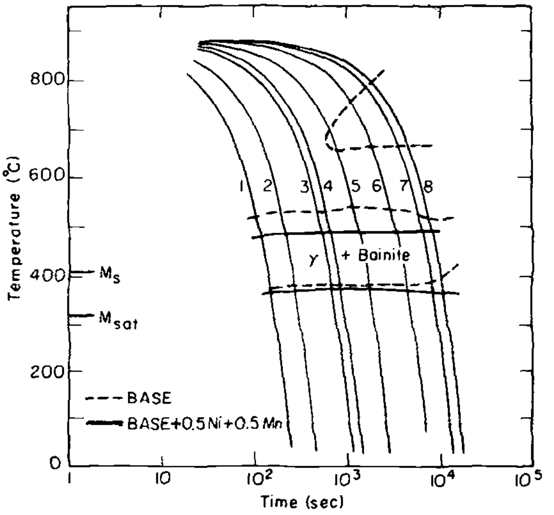

FIG. 2—*CCT diagram of base + 0.5Mn + 0.5Ni alloy (CCT diagram of 2¼Cr-1Mo base is also indicated by dotted line).*

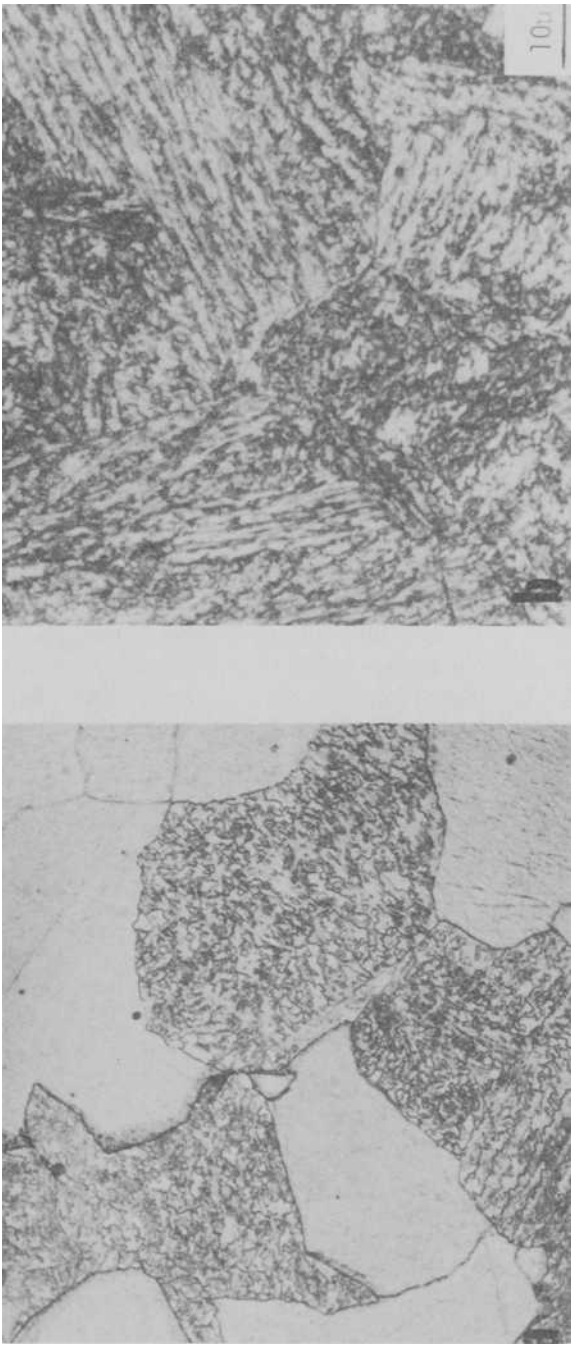

FIG. 3—*Comparison of simulated-cooled (7°C/min) microstructures from base steel and base + 1Mn alloy.*

TABLE 3—*Tensile properties of developmental chromium-molybdenum alloys spray quenched at 7°C/min, plate, ¼T location.*[a]

Type	Yield Strength, MPa (ksi)	Tensile Strength, MPa (ksi)	Elongation, %	Reduction of Area, %	σ_y/σ_{ult}
Base	409.5 (59.4)	705.9 (102.4)	21.5	69.5	0.58
Base + 1Mn	591.5 (85.8)	711.4 (103.2)	25.0	72.8	0.83
Base + 0.5Ni + 0.5Mn	615.0 (89.2)	736.9 (106.9)	24.1	70.0	0.83
Base + 0.5Ni + 0.5Mn[b]	630.8 (91.5)	743.2 (107.8)	25.9	69.8	0.85
Base + 1Ni + 0.5Mn + 0.75Cr	619.7 (89.9)	713.5 (103.5)	26.0	72.3	0.87

[a] Austenitized at 1000°C for 1 h; tempered at 650°C for 4 h (TTP = 34.1)
[b] Grain refined.

TABLE 4—*Tensile properties of developmental chromium-molybdenum alloys spray quenched at 7°C/min, plate, ¼T location.*[a]

Type	Yield Strength, MPa (ksi)	Tensile Strength, MPa (ksi)	Elongation, %	Reduction of Area, %	σ_y/σ_{ult}
Base	499.1 (72.4)	639.8 (92.8)	24.9	71.9	0.78
Base + 1Mn	497.7 (72.2)	643.2 (93.3)	22.8	64.3	0.77
Base + 0.5Mn + 0.5Ni	485.3 (70.4)	631.5 (91.6)	23.8	69.9	0.75
Base + 0.5Ni + 0.5Mn[b]	520.5 (75.5)	649.4 (94.2)	25.2	69.4	0.82
Base + 1.0Ni + 0.5Mn	483.3 (70.1)	633.6 (91.9)	28.7	70.9	0.76
Base + 1.0Ni + 0.5Mn + 0.75Cr	499.1 (72.4)	643.2 (93.3)	27.1	69.7	0.78

[a] Austenitized at 1000°C for 1 h; tempered at 700°C for 4 h.
[b] Grain refined.

Examination of the tensile properties reveals that for the lower TTP (34.1 = 4 h at 650°C) the effect of alloy addition was to cause an increase in the yield strength ranging from 180 to 220 MPa (25 to 35 ksi), whereas for the higher TTP (36.2 = 4 h at 700°C) the modified alloys had tensile properties equivalent to those of the base steel. However, a comparison of the impact properties (Figs. 4 and 5) reveals that the modified alloys were superior for both tempering conditions. For example, as can be seen in Fig. 5, for a TTP of 36.2 the base alloy has a FATT (50 percent brittle) at −14°C, whereas the 0.5Mn + 0.5Ni alloy showed a decrease in FATT to −58°C.

Correlation of Microstructures and Mechanical Properties

In an analyses of the mechanical properties discussed in the previous section, it is important to examine the microstructures in detail in order to explain the observed results. For example, it cannot be said that the elimina-

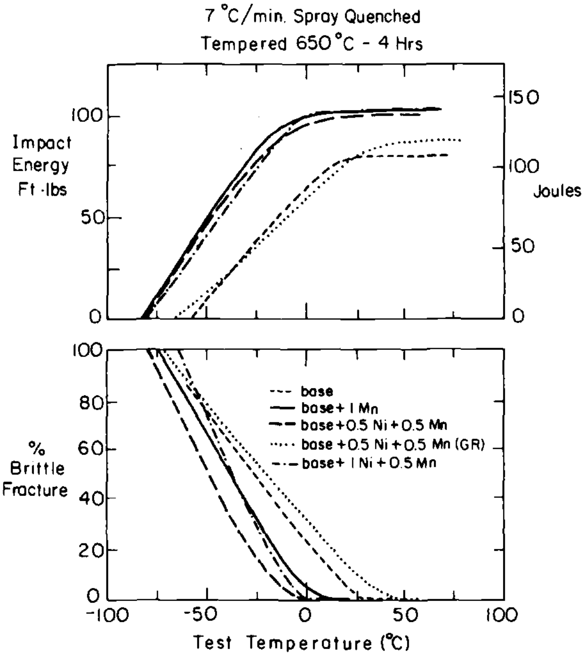

FIG. 4—*Impact properties of modified alloys tempered at 650°C.*

tion of polygonal ferrite from the 7°C/min cooled microstructure is solely responsible for the improvements in mechanical properties [we note that for the higher TTP = 36.2, elimination of the second phase did not result in improved yield strength/ultimate strength ratios (Table 4)]. It is therefore important to examine the as-quenched structures and assess their effect on the mechanical properties of the subsequently tempered plates.

Examination of the base alloy and the nickel-manganese modifications was carried out using transmission electron microscopy. Figure 6 is a series of transmission electron micrographs of 2¼Cr-1Mo steel cooled at 7°C/min which shows the bainitic regions in the steel. As can be seen in Fig. 6*a*, the ferritic laths are in contact with each other and exhibited a fairly high dislocation density. Elongated stringers of interlath carbide (identified as cementite) are barely visible in the bright field, but can be clearly seen in the dark field formed by imaging a cementite spot. Thus the bainite observed in slow-cooled 2¼Cr-1Mo steel can be characterized as upper bainite [*18*], that is, ferritic laths with interlath cementite.

In contrast, examination of the as-quenched structures of the nickel-manganese modified alloys cooled at the same rate (7°C/min) revealed that, apart from the elimination of polygonal ferrite from the microstructure (Fig. 3*b*), the effect of alloy addition was to alter the morphology of the con-

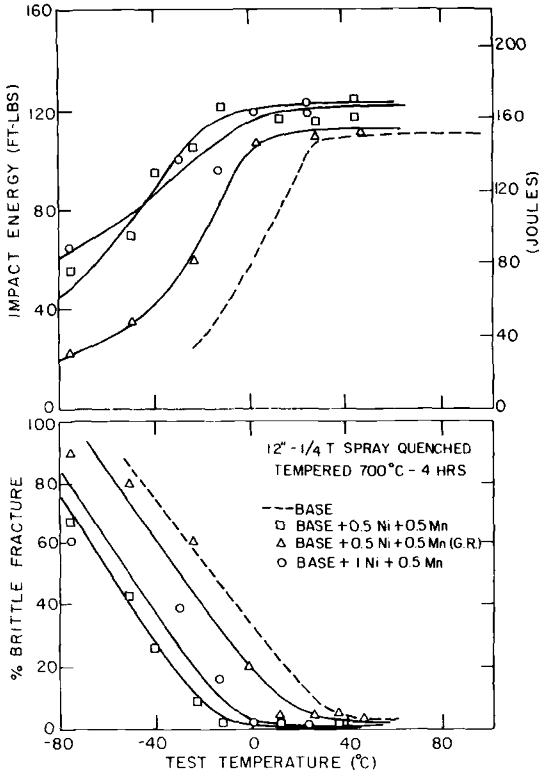

FIG. 5—*Impact properties of modified alloys tempered at 700°C.*

tinuously cooled bainites that formed in these steels. (The bainite in base 2¼Cr-1Mo steel was upper bainite, whereas that observed in the modified steels was primarily lower bainite [*19*], described below.) Figure 7 is a series of transmission electron micrographs of the 1Mn modified alloy cooled at 7°C/min. It can be seen that the structure consisted of dislocated ferritic laths with carbides precipitating internally at an angle of 60 deg with the major axis of the lath. This structure was characteristic of lower bainite [*19*] where carbides precipitate internally at well-defined angles, rather than upper bainite where carbides are interlath in nature [*18*].

It has been pointed out [*7*] that the initial microstructures formed on slow cooling play an important role in controlling the mechanical properties of thick plates on subsequent tempering; for example, the rate of alloy carbide precipitation during tempering is controlled by the dissolution of the cementite. Coarse interlath upper bainitic carbides are fairly resistant to tempering [*20*]; and it was observed that the tempering response of base 2¼Cr-1Mo steel (cooled at 7°C/min and tempered at 650°C) was much slower than that

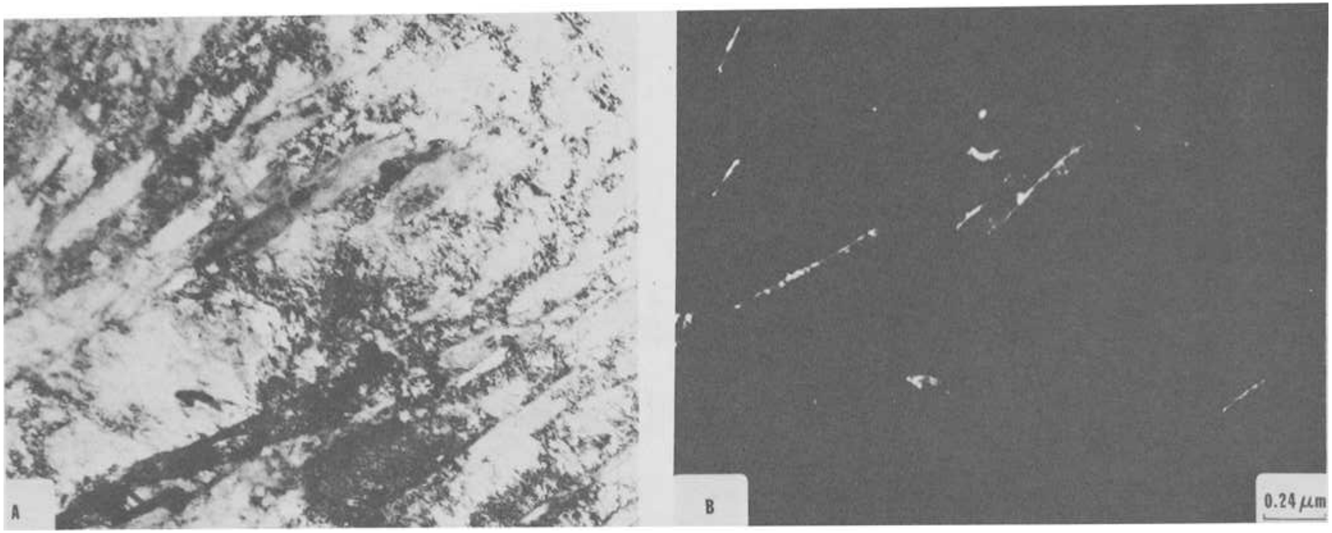

FIG. 6—*Transmission electron micrographs of 7°C/min spray-quenched 2¼Cr-1Mo steel at one-quarter thickness.* (a) *Bright field showing dislocated ferritic laths;* (b) *Dark field showing inter-lath carbides.*

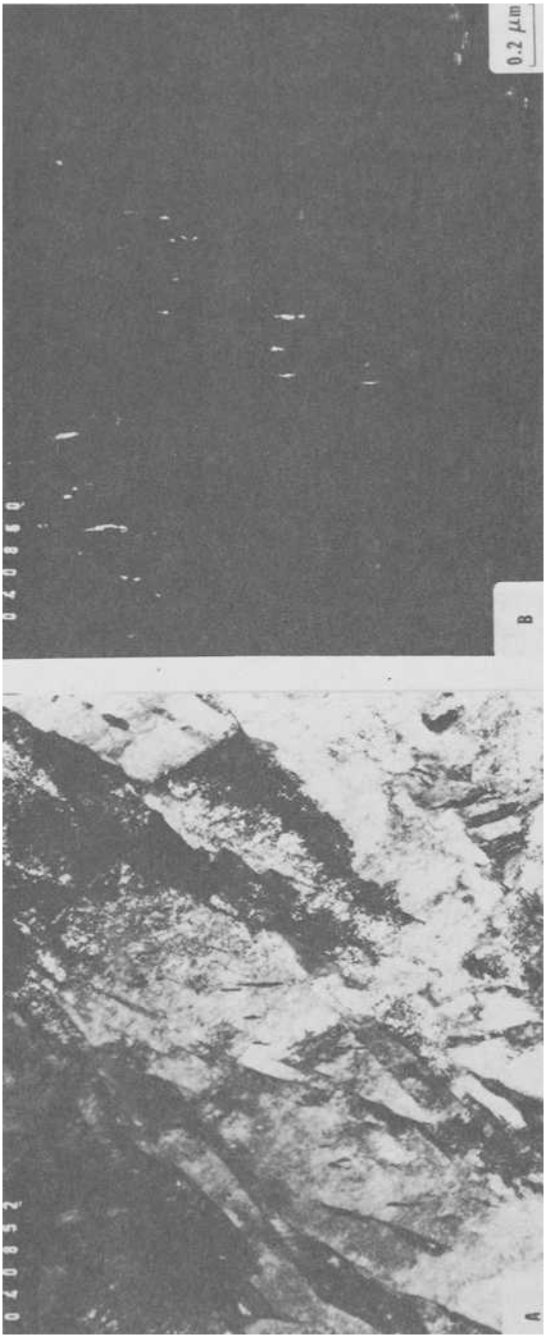

FIG. 7—*Transmission electron micrographs of 7°C/min cooled base + 1Mn steel at one-quarter thickness.* (a) *Bright field showing bainitic laths with internal carbides;* (b) *Dark field of cementite.*

of the modified nickel-manganese alloys where only fine, intralath lower bainitic carbides were found [*7*].

Figures 8*a* and 8*b* are a set of micrographs showing coarse Widmanstatten carbides within the bainitic lath (after tempering) of base 2¼Cr-1Mo steel. In addition, elongated stringers of cementite can be seen precipitated at bainite-polygonal ferrite boundaries. No precipitation of alloy carbide could be detected for this tempering treatment. In contrast, the nickel-manganese modified alloys showed precipitation of alloy carbide on tempering to the same TTP = 34.1. This can be seen in Fig. 9 which shows precipitation of alloy carbide, identified by selected area diffraction as Mo_2C. Coarse Widmanstatten cementite can also be seen within the bainitic laths (Fig. 9*b*).

Therefore, in summary, tempering to a TTP of 34.1 (4 h at 650°C) resulted in improved tensile properties in the modified alloys due to the elimination of polygonal ferrite and the improved tempering response of the lower bainitic microstructure. Further, as shown by Kar [*7*], tempering to a TTP of 36.2 results in extensive coherent alloy carbide precipitation in both the bainitic and ferritic phases of the base alloy and in the bainite of the modified alloys. The alloy carbides play an important role in governing the flow stress of these steels, resulting in equivalent yield strength/ultimate strength ratios. However, the impact properties of the modified alloys are certainly superior to the base alloy even at equivalent strength levels.

Temper Embrittlement Susceptibility

The embrittlement susceptibility of low-alloy steels is known to depend on microstructure, strength, and alloy composition [*21–23*], yet few systematic studies of these variables have been made. As nickel and manganese additions have been found to enhance the temper embrittlement susceptibility of high-chromium steels [*24*], a detailed investigation of the alloy modifications developed at the University of California-Berkeley is in progress to evaluate the effect of both compositional and microstructural variables on the temper embrittlement susceptibility of 2¼Cr-1Mo steel. The alloy compositions chosen were commercial 2¼Cr-1Mo, as the base alloy, Base + 1Mn, Base + 0.5Mn + 0.5Ni. A second series of alloys was chosen to investigate the effect of rare earth additions in reducing the embrittlement susceptibility of 2¼Cr-1Mo steel. All steels had similar levels of phosphorus.

The first series of tests was carried out on quenched and tempered microstructures (corresponding to the surface properties of commercial thick plate). (Viswanathan and Joshi [*23*] have suggested that greater phosphorus segregation is observed in tempered martensite structures than in tempered bainites.) Heat treatments consisted of austenitizing at 1000°C for 1 h, followed by an agitated oil quench, tempered at 650°C for 4 h, and then embrittled by isothermal aging at 483°C for 1000 h. The embrittlement susceptibility was measured by the shift in transition temperature in Charpy tests

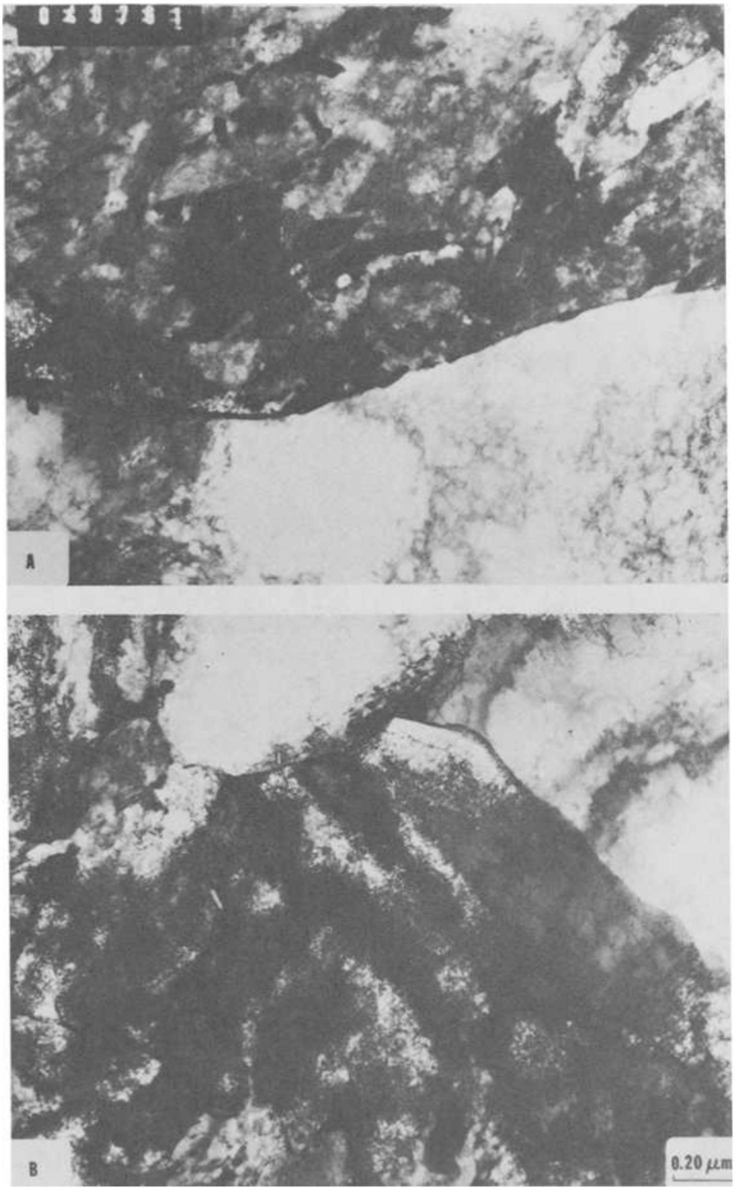

FIG. 8—*Micrographs of 7°C/min cooled 2¼Cr-1Mo steel tempered at 650°C for 4 h. Cementite precipitation within bainite laths and at polygonal ferrite/bainite boundaries is clearly seen.*

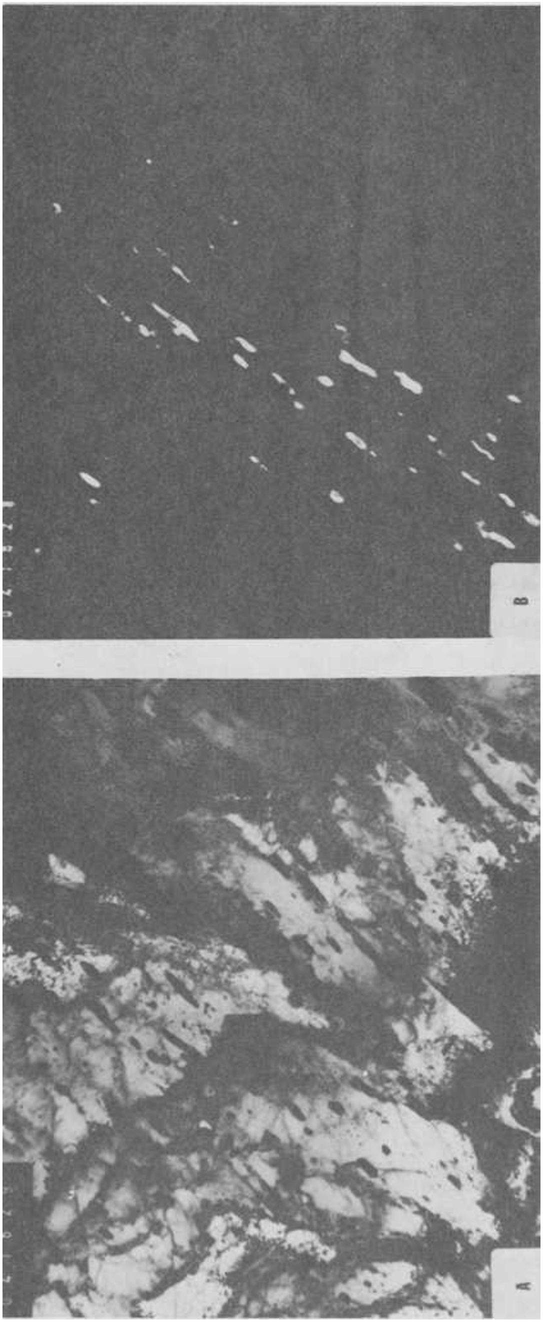
B
A

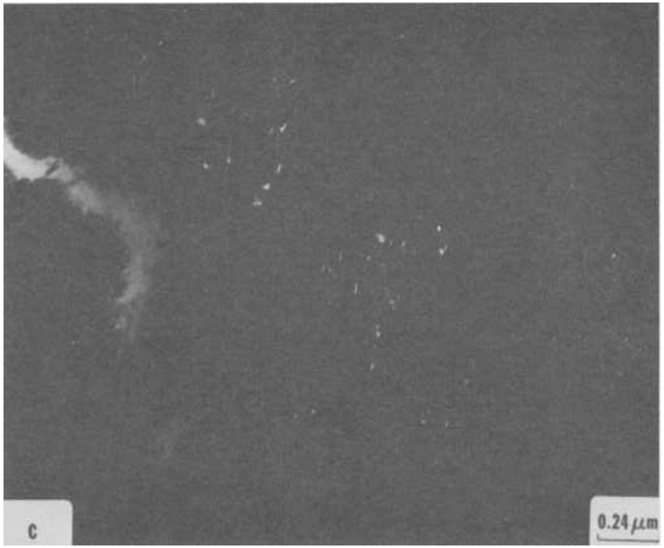

FIG. 9—*Electron micrographs of base + 1Mn alloy cooled at 18°C/min and tempered at 650°C for 4 h.* (a) *Bright field showing dislocated laths with coarse* Fe_3C *and fine alloy carbides (*Mo_2C*);* (b) *Dark field of* Fe_3C*;* (c) *Dark field of* Mo_2C.

carried out for embrittled and nonembrittled specimens. The Charpy impact results are shown in Table 5 and indicate that the base steel and alloy modifications have comparable shifts in 50 ft·lb impact transition temperature ($\Delta T \approx 40$ to 50°C). Figure 10 shows that both the FATT and the 50 ft·lb transition temperature of the modifications lie well below room temperature, and that even after a shift of 40°C (50 ft·lb transition temperature) the properties of the 0.5Mn + 0.5Ni modification appear to be superior to those of base 2¼Cr-1Mo steel.

When the alloy modifications were given a simulated cooling rate of 7°C/min followed by tempering at 650°C and isothermal aging at 483°C for 1000 h, the 50 ft·lb transition temperature increased to −6°C (0.5Mn +

TABLE 5—*Temper embrittlement.*

Alloy	Unembrittled, °C		Embrittled, °C		
	50 ft·lb	Upper Shelf	50 ft·lb	Upper Shelf	ΔT
Base[a]	−63	98	−23	96	40
Base + 1Mn[a]	−47.5	97	−5	93	42.5
Base + 0.5Mn + 0.5Ni[a]	−70	106	−22	100	48
Base + 1Mn[b]	−50	105	+8	...	58
Base + 0.5Mn + 0.5Ni[b]	−45	98	−6	...	39

[a] 1000°C for 1 h; oil quench; 650°C for 4 h; 483°C for 1000 h.
[b] 1000°C for 1 h; simulated cool at 7°C/min; 700°C for 4 h; 483°C for 1000 h.

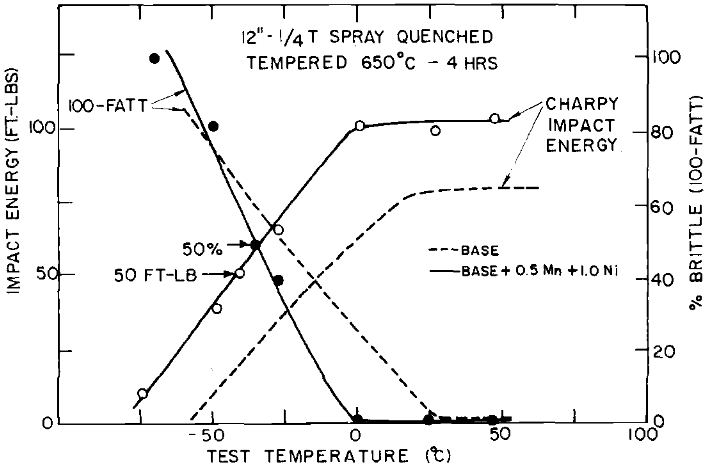

FIG. 10—*Impact properties of base + 0.5Mn + 0.5Ni tempered at 650°C.*

0.5Ni; ΔT = 39°C) and +8°C (1Mn; ΔT = 58°C) (Table 5 and Fig. 11). The properties were comparable with those of the base steel after tempering at 700°C followed by isothermal aging at 483°C for 1000 h.

Some preliminary results have also been obtained from base 2¼Cr-1Mo, a remelt of this steel, and a second remelt with a rare-earth addition. The compositions of these steels are given in Table 2. Several authors [25] have suggested that additions of rare-earth elements may reduce temper embrittlement significantly in steels containing commercial levels of phosphorus. Seah et al [25] have proposed an optimum addition of La = 8.7%S + 2.3%Sn + 4.5%P (wt %) or an equivalent amount of misch metal. Based on this calculation, a laboratory ingot containing 0.11%Ce and 0.03%La was cast. The embrittlement susceptibility of this steel was compared with that of the base steel after a heat treatment consisting of austenitizing at 1000°C for 1 h, simulated cool 7°C/min, temper at 700°C for 4 h, and isothermal aging at 483°C for 1000 h. A tempering temperature of 700°C was used for direct comparison with the data of Seah et al [25]. Preliminary results (Table 6 and Fig. 11) indicate that this addition was effective in reducing the 50 ft·lb impact transition temperature to −42°C (compared with −2°C for the embrittled base steel). The impact fracture surfaces broken at −196°C for the embrittled remelt and remelt + rare-earth addition are shown in Figs. 12 and 13. It can be seen that whereas the remelt exhibited extensive embrittlement (as indicated by decohesion at prior austenite grain boundaries), the rare-

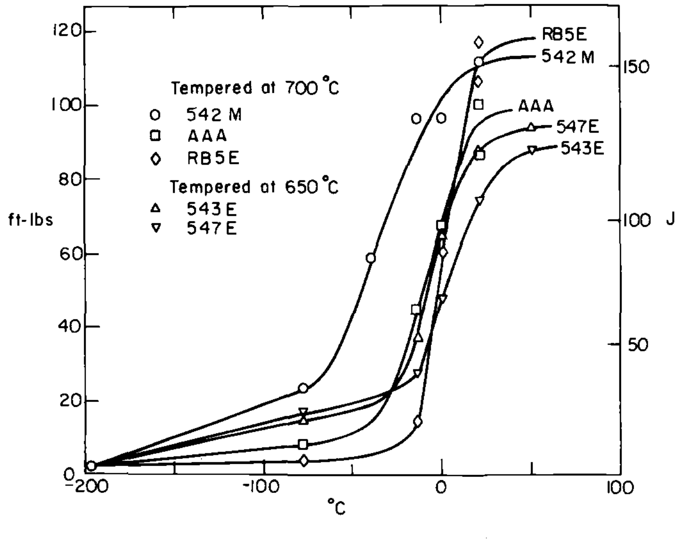

FIG. 11—*Impact properties of temper embrittled modifications and remelted alloys. RB5E = base; 542M = remelt + rare-earth; AAA = remelt; 547 E = base + 0.5Mn + 0.5Ni; 543E = base + 1Mn.*

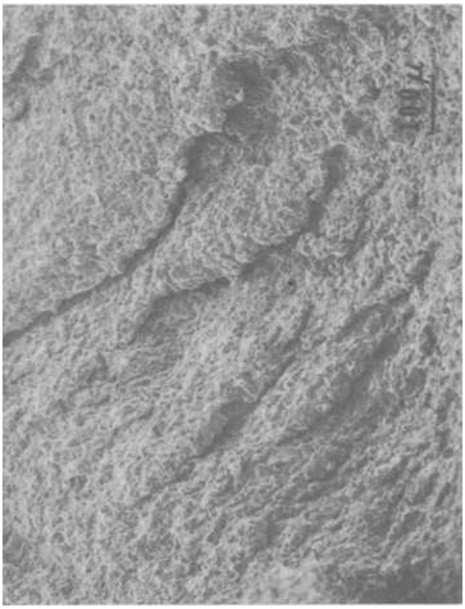
100μ

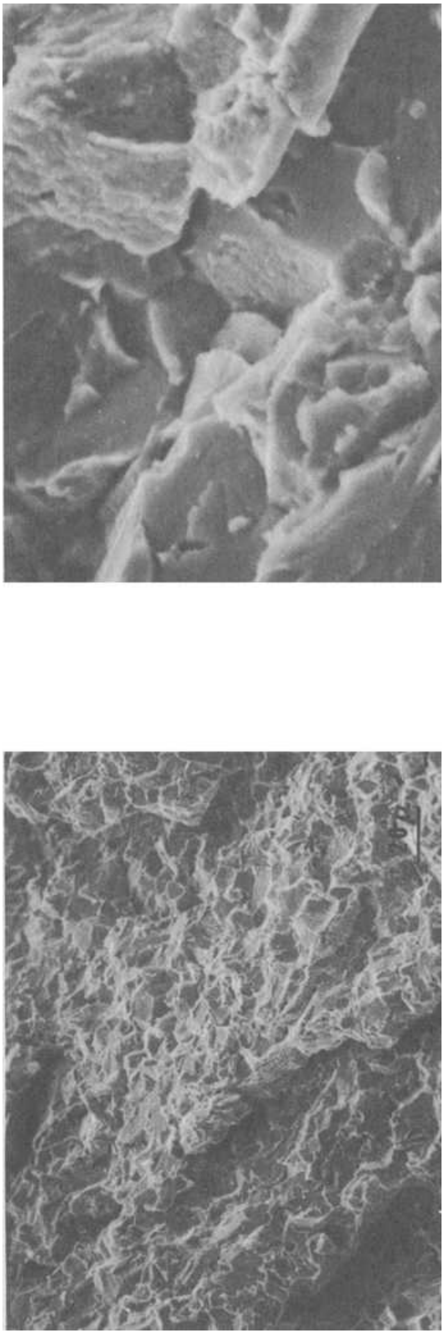

FIG. 12—*Fracture surfaces of isothermally aged remelt (AAA) showing intergranular fracture.*

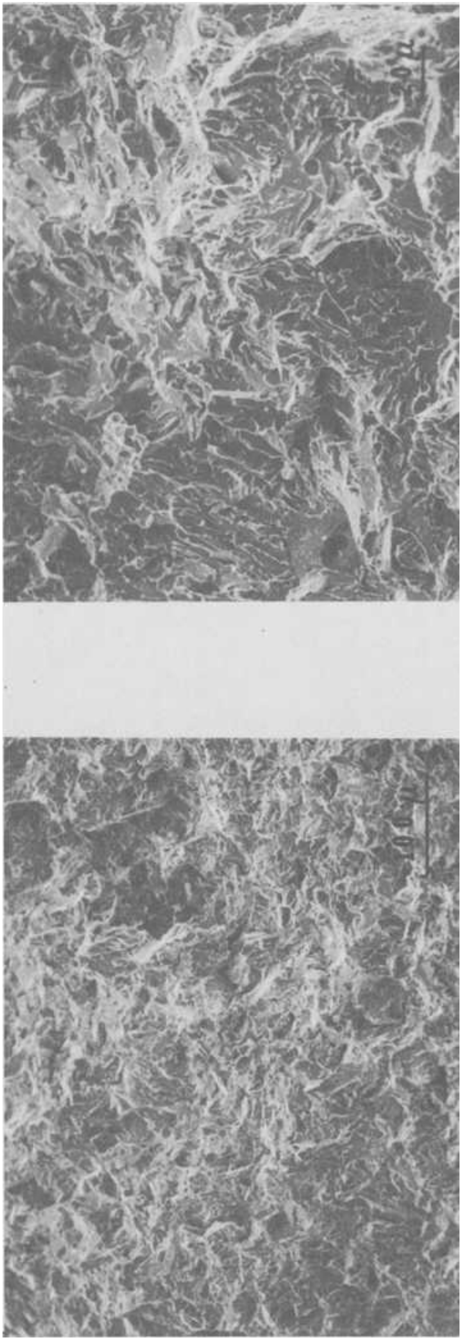
20μ
100μ

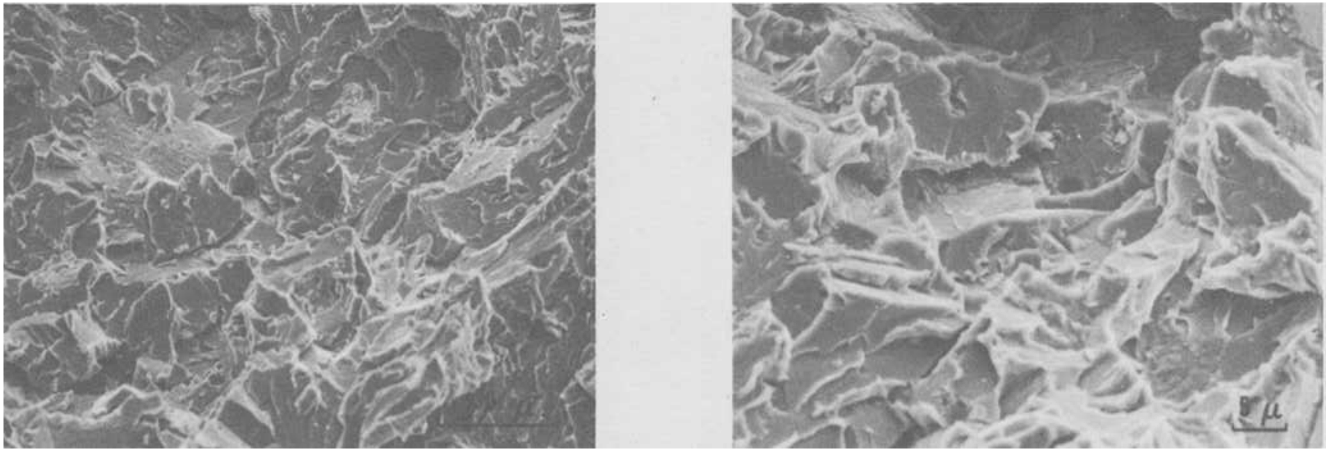

FIG. 13—*Fracture surfaces of isothermally aged remelt plus rare-earth addition showing principally cleavage fracture.*

TABLE 6—*Temper embrittlement.*

Alloy	Unembrittled 50 ft·lb	Unembrittled Upper Shelf	Embrittled 50 ft·lb	Embrittled Upper Shelf	ΔT
Base[a]	−5	105	−2	117	3
Remelt[a]	−5	105	−8	112	−3
Remelt + R.E.[a]	−5	105	−47	112	−37

[a] 1000°C for 1 h; simulated cool at 7°C/min; 700°C for 4 h; 483°C for 1000 h.

earth alloy failed by transgranular cleavage. Further work to investigate the role of the rare-earth additions in reducing temper embrittlement susceptibility of 2¼Cr-1Mo steel is now in progress. In addition, detailed transmission electron microscopy studies of these alloys are also being carried out.

Overview of Current Research Program

Hydrogen Attack—In the past, selection of steels for petrochemical applications has been made on the basis of the well-known Nelson [9] diagrams which indicate temperature-pressure regimes where low-alloy steels would be safe from hydrogen attack. However, little is known about the behavior of 2¼Cr-1Mo steel in hydrogen pressures of 20 700 to 27 580 kPa (3000 to 4000 psi) that would be typical of coal liquefaction systems [2]. In addition, the important factors governing carbide stability are not fully understood. Geiger and Angeles [4] have suggested that precipitation of alloy carbides in 2¼Cr-1Mo steel improves the hydrogen-attack resistance; research is currently in progress to compare the susceptibilities of the base and modified alloys.

Samples of simulated-cooled (7°C/min) 2¼Cr-1Mo steel tempered at 650°C (TTP = 34.1) which showed very little alloy carbide precipitation are being compared with the modified alloys (which had extensive alloy carbide precipitation at 650°C). Samples are being exposed to high-pressure hydrogen at temperatures in the range of 450 to 550°C for time periods of up to 1000 h. The hydrogen-attack susceptibilities will be compared by the reduction in ductility during tensile tests. Further detailed microstructural studies are being undertaken of exposed specimens to establish the role of the noncarbide forming elements, nickel and manganese, in determining the hydrogen-attack resistance.

Weldability—It is well known [26] that increasing the hardenability of low-alloy steels can raise the hardness levels in the heat-affected zone (HAZ) and contributes to problems such as cold cracking of the weldments. The additions of 0.5Mn + 0.5Ni to 2¼Cr-1Mo steel in the present work are thought to be sufficiently low as to have little effect on the weldability of these steels.

However, detailed microstructural characterizations are required to ensure that these alloy additions have no detrimental effect. Rather than begin with a synthetic weld test (such as a Gleeble test), it was decided to run a series of bead on plate tests using the submerged arc welding process so that the "worst case" HAZ microstructures could be examined. Experiments are currently underway to investigate the effects of heat input (40, 80, and 120 kJ/in.) and preheats (300, 400, and 500°F) on the HAZ microstructures. Welds will be evaluated by magnetic particle testing microhardness tests, optical metallography, and bend tests. The weldability of the modified alloys will be compared with 2¼Cr-1Mo steel.

Conclusions

1. The effect of minor alloy additions of nickel and manganese to 2¼Cr-1Mo steel resulted in improved tensile and impact properties for simulations characteristic of spray-quenched 300- to 400-mm-thick plates.
2. Microstructural examination revealed that the effect of alloy modification was to eliminate formation of polygonal ferrite from 2¼Cr-1Mo steel for all the cooling rates used. Further, additions of manganese and nickel altered the morphology of the continuously cooled bainite that formed in 2¼Cr-1Mo steel from upper bainite to lower bainite.
3. Modification of 2¼Cr-1Mo steel through alloy additions of manganese and nickel altered its tempering response so that alloy carbide precipitation occurred at a lower temperature.
4. Preliminary reversible temper embrittlement studies on the manganese-nickel modified alloys indicate that the alloy additions do not appear to alter the temper embrittlement susceptibility of 2¼Cr-1Mo steel for quenched and tempered treatments.
5. The effect of rare-earth additions to 2¼Cr-1Mo steel appears to be effective in reducing the temper embrittlement susceptibility, since isothermal aging of 2¼Cr-1Mo steel modified with cerium and lanthanum did not result in severe temper embrittlement.

References

[1] "Materials for Coal Conversion and Utilization," Department of Energy Conference, Gaithersburg, Md., 9-11 Oct. 1979, pp. 1-31.

[2] Metals Property Council Meeting, Ann Arbor, Mich., 29 April 1980.

[3] Irvine, K. J., Murray, J. D., and Pickering, F. B., "Special Report 70," Iron and Steel Institute, 1961, pp. 246-275.

[4] Geiger, G. H. and Angeles, O. F., "API Publication 945," American Petrochemical Institute, Washington, D.C., June 1975.

[5] Strunck, S. S., Pense, A. W., and Stout, R. D., "Welding Research Council Bulletin 120," Welding Research Council, Feb. 1967.

[6] Kitamura, D. and Moriyama, D., "Nippon Steel Technical Report Overseas Number 7," Nippon Steel Company, Japan, Nov. 1975.

[7] Kar, R. J., "An Investigation of the Microstructure and Mechanical Properties of Thick-Section Cr-Mo Steels," Ph.D. dissertation, University of California, Berkeley, Calif., June 1979.

[8] Horn, R. M., Kar, R. J., Zackay, V. F., and Parker, E. R., "The Design of Steels for Coal Gasification Vessels," *Journal of Materials for Energy Systems*, Vol. 1, 1979.

[9] Nelson, G. A., "Report of Subcommittee on Hydrogen Embrittlement," *Proceedings of the Pressure Vessel Research Committee*, Welding Research Council, 1969.

[10] McMahon, C. J., Jr., *Materials Science and Engineering*, Vol. 25, 1976, pp. 233-239.

[11] Swift, R. A., "Resident Report RDR 77-6," Lukens Steel Company, Coatesville, Pa., 1977.

[12] Kar, R. J., Zackay, V. F., and Parker, E. R., "Department of Energy Annual Report," Sept. 1978; "Low Alloy Steels for Thick Walled Pressure Vessels," Department of Materials Science and Mineral Engineering, University of California, Berkeley, Calif.

[13] Todd, J. A., Zackay, V. F., and Parker, E. R., "Department of Energy Annual Report," Sept. 1978; "Low Alloy Steels for Thick Walled Pressure Vessels," Department of Materials Science and Mineral Engineering, University of California, Berkeley, Calif.

[14] Kinsman, K. R. and Aaronson, H. I., *Symposium on Transportation and Hardenability in Steels*, Climax Molybdenum Company, Mich., 1967, pp. 39-53.

[15] Griffin, R. C. and Emmanuel, G. N., "Welding Research Supplement 9," Welding Research Council, 1961, pp. 393-S-399-S.

[16] Aaronson, H. I., Domian, H. A., and Pound, G. M., *Transactions of the Metallurgical Society*, American Institute of Metallurgical Engineers, Vol. 236, 1966, pp. 768-781.

[17] Aaronson, H. I. and Domian, H. A., *Transactions of the Metallurgical Society*, American Institute of Metallurgical Engineers, Vol. 236, 1966, pp. 781-796.

[18] Shackleton, D. N. and Kelly, P. M., "Physical Properties of Martensite and Bainite," Special Report 93, The Iron and Steel Institute, London, 1965.

[19] Shackleton, D. N. and Kelly, P. M., "Physical Properties of Martensite and Bainite," Special Report 93, The Iron and Steel Institute, London, 1965, p. 132.

[20] Irvine, K. J. and Pickering, F. B., *Journal of the Iron and Steel Institute*, Vol. 194, 1960, pp. 137-157.

[21] Stein, D. F., *Annual Review of Materials Science*, Vol. 7, 1977, pp. 123-153.

[22] McMahon, C. J., Jr., in *Temper Embrittlement in Steel, ASTM STP 407*, American Society for Testing and Materials, 1968, pp. 127-167.

[23] Viswanathan, R. and Joshi, A., *Metallurgical Transactions*, Vol. 6A, 1975, p. 2294.

[24] Low, J. R., Stein, D. F., Turtalo, A. M., and Laforce, R. P., *Transactions of the Metallurgical Society*, American Institute of Metallurgical Engineers, Vol. 242, 1968, pp. 4-24.

[25] Seah, M. P., Spencer, P. J., and Hondros, E. D., *Metal Science*, Vol. 13, No. 5, 1979, pp. 307-314.

[26] Stout, R. D. and Doty, W., *Weldability of Steels*, Welding Research Council, 1971, p. 188.

Fabrication, Welding, and Cladding of Heavy-Gage 2¼Cr-1Mo Steel for Pressure Vessel Applications

J. E. Bonta[1] *and O. G. Sikora*[2]

Fabrication of Heavy-Wall Pressure Vessels

REFERENCE: Bonta, J. E. and Sikora, O. G., **"Fabrication of Heavy-Wall Pressure Vessels,"** *Application of 2¼Cr-1Mo Steel for Thick-Wall Pressure Vessels, ASTM STP 755,* G. S. Sangdahl and M. Semchyshen, Eds., American Society for Testing and Materials, 1982, pp. 255-274.

ABSTRACT: As energy demands steadily increase, industry will require a new generation of pressure vessels to expand the capacities of existing crude oil refineries and to establish synthetic fuels capabilities. These vessels will be a challenge to fabricators. The probable choice of 2¼Cr-1Mo steel will require special attention during fabrication to maintain metallurgical quality. Many of the vessels will be larger than ever; wall thicknesses of 250 to 410 mm (10 to 16 in.) and total weights of 1800 metric tons (2000 tons) and more will be realities. This may necessitate complete field assembly, including welding, nondestructive examination, and postweld heat treatment.

The sizes of the vessel are formidable, but the complexity of the projects is not new and the technology is available. Shop fabrication of components which are then shipped to the site is the typical approach. However, when site location or size of the pressure vessel prohibits transportation, extensive fabrication and complete assembly in the field is required. Lifting equipment can be tailored to the configuration of the vessel and the demands of the project. Heavy plates can be welded with various techniques that ensure good mechanical properties without sacrificing quality. Nondestructive examination (NDE), including radiography, is the same quality available in the shop. Postweld heat treatment (PWHT) can be accomplished in sections, or the entire structure can be insulated and stress relieved in a single operation.

Fabrication of the new generation of large pressure vessels is a natural extension of previous experience in field-assembled structures. The techniques and technology necessary to build quality vessels on schedule exist now.

KEY WORDS: pressure vessels, 2¼Cr-1Mo material, heavy wall thicknesses, field fabrications, preheat, postheat, automatic submerged arc welding, stainless steel overlay, nondestructive examination, machining, erection, postweld heat treatment

A new generation of extremely large pressure vessels will be needed to process synthetic fuels. Pressure vessels with wall thicknesses approximating 380

---

[1] Contracting Engineer, Chicago Bridge & Iron Company, New York, N.Y. 10005.

[2] Area Welding and QA Manager, Corporate Welding Department, Chicago Bridge & Iron Company, Houston, Tex. 77040.

mm (15 in.) and total weights of 1800 metric tons (2000 tons) and more are on designers' drawing boards. Because they will require extensive field fabrication, these vessels pose a formidable challenge to fabricators.

Several recent papers have questioned the adequacy of applying current fabrication techniques in the field to these giant pressure vessels [*1-3*].[3] These papers have issued challenges to industry and to the scientific community to characterize existing materials, to develop new materials, to find faster welding processes without sacrificing mechanical properties, and to improve techniques for nondestructive examination (NDE). Research and development of materials are beyond the scope of this paper, but have been addressed in other papers in this volume. The state of the art of field fabrication and erection indicates that the technology for building quality heavy-wall pressure vessels exists now. In fact, fabricating extremely large pressure vessels in the field is a natural extension of techniques and capabilities already proven in both the petrochemical and the nuclear industries.

Synthetic-Fuels Vessels—Family of Giants

Figure 1 shows an exploded view of a pressure vessel typical of those that will be used for synthetic fuels. The immensity of these vessels is evident when we consider one proposed design:

Diameter = 12.2 m (40 ft)
Tangent length = 38.1 m (125 ft)
Thickness = 318 mm (12.5 in.)
Weight = 3900 metric tons (4250 tons)

While the dimensions and weight cited in this example are impressive, this is not an extreme case. Plates and forgings up to 510 mm (24 in.) thick are commercially available. If the vessel in this example were 410 mm (16 in.) thick, the total weight would be 5150 metric tons (5600 tons)!

Shop versus Field Fabrication

Fabrication Approaches

There are several approaches to fabricating a vessel:

1. A shop built-up vessel (shop BU) is a vessel that is completely fabricated in a shop and shipped to the jobsite as one complete package.
2. A field-erected vessel usually has individual plates or rings, internals, and various components fabricated in the shop and then shipped to the jobsite for erection. The welding, NDE, and postweld heat treatment (PWHT) necessary for the joints are performed in the field.

---

[3] The italic numbers in brackets refer to the list of references appended to this paper.

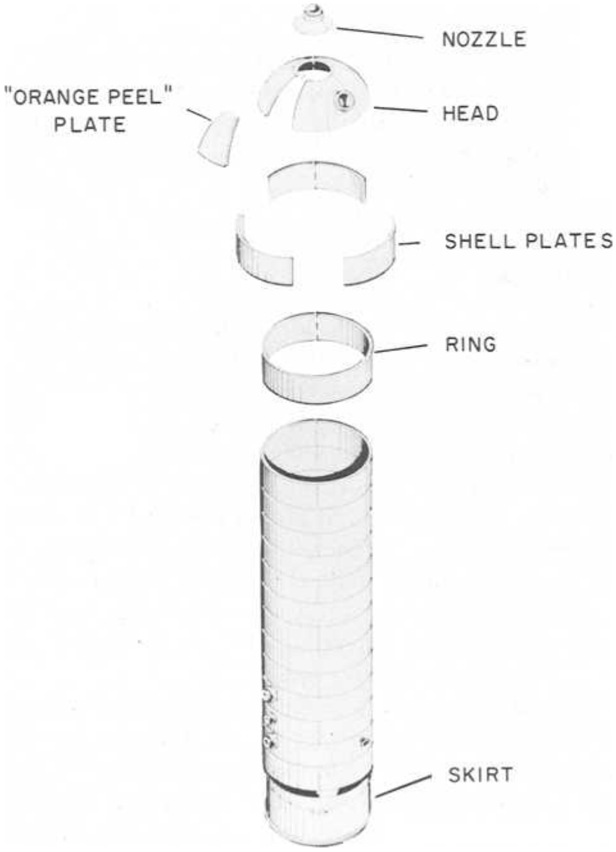

FIG. 1—*Exploded view of typical heavy-wall reactor.*

Size Limitations for Shop BU Vessels

The decision to completely fabricate a vessel in the shop is usually based on size limitations. If navigable waterways exist from the shop to the jobsite, larger vessels can be accommodated than if shipping must be via rail or highway. It should be pointed out that in some cases the size of a vessel may permit barge shipment, but adequate lifting equipment may not be available at the jobsite. A shop BU vessel must be unloaded, transported, and placed in its final position at the site.

Rail shipments are more restrictive than those by barge and are usually limited to overall widths of 4.6 m (15 ft), heights of 6.4 m (21 ft), and weights of approximately 500 metric tons (550 tons). There are length restrictions which vary with the route. Thus a vessel greater than 4 m (13 to 14 ft) in diameter or exceeding 500 metric tons (550 tons) in weight could probably not be completely shop built-up [4].

The magnitude of the synthetic fuels pressure vessels quickly dwarfs these size restrictions and makes field assembly mandatory. But field assembly should not be viewed with pessimism: the technology to build quality vessels to ASME Code requirements is available now and studies have shown field fabrication can be advantageous.

Fabrication Schedules

Comprehensive planning for an entire synthetic fuels plant may be facilitated by field assembly of the pressure vessels. Shop turnover of individual components as opposed to an entire vessel is usually relatively short. Fabrication begins immediately as partially fabricated components are shipped to the site. Shipping time should not be a factor because the field work proceeds as other components are en route to the site. Field fabrication also eliminates the time necessary for shipping and setting a shop BU vessel. Certain construction phases may have to be delayed pending delivery of a large shop BU vessel which requires a special path through the jobsite for clearance. Field assembly, which does not require this site accessibility, can allow construction of the plant to proceed faster [4]. The overall project completion date will not depend on delivery of one vessel.

A 1976 ERDA study of shop assembly versus field assembly of heavy-wall coal gasifier reactor vessels compares overall mechanical plant completion time for a plant with two large field-fabricated pressure vessels and a plant with eleven shop BU vessels. Conservative completion time was 60 months with the field-fabricated vessels and 61 months with the shop BU vessels [5]. This study indicates that construction schedules with field-fabricated vessels are comparable with those for shop BU vessels.

Comparative Costs

The referenced ERDA study conducted an intensive cost comparison of shop assembly versus field assembly of heavy-wall coal gasifier reactor vessels. The project's objectives were to determine and compare costs for a minimal number of field-assembled vessels required for a given plant capacity versus the minimal number of shop-built vessels required for the same capacity. In this case, the minimum number of vessels was two large field-assembled reactors versus eleven smaller shop vessels. This is the only known study to compare capital investments, initial costs, maintenance and operating costs, completion schedules and annual unit production costs. In an effort to take into account the best and the worst conditions, the two cases were considered for two plant locations—one which could utilize barge shipment of large plant components and one limiting all shipments to railway.

The results of the study were conclusive [5]:

> The findings of this study indicate that the utilization of large, field erected gasifiers ... with high unit through-puts will reduce the investment, operating and maintenance costs of coal conversion plants when compared to plants of the same design and total capacity utilizing the largest shop-fabricated gasifiers ... that can be shipped in the United States.

Achievements in Field Erection

The technology of field fabrication is a reality, not a concept. In the past fifteen years, field pressure vessels for nuclear as well as petrochemical applications have been built in full compliance with the ASME Code (Section III for nuclear and Section VIII for petroleum and chemical pressure vessels). Fabricators have successfully field fabricated and assembled numerous large structures. These include:

1. Field-erected full-pressure nuclear containment vessels with diameters up to 46 m (150 ft), heights over 73 m (240 ft), unit weights exceeding 6350 metric tons (7000 tons), and field PWHT of the entire structure.
2. Field-erected heavy-water columns with diameters up to 8.5 m (28 ft), heights in excess of 91 m (300 ft), 1900 metric tons (2080 tons) total unit weight, and field PWHT of the entire structure.
3. Field-erected nuclear reactors with diameters up to 8 m (26 ft), unit weights of 695 metric tons (765 tons), wall thicknesses up to 184 mm (7.25 in.), and field PWHT of the entire structure.
4. Field-erected coal-conversion vessels which involved a fabrication facility in addition to field erection. These vessels had an overall height of 59 m (194 ft), unit weights of 760 metric tons (835 tons) each, and wall thicknesses up to 89 mm (3.5 in.).

The fabrication techniques and processes that were implemented in the construction of these field vessels are the same that will be required to construct the super-large synthetic fuels vessels. These include preheat, welding, NDE, local PWHT, machining, fitting, and final PWHT of the entire structure.

Materials for Synthetic-Fuels Vessels

Materials to be Used

The probable material to be chosen for these pressure vessels is 2¼Cr-1Mo steel (SA 387 Grade 22, SA 336 F22). This steel has been utilized often in petrochemical pressure vessels and has been proven to have good high-temperature tensile strength. The thick-plate material will require quenching and tempering to satisfy the mechanical properties of the ASTM plate specification. Weld metals will match the base metal with a nominal 2¼Cr-1Mo composition. High-alloy weld overlays to protect the low-alloy 2¼Cr-1Mo materials from corrosive environments must be considered. The type and thickness of the overlay will vary depending upon design conditions and exact service of the vessel.

Metallurgical Considerations

These materials—low-alloy base metal, low-alloy weld metal, and high-alloy overlay—are integral parts of a synthetic fuels pressure vessel. There are advantages that necessitate their use, but there are also disadvantages to these materials that require special considerations. Some of these considerations pertain to degradation of various materials properties during extended service at elevated temperatures in a highly pressurized and corrosive environment. Variations in microstructure with thicker sections and accompanying changes in properties may also affect mechanical properties. These properties include fracture toughness characteristics and creep rupture properties. Several research projects to further characterize these properties are in progress.

The materials problems of concern to fabricators are those which may be caused by the fabrication process itself and can be minimized by the fabricator through careful planning and ordering of materials. These problems include lengthy PWHT times required during fabrication, temper embrittlement of the 2¼Cr-1Mo materials, and control of delta-ferrite in austenitic stainless steel weld overlay.

The characteristics of these potential material problems are discussed in detail by Canonico et al [*1*], Scott [*2*], and Dempsey and Tunnell [*3*]. The fabricator can minimize these problems, as summarized below:

1. Lengthy PWHT times necessitated by ASME Code regulations can be reduced by carefully planning construction sequences and providing a vessel with sound weldments prior to final PWHT. This will ensure that any area of the vessel will see minimum final PWHT during fabrication.
2. Temper embrittlement of all 2¼Cr-1Mo plates, forgings, and weld metal can be minimized by ordering all material to chemical specifications which limit the elements that cause temper embrittlement. These elements are phosphorus, silicon, and manganese, and, to a lesser extent, tin, antimony, and arsenic. All materials can also be subjected to special temper embrittlement testing prior to being used in the vessel.
3. An optimum amount of delta-ferrite in the austenitic stainless steel

overlay can be achieved by controlled purchasing of consumables for the overlay and by frequent checking of ferrite levels during production.

Fabrication Precautions

There are several inherent characteristics of 2¼Cr-1Mo material that require special attention during fabrication. These include high hardenability that can result in high heat-affected zone (HAZ) hardnesses, serious susceptibility to hydrogen that can be introduced during welding, and sensitivity to cracking when the material is formed and welded. In addition to compromising the metallurgical integrity of the completed vessel, these problems can cause costly repairs and schedule delays during vessel fabrication. The solution to these problems can be summed up in one word—heat. All joints must be preheated to an adequate temperature prior to welding to minimize the formation of martensite in the HAZ and to minimize hydrogen in the deposited weld. Holding the joint at preheat temperatures (postheat) after the weld is completed allows hydrogen to diffuse out of the weld.

Fabrication of Heavy-Wall Pressure Vessels

Having considered the awesome sizes of the large pressure vessels that will be required for synthetic fuels projects and having discussed the materials problems that must be considered during the manufacture of chromium-molybdenum vessels, it is obvious that field fabrication will be a challenge to fabricators. Figure 2 shows the basic operations in field fabrication of a pressure vessel. Field techniques for preheat, welding, NDE, machining, and PWHT have been developed by transferring knowledge from the shop and adapting it to the rigorous demands of the field. These field capabilities have been proven numerous times on ASME Code pressure vessels. While the heavy thickness of the giant synthetic fuels vessels will require some adaptations of existing equipment, the necessary technology is available. The large field-fabricated pressure vessels can be built with the same quality as shop BU vessels.

Forming

Plate can be formed in existing shop presses and then shipped to the field. Thus it will not be necessary to install costly forming facilities in the field. Shop presses have a capacity of 11 000 metric tons (12 000 tons), which will permit forming plates as thick as 400 mm (16 in.). Shell rings up to 3.9 to 4.3 m (13 to 14 ft) can be fabricated in the shop and shipped to the field. Rings with a greater diameter will be fabricated in the field from components

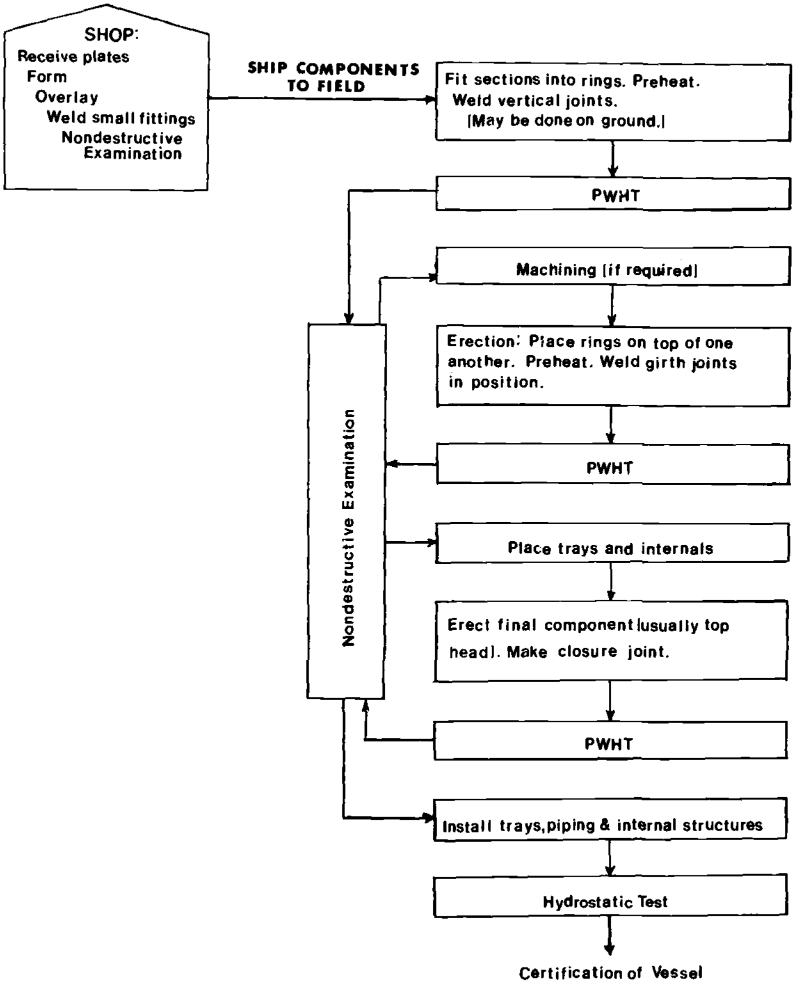

FIG. 2—*Field fabrication of heavy-wall pressure vessels.*

formed in the shop. Components formed in the shop will be trial-fit before shipping to the field. This will alleviate fit-up problems at the site.

Preheat and Postheat

As previously discussed, sound metallurgical reasons require preheating and postheating all 2¼Cr-1Mo welds. In the case of a 9-m (30-ft)-diameter vessel, it could be necessary to maintain preheat on seven or eight vertical joints at one time or on nearly 30 m (100 ft) of girth joint until PWHT can be performed. This must be done in a manner that minimizes fuel consumption while maximizing welder comfort.

Welding Processes

The methods available to weld heavy-wall pressure vessels in the field are subjects of vital concern to those planning synthetic fuels projects. Vessel completion—therefore project completion—can progress only as smoothly and rapidly as the welding can be performed. In addition to the obvious need to produce welds with minimal repairs, there is a demand for automated procedures that can improve welding. The large wall thicknesses create joints requiring huge volumes of weld metal. This volume alone makes the conventional field welding process, shielded metal arc welding (SMA), costly and time consuming. It has been estimated that on one proposed vessel, welding of one girth joint would require 4000 man-hours (mh) or 2 man-years [*3*]. This was estimated on a basis of 80 man-hours per foot of completed weld. Most fabricators will agree that this is a conservative estimate.

In comparing welding processes for heavy-wall fabrication, Weber et al [6] have calculated a joint completion rate (JCR) based on volume of the joint, density of the weld metal, deposition rate, and arc time. The differences in these completion rates can be startling—from 17.7 mh/m (5.4 mh/ft) for a submerged arc vertical joint to 0.49 mh/m (0.148 mh/ft) for an electron beam vertical joint. A JCR may provide an adequate comparison for actual welding times, but it does not take into account the total fabrication time for a joint welded with a given process. For example, the actual welding time for the electron beam process is practically negligible when compared with the time spent on machining and setting up the precision joint. It should be considered that a JCR will vary greatly among fabricators due to different construction sequences and techniques.

Shielded metal arc welding will always be a vital tool used in conjunction with other processes. Recent work indicates automatic submerged arc welding in final position of both vertical and girth joints can be successfully accomplished in the field.

Before discussing various processes for welding thick sections, it must be emphasized that quality welding can only be achieved with proper training and equipment before any welding commences. In the field, all welds must be protected from unfavorable weather conditions, particularly wind and moisture. This can be done with temporary covering or with portable shelters. These shelters will facilitate preheating of the joint, maintaining the preheat until the weld can be heat treated, and could function as a furnace for PWHT. Because one setup can be maintained from preheat through PWHT of the weld, both efficiency and quality can be maximized.

Submerged Arc Welds

Submerged arc welding (SAW) is a high-deposition rate process (in comparison with SMA welding). Because the weld is deposited in multiple passes, the weld metal and the HAZ receive the benefit of grain refinement as subsequent passes are deposited. Good physical properties are attained in 2¼Cr-1Mo submerged arc welds in the PWHT condition (austenitizing heat treatments are not required).

To build a large pressure vessel in the field, vertical welds must be made to join formed plates into shell rings. Horizontal girth welds are made to join the shell rings after they are placed on top of one another. In the shop, the girth joints are made in the downflat position through the use of large positioners and turning rolls. In the field, the girth joints must be welded in position. Until recently, SMA welding has been the only field process for welding vessels of appreciable thickness. Techniques are now available to allow automatic SAW of both vertical and horizontal joints in the field. The submerged arc techniques described next are designed for field application.

Vertical Submerged Arc Welds—The technique of welding thick plates in the vertical position with the submerged arc process was introduced ten years ago by a fabricator of nuclear reactors [7]. Figure 3 is a schematic diagram depicting this "sub-vert" procedure. The plates require a square edge instead of a conventional weld bevel. This edge preparation is less expensive to fabricate and provides a weld joint with 50 to 70 percent less volume than a standard joint detail for SMA welding. The weld metal is deposited in a flatdown position through the thickness of the plate. The numerous layers give a desirable metallurgical structure. The HAZ is small and benefits from grain refinement by subsequent passes. By decreasing volume and welding with a more efficient process, substantial savings over SMA welding can be realized. The vertical welds can be made on the ground and then the completed ring can be erected, or the vertical welds can be made with the ring in final position.

Horizontal Submerged Arc Welds—After the rings are erected, they would be joined with an automatic SAW technique that operates in the horizontal

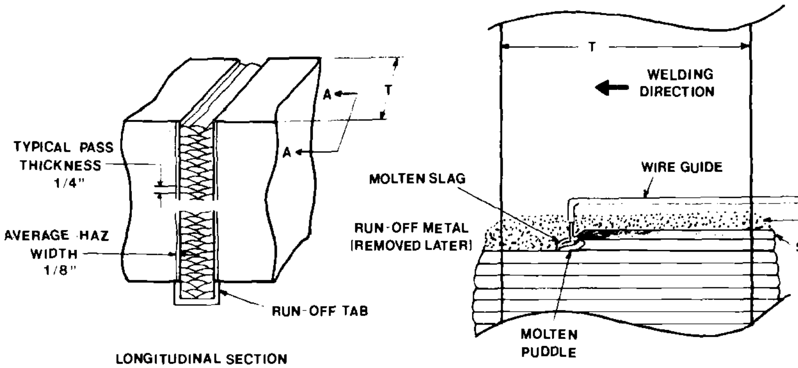

LONGITUDINAL SECTION SHOWING BEAD SEQUENCE

SECT. AA: VIEW THRU SHELL THICKNESS SHOWS WELDING PROGRESSION

FIG. 3—*Sub-vert welding of longitudinal joint.*

position. Horizontal SAW equipment has been used for years in field fabrication of storage tanks and pressure vessels. Maximum wall thicknesses for storage tanks have been 45 mm (1.75 in.) and for pressure vessels 90 mm (3.5 in.). As wall thicknesses increase, the volume of a horizontal manual weld with a conventional joint design becomes prohibitive. The depth of the joint impedes proper flux coverage at the back of the joint. These problems have been solved. Equipment has been developed for horizontal submerged arc welds in plates up to 410 mm (16 in.) thick. By utilizing a "double-V" joint, the working thickness of the weld is decreased to one half the total thickness of the plate. Both sides can be welded at once, minimizing distortion and improving completion time by as much as 50 percent. Figure 4 illustrates horizontal SAW of a heavy-wall joint of 2¼Cr-1Mo material.

The mechanical properties of welds with this setup are good. As with any out-of-position welding, small passes must be deposited to keep the molten weld metal from succumbing to the force of gravity. Small passes usually result in good physical properties, particularly notch toughness characteristics. When proper techniques are used, welds made with the horizontal SAW process have been proven to have low repair rates.

Stainless Steel Overlay

A variety of welding processes will be employed to overlay the internal surfaces of large pressure vessels. Inside surfaces of heads and shell rings re-

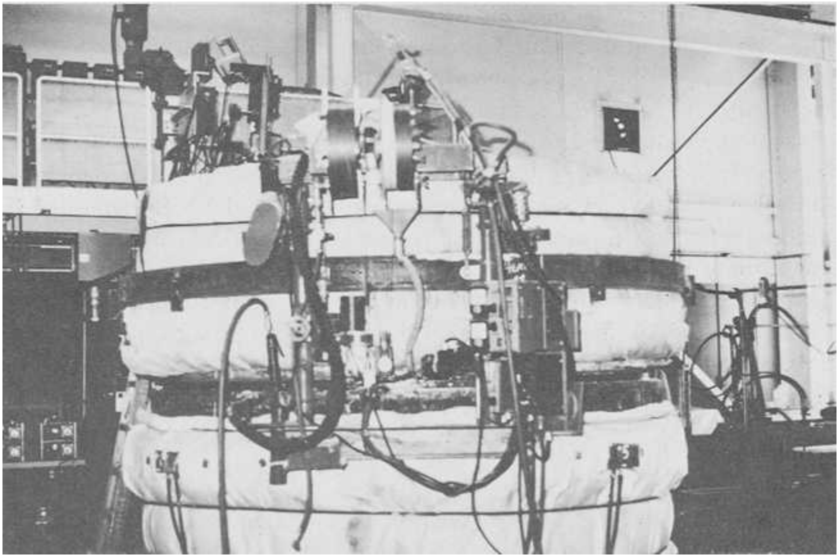

FIG. 4—*Horizontal submerged arc welding.*

quire a high-deposition welding process. Attachments such as nozzles and forgings are often out-of-position or too small to be efficiently automated, so shielded metal arc welding is usually the best method. Some nozzles and forgings have a small diameter and long neck and cannot be reached with an electrode. For these pieces, an automatic gas metal arc system can be devised to overlay the inside surfaces.

The alloy type for the overlay is usually decided by the user of the vessel. The alloy is chosen to withstand the corrosive environment and the operating conditions. Electrode suppliers have developed a complete range of electrodes, wires, and fluxes for most of the austenitic stainless steel alloys.

By far the largest area of overlay will be deposited on the heads and shell rings. There are several high-deposition techniques to accomplish this, but all require welding in the downflat position. In the shop, these large components are placed on turning rolls and positioners. The part moves while the welding head remains stationary. The overlay can then be deposited with a series arc, submerged arc, or strip process. The series arc and submerged arc processes have been the established overlay procedures until the development of strip overlay in the past few years. The strip overlay has better deposition rates than the other two methods, but consumables (metal strip and flux) are expensive.

Several factors are vital to a successful weld overlay operation. The overlay must be continuously bonded to the backing steel. The chemical composition of the overlay must meet the requirements of the specified alloy after dilution with the base metal. Austenitic stainless steel overlay must have an optimum amount of delta-ferrite. Too little delta-ferrite will cause microfissuring in the overlay. Excessive amounts of delta-ferrite can result in ductility loss in the overlay due to increased transformation of delta-ferrite to the brittle sigma phase during PWHT or service at high temperatures.

Usually, the best overlay process is the one the fabricator has proven to be structurally sound and to have optimum metallurgical properties. To facilitate field fabrication of large pressure vessels, the large components will probably be weld overlayed in the shop with one of the high deposition rate techniques. These processes can be performed in the field; however, the need for turning rolls, positioners, and suitable foundations would reduce their cost effectiveness. After being overlayed, the components will then be shipped to the jobsite. Field joints will be overlayed in position by a suitable process, probably shielded metal arc.

Other Welding Processes

There are two welding processes in the developmental stage that may affect fabrication techniques of heavy-wall pressure vessels in the future. These are the narrow-gap gas metal arc process (narrow gap MIG) and the electron beam (EB) process. The narrow-gap MIG process combines the advantages of automation with a narrow weld groove. Welding labor and the cost of weld consumables can be reduced. The process has good out-of-position capabilities, but is dependent on precise operator controls and tight fabrication tolerances. Due to the fast rate at which the welding proceeds, even slight deviations can result in sizeable errors. Narrow-gap MIG has seen shop application by some fabricators, but field application seems questionable at this time.

The most promising process of the future may be electron beam welding. By directly joining plates fit flush together, EB welding eliminates the need for weld consumables. The weld metal has essentially the same properties as the base metal. Other advantages of EB welding are that preheat is not necessary, heat-affected zones are small (relative to other welding processes), and PWHT may not be necessary. At least one manufacturer of electron beam equipment has published satisfactory data on EB welds in 2¼Cr-1Mo material up to 60 mm (2.4 in.) thick [*8*].

The welding time for an EB weld is very low in comparison with other processes. The reduced fabrication time, coupled with the savings in weld consumables, make EB welding a very attractive method for fabricating heavy wall vessels. These advantages are somewhat offset by the fact that setting up an EB process is expensive and all components must be machined to precise tolerances. Machining and fitting require additional fabrication cost and time which must be considered in the overall evaluation of the process.

Techniques for EB welding of thicker sections are now being developed. In addition to private work by suppliers and fabricators, a Department of Energy (DOE) sponsored study on EB welding is in progress [*6*]. The recent development of portable vacuum chambers makes field application of EB welding feasible.

Narrow-gap MIG and electron beam welding, when properly developed, will greatly facilitate fabrication of heavy-wall vessels. The processes must undergo a development period in the shop before they can be used in the field. Fabricators are still a few years away from using either of these processes in the field.

Electroslag

Electroslag welding is basically a shop procedure because of the heat treatment and quenching facilities required. A large number of shop BU vessels have utilized this process. This single pass, high heat input process produces quality welds with high-deposition rates, but the large grain size in both the weld metal and the HAZ results in unacceptable mechanical properties. It is Code-required to austenize, accelerate cool (that is, water quench), and temper electroslag welds to refine these large grains. On large projects where many vessels are to be field fabricated, it might be advantageous to install the necessary facilities at the job site. For projects now being planned, though, vertical joints will probably be welded with the submerged arc process.

Nondestructive Examination

The fabricator must build quality into a vessel from the forming of the first plate until the last weld is checked for defects. Nondestructive examination (NDE) is an essential tool for assuring all components of the vessel—plates and forgings as well as welds—do not contain any defects that exceed the limits specified by the ASME Code or by customer specifications.

There are several methods of NDE; these are summarized in Table 1. Except for visual examination, the ASME Code specifies the procedures for these methods. All NDE except radiography can be performed at preheat and welding temperatures as well as ambient temperatures.

The three techniques that are used to find surface and near-surface defects—visual, dye penetrant, and magnetic particle examination—can be performed in the field as well as in the shop with virtually the same procedures. The techniques that are used to find defects throughout the thickness of the material are ultrasonic and radiographic examination. Radiographic examination requires special considerations for application in the field.

The success of NDE depends on using the correct techniques and procedures for each type of examination and in using the different NDE methods to complement each other. It is also essential to maintain a staff of well-trained people who are familiar with all aspects of NDE. Fabrication sequences must be well planned so that accessibility for in-place examination is maintained from the first to the final examination.

Ultrasonic Examination

The equipment to perform ultrasonic examination (UT) in the field is essentially the same as that used in the shop, but special techniques may be required to examine the thicknesses of the synthetic fuels vessels. Ultrasonic

TABLE 1—*Methods of nondestructive examination.*

Method	Application
Visual	surface defects
Liquid penetrant	surface defects
Magnetic particle	surface and near-surface defects
Radiography	through-thickness defects
Ultrasonic	through-thickness defects

examination of pressure vessels has been perfected in the shop. Ultrasound can be introduced into the metal as either longitudinal or shear waves to detect echo signals from imperfections that are oriented parallel or at an angle to the surface of the plate. As plates and welds become thicker, a new calibration block for every 50 mm (2 in.) of additional thickness must be used to establish the examination procedures. Lack of bonding between dissimilar metals, which may occur with stainless steel overlay, can be found with the proper technique.

Radiographic Examination

Radiographic examination (RT), in the shop or in the field, requires many precautions because of the hazard radiation poses to personnel. Thick plates can only be penetrated by high-energy sources such as a linear accelerator. The high-energy source and the extensive X-rays emitted require more protective shielding. Shops equipped with linear accelerators have permanent X-ray buildings with thick concrete walls and sometimes earthen reinforcement to contain the X-rays. Field RT has been limited to thicknesses that can be examined by lesser sources such as X-ray machines or radioactive isotopes. Reliable portable linear accelerators are commercially available, and operating licenses can be obtained from the states where the equipment would be used.

The portable linear accelerators (Linacs) penetrate steel from 76 to 550 mm (3 to 22 in.) thick to Code requirements. Manufacturers can furnish an overhead bridge crane for support and maneuvering the X-ray head.

At least one state has responded favorably to an inquiry about licensing a field linear accelerator. As long as all Federal and State regulations are upheld, an operating license can be obtained.

Proper shielding to protect jobsite personnel and surrounding areas requires extensive planning, but it can be accomplished. One approach is to provide a shelter for examining joints welded on the ground (vertical seams, nozzles). A larger shelter can be built to encompass a portion or all of the vessel, which allows radiography in place. This concept is shown in Fig. 5. In addition to adequate shielding, field RT with a linear accelerator will be scheduled during night or off shifts to minimize the chance of personnel exposure. The first priority of radiography work is safety.

Machining

Field erection of nuclear reactors and containment vessels necessitated the development of sophisticated machining capabilities that can be performed in the field. The cover of a containment vessel was field fabricated in 1966, in which the plate flanges were welded, PWHT, and field machined to contract requirements. Figure 6 depicts a setup for field machining. If required, past

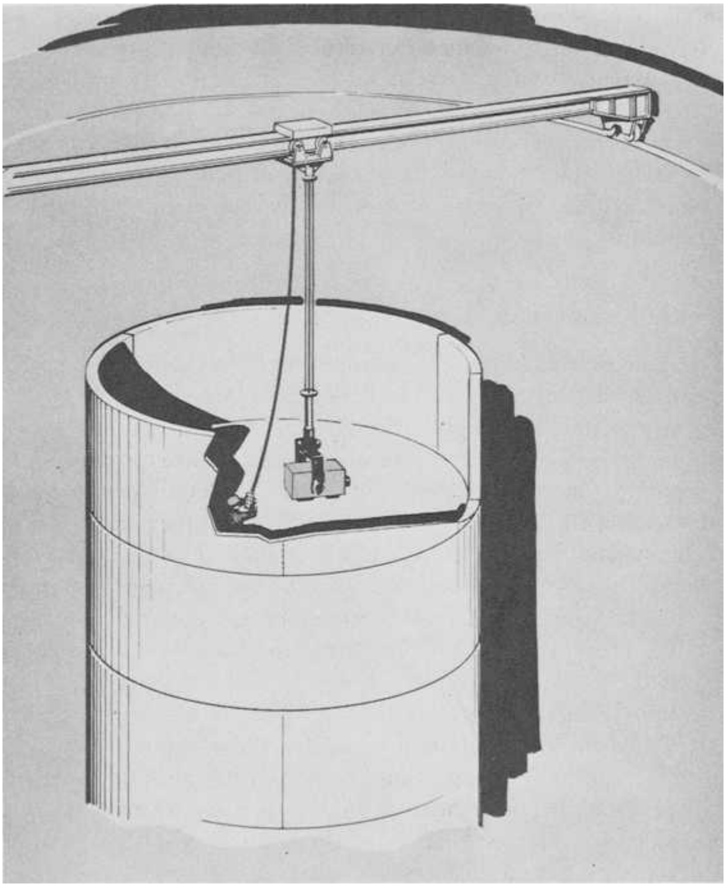

FIG. 5—*Radiographic examination "in the air".*

experience indicates extensive machining can be readily accommodated in the field.

Erection

After shell rings are fabricated on the ground, they will be lifted into place and the horizontal girth joints made. Other typical lifts will include internal fittings. The last major lift will be the top head, which closes the vessel. A typical field lift is seen in Fig. 7. In this photo, a 43-m (140-ft)-diameter ring weighing approximately 109 metric tons (120 tons) is lifted into place on a nuclear containment vessel. The Ringer Crane which is being used to make the lift is a commercially available piece of equipment which has been

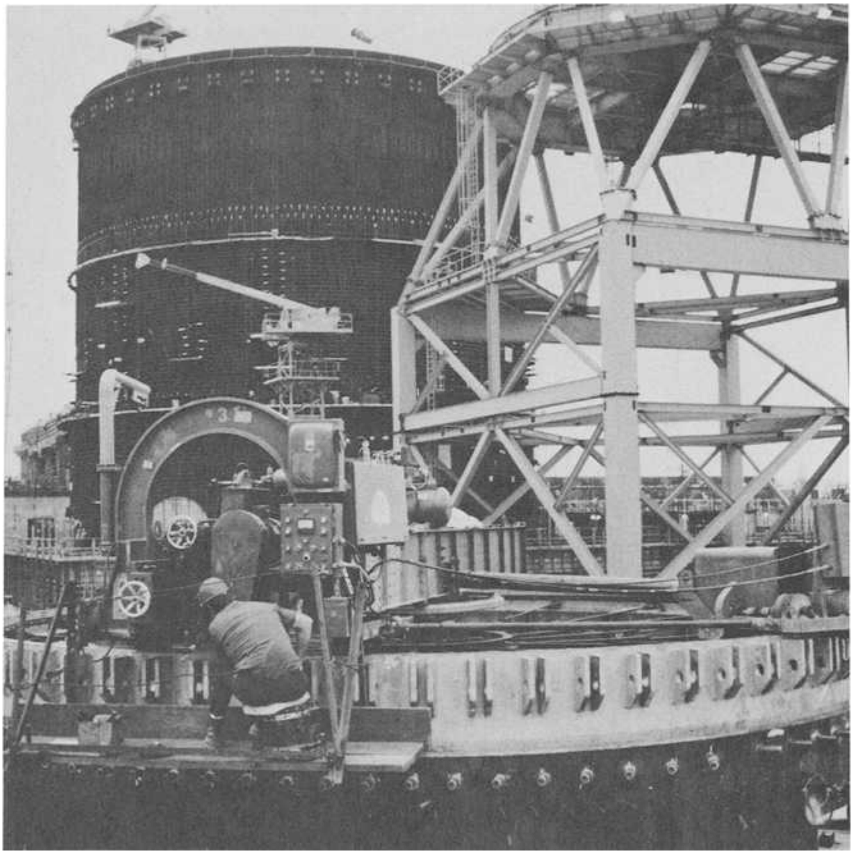

FIG. 6—*Field machining equipment used for preparing flange surfaces of large opening in field-erected structure.*

mounted on a tower to accommodate the height of the vessel. The lift being made here requires only about 20 percent of the capacity of the Ringer.

The size of a lift is usually a matter of economics. With the proper planning, maximum capacity lifts can be made to benefit schedule and costs. When field fabricating pressure vessels, the vessel can be built horizontally and lifted into place in one piece, or the vessel can be erected in position utilizing multiple lift techniques. The latter approach is usually the most economic.

Shop fabricators now have the equipment to make lifts up to 910 metric tons (1000 tons). Rigging companies advertise capabilities of 1800 metric tons (2000 tons). A competent fabricator will be able to meet any erection demands made by the synthetic fuels vessels.

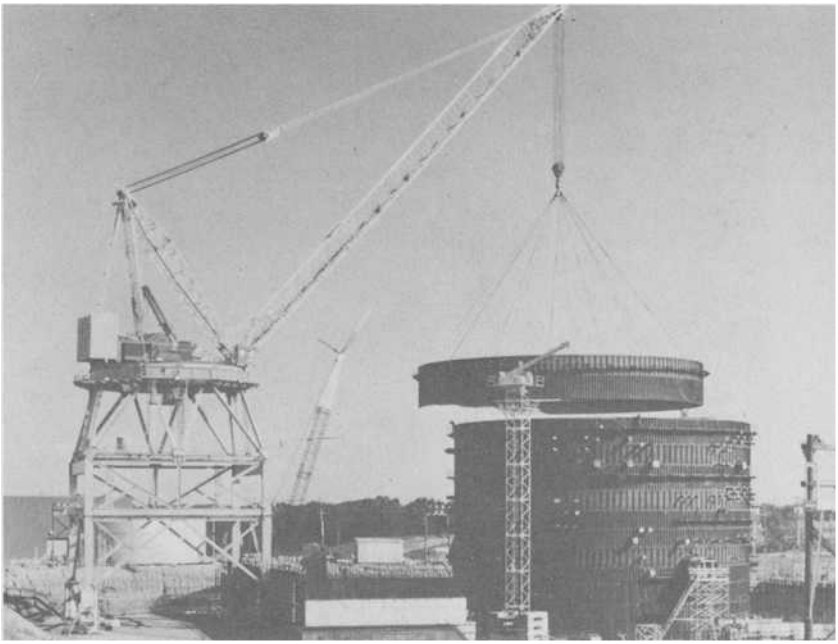

FIG. 7—*Ringer crane setting 110-metric-ton (120-ton) ring in place.*

Postweld Heat Treatment

As explained earlier, the 2¼Cr-1Mo material will receive intermediate PWHT during fabrication as well as a final, Code-required PWHT. Fabrication of these pressure vessels will require welding of several joints simultaneously. This is particularly true if more than one vessel is being fabricated.

PWHT on one joint or an area of a vessel can be accomplished in several ways. If the component is not in position on the vessel, PWHT of the weldment can be accomplished in a PWHT furnace. This same furnace could have served as a shelter during preheat and welding. If the component is in place, the joint can be insulated and given a local PWHT or a portable PWHT furnace can be built around the joint. The PWHT setup must include a sufficient number of reliable thermocouples and recording equipment so that the piece is adequately monitored. The area to be given the PWHT, as well as the surrounding metal, must be analyzed for thermal gradients. Improper heating of sections of a vessel can create undesirably high stresses in adjacent areas of the vessel.

Final PWHT can be accomplished in sections (local PWHT) as the vessel is fabricated. In some cases, the entire structure may be PWHT at one time. This minimizes the amount of PWHT time any one area of the vessel receives.

Figure 8 shows a nuclear containment vessel being insulated for final PWHT. The vessel when insulated becomes its own furnace. Luminous flame burners are placed at strategic openings in the vessel. Other openings for nozzles and flanges are closed off except for the outlet. The fabricator must perform detailed stress analysis which requires knowledge of the properties of the materials at PWHT temperatures to ensure that the structure is self-supporting throughout the heat treating cycle.

Field PWHT of large structures to Code requirements has been proven many times. Recently, the largest known single structure in the world was

FIG. 8—*Nuclear containment vessel being insulated for PWHT.*

successfully PWHT in one operation. This nuclear containment vessel had a maximum wall thickness of 115 mm (4.5 in.), a diameter of 46 m (150 ft), and a height of approximately 67 m (220 ft). The total weight was about 5450 metric tons (6000 tons). This vessel was fabricated from a carbon-manganese steel, so the final PWHT temperature was lower than that the Code requires for 2¼Cr-1Mo material. However, field PWHT experience with 2¼Cr-1Mo material has shown that attaining and holding the necessary temperature can be accomplished.

Conclusion

The intention of this paper has been to provide a state-of-the-art view of field fabrication of the super-large pressure vessels that will be an integral part of synthetic fuels system. A few large pressure vessels have been shown to have economic as well as scheduling advantages over several smaller, shop BU vessels. These vessels will probably be fabricated from 2¼Cr-1Mo materials. In order to appreciate the challenge these pressure vessels will be to fabricators, one must recognize the technical problems inherent in the 2¼Cr-1Mo material. While structures with wall thicknesses as great as 410 mm (16 in.) have not been fabricated in the field to date, the technology to accomplish this is currently available. Present research and development programs may reduce the initial cost of these vessels. However, current techniques—including welding, NDE, machining, erection, and PWHT—can be utilized in the field to build pressure vessels to Code requirements. These field-fabricated vessels will be supplied to the same high-quality standards as shop-fabricated vessels.

References

[*1*] Canonico, D. A. et al, "Assessment of Materials Technology for Gasifier and Reaction Pressure Vessels and Piping for Second Generation Commercial Coal Conversion Systems," Oak Ridge National Laboratories, OPNL-5238, 1979.

[*2*] Scott, T. E., *Materials for Coal Liquefaction*, Iowa State University, Ames, Iowa, 1979.

[*3*] Dempsey, P. E. and Tunnell, Gerald, "The Challenges of Gigantic Pressure Vessels," presentation to American Welding Society at Colorado School of Mines, 27 April 1979.

[*4*] Hicklen, W. L., "The Construction of Coal Conversion Vessels," presented at the Clean Fuels from Coal Conference, 23-27 June 1975.

[*5*] "Cost Study, Shop Assembly vs. Field Assembly of Heavy Wall Coal Gasifier Reactor Vessels," Final Report, FE-2009-13, Chicago Bridge & Iron Company, Dec. 1976.

[*6*] Weber, C. M. et al, "Factors Influencing the Welding of Coal Gasification Vessels—Report of Some Recent Developments," presented to Materials Developments for the Coal Conversion Industry Symposium, National Association of Corrosion Engineers, Atlanta, 12-16 March 1979.

[*7*] Bunn, W. B. and Berger, C. F., "Reactor Welding with Bead Axis Perpendicular to Joint Axis," *Welding Journal*, March 1970.

[*8*] Steigerwald Strahltechnik, private communication.

O. V. Serrano,[1] *G. R. Edwards,*[2] *and R. H. Frost*[2]

A Comparison of As-Welded and Stress-Relieved 2¼Cr-1Mo Steel Electroslag Weldments: Microstructure and Properties

---

REFERENCE: Serrano, O. V., Edwards, G. R., and Frost, R. H., "**A Comparison of As-Welded and Stress-Relieved 2¼Cr-1Mo Steel Electroslag Weldments: Microstructure and Properties,**" *Application of 2¼Cr-1Mo Steel for Thick-Wall Pressure Vessels, ASTM STP 755,* G. S. Sangdahl and M. Semchyshen, Eds., American Society for Testing and Materials, 1982, pp. 275–296.

ABSTRACT: Electroslag weldments of 102-mm (4-in.)-thick annealed 2¼Cr-1Mo steel have been microstructurally and mechanically evaluated in the following conditions: as-welded, stress relieved at 690°C, and stress relieved at 760°C. The fusion zones and heat-affected zones were significantly toughened by postweld heat treatment, a result attributed to changes in the carbide composition and morphology caused by tempering.

KEY WORDS: electroslag welding, chromium-molybdenum steel, microstructure

Background and Scope

Electroslag welding is a very high deposition rate welding process for joining heavy-steel sections. This method has been used to join various structures such as pressure vessels, ship hulls, and structural bridge tension members. The current criticism of electroslag welding is that to obtain satisfactory properties, the weldments must be reaustenitized after welding [*1-6*].[3] Numerous attempts have been made to improve the properties of electroslag weldments without resorting to reheat treatment. Khakimov et al [*7*] employed forced cooling and powder filler metal additions to improve the toughness of electroslag welds in 10G2FR steel. Makara et al [*8*] used inter-

---

[1] Politechnica del Litoral, Gauyaquil, Ecuador.

[2] Professor, Department of Metallurgical Engineering, Colorado School of Mines, Golden, Colo. 80401.

[3] The italic numbers in brackets refer to the list of references appended to this paper.

critical anneals on 09G2S and 16GS steels to improve impact strength, as did Malinovska and Hrivnak on 13123 and 13030M boiler steels [*9*]. Makara et al [*10,11*] later employed various filler metal additions to improve properties of the chromium-molybdenum steels 20Kh2Ma and 12KhM. In the latter studies, it was demonstrated that filler metal chromium contents greater than 1.8 percent, with 0.1 to 0.2 percent zirconium or 0.24 percent titanium, significantly improved toughness of the weld metal.

There have been previous research efforts to improve the properties of electroslag welds in 2¼Cr-1Mo steel. For example, Okurmura et al [*12*] have reported good fusion zone toughness in 2¼Cr-1Mo electroslag weldments joined with a modified filler wire. These investigators also studied the influence of postweld heat treatment on the properties of the weldments. It was reported that weld metal compositions of 0.85 percent manganese and 0.02 percent vanadium showed hot tensile strengths over 441 MPa (64 ksi) at 435°C and Charpy V-notch (CVN) impact energies over 98 J (72 ft · lb) at 0°C when quenched at a cooling rate of 134°C/min (274°F/min) and then stress relieved under conditions corresponding to a temper parameter (TP) of 19.9 to 20.7 K. The toughness and strength were still satisfactory when the cooling rate was reduced to −8.9°C/min (16°F/min). A rapid cooling rate after stress relieving increased the toughness of the weld metal.

The purpose of this investigation was to apply commercial electroslag welding techniques to the joining of thick-section 2¼Cr-1Mo steel, and then to thoroughly characterize the weldment with respect to microstructure and CVN toughness. A major emphasis was to compare the microstructure and mechanical properties in as-welded specimens with those of postweld stress-relieved specimens. The aim of this study was to evaluate the potential of developing a suitable electroslag welding technique for thick-section 2¼Cr-1Mo steel which did not require a reaustenitizing postweld heat treatment.

Microstructure and Thermal History

More comprehensive discussions of the transformations in 2¼Cr-1Mo steel can be found in other papers in this volume. However, because thick-section electroslag weldments experience a complex thermal history and consequently develop complex microstructures, a brief summary of microstructures and thermal history will help to orient the reader.

Austenitizing of 2¼Cr-1Mo steel occurs at about 927°C and above. Slow cooling produces the annealed structure, consisting of equiaxed proeutectoid ferrite with typically about 20 percent upper bainite. The upper bainite in this structure often has a lamellar appearance similar to pearlite. A cooling rate on the order of 300°C/h (similar to normalizing) creates a microstructure with a ratio of proeutectoid ferrite to bainite of about 55:45 [*13*]. The resulting bainite has a lath-like morphology with cementite distributed at the ferrite lath boundaries. In addition, a small amount of acicular Mo_2C is present in the normalized structure as fringes on the ferrite side of the ferrite-bainite boundaries.

Quenching 2¼Cr-1Mo steel yields a microstructure which is predominately bainite, with the carbide precipitates in a Widmanstatten array. It is difficult to form any martensite in 2¼Cr-1Mo steel just as it is difficult to form pearlite. The structure of 2¼Cr-1Mo steel, therefore, is typically a combination of proeutectoid ferrite and bainite, with the relative amounts of each being dependent on the rate of cooling from the austenitizing temperature.

The sequence of carbide formation during tempering, as discussed by Baker and Nutting [*13*], is shown diagrammatically in Fig. 1 for both the quenched and normalized conditions. For the quenched steel, tempering for short times at 500°C resulted in the precipitation of large lenticular carbides, especially at the ferrite lath boundaries. On further tempering, the carbide precipitate thickened, accompanied by an increase in the amount of cementite. Long tempering times at 500°C (1000 h) produced a well-dispersed and fine Mo_2C precipitate within the ferrite, accompanied by a decrease in the amount of cementite.

For the normalized steel, an early local precipitation of Mo_2C in the ferrite occurred, and this phase persisted. Tempering at 400°C produced no change in the ferrite regions, but the bainite carbides gradually thickened. At 500°C, the bainitic carbides became thicker, and fringes of Mo_2C were detected at the ferrite/bainite boundaries. Tempering at 600°C resulted in a marked spheroidization of the bainitic carbides. At 650°C, the cementite spheroidized and the Mo_2C precipitated more rapidly.

The remainder of the carbide precipitation reactions resulting from tempering were found by Baker and Nutting [*13*] to be similar for both the quenched and normalized conditions. Fe_3C, Cr_7C_3, $M_{23}C_6$, and M_6C were formed by nucleation at carbide particles already present. Cr_7C_3 formed by nucleation either within the cementite particles or at the ferrite/cementite interfaces. M_6C nucleated at cementite boundaries where Cr_7C_3 was not already present. M_6C grew at the expense of both cementite and Mo_2C, thus reducing the number of particles. It was suggested that all carbides eventually form M_6C.

In summary, the difference between the as-quenched and normalized conditions is primarily a difference in the precipitation of Mo_2C. Although most of the carbides formed during tempering tend to nucleate on previous carbides within the structure, Mo_2C forms by separate nucleation within the ferrite matrix. In quenched 2¼Cr-1Mo steel, this nucleation occurs within the ferrite portion of the bainite, whereas in normalized 2¼Cr-1Mo steel the Mo_2C precipitates on the ferrite side of proeutectoid ferrite-bainite boundaries.

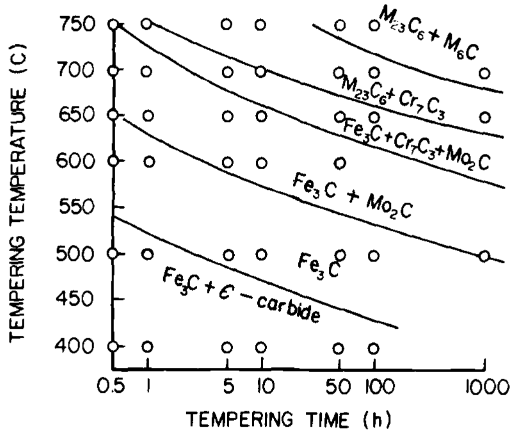

QUENCHED

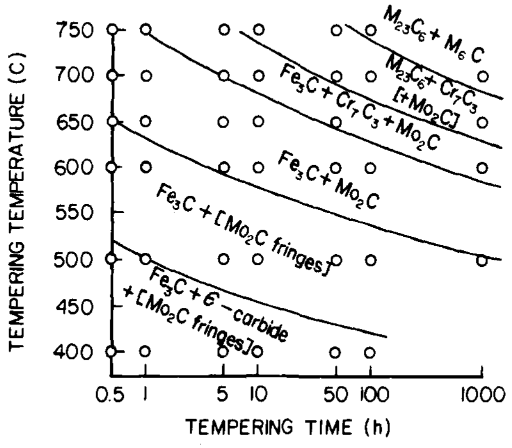

NORMALIZED

FIG. 1—*Carbide stability diagram for 2¼Cr-1Mo steel in both the quenched and normalized conditions, as determined by Baker and Nutting* [13].

Experimental Procedure

The base metal for this investigation was 102-mm (4-in.)-thick 2¼Cr-1Mo steel seamless pipe in the annealed condition [ASTM Specification for Seamless Ferritic Alloy-Steel Pipe for High-Temperature Service (A 335-80), P22]. Annealed steel would not be used to fabricate an actual pressure vessel, of course. Current technology typically requires a quench and temper heat treatment [ASTM Specification for Pressure Vessel Plates, Alloy Steel, Chromium-Molybdenum (A 387-79b)] for 2¼Cr-1Mo steel to ensure adequate base metal toughness. However, this initial electroslag welding study concentrated primarily on the characteristics of the fusion zone (FZ), and properties of the fusion zone after welding are not sensitive to the prior condition of the base metal (BM). Although characteristics of the heat-affected zone (HAZ) are reported in this study for the sake of completeness, the reader is reminded that a truly adequate evaluation of the effect of electroslag welding on the HAZ will require the use of clean base plate in the quenched and tempered condition.

Steel sections 178 mm wide by 229 mm high were oxyacetylene flame cut, and then a starting tab and two 38-mm-thick lateral hot shoes (also 2¼Cr-1Mo steel) were welded to the plates to bound a 102 by 229 by 28.6 mm weldment cavity. Welding was performed with a Hobart Porta-Slag unit. The welding parameters are given in Table 1, and the welding consumables are listed in Table 2. The thermal history of the welding process was recorded by an embedded array of Type K thermocouples, and then transposed to a typical continuous cooling diagram [*14*] as illustrated in Figs. 2 and 3. Cooling rates to a temperature of 543°C are shown in Table 3.

For this investigation, two different stress-relief heat treatments in accordance with ANSI Code B-31-1 were performed. The weldments were held at 690 and 760°C for 177 s/mm (1.25 h/in.) and 142 s/mm (1 h/in.), respectively, and then air cooled. The corresponding temper parameters for these

TABLE 1—*Welding parameters.*

Voltage, V	48
Current, A	750
Wire speed, mm/s	167

TABLE 2—*Welding consumables.*

Arcos Chromenar 521U Filler Wire
Size: 2.38 mm (3/32 in.)

Composition							
C	Mn	P	S	Si	Cr	Mo	Cu
0.11	0.64	0.007	0.014	0.15	2.48	0.95	0.11

Hobart Guide (#48)

Fluxes
Hobart PF-203 (starting)
Hobart PF-201 (running)

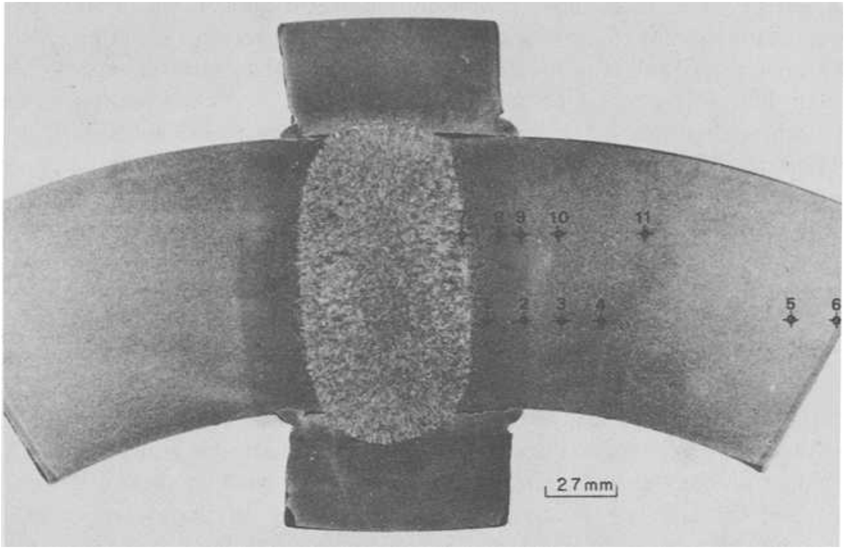

FIG. 2—*Macro-etched specimen of an electroslag weldment in 102-mm (4-in.)-thick 2¼Cr-1Mo steel. This weldment was postweld stress relieved at 760°C. Both the thermocouple placements and the macroscopic grain structure are illustrated.*

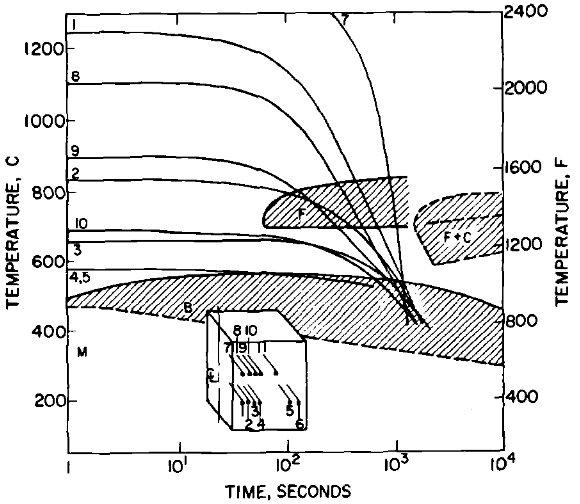

FIG. 3—*Cooling rates observed at the thermocouple positions shown in Fig. 2 relative to a typical continuous cooling diagram for 2¼Cr-1Mo steel* [14].

TABLE 3—*Cooling rates recorded by thermocouples—as-welded condition.*

Thermocouple No.	Peak Temperature, °C	Time to 543°C, s	Cooling Rate, °C/s
1	1271	1256	0.58
2	832	1049	0.28
3	660	850	0.14
4	577	502	0.03
5	577	384	0.09
6	<543	...	...
7	>1370	1034	0.80[a]
8	1104	990	0.57
9	899	842	0.42
10	693	709	0.21
11	<543	...	...

[a] Cooling rate calculated with 1370°C as peak temperature.

postweld heat treatments were 19.9 and 21.32 K, respectively. Weldments were analyzed using optical microscopy, hardness profiles, Charpy impact testing, and scanning electron microscopy. Standard Charpy V-notch specimens, spaced approximately at 6.4-mm (¼-in.) intervals across the fusion and heat-affected zones and into the base metal, were obtained to (*1*) evaluate CVN toughness versus position at room temperature, and (*2*) determine the transition temperature of each major weldment region. Typical locations of Charpy V-notch specimens are superimposed on a profile of a transverse slice in Fig. 4. Impact tests were performed in accordance with ASTM Methods and Definitions for Mechanical Testing of Steel Products (A 370-77) and the fractures were subsequently evaluated.

Results

Macroscopic Observations

The overall effect of the electroslag welding process and subsequent heat treatment on the macroscopic grain structure of 2¼Cr-1Mo steel is shown in Fig. 2. (This section is of a weldment that was postweld stress relieved at 760°C.) The fusion zone is characterized by large columnar grains which grow radially inwards from the walls of the base metal plates and hot shoes, and upwards in the preferential direction of heat removal. (In the transverse section shown in Fig. 2, these grains appear equi-axed.) In the heat-affected zone adjacent to the fusion line, large equi-axed grains, typical of those found in thick-section electroslag weldments, appear. This region of the HAZ in electroslag weldments sees temperatures well above the Ac_3, and significant grain growth can occur without careful process control.

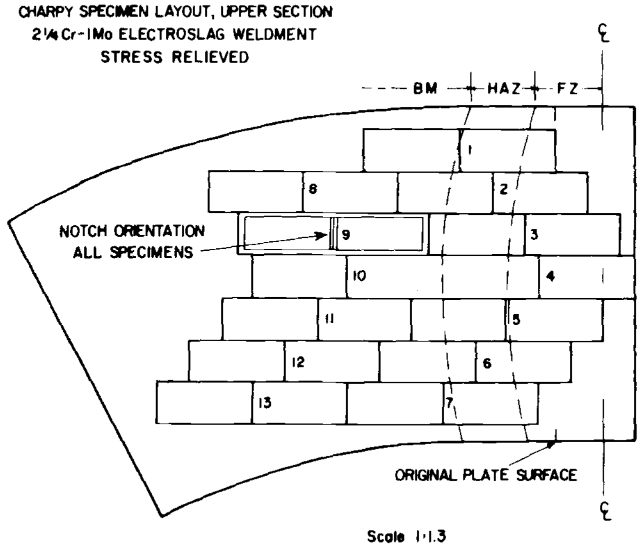

FIG. 4—*Typical layout for Charpy specimens from 102-mm (4-in.)-thick 2¼Cr-1Mo electroslag welded steel.*

Microscopic Observations

Weld zone microstructures at positions of recorded thermal history are shown in Fig. 5. The microstructures at thermocouple positions 3, 4, 5, 6, and 11 are of the base metal, and show the typical polygonal ferrite and coarse upper bainite of the annealed steel. Note the fine dispersion of Mo_2C within the ferrite.

Thermocouple positions 1, 2, 8, and 9 in Fig. 5 are in the HAZ, and the microstructures illustrate the sensitivity of the ferrite/bainite ratio to cooling rate. Microstructures at positions 1 and 8, both near the fusion line, are predominately bainite containing moderately large spheroids of carbide, probably Fe_3C. Microstructures at positions 2 and 9 contain significantly larger fractions of ferrite (free of Mo_2C precipitates) and coarse upper bainite. Note also the change in morphology of the ferrite, from patchy, almost acicular near the fusion line to quite equiaxed at a distance of 20 mm from the fusion line.

The thermocouple positions and corresponding microstructures after electroslag welding and a 760°C postweld stress relief are shown in Fig. 6. Carbide coarsening in the base metal (positions 4, 5, 9, 10, and 11), especially at ferrite grain boundaries, resulted from postweld heat treatment at 760°C. A similar effect can be observed in the regions of the HAZ closest to the base metal (for example, compare microstructures at position 2 in both Figs. 5 and 6).

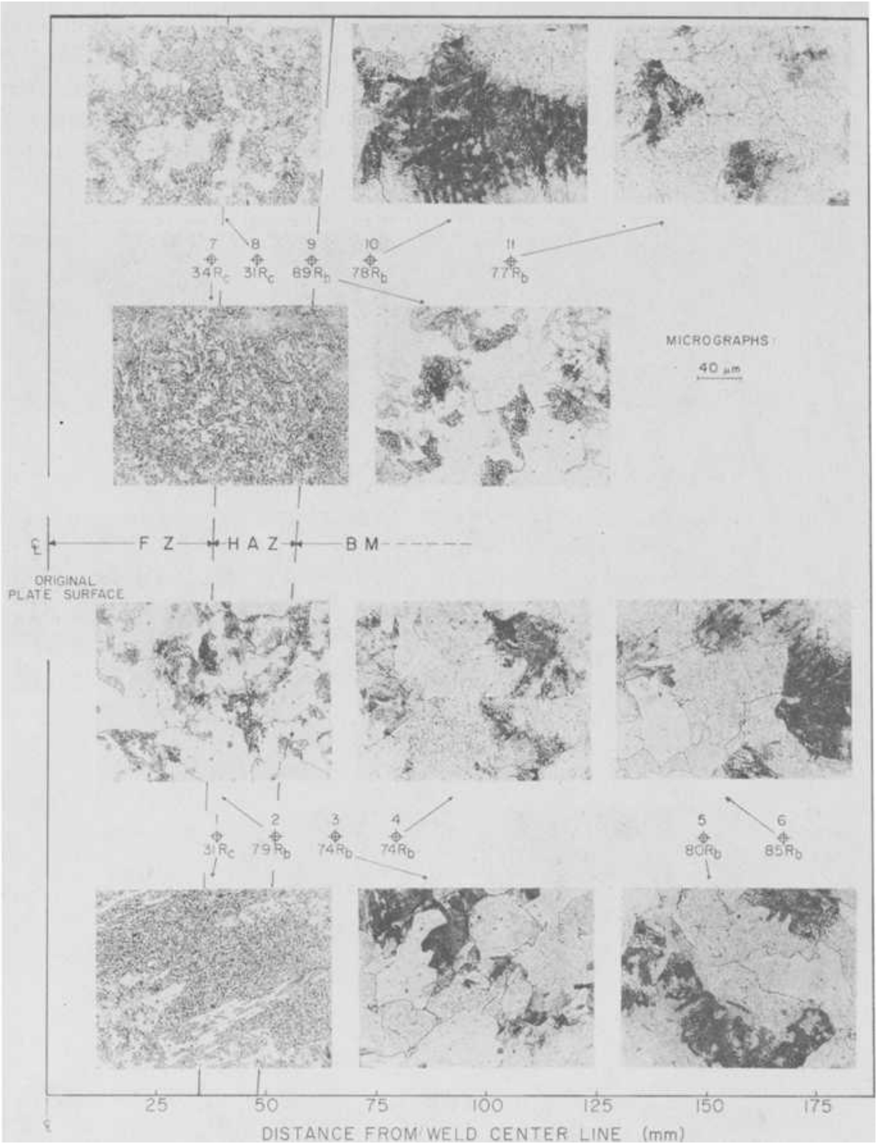

FIG. 5—*Microstructures of a 2¼Cr-1Mo steel electroslag weldment in the as-welded condition.*

In contrast, regions of the HAZ near the fusion line have undergone carbide transitions which appear to have homogenized and refined the carbide distribution, probably by converting Fe_3C to Mo_2C (for example, compare microstructures at either position 1 or 7 in both Figs. 5 and 6). Recovery processes during the 760°C stress-relief heat treatment also coarsened the substructure of the HAZ adjacent to the fusion line, a result also seen in comparing microstructures at positions 1 and 7 in both Figs. 5 and 6.

Selected metallographic samples from the different weldments and from the as-received base material were observed at high optical magnification to further clarify the microstructural differences. The microstructures of the fu-

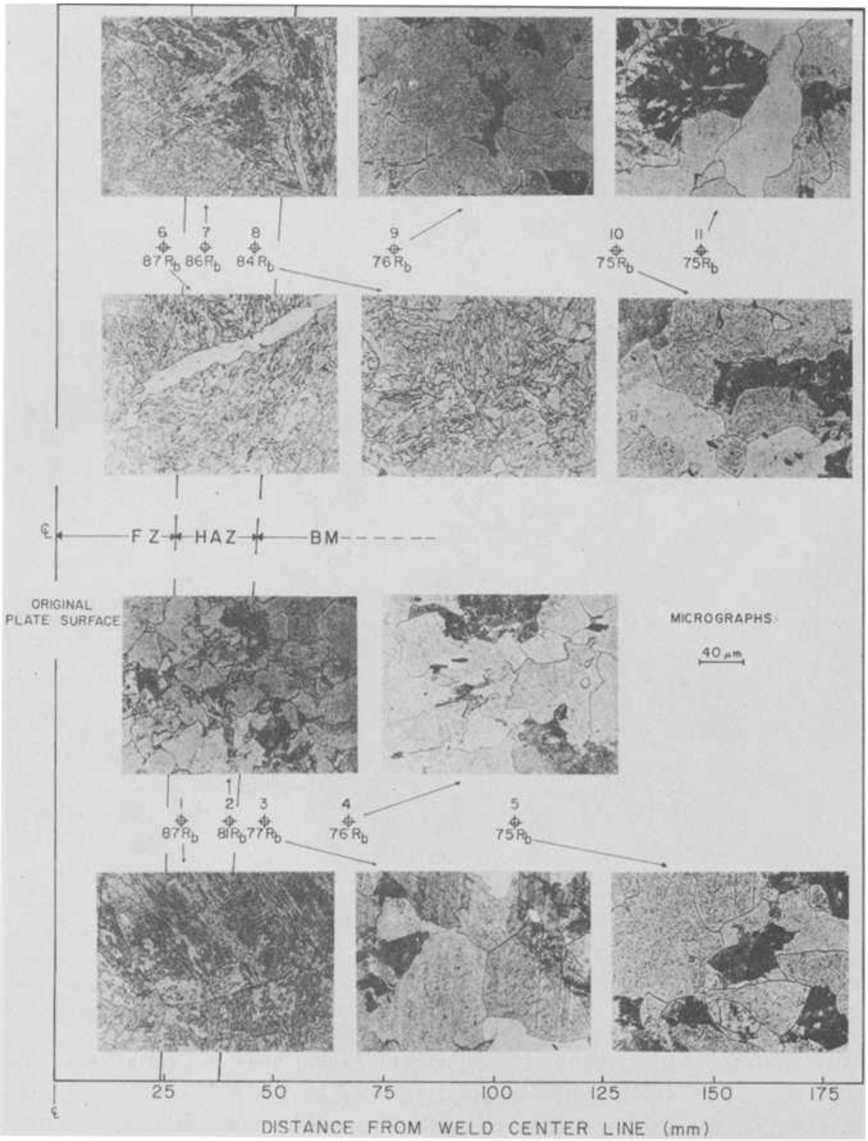

FIG. 6—*Microstructures of a 2¼Cr-1Mo steel electroslag weldment after stress relieving at 760°C.*

sion zone and base metal of the as-welded, stress-relieved at 690°C, and stress-relieved at 760°C electroslag weldments are shown in Fig. 7. A definite coarsening of the fine ferrite laths in the fusion zone was observed after stress relieving, with the most noticeable coarsening occurring at 760°C. Perhaps more significant was the fact that the carbides were finer and more homogeneously distributed after stress relieving, especially in the 760°C

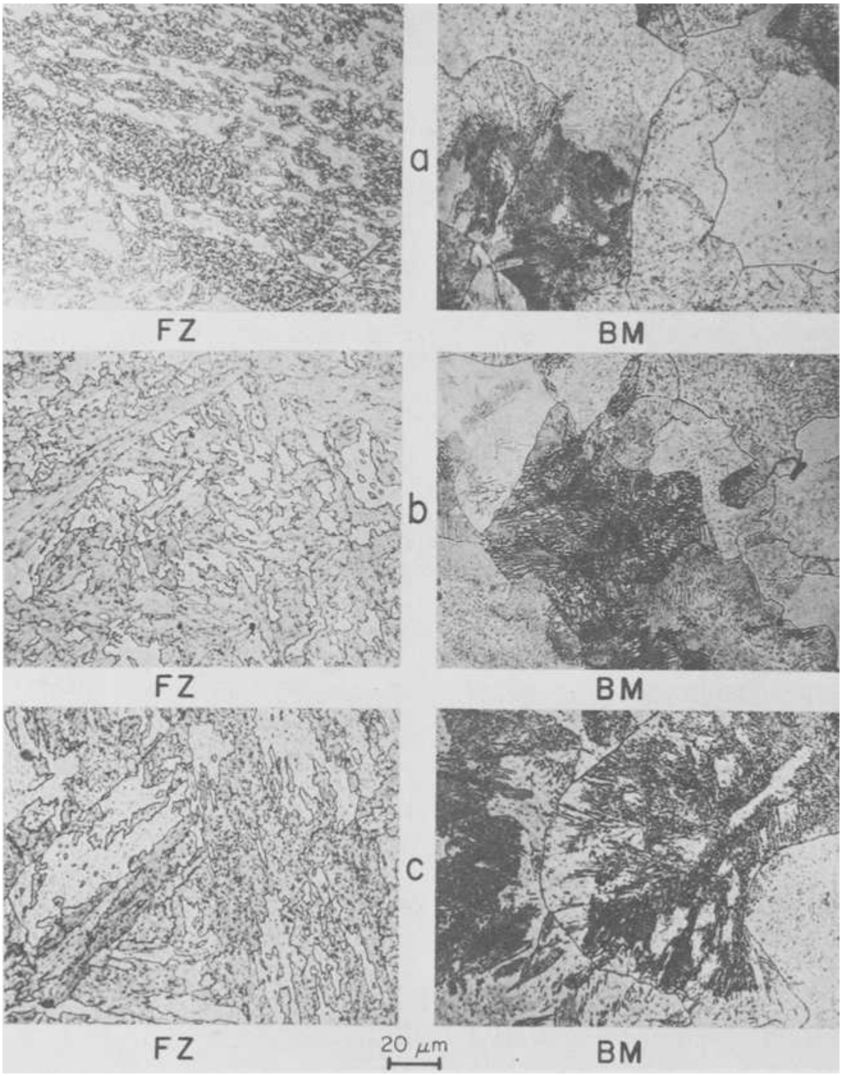

FIG. 7—*Microstructures from the fusion zone (FZ) and the base metal (BM) of 2¼Cr-1Mo steel electroslag weldments. Conditions are* (a) *as-welded,* (b) *stress relieved at 690°C, and* (c) *stress relieved at 760°C.*

specimen. This result is more clearly seen in the high-magnification micrographs of Fig. 8. Micron-size carbides, probably Fe_3C in a nearly continuous morphology at the ferrite lath boundaries of the as-welded bainite, are replaced by a finely divided and uniformly dispersed Mo_2C after stress relieving, especially at 760°C.

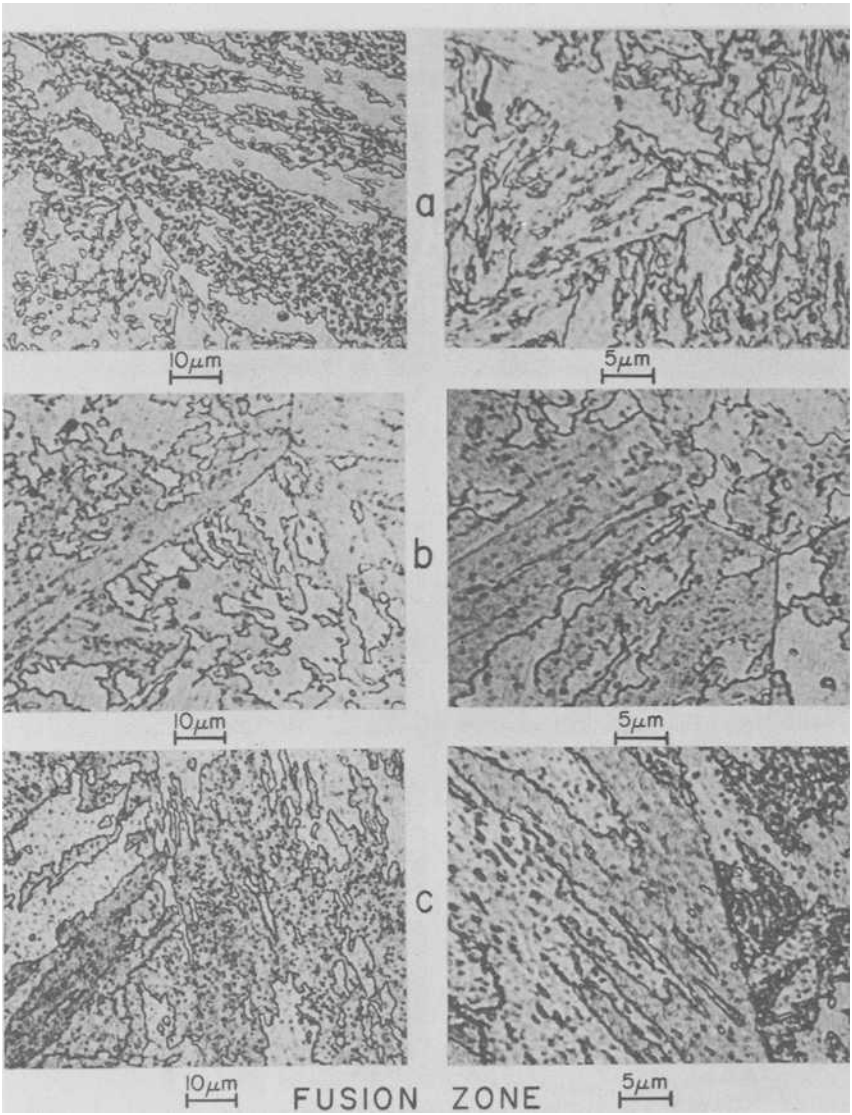

FIG. 8—*Fusion zone of 2¼Cr-1Mo steel electroslag weldments at high optical magnifications. Conditions are* (a) *as-welded,* (b) *stress relieved at 690°C, and* (c) *stress relieved at 760°C. Note the recovery in the ferrite laths and the refinement of the carbides caused by postweld heat treatment.*

The effect of postweld heat treatment on the microstructure of the annealed base metal was less obvious. Some coarsening and redistribution of carbides during stress relieving is indicated in Fig. 7, and shown clearly in the high-magnification micrographs of Figs. 9 and 10. Both coarsening and spheroidization of the Fe_3C in the upper bainite during stress relieving is shown in Fig. 9, while in Fig. 10, thickening of the carbide (probably Fe_3C)

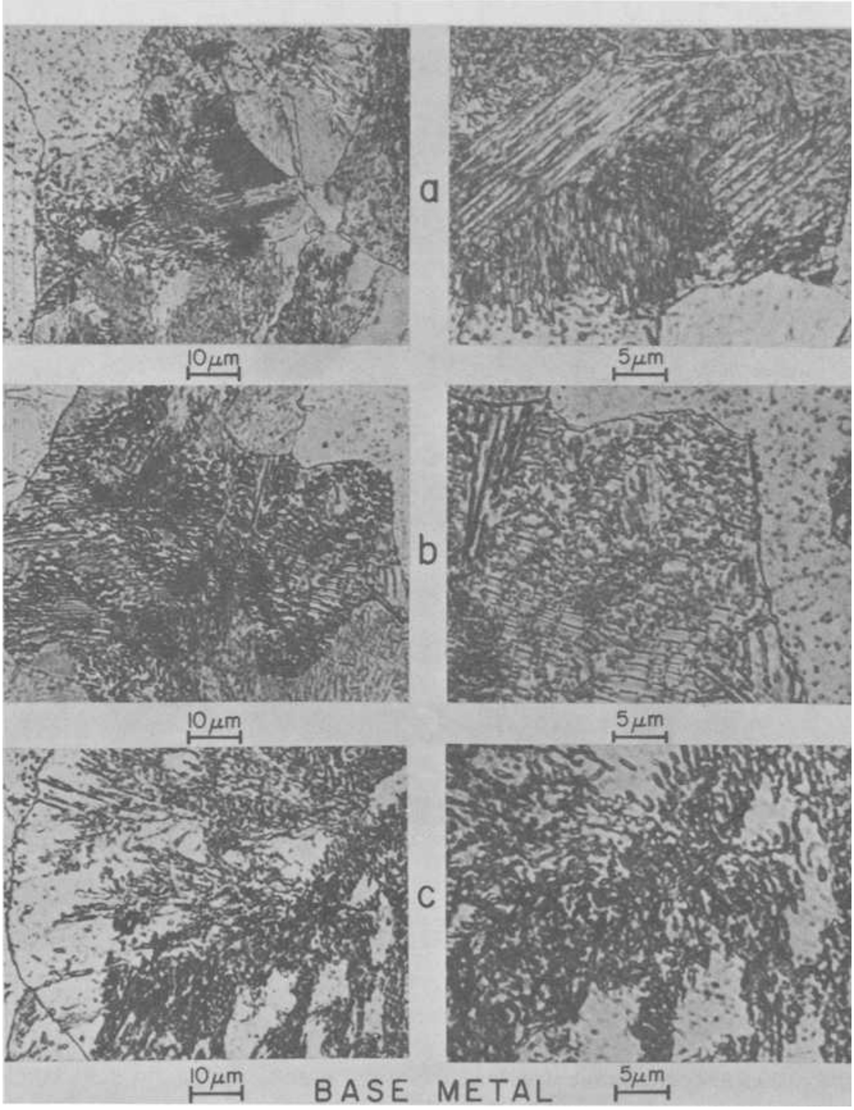

FIG. 9—*Bainite portion of the base metal in 2¹/₄Cr-1Mo steel electroslag weldments. Conditions are* (a) *as-welded,* (b) *stress relieved at 690°C, and* (c) *stress relieved at 760°C.*

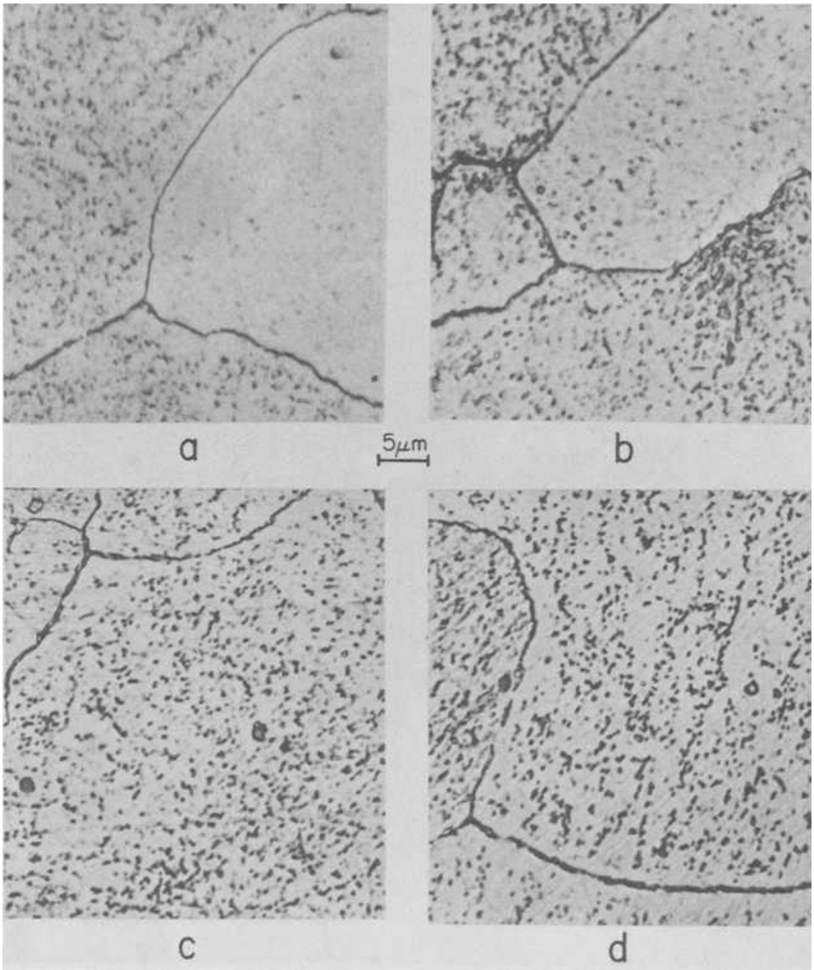

FIG. 10—*Ferrite portion of the base metal in 2¼Cr-1Mo steel electroslag weldments. Conditions are* (a) *as-received base metal,* (b) *as-welded,* (c) *stress relieved at 690°C, and* (d) *stress relieved at 760°C.*

at the ferrite grain boundaries can be seen to result from a stress-relief heat treatment. The morphology of Mo_2C within the ferrite grains was not markedly affected by postweld heat treatment.

The grain sizes for both the as-welded and stress-relieved specimens were measured as a function of position, and the results are plotted in Fig. 11. At the fusion line, the grain structure was quite coarse, with grain sizes larger than ASTM 1 [ASTM Methods for Estimating the Average Grain Size of Metals (E 112-80)]. Grain size decreased rapidly with distance away from the

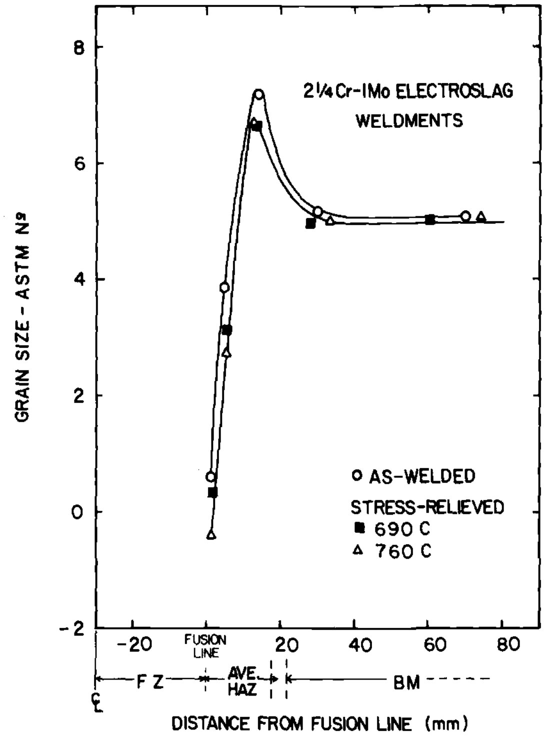

FIG. 11—*Grain sizes resulting from electroslag welding and stress relieving of 2¼Cr-1Mo steel.*

fusion line, peaking at a grain size of about ASTM 7 at 20 mm from the fusion line, then increasing to a nominal ASTM 5 grain size characteristic of the base metal. Differences in grain size caused by postweld heat treatment were not significant.

Mechanical Properties

Cylindrical test specimens traversing the entire region of microstructural change were machined from as-welded samples and from samples stress relieved at 690 and 760°C. These specimens were subjected to both tensile testing and low-cycle (tension-tension) fatigue testing at ambient temperature to determine the "weakest link" region of each microstructural condition. All tensile failures occurred in the base metal, and tensile properties were not markedly altered by postweld heat treatment. Nominal tensile properties of the annealed base metal (long transverse orientation) were 234 MPa (34 ksi) yield strength, 496 MPa (72 ksi) ultimate tensile strength, and 50 percent reduction in area. These values after a 760°C stress relief were 234

MPa (34 ksi) yield strength, 469 MPa (68 ksi) ultimate tensile strength, and 57 percent reduction in area.

Cyclic loading [31 to 310 MPa (4.5 to 45 ksi)] of tensile specimens also resulted in base metal failure, regardless of microstructural condition. Fatigue life under such conditions was approximately 10^6 cycles, and crack propagation in the base metal was found to be transgranular.

Thus both tensile and low-cycle fatigue testing indicated the base metal to be the weakest section of all weldments. Since these data did not differentiate the three microstructural conditions of weldments emphasized here, further details are omitted for the sake of brevity.

The hardness profiles for the as-welded and both stress-relieved conditions are given in Fig. 12. A change in hardness from HRC 32 in the fusion zone to HRB 79 in the base metal for the as-welded specimen is consistent with the microstructural changes shown in Fig. 5. Stress relieving reduced the hardness of the fusion and heat-affected zones by coarsening the substructure of the bainite, as evidenced by a comparison of micrographs in Figs. 5 and 6.

Extensive Charpy V-notch impact testing was performed on specimens in

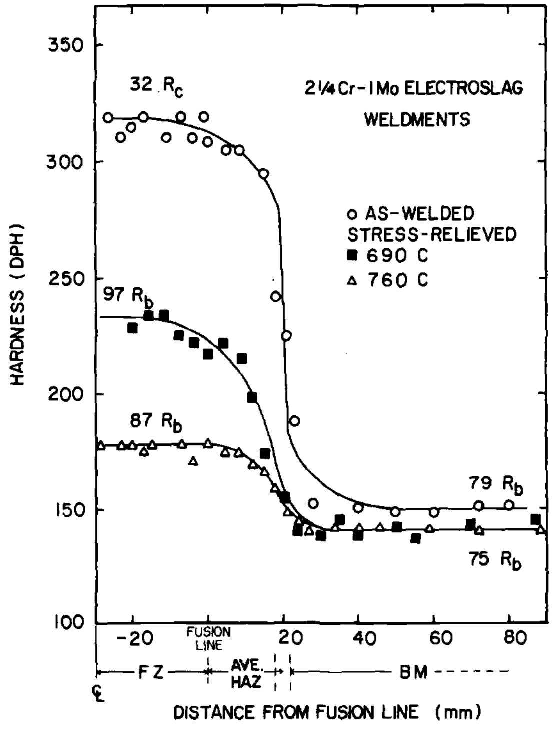

FIG. 12—*Rockwell hardness profiles resulting from electroslag welding and stress relieving of 2¼Cr-1Mo steel.*

the as-welded and both stress-relieved conditions. Specimens were taken from closely spaced locations across the weld zones of all three weldments, broken at ambient temperatures, and analyzed as shown in Fig. 13. Both the energy absorbed and the fracture appearance (percent shear) were plotted as a function of distance from the fusion line. In the as-welded condition, Charpy impact energies were found to be low [a nominal 20 J (15 ft · lb)] and

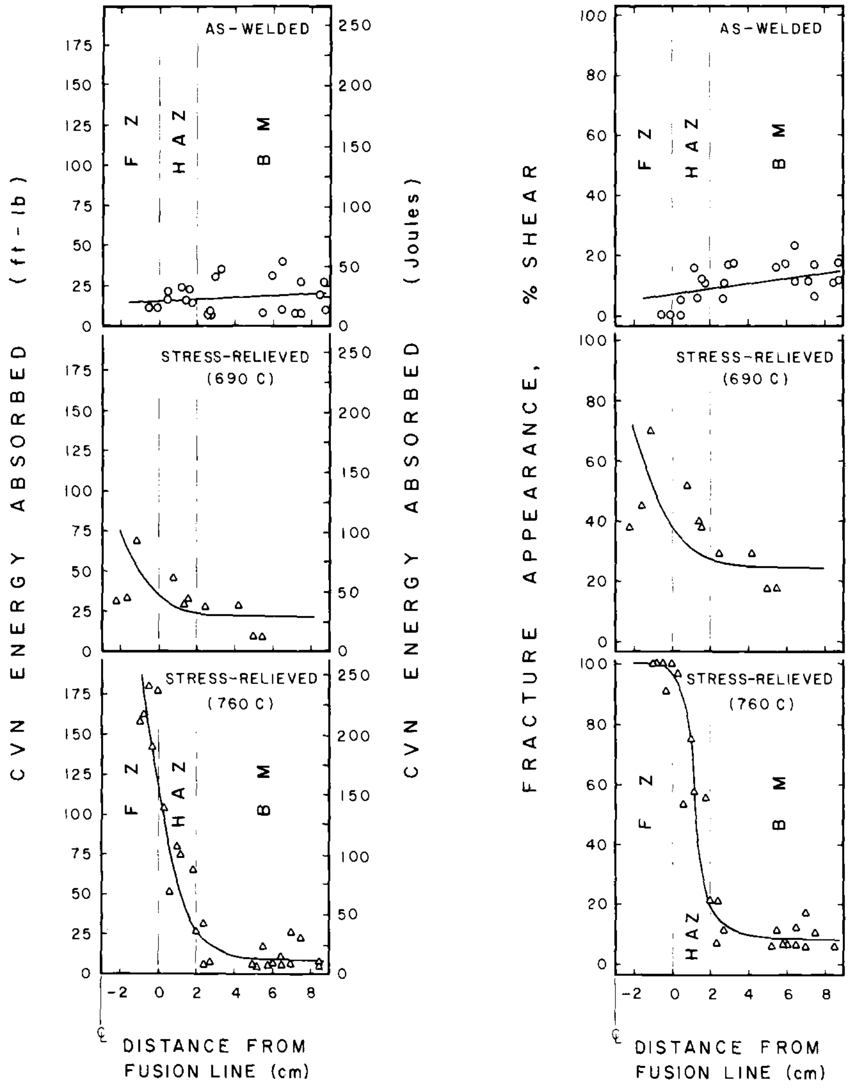

FIG. 13—*Ambient temperature CVN toughness as a function of distance from the fusion line for 2¼Cr-1Mo steel electroslag weldments. Data are shown for weldments in the following conditions: as-welded, stress relieved at 690°C, and stress relieved at 760°C.*

essentially constant across the entire weld zone. In contrast, the CVN toughness of the fusion and heat-affected zones of the weldments were dramatically improved by the postweld heat treatments. Note, however, that the base metal lost impact strength when stress relieved at 760°C.

Figure 14 compares the transition temperatures observed in the fusion

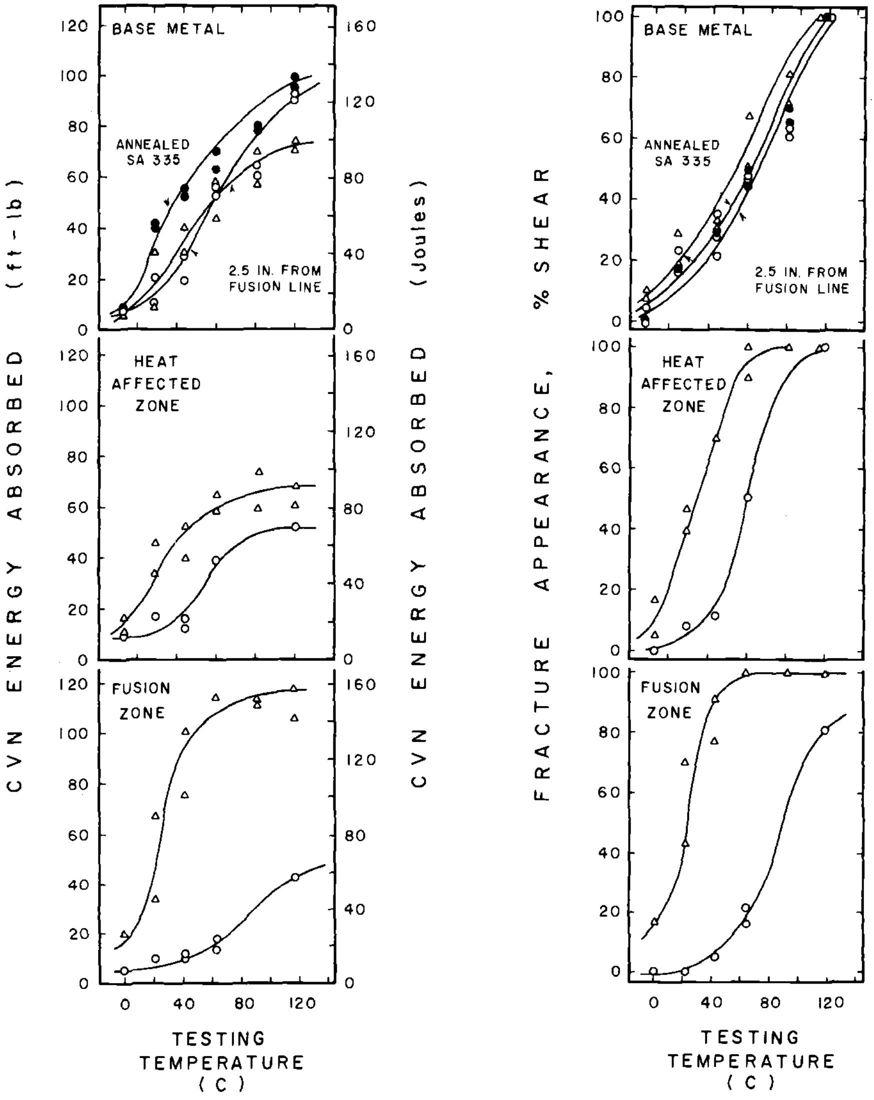

FIG. 14—*CVN toughness as a function of temperature for $2^1/_4$Cr-1Mo steel electroslag weldments. Data are shown for weldments in the as-welded (○) and the stress relieved (△) (690°C) conditions. Transition temperatures were determined for the base metal, the heat-affected zone, and the fusion zone as indicated.*

zone, heat-affected zone, and base metal for the as-welded specimen and the specimen stress-relieved at 690°C. Note that toughness has been slightly reduced by welding in a region which would normally be considered the base metal (64 mm from the fusion line). The salient feature of Fig. 14, however, is the improvement in both upper shelf energies and transition temperatures caused in the fusion and heat-affected zones by postweld heat treatment at 690°C. A summary of the Charpy impact testing results for this study is given in Table 4. Transition temperatures, whether taken as the temperature at 54 J (40 ft·lb) (TT40) or the temperature at a fracture appearance of 50 percent shear (FATT), were reduced over 65 degrees Celsius in the fusion zone and over 35 degrees Celsius in the heat-affected zone by a stress relief at 690°C.

Fractographic Observations

Scanning electron fractographs representative of the fusion zone, heat-affected zone, and base metal in each of the three weldments studied are shown in Fig. 15. In the as-welded specimen, all regions manifest a brittle nature; however, the characteristics of fracture in the fusion and heat-affected zones are quite different from those of the base metal. A fine structured quasi-cleavage mode is shown for the fusion and heat affected zones, while a coarse cleavage with river patterns is found in the base metal. Fracture between the carbide-decorated subboundaries in the bainite of the weld zones, and fracture unimpeded by the carbide-laden ferrite boundaries in the

TABLE 4—*Charpy V-notch impact data for annealed 2¼Cr-1Mo steel and electroslag weldments.*

	Properties at Room Temperature			Transition Temperature at	
Condition	Specimen Orientation/ Location	Average CVN Energy, J (ft·lb)	Average Fracture Appearance, % shear	54 J (40 ft·lb), °C (°F)	50% Shear, °C (°F)
Annealed	longitudinal	16 (12)	17	63 (145)	68 (155)
Annealed	transverse	42 (31)	22	26 (78)	68 (155)
As-welded	FZ	12 (9)	0	114 (237)	91 (195)
	HAZ	24 (18)	8	70 (158)	67 (152)
	BM	28 (21)	20	56 (132)	72 (162)
Stress-relieved (690°C)	FZ	61 (45)	50	17 (63)	25 (77)
	HAZ	50 (37)	42	29 (85)	31 (87)
	BM	26 (19)	20	52 (125)	57 (135)
Stress-relieved (760°C)	FZ	222 (164)	100	ND[a] ND	ND ND
	HAZ	102 (75)	61	ND ND	ND ND
	BM	16 (12)	10	ND ND	ND ND

[a] ND: Not determined.

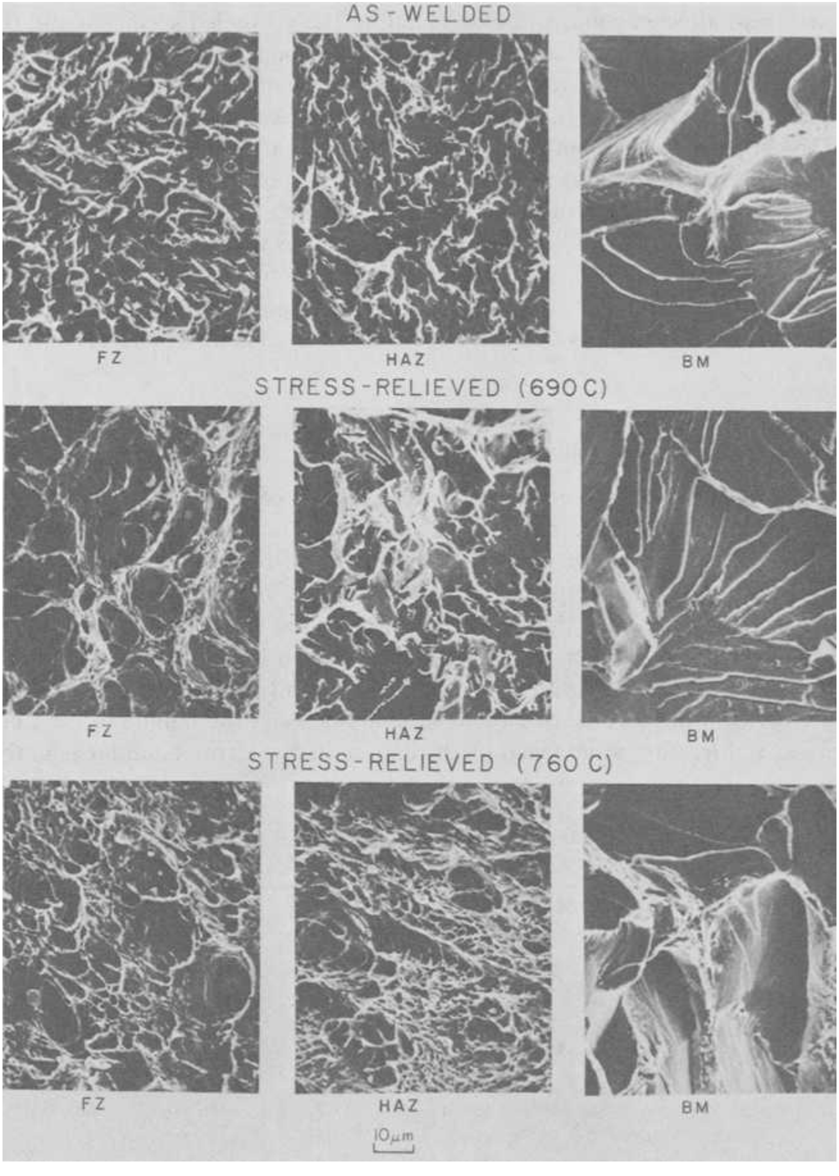

FIG. 15—*Scanning electron micrograph of the fractures surfaces from the ambient temperature Charpy tests summarized in Fig. 13.*

base metal could yield the results shown. Stress relieving resulted in ductile rupture by microvoid coalescence in the fusion zones, and, in the case of the 760°C stress relief, in the heat-affected zone. Stress relieving did not significantly alter the fracture mode in the base metal.

Discussion

The cooling rates measured during electroslag welding of 102-mm (4-in.)-thick 2¼Cr-1Mo steel, and the microstructures which resulted, suggest that the bainite created in the fusion and heat-affected zone by the welding process was upper bainite, in which carbides are dispersed along the ferrite lath boundaries [*15*, *16*]. Such a structure is not particularly tough, because neither the low angle boundaries between ferrite laths nor the carbide concentrated at the lath boundaries provides major barriers to a cleavage crack [*16*]. Furthermore, upper bainite is not generally considered to be responsive to tempering because the low angle boundaries undergo sluggish recovery processes [*15*]. Clearly, the bainite in the fusion zones and heat-affected zones of this study responded to tempering, however, and a refinement and redistribution of precipitates was observed. We have attributed these microscopic observations and the marked increase in fusion and heat-affected zone toughness with stress relieving to the dissolution of Fe_3C and the formation of homogeneously distributed Mo_2C, known to nucleate within the ferrite [*13*]. Similar toughening effects have been observed in 10Ni-8Co-2Cr-1Mo steels by Speich and Leslie [*17*]. This change in carbide composition and morphology, coupled with the coarsening of the ferrite lath structure by recovery processes, apparently produced a tough microstructure. These results are promising and suggest that a careful stress relieving of quenched and tempered 2¼Cr-1Mo plate after electroslag welding may produce a sufficiently tough microstructure across the entire weldment. Postweld heat treatment without austenitizing would require a change in the current ASME code, and thus a very thorough demonstration must be made before this mode of electroslag welding receives serious consideration by fabricators. Additional improvement of toughness would result from increasing the hardenability of the fusion zone by filler metal additions [*10–12*], and by other grain refinement techniques, since grain size refinement is known to be effective in increasing the toughness of upper bainite [*16*]. Finally, numerous researchers [*18–21*] have demonstrated the effect of cleanliness on improving the toughness of 2¼Cr-1Mo steel. It can be speculated that improving base metal cleanliness would likewise simplify thick-section welding of this steel, simply by reducing the magnitude of the impurity segregation that can occur in the HAZ during welding.

Conclusions

1. Electroslag welding of 102-mm (4-in.)-thick 2¼Cr-1Mo steel creates bainitic fusion zones which can be dramatically toughened by stress-relief heat treatments.
2. The heat-affected zones in 102-mm (4-in.)-thick 2¼Cr-1Mo steel electroslag weldments are microstructurally complex. Nonetheless, these heat-affected zones can be significantly toughened by stress-relief heat treatments.

3. Sufficient potential for making adequately tough electroslag weldments in thick-section 2¼Cr-1Mo steel plate has been demonstrated. Further study is warranted, and future efforts should include evaluation of weldments made from quenched and tempered plate, fusion-zone grain refinement studies, and evaluation of weldments from plates of improved cleanliness.

Acknowledgments

This work was sponsored by the Department of Energy's Fossil Energy Materials Program. The assistance of our academic colleagues Drs. D. L. Olson and J. E. Jones is greatly appreciated. P. E. Dempsey of Stearns-Roger Corporation and W. Clay of Eur-Control, Inc., also made significant contributions to this work. The steel for this research was supplied by Stearns-Roger Corporation.

References

[*1*] Paton, B. E., *Welding Journal*, Vol. 41, No. 12, Dec. 1962, pp. 1115-1122.

[*2*] Norcross, J. E., *Welding Journal*, Vol. 44, No. 3, March 1965, pp. 176-186.

[*3*] Woodley, C. C. et al, *British Welding Journal*, March 1966, pp. 165-173.

[*4*] Zeke, J., *British Welding Journal*, May 1966, pp. 258-268.

[*5*] Naganathan, S. et al, *Welding Journal*, Research Supplement, Vol. 52, No. 3, March 1973, pp. 125s-134s.

[*6*] Culp, J. D., *Welding Journal*, Vol. 58, No. 7, July 1979, pp. 27-41.

[*7*] Khakimov, A. N. et al, *Svarochnoe Proizvodstvo*, No. 1, pp. 24-26.

[*8*] Makara, A. M., Yegorova, S. V., and Novikov, I. V., *Avtomaticheskaia Svarka*, No. 12, 1969, pp. 1-5.

[*9*] Malinovska, E. and Hrivnak, I., *British Welding Journal*, Oct. 1967, pp. 527-532.

[*10*] Makara, A. M. et al, *Avtomaticheskaia Svarka*, No. 3, 1972, pp. 69-70.

[*11*] Makara, A. M. et al, *Avtomaticheskaia Svarka*, No. 7, 1974, pp. 51-54.

[*12*] Okurmura, M., Kumagai, M., Nakamura, H., and Kohira, K., *Welding Journal*, Research Supplement, Vol. 55, No. 12, Dec. 1976, pp. 389s-399s.

[*13*] Baker, R. G. and Nutting, J., *Journal of Iron and Steel Institute*, July 1959, pp. 257-267.

[*14*] Habraken, L. J. and Economopoulous, M., *Transformation and Hardenability in Steels Symposium*, Climax Molybdenum Company, Ann Arbor, Mich., 1967, p. 71.

[*15*] Honeycombe, R. W. K. and Pickering, F. B., *Metallurgical Transactions*, Vol. 3, 1972, p. 1099.

[*16*] Pickering, F. B., *Transformations and Hardenability in Steels Symposium*, Climax Molybdenum Company, Ann Arbor, Mich., 1967, p. 109.

[*17*] Speich, G. R. and Leslie, W. C., *Metallurgical Transactions*, Vol. 3, 1972, pp. 1043-1054.

[*18*] Copeland, J. F., *Journal of Pressure Vessel Technology, Transactions of American Society for Mechanical Engineers*, May 1976, pp. 135-142.

[*19*] Wada, T. and Hagel, W. C., *Metallurgical Transactions*, Vol. 7A, Sept. 1976, pp. 1419-1426.

[*20*] Gulya, J. A. and Swift, R. A. in *Conference Proceedings*, American Society of Mechanical Engineers, Petroleum Mechanical Engineers Conference, Mexico City, Sept. 1976.

[*21*] Swift, R. A., *Metallurgical Progress*, Vol. 103, May 1973, pp. 75-81.

W. J. Farrell[1]

A Portable 100-kW Electron Beam Welding System for Pressure Vessel Fabrication

---

REFERENCE: Farrell, W. J., "**A Portable 100-kW Electron Beam Welding System for Pressure Vessel Fabrication,**" *Application of 2¼Cr-1Mo Steel for Thick-Wall Pressure Vessels, ASTM STP 755*, G. S. Sangdahl and M. Semchyshen, Eds., American Society for Testing and Materials, 1982, pp. 297-325.

ABSTRACT: A program to demonstrate the application of a 100-kW portable electron beam (EB) welding system to the production of girth welds in several pressure vessel shells in an industrial environment is detailed. Three-metre-diameter shells, one 80-mm-thick 304L, the other 135-mm-thick ASTM A 533 Type B, were EB welded to ASME Boiler and Pressure Vessel code requirements without the use of a large vacuum chamber. Drawing upon this experience, the author presents a manufacturing plan for applying EB welding in the fabrication of thick-wall pressure vessels.

Potential fabrication cost savings are described in terms of a measure of welding time called Joint Completion Rate expressed in hours per foot of completed weld seam for 203-mm (8-in.)-thick plate. The values are: submerged arc welding (downhand), 3.0 h/ft; manual arc welding, 40 h/ft; and EB welding, 0.067 h/ft. Energy input is calculated for 135-mm-thick plate to be 7338 kJ/in. for submerged arc and 636 kJ/in. for EB welding.

The results of testing a series of EB butt welds in 63.5-mm (2½-in.)-thick ASTM A 387 Grade 22 (2¼Cr-1Mo) produced without preheat or postheat, and subjected to various postweld heat treatments, are summarized. A T1 of −107°C (−160°F) and a T2 of −50°C (−58°F) were obtained.

Additional inherent benefits of EB welding thick plate are described.

KEY WORDS: portable electron beam, thick-wall pressure vessels, potential fabrication cost savings, properties of electron beam weld 2¼Cr-1Mo steel

Our technology, and indeed our civilization, is based upon the abundant supply of low-cost, highly concentrated energy in several forms. These forms are petroleum, natural gas, and coal. The most useful form of such energy

---

[1] Senior Vice President, Sciaky Brothers, Inc., Chicago, Ill. 60638.

has been petroleum, which we have consumed prodigiously; thus we are rapidly depleting this bountiful, but finite, resource.

Civilization will have to replace this natural store of energy with machines that create concentrated energy from sources and raw materials other than petroleum or natural gas. The design and manufacture of these machines, which will substitute for the energy concentrated by nature over billions of years, will require a tremendous organized long-term effort.

The "energy machines" that convert one form of natural stored energy, such as oil shale or coal, to another form, such as synthetic liquid petroleum, are characterized by the utilization of heat and pressure. Therefore these machines are essentially high-temperature pressure vessels, and will require welded heavy sections of low-alloy steel. A significant portion of the total quantity of labor expended in fabricating a large thick-wall pressure vessel by today's methods is utilized to produce the welded joints. For example, the joint completion rate for a butt-welded 203-mm (8-in.)-thick plate utilizing the automatic subarc process in the downhand position (shop fabrication) is reported to be 3.0 h/ft.[2] If field closure is required, with the vessel in the vertical position, manual arc welding must be utilized and the joint completion rate becomes 40 h/ft. In contrast, the electron beam (EB) is potentially capable of welding 203-mm (8-in.)-thick plate at 3 in./min in one pass, for a joint completion rate of 0.067 h/ft!

Electron beam welds are characterized by (*1*) virtually unlimited penetration, producing a parallel sided weld in a single pass; (*2*) high welding speed; (*3*) minimal distortion and shrinkage; (*4*) no filler material or fluxes required; and (*5*) inherent precision control of welding parameters, providing repeatability of developed procedures.

These characteristics make EB welding economically attractive for welding heavy structures, such as very large pressure vessels. Therefore Sciaky decided to develop a portable welding system suitable for large pressure vessel fabrication that could be used in field erection as well as in shop fabrication. At the time of this decision, the most powerful EB welder produced a maximum power of 42 kW. Our first step was to extrapolate this design to 60 kW, and we produced such an experimental system in 1970. Working with this system over the next several years provided insight into the requirements of an electron gun (EG) for one pass welding of very heavy sections.

We recognized that a more rigorous design approach was required if the EG were to produce a stable beam of the proper characteristics, and to demonstrate operating reliability. We therefore began the development of sophisticated computer programs which solve the differential equations defining the characteristics of the EB and permit optimization of the shapes

---

[2] Weber, C. M. et al, "Factors Influencing the Welding of Coal Gasification Vessels-Report on Some Recent Developments," paper presented at Corrosion '79.

of the electron gun components (cathode, anode, magnetic coils) as well as the magnitude of the accelerating voltage.[3]

Finally, a 100-kW EG was designed utilizing these computer programs. This EG (and its associated power supplies) was designed to the following criteria:

1. Produce an EB concentrated to a diameter capable of penetrating up to 254-mm (10-in.)-thick alloy steel at a welding speed of 6 in./min. Extrapolating from our previous work at 42 and 60 kW beams, resulted in our specifying a 100-kW EB, 2 mm in diameter.
2. The EG must be small and rugged for maximum mobility. Our objective was to eliminate the need for a large vacuum chamber, and to move the EG and its associated apparatus from work station to work station.
3. Small anode hole diameter to avoid interelectrode flash-over by excluding metallic vapors from the cathode region.
4. Long emitter life.

These considerations led to the development of a compact EG producing a 1-A beam at 100 kW. The lifetime of the emitter is 50 h.

Electron Beam Welding Process

Electron beam welding is a fusion welding process, in that the weld is produced by local melting and coalescence. The energy source is a concentrated beam of very high velocity electrons which is directed at the joint to be welded. Upon striking the surfaces to be joined, each electron penetrates a small distance into the thickness of the material, giving up its kinetic energy in the form of heat.

The energy density of the EB is so high that it literally bores a hole through the thickness of the material being welded. The hole is moved along the joint by advancing either the EG or the work. As the beam advances, it comes into contact with solid material at the leading edge of the hole. This material is melted, flows around the bore of the hole, and solidifies behind it to make the weld.

The mechanisms of the formation of the hole or cavity are not completely understood. The theoretical penetration of an electron, accelerated by a voltage *V*, into the metal, is not enough to explain the great depths of the welds produced.

Several models have been proposed to explain the cavity formation, none of which clearly account for the great depth of the penetration attainable with the EB. It is sufficient for our purposes to state that the following phenomena play a role in the cavity formation: (*1*) metal vaporization and

---

[3] Sayegh, G. and Dumonte, P., "Theoretical and Experimental Techniques for Design of EB Welding Guns," in *Third International Processing Seminar*, March 1974, pp. 3a1-3a87.

pressure on the molten pool created by vaporization; (*2*) the pressure of the EB due to the mass, velocity, and number of electrons striking the work surface per unit of time; and (*3*) the pressure of the metal vapors.

It has been demonstrated by countless experiments that once the specific power of the incident EB is sufficiently high for the cavity to form, the cavity becomes progressively deeper until the depth reached is such that the total beam power is absorbed by the plasma trapped in the cavity before reaching the bottom.[4] To fully penetrate a given thickness of plate, therefore, requires sufficiently high specific power for the cavity to form, and sufficiently high total beam power for the cavity to extend through the bottom of the plate. Such a beam of electrons, directed at the surface of a plate somewhere within its boundaries, will produce a full-penetration weld bead as it advances. If this process is applied along the line of junction of the butting faces of two plates, one obtains by melting a continuity of the materials over their entire thickness, and, upon solidification, a weld. This is illustrated in Fig. 1.

The first distinguishing characteristic of an EB as applied to welding is thus seen to be its ability to penetrate completely through the maximum thickness of plate for which a given EB welding system is designed. Thus square butt joints are most suitable for this process. In contrast, the conventional fusion welding processes, such as submerged arc, are limited in penetration by heat transfer considerations. Therefore one must gouge a trench on each side of the butting edges of the plates to be joined in order to give the energy source access to the midpoint of the plate thickness. These

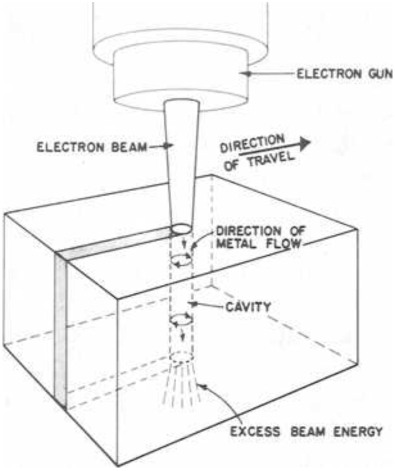

FIG. 1—*Representation of the mechanism of full-thickness penetration EB welding.*

---

[4] Farrell, W. J., " The Use of the EB to Fabricate Structural Members," Creative Manufacturing Seminar, American Society of Tool and Manufacturing Engineers, 1962-63.

trenches must then be filled by expensive welding wire, in very many passes, to provide a weld joint through the entire thickness of the plate.

The EB is produced by a device called an electron gun (EG). The principles embodied in the EG are illustrated schematically in Fig. 2. This figure depicts the 100-kW EG developed for welding heavy plates, revealing some of the features uniquely designed to satisfy the requirements of its intended applications.

Conventional electron guns utilize a resistance heated formed wire or strip for the emitter. Because this EG was developed to make very long duration continuous welds in very heavy plate, the indirectly heated slug emitter was developed in order to provide long life before failure. Another unique aspect is the fact that the EG housing is sealed, and fitted with a turbo-molecular pump. This tiny, purely mechanical pump is able to maintain a vacuum of 1×10^{-5} torr within the gun housing, with the complete gun assembly immersed in an enclosure at a pressure of 6×10^{-2} torr. The fact that the hole through the anode communicates with the volume at the higher pressure appears to contradict the earlier statement that the gun housing is sealed and separately pumped to a high vacuum. However, the hole in the anode is very

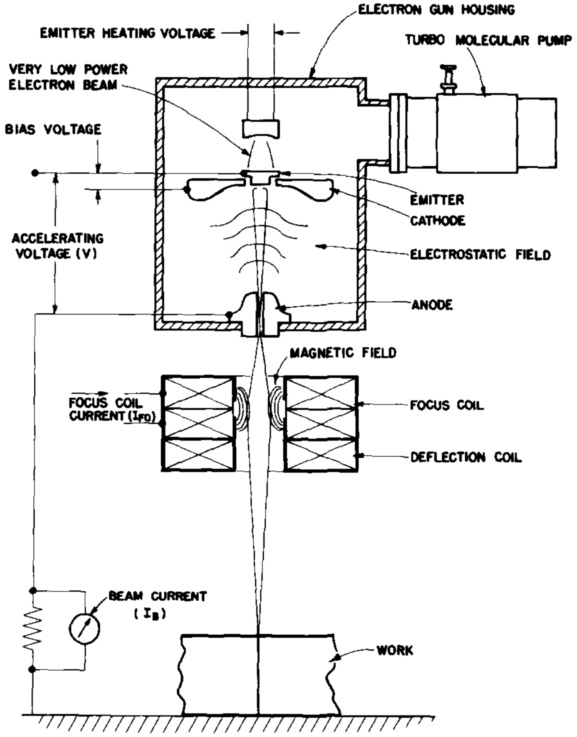

FIG. 2—*Schematic representation of the Sciaky 100-kW electron gun.*

small in diameter, and quite long. The high vacuum in the gun, and the intermediate vacuum in the welding enclosure are both at sufficiently reduced pressure that the mean free path of the gas molecules approach system dimensions, and the gas molecules cease to interact. Under such circumstances, termed the molecular flow region, such an orifice acts to block the passage of gas molecules from one region to the other.

A high vacuum is needed in the region where the electrons are emitted and accelerated, both to protect the emitter from oxidation, and to avoid interference with the electrons when they are still at a low velocity. An intermediate vacuum level is desirable in the welding enclosure to make the portable EB welding system concept practical. The small, lightweight, mobile, and efficient turbo-molecular pump makes this possible.

In the case of the 100-kW EG, two 100 L/s turbo-molecular pumps are mounted diametrically to the gun body. When the gun housing is at atmospheric pressure (local vacuum chamber situation) a small mechanical fore-pump is connected to the outlet port of the turbo-molecular pumps. When the gun is within an enclosure to be evacuated to the 10^{-2} torr range, a fore-pump is unnecessary. The turbo-molecular pumps simply exhaust into the main enclosed volume being pumped by the two stage mechanical pumps.

Characteristically, the energy input for an EB weld is a small fraction of that associated with an electric arc weld.

Since submerged arc welding in the flat or downhand position is the accepted electric arc welding process exhibiting the highest deposition rate (resulting in the smallest number of passes to fill a joint), welding procedures for butt welds in 135-mm-thick Specification for Pressure Vessel Plates, Alloy Steel, Quenched and Tempered, Manganese-Molybdenum and Manganese-Molybdenum-Nickel (A 533-80) Type B alloy steel were obtained from several prominent pressure vessel manufacturers. The energy input for each procedure obtained was calculated. The spread in values for the identical thickness and alloy was surprising. Generalizing from this relatively small sample, it appears that machined joints result in the smallest volume to be filled and the lowest energy input.

In any event, we chose the lowest energy input submerged arc process to compare with EB welding. Figure 3 shows this comparison. The values are: submerged arc welding, 7338 kJ/in.; EB welding, 636 kJ/in. of weld length. This substantial reduction results in energy cost savings and considerably less distortion of the weldment. In addition, the cost of welding wire and flux, plus, in the case of ASTM A 533 Type B and 2¼Cr-1Mo, the cost of preheating, are eliminated, a rather significant savings.

In the modern EB welder, the process parameters are precisely controlled by closed-loop servo systems. These parameters therefore are accurately regulated and highly reproducible. Experience has shown that the EB welding process exhibits a similarly high level of reproducibility. This is

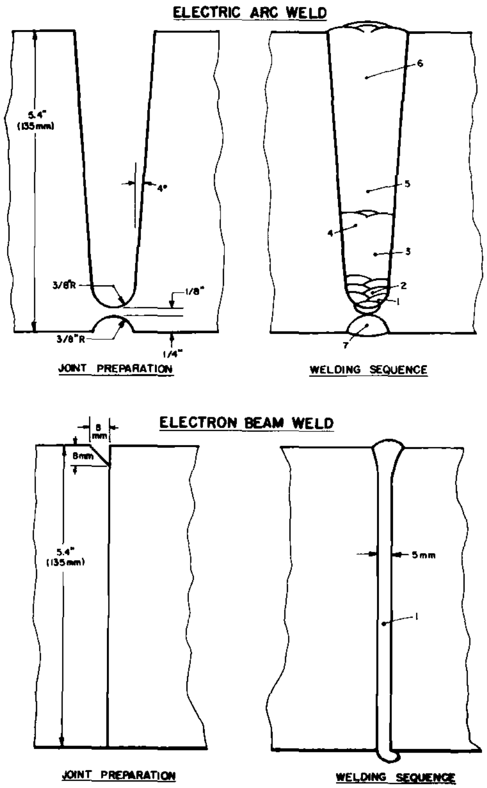

ENERGY INPUT
KILO-JOLES PER INCH OF
JOINT LENGTH

ELECTRIC ARC WELD

SEQUENCE NO	BEAD NO	PROCESS	I AMPS	V VOLTS	S IPM	ENERGY INPUT KJ/IN
1	1	Metal Arc	168	23.5	--	Manual Weld
2	2 - 3	"	230	23.5	--	"
3	4 - 5	Sub-Arc	500	34	19	107.4
4	6 - 9	Sub-Arc	600	34	19	257.7
5	10 - 13	Tandem Sub-Arc				
		Leading	700	34.5	28	207.0
		Trailing	600	36.5	28	187.7
6	14 - 66	Tandem Sub-Arc				
		Leading	850	34.5	28	3,330.5
		Trailing	750	36.5	28	3,109.0
7	B-1	Sub-Arc	700	33	10	138.6

TOTAL ENERGY INPUT - 7,337.9 KJ/IN

NOTES:

1. Manual weld passes not included in energy input calculations
2. Filler Wire - 5 32" ∅, AC current source
3. Preheat to 300°F
4. Welding position - Flat (1G)
5. Source - Welding Instruction Sheet
   Pressure Vessel Fabricator

ELECTRON BEAM WELD

SEQUENCE NO.	I AMPS	V VOLTS	S IPM	ENERGY INPUT KJ/IN
One Pass Full Penetration	0.625	80,000	4.72	635.6

TOTAL ENERGY INPUT - 635.6 KJ/IN

NOTES:

1. No Preheat
2. Welding position - Horizontal
3. Source - Procedure Qualification Record
   Sciaky - Applications Development Program

FIG. 3—*Input comparison of electric arc versus EB butt weld in 135-mm-thick ASTM A 533 Grade B.*

probably the result of the fact that the transfer of energy from the source (EG) to the work is at very high efficiency (no radiation or convection losses). As a result, EB parameters can be developed on relatively small test blocks, and then repeated without modification for production welding of large structures of the same alloy and thickness as the test blocks.

It should be noted that the statement "relatively small test blocks" deserves quantification. If the test block is too narrow in width, the temperature distribution and the gradient during solidification of the molten zone will be affected. We have found that the test block should be 1.5 to 2 times the weldment thickness.

Application Technology Demonstration Program

Sciaky is nearing completion of a program to demonstrate the application of its portable 100-kW EB welding system to the welding of the girth joints in several pressure vessels to code requirements in an industrial environment. This program was financed largely by an international group of pressure vessel fabricators. Two typical cases for the Application Technology Demonstration Program were chosen by the sponsoring group:

1. *A simulated Reactor Core Barrel* consisting of six cylindrical sections, 3 m in diameter, constructed of 80-mm-thick 304L stainless steel. The relatively distortion-free weldments produced by this process, in addition to the inherent cost savings, were the driving forces for this choice.
2. *A simulated Reactor Containment Vessel* consisting of three cylindrical sections, 3 m in diameter, constructed of ASTM A 533 Type B alloy steel of 135 mm thickness. This selection allows resolution of the question of EB welding magnetic material in heavy sections; demonstration of acceptable weld mechanical properties, including Charpy V-notch; development of procedures for one pass welding of heavy-section alloy steel; verification that EB welding does not require preheating as does conventional fusion welding; and investigation of postweld heat treating.

This program required the development of EB welding procedures, determination of maximum joint gaping and mismatch, development of slope out procedures, and nondestructive inspection of complete girth welds, verified by metallographic examination.

At this writing, the program is nearing completion; welding procedures and all required data have been developed, the 304L cylindrical sections have been welded and tested, and the first pair of ASTM A 533 Type B rings have been welded. The concept of utilizing the pressure vessel being welded to enclose the vacuum welding environment has been reduced to practice.

In all cases, joint preparation is a simple square butt, incorporating a small groove for electromechanical tracking of the joint. Recent technological advancements will allow elimination of the tracking groove.

Figure 4 depicts the concept utilized to weld the cylindrical sections with the general purpose portable EB system. The lower ring is placed on a fabricated base, resting on a large diameter O-ring to provide a vacuum seal. The upper ring is placed on top of and aligned with the lower ring. The square butt joint configuration, the optimum joint configuration for EB welding, makes it possible to utilize the force of gravity for positioning and sealing. Next, the small local chamber (sealing belt) is installed, straddling the two rings in order to seal the joint, which may contain relatively wide gaps. Finally, the cover plate assembly is lowered in place by an overhead crane. It contains a large O-ring that seals against the top surface of the upper ring.

The cover plate assembly is fitted with a mechanism to rotate the EG at preset welding speed. The EG is attached, through a servo-controlled cross slide, to a rigid bracket fixed to the rotating mechanism. Welding travel is provided by rotating the EG, fixed at a suitable lever arm with respect to the

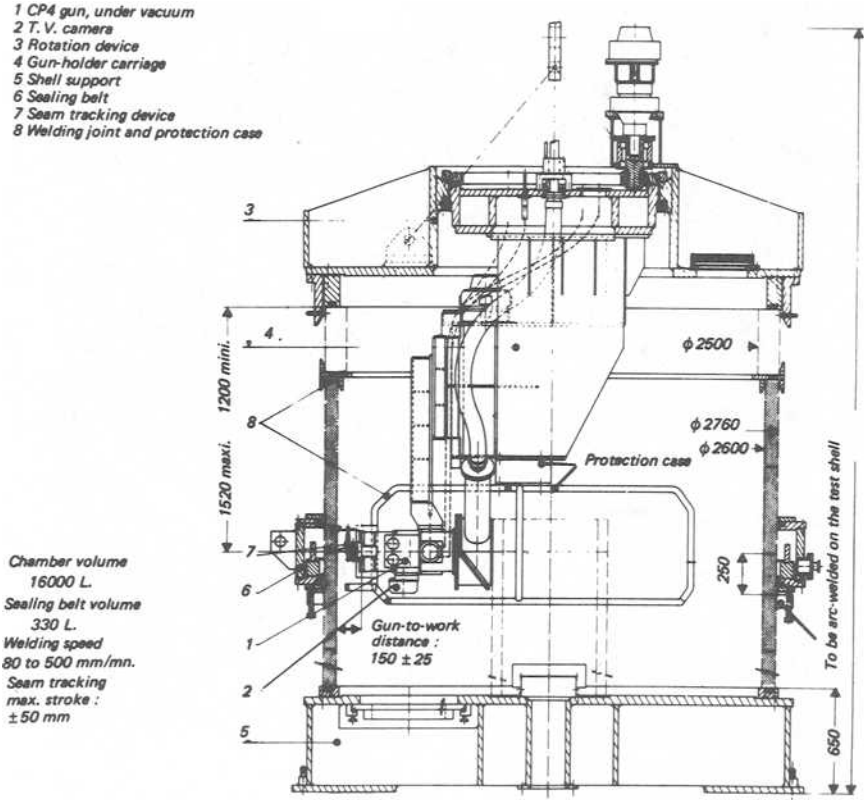

FIG. 4—*Portable EB welding system for welding rings to form pressure vessel shell.*

cylinder axis. This dimension is adjustable for rings of different diameters. Beam-to-seam alignment is maintained dynamically by the cross-slide servo mechanism in response to the output of the tracking device.

With the cover in place, the two rings form the welding vacuum chamber. The interior enclosed space is pumped through a port in the base plate. Mechanical pumps only are required, since the system is designed to operate in an intermediate vacuum of approximately 6×10^{-2} torr.

Figure 5 shows two ring sections in position ready to be EB welded, with the cover being lowered in place. The O-ring seal and the EG are clearly evident. Figure 6 displays the apparatus in place, pumpdown completed, and

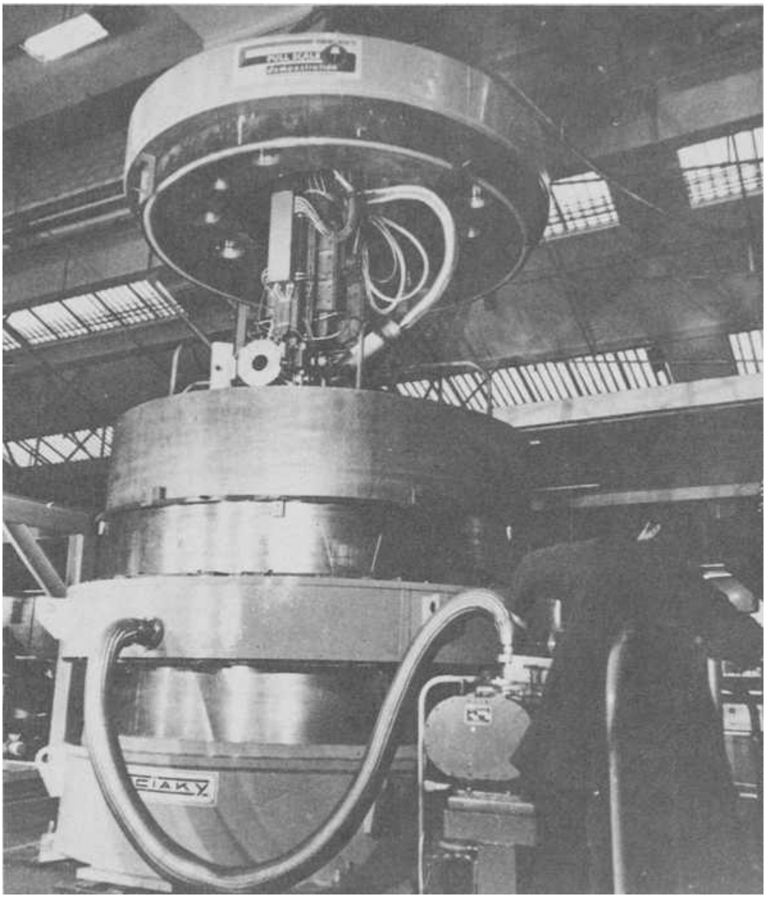

FIG. 5—*Lowering upper plate assembly into position. This is the final step in preparing to weld 3-m-diameter, 80-mm-thick 304L stainless steel rings from the inside.*

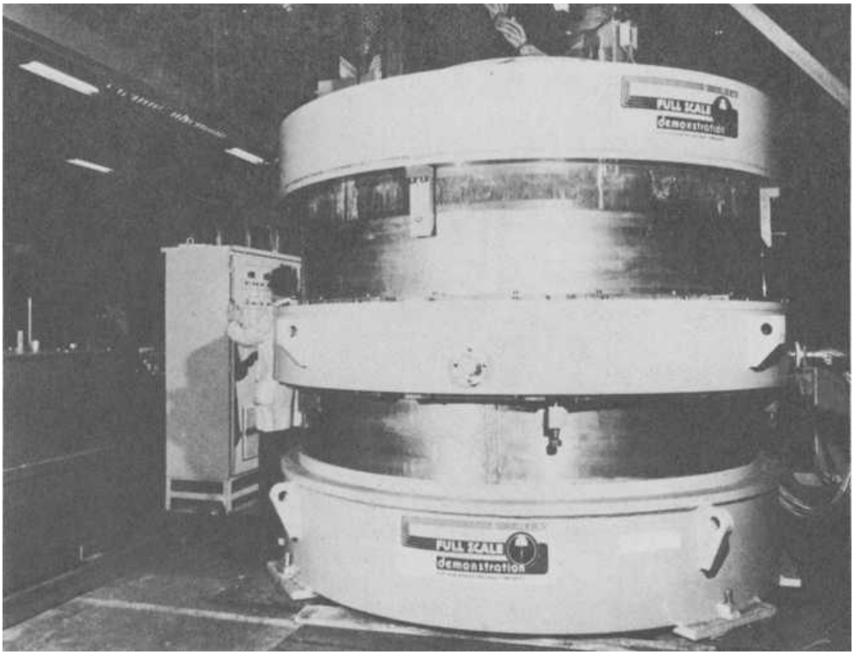

FIG. 6—*Setup completed and interior at vacuum. Ready to EB weld two 3-m-diameter rings from the inside.*

the girth welding ready to start. A closed-circuit television camera, mounted to the EG, allows observation of the welding process by a TV monitor. The completed EB welded 304L rings are shown in Fig. 7. The welding procedure utilized is described in Fig. 8. The welding time for the complete girth weld was 55 min. The welding time for the 135-mm-thick ASTM A 533 Type B rings was 70 min.

Figure 9 shows cross sections through a weld joining two 304L rings. The mismatch encountered when the rings were assembled is evident. It is clear that the magnitude of mismatch and gapping encountered is not deleterious to the weld quality. A macrograph of an EB weld in 130-mm-thick ASTM A 533 Type B is reproduced in Fig. 10. Figure 11 shows the ease with which EB welds can be repaired. The original weld was intentionally misaligned with respect to the joint. The repair weld was made by simply indexing the EG to the correct location with respect to the joint, turning on the power and re-welding. It is not necessary, or even helpful, to grind out the original weld. Portable apparatus for welding the longitudinal joints in rings, and for welding nozzles have also been developed for use with the 100-kW system.

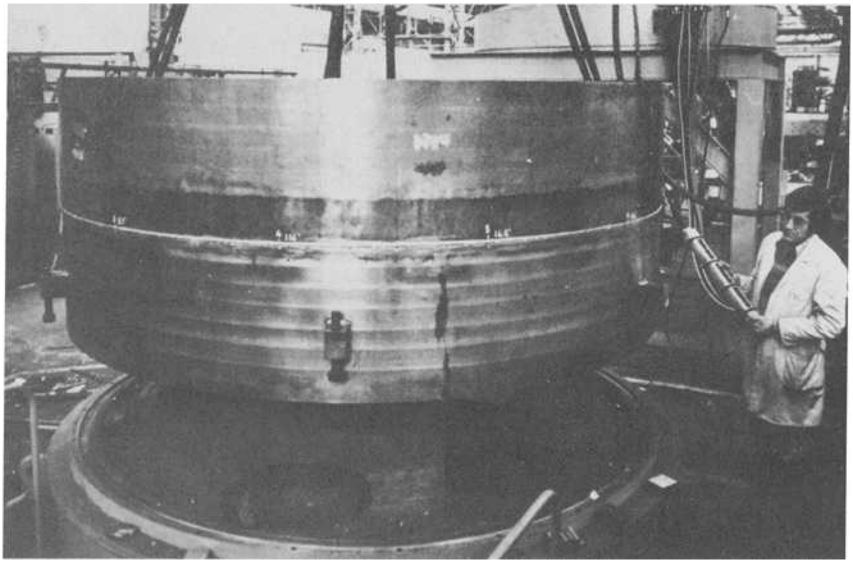

FIG. 7—*Five 80-mm-thick, 3-m-diameter rings EB welded from inside.*

Manufacturing Plan

A manufacturing plan for applying EB welding in the fabrication of pressure vessels has been formulated. This plan is built upon the following set of typical requirements:

1. Production facilities for:
    1.1 Longitudinal welds in cylindrical sections up to 15 ft long.
    1.2 Nozzle to cylinder welds; nozzle weld diameter up to 5 ft.
    1.3 Girth welds joining cylindrical sections varying from 5 to 15 ft diameter.
2. A facility for welding procedure development and for producing welded plates for procedure qualification.

Since the EB equipment was designed to be portable, the plan requires a single 100-kW EG with its high-voltage cable, controls, and power supplies, plus a single pumping system shared between the following equipment units:

1. A simple vacuum chamber for procedure development.
2. A local chamber for longitudinal welds in rings.
3. A local chamber for welding nozzles to rings.
4. An apparatus for girth welds, providing a localized intermediate vacuum environment inside the pressure vessel shell.

MAY 22, 1979

WELD NO. 6: 10 METER Ø BARREL SECTIONS
80 MM THICK 304L STAINLESS STEEL

1. JOINT PREPARATION

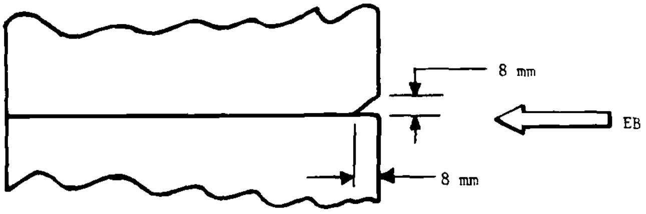

2. EMITTER HISTORY

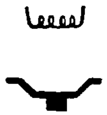

FILAMENT - 136 hours

EMITTER - 8 hours

3. VACUUM LEVELS

Barrel - 2×10^{-3}
Back-up - 2×10^{-3}
EB Gun - 1×10^{-5}

4. WELDING PARAMETERS

Accelerating Voltage = 65KV
Beam Current = 500 MA
Focus = Close to top surface
Oscillation = 35 HZ circular 3.0 MM amplitude
Deflection = 4 CM trailing (8°)
Speed = 15.8 mm/min. = 6.22 IPM

5. WELD WIDTH

5 mm - Parallel Sided

6. AXIAL SHRINKAGE

Measured axial shrinkage after welding - 0.7 mm

FIG. 8—*Sciaky vitry full-scale demonstration.*

Considering the inherently short EB welding time, such a sharing scheme is reasonable in the pressure vessel industry.

The knowledge gained in carrying out the Applications Technology Demonstration Program was employed in specifying the EB system to be utilized with the aforementioned apparatus.

The EG and its power supplies must be integrated with a system to provide logic and process control. Therefore the system utilizes a general purpose minicomputer, interface hardware, and a powerful software package to provide process control, numerical control, digitizing, and quality assurance

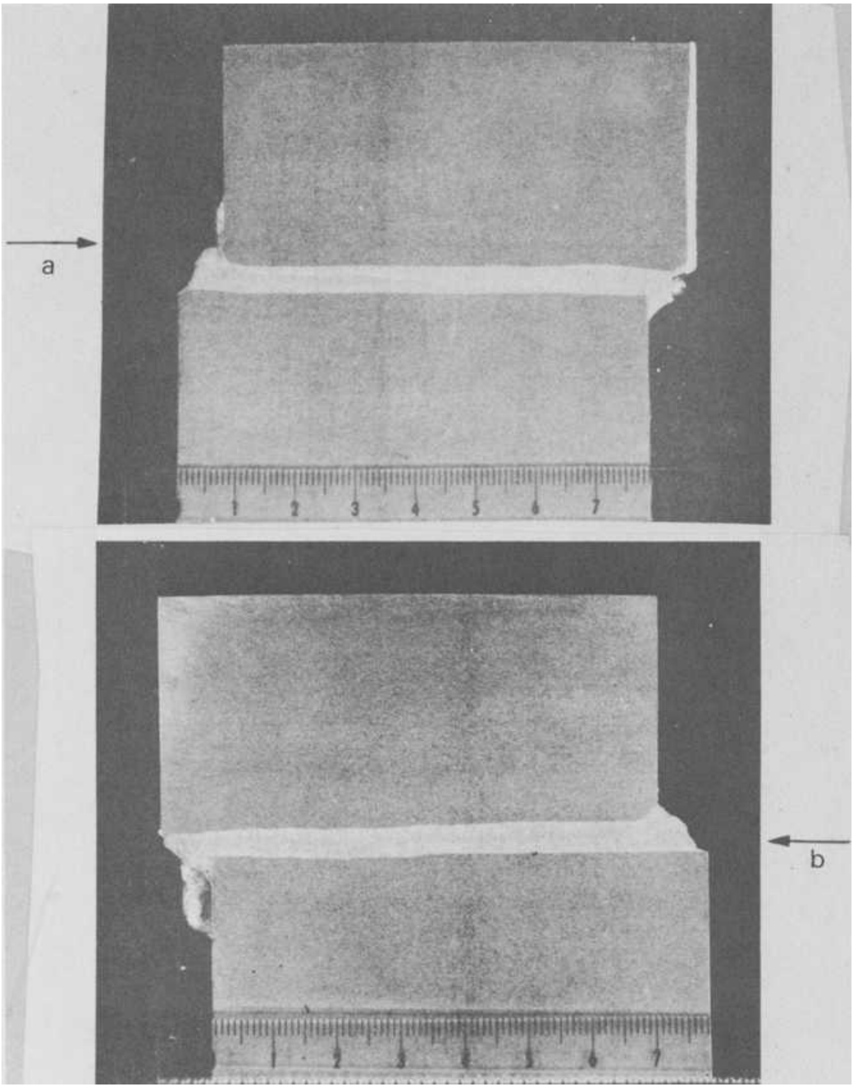

FIG. 9—*Macrographs of EB welds in 80-mm-thick 304L stainless steel:* (a) *square butt joint displaying negative mismatch;* (b) *square butt joint with 6 mm positive mismatch and 0.2 mm gap.*

monitoring in a complete integrated package. The machine sequencing logic is in software. A number of diagnostic programs are provided to simplify system maintenance.

Interactive communications are provided by an alphanumeric keyboard

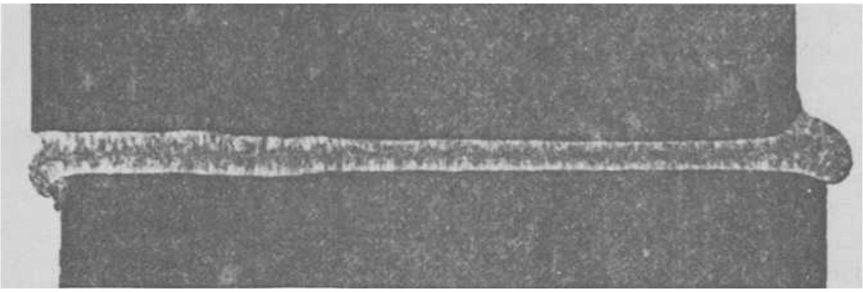

FIG. 10—*Square butt joint displaying positive mismatch.*

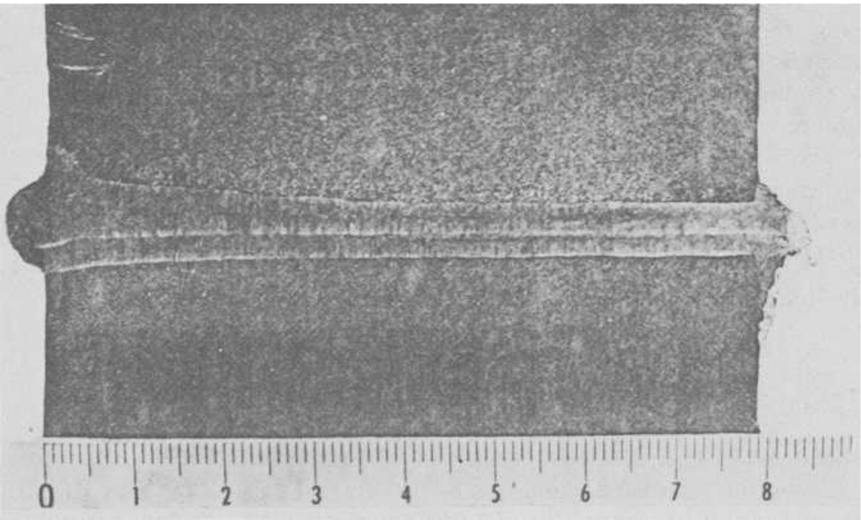

FIG. 11—*Joint rewelded by vertically displacing gun for second pass in order to demonstrate repair technique.*

and a 304.8 mm (12 in.) diagonal screen CRT. Special operator instructions can be included within the part program test and displayed on the CRT.

Some of the capabilities which characterize the control system that are significantly important to the implementation of the manufacturing plan include:

1. Precision control and programmability of welding parameters. The welding parameters (accelerating voltage, beam current, focus, and travel speed) are controlled within ±1 percent of commanded values by closed-loop systems. These parameters are controlled from a stored program with the same precision and repeatability.

2. The tie-in at the overlap area of the penetration and girth welds, and the subsequent slope out of the full-thickness penetration makes special demands on the control system when welding plate of 101.6 mm (4 in.) thickness or greater. The system must provide precision modulation of the beam current and of the beam focus magnitudes, with the relationship between the resultant constantly changing values accurately controlled. With the system provided, these parameters are programmable as a function of travel distance or of time. The rate of parameter value change is programmed by a set of discrete values, with the system providing linear interpolation between the programmed points. Their relationship is controlled with the accuracy of a precision shaft encoder or a crystal clock.

3. The ability to document and store each welding procedure once it has been developed, together with any special instructions text, is important considering the large number of plate thickness and material combinations characteristic of this industry.

4. On-line continuous monitoring of welding parameters for quality assurance, with the capability to document the performance of each weld.

5. The Multi-Beam technique developed for EB heat treating is proving to be beneficial for welding as well. In limited tests to date, this technique has allowed increasing the maximum joint gap dimensions, has provided unique control over weld geometry, and has been beneficial in slope-out.

The proposed manufacturing plan is illustrated in the figures and text that follow.

Figure 12

This drawing illustrates the intermediate vacuum chamber and work carriage, plus the associated multi-use equipment as utilized for procedure development and the production of qualification test plates. Included are:

100-kW EB gun.

EB gun traversing mechanism, including a sliding seal and seal plate, which can be mounted in any one of two positions for vertical, horizontal, or downhand procedure development. In the vertical up position, the EG axis (Z in this setup), in combination with the work table axis (X), provides a circular weld path of selectable diameter and welding speed. Circular interpolation is provided through the control system to simplify keyboard programming of such welding procedures. Position read-out for each axis is provided on the CRT, as are all welding parameters, deflection parameters, etc. The mechanism for translating the EG is self-contained, and can also be utilized as a local vacuum chamber to produce straight line welds of 1.2 m (4 ft) maximum length. The seal slides on a continuous ground surface, is properly lubricated, is protected from environmental contamination, and is not exposed to the intense heat of the welding process.

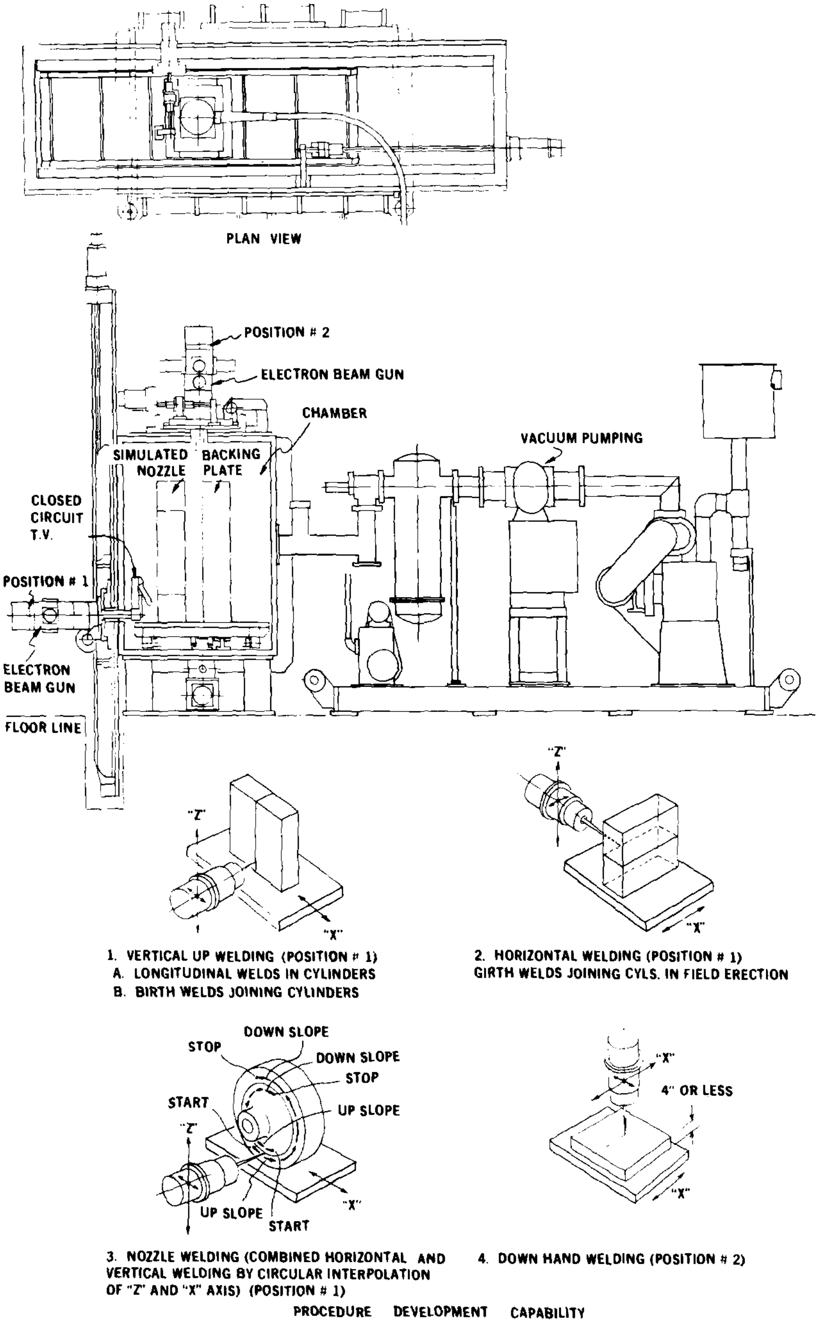

FIG. 12—*Intermediate vacuum chamber for procedure development with portable EB welding and vacuum pumping systems applied.*

Minicomputer-based control system, high voltage tank, and automatic voltage regulator, mounted on a sturdy base fitted with crane hooks. Welding parameters can be commanded and programmed for welding interval and for up and down slope functions. The functions (accelerating voltage, beam current, and focus) are keyboard programmed with manual over-ride precision potentiometers for development convenience. Interpolation between programmed points provides complete control and all possibilities for up-and-down slope procedure development. Multiple time shared EB capability is provided, as are circular and elliptical beam oscillation. The Multi-Beam and the ellipse are steered to maintain any designated orientation with respect to the direction of the weld path. The multiple time shared beam capability provides a new direction in the EB welding process.

TV camera mounted to the EB gun allows observation of the weld pool while the EB weld is in progress. Beam to weld joint alignment is facilitated by the joint scanning function of the system.

Vacuum system is generously sized for this chamber, as it is intended for the production case as well. It will evacuate the chamber to 6×10^{-2} torr on the order of 4 to 5 min. It is also equipped with a large and effective filter to protect the pumps over the long haul.

On the lower portion of the drawing are shown the basic welding procedures to be developed, together with the machine setup associated with each procedure. Each procedure shown ties in with the production welding of heavy-wall pressure vessels in the figures that follow. A fourth procedure, downhand welding of relatively thin plate, can also be practiced with the production apparatus shown.

Figure 13

This drawing illustrates the production utilization of the EB equipment provided with the procedure development chamber for subsequent production application. This is the first step in the welding of the pressure vessel-the longitudinal seams in the cylindrical sections. The pumping system, gun, high voltage cable, console, and control systems are taken from the procedure development chamber.

It is only necessary to add the local vacuum chamber to perform these longitudinal welds.

Figure 14

This drawing shows the welding of nozzles to rings. Again, the same EG, controls and pumps are utilized. The addition of only the local chamber which contains the drive for translating the gun along the circular path is required.

As the local chamber is shown, the nozzle flange size adjustment is from

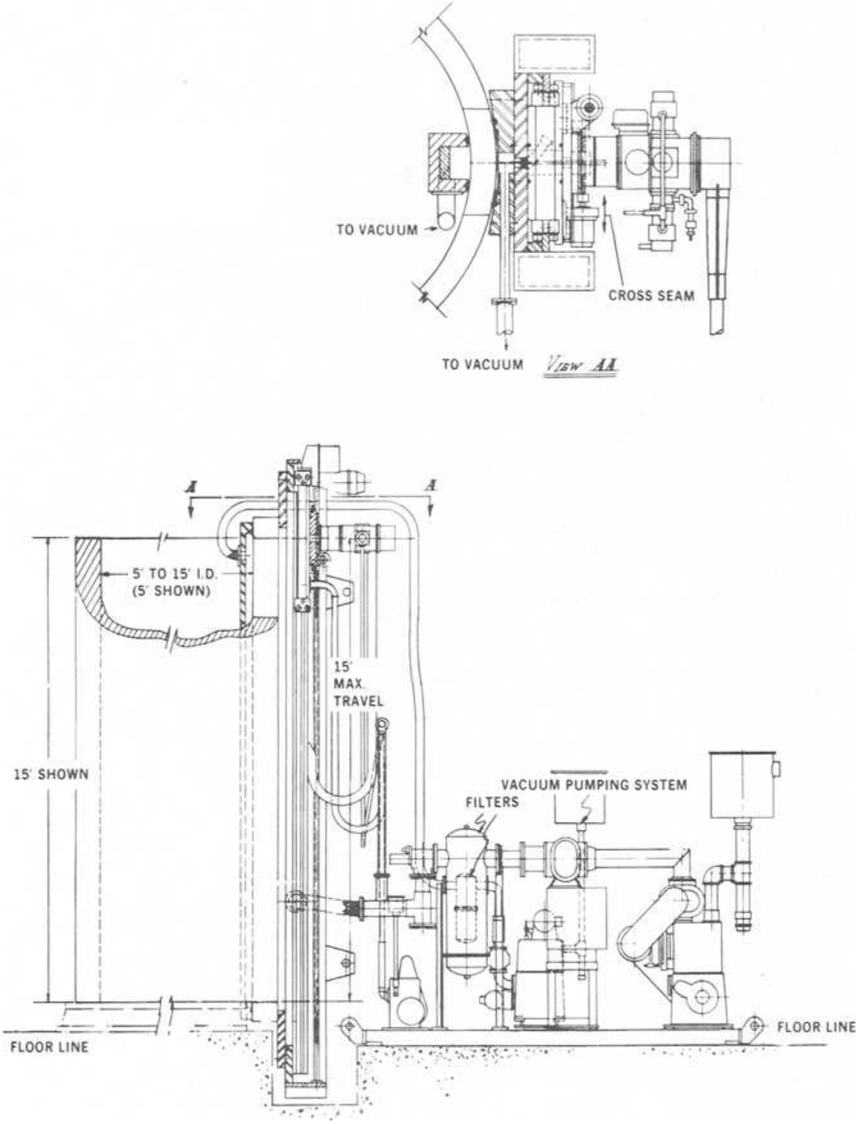

FIG. 13—*Local vacuum chamber for longitudinal weld in rings, utilizing portable EB and vacuum pumping systems.*

101.6 to 762 mm (4 to 30 in.) radius. The path radius is adjusted and the surface contour adapter replaced as the penetration and the ring diameters change from one job to the next. A similar apparatus has already been proved in production application.

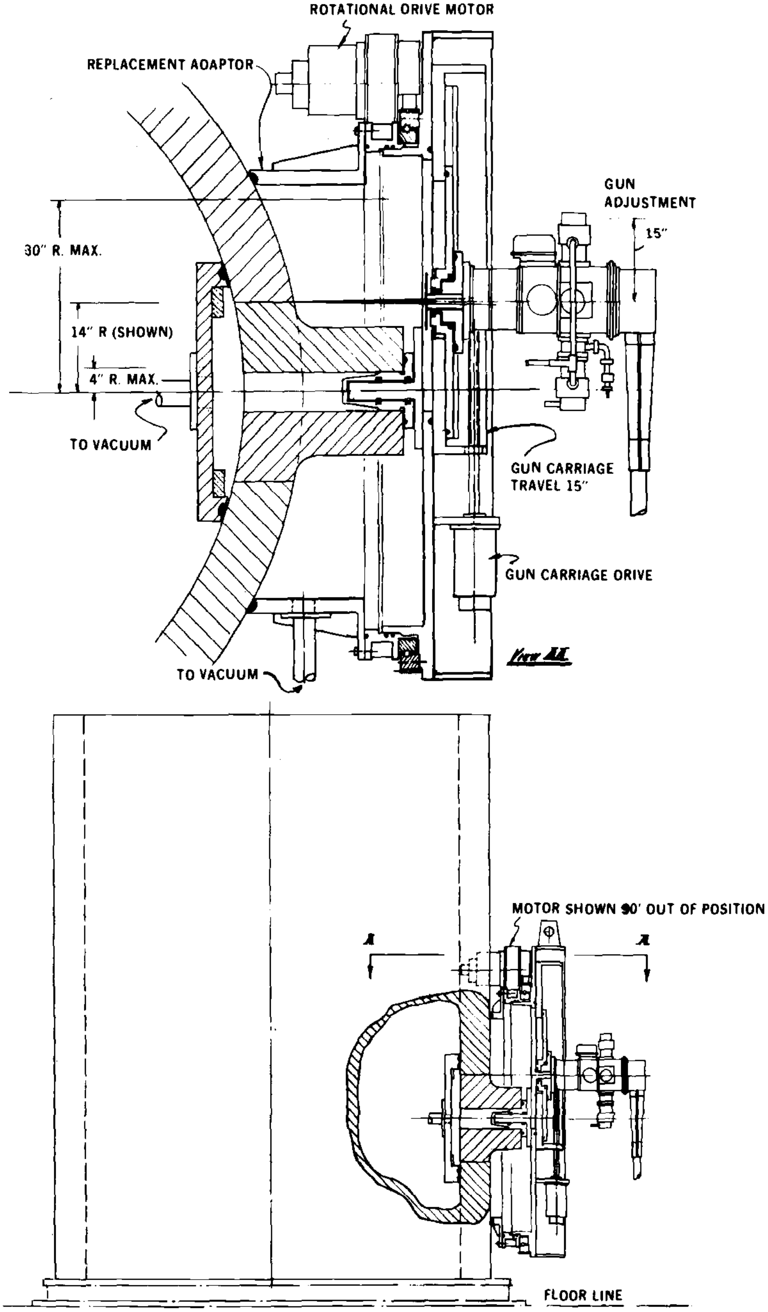

FIG. 14—*Local chamber for welding nozzles to rings.*

Figure 15

Cylindrical sections can be joined to form the shell as previously described with their axes in the vertical plane or with their axes in the horizontal plane.

This drawing is an overall view of the apparatus for producing girth welds with the cylinder axis in the horizontal plane. The cylindrical sections are mounted on existing turning rolls. The welding apparatus accepts the same EB gun and high voltage cable, and after installation in the cylindrical sections, will be plug connected to the existing control and pumping systems.

As the apparatus is shown, the EG is stationary (except for cross-seam travel) in the nine o'clock position, and the cylindrical section is rotated by the rolls to provide travel speed.

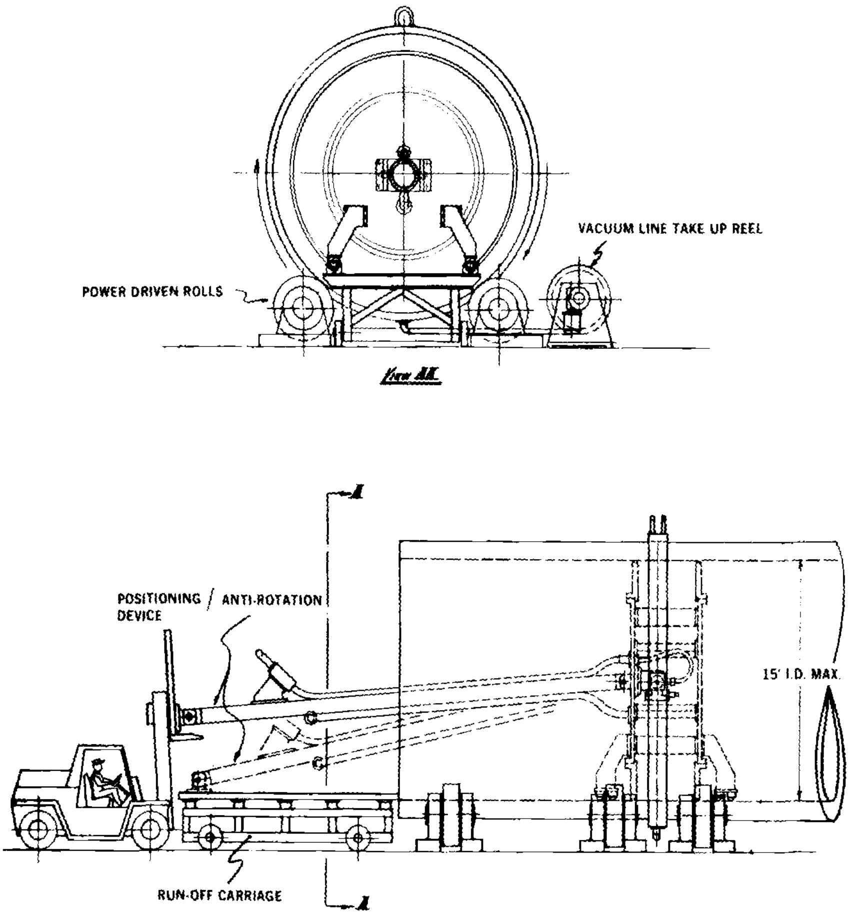

FIG. 15—*Apparatus providing local evacuated enclosure for portable EB system to girth weld rings to produce pressure vessel shell.*

A number of options are available as to the method of positioning the welding apparatus, and of fixing it to take the reaction from the antifriction bearings and O-ring seals while the cylinder is rotating. One possible method is shown.

Figure 16

This drawing, a conceptual floor plan of a pressure vessel fabrication shop, shows how the portable 100-kW EB system is used successively for producing longitudinal welds in cylindrical sections, for welding nozzles to cylinders, and for girth welding cylinder to cylinder. The same EG, power supplies, controls, and vacuum pumping apparatus are utilized for each welding operation as required. Specialized equipment is minimized. There is no need for large vacuum chambers, although large chambers operating at the intermediate vacuum level can exhibit high throughput, and prove economical where production volume is sufficiently high.

Mechanical Properties of Electron Beam Welded 2¼Cr-1Mo Alloy Steel

A program was conducted to verify the feasibility of electron beam welding the 2¼Cr-1Mo alloy steel without preheat or postheat, and to evaluate the resultant weldments for mechanical properties at various degrees of postweld heat treatment.[5]

The program consisted in welding a number of square butt joints in 63.5-mm (2.5-in.)-thick ASTM Specification for Pressure Vessel Plates, Alloy Steel, Chromium-Molybdenum (A 387-79b) Grade 22, which, for reasons of availability, were cut from a heat not melted to special practice. Accordingly, the gas content was relatively high (1920 ppm), as were the sulphur (0.029) and the phosphorus (0.011). Therefore this test program could be considered a "worst case" condition from the materials standpoint, which makes the excellent mechanical properties achieved even more remarkable.

The test plates were electron beam welded by Sciaky in Chicago, and shipped to Houston for postweld heat treatment (PWHT) and mechanical testing by CBI. The welded plates were subjected to the following tests: (*1*) reduced section tensile, (*2*) transverse side bend, (*3*) hardness test (Rockwell C, Vickers), and (*4*) Charpy V-notch. All of these tests were performed on each of the six welded plates, each plate being given a different PWHT. The heat treatments were (*1*) no heat treatment (as-welded); (*2*) minimum PWHT; (*3*) maximum PWHT; (*4*) minimum PWHT, step cool; (*5*) quench

---

[5] Dickenson, J. C., "Evaluation of 2¼Cr-1Mo Welded with the Electron Beam Process," Research Contract R-0363, CB&I Welding R&D Internal Report, 29 Dec. 1980.

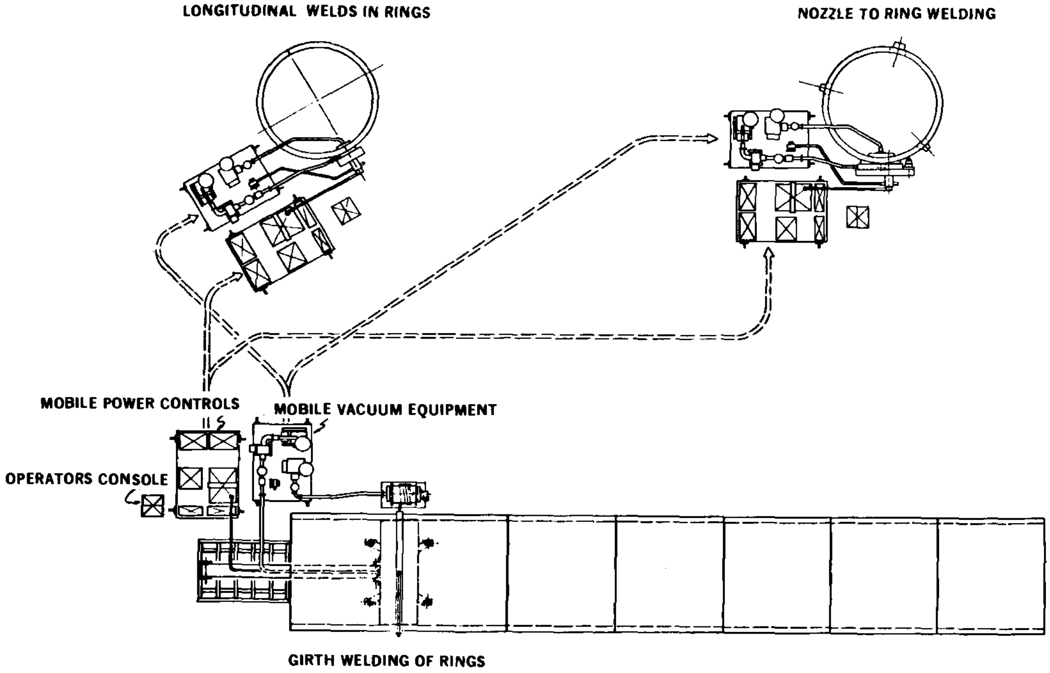

FIG. 16—*Floor plan of pressure vessel fabrication facility illustrating sequential utilization of the portable EB and vacuum pumping systems.*

and temper, minimum PWHT; and (*6*) quench and temper, maximum PWHT.

Figure 17 is a cross section showing the electron beam weld in the test weldment receiving minimum PWHT. Rockwell C and Vickers hardness traverses were made on the top and bottom of such polished and etched weld cross sections in order to measure the base metal, heat-affected zone (HAZ), and weld metal hardness. The specimen subjected to minimum PWHT exhibited a hardness range of 9.5 to 11 R_c; that receiving the maximum PWHT of 8.5 to 9.5 R_c. The quench and tempered specimens showed the following values: with minimum PWHT, a range of 7.5 to 9.0 R_c; with maximum PWHT, a hardness range of 7.0 to 9.0 R_c. The Vickers (30-kg load) tests verify the general trends, but with a smaller degree of scatter, as should be expected for R_c-values lower than twenty. The PWHT plates and the quenched and tempered and PWHT plates exhibited a maximum hardness of 202

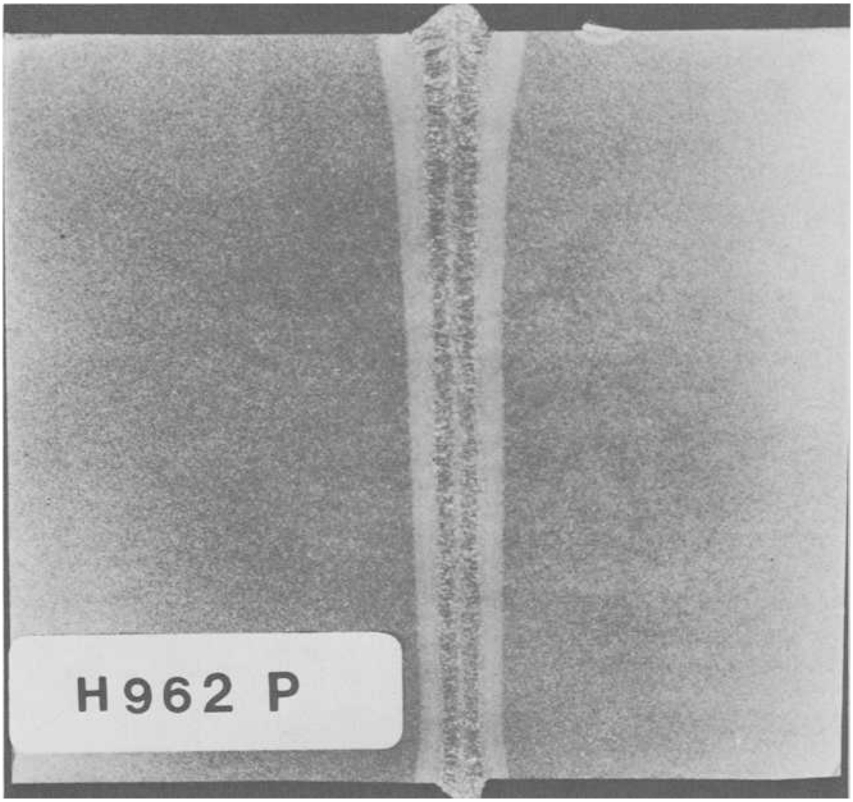

FIG. 17—*Cross section of EB weld in 63.5-mm (2½ in.)-thick 2¼Cr-1Mo. This section has had the minimum PWHT (Nital etch; X2.5).*

D.P.H. and a minimum hardness of 188 D.P.H. The "as welded" test plate showed a HAZ maximum hardness of 318 to 350 Vickers (DPH) while the maximum hardness of the weld metal ranged from 332 to 339 DPH. These data indicate that martensite was present in the "as welded" microstructure.

Metallographic examination revealed that the microstructure is predominantly of a lath type of martensite (Fig. 18). The hardness test data indicate that the PWHT reduces the hardness to a specific value from which no further reduction occurs by either extended PWHT or by quench and temper followed by PWHT. Thus it may be concluded that once an electron beam welded joint has been subjected to PWHT, subsequent PWHT will not soften its microstructure. Since the heat from which the test plates were cut had a carbon content of 0.120 percent, the hardness of all the samples subjected to any of the postweld heat treatments employed in this program would indicate a tempered martensitic microstructure.

The ultimate tensile strength was above 572 MPa (83 ksi) with elongations of above 27 percent for the reduced section tension tests of all the PWHT test plates. The transverse side bend tests for all the test plates were satisfactory.

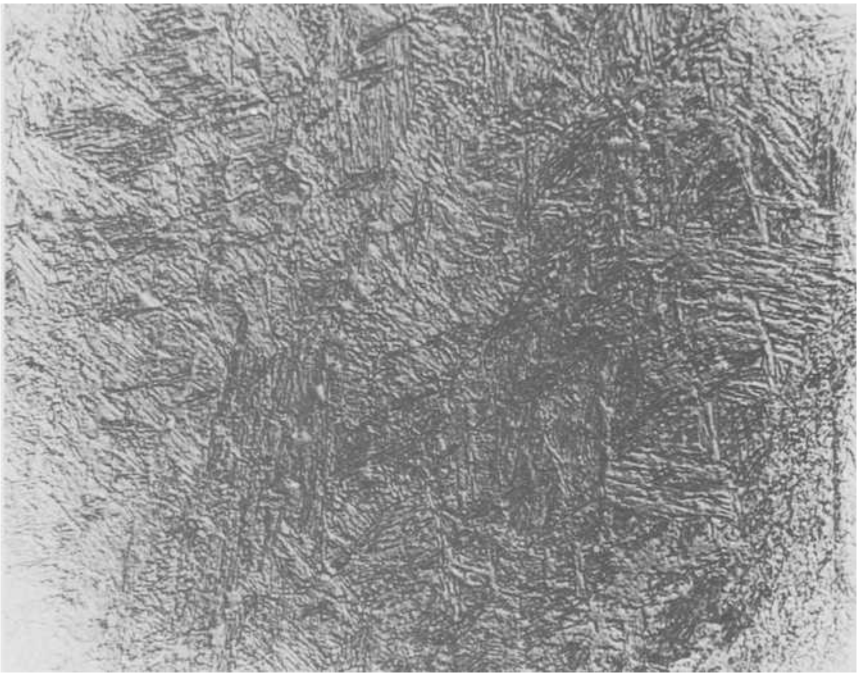

FIG. 18—*Weld metal microstructure of the "as welded" sample. The structure is one of lath martensite.*

Charpy V-notch impact tests were taken at 1.6 mm (1/16 in.) depth, ¼ *T* depth, and ½ *T* depth. The data are summarized in Table 1 for each of the PWHT conditions.

Alloy steels, such as the 2¼Cr-1Mo tested in this program, are subject to temper embrittlement, a phenomenon whereby the notch toughness is considerably reduced. The degree of temper embrittlement experienced by the EB welded joints was measured by a combination of three values: T1, T2, ΔT.

T1 is the temperature at which 54 J (40 ft·lb) of Charpy impact value is reached after the test specimen has been subject to a minimum PWHT. T2 is the temperature at which the 54 J (40 ft·lb) transition is achieved after the test plate is given a minimum PWHT plus a step cool. The difference between these two values is ΔT. This investigation yielded the following values:

$$\mathrm{T1} = -107^\circ\mathrm{C}\ (-160^\circ\mathrm{F})$$

$$\mathrm{T2} = -50^\circ\mathrm{C}\ (-58^\circ\mathrm{F})$$

$$\Delta\mathrm{T} = 57^\circ\mathrm{C}\ (102^\circ\mathrm{F})$$

Temper embrittlement acceptance requires fulfilling one of the following relations:

$$\mathrm{T2} \leq -29^\circ\mathrm{C}\ (-20^\circ\mathrm{F})$$

$$\mathrm{T1} + 2\tfrac{1}{2}\,\Delta\mathrm{T} \leq 38^\circ\mathrm{C}\ (100^\circ\mathrm{F})\ (\text{socal factor})$$

$$\mathrm{T1} + 1\tfrac{1}{2}\,\Delta\mathrm{T} \leq 10^\circ\mathrm{C}\ (50^\circ\mathrm{F})$$

TABLE 1—*Impact test data.*

Test Plate Condition	54 J (40 ft·lb) Transition Temperature, °C (°F)	Maximum Impact Value	
		J (ft·lb)	at °C (°F)
As welded	−8 (18)	105 (78)	79 (175)
Minimum PWHT	−107 (−160)	247 (182)	−1 (30)
Maximum PWHT	−79 (−110)	235 (173)	−34 (−30)
Minimum PWHT, step cool	−50 (−58)	194 (143)	32 (90)
Quenched and tempered, minimum PWHT	−111 (−168)	142 (105)	−73[a] (−100)
Quenched and tempered, maximum PWHT	−106 (−158)	157 (116)	−90[a] (−130)

[a] The maximum testing temperature for these specimens was −73°C (−100°F).

The electron beam welds passed all of the aforementioned requirements:

$$T2 = -50°C\ (-58°F)$$

$$T1 + 2\frac{1}{2}\,\Delta T = 35°C\ (95°F)$$

$$T1 + 1\frac{1}{2}\,\Delta T = -21°C\ (-7°F)$$

Since the test plate material was not melted to special temper embrittlement practices, this indicates very satisfactory performance for large pressure vessel fabrication of EB welded butt joints in 2¼Cr-1Mo material. It should be recalled that neither preheating nor postheating was employed while electron beam welding the test plates.

Conclusion

An integrated manufacturing plan for applying EB welding for the fabrication of pressure vessels has been presented. The plan encompasses procedure development and qualification, longitudinal welding of rings, penetration to ring welding, and girth welding of rings with a single EB welding and vacuum pumping system. Specialized, yet flexible local chambers avoid the need for very large vacuum chambers. Electron beam welding is accomplished at a vacuum level in the range of 5×10^{-3} to 6×10^{-2} torr to preclude the need for diffusion pumps and excessively long pumpdown times.

The substantial cost savings that can be realized by utilizing EB welding to replace conventional fusion welding was mentioned in the introduction. In addition to such cost advantages, EB welding offers several less obvious benefits for pressure vessel fabrication.

1. *Hydrogen-Induced Weld Metal and Heat-Affected Zone Cracking*—Pressure vessels are designed to stringent code criteria, resulting in very generous safety factors. Accordingly, the chemistry of the constructional steels is enriched, and the resultant alloys are heat treated in order to provide sufficiently high physical properties to permit a practical design. Such steels are subject to weld metal and heat-affected zone cracking as a result of hydrogen pickup during conventional fusion welding. There can be no hydrogen pickup in even an intermediate vacuum EB welding process.

2. *Preheating*—Many of the constructional steels for pressure vessels require preheating for successful conventional fusion welding. Sciaky has successfully EB welded ASTM A 533 Type B and 2¼Cr-1Mo without preheat. Babcock & Wilcox has shown that 516 Grade 70 steel can be EB welded without preheating. These steels must be preheated prior to welding by submerged arc or stick electrode methods. The elimination of preheating

represents a cost and energy savings. It is probable that preheating can be eliminated while EB welding many of the other alloy steels of interest.

3. *Welding Position*—EB welding of plate thicknesses in excess of 102 mm (4 in.) is constrained to the horizontal and vertical positions. It cannot be applied to the welding of heavy plate sections in the downhand position. Submerged arc welding is usually constrained to the downhand position. This latter limitation eliminates submerged arc welding for many field erection tasks, thus giving an additional economic edge to EB welding.

4. *Weld Geometry*—The geometry of the EB weld, that is, essentially straight parallel sided, is favorable when the weld is placed in a high-stress field. The geometry of conventional welds, that is "V" or "hour-glass" shaped, is unfavorable under these conditions.

5. *Joint Preparation*—Square butt joints are less expensive to prepare and far simpler to align than are double "V" or "J" groove joints.

6. *Weld Repair*—Weld repairs are effected by simply re-welding the joint. Grinding out the defective weld is not necessary or beneficial.

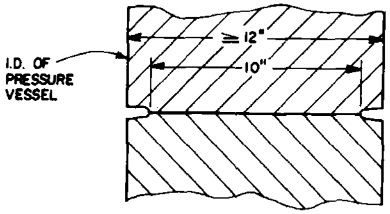

1. JOINT PREPARATION

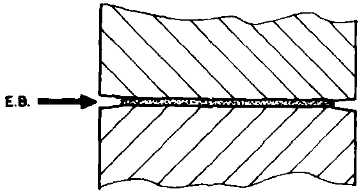

2. EB WELD 10" LAND IN ONE PASS

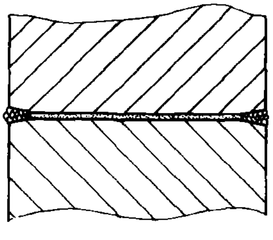

3. COMPLETE JOINT BY FUSION WELDING

FIG. 19—*Method for composite welding 305 to 457 mm (12 to 18 in.) thick-wall pressure vessels.*

7. *Quality Assurance*—EB welding parameters are inherently amenable to precise control and repeatability. Therefore, with the computer-based control system, the welding procedure for a given combination of alloy and thickness, once developed, is documented and can be filed for later retrieval whenever the same combination repeats. Furthermore, the system has the ability to document the performance of each weld in hard copy, thus providing permanent quality control records for every EB welded pressure vessel.

8. *Environmental Considerations*—EB welding takes place in a vacuum. Any gases liberated or evolved from the metal pass through the vacuum pumps and are exhausted to the outside after passing through a filter. Such gases are necessarily in extremely small quantities, since they must evolve from the metal itself, as no organic material containing flux or electrode covering is utilized in the process. Metal vapors plate on surfaces inside the vacuum enclosure. Consequently, no airborne particles or metallic aerosols are possible.

9. *Mechanical Properties*—In the case of the specific alloy of interest, 2¼Cr-1Mo, superior mechanical properties are exhibited by EB butt welds produced without preheat or postheat and subjected to PWHT.

10. *Limitations*—This portable EB welding system was conservatively designed to butt weld a maximum of 254-mm (10 in.)-thick alloy steel plate in one pass. Although this limitation will probably be exceeded in practice, it is unlikely that the maximum capacity will be stretched beyond 120 percent. Nevertheless, EB welding can be practically and economically applied in welding pressure vessels of, say, 406 mm (16 in.) wall thickness by the method shown in Fig. 19.

V. M. Calvo,[1] *R. R. Ruiz,*[2] *and Yoshito Mitani*[2]

Case Study on Hydrocracking Reactor Inspection after an Emergency Shutdown

---

REFERENCE: Calvo, V. M., Ruiz, R. R., and Mitani, Yoshito, "**Case Study on Hydrocracking Reactor Inspection after an Emergency Shutdown,**" *Application of 2¼Cr-1Mo Steel for Thick-Wall Pressure Vessels, ASTM STP 755,* G. S. Sangdahl and M. Semchyshen, Eds., American Society for Testing and Materials, 1982, pp. 326-339.

ABSTRACT: Since 1973 hydrocracking reactors have been operating in the oil refinery of Salamanca, Mexico. These reactors are composed basically of 2¼Cr-1Mo steel, overlaid with 347 stainless steel, of 262 mm total thickness. In early 1979 one of these reactors experienced an emergency shutdown caused by a fire originating in the recirculation pump. In this paper several observations made during a field inspection are presented. It was found by ultrasonic methods that some parts of the reactor suffered overlay separations, including a total of about 12 percent of the surface area on the first ring. Metallographic analysis was carried out to find whether the material had suffered damage due to the emergency cooling conditions. Possible causes of the overlay separation and its behavior after re-starting operations are reported.

KEY WORDS: nondestructive testing, ultrasonic tests, inspection, calibration, test blocks, steels, pressure vessels

The emergency shutdown due to a fire at the finishing unit originated with a large leakage of hydrogen and hydrocarbons at the bottom of the reactor. It raised an important question as to the reactor's safety. According to the technical report, the shutdown procedure was as described in the following section. The temperature profile was as shown in Fig. 1.

Shutdown Procedure

In approximately 20 min the reaction section was depressurized from 20 MPa down to 0.5 MPa, with the temperature at approximately 420°C. These conditions were maintained for 3 h. Cooling oil at 205°C was introduced to

---

[1] Coordinator of Inspection, RIAMA-PEMEX, Salamanca, Mexico.
[2] Senior Lecturer, ESIQIE-IPN, Mexico City, Mexico.

maintain the temperature below the ignition temperature of the cracking products, which were still leaking.

The temperature at the bottom of the reactor was 235°C 19 h later. Under this condition, with a pressure of 0.9 MPa, outgassing took place for approximately 150 h, followed by steady cooling for 45 h, reaching the temperature of 86°C while the pressure remained constant. Then, after repair of the damage, which was located at the seal oil cooling coil of the recirculation pump, the temperature was raised to 300°C and maintained for 72 h in order to complete the hydrogen outgassing. Since the leaking oil ignited in contact with the air, water was sprayed by fire hoses until the temperature was 86°C. Before starting operation again the following questions had to be considered:

1. Did the reactor suffer any damage due to the aforementioned shutdown procedure?
2. Is it possible to determine the underlying cause?
3. Does the damage, if any, allow a safe operation?

With these questions in mind, in addition to the visual and dye penetrants inspection, ultrasonic inspection was employed. Based on these results the effects of temper embrittlement, hydrogen-assisted cracking, and fracture mechanics analysis were considered.

Ultrasonic Inspection

Calibration Block for Ultrasonic Testing

In accordance with the ASME Code, Section VIII, Division 2, 1968 ed., the manufacturer carried out an ultrasonic inspection at the time of construction, using a reference test block containing a 19-mm ($^{3}/_{4}$-in.)-diameter flat-bottomed hole machined in the base metal to the overlay/base metal interface. For the present inspection, another reference test block was prepared. Originally, the manufacturer supplied a test block with 9.5-mm ($^{3}/_{8}$-in.) reference holes without an overlay (which was overlay welded in the workshop later). For further reference, several 1.6-mm ($^{1}/_{6}$-in.) holes and 2.4-mm ($^{3}/_{32}$-in.) slits at different depths were machined as shown in Fig. 2 to obtain the standard attenuation curves (Figs. 3 and 4) and standard reflection (Fig. 5*a*). For the overlay inspection, the 19-mm ($^{3}/_{4}$-in.) hole was machined from the overlay side to the interface, for which the back reflections were observed, depending on the area scanned by a longitudinal beam transducer of 25.4 mm (1 in.) diameter with a frequency of 2.55 MHz.

Field Inspection

The areas inspected are indicated in Fig. 6. For comparison, five zones (A to E) were chosen: of these, C and D were the most rapidly water cooled;

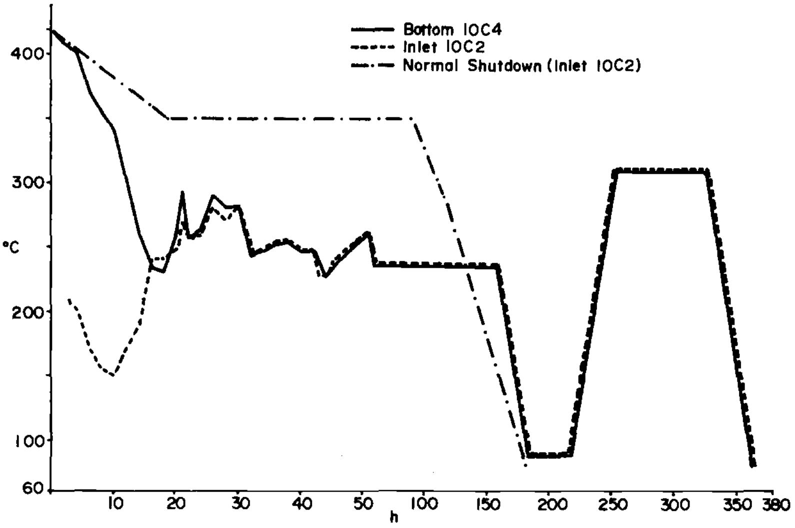

FIG. 1—*Temperature control during the shutdown procedure.*

these zones include the bottom head and the welds at the nozzles. B is the intermediate neighboring area, A is the top zone of the reactor, and E is the reference zone. The inspection was carried out mainly from the outside diameter (backing steel side) with a longitudinal beam probe, accompanied by an angled beam probe for complementary inspection in several areas.

The inspection results are summarized as follows:

1. There was no significant defect in the wall which could be considered a crack.

2. In Zone C, a defect pattern similar to the calibration block was obtained in several areas (Fig. 5*b*). It is quite clear, comparing patterns C and D in the same figure, that the back reflection due to the inside wall disappeared; that is, the back reflection came from the overlay-base metal interface, which is indicative of overlay detachment.

From these results it can be concluded that the main damage suffered by the reactor was the localized overlay detachment in Zone C, amounting to around 12 percent and whose distribution is shown in Fig. 7.

As the detailed topography in Figs. 8 and 9 shows, the separation is located at the interface between the overlay and the base metal. The previous visual and penetrants inspections of the inside wall (overlay side) revealed that no crack was present in these areas, which confirms that only overlay detachment occurred and that the overlay still provided a protective barrier. This evidence may be very favorable for a safe operation. In addition, it is quite interesting to note that the detachment has not occurred in other areas

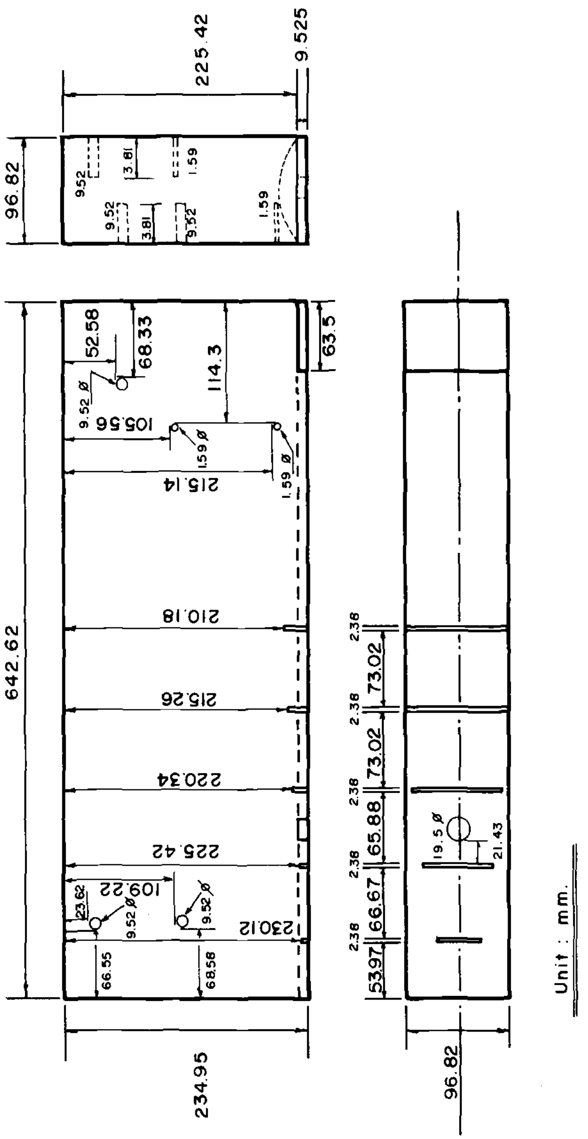

FIG. 2—*Calibration block for ultrasonic inspection.*

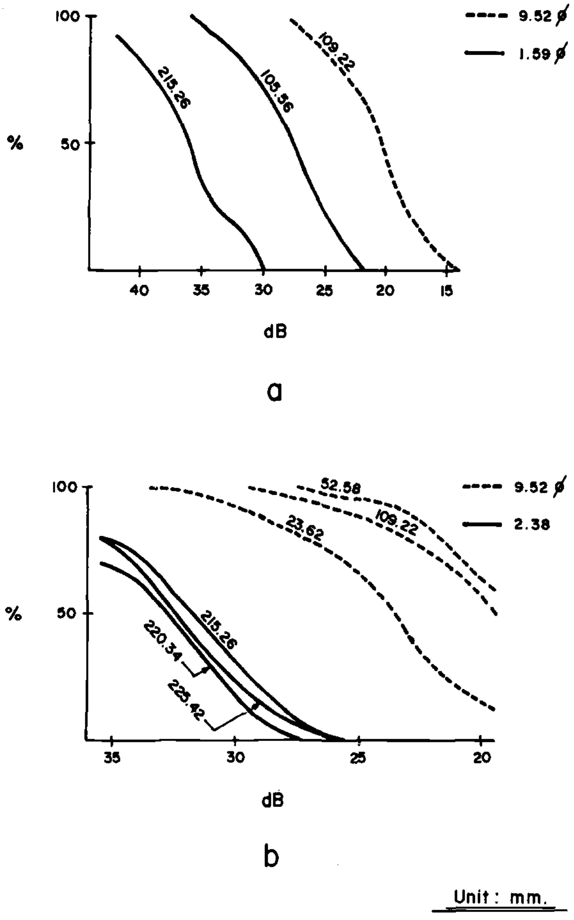

FIG. 3—*Reference attenuation curves with longitudinal beam.*

except for a few points in Zone E. This fact suggests water cooling by spraying with hoses was the reason for this detachment; in other words, the bimetallic stresses due to the drastic water cooling spray, which was employed mainly in this zone, might have induced the separation.

Discussion

It has been pointed out that the principal problems to be considered in this type of reactor are temper embrittlement of 2¼Cr-1Mo steel and hydrogen-assisted cracking due to hydrogen charged under operation with high hydrogen content atmospheres, temperature, and pressure. In both cases, it is important to take into account the real or potential crack size, which may

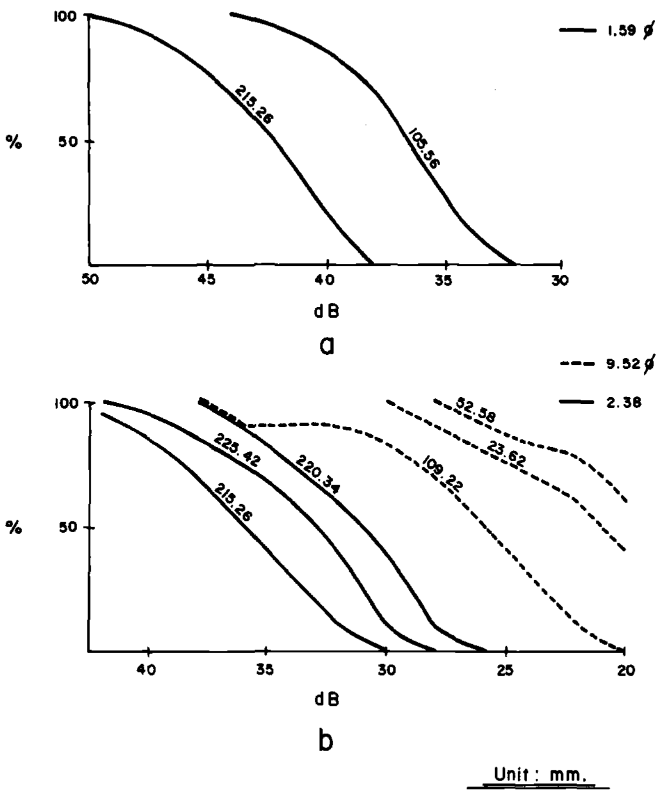

FIG. 4—*Reference attenuation curves with angled beam.*

be called a critical crack size. According to the present inspection, the existence of such crack-like defects have not been detected, but circumferential defects due to overlay detachment were evident. The following safety analysis is based on the assumption of the existence of a crack; also, the possible cause of overlay separation is considered.

Temper Embrittlement

It is now widely accepted that the 2¼Cr-1Mo steel is susceptible to temper embrittlement. Its Charpy V-notch (CVN) impact upward shift of energy transition temperature, after exposure to temperatures in the range of 400 to 480°C, can be as high as 150°C to a maximum 54 J (40 ft·lb) transition temperature of 175°C. As extreme examples, Sawada et al [*1*][3] presented two cases of 2¼Cr-1Mo steel that was temper embrittled after long-time

---

[3] The italic numbers in brackets refer to the list of references appended to this paper.

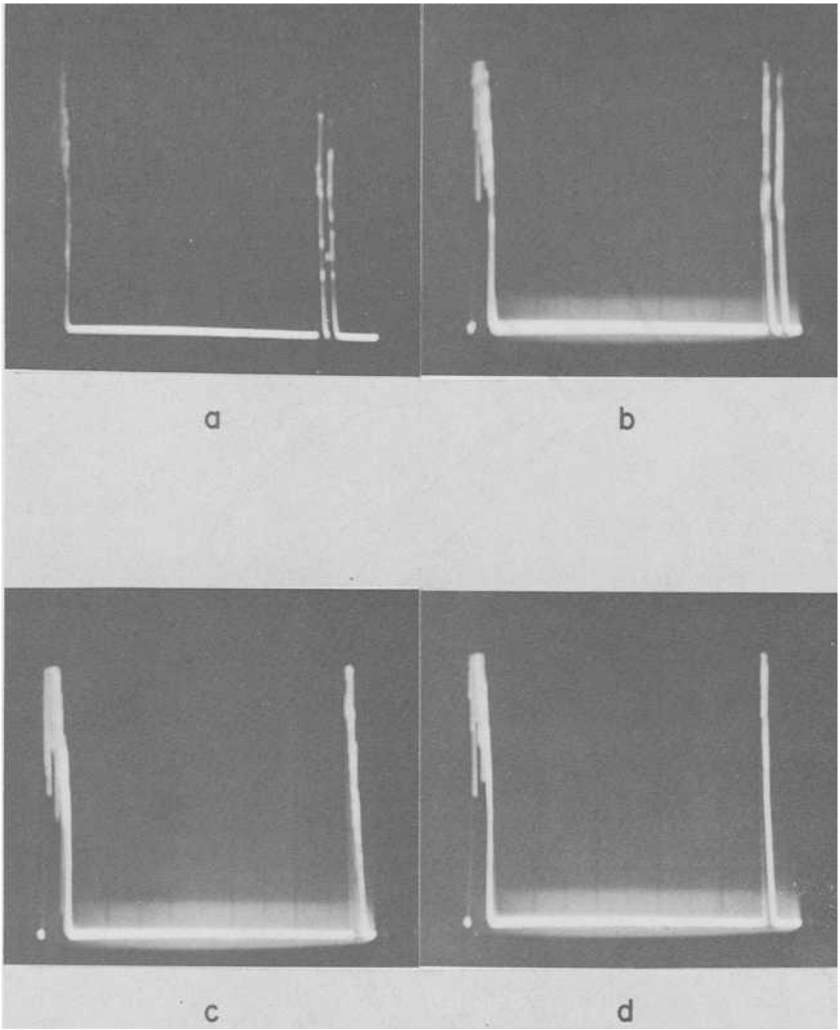

FIG. 5—*Reflection patterns of overlay separation.*

hydrocracking service in the range of 349 to 449°C. In these cases, the shift in the 54 J (40 ft·lb) CVN transition temperature was about 90 and 115°C after 30 000 and 60 000 h, respectively.

Despite the fact that Reactor 10C-2 may be temper embrittled to some degree after 32 000 h service, no cracking was found on inspection following the emergency shutdown. The major reason for this is that the reactor pressure was reduced to a pressure of 0.5 MPa before the reactor was allowed to cool below 175°C, which is in accordance with ASME Code procedures to

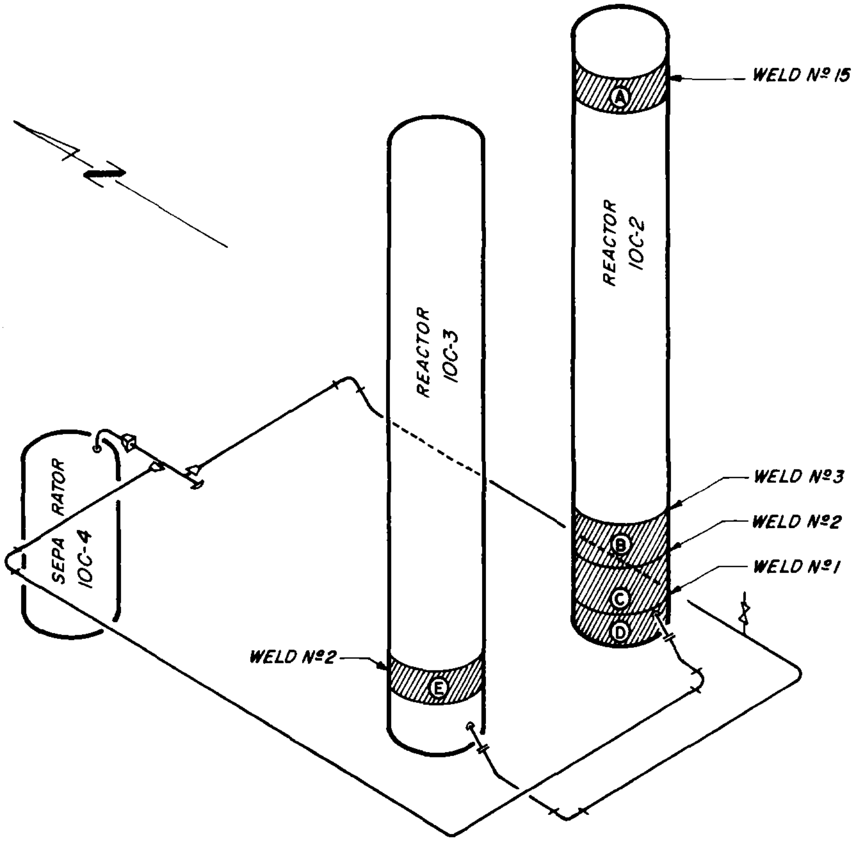

FIG. 6—*Schematic representation of field inspection zones.*

avoid massive brittle fracture in pressure vessels [2]. With reduced pressure, stresses are significantly reduced in the vessel, and brittle fracture does not occur even in situations when the toughness of the steel may be degraded by temper embrittlement. Watanabe et al [3] have proposed a method of fracture-safe analysis for temper embrittled materials that follows the method of pressure reduction below a minimum temperature, which is generally practiced in regard to operation of hydrocracking reactors. It is interesting to note that the microphotographs do not reveal any evidence of microscopic changes due to temper embrittlement (Fig. 10).

Hydrogen Effects

A major concern in an emergency shutdown is the possibility that an accumulation of hydrogen will cause cracking when the reactor is rapidly cooled. A reactor shutdown under normal circumstances involves slow cooling or

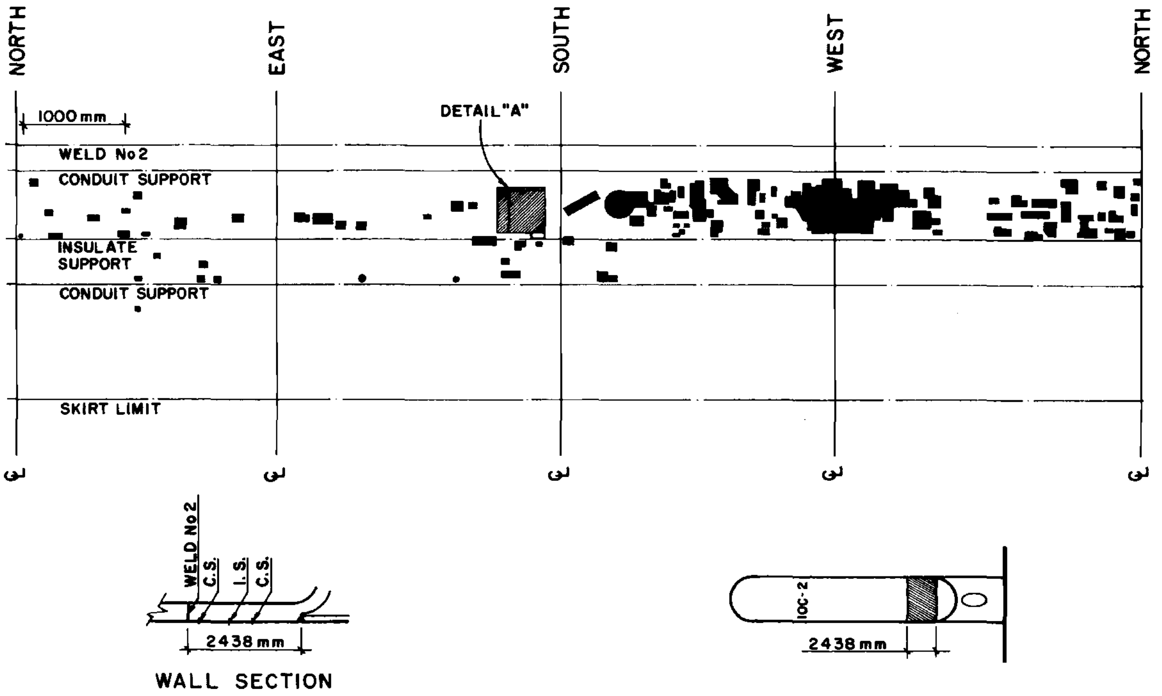

FIG. 7—*Distribution of overlay separation of Zone C.*

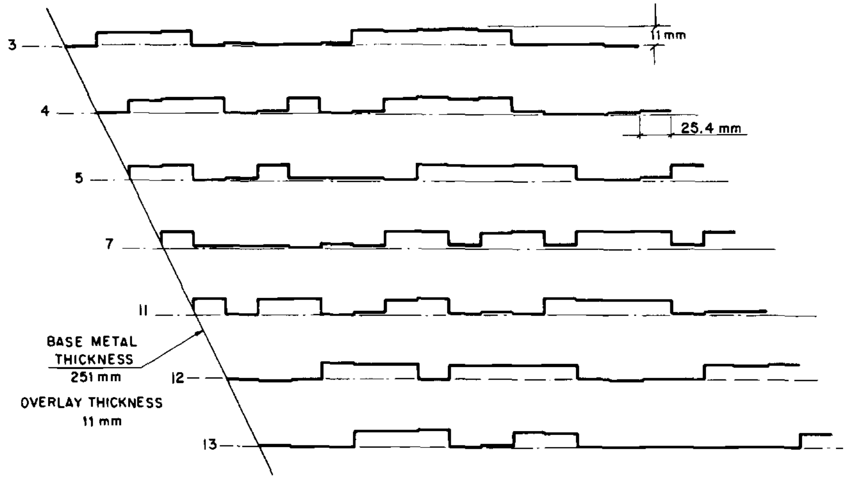

FIG. 8—*Topography of overlay separation of Detail A in Fig. 7.*

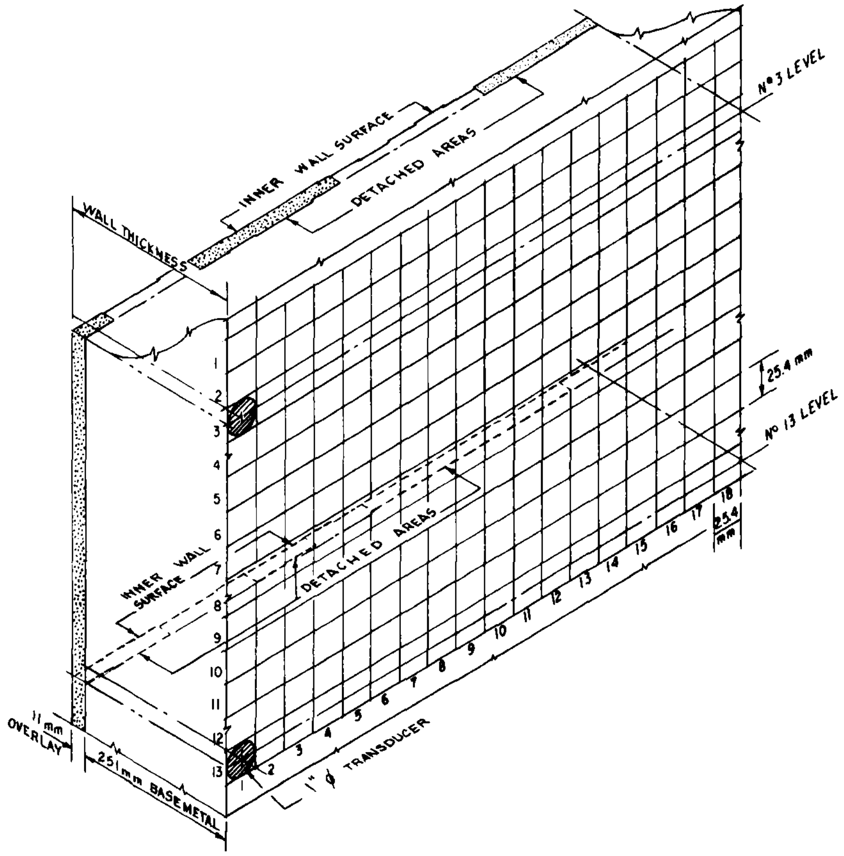

FIG. 9—*Overlay detachment profile at No. 3 and No. 13 levels (scale: none; Detail A of Fig. 7).*

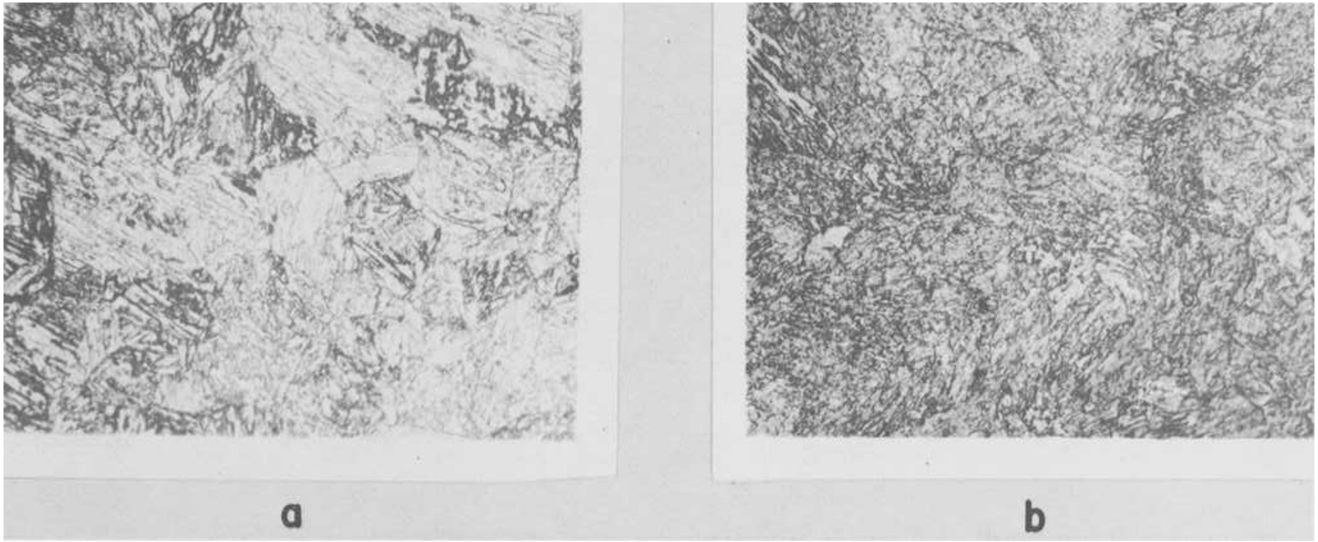
a
b

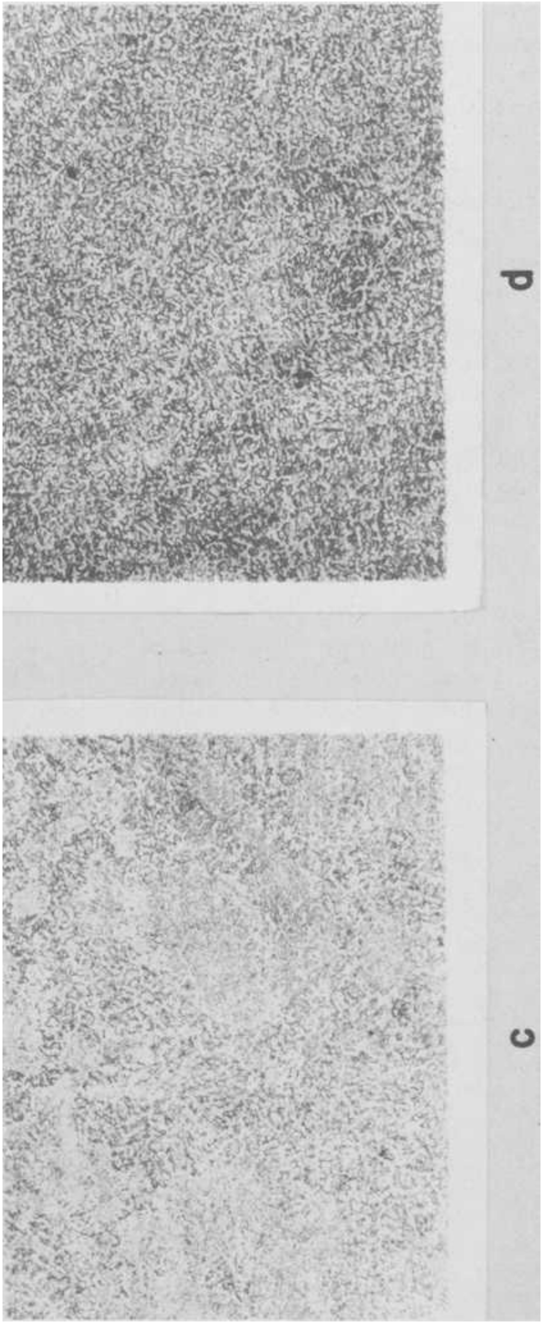

FIG. 10—Photomicrographs of Reactor 10C-2 after the accident.

sometimes a hold period at elevated temperature under reduced pressure to outgas hydrogen dissolved in the steel during operation. As shown in Fig. 1, during the emergency shutdown the reactor reached a minimum temperature of 150°C in about 10 h, which would not have been sufficient time to fully outgas the reactor. Results of the ultrasonic inspection, as mentioned before, found that no significant cracking occurred in the reactor despite the rapid cooling experienced.

Kerr et al [*4*] studied the susceptibility to hydrogen cracking of 2¼Cr-1Mo steel at different strength levels. They found that 2¼Cr-1Mo steel with UTS below 689 MPa (100 ksi) was resistant to cracking due to hydrogen, while the same steel with UTS above 827 MPa (120 ksi) was highly susceptible to cracking by hydrogen. Because the UTS of 2¼Cr-1Mo steel in Reactor 10C-2 is 641 MPa (93 ksi), from Table 1, it is not surprising to find no cracks even after the emergency shutdown. This finding demonstrates that when large flaws do not exist in a vessel prior to shutdown, 2¼Cr-1Mo steel with UTS below 689 MPa (100 ksi) is almost immune to hydrogen cracking, in agreement with the findings of Kerr et al.

Overlay Separation

Conditions are encouraging to date for a safe re-starting operation in spite of the overlay separation, whose origin has not been discussed. Vinckier and Pense [5] reviewed underclad cracking in pressure vessel components, which is generally produced during postweld heat treatment due mainly to susceptible microstructure, a critical residual stress pattern, and a thermal treatment

TABLE 1—*Technical data of Reactor 10C-2.*

Dimensions	
Internal shell diameter thickness	2905 mm
Base metal 2¼Cr-1Mo	251 mm
Overlay 309 and 347	11 mm
Mechanical Properties—Shell C	
Yield stress	500 MPa
UTS	641 MPa
Elongation in 50.8 mm	26.6%
Reduction of area	75.7%
Charpy V-notch (CVN) at 7°C	310 J
Operation Conditions	
Pressure	20 MPa
Hydrogen partial pressure	15 MPa
Temperature	425°C
Statistics	
Total hours of operation[a]	32 376
Total number of shutdowns	50

[a] Including the recirculation period under the conditions: temperature at 350 to 380°C; pressure at 19 MPa; natural gas.

between 600 and 650°C. Since laboratory tests show that 2¼Cr-1Mo steel clad with austenitic steel is not susceptible to cracking under normal conditions, it is necessary to investigate under similar operational conditions. Observing the distribution of the overlay separation, one might say that the main cause of its localized appearance seems to be the drastic outer surface cooling by water.

Conclusions

The reactor wall is in good condition for operation in spite of the localized overlay separation. It is necessary to study further the cause of overlay separation under fully operational conditions and to continue monitoring its behavior during further cycles of operation.

Acknowledgments

The authors wish to thank J. J. Corres, General Superintendent, RIAMA-PEMEX, for permission to publish this work. They also acknowledge the cooperation of A. Murguiondo and H. Islas, Superintendents, and the technical staff of RIAMA-PEMEX. Thanks are also due M. Pardo-Salas of IMP for providing the metallographic data.

References

[*1*] Sawada, S., Ohhashi, T., Okamoto, M., and Watanabe, J., *Ductility and Toughness Considerations in Elevated Temperature Service,* ASME/MPC, New York, 1978, pp. 167-186.

[*2*] ASME Boiler and Pressure Vessel Code, Paragraph AD-155, Sect. VIII, Div. 2, American Society for Mechanical Engineers.

[*3*] Watanabe, J., Murakami, Y., Yoshito, Y., Iwadate, T., and Mima, S., "A Fracture Safe Analysis of Pressure Vessels Made of 2¼Cr-1Mo Steel," Paper No. 126, presented at Corrosion/76, NACE, 22-26 March 1976, Houston, Tex.

[*4*] Kerr, J. G., Coombs, J. W., Purgalis, P., and Olsen, R. J., in *Proceedings of Division of Refining,* American Petroleum Institute, Vol. 52, Midyear Meeting, 8-11 May 1972, New York, pp. 890-905.

[*5*] Vinckier, A. G. and Pense, A. W., "A Review of Underclad Cracking in Pressure-Vessel Components," Welding Research Council Bulletin No. 197, Aug. 1974.

Studies of Heat Treating and Temper Embrittlement of $2^{1}/_{4}$Cr-1Mo Steel

Tsuguyasu Wada[1] *and G. T. Eldis*[2]

Transformation Characteristics of 2¼Cr-1Mo Steel

REFERENCE: Wada, Tsuguyasu and Eldis, G. T., **"Transformation Characteristics of 2¼Cr-1Mo Steel,"** *Application of 2¼Cr-1Mo Steel for Thick-Wall Pressure Vessels, ASTM STP 755,* G. S. Sangdahl and M. Semchyshen, Eds., American Society for Testing and Materials, 1982, pp. 343-362.

ABSTRACT: For application to heavy-thickness plates, steels based on the 2¼Cr-1Mo system should have sufficient hardenability to provide the appropriate microstructure and mechanical properties. This investigation was undertaken to evaluate the effects of several composition variations on the hardenability of 2¼Cr-1Mo steel, and thereby to provide useful information in applying this steel in sections up to 400 mm thick. Continuous cooling transformation diagrams were determined by dilatometry for variations of carbon, manganese, and minor additions such as nickel and vanadium. The critical cooling rate for polygonal ferrite formation, K_f, defined as the slowest rate at which the material can be cooled and still result in a microstructure free of polygonal ferrite, is considered the parameter of greatest significance. In terms of the average cooling rate between 800 and 500°C, K_f for 2¼Cr-1Mo steels containing 0.11 to 0.13 percent carbon is approximately 30°C/min; this corresponds to the cooling rate at the center of a 200-mm-thick plate during water quenching. Variations in carbon and manganese content and in the content of minor elements such as nickel significantly affect K_f. Vanadium does not significantly increase hardenability (decrease K_f), but it does increase temper resistance and hence the final strength after tempering and stress relieving. The average cooling rate (800 to 500°C) at the center of a 400-mm-thick plate during water quenching is about 8°C/min. A 2¼Cr-1Mo steel on the high side of the ASTM A 387 Grade 22 composition range and containing about 0.5 percent nickel has a fully bainitic microstructure after cooling at this rate. Maximum hardenability was observed in an experimental steel containing 0.15 percent carbon, 0.60 percent manganese, 2.37 percent chromium, 1.10 percent molybdenum, 0.50 percent nickel, and 0.08 percent vanadium that exhibited no polygonal ferrite after cooling at about 4°C/min. After tempering at 700°C for 120 h, this steel had a tensile strength of 590 MPa.

KEY WORDS: 2¼Cr-1Mo steel, hardenability, transformation, CCT diagram, critical cooling rate for polygonal ferrite formation, pressure vessels, Ac_1 temperature, Ac_3 temperature, bainite

---

[1] Staff Metallurgist, Climax Molybdenum Company of Michigan, Ann Arbor, Mich. 48105.

[2] Manager, Ferrous Metallurgy, Climax Molybdenum Company of Michigan, Ann Arbor, Mich. 48105.

The 2¼Cr-1Mo steel has been widely used for pressure vessels and reactors in the petrochemical industry. The manufacture of vessels up to 200 mm wall thickness is quite common. Some vessels of greater wall thickness have been produced, but experience with these has been limited. Another relatively new application for this steel, where experience is also limited, is in the manufacture of heavy-section well-head equipment, in which high resistance to sulfide stress cracking is required. The purpose of this paper is to provide information on the transformation characteristics of 2¼Cr-1Mo steel and to evaluate the effects of compositional variations on hardenability. Such information is of value in the application of this steel for heavy-section plates up to 400 mm thick.

Among the metallurgical features of 2¼Cr-1Mo steel, probably the most important are (*1*) high bainitic hardenability, and (*2*) formation of stable and competing alloy carbides. A high bainitic hardenability means that 2¼Cr-1Mo steel transforms to a fully bainitic microstructure over a wide range of cooling rates. This feature makes the steel suitable for heavy-section applications. The well-balanced chromium and molybdenum contents of the steel ensure that the stabilities of various alloy carbides such as M_2C, M_7C_3, and $M_{23}C_6$ are close to each other. Thus, the transformation of one carbide species to another is sluggish, which gives a high elevated temperature stability to the steel. Alloy carbide formation also provides resistance to hydrogen attack. The present study focuses primarily on the hardenability of 2¼Cr-1Mo steel.

The continuous-cooling transformation (CCT) diagram provides useful information on hardenability, defining quite accurately the cooling rates at which various transformation products will form. In this study, quench dilatometry combined with metallographic observations were used for constructing the CCT diagram. In addition, mechanical properties were determined on specimens that were heat treated to simulate heavy-section plates.

Experimental Procedures

Materials

The steels examined in this study are listed in Table 1. Steels B and I are commercial heats, while all others are laboratory heats. All laboratory heats were 25 to 30 kg in size, melted in a vacuum induction furnace and cast in cylindrical ingot molds under an argon atmosphere. The ingots were forged and rolled to 13 to 25 mm thick plates before heat treatment.

Transformation Studies

CCT diagrams were established by dilatometry, using a Formastor-F quench dilatometer. This instrument employs induction heating of the test

TABLE 1—*Chemical composition of test steels.*

Type of Steel	Designation	Element, %										
		C	Mn	Si	Cr	Mo	Ni	P	S	N	Al	Other
Standard 2¼Cr-1Mo	A	0.11	0.58	0.22	2.17	0.95	[a]	0.018	0.015	0.005	0.010	...
	B	0.12	0.51	0.30	2.29	1.01	0.30	[b]	[b]	[b]	[b]	...
	C	0.13	0.40	0.21	2.22	0.98	[a]	0.014	0.015	0.008	0.026	...
Higher-C 2¼Cr-1Mo	D	0.20	0.50	0.14	2.24	1.00	0.05	0.008	0.011	0.0043	0.025	...
	E	0.21	0.58	0.22	2.17	0.95	[a]	0.018	0.015	0.005	0.010	...
	F	0.31	0.56	0.22	2.21	0.96	[a]	0.019	0.014	0.005	0.005	...
2¼Cr-1Mo-0.5Ni	G	0.16	0.58	0.26	2.46	1.02	0.48	0.012	0.010	0.0094	0.016	...
	H	0.15	0.60	0.23	2.37	1.10	0.50	0.008	0.013	0.0066	0.007	0.08V
	I	0.19	0.50	0.16	2.17	0.95	0.50	0.007	0.015	0.017	0.059	...
2¼Cr-1Mo-V	J	0.13	0.42	0.20	2.22	0.99	[a]	0.014	0.016	0.009	0.029	0.15V
	K	0.12	0.43	0.23	2.22	0.97	[a]	0.013	0.016	0.009	0.017	0.28V
	L	0.12	0.44	0.21	2.22	0.98	[a]	0.013	0.017	0.010	0.022	0.36V
3Cr-Mo	M	0.10	1.42	0.23	2.97	1.49	0.10	0.011	0.010	0.0069	0.005	0.08V

[a] None added and not analyzed; assumed less than 0.01 percent.

[b] Not analyzed.

specimens *in vacuo* and allows controlled cooling over a wide spectrum of cooling rates. The specimen length and temperature are simultaneously recorded during heating and cooling. In the present study, the cooling rates employed ranged from 7000 to 0.6°C/min.[3] For the faster cooling rates ($\geq$1200°C/min), helium gas quenching was employed. Slower cooling rates were attained by controlled radiation cooling.

All dilatometer specimens were of cylindrical geometry, 3 mm diameter by 10 mm long. A 2-mm-diameter hole was drilled axially into one end to a depth of 5 mm to accommodate a thermocouple spot-welded in place for temperature measurement and control. Specimens were taken from the plates in the as-rolled condition.

The Ac_1 and Ac_3 temperatures were determined using the same Formastor-F dilatometer by heating the specimen at a constant rate of 2°C/min from 600 to 960°C. The Ac_3-temperature thus determined on each test steel provided a basis for selecting the austenitizing temperatures in determining the CCT diagram; that is, Ac_3 plus 30°C.

All test specimens were austenitized in the dilatometer for 20 min prior to cooling. Construction of each CCT diagram was based on the dilatometer cooling records and metallographic observations of the transformed specimens. Metallography was performed on specimens mounted in epoxy resin and with at least 1.5 mm ground from the surface prior to final mechanical polishing and etching. Hardness was determined on the same surface using a Vickers hardness indenter with a 10-kg load.

Mechanical Testing

Tensile tests were performed on specimens machined from 13 to 25-mm-thick plates heat treated to simulate much heavier section sizes. The required slower cooling rates were attained by enclosing the thinner plates in boxes made of insulating firebrick and/or steel and air cooling the entire box-and-plate assembly. Temperatures were monitored during heat treatment via thermocouples attached to the enclosed plates. The finished tensile specimen geometry was cylindrical, with 6.35 mm gage diameter and 25.4 mm gage length.

Results and Discussion

General CCT Behavior

Figure 1 shows the CCT diagram for a "standard" 2¼Cr-1Mo steel, Steel A in this study (see Table 1). The reader unfamiliar with the general features

---

[3] All cooling rates specified herein are based on the time to cool the specimen from 800 to 500°C.

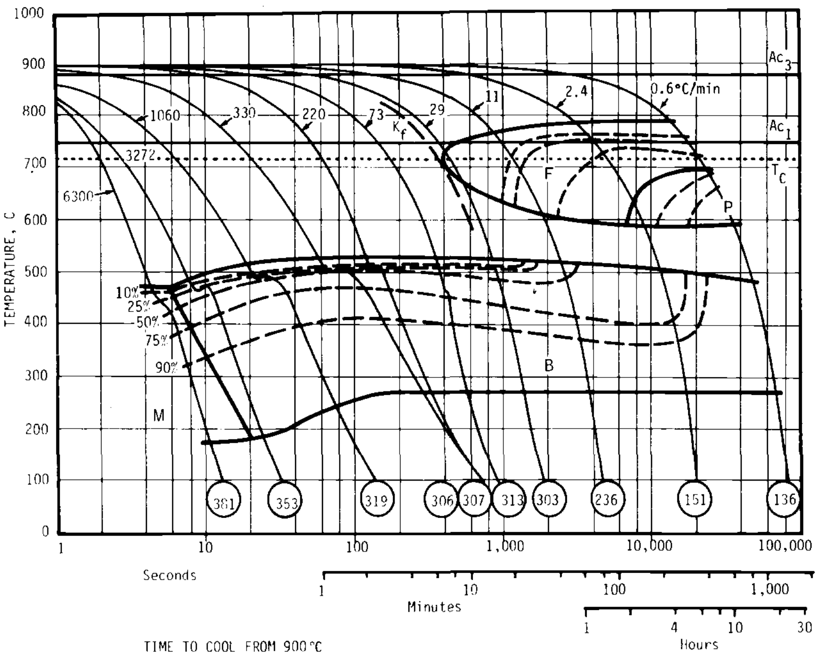

FIG. 1—*CCT diagram for 0.1 percent carbon 2¼Cr-1Mo steel (Steel A); ASTM grain size No. 7; F = polygonal ferrite; P = pearlite; B = bainite; M = martensite.*

of such diagrams or the manner in which they are constructed from the original dilatometer records is referred to the literature [*1*].[4] In Fig. 1, the numbers written adjacent to the cooling curves near the top of the diagram are the cooling rates (°C/min) associated with the respective curves. The number inscribed in a circle at the end of each cooling curve gives the hardness (HV10) of the respective dilatometer specimen cooled as indicated.

One of the most striking features of the CCT diagram for 2¼Cr-1Mo steel is the wide range of cooling rates over which bainite is the predominant austenite transformation product. For Steel A (Fig. 1), cooling rates ranging from about 3300 to about 30°C/min result in a fully bainitic microstructure. A convenient parameter for expressing this bainitic hardenability is the critical cooling rate for ferrite formation, K_f. This is the slowest rate at which the steel can be cooled and still attain a structure free of polygonal ferrite. A portion of a hypothetical cooling curve associated with K_f is shown as a dashed curve in Fig. 1; tangent to the knee of the polygonal ferrite transformation region.

The polygonal ferrite that forms on cooling at rates slower than K_f affects

---

[4] The italic numbers in brackets refer to the list of references appended to this paper.

the mechanical properties. This is illustrated in Fig. 2, where hardness is plotted as a function of cooling rate. Beyond K_f, hardness decreases rapidly as the softer microconstituent, polygonal ferrite, becomes an increasing portion of the microstructure.

Examples of the bainitic transformation products obtained in 2¼Cr-1Mo steel are shown in Figs. 3 and 4. Figure 3 shows optical micrographs of Steel C cooled at rates faster than K_f (Fig. 3*a*), and just slightly slower than K_f (Fig. 3*b*). The polygonal ferrite that forms at the slower cooling rate is indicated by an arrow. Figure 4 shows scanning electron micrographs of the bainite formed in Steel A and illustrates a rather characteristic feature of the bainitic microconstituent in 2¼Cr-1Mo steels. Whereas in lower alloy steels the bainite consists of laths of dislocated ferrite and particles of M_3C carbides, the bainite in 2¼Cr-1Mo steel is generally free of the carbide phase. In place of the carbides one finds "islands" of martensite plus retained austenite (MA constituent). Whether or not the bainite contains carbides or MA appears to be dependent on both composition and cooling rate. In this work, the authors noted a general trend toward more carbide and less MA in the bainite as the carbon content of the steel was increased and as the cooling rate was decreased. The cooling rate effect can be seen by comparing Figs. 4*a* and 4*b*.

The CCT diagram in Fig. 1 indicates three critical temperatures for the 2¼Cr-1Mo steel: the usual upper and lower critical temperatures, Ac_3 and Ac_1, and a third temperature designated as Tc.

There is some disagreement among the reported Ac_1-values in the literature. Table 2 shows Ac_1-temperatures measured in this study as well as

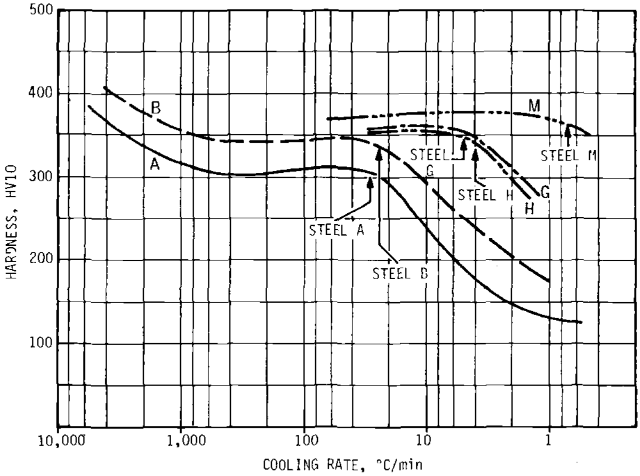

FIG. 2—*Hardness versus cooling rate for several of the steels investigated. Vertical arrows denote* K_f *for the steels.*

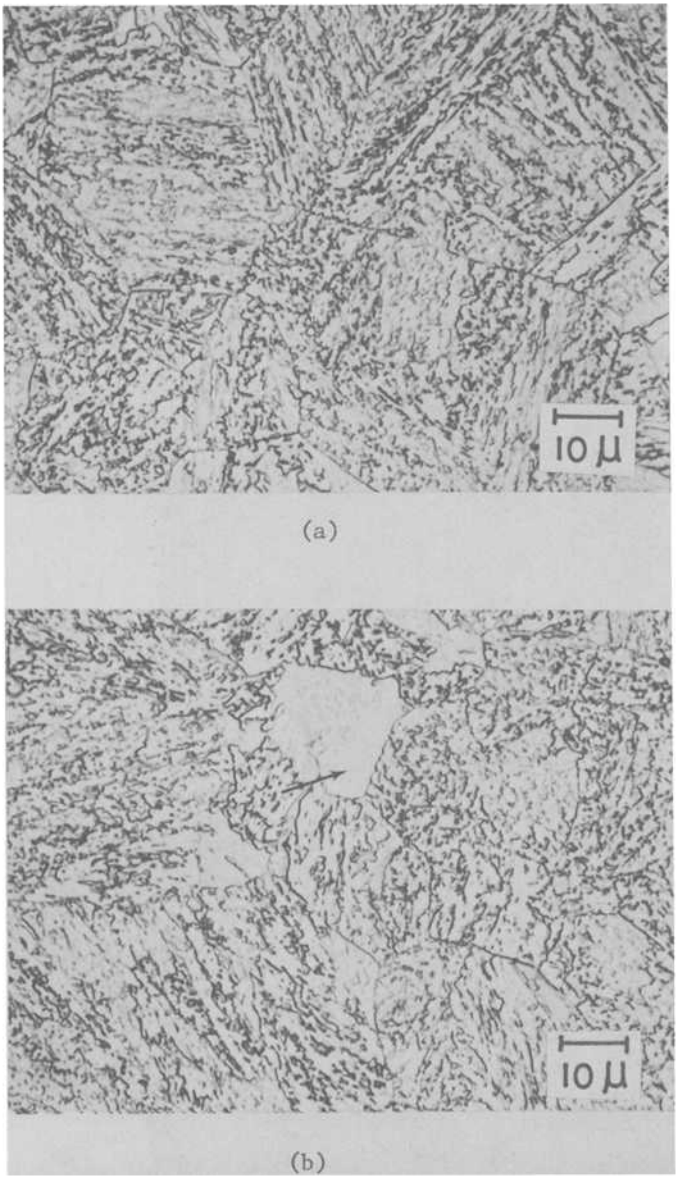

FIG. 3—*Microstructure of Steel C after CCT. Arrow indicates polygonal ferrite.* (a) *Cooled at 70°C/min;* (b) *Cooled at 30°C/min.*

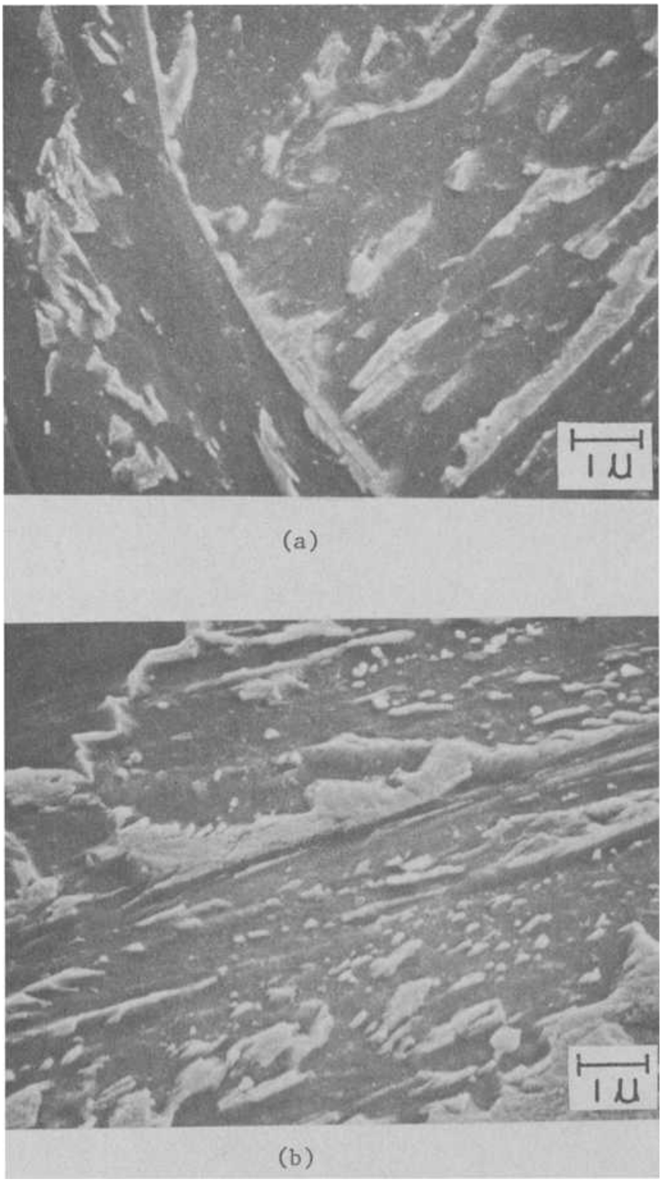

(a)

(b)

FIG. 4—*Scanning electron micrographs of Steel A after CCT.* (a) *Cooled at 400°C/min;* (b) *Cooled at 11°C/min.*

TABLE 2—*Ac_1 temperatures of standard 2¼Cr-1Mo steels.*

Observer	Reference	Ac_1-Temperature,°C
This study—Steel A		750
This study—Steel B		750 to 778 (see Table 3)
This study—Steel C		760
Rose et al	*2*	780
Kunitake et al	*3*	773
Atkins	*4*	735
Leymonie et al	*5*	815

data reported by others [*2-5*]. (The compositions of the steels from Refs *2* to *5* are given in Table 4.) Atkins [*4*] reports the lowest Ac_1-value, 735°C, while Leymonie et al [*5*] give a value of 815°C. Except for these two extremes, the data fall within a reasonably narrow range of 750 to 780°C.

Because of the variation in reported data, an experiment was performed to determine the extent to which prior heat treatment might affect the Ac_1-measurement. The heat treatments employed and the Ac_1-temperatures subsequently measured are shown in Table 3. Figure 5 shows some of the actual dilatometer records. Clearly, Ac_1 is dependent on prior treatment, ranging from a low value of 750°C to a high of 778°C. Metallographic examination of a specimen tempered in a gradient furnace and subsequently quenched confirmed the dilatometric results. A portion of that specimen heated to 780°C is shown in Fig. 6. The presence of fresh martensite indicates that transformation to austenite occurred at this or a lower temperature. The most frequent nucleation site for the austenite appears to be at grain boundary triple points, which may indicate that grain boundary diffusion has a role in the transformation.

The dilatometer records obtained during heating (Fig. 5) show a deviation from normal thermal expansion behavior in the vicinity of 730 to 740°C, indicating some phase transformation occurs in this region. Specimens tempered in this range did not reveal any positive metallographic evidence of austenite formation. The authors believe the observed phenomenon is due to the formation of alloy carbides, or the transformation of one alloy carbide

TABLE 3—*Effect of prior heat treatment on Ac_1 temperature. Test steel—Steel B.*

Condition	Ac_1-Temperature, °C
As-received	750
930°C, 1 h, A.C.[a] plus 630°C, 45 min	778
930°C, 1 h, A.C.[a] plus 730°C, 3 h	770
930°C, 1 h, A.C.[a] plus 730°C, 20 h	764

[a] Air-cooled as 16 mm square bars.

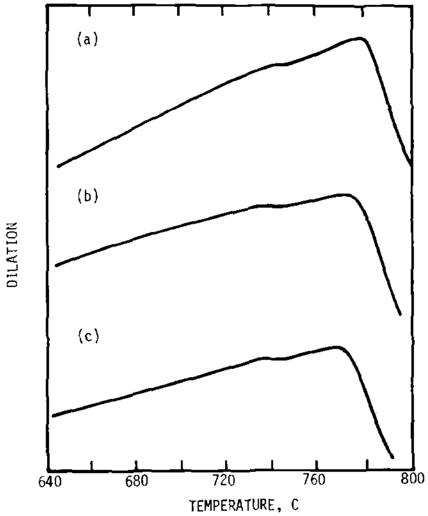

FIG. 5—*Examples of dilatometric curves during heating. Heating speed: 2°C/min. Steel B, air cooled from 930°C. and* (a) *tempered at 630°C. 45 min:* (b) *tempered at 730°C. 3 h:* (c) *tempered at 730°C. 20 h.*

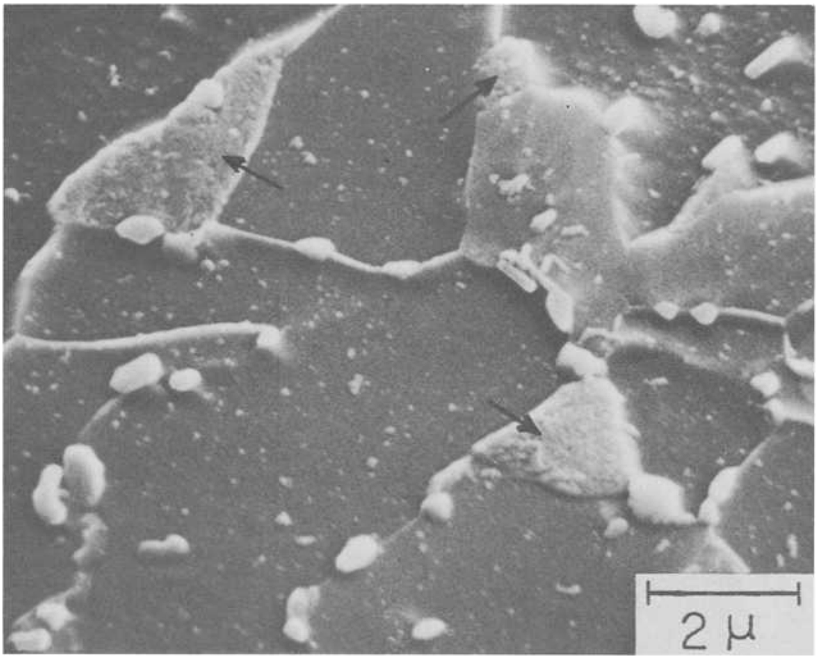

FIG. 6—*Scanning electron micrograph of Steel B after normalizing from 950°C and tempering at 780°C for 45 min. Arrows show fresh martensite particles.*

species to another, at the slow heating rate (2°C/min) employed. The subcritical transformation is indicated as Tc on the CCT diagram in Fig. 1.

Effect of Composition on Hardenability

Figure 2 shows hardness versus cooling rate for several of the steels examined and indicates the shifts in K_f resulting from compositional changes. Table 4 gives the K_f-values determined in this work, as well as some data from the literature. For standard 2¼Cr-1Mo steel (0.15 percent maximum carbon, 0.5 percent maximum silicon, 0.30/0.60 percent manganese, 2.00/2.50 percent chromium, and 0.90/1.10 percent molybdenum), K_f is generally in the range of 15 to 35°C/min. The cooling rate at the center of water-quenched 200-mm-thick plate is about 30°C/min. Thus standard 2¼Cr-1Mo would generally be suitable for section sizes up to 200 mm. The reason for the exceptionally high K_f-value (low hardenability) reported by Rose et al [*2*] is not clear.

Additions of carbon, manganese, chromium, and molybdenum are all known to increase the hardenability of steel. In this work, the effects of carbon and vanadium were systematically studied in some detail using steels in which all other elements were held at a constant level. Steels A, E, and F formed a series with a carbon variable, while Steels C, J, K, and L formed a series with vanadium as the variable. The effects of carbon and vanadium on K_f are shown in Fig. 7. Carbon strongly increases hardenability (decreases K_f). The carbon effect can be described by the relation

$$\log K_f\,(°\mathrm{C/min}) = 2.03 - 5\,(\%\ \mathrm{carbon}) \tag{1}$$

Vanadium has relatively little effect on hardenability, resulting in a modest decrease with additions of up to about 0.3 percent, and a relatively small increase with further additions [*6*]. Vanadium does contribute to the mechanical properties of the steel, however, as discussed below.

Table 4 also illustrates the effects of chromium and nickel compositional variables. The data of Kunitake et al [*3*] show that chromium additions are relatively ineffectual; that is, raising chromium to as high as 3 percent has little effect on K_f. In contrast, the addition of 0.5 percent nickel to 2¼Cr-1Mo has a potent effect, decreasing K_f by nearly an order of magnitude compared with the standard composition. As discussed further below, these nickel-modified steels would yield fully bainitic microstructures if water quenched in sections as heavy as 400 mm.

Two of the steels in Table 4, Steel I and Steel M, show exceptionally high hardenability. Steel I is a higher carbon modification of the standard grade plus 0.5 percent nickel. This steel was prepared as a commercial trial heat intended for oil well components. The other high-carbon steels in Table 4 have also been proposed and examined by the Climax Laboratory for oil field ap-

TABLE 4—*Critical cooling rate for ferrite formation.* K$_f$, *of standard 2¼Cr-1Mo and modified chromium-molybdenum steels.*

Type of Steel	Designation of Steel	Chemical Composition							K_f, °C/min	Observer	Reference
		C	Mn	Si	Cr	Mo	Ni	Other			
Standard 2¼Cr-1Mo	A	0.11	0.58	0.22	2.17	0.95	. . .	. . .	30	this study	
	B	0.12	0.51	0.30	2.29	1.01	0.30	. . .	26	this study	
	C	0.13	0.40	0.21	2.22	0.98	. . .	. . .	33	this study	
		0.11	0.47	0.21	2.29	1.02	0.14	. . .	60	Rose et al (Max-Planck Inst.)	2
		0.10	0.48	0.37	2.16	0.96	. . .	. . .	35	Kunitake et al (Sumitomo)	3
		0.14	0.46	0.23	2.28	1.05	0.21	. . .	35	Atkins (BSC)	4
		0.15	0.74	0.36	2.40	0.99	. . .	. . .	15	Leymonie et al (Babcock-Atlantique)	5
Higher-C 2¼Cr-1Mo	E	0.21	0.58	0.22	2.17	0.95	. . .	. . .	9	this study	
	F	0.31	0.56	0.22	2.21	0.96	. . .	. . .	3.2	this study	
2¼Cr-1Mo-0.5Ni	G	0.16	0.58	0.26	2.46	1.02	0.48	. . .	5	this study	
	H	0.15	0.60	0.23	2.37	1.10	0.50	0.08V	4	this study	
	I	0.19	0.50	0.16	2.17	0.95	0.50	. . .	0.75	this study	
2¼Cr-1Mo-V	J	0.13	0.42	0.20	2.22	0.99	. . .	0.15V	40	this study	
	K	0.12	0.43	0.23	2.22	0.97	. . .	0.28V	45	this study	
	L	0.12	0.44	0.21	2.22	0.98	. . .	0.38V	18	this study	
3Cr-Mo		0.08	0.45	0.37	3.01	0.93	0.06	. . .	33	Kunitake et al (Sumitomo)	3
	M	0.10	1.42	0.23	2.97	1.49	0.10	0.08V	0.7	this study (also see Ref 7)	

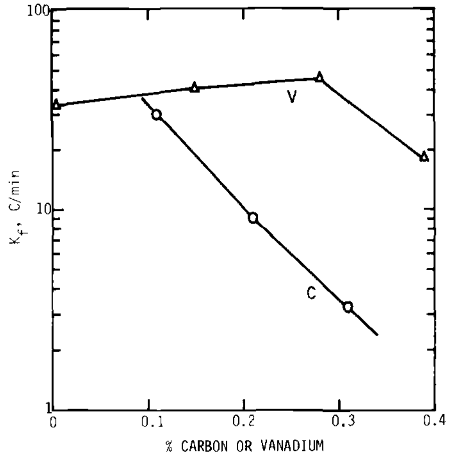

FIG. 7—*Effects of carbon and vanadium on* K_f *in 2¼Cr-1Mo steel.*

plications. Steel M was developed by Wada et al [7] and designed for air-cooled plates of 200 to 300 mm thickness.

Tensile Properties

The tensile properties after heat treatment of several of the steels investigated here are summarized in Figs. 8 and 9. Data from the literature [*8*, *9*] are also presented.

As noted previously, vanadium does not contribute significantly to hardenability of 2¼Cr-1Mo steel. However, it does contribute significantly to the strength of the steel after heat treatment. As shown in Fig. 8, the addition of 0.28 percent vanadium raises both the yield and tensile strengths at room temperature in the quenched and tempered condition by about 150 MPa. The strengths at 425°C are increased about 100 MPa by the vanadium addition.

The aim tensile strength of 400-mm-thick 2¼Cr-1Mo steel plate would be that of ASTM Specification for Pressure Vessel Plates, Alloy Steel, Chromium-Molybdenum (A 387-79b) Grade 22, Class 2; that is, 517 to 690 MPa (75 to 100 ksi). Accelerated cooling with dip- or spray-water quenching would be useful to maintain this strength after tempering and stress relieving. Depending on the amount of tempering, the tensile strength could be on the very low side of the specified range. If tempering and postweld stress relieving take, for example, the equivalent of 30 h at 730°C, the tempering parameter T.P. $= T(K)\ [20 + \log t\ (\text{h})]$ is about 21.5×10^3. As shown in Fig. 9, the tensile strength of standard 2¼Cr-1Mo steel [*8*, *9*] is quite marginal after such tempering. Two of the 2¼Cr-1Mo-0.5Ni steels studied

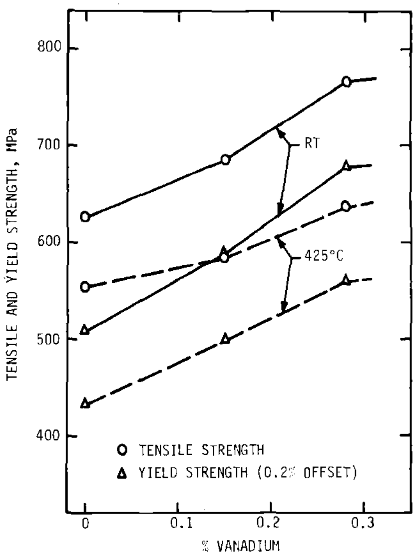

FIG. 8—*Effect of vanadium on tensile and yield strength of 2¼Cr-1Mo steel. Heat treatment: cooled from 955°C at 50°C/min and tempered at 730°C for 2 h.*

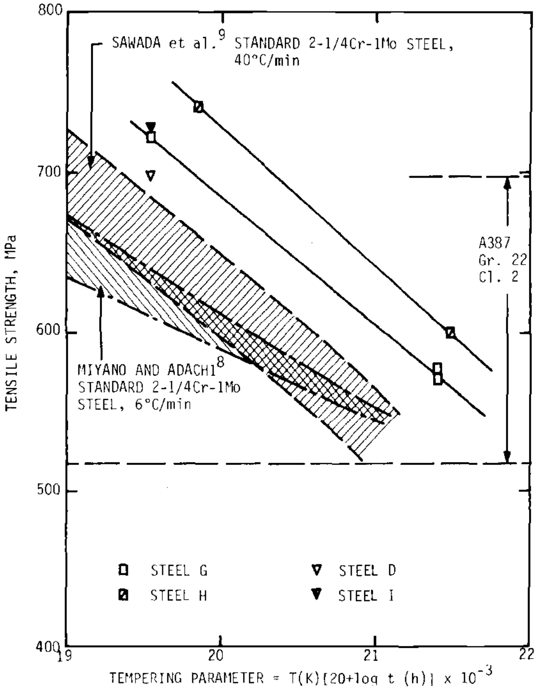

FIG. 9—*Tensile strength of 2¼Cr-1Mo steels after tempering.*

here, Steels G and H, one with and one without 0.08 percent vanadium, exhibit much higher strength than the standard steels after similar tempering. Vanadium certainly improves the tensile strength, but even Steel G, without vanadium, exhibits satisfactory tensile strength after tempering to T.P. = 21.5×10^3.

Tempering of 2¼Cr-1Mo steel at high temperatures (high T.P. values) is desirable to maintain high resistance to hydrogen attack [*10*] or to decarburization [*11*]. The increased stability of alloy carbides resulting from tempering is the reason for this resistance to hydrogen attack and decarburization.

General Discussion

The cooling rates of heavy-section plates during heat treatment have been reported in several papers [*12-18*]. The articles by Stout [*12*], Lorentz [*13*], and Struck et al [*14*] contain good summaries of the cooling rates. Figure 10 shows the cooling rates in both water-quenched and air-cooled plates from these sources, after converting their data to the cooling rate definition used in this work, namely, the average cooling rate between 800 to 500°C. Data from two more recent papers [*17,18*] are also included in Fig. 10. There is good agreement among the various authors.

According to Fig. 10, the cooling rate at the center of a 400-mm-thick plate is only about 8°C/min during water quenching. The cooling rate in water-quenched 200-mm plate would be about 30°C/min, which is approximately the same as the K_f of standard 2¼Cr-1Mo steel. This means that avoiding ferrite formation in standard 2¼Cr-1Mo steel plates at thicknesses greater than 200 mm may not be easy, even by water quenching. A small amount of ferrite may not be harmful to mechanical properties; Table 5 presents data from unpublished work of one of the authors (Wada) which show that 2 percent polygonal ferrite in Steel D (0.2 percent carbon 2¼Cr-1Mo) does not significantly affect the mechanical properties. However, it is apparent that some adjustment in chemistry is necessary to maintain hardenability sufficient for 400 mm thickness; for instance, at the 8°C/min cooling rate involved, standard 2¼Cr-1Mo steel could contain 50 or more percent polygonal ferrite (see Fig. 1).

The 2¼Cr-1Mo-0.5Ni steels tested in this study exhibit sufficient hardenability to produce a fully bainitic microstructure in water-quenched 400-mm-thick plates. Since a few percent polygonal ferrite in the structure would not significantly affect the mechanical properties after tempering, the chemical compositions of Steels G and H are probably more than adequate for 400-mm-thick plates. A steel in the range of 0.13 to 0.15 percent carbon, 0.55 to 0.6 percent manganese, and 0.3 to 0.5 percent nickel would be adequate for this section size.

Although vanadium does not increase hardenability, it does retard soften-

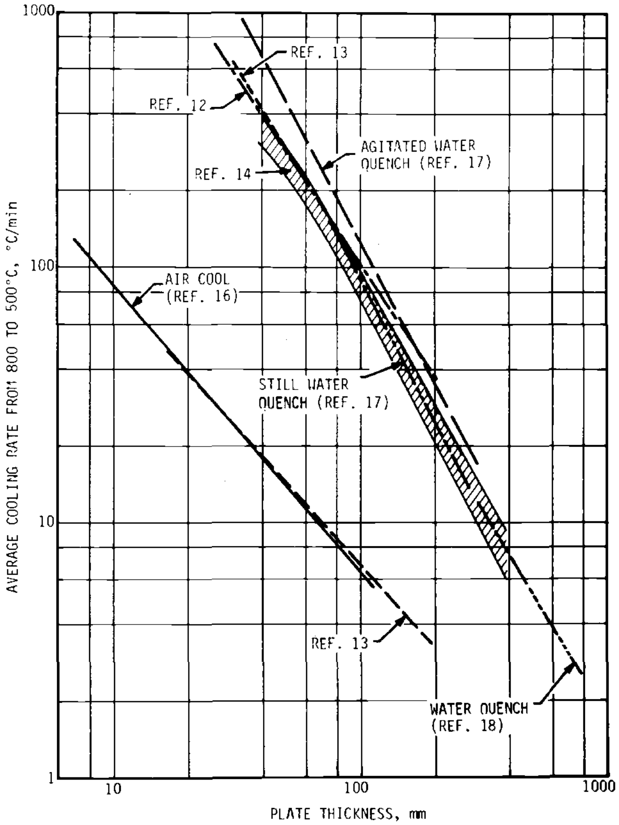

FIG. 10—*Cooling rates at center of steel plate.*

ing during tempering and this increases tensile strength after heat treatment. Its addition to the steel might therefore be advantageous where weldability is concerned. A beneficial effect of addition of 0.02 percent vanadium to heavy-section electroslag welds has been reported by Okumura et al [*19*].

Temper embrittlement susceptibility should be carefully evaluated when the chemistry of 2¼Cr-1Mo steel is modified. There are results [*20,21*] which show that nickel in 2¼Cr-1Mo steel at residual element levels does not significantly influence the temper embrittlement susceptibility, but the effect of 0.3 to 0.5 percent nickel is not well known. Manganese has a mildly adverse effect on temper embrittlement resistance [*21,22*]. However, the effect of increasing manganese to the highest level within the ASTM A 387 Grade 22 composition range could be offset by careful control of phosphorus and silicon.

TABLE 5—*Effects of cooling rate from the austenitizing temperature on tensile and impact properties of Steel D.*[a]

Cooling Rate from Austenitizing Temperature,[a] °C/min	Simulating Plate Thickness, mm	Microstructure	0.2 % Offset Yield Strength, MPa	Tensile Strength, MPa	Elongation, %	Charpy V-Notch Impact Value	
						Room Temperature Impact Energy, J	FATT, °C
18	250	full bainite	550	692	25	213	−40
8	400	2 % ferrite + bainite	558	698	25	203	−35

[a] Heat treatment condition: Austenitized at 955°C for 1 h, cooled as indicated, tempered at 690°C for 2 h, and air cooled.

Conclusions

1. The 2¼Cr-1Mo steel has a high bainitic hardenability which, in conjunction with its high elevated temperature strength and resistance to hydrogen attack, makes the steel well suited for heavy-section pressure vessel applications.

2. The critical cooling rate for polygonal ferrite formation, K_f, of standard 2¼Cr-1Mo steel is about 30°C/min, which is approximately equivalent to the cooling rate at the center of water-quenched 200-mm-thick plates.

3. Slightly modified steels, such as one containing carbon and manganese at the high side of the specified ranges and 0.5 percent nickel, exhibit a fully bainitic microstructure in water-quenched 400-mm-thick plates.

4. The tensile strength of these modified steels is satisfactory for ASTM A 387 Grade 22, Class 2, that is, 517 to 690 MPa (75 to 100 ksi), even after tempering to a parameter $T.P. = T(K)\,[20 + \log t\ (h)] = 21.5 \times 10^3$, which is equivalent to 730°C for 30 h or 700°C for 120 h.

References

[1] Eldis, G. T. in *Hardenability Concepts with Applications to Steel*, D. V. Doane and J. S. Kirkaldy, Eds., AIME, 1978, pp. 126–149.

[2] Rose, A. et al, *Atlas zur Wärmebehandlung der Stähle*, Teil II, Max-Planck-Institut für Eisenforschung, 1958.

[3] Kunitake, T., Yukitoshi, T., Yoshikawa, K., and Ohtani, H., *Sumitomo Kinzoku*, Vol. 22, No. 2, 1970, p. 189.

[4] Atkins, M., *Atlas of Continuous Cooling Transformation Diagrams for Engineering Steels*, British Steel Corporation, 1977.

[5] Leymonie, C., Hennion, J., and Cadiou, L., *Revue de Metallurgie*, Vol. 71, 1974, p. 684.

[6] Wada, T., "2¼Cr-1Mo Steel Modified with Vanadium Addition," Climax Report RP-32-75-03, 22 Feb. 1977.

[7] Wada, T., Grobner, P. J., and Sponseller, D. L., "Hydrogen-Resistant Steel for Service in Thick-Walled Pressure Vessels at Elevated Temperatures," in *Applications of Materials for Pressure Vessels and Piping, MPC-10*, edited by G. V. Smith, Metal Properties Council, 1979.

[8] Miyano, K. and Adachi, T., *Transactions of the Iron and Steel Institute of Japan*, Vol. 11, 1971, p. 54.

[9] Sawada, S., Matsumiya, J., and Nonaka, K., *Kawasaki Steel Technical Report*, Vol. 6, 1974, pp. 249–264.

[10] Murakami, Y., Watanabe, J., and Mima, S., "Heavy Section Cr-Mo Steels for Hydrogenation Services," a paper presented at the 17th CIM Annual Conference, Montreal, 27–30 Aug. 1978.

[11] Moroishi, T. and Shida, Y., *Journal of the Japan Institute of Metals*, Vol. 40, 1976, pp. 1184–1192.

[12] Stout, R. D., *Welding Journal*, Vol. 39, 1960, pp. 273-S-283-S.

[13] Lorentz, R. E., Jr., *Welding Journal*, Vol. 41, 1962, pp. 433-S-447-S.

[14] Struck, S. S., Pense, A. W., and Stout, R. D., "The Properties and Microstructure of Spray-Quenched Thick-Section Steels," *Welding Research Council Bulletin*, No. 120, Feb. 1967, pp. 1-15.

[15] Kottcamp, E. H., Canonico, D. A., and Stout, R. D., *Welding Journal*, Vol. 41, 1962, pp. 350-S-354-S.

[16] Kramer, I. R., Gorsuch, P. D., and Newhouse, D. L., *Transactions of AIME*, Vol. 172, 1947, pp. 244–272.

[*17*] Hara, H. and Yoshimura, S., Kawasaki Steel Technical Report, Vol. 6, 1974, pp. 295-304.

[*18*] Saeki, T., Tahara, T., Fujioka, K., Tokuda, A., and Mima, S., Japan Steel Works Technical Report, No. 38, 1978, pp. 5-17.

[*19*] Okumura, M., Kumagai, M., Nakamura, H., and Kohira, K., *Welding Journal*, Vol. 55, 1976, pp. 389-S-399-S.

[*20*] McMahon, C. J., Jr., private communication.

[*21*] Nakao, H., Yamaba, R., and Yamamoto, H., *Tetsu-To-Hagane*, Vol. 64, 1976, p. S-283.

[*22*] Yu, Jin and McMahon, C. J., Jr., *Metallurgical Transactions A*, Vol. 11A, 1979, pp. 291-300.

DISCUSSION

R. J. Kar[1] *and J. A. Todd*[2] (*written discussion*)—We find it difficult to agree with your interpretation of your scanning electron micrographs of 2¼Cr-1Mo steel cooled at 11°C/min (Fig. 4) as being bainite with "islands" of retained austenite and martensite. Habraken and Economopoulos[3] undoubtedly have shown such "islands" to exist in 2¼Cr-1Mo steel cooled at 220°C/min; however, the cooling rates you have referred to in your presentation are one order of magnitude slower. Further, as discussed in our paper,[4] we have examined the microstructure of 2¼Cr-1Mo steel in detail after slow cooling at similar rates, and have failed to detect retained austenite either through transmission electron microscopy or X-ray analysis. The microstructure we have observed consisted of mixtures of polygonal ferrite and lower and upper bainite, and is in agreement with the findings of Lonsdale and Flewitt,[5] who failed to observe retained austenite in normalized 2¼Cr-1Mo steel.

Tsuguyasu Wada and G. T. Eldis (*authors' closure*)—As we noted in the text, the formation of so-called MA constituent (Fig. 4*a*) is both composition and cooling rate dependent. In 2¼Cr-1Mo steels, carbon content appears to have a particularly strong effect. For example, at 0.1 percent carbon (Steel A), at all cooling rates resulting in fully bainitic transformation (see Fig. 1), MA was the only "second phase" observed in the microstructure. Carbides were observed only at cooling rates slow enough to result in some transformation to polygonal ferrite prior to the start of the bainite reaction, as shown in Fig. 4*b*. At 0.2 percent carbon (Steel E), the bainitic transformation product contained both carbides and MA at all cooling rates investigated, the relative

[1] Senior Metallurgist, Anamet Laboratories, Inc., Berkeley, Calif. 94710.

[2] Assistant Research Engineer, University of California, Berkeley, Calif. 94710.

[3] Habraken, L. J. and Economopoulos, M., "Symposium on Transformation and Hardenability in Steels," Feb. 1967, Climax Molybdenum Company of Michigan, Ann Arbor, Mich.

[4] This publication, pp. 228-252.

[5] Lonsdale, D. and Flewitt, P. E. J., *Metallurgical Transactions*, Vol. 9A, 1978, pp. 1619-1623.

amount of MA decreasing and the amount of carbide increasing with decreasing cooling rate. At 0.3 percent carbon (Steel F), carbide was the only second phase present in the bainitic transformation product, regardless of cooling rate.

You investigated[4] slow-cooled 2¼Cr-1Mo steels containing 0.15 percent carbon or higher and did not observe any MA islands. Habraken and Economopoulos[3] observed the islands in a 0.11 percent carbon 2¼Cr-1Mo steel cooled at 220°C/min. They did not investigate a specimen cooled at a rate between 220 and 1.1°C/min. We think that these results do not conflict with our results; rather, these confirm our observations on the conditions under which the MA islands form.

We used the term martensite-plus-austenite (MA) islands according to the conventional terminology for this type of microstructure. In many cases, low-alloy steels form austenite islands instead of carbides during bainite transformation. These austenite islands partially transform to martensite during further cooling. What portion of austenite islands eventually transforms to martensite is dependent on the composition of steel; it is possible that the portion of martensite is very high in chromium-molybdenum steels. The point which we would emphasize is that 2¼Cr-1Mo steel can transform, under certain conditions, to ferrite plus austenite islands rather than ferrite plus carbides. This does not necessarily mean that 2¼Cr-1Mo steel contains large amounts of retained austenite after cooling to room temperature.

Shingo Sato,[1] *Susumu Matsui,*[1] *Teiichi Enami,*[1]
and Toshikazu Tobe[2]

Strength and Temper Embrittlement of Heavy-Section 2¼Cr-1Mo Steel

REFERENCE: Sato, Shingo, Matsui, Susumu, Enami, Teiichi, and Tobe, Toshikazu, **"Strength and Temper Embrittlement of Heavy-Section 2¼Cr-1Mo Steel,"** *Application of 2¼Cr-1Mo Steel for Thick-Wall Pressure Vessels, ASTM STP 755,* G. S. Sangdahl and M. Semchyshen, Eds., American Society for Testing and Materials, 1982, pp. 363-382.

ABSTRACT: The effects of austenitizing temperature and manganese, silicon, and phosphorus contents on temper embrittlement of 2¼Cr-1Mo steel associated with its strength were studied using laboratory heats.

High manganese content or high austenitizing temperature improves the strength and the initial toughness by suppressing the formation of ferrite. Once a fully bainitic structure is obtained, the increase in strength and the decrease in toughness are small even if the manganese content or the austenitizing temperature increases.

The manganese content should be as low as possible under the condition where the fully bainitic structure is obtained for toughness in the step-cooled condition. The increase in susceptibility to temper embrittlement caused by a high austenitizing temperature is small. It may be compensated for by reducing manganese, silicon, or phosphorus content.

The addition of silicon, intended to obtain higher strength, must be compensated for by lowering the phosphorus content to decrease the susceptibility to temper embrittlement.

On the basis of the laboratory experiments, a 2¼Cr-1Mo steel forging with a thickness of 397 mm was produced. The forging exhibited a good combination of strength and toughness in the step-cooled condition.

KEY WORDS: strength, toughness, temper embrittlement, austenitizing temperature, austenite grain size, manganese, silicon, phosphorus

---

[1] Senior Researcher, Mizushima Laboratory, Research Laboratories, Kawasaki Steel Corporation, Kurashiki, Japan.

[2] Assistant Manager, Casting and Forging Department, Mizushima Works, Kawasaki Steel Corporation, Kurashiki, Japan.

In the petrochemical industry, 2¼Cr-1Mo steel is widely used for pressure vessels such as desulfurization and reforming reactors. This steel must maintain good toughness even after being subjected to elevated temperatures for long times which can cause temper embrittlement. This requires improved initial toughness and low susceptibility to temper embrittlement. Also, this steel is often required to have a strength at elevated temperatures which requires a higher strength at room temperature than the minimum specified value of ASTM Specification for Steel Forgings, Alloy, for Pressure and High-Temperature Parts (A 336-80a) Class F22 steel forging or ASTM Specification for Pressure Vessel Plates, Alloy Steel, Chromium-Molybdenum (A 387-79b) Grade 22 Class 2 steel plate. In addition, for the manufacturing of larger vessels, heavier section steels are required.

High hardenability is required to prevent a decrease in strength and initial toughness, which can result from a decrease in cooling rate during the quenching of heavier section steels. Most of the factors which decrease susceptibility to temper embrittlement [*1-3*],[3] however, cause a decrease in hardenability. Therefore it is necessary to find suitable procedures to obtain high strength and toughness and to keep low susceptibility in heavier section steel.

This study is conducted to examine the effects of austenitizing temperature and manganese content on hardenability and susceptibility to temper embrittlement. The effects of silicon and phosphorus contents on the susceptibility were also studied.

Experimental Procedure

The steels used in the experiment were induction-melted 50-kg ingots. Their chemical compositions are given in Table 1. These ingots were heated at 1250°C and forged to 20-mm-thick plates. Subsequently the plates were subjected to the following heat treatments.

Experiment 1—To examine the effect of manganese content, Steels A-1 to A-5 were used. For comparison, a low-silicon steel, A-6, was included in the experiment. After normalizing at 950°C for 5 h, the steels were reaustenitized at 950°C for 3 h, and subsequently controlled cooled to ambient temperature. The cooling rates for controlled cooling were 65 and 22°C/min (average rate from 800 to 400°C). The cooling rate is defined in this manner throughout the study. These cooling rates are equivalent to those at mid-thickness of 140- and 250-mm-thick plates, respectively, during water quenching. They were subsequently tempered at 690°C for 7.5 h, air cooled, and finally step cooled (Fig. 1).

Experiment 2—To examine the effect of austenitizing temperature, Steel B-1, normalized at 950°C for 2 h, was reaustenitized at 950, 1050, or 1200°C

---

[3] The italic numbers in brackets refer to the list of references appended to this paper.

TABLE 1—*Chemical compositions of steels used (weight percent).*

Steel	C	Si	Mn	P	S	Cr	Mo	Al	N	Others
A-1	0.13	0.26	0.10	0.010	0.003	2.42	1.00	0.013	0.0054	V:0.013
A-2	0.12	0.26	0.30	0.010	0.003	2.42	1.00	0.013	0.0054	V:0.013
A-3	0.13	0.27	0.50	0.009	0.004	2.42	1.00	0.012	0.0048	V:0.014
A-4	0.14	0.27	0.69	0.010	0.004	2.40	1.00	0.013	0.0046	V:0.014
A-5	0.13	0.27	0.97	0.010	0.004	2.40	1.00	0.013	0.0046	V:0.014
A-6	0.14	0.07	0.50	0.009	0.004	2.42	1.00	0.013	0.0050	V:0.014
B-1	0.14	0.26	0.15	0.004	0.004	2.48	1.02	0.010	0.0075	Cu:0.12, Ni:0.20
C-1	0.13	0.02	0.50	0.008	0.006	2.25	1.04	0.010	0.0085	...
C-2	0.12	0.02	0.50	0.014	0.007	2.25	1.07	0.011	0.0083	...
C-3	0.11	0.02	0.49	0.021	0.003	2.16	1.00	0.017	0.0076	...
C-4	0.11	0.16	0.50	0.009	0.003	2.20	1.03	0.014	0.0073	...
C-5	0.12	0.16	0.51	0.015	0.003	2.19	1.05	0.016	0.0080	...
C-6	0.12	0.26	0.51	0.009	0.003	2.22	1.05	0.016	0.0067	...
C-7	0.12	0.25	0.51	0.016	0.007	2.21	1.04	0.014	0.0076	...
C-8	0.12	0.36	0.50	0.005	0.004	2.20	1.04	0.013	0.0077	...
C-9	0.10	0.45	0.54	0.009	0.010	2.58	1.04	0.003	0.0019	...

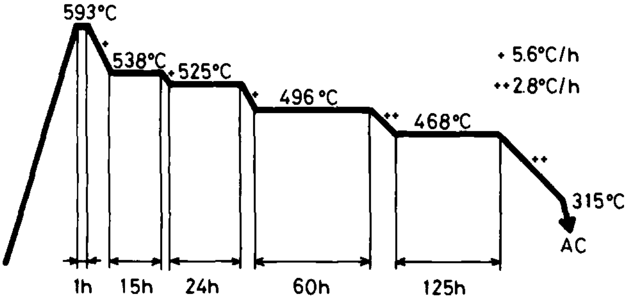

FIG. 1—*Step-cooling treatment used in the experiment.*

for 2 h, and controlled cooled to ambient temperature at the rate of 5°C/min. This was to simulate the cooling condition at midthickness of a 500-mm-thick plate during water quenching. It was then tempered at 690°C for 19 h, furnace cooled, and subsequently step cooled (Fig. 1).

Experiment 3—To examine the effects of manganese, silicon, and phosphorus contents on susceptibility to temper embrittlement in steels with fine or coarse austenite grain, Steels A-1 to A-5 and C-1 to C-9, after normalizing at 930°C for 3 h, were reaustenitized at 900 and at 1200°C for 2 h, and oil quenched at the rate of 500°C/min. This was intended to magnify the susceptibility to embrittlement. They were then tempered at 690°C for 17 h, and subsequently water cooled to minimize embrittlement during cooling, followed by step cooling (Fig. 1).

Tension tests at room temperature were performed after tempering using 12.5-mm-diameter specimens with a 50-mm gage length.

Impact tests were carried out before and after step cooling using the 2-mm V-notch Charpy specimen [the Type A specimen of Fig. 11 indicated in ASTM Methods and Definitions for Mechanical Testing of Steel Products (A 370-77)]. For one condition, 15 specimens were prepared, and the tests were performed at intervals of 20°C, sometimes at intervals of 10°C, using two or three specimens at each temperature. All of the broken specimens were subjected to measuring of the length and width of the cleavage portion of the fracture surface, and the percent shear fracture was determined at intervals of 5 percent. From the plots of the average value of the absorbed energy and the percent shear fracture against the test temperature, the 40 ft·lbf (54 J) energy transition temperature (TT_{40}) and 50 percent shear fracture appearance transition temperature (FATT) were determined by graphic interpolation. The shift of FATT (ΔFATT) and that of TT_{40} (ΔTT_{40}) were also determined. By regression analysis using the obtained data shown in Tables 2 to 4, the relation between FATT and TT_{40}, and that between ΔFATT and ΔTT_{40}, are calculated by the following equations:

$$\text{FATT}\ (^\circ\text{C}) = 1.14 \times TT_{40}\ (^\circ\text{C}) + 21.6$$

Coefficient of correlation: 0.971
Standard deviation: 7.5°C

$$\Delta\text{FATT}\ (^\circ\text{C}) = 1.20 \times \Delta TT_{40}\ (^\circ\text{C}) + 2.6$$

Coefficient of correlation: 0.977
Standard deviation: 6.4°C

The austenite grain size number (G) was determined by counting the number of grains per unit area (N), using the following equation:

$$N\ (\text{mm}^{-2}) = 2^{G+3}$$

Results and Discussion

Strength and Toughness

Figure 2 shows typical microstructures of steels with various manganese contents and a low-silicon steel. Steels with 0.10 and 0.30 percent manganese contents, cooled at a rate of 22°C/min, developed microstructures with ferrite of 70 and 50 percent, respectively. Steels with manganese contents more than 0.50 percent, and even the 0.10 percent manganese steel cooled at a rate of 65°C/min, exhibit fully bainitic structure.

Figure 3 shows the strength and FATT of these steels. They are closely dependent on the microstructures. As seen in Fig. 3*b*, below the critical manganese content that is required to achieve a fully bainitic structure, the strength rapidly decreases and the FATT rises, with an increasing fraction of

TABLE 2—*Effects of manganese and silicon contents on tensile and impact properties.*

		Tensile Properties				Impact Properties							
		Unembrittled				Unembrittled			Step-Cooled			Shift	
Steel	Average Cooling Rate, °C/min	YS, MPa	TS, MPa	El, %	RA, %	Eus, J	FATT, °C	TT_{40}, °C	Eus, J	FATT, °C	TT_{40}, °C	ΔFATT, °C	ΔTT_{40}, °C
A-1	65	470	589	28	80	286	−83	−88	293	−78	−80	5	8
A-2		471	593	27	79	289	−65	−69	291	−60	−70	5	−1
A-3		475	600	28	79	289	−78	−86	ND	−60	−69	18	17
A-4		465	594	29	78	281	−83	−88	274	−46	−55	37	33
A-5		479	604	28	76	271	−68	−77	ND	−5	−22	63	55
A-6		465	578	29	81	294	−83	−88	292	−78	−87	5	1
A-1	22	329	512	33	79	291	−33	−38	294	−34	−46	−1	−8
A-2		369	542	28	79	292	−48	−55	292	−38	−47	10	8
A-3		470	606	28	76	289	−76	−86	270	−42	−59	34	27
A-4		468	608	27	76	268	−54	−74	ND	−29	−44	25	30
A-5		476	619	28	74	255	−46	−57	ND	11	−8	57	49
A-6		451	579	29	79	293	−78	−86	293	−66	−72	12	14

Unembrittled: quenched and tempered. Step-Cooled: see Fig. 1.
YS: 0.2% yield strength. TS: tensile strength. El: elongation. RA: reduction of area.
Eus: upper shelf energy. FATT: 50 % shear fracture appearance transition temperature.
TT_{40}: 40 ft·lbf (54 J) energy transition temperature.
ΔFATT, ΔTT_{40}: shift of FATT and TT_{40}, respectively, by step cooling.
ND: not determined.

TABLE 3—*Effect of austenitizing temperature on tensile and impact properties (Steel B-1).*

Austenitizing Temperature, °C	Austenite Grain Size Number (*G*)	Tensile Properties				Impact Properties							
		Unembrittled				Unembrittled			Step-Cooled			Shift	
		YS, MPa	TS, MPa	El, %	RA, %	Eus, J	FATT, °C	TT_{40}, °C	Eus, J	FATT, °C	TT_{40}, °C	ΔFATT, °C	ΔTT_{40}, °C
950	6.9	307	528	30	77	294	−5	−17	286	−5	−17	0	0
1050	3.9	499	619	25	75	266	−30	−43	267	−28	−41	2	2
1200	0.1	510	622	22	73	ND	−15	−30	241	−10	−21	5	9

Unembrittled: quenched and tempered. Step-Cooled: see Fig. 1.
YS: 0.2% yield strength. TS: tensile strength. El: elongation. RA: reduction of area.
Eus: upper shelf energy. FATT: 50% shear fracture appearance transition temperature.
TT_{40}: 40 ft·lbf (54 J) energy transition temperature.
ΔFATT, ΔTT_{40}: shift of FATT and TT_{40}, respectively, by step cooling.
ND: not determined.

TABLE 4—*Effects of austenitizing temperature and manganese, silicon, and phosphorus contents on impact properties.*

Steel	Austenitizing Temperature, °C	Austenite Grain Size Number (G)	Impact Properties									
			Unembrittled			Step-Cooled			Shift		Grain Size Dependence	
			Eus, J	FATT, °C	TT_{40}, °C	Eus, J	FATT, °C	TT_{40}, °C	ΔFATT, °C	ΔTT_{40}, °C	$\Delta\Delta$FATT/ $(-\Delta G)$, °C	$\Delta\Delta TT_{40}$/ $(-\Delta G)$, °C
A-1	900	7.6	286	−88	−94	282	−75	−84	13	10	1.7	2.0
	1200	−0.5	276	−107	−118	286	−80	−92	27	26		
A-2	900	7.1	293	−95	−97	290	−68	−73	27	24	1.8	1.4
	1200	2.1	275	−88	−93	272	−52	−62	36	31		
A-3	900	7.3	287	−101	−110	253	−62	−79	39	31	2.7	2.9
	1200	2.1	282	−108	−128	267	−55	−82	53	46		
A-4	900	6.7	276	−96	−105	286	−27	−61	69	44	2.2	3.1
	1200	1.6	ND	−95	−101	ND	−15	−41	80	60		
A-5	900	6.2	ND	−94	−108	ND	10	−30	104	78	6.4	5.0
	1200	2.6	287	−102	−112	282	25	−16	127	96		
C-1	900	8.3	287	−98	−100	278	−88	−96	10	4	0.8	0.4
	1200	0.4	285	−84	−84	289	−68	−77	16	7		
C-2	900	8.9	293	−81	−90	282	−85	−94	−4	−4	ND	ND
C-3	900	9.9	291	−105	−109	263	−64	−71	41	38	2.2	0.8
	1200	2.5	281	−99	−106	292	−42	−62	57	44		
C-4	900	9.2	292	−81	−86	266	−93	−97	−12	−11	4.5	3.6
	1200	0.5	280	−91	−94	292	−64	−74	27	20		
C-5	900	8.9	292	−84	−84	264	−63	−74	21	10	1.8	2.2
	1200	2.1	280	−80	−90	293	−47	−65	33	25		
C-6	900	9.0	293	−81	−88	280	−64	−86	17	2	1.2	1.6
	1200	0.8	281	−85	−85	288	−58	−70	27	15		
C-7	900	9.5	272	−80	−82	ND	−44	−48	36	34	2.6	1.7
	1200	1.8	271	−87	−94	293	−31	−47	56	47		
C-8	900	8.6	283	−80	−84	ND	−65	−85	15	−1	0	0.2
	1200	0	284	−85	−94	293	−70	−93	15	1		
C-9	900	7.9	242	−81	−92	240	−22	−47	59	45	4.8	4.2
	1200	1.9	224	−82	−96	ND	6	−26	88	70		

Unembrittled: quenched and tempered. Step-Cooled: see Fig. 1. Eus: upper shelf energy.

FATT: 50% shear fracture appearance transition temperature. TT_{40}: 40 ft·lbf (54 J) energy transition temperature.

ΔFATT, ΔTT_{40}: shift of FATT and TT_{40} by step cooling, respectively.

$\Delta\Delta$FATT, $\Delta\Delta TT_{40}$, ΔG: shift of ΔFATT, ΔTT_{40} and austenite grain size number (G), respectively, caused by raising austenitizing temperature from 900 to 1200°C.

ND = not determined.

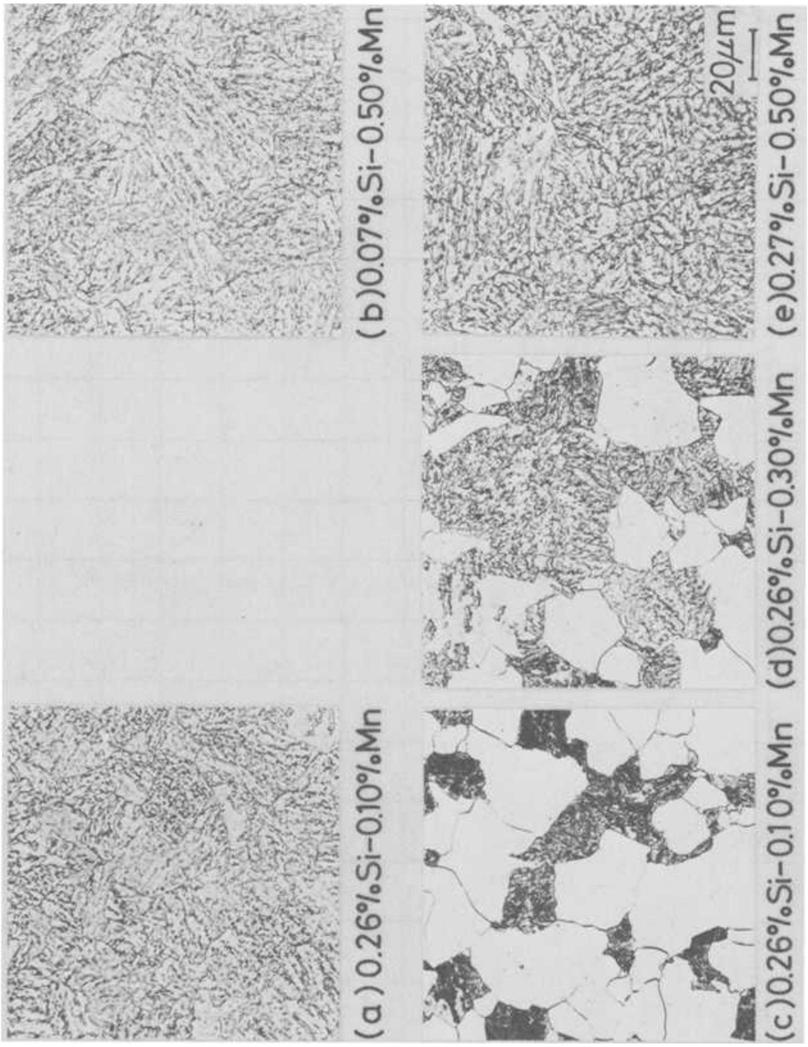

(a) 0.26%Si-0.10%Mn

(b) 0.07%Si-0.50%Mn

(c) 0.26%Si-0.10%Mn

(d) 0.26%Si-0.30%Mn

(e) 0.27%Si-0.50%Mn

FIG. 2—*Typical examples of microstructures of various manganese containing steels and a low-silicon steel. Austenitizing condition is 950°C for 3 h; cooling rates are* (a) *65°C/min and* (b)-(e) *22°C/min.*

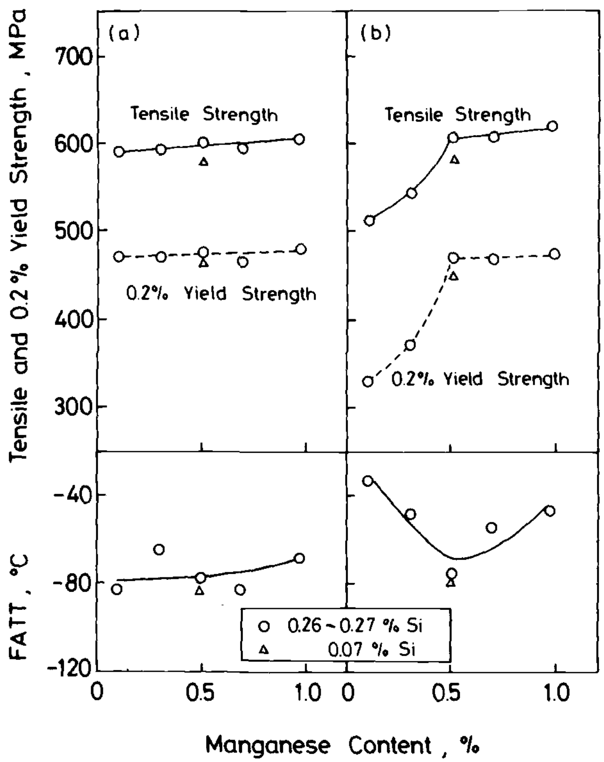

FIG. 3—*Strength and FATT plotted against manganese content in steels with two levels of silicon content. Austenitizing condition is 950°C for 3 h; cooling rates are* (a) *65°C/min and* (b) *22°C/min. Tempering condition is 690°C for 7.5 h, followed by air cooling.*

ferrite. As long as the microstructure consists of fully bainitic structure, the strength and the FATT increase gradually with increasing manganese content. The low-silicon steel has a slightly lower FATT, but lower strength. For example, when cooled at 65°C/min, even the 0.10 percent manganese steel exhibits higher strength than the low-silicon steel. It is shown that the strengthening effect of silicon is larger than that of manganese in the ferrite and pearlite structure [*4*]. This effect is also observed in the bainitic structure of this study. As for the TT_{40}, the same tendency is observed as for the FATT (see Table 2).

The effect of austenitizing temperature on microstructure in Steel B-1 is shown in Fig. 4. A microstructure austenitized at 950°C has 50 percent ferrite, while that austenitized at 1050 or 1200°C exhibits fully bainitic structure; prior austenite grain size numbers are 6.9, 3.9 and 0.1, respectively.

Figure 5 shows the effect of austenitizing temperature on strength and FATT. There is good correspondence between the microstructure and these properties. When the microstructure consists of bainite and ferrite, the

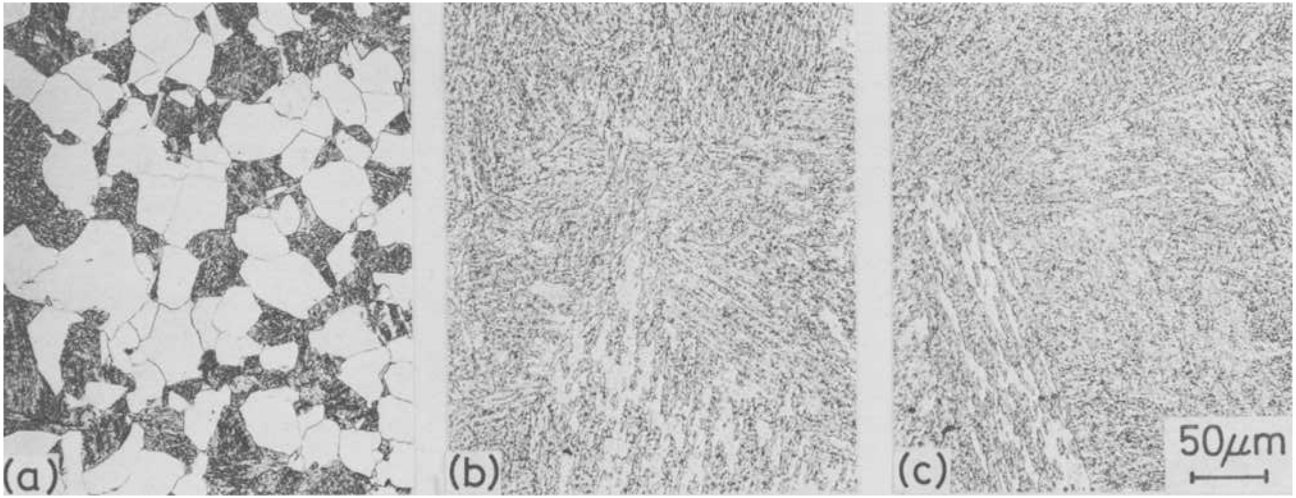

FIG. 4—*Effect of austenitizing temperature on microstructure in Steel B-1. Austenitizing conditions are* (a) *950°C for 2 h,* (b) *1050°C for 2 h, and* (c) *1200°C for 2 h; cooling rate is 5°C/min.*

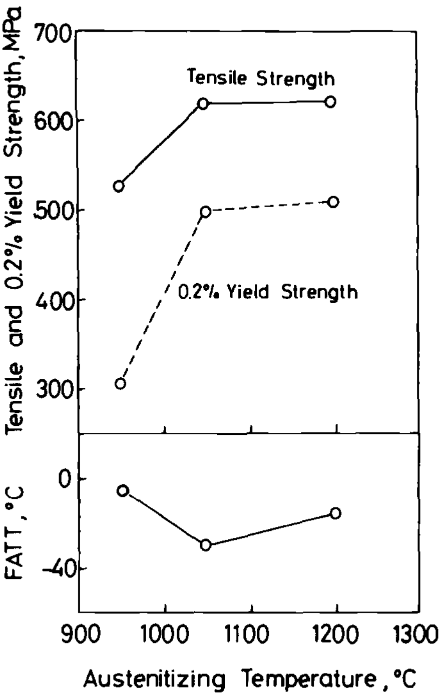

FIG. 5—*Effect of austenitizing temperature on strength and FATT in Steel B-1. Cooling rate from austenitizing temperature is 5°C/min. Tempering condition is 690°C for 19 h, followed by furnace cooling.*

strength is low and the FATT is high, whereas a microstructure consisting fully of bainite exhibits low FATT and much higher strength. Once the microstructure becomes completely bainitic, the strength and FATT increase slightly with increasing austenitizing temperature. The lowest FATT is obtained at 1050°C. The TT_{40} varies almost in the same manner as the FATT does (see Table 3).

When steel is cooled from various austenitizing temperatures at a constant cooling rate, it is sometimes observed that FATT is lower for a higher austenitizing temperature than for lower one. This is well explained in terms of changes in unit crack path and microstructure [5].

Figure 6 shows the brittle-fractured surface of the Charpy specimens revealed by a scanning electron microscope. The unit crack path of the specimen with a fully bainitic structure austenitized at 1050 or 1200°C is slightly finer than that of the specimen with a large amount of ferrite austenitized at 950°C. In addition, the latter exhibits cleavage fracture with river patterns, while the former exhibits quasi-cleavage fracture with many tear ridges. These observations suggest that a fully bainitic structure has a larger resistance to brittle fracture than a structure with a large amount of

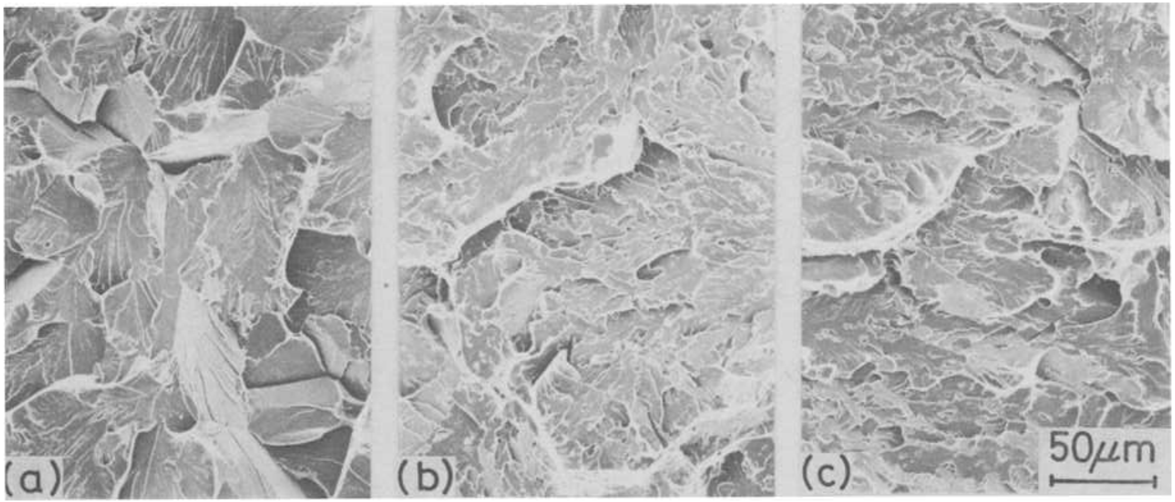

FIG. 6—*Fractographs of brittle-fractured surfaces of the Charpy impact specimens. Austenitizing conditions are* (a) *950°C for 2 h,* (b) *1050°C for 2 h, and* (c) *1200°C for 2 h; cooling rate is 5°C/min. Tempering condition is 690°C for 19 h, followed by furnace cooling.*

ferrite owing to smaller unit crack path and many tear ridges. Therefore it is important to obtain a fully bainitic structure, even though the prior austenite grain becomes coarser.

Temper Embrittlement

Figure 7 shows the FATTs in the unembrittled and step-cooled conditions, and the ΔFATT of the steels with various manganese contents, as well as the low-silicon steel. In Fig. 7*a*, all of the steels have fully bainitic structure, and in this case, the FATT increases abruptly with increasing manganese content in step-cooled condition. In Fig. 7*b*, a fully bainitic structure is obtained when the manganese content is more than 0.50 percent, and in this case, the FATT behaves in the same manner as in Fig. 7*a*. On the other hand, below 0.50 percent manganese, where the microstructure consists of bainite and ferrite, the FATT decreases with increasing manganese content in the step-cooled condition. The lowest FATT is obtained at manganese content of 0.50 percent, where bainite becomes just 100 percent. These results imply that so long as a fully bainitic structure is formed, manganese content should be as low as possible for toughness in the step-cooled condition. The low-silicon

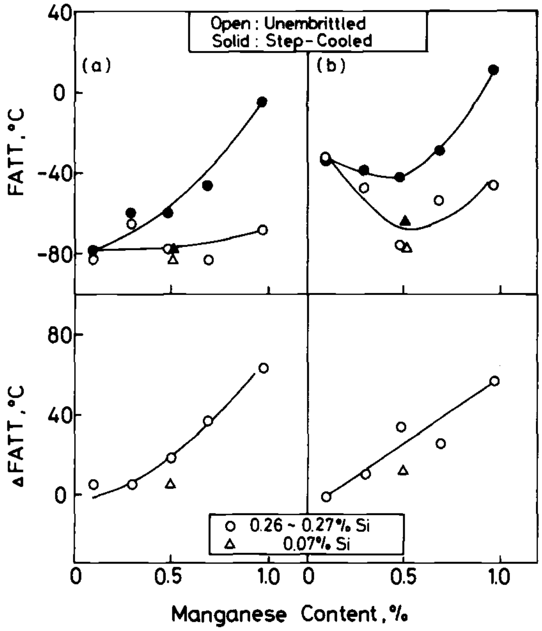

FIG. 7—*FATTs in unembrittled and step-cooled conditions and ΔFATT plotted against manganese content in steels with two levels of silicon content. Austenitizing condition is 950°C for 3 h: cooling rates are* (a) *65°C/min and* (b) *22°C/min. Tempering condition is 690°C for 7.5 h, followed by air cooling.*

steel has low susceptibility to temper embrittlement, and therefore a low value of FATT in the step-cooled condition. The same tendency is observed for the TT_{40} and ΔTT_{40} (see Table 2).

Figure 8 shows the effect of austenitizing temperature on the FATT in the unembrittled and step-cooled conditions, and the ΔFATT. Ferrite and bainite mixed structure and fully bainitic structure are obtained for 950°C and more than 1050°C, respectively (see Fig. 4). The lowest FATTs are obtained at 1050°C in both unembrittled and step-cooled conditions. This is the lowest temperature required to obtain the fully bainitic structure; it is the same for the TT_{40} (see Table 3).

Capus has studied the effect of austenite grain size on temper embrittlement, using a nickel-chromium steel with 0.023 percent phosphorus or 0.074 percent tin, as well as a base steel, and showed that temper embrittlement depended less on grain size for the pure steel than for the steel with 0.023 percent phosphorus or 0.074 percent tin [*6*]. To confirm this tendency, an additional study was conducted using Steels A-1 to A-5 with different manganese contents and C-1 to C-9 with different silicon and phosphorus contents.

Figure 9*a* shows the effects of manganese content and austenite grain size on susceptibility to temper embrittlement. Figure 9*b* shows the effect of manganese content on the grain size dependence of susceptibility, $\Delta\Delta$FATT/$(-\Delta G)$, where $\Delta\Delta$FATT and ΔG are shifts of ΔFATT and G, respectively, caused by raising the austenitizing temperature from 900 to 1200°C. It is noteworthy that even with coarse austenite grain size, caused by higher austenitizing temperature, the susceptibility can be sufficiently decreased by

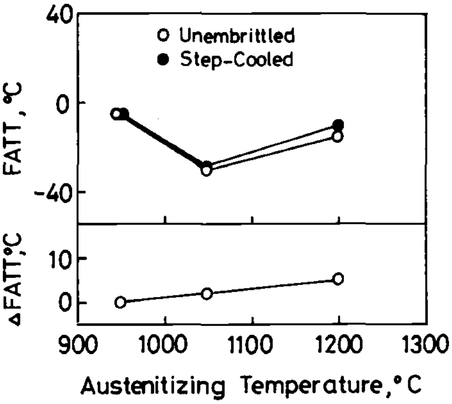

FIG. 8—*Effect of austenitizing temperature on FATTs in unembrittled and step-cooled conditions and ΔFATT in Steel B-1. Cooling rate from austenitizing temperature is 5°C/min. Tempering condition is 690°C for 19 h, followed by furnace-cooling.*

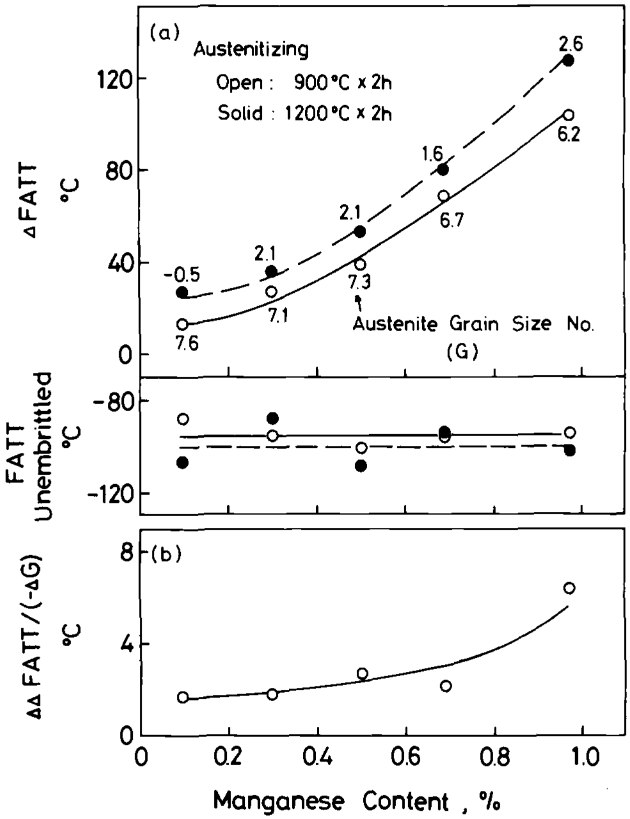

FIG. 9—(a) *Effects of manganese content and austenite grain size on FATT in unembrittled condition and ΔFATT. Austenitizing conditions are 900°C for 2 h (open mark) and 1200°C for 2 h (solid mark); cooling rate is 500°C/min. Tempering condition is 690°C for 17 h, followed by water cooling.* (b) *Effect of manganese content on austenite grain size dependence of susceptibility to temper embrittlement, ΔΔFATT/(−ΔG), where ΔΔFATT and ΔG are shift of ΔFATT and G, respectively, caused by raising austenitizing temperature from 900 to 1200°C.*

reducing the manganese content. This is because lower manganese content results in a decrease not only in susceptibility to temper embrittlement, but also in the increase in susceptibility caused by coarsening of austenite grain size (Fig. 9*b*).

Figure 10 shows the same tendency in steels with different silicon and phosphorus contents. This figure also shows that a lower phosphorus content compensates for the increase in susceptibility to temper embrittlement caused by silicon. For example, the steel with 0.36 percent silicon and 0.005 percent phosphorus contents shows low ΔFATT even when the austenite grain size becomes coarser. This tendency is also observed for the TT_{40} (see Table 4).

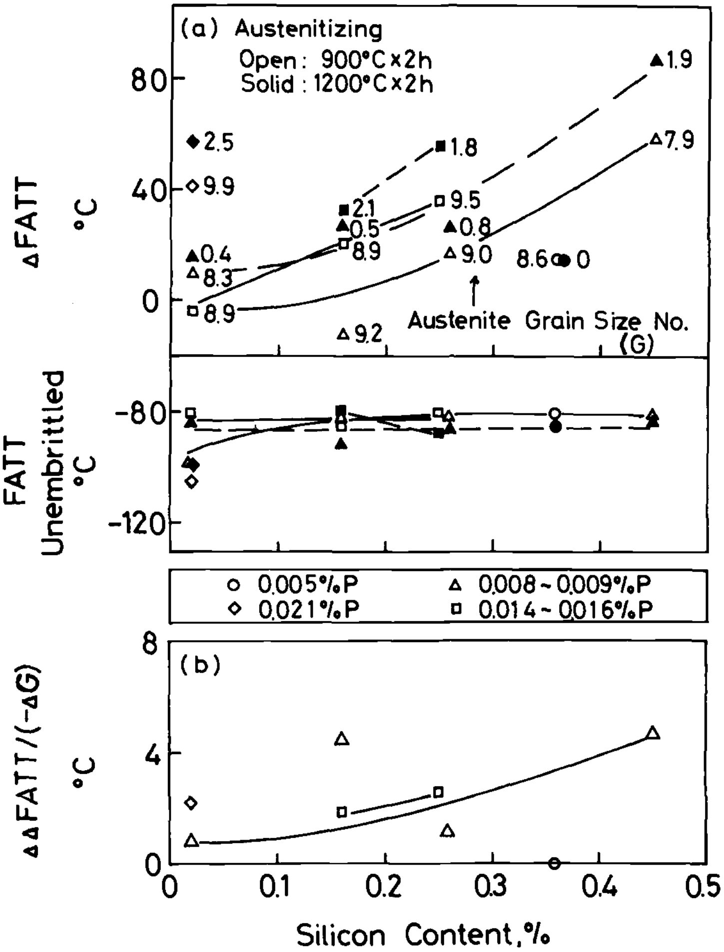

FIG. 10—(a) *Effects of silicon and phosphorus contents and austenite grain size on FATT in unembrittled condition and ΔFATT. Austenitizing conditions are 900°C for 2 h (open mark) and 1200°C for 2 h (solid mark); cooling rate is 500°C/min. Tempering condition is 690°C for 17 h, followed by water cooling.* (b) *Effects of silicon and phosphorus contents on austenite grain size dependence of susceptibility to temper embrittlement, ΔΔFATT/(−ΔG), where ΔΔFATT and ΔG are shift of ΔFATT and G, respectively, caused by raising austenitizing temperature from 900 to 1200°C.*

Manufacture of Actual Size Forging

A 2¼Cr-1Mo steel nozzle forging with a maximum thickness of 397 mm was manufactured. The material was required to meet the following specifications:

1. Austenite grain size number is greater than 4.
2. 0.2 percent yield strength is more than 314 MPa at both room temperature and 425°C.
3. Tensile strength is 520 to 686 MPa at room temperature.
4. $TT_{40} + (1.5 \times \Delta TT_{40})$ is less than 38°C.

The steel was refined by a basic oxygen furnace and a ladle refining furnace, and poured into an 18-ton ingot. The ingot was healed at 1250°C and hollow forged by a 6000-ton press. The forging was normalized at 950°C for 12 h, and machined into the shape shown in Fig. 11. Then it was austenitized at 1000°C for 11.8 h to obtain high hardenability while satisfying the requirement for the austenite grain size, and quenched in water. Subsequently it was tempered at 680°C for 15.5 h, followed by air cooling. A test coupon was cut from the location shown in Fig. 11, simulated postweld heat treated at 690°C for 19 h, followed by furnace cooling, and finally step cooled (see Fig. 1).

The chemical composition of the steel is given in Table 5. Manganese content was adjusted so as to obtain fully bainitic structure, and silicon was added to obtain higher strength. Phosphorus content was reduced to an extremely low level to compensate for temper embrittlement caused by silicon.

Tension and impact test specimens were prepared from the coupon. Their axes were parallel to the tangential direction. Tension tests at room temperature and impact tests were performed under the same conditions as those in the laboratory experiment. Tension tests at elevated temperatures were carried out using 12.5-mm-diameter specimens with a 50-mm gage length.

Figure 12 shows that a fully bainitic structure is obtained. A prior austenite grain size number is 4.6.

Table 6 shows the mechanical properties in the unembrittled and step-cooled conditions. The forging has high strength and low susceptibility to temper embrittlement, and therefore has good toughness even in the step-cooled condition.

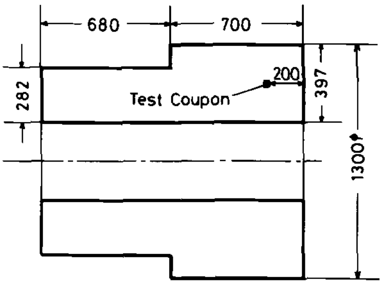

FIG. 11—*Cross section of 2¼Cr-1Mo steel forging.*

TABLE 5—*Chemical composition of 2¼Cr-1Mo steel forging (weight percent).*

C	Si	Mn	P	S	Cu	Ni	Cr	Mo	Al	N	Sn	Sb	As
0.13	0.25	0.53	0.003	0.003	0.16	0.15	2.33	0.96	0.011	0.0048	0.001	0.0003	0.002

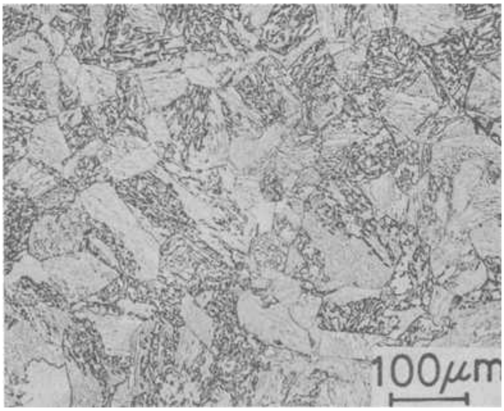

FIG. 12—*Microstructure of 2¼Cr-1Mo steel forging.*

TABLE 6—*Tensile and impact properties of 2¼Cr-1Mo steel forging.*

Test Temperature	0.2 % Yield Strength, MPa	Tensile Strength, MPa	Elongation, %	Reduction of Area, %
Room temperature	460	584	29	79
	462	586	27	78
400°C	400	495	19	72
425°C	391	479	21	73
	385	477	20	74
450°C	380	469	22	73
500°C	369	431	24	79
550°C	353	383	28	84

Quenched, Tempered, and Postweld Heat Treated								
Unembrittled			Step-Cooled			Shift		
Eus, J	FATT, °C	TT_{40}, °C	Eus, J	FATT, °C	TT_{40}, °C	ΔFATT, °C	ΔTT_{40}, °C	$TT_{40} + (1.5 \times \Delta TT_{40})$, °C
289	−59	−71	289	−46	−61	13	10	−56

Unembrittled: quenched, tempered, and postweld heat treated.
Step-Cooled: see Fig. 1.
Eus: upper shelf energy.
FATT: 50% shear fracture appearance transition temperature.
TT_{40}: 40 ft·lbf (54 J) energy transition temperature.
ΔFATT, ΔTT_{40}: shift of FATT and TT_{40}, respectively, by step cooling.

Conclusions

1. High manganese content or high austenitizing temperature improves the strength and initial toughness by suppressing the formation of ferrite. Once a fully bainitic structure is obtained, the increase in strength and the decrease in toughness are small even if the manganese content or the austenitizing temperature increases.
2. The manganese content should be as low as possible under the condition where the fully bainitic structure is obtained for toughness in the step-cooled condition. The increase in susceptibility to temper embrittlement caused by a high austenitizing temperature is small. It may be compensated for by reducing manganese, silicon, or phosphorus content.
3. The addition of silicon, intended to obtain higher strength, must be compensated for by lowering the phosphorus content to decrease the susceptibility to temper embrittlement.
4. On the basis of the laboratory experiments, a 2¼Cr-1Mo steel forging with a thickness of 397 mm was produced. The forging exhibited a good combination of strength and toughness in the step-cooled condition.

References

[1] Wada, T. and Hagel, W. C., *Metallurgical Transactions A*, Vol. 7A, Sept. 1976, pp. 1419-1426.
[2] Watanabe, J., Shindo, Y., and Murakami, Y., *Tetsu To Hagane*, Vol. 61, No. 12, Sept. 1975, p. s726.
[3] Kanazawa, S., Kado, S., Otoguro, Y., Shiotsuka, K., and Hashimoto, K., *Tetsu To Hagane*, Vol. 62, No. 4, March 1976, p. s285.
[4] Irvine, K. J. and Pickering, F. B., *Journal of the Iron and Steel Institute*, Vol. 201, Part 11, Nov. 1963, pp. 944-959.
[5] Kunitake, T., Terasaki, F., Ohmori, Y., and Ohtani, H. in *Proceedings, Symposium Toward Improved Ductility and Toughness*, sponsored by Climax Molybdenum Company, Kyoto, Japan, 25-26 Oct. 1971, pp. 83-100.
[6] Capus, J. M., *Journal of the Iron and Steel Institute*, Vol. 200, Part 11, Nov. 1962, pp. 922-927.

Y. Murakami,[1] *T. Nomura,*[1] *and J. Watanabe*[2]

Heavy-Section 2¼Cr-1Mo Steel for Hydrogenation Reactors

REFERENCE: Murakami, Y., Nomura, T., and Watanabe, J., **"Heavy-Section 2¼Cr-1Mo Steel for Hydrogenation Reactors,"** *Application of 2¼Cr-1Mo Steel for Thick-Wall Pressure Vessels. ASTM STP 755,* G. S. Sangdahl and M. Semchyshen, Eds., American Society for Testing and Materials, 1982, pp. 383-417.

ABSTRACT: 2¼Cr-1Mo steel has been widely used for high-temperature, high-pressure hydrogenation reactors such as hydrodesulfurizing reactors. Material degradations that have been found to occur during the service life of such equipment are hydrogen damage, creep embrittlement, and temper embrittlement. A brief review is made of these embrittlements, among which the latter has been considered the most serious. A study of the effect of chemical composition on temper embrittlement showed that susceptibility of 2¼Cr-1Mo steel to temper embrittlement can be well expressed by the J-factor [(Si + Mn) (P + Sn) × 10^4] and therefore can be reduced by lowering the J-factor value. 2¼Cr-1Mo steel with very low J-factor is easily obtained by lowering silicon content by applying the vacuum carbon deoxidation (VCD) process. Temper embrittlement susceptibility of the weld heat affected zone can be also minimized by the same compositional countermeasures as in the base metal. Temper embrittled steel was found to be further deteriorated by the presence of hydrogen so as to exhibit extremely low fracture toughness. Such hydrogen embrittlement can be reduced by minimizing temper embrittlement susceptibility. Seeking the scale merit of units and to meet the future requirements of coal liquefaction processes, reactors of considerable size (much larger than now exist) are being considered. From this viewpoint, availability of material for heavy-section pressure vessels is discussed based on the heat-treatment characteristics of 2¼Cr-1Mo steel. The formation of polygonal ferrite must be avoided in order to ensure adequate mechanical properties of 2¼Cr-1Mo steel. This was found possible for a thickness up to about 450 mm when accelerated cooling in water was applied. Mechanical properties of a heavy-section, low-silicon 2¼Cr-1Mo steel with thicknesses of 450 and 300 mm were also studied, and sufficient and homogeneous properties were confirmed.

KEY WORDS: cracking, creep, ductility, fracture toughness, heat treatment, heat affected zone (HAZ), homogeneity, hydrogen attack, hydrogen embrittlement, isothermal treatment, mechanical properties, notch toughness, phosphorus, pressure vessels, silicon, steels, step cooling, temper embrittlement, tin, transition temperature

---

[1] Research Laboratory, Muroran Plant, The Japan Steel Works, Ltd., Muroran, Japan.
[2] Material Research Laboratory, The Japan Steel Works, Ltd., Muroran, Japan.

In the oil refining industry, many hydrogenation units, such as hydrocracking, hydrodesulfurizing, and catalytic reforming, are in operation. 2¼Cr-1Mo steel has been one of the most familiar reactor materials in the hydrogenation unit, mainly because of its excellent resistance to hydrogen attack and its high temperature strength. Additionally, long industrial experience has shown that 2¼Cr-1Mo steel has good stability of metallurgical and mechanical properties. However, recent studies pointed out the possibility of environmental degradation of 2¼Cr-1Mo steel during service, and the importance of minimizing the degradation in order to ensure reactor safety [*1,2*].[3] Such material degradation problems and their countermeasures will be discussed.

In an effort to upgrade the service condition and to search the scale merit, larger and thicker reactors are required in hydrogenation processes. At the same time, coal liquefaction technology, which is considered one of the major alternative energy technologies, also requires the large-size reactor in order for the process to be economical. From this point of view, availability of heavy-section 2¼Cr-1Mo steel will be discussed based on its heat-treatment characteristics.

Finally, mechanical properties and homogeneity of the heavy-section 2¼Cr-1Mo steel forging made by the vacuum carbon deoxidation (VCD) process, which is recommended in view of temper embrittlement, will be presented.

Requirements for 2¼Cr-1Mo Steel for Hydrogenation Services

It is common practice to design, fabricate, and inspect pressure vessels in accordance with the American Society of Mechanical Engineers (ASME) Boiler and Pressure Vessel Code. The Code calls for the following material properties: (*1*) strength necessary for the guarantee of the allowable stress, including room and design temperature tensile, creep, and fatigue properties, (*2*) notch toughness at the lowest operating (including the pressure test) temperature, and (*3*) weldability.

In addition to these minimum Code requirements for the as-fabricated condition, 2¼Cr-1Mo steel for high-temperature, high-pressure hydrogenation services is required to have good resistance to such environmental degradation problems during long-time operation as toughness deterioration due to temper embrittlement, hydrogen damages, and creep cracking.

Notch Toughness

Many hydrogenation reactors made of chromium-molybdenum steels are operating at the temper embrittlement temperature range of 325 to 575°C.

---

[3] The italic numbers in brackets refer to the list of references appended to this paper.

Figure 1 illustrates the change in fracture toughness for a 2¼Cr-1Mo steel that was temper embrittled during approximately seven years of service life of a hydrodesulfurizing reactor [*3*]. Thus temper embrittlement reduced fracture toughness and then the critical flaw size for the brittle fracture. A prediction method of the fracture toughness from Charpy-V notch impact properties and yield strength has been proposed for 2¼Cr-1Mo steel [*3,4*]. Temper embrittlement susceptibility of various Cr-Mo steels (Tables 1 and 2) was compared by means of a step cooling (Fig. 2), which is an accelerated embrittling treatment used to predict temper embrittlement susceptibility in relatively short test period. The results are shown in Fig. 3. Temper embrittlement susceptibility of 2¼Cr-1Mo steel is very high among Cr-Mo steels and ranks next to (but almost equal to) that of 3Cr-1Mo steel. Though studies on the mechanisms of temper embrittlement and on the less sensitive steels are still continuing [*5,6*], effective countermeasures are desired for 2¼Cr-1Mo steel, whose manufacturing and service experiences in the hydrogenation process cannot be easily replaced by other materials.

Effect of Chemical Composition—In order to predict the temper embrittlement susceptibility of 2¼Cr-1Mo steel, *J*-factor $(\text{Si} + \text{Mn})(\text{P} + \text{Sn}) \times 10^4$ has been proposed [*7*]. The other known contributors to temper embrittlement, arsenic and antimony, are less effective in 2¼Cr-1Mo steel when they are controlled under 0.020 and 0.004 percent, respectively. Figures 4 and 5 show relations between *J*-factor and 50 percent shear fracture appearance transition temperature (FATT) in the various embrittling conditions, which were obtained from tests on 48 heats of 2¼Cr-1Mo steel forgings and plates with thicknesses ranging from 64 to 450 mm. Good correlations between *J*-factor and temper embrittlement susceptibility are obtained in spite of a wide

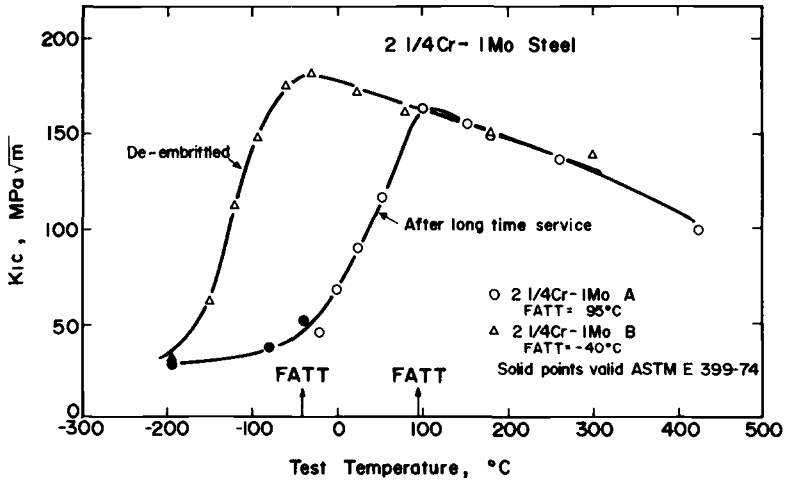

FIG. 1—*Fracture toughness versus temperature behavior of 2¼Cr-1Mo steel* [3].

TABLE 1—*Chemical compositions of chromium-molybdenum steels examined.*[a]

Steel	C	Si	Mn	P	S	Cr	Mo	Al	As	Sn	Sb
1Cr-½Mo	0.16	0.24	0.58	0.007	0.007	1.06	0.55	0.018	0.012	0.018	0.0022
1¼Cr-½Mo	0.15	0.71	0.56	0.008	0.005	1.39	0.51	0.022	0.015	0.016	0.0027
2¼Cr-1Mo	0.15	0.31	0.61	0.009	0.011	2.35	1.10	0.020	0.010	0.021	0.0032
3Cr-1Mo	0.15	0.26	0.58	0.009	0.009	3.04	1.01	0.014	0.011	0.016	0.0032
5Cr-½Mo	0.16	0.17	0.58	0.008	0.015	4.92	0.52	0.005	0.014	0.013	0.0029
9Cr-1Mo	0.17	0.60	0.55	0.010	0.017	8.84	1.01	0.010	0.014	0.009	0.0024

[a] In weight percent.

TABLE 2—*Thickness and heat treatments of chromium-molybdenum steels examined.*

Steel	Thickness, mm	Normalizing Conditions		Tempering[a]
		Austenitizing	Cooling	
1Cr-½Mo	117	920°C for 5 h	accelerated cooling in water	670°C for 5 h + 680°C for 9 h
1¼Cr-½Mo	133	920°C for 3 h	accelerated cooling in water	650°C for 30 h
2¼Cr-1Mo	127	920°C for 5 h	accelerated cooling in water	650°C for 5 h + 690°C for 20 h
3Cr-1Mo	140	920°C for 5 h	accelerated cooling in water	670°C for 8 h + 710°C for 10 h
5Cr-½Mo	120	930°C for 2 h	programmed cooling[b]	750°C for 5 h
9Cr-1Mo	120	930°C for 2 h	programmed cooling[b]	750°C for 5 h

[a] The cooling rate from the final tempering temperature is 50°C/h.

[b] Average cooling rate at the programmed cooling is 20°C/min in the range of 930 to 450°C.

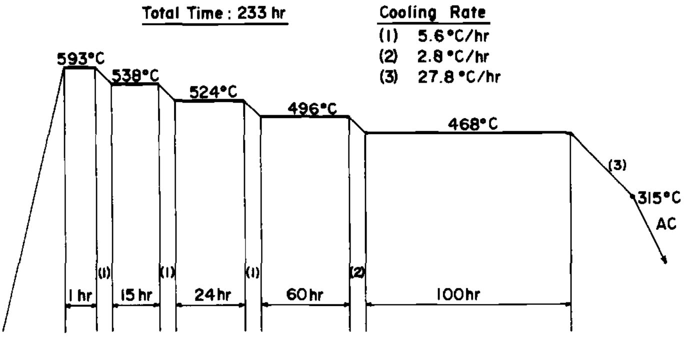

FIG. 2—*Step cooling used in this study.*

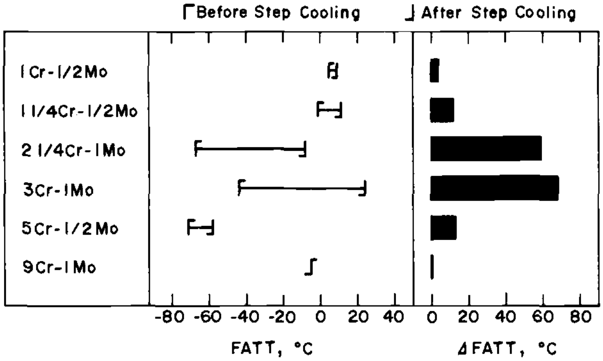

FIG. 3—*Comparison of temper embrittlement susceptibility among chromium-molybdenum pressure vessel steels.*

variety of manufacturing variables, such as thickness, heat treatment, and other chemical compositions.

It is a known countermeasure for the temper embrittlement of 2¼Cr-1Mo steel to lower phosphorus content [*8, 9*] by which the *J*-factor can be significantly reduced. Figure 6 shows the relation between silicon content and shift of FATT (ΔFATT) caused by a step cooling. Susceptibility of the steel depends noticeably on silicon content, and with silicon content less than 0.10 percent, ΔFATT is very small. It may be thus concluded that lowering silicon content is also a good tool for minimizing temper embrittlement susceptibility of 2¼Cr-1Mo steel. 2¼Cr-1Mo steels with very low silicon content can be made by the vacuum carbon deoxidation (VCD) process.

An isothermal temper embrittlement characteristic of a recently manufactured 2¼Cr-1Mo VCD steel with low silicon content is shown in Fig. 7 compared with the embrittlement behavior of a high silicon steel which was embrittled during approximately 30 000 h service at 332 to 432°C. Figure 8

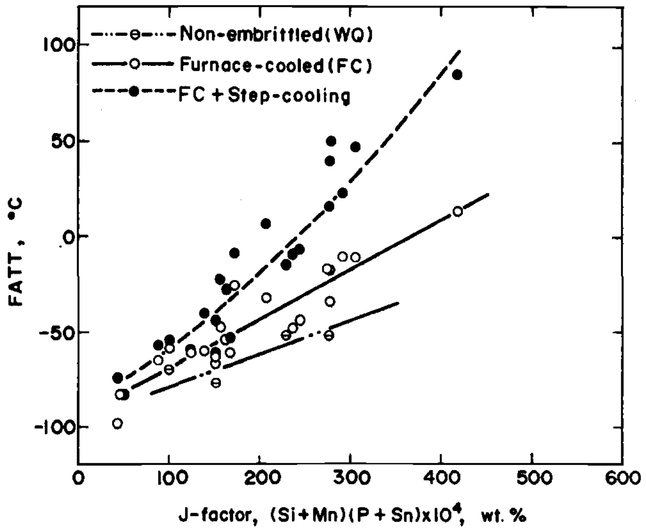

FIG. 4—*Effect of J-factor on FATT of 2¼Cr-1Mo steel forgings in nonembrittled (WQ), furnace-cooled (FC), and step-cooled (SC) conditions (WQ: water quenched from tempering temperature; FC: furnace cooled from tempering temperature at 50°C/h; SC: FC plus step cooling).*

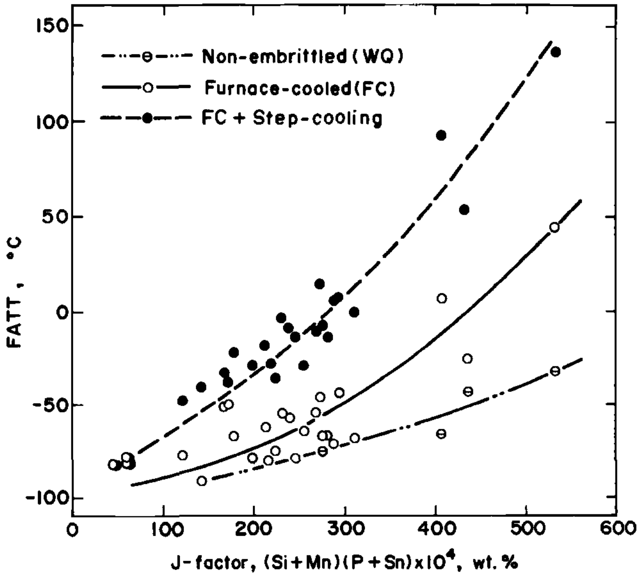

FIG. 5—*Effect of J-factor on FATT of 2¼Cr-1Mo steel plates in nonembrittled (WQ), furnace-cooled (FC), and step-cooled (SC) conditions (WQ: water quenched from tempering temperature; FC: furnace cooled from tempering temperature at 50°C/h; SC: FC plus step cooling).*

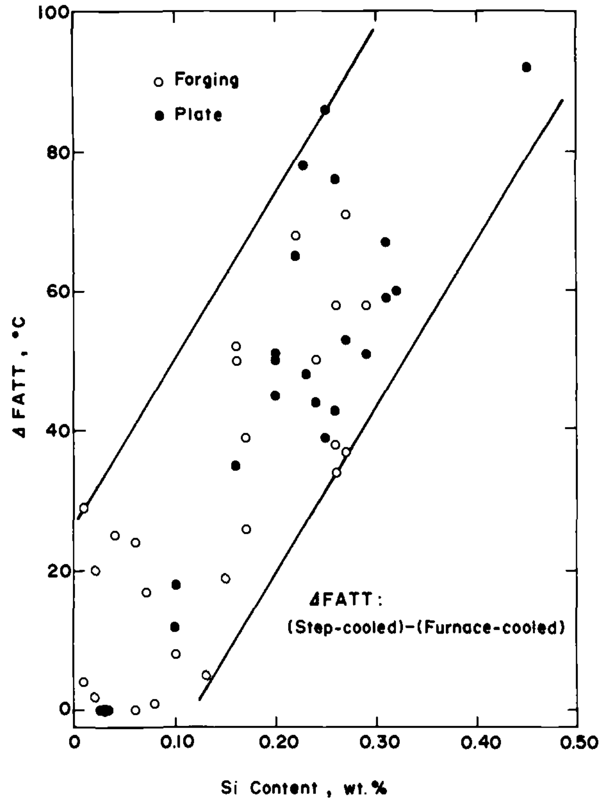

FIG. 6—*Effect of silicon content on the shift of FATT (ΔFATT) of 2¼Cr-1Mo steel caused by step-cooling.*

shows the effect of *J*-factor on FATT after 10 000 h exposure at 427, 454, and 482°C. These experimental data proved that lowering silicon content and thus *J*-factor is effective in minimizing the susceptibility of 2¼Cr-1Mo steel to temper embrittlement caused by isothermal aging as well as by a step cooling.

Temper Embrittlement Susceptibility of the Heat-Affected Zone—Sometimes in the weld heat-affected zone (HAZ), metallurgical and mechanical discontinuities co-exist, and then it is considered meaningful to evaluate its susceptibility to temper embrittlement to secure the pressure vessel safety. Temper embrittlement behavior of the HAZ coarse region of various chromium-molybdenum steels synthetically produced by heating specimens at a peak temperature of 1350°C were compared by means of a step cooling; the results are shown in Fig. 9 [*10*].

1Cr-½Mo steel exhibits almost no temper embrittlement susceptibility even in HAZ. The microstructure of 1¼Cr-½Mo steel changes from the fine

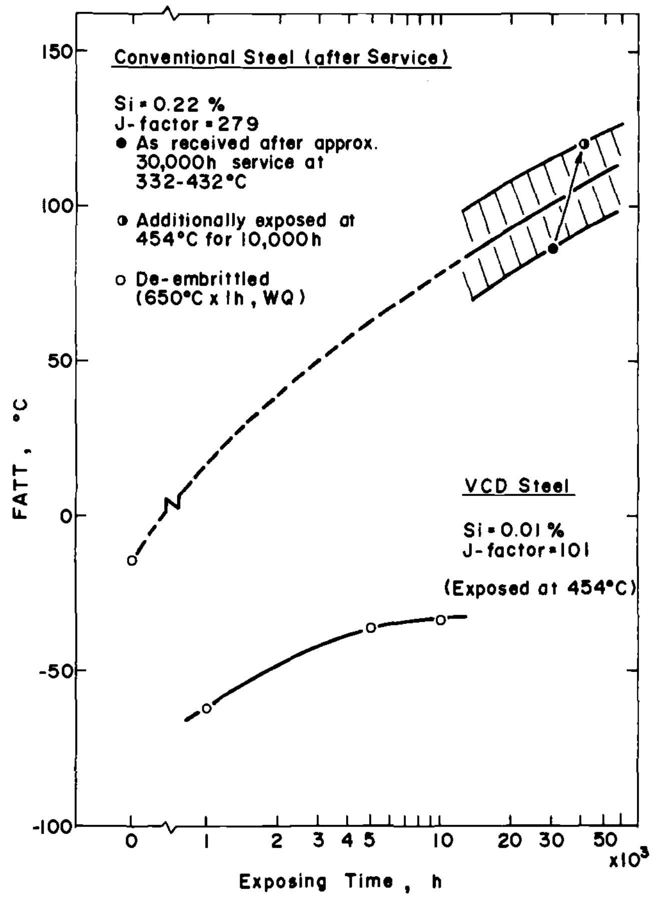

FIG. 7—*Comparison of temper embrittlement behavior between a conventional and a low silicon, vacuum carbon deoxidized 2¼Cr-1Mo steel.*

mixed structure of ferrite, pearlite, and bainite to the coarse bainitic structure by the synthetic heat treatment of HAZ (Figs. 10*a* and 10*b*), and this microstructural change significantly increases temper embrittlement susceptibility of HAZ of the high-silicon, high-impurity steel. It was proved, however, that lowering silicon content (silicon: 0.50 to 0.60 percent) and impurity control ($P + Sn \leq 0.030$ percent) was effective in reducing temper embrittlement susceptibility of HAZ of 1¼Cr-½Mo steel to the sufficiently low level just as proved in the base metal.

Though the microstructural change in 2¼Cr-1Mo and 3Cr-1Mo steels due to HAZ heat cycle is not so remarkable as in 1¼Cr-½Mo steel, a certain increase in temper embrittlement susceptibility, probably attributable to the grain coarsening, is observed. The susceptibility of HAZ in these steels clearly

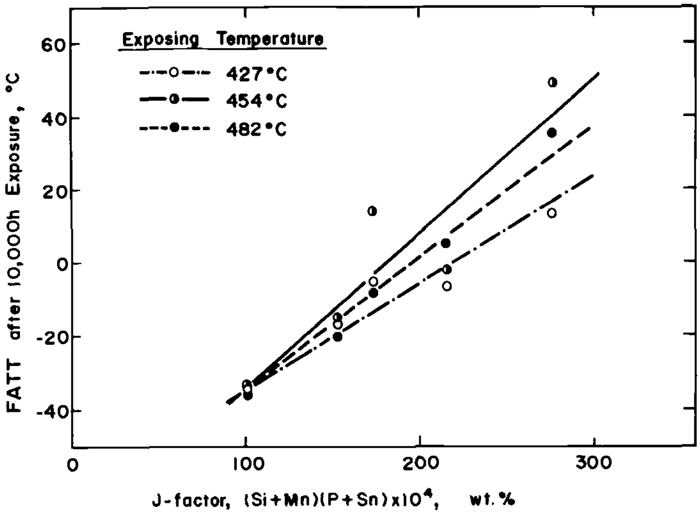

FIG. 8—*Relation between J-factor and FATT of 2¼Cr-1Mo steel after 10 000 h exposure at 427, 454, and 482°C.*

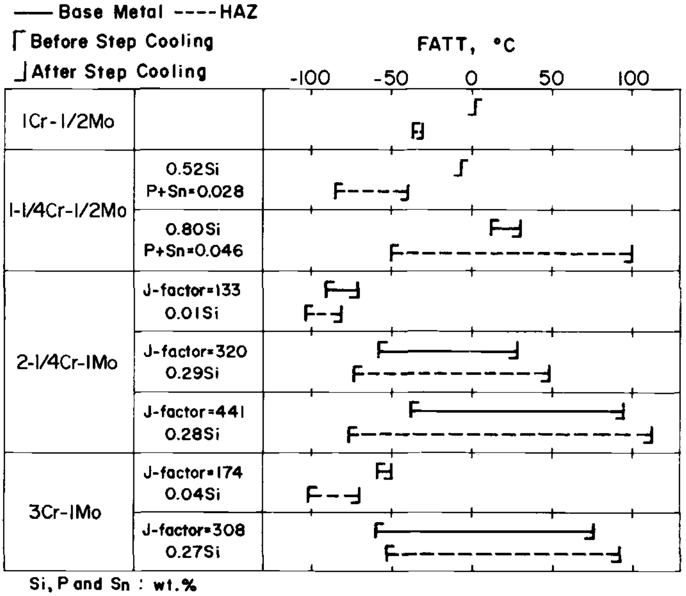

FIG. 9—*FATT of base metal and synthetic HAZ (peak temperature: 1350°C) of various chromium-molybdenum steels before and after a step cooling (PWHT—1Cr-½Mo and 1¼Cr-½Mo: 20 h at 650°C; 2¼Cr-1Mo and 3Cr-1Mo: 20 h at 690°C)* [10].

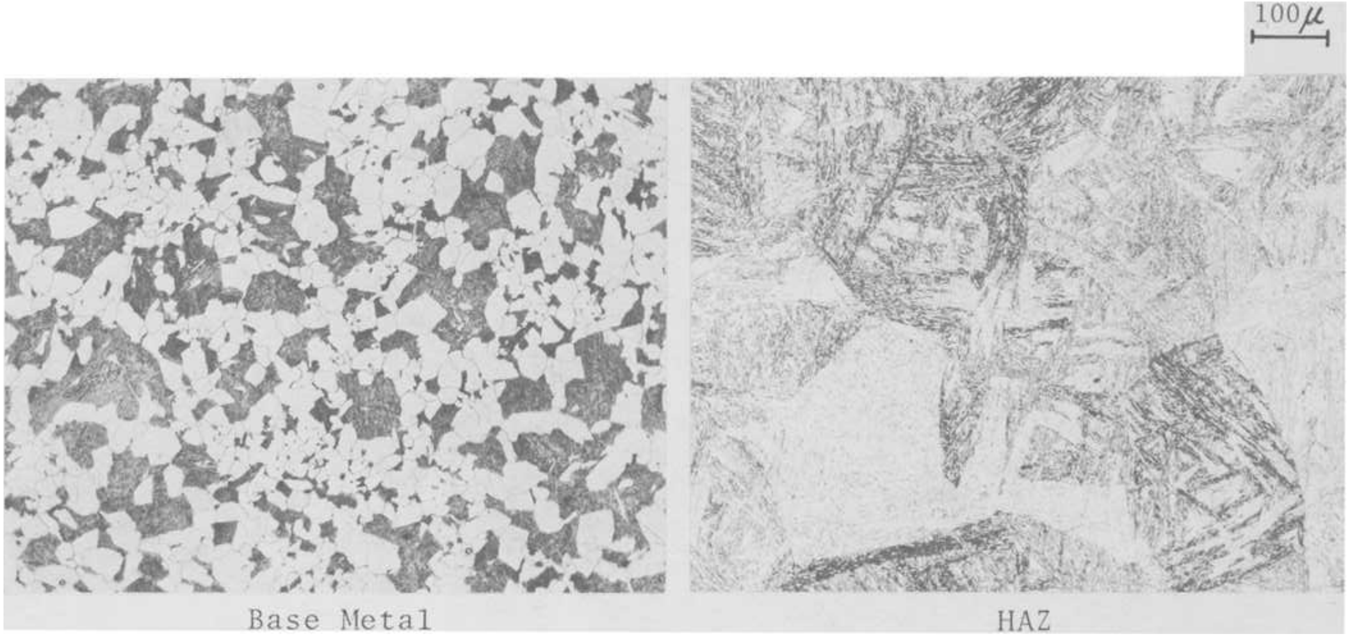

FIG. 10a—*Microstructural change in 1¼Cr-½Mo steel caused by a synthetic heat cycle of HAZ (peak temperature: 1350°C).*

FIG. 10*b*—*Microstructural change in 2¼Cr-1Mo steel caused by a synthetic heat cycle of HAZ (peak temperature: 1350°C).*

depends on the *J*-factor. FATT after a step cooling of the low-silicon, low-*J*-factor steel is well below that of the base metal, showing that lowering silicon content and *J*-factor control are effective countermeasures for HAZ as in the base metal.

Figure 11 shows the effect of peak temperature on FATT of the synthetically produced 2¼Cr-1Mo HAZ before and after a step cooling. In addition to this single heat cycle study, effects of multiple heat cycle in the synthetic HAZ of 2¼Cr-1Mo steel have been discussed elsewhere [*11*]. From these results, the following brief summary can be made for temper embrittlement of HAZ of 2¼Cr-1Mo steel:

1. Temper embrittlement susceptibility of the high-silicon, high-*J*-factor steel is increased by the low-temperature heat input below A_{C1}.
2. In the high-silicon, high-*J*-factor steel, the susceptibility decreases in the grain refining condition (peak temperature: 800 to 1000°C) and increases in the grain coarsening condition (peak temperature: over 1100°C).
3. In the low-silicon, low-*J*-factor steel, FATT of HAZ after a step cooling is lower than that of the base metal even in the grain coarsening condition.

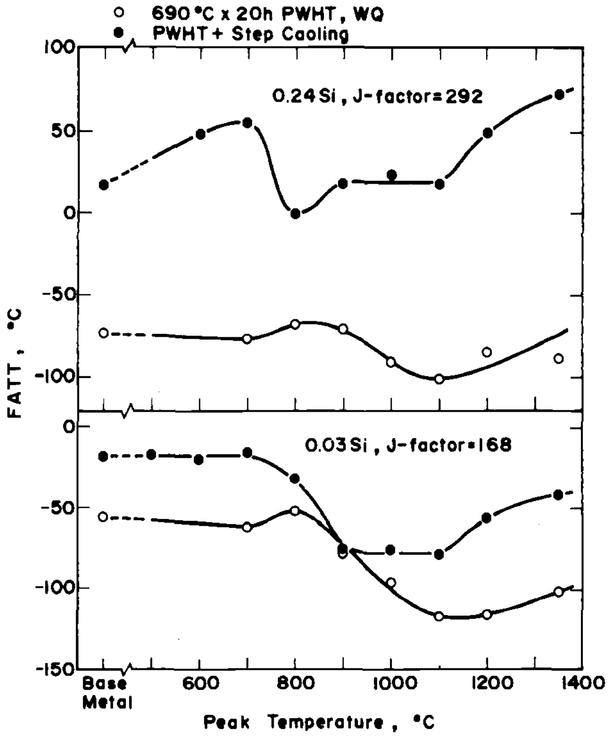

FIG. 11—*Effect of peak temperature on FATT of synthetic HAZ of 2¼Cr-1Mo steel before and after step cooling* [11].

4. Effects of the multiple heat cycles of HAZ beyond A_{C1} temperature may be determined by the peak temperature of the last heat cycle.
5. The HAZ of the actual multi-pass weldment probably has the same level of temper embrittlement susceptibility as in the base metal because of the alternate repetition of the coarse and fine grained regions.

It can be concluded that temper embrittlement susceptibility of HAZ in chromium-molybdenum steels can be controlled to the minimum level by a proper selection of the base metal chemistry.

Effect of Hydrogen Environment

Hydrogen Attack—The first consideration to be given in selecting materials of the pressure vessels for a hydrogenation unit is hydrogen attack. At higher temperatures, hydrogen diffused in a steel can react with carbon atoms to form methane. The accumulation of methane at certain locations in steels, such as grain boundaries and nonmetallic inclusions, causes the irreversible loss of strength and ductility. Elevated temperature exposure in hydrogen sometimes results in surface decarburization. These damages in the steel are called hydrogen attack. The Nelson curve [*12*] gives a guide to selecting a material resistant to hydrogen attack at a given hydrogen pressure and temperature. The curve has been established from research and long-term performance information and gives the basis to select steel chemistry, such as chromium and molybdenum. However, it must be noted that the resistance to hydrogen attack is affected by other metallurgical factors, such as the effects of tempering and postweld heat treatment, which are not reflected in the Nelson curve.

The as-quenched steel shows severe loss of ductility due to the exposure in the high-temperature, high-pressure hydrogen, and the higher the tempering temperature the more resistance is observed [*13*]. Figure 12 shows the effect of the postweld heat treatment on hydrogen attack of the weld joint. It shows a remarkable improvement in the tensile ductility by a postweld heat treatment. Yamazaki et al [*14*] report that if a postweld heat treatment of the 2¼Cr-1Mo steel weldment is omitted, it will be hydrogen attacked at temperatures about 100°C below the temperature the Nelson curve illustrates. Figure 13 shows typical intergranular cracks caused by hydrogen attack in the coarse grain region of HAZ of a 2¼Cr-1Mo steel weldment. These facts show that the stability of carbides has an important role in hydrogen attack and that a selection of a material by the Nelson curve should be limited to materials which receive sufficient tempering or postweld heat treatment.

As clearly marked in Fig. 12, weld joint tensile specimens fail at HAZ when the severe condition of hydrogen attack is applied, even though they have been sufficiently postweld heat treated. This means that the damage in HAZ may be a critical problem in hydrogen attack of such a pressure vessel

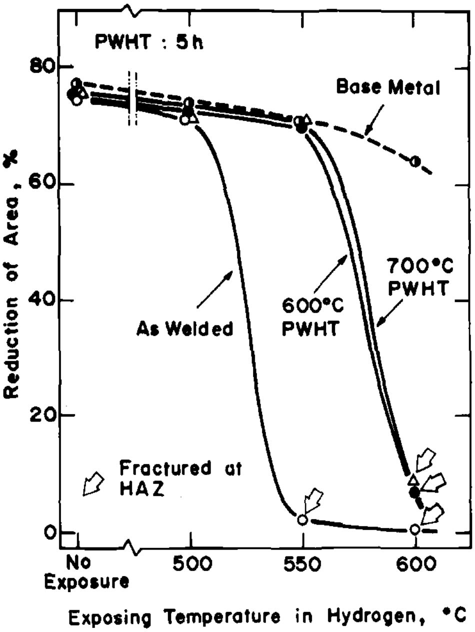

FIG. 12—*Effect of postweld heat treatment on resistance to hydrogen attack of 2¼Cr-1Mo weld joint (hydrogen pressure: 29.4 MPa: exposure time: 360 h)* [13].

weldment. In some coal liquefaction processes, the new reactor design being considered is severer than ever experienced in hydrocracking or hydrodesulfurizing reactors in both temperature and hydrogen partial pressure. It would therefore be very desirable to accumulate the supporting data of the upper operation limit of 2¼Cr-1Mo steel in the Nelson curve with special attention given to HAZ [*15*].

Reversible Hydrogen Embrittlement—The base metal of the hydrogenation reactor absorbs hydrogen during operation under the equilibrium condition. Groeneveld [*16*] reported that the absorbed hydrogen content in 2¼Cr-1Mo base metal in such reactors is about 4 to 5 ppm when the temperature and hydrogen partial pressure are 454°C and 17.2 MPa. Since some of the absorbed hydrogen may remain in the steel after cooling down the reactor, the possibility of damage owing to reversible hydrogen embrittlement should be considered. Groeneveld [*16*] gives an experimental result which shows that in normalized and tempered 2¼Cr-1Mo steel with an ordinary tensile strength level of 550 to 650 MPa the threshold stress intensity for the hydrogen-assisted crack growth (K_{ISCC}) is higher than about 100 MPa$\sqrt{m}$. With this high K_{ISCC}, the possibility of hydrogen-assisted cracking is very limited in so far as sufficient postweld heat treatment is carried out to eliminate the susceptible hardened HAZ.

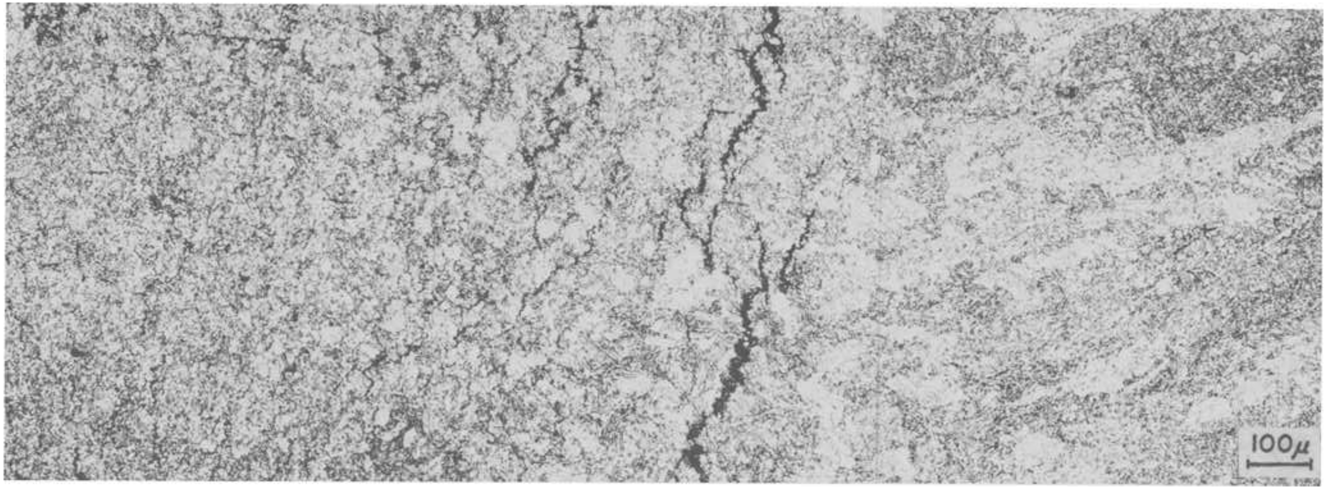

FIG. 13—*A crack due to hydrogen attack observed in HAZ of 2¼Cr-1Mo steel (hydrogen pressure: 29.4 MPa; exposure temperature: 550°C; exposure time: 360 h)* [13].

Combined Effect of Temper Embrittlement and Hydrogen Embrittlement—As already mentioned, 2¼Cr-1Mo steel of the normal strength level is considered as a resistant material to the reversible hydrogen embrittlement. However, when it is temper embrittled by long-time service, a study should be taken as to whether the steel could be further deteriorated by the combined effect of temper embrittlement and hydrogen embrittlement. Through recent studies on the ultrahigh strength steels, such as HY-130 and 4340 steels [*17,18*], the combined effect between both embrittlement phenomena has been discussed and the relation between them is now gradually being understood. However, knowledge of the combined effect in the lower-strength, less-sensitive 2¼Cr-1Mo steel is needed when discussing the safety of hydrogenation reactors.

Figure 14 shows the effect of temper embrittlement on the delayed failure characteristics studied for 2¼Cr-1Mo steel in 500 ppm H_2S solution [*19*]. Both time to failure and the lower critical stress in the static fatigue curve markedly decreased. Apparently hydrogen embrittlement susceptibility is raised by temper embrittlement. Fracture mode shifted from the quasi-cleavage type to the intergranular type with temper embrittlement (Figs. 15 and 16).

Correlation between the threshold stress intensity for hydrogen assisted crack growth (K_{IH}) (the same concept as K_{ISCC} defined by Groeneveld [*16*]) and FATT is shown in Fig. 17 in comparison with the change of K_{IC}, where the absorbed hydrogen level ranged from 2.1 to 2.6 ppm [*19*]. Based on these experimental results, the correlation between temper embrittlement and

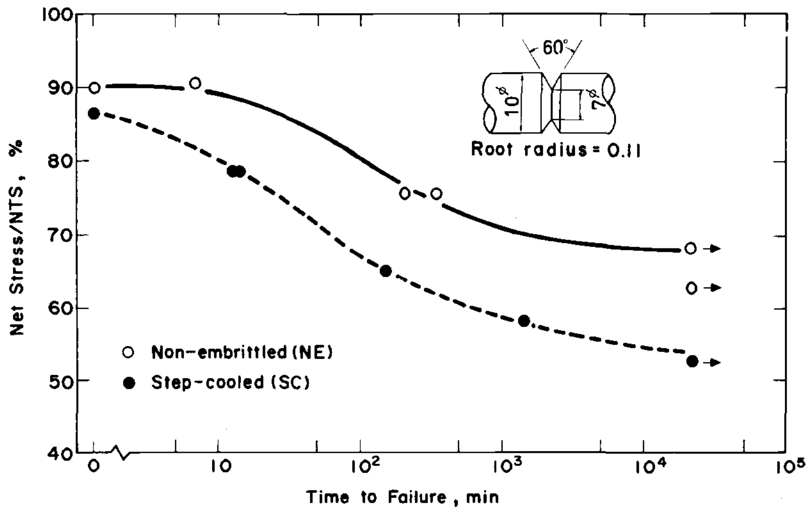

FIG. 14—*Effect of temper embrittlement on static fatigue strength of 2¼Cr-1Mo steel tested in 500 ppm H_2S solution (notch tensile strength—NE: 970 MPa; SC: 934 MPa)* [19].

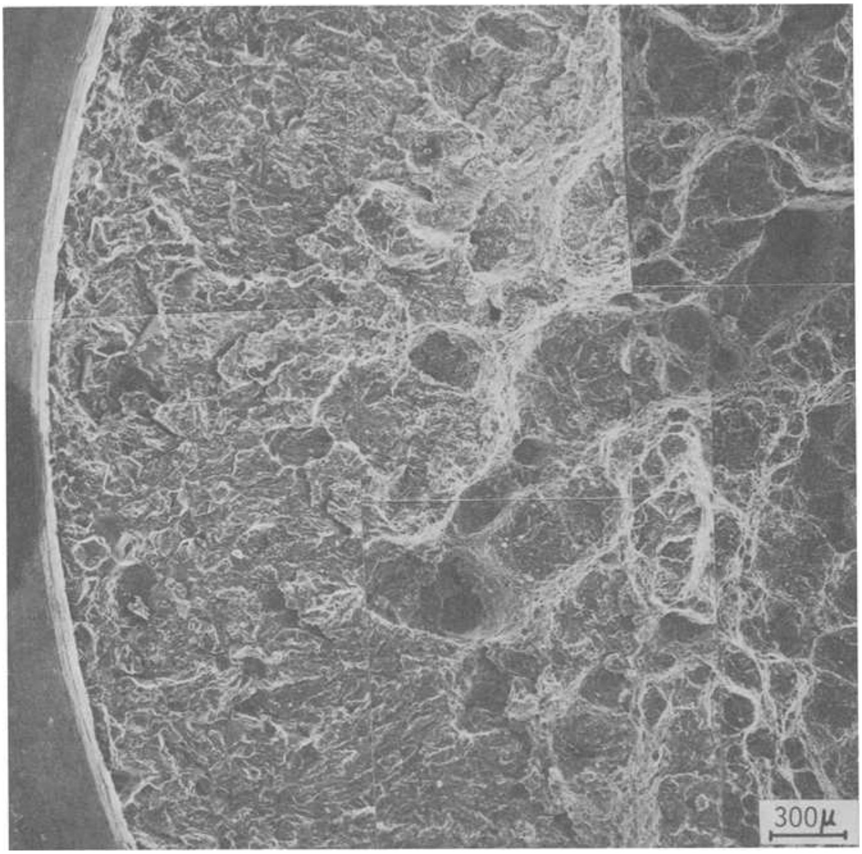

FIG. 15—*Fracture appearance of the static fatigue test specimen in the nonembrittled condition* [19].

hydrogen embrittlement can be expressed schematically as shown in Fig. 18, showing the following features:

1. In the range of low FATT, temper embrittlement itself is very limited and there would be no significant effect of temper embrittlement on K_{IH}.
2. In the range of extremely high FATT, the difference between K_{IC} and K_{IH} is small, because the fracture mode of the K_{IC} (J_{IC}) specimen has changed to the intergranular type through temper embrittlement, and then change of fracture mode due to hydrogen absorption is slight. K_{IH} in this range approaches the certain limit with increase of FATT.
3. In the range of intermediate FATT, the difference between K_{IC} and K_{IH} is very remarkable. It is considered that loss of grain boundary coherency due to hydrogen becomes larger with the grain boundary segregation, and

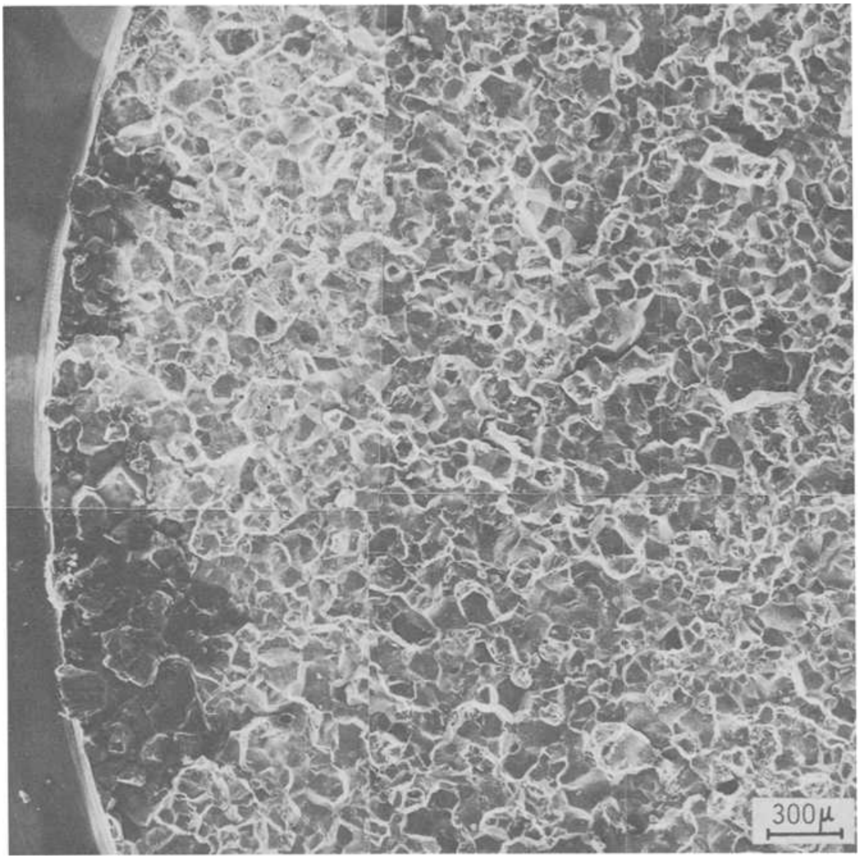

FIG. 16—*Fracture appearance of the static fatigue test specimen in the step-cooled condition* [19].

that the consequent preference of intergranular fracture mode in the more temper embrittled condition probably controls the phenomenon.

Although it must be confirmed, change of K_{IH} might be expressed by FATT, a tentative parameter of the degree of temper embrittlement, and hydrogen embrittlement would be minimized by suppressing temper embrittlement.

High-Temperature Creep

Creep strength data have been gathered for the high-temperature design of pressure vessels. However, recent experience reveals that attention should be paid to the creep ductility in order to avoid creep cracking. Figure 19 shows a

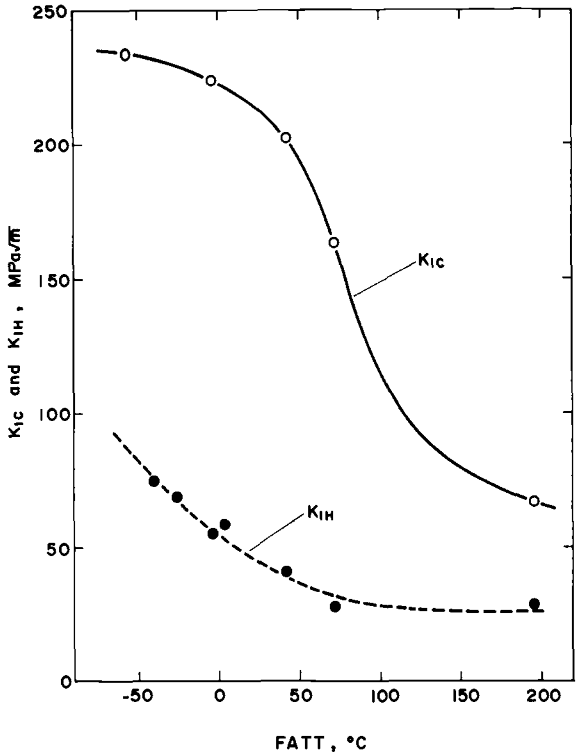

FIG. 17—*Room temperature (*K_{IC} *and* K_{IH}*) versus FATT of 2¼Cr-1Mo steel* [19].

crack observed at a nozzle attachment weld of a reactor made of 1¼Cr-½Mo steel after approximately eight years of operation at about 530°C. The crack started at the weld toe and propagated along the coarse grain region of HAZ. Typical intergranular creep voids are observed near the main crack and in the crack tip area (Figs. 20 and 21), and the crack is judged to be a creep crack. The same type of cracking is often detected by recent careful in-service inspection at other stress raisers, such as attachment welds of skirts, external lugs, and pads. 1Cr-½Mo steel is also found to be a sensitive material to the cracking. Relatively high operational temperatures, the peak stress at the weld toe, and poor creep ductility of HAZ are considered factors that work together.

Creep test results at 550°C of smooth and notched specimens of the synthetic coarse grain region of HAZ (peak temperature: 1350°C) are compared for 1¼Cr-½Mo and 2¼Cr-1Mo steels in Fig. 22. A remarkable difference of creep ductility is observed between those steels. In the less ductile 1¼Cr-½Mo steel, the notch weakening effect observed explains the cracking. On the other hand, 2¼Cr-1Mo steel is considered more resistant to the cracking

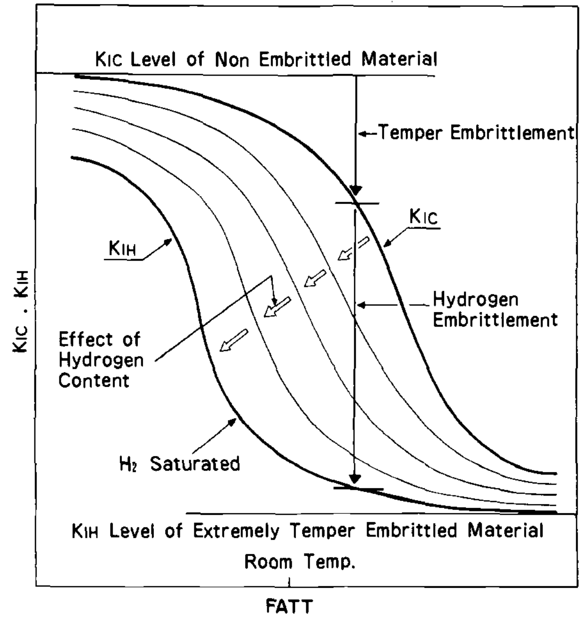

FIG. 18—*Schematic illustration of the correlation between room temperature (*K_{IC} *and* K_{IH}*) and FATT* [19].

based on its excellent creep ductility and the consequent notch strengthening effect.

In summary, a design to minimize the stress concentration at the weldment is needed. At the same time, 2¼Cr-1Mo steel should be considered as a candidate material for a high-temperature reactor when its operation temperature exceeds about 500°C. Careful in-service inspection is also required for the safe operation of existing reactors.

Manufacturing of Heavy-Section 2¼Cr-1Mo Steel

Reactors for hydrogenation units have been continuously getting larger and thicker as operators seek economic efficiency. (The largest hydrogenation reactor fabricated to date has a 4500 mm inside diameter, 297 mm wall thickness, and 850 ton weight.) Because 2¼Cr-1Mo steel will still be used so far as the Nelson curve permits, two questions are of major concern from the standpoint of material manufacturing:

1. What is the maximum thickness of 2¼Cr-1Mo steel with standard mechanical and metallurgical properties?
2. Are the properties of heavy-section 2¼Cr-1Mo steels sufficient and homogeneous?

FIG. 19—*A crack observed at a nozzle attachment weld of a reactor made of* $1\frac{1}{4}$*Cr-*$\frac{1}{2}$*Mo steel after approximately eight years of operation at about 530°C.*

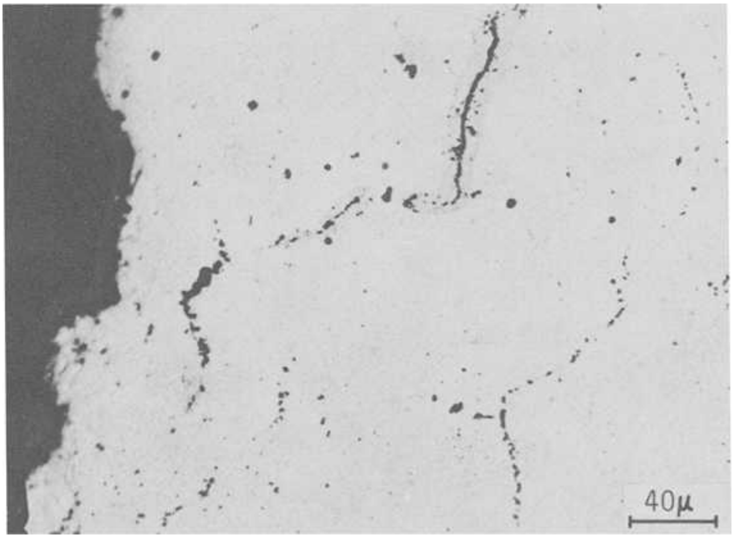

FIG. 20—*Intergranular creep voids observed in the vicinity of the main path of the creep crack shown in Fig. 19.*

Our knowledge of 2¼Cr-1Mo steel will now be summarized with special attention given to these questions.

Heat-Treatment Characteristics of 2¼Cr-1Mo Steel

Recent improvements in steel-melting, refining, and ingot-making technology are remarkable. Large sound ingots for heavy-gage plates and forgings for large pressure vessels are now available. Troubles such as nonmetallic inclusions, laminations, and flakes have been almost eliminated. Currently, a major concern in pressure-vessel steel manufacturing is the heat treatment needed to obtain good, uniform mechanical properties in heavy-section steels.

Effects of the cooling rate from the austenitizing temperature on the mechanical properties of 2¼Cr-1Mo steel are shown in Figs. 23, 24, and 25, where the cooling rate is the average value in the range of 920 to 450°C. 2¼Cr-1Mo steel has good hardenability, and a cooling rate from the austenitizing temperature faster than 5°C/min is enough to obtain good tensile and impact properties. With that cooling rate the polygonal ferrite in the microstructure disappears (Fig. 26).

Change in the notch toughness of the steel during tempering is shown in Fig. 27. A drop of toughness due to the overaging that is observed in 1Cr-½Mo and 1¼Cr-½Mo steels appears only when they are tempered a long time at high temperatures, beyond the practical tempering or postweld heat-

FIG. 21—*Crack-tip area of the creep crack shown in Fig. 19.*

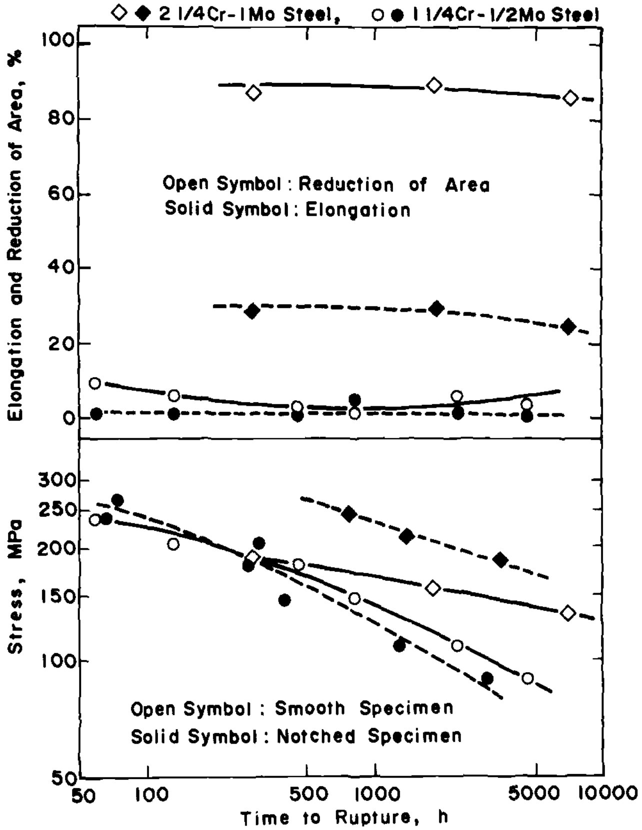

FIG. 22—*Creep test results at 550°C of smooth and notched specimens of the synthetic HAZ (peak temperature: 1350°C) of 1¼Cr-½Mo and 2¼Cr-1Mo steel (theoretical stress concentration factor of the notched specimen: 1.9).*

treatment conditions. Accordingly, tempering conditions can be determined only with an attention to the required strength level. Figure 28 illustrates the strength reduction due to tempering of heavy-section, low-silicon-type plates and forgings with 108 to 450 mm thickness. The total tempering, including the effect of the postweld heat treatments, should be controlled within the permissible range.

Estimated Maximum Thickness with Uniform Properties

As shown previously, the cooling rate from the austenitizing temperature controls the mechanical properties of 2¼Cr-1Mo steel, and the minimum required rate to obtain good properties is about 5°C/min. The correlations between the cooling rate during normalizing and the plate thickness were studied for various cooling methods and are shown in Fig. 29. This figure shows that

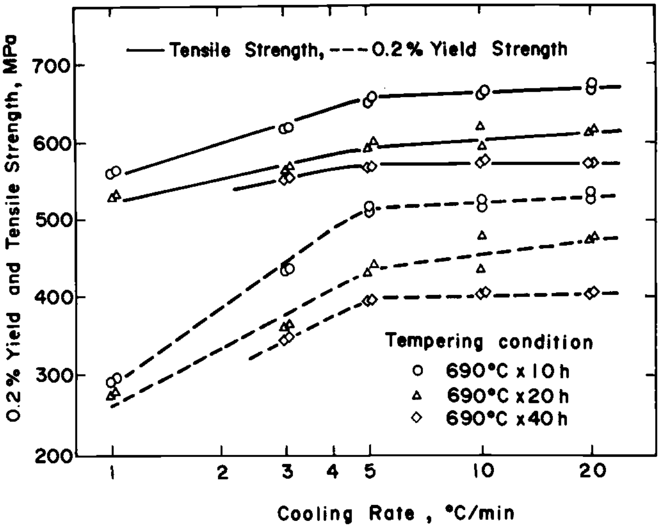

FIG. 23—*Effect of cooling rate from the austenitizing temperature on room temperature yield strength and tensile strength of 2¼Cr-1Mo steel tempered at various conditions.*

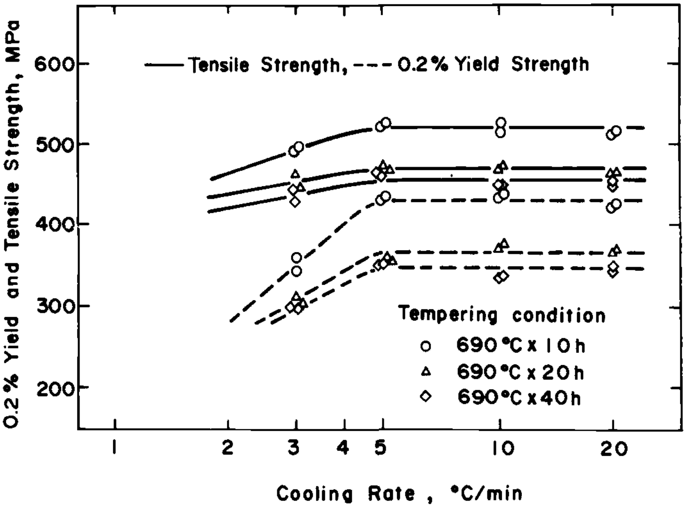

FIG. 24—*Effect of cooling rate from the austenitizing temperature on yield strength and tensile strength at 450°C of 2¼Cr-1Mo steel tempered at various conditions.*

the application of the accelerated cooling method is necessary to obtain sufficient cooling rate in a heavy-section steel. When the immersion quenching in water which gives the fastest cooling rate is applied, the maximum heat-treated thickness with uniform properties through the wall is about 500 mm.

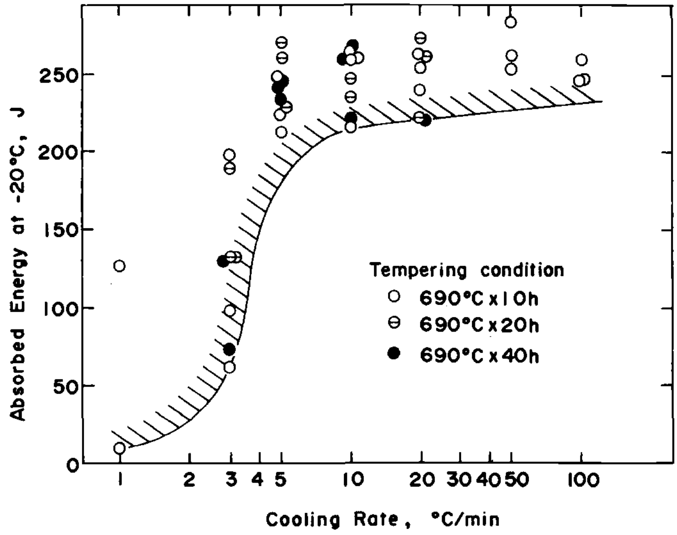

FIG. 25—*Effect of cooling rate from the austenitizing temperature on the Charpy-V absorbed energy at −20°C of 2¼Cr-1Mo steel tempered at various conditions.*

From this heat-treated thickness, approximately 450-mm-thick 2¼Cr-1Mo forged shell can be machined out.

Mechanical Properties of Heavy-Section 2¼Cr-1Mo Steel Made by the Vacuum Carbon Deoxidation (VCD) Process

Properties of a 450-mm-Thick Nozzle Forging—Mechanical properties of a nozzle forging with 450 mm machined thickness and chemical composition as shown in Table 3 were studied. A 90-ton ingot was made by the vacuum carbon deoxidation (VCD) process. It was then forged and machined to the following dimensions prior to heat treatment: 780 mm inside diameter, 480 mm thickness, and 3350 mm length. The normalizing was carried out by accelerated cooling in water after austenitizing at 910°C for 15 h, and then tempering at 645°C for 17.5 h and postweld heat treating at 620°C for 32.5 h plus at 690°C for 17 h were also carried out. The cooling rate from the final postweld heat treatment was 50°C/h. After the heat treatments, a 450-mm-thick product was machined out.

Figure 30 shows microstructures observed at ¼ *T* and ½ *T* locations; in the latter, the very slight area of the polygonal ferrite can be observed. This means that the cooling rate at the ½ *T* location in this case is judged to be just around the critical rate for the disappearance of the polygonal ferrite. Excellent notch toughness and strength in the allowable level were confirmed even at midthickness (Table 4). These results proved the previous estimation

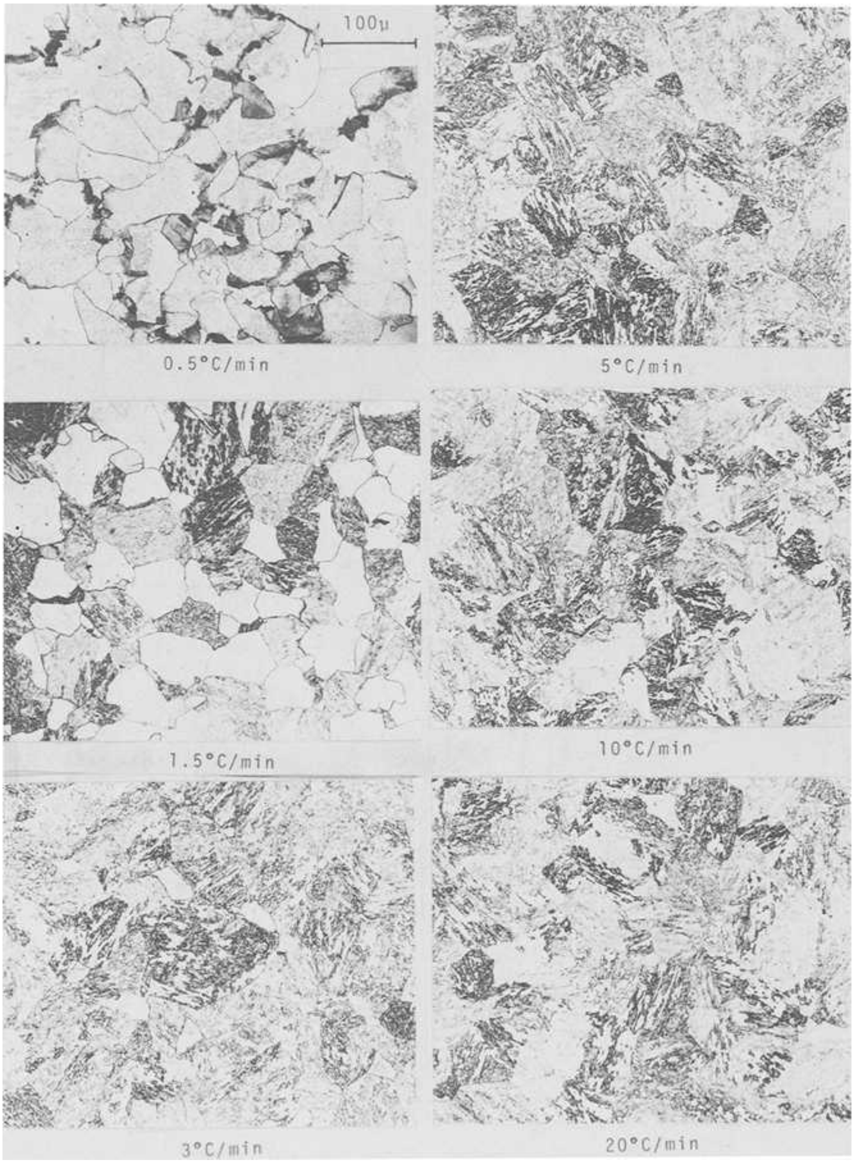

FIG. 26—*Effect of cooling rate from the austenitizing temperature on the microstructure of 2¼Cr-1Mo steel.*

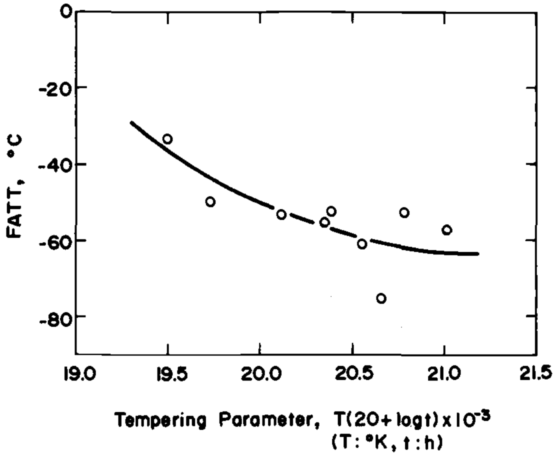

FIG. 27—*Relation between tempering parameter and FATT of 2¼Cr-1Mo steel.*

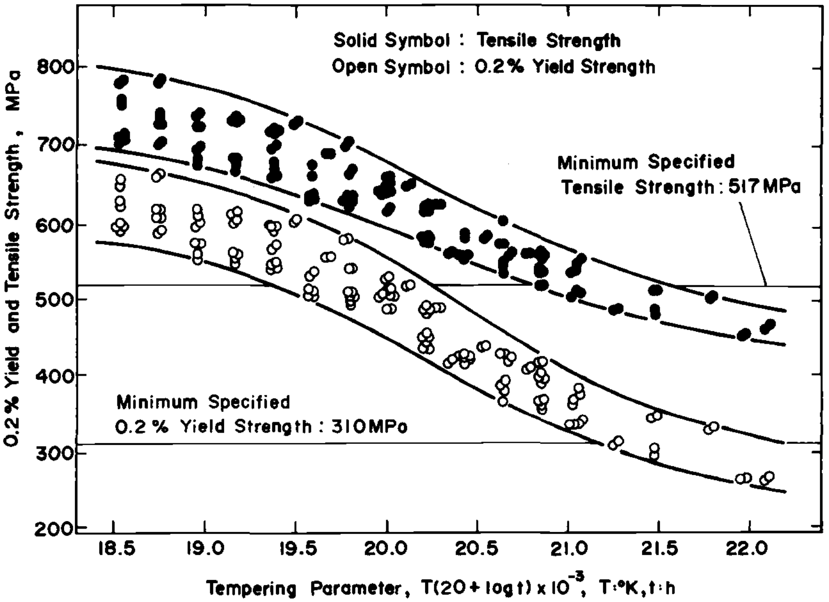

FIG. 28—*Relation between tempering parameter and room temperature strength of low-silicon, heavy-gage 2¼Cr-1Mo forgings and plates (number of heats examined: 10; thickness range: 108 to 450 mm).*

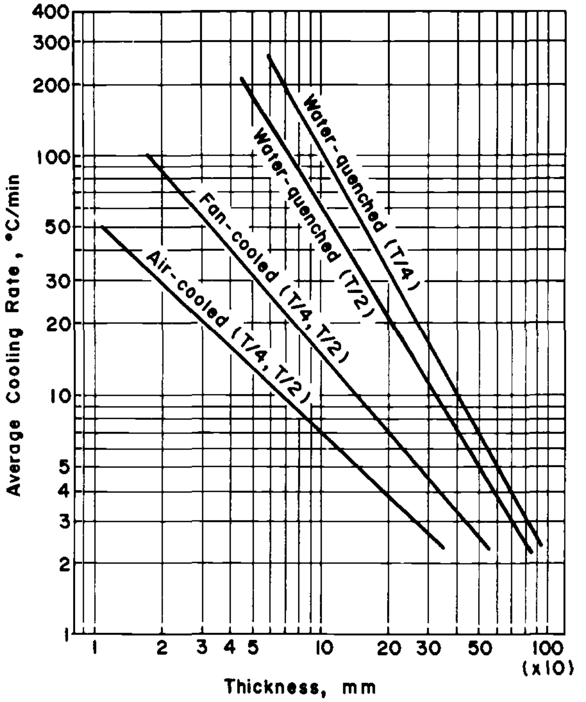

FIG. 29—*Average cooling rates between the austenitizing temperature and 450°C during normalizing by various cooling methods.*

that 450 mm is the maximum thickness of 2¼Cr-1Mo steel product with uniform properties.

Properties of 300-mm-Thick Shell Forging—Mechanical properties of a 300-mm-thick shell forging were also studied. The test material was removed from the excess part of an actual ring forging for a shell course of a pressure vessel. The chemical composition is shown in Table 3. From a 180-ton ingot made by the VCD process, a shell forging of the following approximate heat treated size was forged out; 4400 mm inside diameter, 370 mm thickness, and 3050 mm length. The normalizing was carried out by accelerated cooling in water after austenitizing at 920°C for 19 h and followed by tempering at 650°C for 10 h plus at 690°C for 26 h.

Charpy-V impact properties at various thicknesses were examined before and after a step cooling, and the results shown in Fig. 31 and Table 5 were obtained. The tensile properties at room temperature and 450°C are also shown in Table 5. In addition to the very uniform and excellent mechanical properties, these results clearly indicate that lowering the silicon content of 2¼Cr-1Mo steels by the VCD process has a remarkable effect on minimizing temper embrittlement susceptibility, causing improved notch toughness.

TABLE 3—*Chemical compositions of heavy-section 2¼Cr-1Mo forgings.*[a]

	C	Si	Mn	P	S	Cr	Mo	Al	As	Sn	Sb
300-mm-thick forged shell	0.15	0.01	0.51	0.007	0.008	2.39	0.99	0.006	0.007	0.010	0.0025
450-mm-thick nozzle forging	0.15	0.01	0.52	0.007	0.008	2.41	1.07	0.006	0.006	0.012	0.0023

[a] In weight percent.

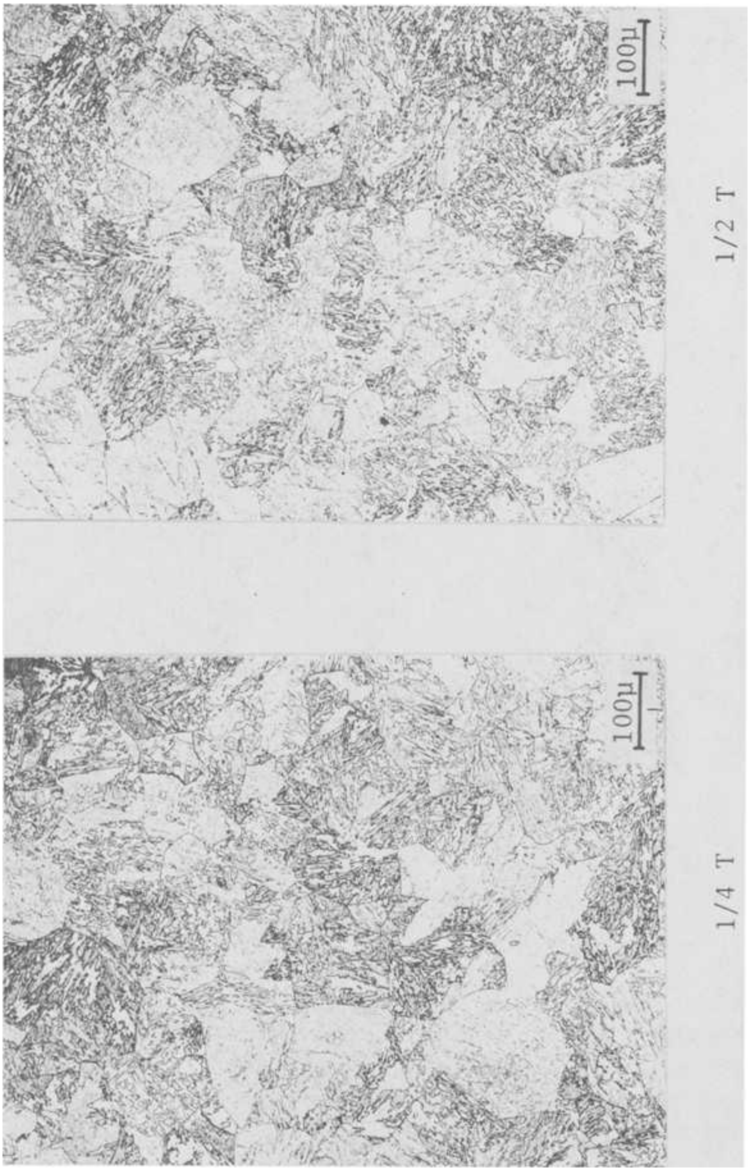

FIG. 30—*Micrographs of a 450-mm-thick 2¼Cr-1Mo steel forging at ¼ T and ½ T.*

TABLE 4—*Mechanical properties of a 450-mm-thick 2¼Cr-1Mo nozzle forging.*

Location	0.2 % Yield Strength, MPa	Tensile Strength, MPa	Elongation,[a] %	Reduction of Area, %	vTrs, °C
¼-*T*	421.7 418.7	560.0 557.0	27.8 28.0	79.4 80.5	−68
½-*T*	395.2 394.2	541.3 541.3	28.9 29.0	78.6 80.8	−71

[a] Specimen diameter and gage length are 12.7 mm and 50 mm, respectively.

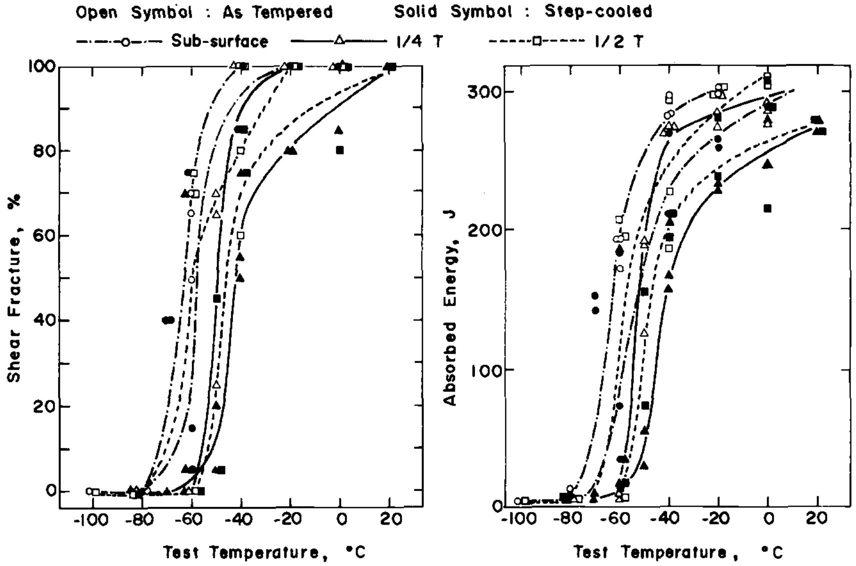

FIG. 31—*Charpy-V impact transition curves of a 300-mm-thick 2¼Cr-1Mo steel forging before and after step cooling.*

Summary

2¼Cr-1Mo steel is a very common pressure-vessel steel used in hydrogenation units which play an important role in the petroleum refining industry. Properties required for 2¼Cr-1Mo steel for high-temperature, high-pressure hydrogenation service and related material problems were discussed and the following points were brought out:

1. 2¼Cr-1Mo steel for hydrogenation service needs adequate resistance to environmental degradation phenomena such as temper embrittlement, hydrogen damage, and creep cracking.
2. The temper embrittlement susceptibility of 2¼Cr-1Mo steel may be

TABLE 5—*Mechanical properties of a 300-mm-thick 2¼Cr-1Mo shell forging.*

Location	Test Temperature, °C	0.2 % Yield Strength, MPa	Tensile Strength, MPa	Elongation, %	Reduction of Area, %	vTrs, °C		
						As-tempered	Step-cooled	Shift
Surface	25	422.7	560.9	30.6	80.1	−63	−58	5
		424.6	560.9	30.8	80.1			
	450	340.3	441.3	19.8	76.9			
		341.3	435.4	19.5	77.3			
¼-*T*	25	421.7	558.0	29.6	80.6	−49	−43	6
		416.8	554.1	29.2	79.9			
	450	340.3	439.3	19.2	76.8			
		337.3	433.5	19.4	77.4			
½-*T*	25	400.1	553.1	31.3	80.1	−60	−47	13
		400.1	559.0	30.6	78.5			
	450	332.4	432.5	19.6	75.4			
		329.5	431.5	19.8	76.8			

suppressed by control of J-factor [(Si + Mn) (P + Sn) × 10^4]. To reduce J-factor, lowering silicon content is very effective. Control of impurities such as phosphorus and tin is also effective. Temper embrittlement susceptibility of HAZ can be significantly minimized by the same compositional countermeasures as in the base metal.

3. In order to avoid hydrogen attack, pressure-vessel materials for hydrogenation services should receive sufficient tempering or postweld heat treatment, or both, in addition to their selection by the Nelson curve. Considering the upgrading of future design conditions, an accumulation of data on the upper operation limit of 2¼Cr-1Mo steel with special attention to the attack in HAZ is needed.

4. 2¼Cr-1Mo steel of standard strength has sufficient resistance to hydrogen-assisted cracking. When it is temper embrittled by long-time service, however, the steel apparently becomes susceptible to hydrogen-assisted cracking. Based on the experimental results on the combined effect of temper embrittlement and hydrogen embrittlement, the possible correlation between both embrittlements was proposed. Suppressing temper embrittlement is important in lowering the susceptibility to subcritical hydrogen-assisted cracking.

5. Creep crackings in some high-temperature reactors made of 1Cr-½Mo and 1¼Cr-½Mo steels are considered attributable to the coincidence of the peak stress at the weld toe with the poor creep ductility of HAZ. The cracking may be avoided by a design to reduce stress concentration at weldments. Ap-

plication of 2¼Cr-1Mo steel with excellent creep ductility will completely eliminate the problem.

In order to meet the upgrading of service conditions in hydrogenation units and the future requirements in coal liquefaction processes, establishment of the manufacturing technology of larger and thicker pressure vessels is required. From this standpoint, availability of heavy-section 2¼Cr-1Mo steel for large-size pressure vessels was studied and the following points were brought out:

1. To obtain good mechanical properties, the cooling rate from the austenitizing temperature shall be faster than 5°C/min, that is, the critical rate for the disappearance of the polygonal ferrite.
2. When water-immersion quenching is applied, the rate can be obtained up to approximately 500-mm heat-treated thickness, and about 450-mm-thick forging can be machined out from it.
3. Mechanical properties of 300-mm-thick and 450-mm-thick 2¼Cr-1Mo forgings made by the VCD process were investigated. The results showed good, uniform through-thickness properties and low temper embrittlement susceptibility.

References

[*1*] Watanabe, J., Shindo, Y., Ohnuma, H., Ishigaki, S., Kawakami, K., and McGuire, W. J. in *Proceedings*, 1976 Elevated Temperature Design Symposium, International Joint Petroleum Mechanical Engineering and Pressure Vessel and Piping Conference, Mexico City, American Society of Mechanical Engineers, 1976, pp. 7-13.

[*2*] Mima, S., Watanabe, J., Nakajo, Y., Murakami, Y., and McGuire, W. J. in *Proceedings*, 1976 Elevated Temperature Design Symposium, International Joint Petroleum Mechanical Engineering and Pressure Vessel and Piping Conference, Mexico City, American Society of Mechanical Engineers, 1976, pp. 15-23.

[*3*] Iwadate, T., Karaushi, T., and Watanabe, J., "Fracture Toughness of Temper Embrittled 2¼Cr-1Mo and 3.5Ni-Cr-Mo-V Steels," Joint USA-Japan Seminar on Fracture Mechanics of Ductile and Tough Materials and Its Application to Energy Related Structures, Hayama, Japan, 1979.

[*4*] Iwadate, T., Karaushi, T., and Watanabe, J. in *Flaw Growth and Fracture, ASTM STP 631*, American Society for Testing and Materials, 1977, pp. 493-506.

[*5*] Yu, J. and McMahon, C. J., Jr., *Metallurgical Transactions A*, Vol. 11A, 1980, pp. 277-289.

[*6*] Yu, J. and McMahon, C. J., Jr., *Metallurgical Transactions A*, Vol. 11A, 1980, pp. 291-300.

[*7*] Watanabe, J., Shindo, Y., Murakami, Y., Adachi, T., Ajiki, S., and Miyano, K., "Temper Embrittlement of 2¼Cr-1Mo Pressure Vessel Steel," 29th Annual Petroleum Mechanical Engineering Conference, Dallas, American Society of Mechanical Engineers, 1974.

[*8*] McMahon, C. J., Jr., Murza, J. C., Yu, J., and Swift, R. A. in *Proceedings*, 42nd Midyear Meeting of Refining Department, American Petroleum Institute, 1977, pp. 17-25.

[*9*] Katsumata, M., Takada, H., Hirano, H., Takano, M., and Makioka, M., *Tetsu-To-Hagane (Journal of the Iron and Steel Institute of Japan)*, Vol. 63, 1977, pp. A155-A158.

[*10*] Murakami, Y., Nitta, Y., Nomura, T., and Nakajo, Y. in *Preprints*, National Meeting of Japan Welding Society, Autumn 1979, No. 25, pp. 40-41.

[*11*] Murakami, Y., Muro, M., Nomura, T., and Nakajo, Y. in *Preprints*, National Meeting of Japan Welding Society, Autumn 1979, No. 25, pp. 42-43.

[*12*] "Steels for Hydrogen Service at Elevated Temperatures and Pressures in Petroleum Refineries and Petrochemical Plants," API Publication 941, 2nd ed., Refining Department, American Petroleum Institute, June 1977.

[*13*] Watanabe, J., Ishizuka, H., Ohnishi, K., and Chiba, R. in *Proceedings*, 20th Japan National Symposium on Strength, Fracture and Fatigue, 1975, pp. 101-111.

[*14*] Yamazaki, D., Shinkawa, T., Makimoto, H., and Oe, T., *Journal of the Japan Petroleum Institute*, Vol. 19, 1976, pp. 27-32.

[*15*] Cooperative Study Program, Subcommittee on Hydrogen Embrittlement, Materials Division of the Japan Pressure Vessel Research Council, April 1979.

[*16*] Groeneveld, T. P., "Hydrogen-Assisted Crack Growth in 2¼Cr-1Mo Steels," 29th Annual Petroleum Mechanical Engineering Conference, Dallas, Tex., American Society of Mechanical Engineers, 1974.

[*17*] Briant, C. L., Feng, H. C., and McMahon, C. J., Jr., *Metallurgical Transactions A*, Vol. 9A, 1978, pp. 625-633.

[*18*] Viswanathan, R. and Hudak, S. J., Jr., *Metallurgical Transactions A*, Vol. 8A, 1977, pp. 1633-1637.

[*19*] Murakami, Y., Nomura, T., and Ohnishi, K., *Journal of the High Pressure Institute of Japan*, Vol. 19, 1981, pp. 132-139.

Eiji Takahashi[1] *and Kenji Iwai*[1]

Omission of Intermediate Postweld Heat Treatment (PWHT) by Utilizing Low-Temperature PWHT for Welds in Pressure Vessels

---

REFERENCE: Takahashi, Eiji and Iwai, Kenji, **"Omission of Intermediate Postweld Heat Treatment (PWHT) by Utilizing Low-Temperature PWHT for Welds in Pressure Vessels,"** *Application of 2¼Cr-1Mo Steel for Thick-Wall Pressure Vessels, ASTM STP 755*, G. S. Sangdahl and M. Semchyshen, Eds., American Society for Testing and Materials, 1982, pp. 418-450.

ABSTRACT: This study was conducted in order to establish a procedure for a low-temperature postweld heat treatment (LTPWHT) to replace conventional stress relief annealing utilized as postweld heat treatment, when pressure vessels are fabricated.

From the standpoint of preventing only hydrogen-induced weld cracks during fabrication before the final PWHT, the appropriate conditions of the LTPWHT for preventing the cracks in heavy-section 2¼Cr-1Mo steel weldments were obtained by clarifying the following items: (*1*) the causes and characteristics of a crack, (*2*) the hydrogen concentration at the location of the crack initiation by applying various welding conditions, (*3*) the relation between the reduction of the hydrogen concentration through LTPWHT and its treating conditions, and (*4*) a critical hydrogen concentration below which cracking does not occur.

As a result of the establishment of the LTPWHT, not only the hydrogen-induced weld crack, but also stress relief cracking can be prevented. Moreover, the deterioration of the toughness and the strength of the material caused by the repetitious stress relief annealing can be avoided, and then the condition of the final PWHT specified in pressure vessel codes can be optimized in each weld zone.

An additional study was completed for welds using a newly developed flux material.

KEY WORDS: postweld heat treatment (PWHT), ISR, 2¼Cr-1Mo steel, hydrogen induced weld cracking (transverse crack), pressure vessel, diffusible hydrogen, submerged arc welding, multipass welds, flux, hydrogen concentration

In recent years, thicker materials with higher strengths have been required to meet the needs of large-size, efficient equipment in heavy industry. Ex-

---

[1] Central Research Laboratory, Kobe Steel, Ltd., Kobe-City, Japan.

amples are high-pressure vessels used in the chemical industry and nuclear reactor pressure vessels having wall thicknesses in the range of 200 to 300 mm. These vessels are usually fabricated by the submerged arc welding process.

When thick materials are joined by the submerged arc welding process, cracking transverse to the weld direction sometimes occurs in the weld metal, and in some cases, cracks propagate through total thickness [*1*].[2] To avoid this kind of cracking, an intermediate stress relief annealing (ISR) in a furnace has been utilized as the usual process of construction. However, the heavier the structure, the more the intermediate stress relief annealing is required, and in consequence deterioration of the toughness and the strength of the material may be induced; there is also the great disadvantage of the cost of the construction. For these reasons, a postweld heat treatment under a temperature of about 200 to 300°C, by which the diffusible hydrogen concentrations which are considered to be closely related to the crackings may be decreased, was recently recommended instead of the conventional ISR [*2,3*]. However, the basic study concerning the treatment had not yet been performed.

This research, then, was conducted in order to establish a low-temperature postweld heat treatment (LTPWHT) that would supersede ISR. 2¼Cr-1Mo steel was selected because it has been commonly used as a material for high-temperature and high-pressure vessels. And, regarding LTPWHT as a method for preventing the hydrogen-induced weld crackings which are apt to occur at the intermediate step of fabrication of a thick-wall pressure vessel, its preventing conditions through LTPWHT were evaluated first by investigating the characteristics and causes of the cracks and next by clarifying experimentally and analytically the behavior of hydrogen diffusion both during welding and during LTPWHT.

Necessity of Omitting ISR

As the fabrication process of a pressure vessel becomes complicated (Fig. 1), the difference of the number of ISR between each component increases, so that one can not always give the optimal condition of final PWHT equally to each part of a vessel. Moreover if all of the ISRs are performed in an annealing furnace, the fabrication schedule will be disturbed because the furnace needs to be made readily available when a welding is completed. It also means consumption of a great deal of energy by heating a batch of furnace.

Figure 2 indicates the relation between the Vicker's hardness number of 2¼Cr-1Mo steel and PWHT conditions, where the abscissa represents the Larson-Miller parameter. This relation was obtained for a 25-mm-thick plate which had been reheated to a temperature of 950°C (1742°F) for 2 h in order

---

[2] The italic numbers in brackets refer to the list of references appended to this paper.

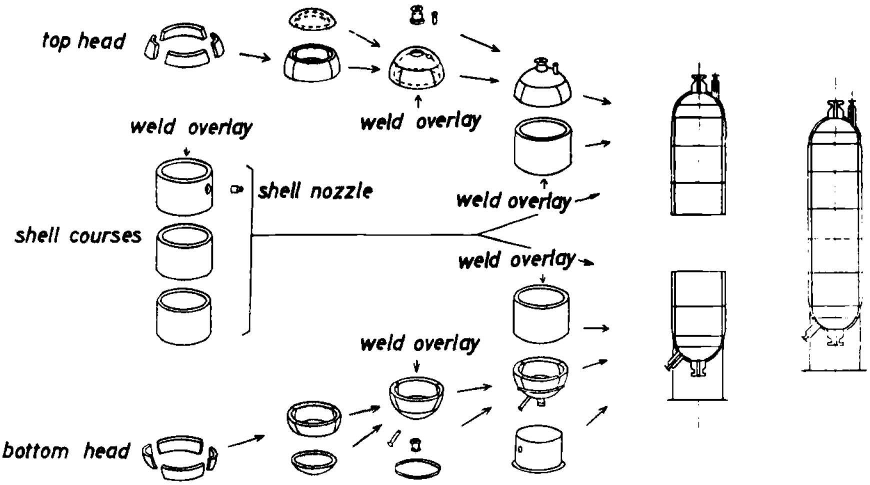

FIG. 1—*Schematic illustration of assembly of major pressure vessel components.*

to be austenized and then cooled at the rate of about 40°C (72°F)/min from 800 to 500°C (1472 to 932°F) to make the same microstructure as that obtained at the position of one-fourth thickness of about 250-mm-thick plate by water quenching. A heat treatment, of which temperature and holding time were 600°C (1112°F) for 25 to 200 h, 650°C (1202°F) for 5 to 470 h, or 700°C (1292°F) for 1 to 150 h, followed. Thus this heat treatment can be regarded as the treatment including temper, ISR, and final PWHT. It shows that the relation between the hardness and *P*-value becomes linear, as is well known. Therefore repetitious ISR as well as excessive final PWHT may cause the fatal reduction of the material strength. In the same way, Fig. 3 indicates the relation between fracture transition temperature vTrs and PWHT conditions for the same material. Location and orientation of test samples are the center portion of the thickness and transverse final rolling directions, respectively. Figure 3 shows that optimal condition of PWHT exists. It is found from these figures that excessive postweld heat treatment, including ISR and final PWHT, should be avoided.

In addition, ISR contains a possibility of stress relief cracking during the treatment. Figure 4 shows the effects of the initial stress, σ_i, and stress concentration factor, K_t, upon the occurrence of the crack. An anisothermal stress relaxation test was carried out on the notched specimen with the synthetic heat-affected zone (HAZ) coarse structure. It is seen in Fig. 4 that the removal of the excess reinforcement of weld before ISR has a good effect on the prevention of the crack. However, grinding is not easy because the welds should be kept at a temperature that is too high for the usual grinding wheel; otherwise hydrogen-induced weld cracks will occur.

Accordingly, in order to solve these problems pertaining to repetitious

ISR, the establishment of LTPWHT by gas burners superseding conventional ISR has been urgently required.

Hydrogen-Induced Weld Cracks Apt to Occur in Heavy-Section Weldments of 2¼Cr-1Mo Steel

Preventing hydrogen-induced weld cracking is one of the most important objects at the intermediate step of fabrication of a pressure vessel, and from this standpoint ISR is conventionally being utilized. This section investigates the causes and characteristics of the transverse crack induced in heavy-section weldments, which is the most difficult crack to be prevented. Moreover it is experimentally shown that the LTPWHT is a promising method for preventing the cracks and makes it possible for the conventional ISR to be omitted.

Experiment

Material—The base metal used in this study is ASTM Specification for Pressure Vessel Plates, Alloy Steel, Chromium-Molybdenum (A 387-79b),

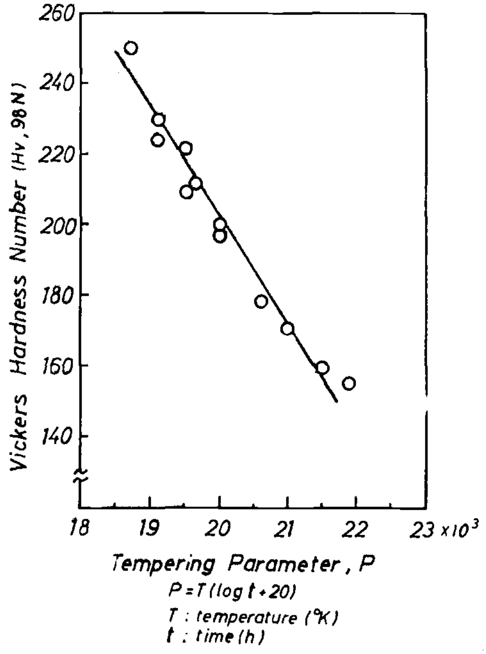

FIG. 2—*Relation between Vickers hardness number and tempering parameter* P *(material: 2¼Cr-1Mo steel).*

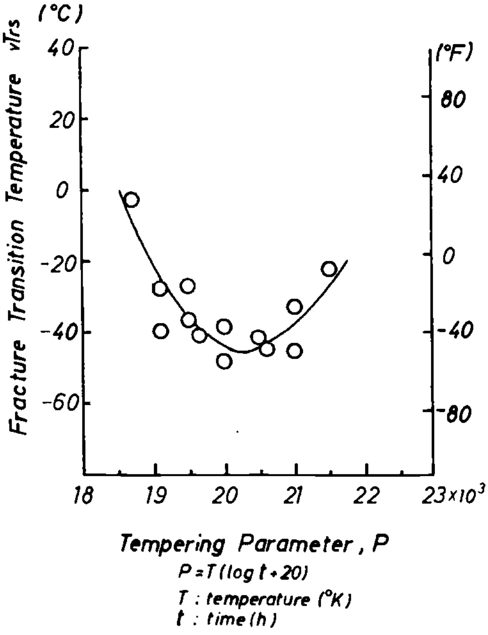

FIG. 3—*Relation between fracture transition temperature vTrs and tempering parameter* P *(material: 2¼Cr-1Mo steel).*

Grade 22, 2¼Cr-1Mo steel of 200 mm thickness. Its chemical compositions and mechanical properties are listed in Table 1.

Cracking Tests on Restraint Test Specimens—Various sizes of restraint test specimens (Fig. 5), to which the mild steels of 50 mm thickness were attached to restrain angular distortion along the weld line, were prepared for the cracking tests.

Cracking tests were carried out by changing combinations of parameters of plate thickness and interpass temperature during welding. The method of welding was the submerged arc process using combinations of the conventionally utilized wire and flux. The chemical compositions and mechanical properties of the weld metals obtained are listed in Table 1. The welding conditions are shown in Table 2.

The restraint test specimen after welding was kept at room temperature for a week, and then two plates were cut off from the weld metals parallel to the weld line. Magnetic particle examination was applied to the plate surfaces, and cracks in these plates were checked.

Measurement of the Distribution of Residual Stresses Parallel to the Weld Line Through the Thickness—There had been no established method to measure residual stresses induced in heavy-section weldments. Hence the

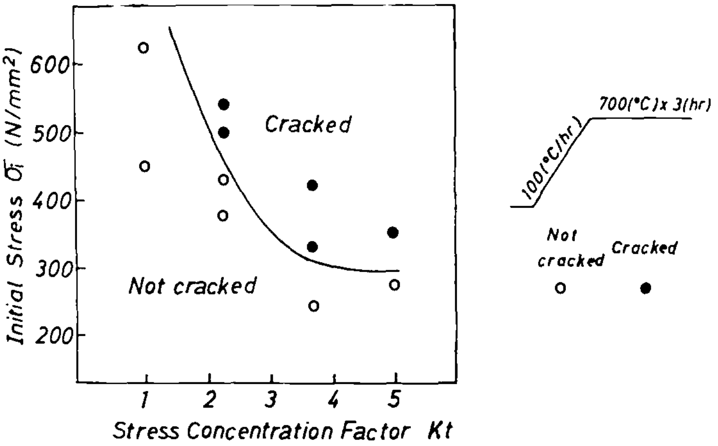

FIG. 4—*Stress relief cracking characteristics in bond area of 2¼Cr-1Mo steel weldments.*

authors in cooperation with Professor Satoh of Osaka University developed a method for this purpose [*4*].

Measurement of residual stresses was conducted on restraint test specimens in the thickness range of 50 to 150 mm by applying this method.

Measurement of Diffusible Hydrogen Concentration Distribution Through the Plate Thickness—In order to investigate the effects of interpass temperature and plate thickness on diffusible hydrogen concentrations which are considered to be related to the formation of the transverse cracks, the distribution of diffusible hydrogen concentrations through the plate thickness was measured. Measurement was carried out just after the final bead of welds was cooled to an interpass temperature. Further, in order to investigate the usefulness of LTPWHT for decreasing the diffusible hydrogen concentration in the weld metal, its distribution throughout the thickness of the weld metals was measured right after LTPWHT following welding which was done with the interpass temperature kept at 200°C (392°F) using a restraint test specimen of 55 mm thickness.

It is very important to be careful in cutting the test specimens loose from welded joint. Cutting must be performed with the welded joint as cold as possible. Taking such a condition into account, restraint test specimens provided with cold baths on the top surface (Fig. 6) were used. They were immersed into water immediately after the final bead of welds was cooled to an interpass temperature or after LTPWHT following welding was finished, and then they were put into a bath of solution of calcium chloride cooled by dry ice to a temperature of about −50°C (−58°F). Moreover, to prevent hydrogen from diffusing in the course of saw cutting, the solution of calcium chloride cooled to a temperature of about −50°C (−58°F) was constantly

TABLE 1—*Chemical compositions and mechanical properties of 2¼Cr-1Mo steel and weld metal.*

	Chemical Composition, %							Mechanical Properties		
	C	Si	Mn	P	S	Cr	Mo	Elongation, %	Yield Point, N/mm^2	Tensile Strength, N/mm^2
ASTM A 387, Grade 22	0.13	0.30	0.47	0.01	0.01	2.39	1.00	23.6	341	577
Weld metal	0.09	0.24	0.73	0.01	0.01	2.37	1.03	18	843	931

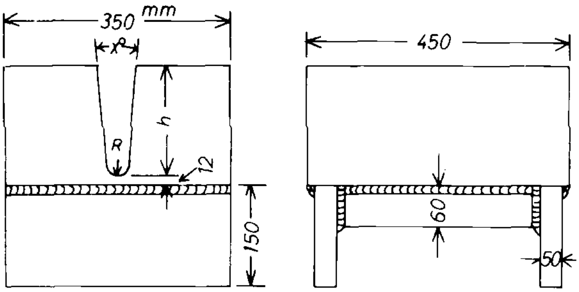

h, mm	50	100	150	200
X, deg[b]	8	7	5.5	4
R, mm	8	8	8	8

FIG. 5—*Restraint test specimen.*

TABLE 2—*Welding conditions.*

Wire, mm	Flux	Current, A	Voltage, V	Heat Input, kJ/cm
SFA-5.23 EG (corresponding to EB-3), 4.8 diameter	F92-EG-G	650	36	40

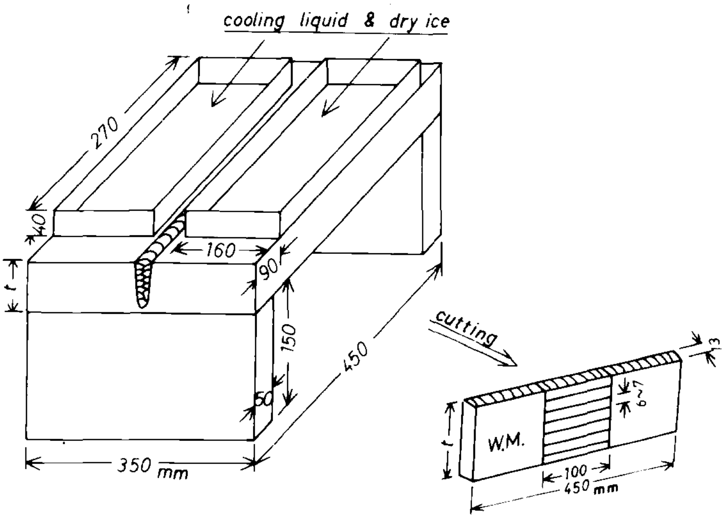

FIG. 6—*Test specimen used for measurement of diffusible hydrogen concentration.*

poured over the specimen, and the sections newly exposed to the air were covered with crushed dry ice.

For measurement of diffusible hydrogen, a vacuum extraction system was used [*5*]. It was first developed by Dr. Uda, National Research Institute for Metal in Japan, and its accuracy has been well confirmed. Test specimens were kept in a jar of liquid nitrogen, and after cleaning with ethyl alcohol they were put into glass bottles from which the air was extracted immediately to a vacuum of 10^{-2} torr. They were kept at room temperature for about 10 days. This was long enough for the hydrogen to completely diffuse out because the test specimens in this experiment were small enough (6 by 13 by 100 mm). Diffusible hydrogen accumulated in the bottle was led to a burette with a minimum graduation of 0.02 mL, where the hydrogen volume was measured under the atmospheric pressure.

Results

Configuration of the Transverse Crack—The macroscopic configuration of the transverse cracks is shown in Fig. 7. It shows the result of magnetic particle inspection of a vertical section of the weld metal obtained under the conditions of 55 mm thickness and 100°C (212°F) interpass temperature. Two kinds of cracks are identified. One is the transverse crack that penetrates through total thickness, and the other is small cracks that stop inside of the weld metal without propagating to the top surface. The latter cracks lie at the same distance from the top surface of the finishing bead. This implies that all the cracks initiate at the same distance below the top surface of the finishing bead and then propagate both to the top surface and to the bottom surface of the plate. The cracks observed in other specimens, which were welded under different conditions of plate thickness and interpass temperature, indicated

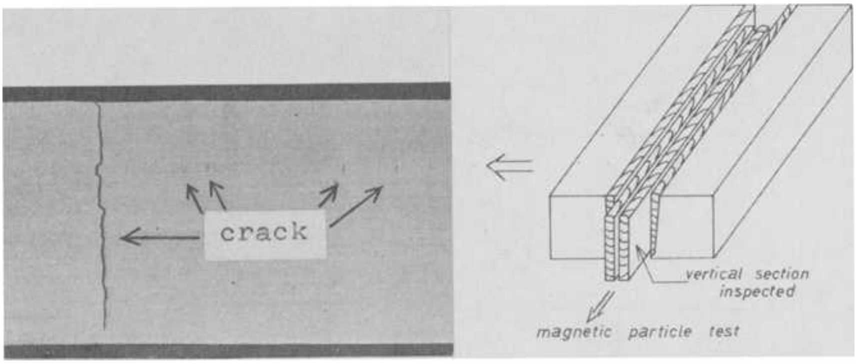

FIG. 7—*Macroscopic view of transverse cracks observed in a vertical section of weld metal [plate thickness: 55 mm; interpass temperature: 100°C (212°F)].*

the same characteristics. Preheating and interpass temperatures for prevention of cracks were found to be about 150 to 175°C (302 to 347°F) in the thickness range of 50 to 100 mm and about 200 to 225°C (392 to 437°F) in the thickness range over 150 mm [*6*]. However, taking into account the fact that the width of a welded structure is usually larger than that of the restraint test specimen used here, it seems that the interpass temperature during welding of real structures has to be kept higher than the aforementioned value, because the cooling rate during welding increases with an increase in width of a welded structure as well as in plate thickness. This problem is dealt with in the next section.

Residual Stress Distribution Through the Plate Thickness—Residual stress distributions through the plate thickness of 100 mm are presented in Fig. 8. It is seen that residual stresses reach their maximum values at a distance of about 10 to 20 mm below the top surface of the finishing bead, where the initiation of the transverse crack is limited to as described before.

Figure 9 shows the relation between the highest longitudinal residual stress, which is considered to be related to the occurrence of the crack, and the plate thickness. The highest longitudinal residual stress becomes almost constant in the thickness range over 50 mm, and therefore it can be considered that the influence of the residual stress upon the occurrence of the crack becomes constant regardless of the plate thickness.

Distribution of Diffusible Hydrogen Concentrations Through the Thickness—Figure 10 shows the results of measuring the distribution of diffusible hydrogen concentrations just after the temperature of the finishing bead has dropped to an interpass temperature. The vertical axis indicates the distance from the top surface of the final layer of welds, and the horizontal axis indicates hydrogen concentration in mL/100 g NTP.

The results indicate that the diffusible hydrogen concentration reaches its

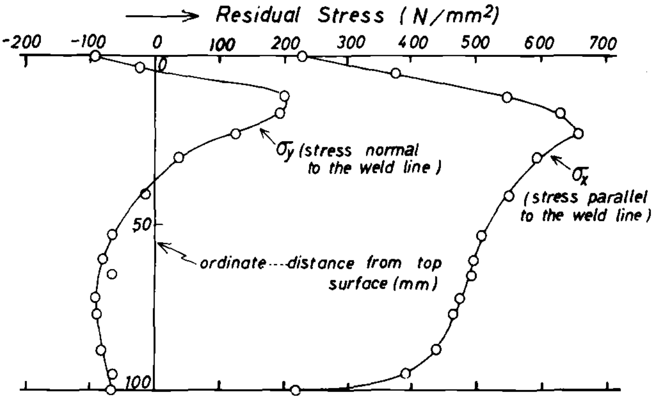

FIG. 8—*Residual stress distributions through plate thickness of 100 mm.*

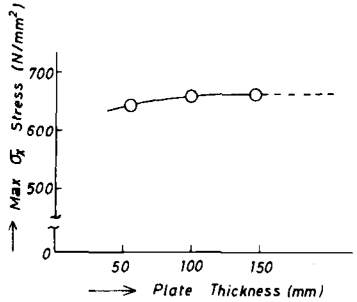

FIG. 9—*Relation between the highest longitudinal residual stress, σ_x, and plate thickness.*

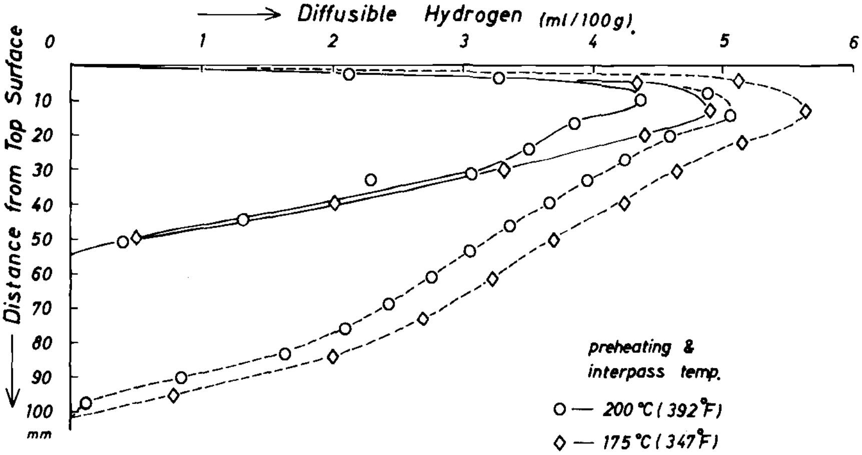

FIG. 10—*Distributions of hydrogen concentrations across the thickness when plate thickness is changed.*

maximum value about 10 mm below the top surface of the finishing bead and shows an almost linear decrease with an increased depth. The location where the highest concentration of diffusible hydrogen appears is considered to differ somewhat depending on the cooling time of a specimen in water. However, it relates closely to that of crack initiation, as does the location of the highest longitudinal residual stress. It is also found that the highest concentration has a tendency to decrease with an increase in preheating and interpass temperatures; at the same time, it has a tendency to increase with an increase in plate thickness. This is owing to the fact that cooling rate increases with an increase in plate thickness, which is probably the reason prevention of the cracks necessitates an increase in preheating and interpass temperatures with an increase in plate thickness as referred to before.

Judging from these results, it is clear that the transverse crack is a cold cracking induced in the weld metal both by high longitudinal residual stress and by high concentration of diffusible hydrogen. Moreover, taking into account the aforementioned fact that the highest longitudinal residual stress is nearly constant regardless of the plate thickness of the butt welded joint, it is easily seen that prevention of the cracks can be made possible only by decreasing the concentration of diffusible hydrogen. Accordingly, we next consider the effect of LTPWHT to decrease it.

Figure 11 shows the distribution of hydrogen concentration across the thickness when LTPWHT is employed. Preheat and interpass temperatures during welding were 200°C (392°F) and the temperature of LTPWHT was changed as shown in Fig. 11; the time was about 2 h. The results indicate that LTPWHT is a very useful method for decreasing the concentration of diffusible hydrogen, and its effect increases with an increase in temperature. Consequently, this treatment is considered a promising method for avoiding the kind of crackings superseding the conventional intermediate stress relief annealing.

Prevention of the Transverse Crack Through LTPWHT

Unlike the conventional ISR that is expected to lower the two causes of the cracks—namely, residual stress and hydrogen concentration—LTPWHT is a method for preventing the cracks by decreasing only hydrogen concentration. Accordingly, in order to make a practical application of LTPWHT possible that would supersede ISR, the following points must be made clear: (*1*) the

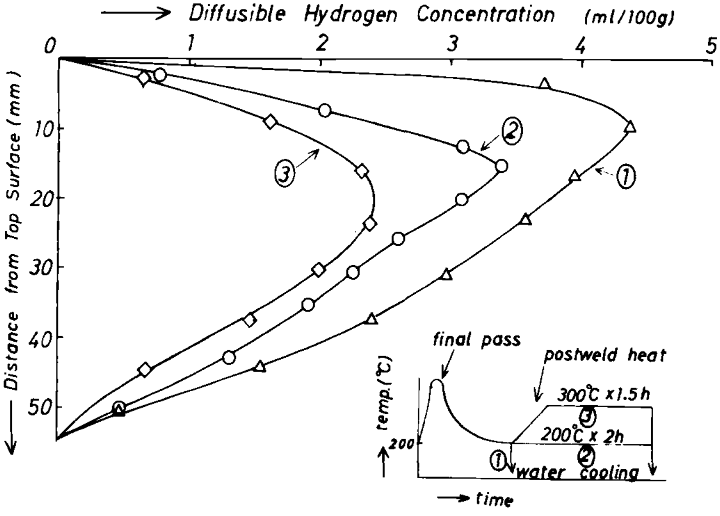

FIG. 11—*Distributions of hydrogen concentrations across the thickness when LTPWHT is employed.*

relation between the hydrogen concentration at the point of the crack initiation and the practical welding conditions, (*2*) the relation between the change of the hydrogen concentration during LTPWHT and its treating conditions, and (*3*) a critical hydrogen concentration to prevent the cracks.

Correlation Between the Hydrogen Concentration Just After Welding and Welding Conditions

Calculating Hydrogen Diffusion during Welding—In order to deal experimentally with hydrogen diffusion during a practical welding, it is first necessary to simulate the welding thermal cycles. However, as the plate thickness considered in this research is over 50 mm, the number of weld passes is considerable; moreover, the submerged arc welding process provides high heat input to the plate, so that it is almost impossible to simulate experimentally the thermal cycles, which are brought about in the welding of a real structure, using a test plate. Accordingly, the necessity of resorting to some analytical method arises in order to deal with hydrogen diffusion during practical multipass welds. Two numerical methods exist for analyzing the structure of an arbitrary shape and dimensions; the finite element method and the finite difference method. Since the atmospheric boundaries in analyses both on the heat flow and on hydrogen diffusion during multipass welds have an abrupt change when the next bead of welds is deposited, we used the former method in this research. This treats those boundary changes more easily than the latter. Now, let us refer to the various conditions with which the computer program was set up when the thermal history and hydrogen diffusion were calculated.

The submerged arc welding process brings about a high rate of penetration and, in the case of the heat input being 40 kJ/cm, it reaches about 60 percent. On account of this, the welded joint was divided into such small elements that the penetration was 60 percent (Fig. 12) where the weld was regarded as an I-groove weld with each layer composed of two passes.

The calculation of the welding thermal cycles was carried out asuming that the welding heat input and its efficiency were 40 kJ/cm and 65 percent, and that this was evenly distributed between the deposit and penetration areas when each pass of welds was deposited. The temperature change during the cooling stage of welding was calculated by using the thermal constants indicated in Fig. 13. Heat transfer coefficient, heat conductivity, and specific heat were considered to have such temperature dependences as indicated in the figure, but density was considered to be constant regardless of temperature change.

A time increment in the analysis was changed within the range of 1 to 10 s in response to the change of the cooling rate. When the temperature at the point 10 mm inside the groove face and 15 mm below the top surface of the plate reached a fixed value, the next pass of welds was deposited, and that

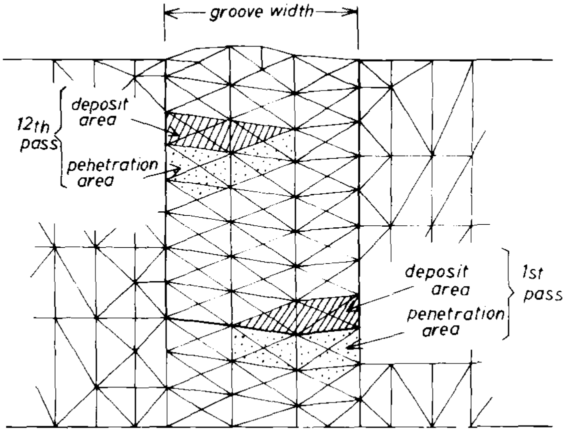

FIG. 12—*Element division for the analysis of hydrogen diffusion during welding.*

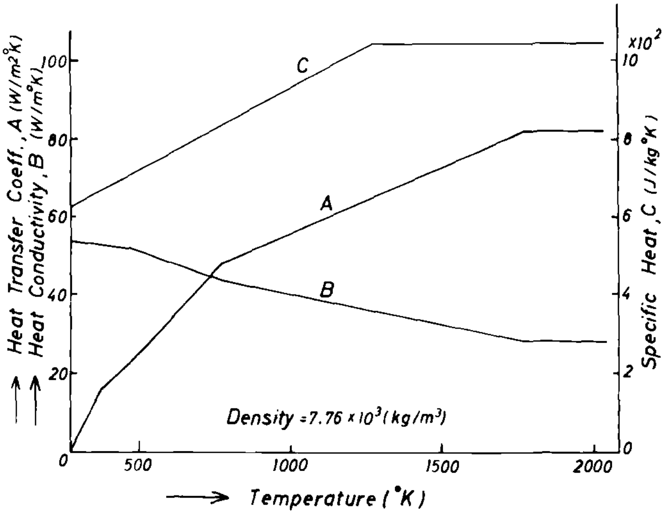

FIG. 13—*Temperature dependences of the thermal constants used for the analysis of welding thermal cycles.*

temperature was regarded as an interpass temperature. When welding thicker plate, the point in the thickness direction measuring an interpass temperature was changed with the progress of welding. This was for the purpose of making the thermal condition in the analysis correspond to that of experiments for obtaining the hydrogen distributions in the welded region which were presented in the previous section.

The hydrogen diffusion is known to be influenced by, besides the gradient of hydrogen concentration, the gradient of such hydrostatic pressure as produced by residual stresses and, microstructurally, the existence of such defects as voids, dislocations, and inclusions. However, since 2¼Cr-1Mo steel is usually welded with its welded region held at over 200°C (392°F), those influences, besides the gradient of hydrogen concentration, on the hydrogen diffusion are likely to become negligibly small. Accordingly, hydrogen diffusion during welding was analyzed under the assumption that it obeys Fick's second law.

The hydrogen concentration at the latest bead just after its bead is deposited may be considered to increase with an increase in the number of welding passes. The reason is that the amount of hydrogen contained in the latest bead just after its welding is the sum of the dissolved hydrogen from the arc column and the residual hydrogen in the penetration area, and that it is evenly distributed between the deposit area and the penetration area. Then, considering the dissolved hydrogen from the arc column at the time of welding of each pass to be constant and adding this to the residual hydrogen in the penetration area, the average value, which was obtained by dividing its total amount of hydrogen by the total weight of the deposit area and the penetration area, was evenly distributed as an initial hydrogen concentration between the two areas.

Hydrogen diffusion during the cooling stage of welding was calculated by using the hydrogen diffusivity coefficient indicated in Fig. 14 by the solid lines. Research into hydrogen diffusivity has shown that it depends strongly upon the microstructure of steel, particularly in the low-temperature range [*7-10*]. The apparent diffusivity of hydrogen of the welded joint made by the submerged arc welding process was also measured in this research, and these measurements are presented in Fig. 14 as open circles. More detailed description of the measurements is given later.

In addition, the hydrogen concentrations at the external boundary nodes were considered to be kept at zero throughout the analysis.

Comparison Between Calculated Values and Measurements—Figure 15 shows measured and calculated values of welding thermal cycles of the 1st to 5th and the 10th to 14th pass of welds for a 55-mm-thick restraint test specimen welded with an interpass temperature kept at 200°C (392°F). The solid lines represent the measurements of the temperature change at the point 10 mm inside the groove face and 15 mm below the top surface of the plate, and the values represented by "X" are the calculated ones at that point. It is seen that the calculated values of the temperature change during welding coincide very well with the measurements, and that there is not any problem with calculating the welding thermal cycles by means of this program.

Figure 16 shows both the calculated and the experimental values of the hydrogen distributions in the weld metal's region just after the final pass of welds cooled to an interpass temperature. The circle ○, triangle △, and lozenge ◇ represent the experimental values of hydrogen distributions which

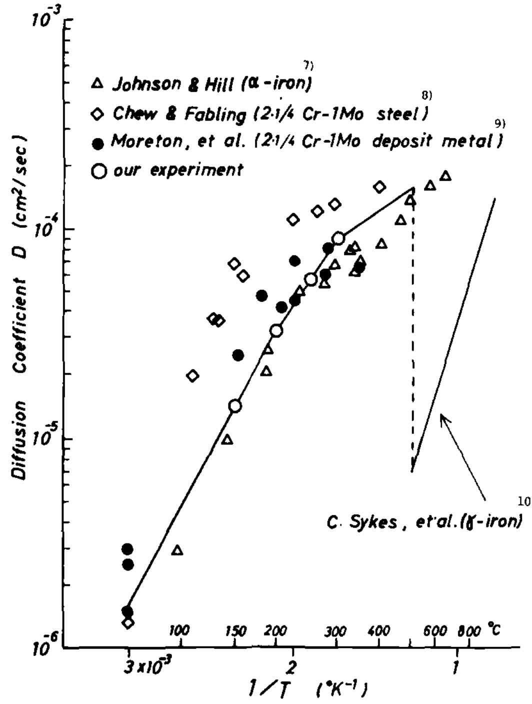

FIG. 14—*Temperature dependences of hydrogen diffusivity coefficient.*

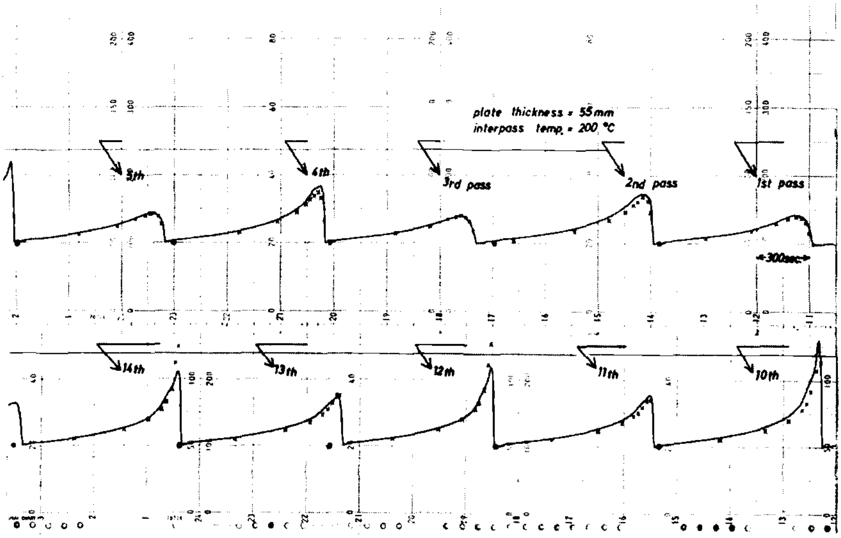

FIG. 15—*An example of welding thermal cycles.*

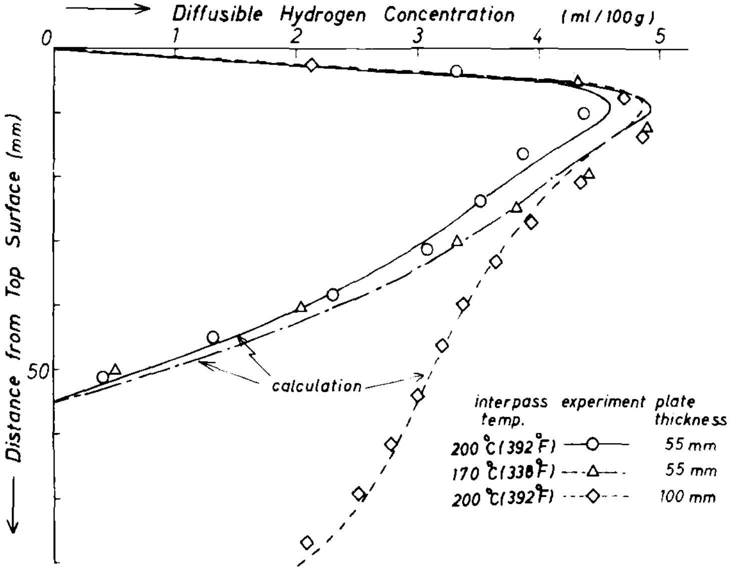

FIG. 16—*Comparison between measured and calculated distributions of hydrogen concentrations at the time when the final pass of welds attains to an interpass temperature.*

have been already shown in Fig. 10; the curves represent the analytical results. A comparison of the experimental with the calculated results shows that both distributions reach their maximum values just below the final layer of welds, and that those values increase with a decrease in the preheat and interpass temperatures or with an increase in the plate thickness. Moreover the calculated values in general coincide with the experimental ones.

These calculated values were obtained by assuming that the amount of hydrogen of 11.86 mL/100 g deposit metals dissolved from the arc atmosphere at the time of each pass of welds being deposited. Taking into account the penetration of 60 percent, its average concentration over the welded zone containing penetration just after the initial pass of welds is deposited—represented here by $C_{o,o}$—is 4.74 mL/100 g.

Figure 17 indicates the relation between the hydrogen concentration just below the penetration area of the latest bead right after its bead is deposited and the number of passes. The hydrogen concentration just below the latest bead right after its welding shows an almost linear increase with an increase in the number of passes. However, it becomes almost constant from about sixth pass to the final pass. This indicates that the amount of hydrogen which diffuses out from the welded region during each welding thermal cycle becomes constant over the sixth pass of welds. It varies, of course, depending upon the welding thermal cycles.

Correlation Between the Hydrogen Concentration Just Below the Final

Layer of Welds and a Parameter τ of Hydrogen Diffusion During Welding—It is very important, from the standpoint of preventing the transverse cracks, to clarify the correlation between the hydrogen concentration just below the final layer of welds and practical welding conditions.

The hydrogen concentration, at the point just below the latest bead immediately after its bead is deposited, can be determined by the amount both of the dissolved hydrogen from the arc column and the residual hydrogen around its penetration area, and the latter can be easily presumed to be determined both by the dissolved hydrogen from the arc column of each weld pass and by the welding thermal cycles up to its pass. (The amount of dissolved hydrogen from the arc column of each weld pass is considered to be the same, and so may be each welding thermal cycle; this we can judge from the fact that when the number of weld passes is over six in Fig. 17, the hydrogen concentration just below the penetration area of the latest bead is almost constant regardless of the number of the weld passes.)

Consequently, it seems that the hydrogen concentration, just below the penetration area of the final pass of welds right after its bead is deposited, will be determined provided the average hydrogen concentration over the welded region just after the initial pass of welds is deposited and one welding thermal cycle near the final layer of welds are given.

Accordingly, paying attention to the neighborhood of the final layer of welds in which the transverse cracks occur most frequently and using the

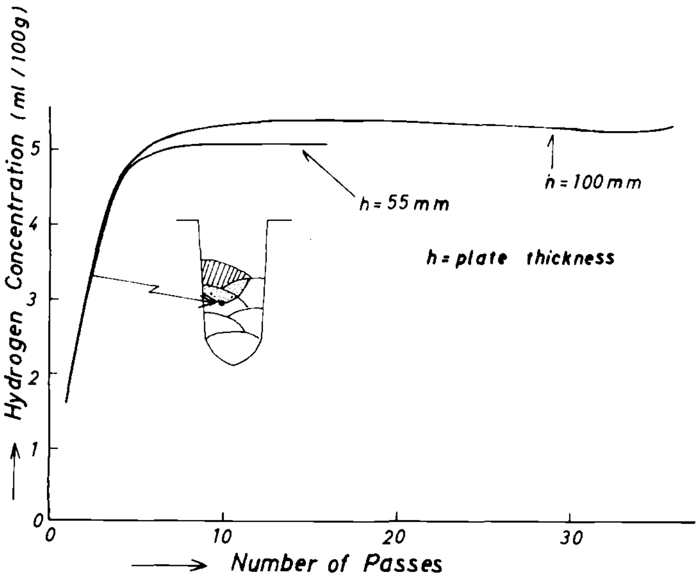

FIG. 17—*Relation between the number of passes and the hydrogen concentration just below the latest bead immediately after its bead is deposited.*

aforementioned computer program, we investigated the correlation between the hydrogen concentration just below the penetration area of the final pass of welds immediately after its bead was deposited and the parameter $\Sigma_i D_i \cdot \Delta t_i$ [obtained by dividing its thermal history successively by a small time increment Δt_i and then by summing up each $D_i \cdot \Delta t_i$ that was obtained by multiplying the hydrogen diffusivity coefficient D_i corresponding to the temperature at each time by Δt_i].

The result is shown in Fig. 18, where the horizontal axis represents the parameter of $\Sigma_i D_i \cdot \Delta t_i$ that is denoted by τ, and the vertical axis represents nondimensional hydrogen concentration obtained by dividing the hydrogen concentration just below the final pass of welds right after welding by the average hydrogen concentration over the welded region right after welding of the initial pass. The calculated values shown in the figure were obtained by changing widely the welding conditions, such as plate thickness, plate width, preheat and interpass temperatures, etc.

It is seen from Fig. 18 that the hydrogen concentration just below the final pass of welds right after the welding is determined by a parameter of τ which is a function both of welding thermal cycle and of the hydrogen diffusivity coefficient. Even though the average hydrogen concentration over the welded

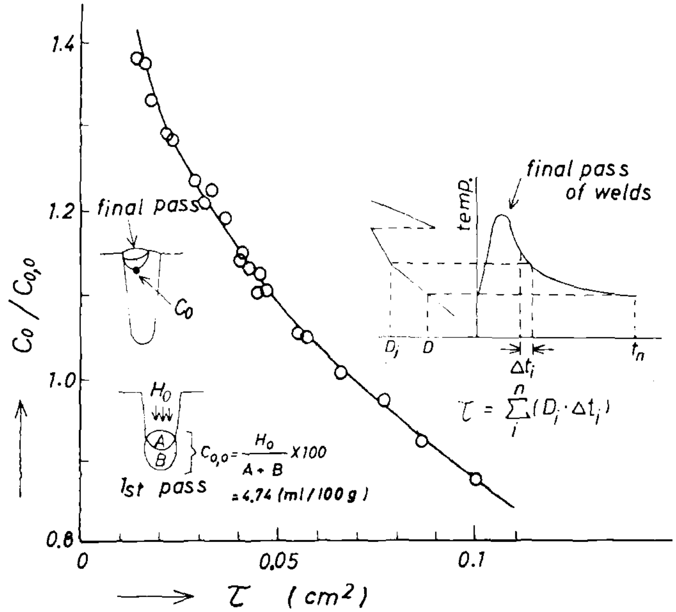

FIG. 18—*Correlation between hydrogen diffusion parameter during welding,* τ, *and the hydrogen concentration just below the final pass of welds right after its welding.*

region of the initial pass—namely, $C_{o,o}$—is changed because of the change of the flux used, or the hydrogen diffusivity is changed because of the change of the steel welded, using this figure we can readily estimate the hydrogen concentration just below the final pass of welds right after the finish of welds without carrying out the same calculations, provided that the values of $C_{o,o}$, the welding thermal cycle, and the hydrogen diffusivity are given.

Correlation Between a Parameter of Hydrogen Diffusion (τ) and Welding Conditions—The results described in the preceding paragraph are obtained by assuming that each pass of welds is deposited when the temperature of its preceding bead cools to an interpass temperature. In practical welding, however, if the size of a welded structure—for example, the diameter of a pressure vessel in the case of its circumferential welding—is large, the pass-intervals of welding will be long and an interpass temperature will decrease gradually. In order to maintain an interpass temperature during welding, a compensatory heating by gas burners is widely utilized.

Accordingly, we next investigated the effect of the compensatory heating on the parameter of hydrogen diffusion (τ), assuming that the temperature of a weld bead was kept constant by the compensatory heating from the time when the temperature of the bead attained an interpass temperature to the time when the next bead was deposited. Utilizing the compensatory heating, the parameter of τ can be estimated by adding the contribution of the compensatory heating, namely, $D \cdot \Delta t_a$, to the value of τ indicated in Fig. 18, where D is the hydrogen diffusivity coefficient at the interpass temperature and Δt_a is the interval from the time for a weld bead to attain the interpass temperature to the time for the next bead to be deposited. The value of Δt_a is changed by the welding conditions, such as plate thickness, interpass temperature, welding speed, and welding length—for example, the shell diameter of a pressure vessel in the case of its circumferential welding.

Figure 19 shows the correlation between the pass-intervals and the parameter τ obtained under the aforementioned assumption in the case of an infinitely wide plate being welded. Broken lines in the figure represent the relations between the intervals from the time right after the final pass of welds is deposited to the time when its temperature attains the interpass temperature, and the value of τ obtained by using its thermal history, namely, the value of $\Sigma_i D_i \cdot \Delta t_i$ presented in Fig. 18.

On the other hand, solid straight lines extending from a broken line represent the relation of the intervals from the time when the temperature of a weld bead attains the interpass temperature to the time when the next bead is deposited—that is, Δt_a versus an increase of τ attributed to the compensatory heating, namely, $D \cdot \Delta t_a$. Therefore the slope of the straight lines equals the diffusivity coefficient at interpass temperature.

As seen in Fig. 19, the pass intervals have a great influence on the value of τ considering the compensatory heating.

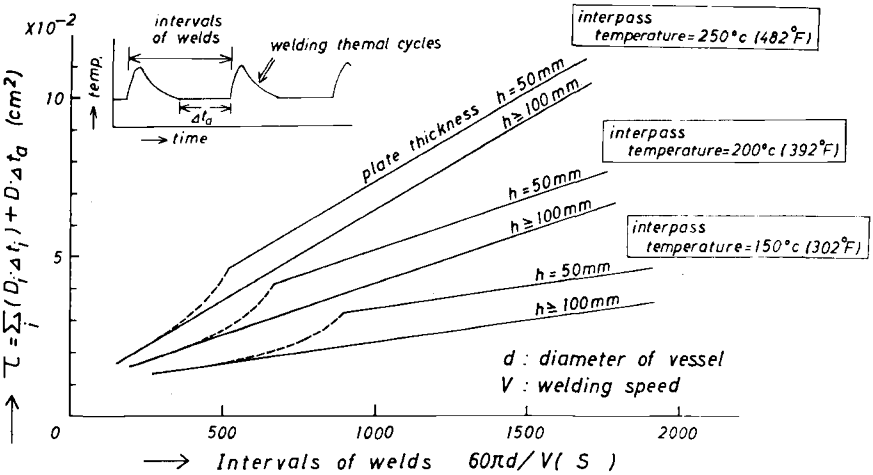

FIG. 19—*Correlation between the parameter of hydrogen diffusion, τ, and the welding conditions obtained by taking the compensatory heating by gas burners into account.*

Taking the aforementioned results into account, the hydrogen concentration, right after the final pass of welds is deposited under practical welding conditions, can be determined readily by putting the value of τ obtained from Fig. 19 into that of Fig. 18.

Correlation Between Reduction of Hydrogen Concentration Through LTPWHT and Its Treating Conditions

Method for Calculating Hydrogen Diffusion During LTPWHT—In order to clarify the relation between the reduction of hydrogen concentration through LTPWHT and its treating conditions, and the influences of the dimensions of the weldments upon the relation, analyses on hydrogen diffusion during LTPWHT were carried out. As the diffusion of hydrogen is known to be influenced by the gradient of the hydrostatic stress, the diffusion of hydrogen during LTPWHT is considered to be influenced by the residual stress distribution induced by welding. Therefore it is desirable to take this fact into consideration, because the transverse cracks are apt to occur in the region where the residual stresses are so high as to retard the diffusion of hydrogen.

Taking the gradient of hydrostatic stress into consideration, the flow of hydrogen—that is, the total amount of hydrogen passing through unit area per unit time—can be described by adding a term that depends on the gradient of hydrostatic stress to Fick's first law of diffusion:

$$J = -D\cdot\nabla C + M\cdot C\cdot\nabla_{\sigma_h};\ M = D\cdot V^*/RT \qquad (1)$$

where D, ∇C, ∇_{σ_h}, and V^* represent the diffusion coefficient, the gradient of hydrogen concentration, the gradient of hydrostatic stress, and the partial molar volume of hydrogen, respectively.

In this research the analyses were carried out by replacing this partial differential equation by the finite-difference equation described as follows.

Firstly, a welded structure is divided into small triangles (Fig. 20). Now, considering the amount of hydrogen which flows from point i into point n during time dt, it can be expressed as

$$J_i \cdot S_i \cdot dt = (-D_n \cdot \partial C/\partial_{X_i} + M_n \cdot C_n \cdot \partial_{\sigma h}/\partial_{X_i}) S_i \cdot dt \qquad (2)$$

where S_i and X_i represent the cross-sectional area and the distance between points n and i, respectively. Similarly, considering each amount of hydrogen which flows from the surrounding points of j, k, l, and so on into point n, adding them up and dividing the total amount by the volume V_n of point n enclosed with oblique lines as indicated in Fig. 20, the change of the hydrogen concentration at point n during time dt, namely, dC_n, can be described by the following equation:

$$dC_n = \sum_m J_m \cdot S_m \cdot dt/V_n = \sum_m (-D_n \cdot \partial C/\partial_{X_m} + M_n \cdot C_n \cdot \partial_{\sigma h}/\partial_{X_m}) S_m \cdot dt/V_n \qquad (3)$$

Next, we replace $\partial C/\partial_{X_m}$, $\partial_{\sigma h}/\partial_{X_m}$, and so on by the difference form as follows:

$$\partial C/\partial_{X_m} = (C_{n,t} - C_{m,t})/X_m,\ \partial_{\sigma h}/\partial_{X_m} = (\sigma_{h,n} - \sigma_{h,m})/X_m;$$
$$dt = \Delta t,\ dC_n = C_{n,t+\Delta t} - C_{n,t} \qquad (4)$$

where

$\sigma_{h,n}$, $\sigma_{h,m}$ = hydrostatic stress at point n and its arbitrary surrounding point m, respectively,

$C_{n,t}$, $C_{m,t}$ = hydrogen concentration at point n and point m at time t, respectively, and

$C_{n,t+\Delta t}$ = hydrogen concentration at point n at time $t + \Delta t$.

Substituting these equations into Eq 3 and solving it with respect to $C_{n,t+\Delta t}$ yields

$$C_{n,t+\Delta t} = [1 - D_n \cdot \Delta t \cdot \sum_m (S_m/X_m)/V_n + M_n \cdot \Delta t \cdot \sum_m \{(\sigma_{h,n} - \sigma_{h,m}) S_m/X_m\}/V_n] \cdot C_{n,t} + D_n \cdot \Delta t \cdot \sum_m (S_m \cdot C_{m,t}/X_m)/V_n \qquad (5)$$

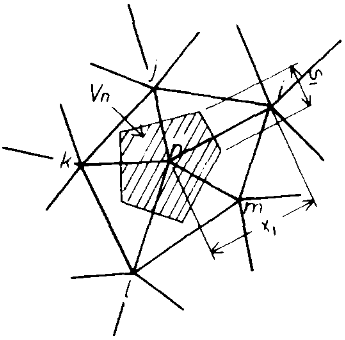

FIG. 20—*Element division for the analysis of hydrogen diffusion during LTPWHT.*

Substituting the distribution of the hydrogen concentrations at time t into Eq 5, the distribution of the hydrogen concentrations after time Δt can be calculated. The distribution of the hydrogen concentrations at the time when the final pass of welds attained an interpass temperature was first calculated with the aid of the computer program developed for the calculation of the hydrogen diffusion during welding, and taking it as an initial distribution of the hydrogen concentrations, the analysis of the diffusion of hydrogen during LTPWHT was performed on the cross section as indicated in Fig. 12.

V^*, indicated in Eq 1, has a temperature dependence and its value decreases with a rise in temperature, so that the influence of the gradient of hydrostatic stress on the diffusion of hydrogen decreases. This experimental value has not been made sufficiently clear. Accordingly, referring to the value obtained by Bockris et al [*11*], it was assumed to be 2.14 $\text{cm}^3/\text{g}\cdot\text{atom}$ at 0°C (32°F) and zero at 700°C (1292°F). Within the temperature range, it was approximated by a straight line joining both values.

Meanwhile, the hydrostatic stress σ_h in the weld zone was given by $(\sigma_x + \sigma_y)/3$ using the aforementioned residual stress distributions measured experimentally, where σ_x and σ_y are the residual stresses both in the weld direction and in the transverse direction; therefore the residual stress in the thickness direction was ignored. On the other hand, σ_h in the region of base metal was distributed so that it could balance with the hydrostatic stress in the weld zone.

Apparent Diffusion Coefficient of Hydrogen in the Welded Joint—In order to determine the diffusion coefficient, the distributions of the hydrogen concentrations throughout the thicknesses of the restraint test specimens both right after welding and after LTPWHT were first measured experimentally and then compared with those obtained analytically under the same conditions.

For this purpose, two test specimens were first welded simultaneously. For one the distribution of the hydrogen concentrations was measured right after the final pass of welds attained an interpass temperature, and for the other the distribution of the hydrogen concentrations right after LTPWHT being performed was measured. If two test specimens are welded simultaneously like this, they have the same distribution of hydrogen concentrations just after welding. Therefore the reduction of the hydrogen concentration through LTPWHT can be evaluated accurately.

Next, the analyses of the diffusion of hydrogen both during welding and LTPWHT were carried out under the same conditions as the experimental ones. The procedures are as follows. As the first step of the analyses, the distribution of the hydrogen concentrations just after welding is calculated by assuming an arbitrary value for the amount of hydrogen H_0 that dissolves from the arc atmosphere into the weld zone when each pass of welds is deposited. As the calculated values obtained at that time are directly proportional to H_0, the correct value of H_0 can be so determined that the calculated values on the distribution of the hydrogen concentrations become equal to the measured values. Given such a distribution of the hydrogen concentrations obtained like this, as an initial distribution, the analysis of the diffusion of hydrogen during LTPWHT proceeded.

It is found from Eq 5 that the analysis can proceed step by step by taking a parameter $D \cdot \Delta t$ in place of the time increment Δt, so that the results obtained can be arranged by a parameter $D_p t_p$ that is the product obtained by multiplying the diffusion coefficient at the temperature of LTPWHT, that is, D_p, by its holding time t_p. Then, comparing the measured values of hydrogen concentration with the calculated values, the parameter $D_p t_p$, at which the calculated values of hydrogen concentration coincide most closely with the measured values, can be determined. Accordingly, substituting the holding time of LTPWHT, that is, t_p, into this value $D_p t_p$, the diffusion coefficient D_p at the temperature of LTPWHT can be obtained.

Both examples of measured and calculated results concerning the distributions of hydrogen concentrations through the thickness of the restraint test specimens are shown in Fig. 21. In this case, welding was performed with the interpass temperature kept at 200°C (392°F), and LTPWHT occurred by heating the test specimen from 200 to 300°C (392 to 572°F) at the rate of 200°C/h (360°F/h) and then holding it at 300°C (572°F) for 90 min. The distribution of the hydrogen concentrations just after the final bead of welds attains the interpass temperature is denoted by "1" in the figure; the other distributions, denoted by "2," show hydrogen concentrations obtained where LTPWHT occurred. Moreover, the analytical results, together with the measured values denoted by circles, are shown by curves in the figure. The broken line means that the analysis was carried out by assuming that the diffusion of hydrogen conformed to Fick's second law. On the other hand, the solid line means that the analysis was made considering the effect of the residual stress distributions on the diffusion of hydrogen.

Taking into consideration the effect of the residual stress distributions, the

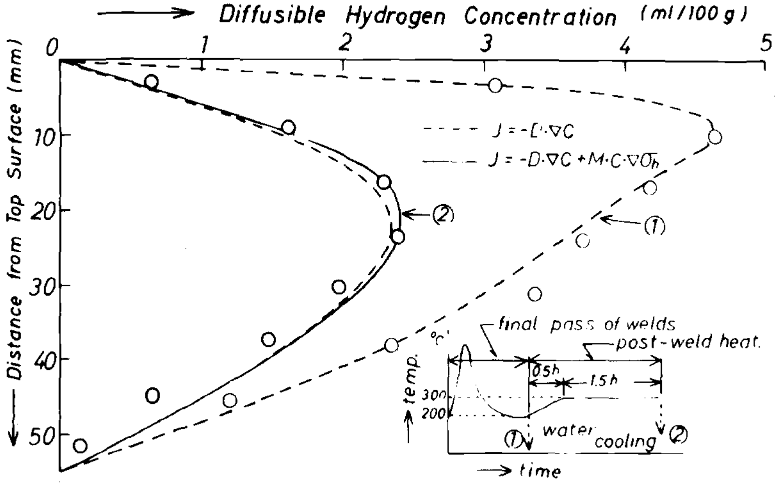

FIG. 21—*One example of the distributions of the hydrogen concentrations in the weld zone used for determining the apparent diffusivity coefficient in the welded joint.*

diffusion of hydrogen during LTPWHT is somewhat retarded in the high-stress region, as can be seen from Fig. 21 by comparing the solid line with the broken one denoted by "2". Meanwhile, the diffusion coefficient obtained from the results is 8.99 × 10^{-5} cm^2/s at 300°C (572°F).

Figure 14 shows the temperature dependence of the diffusion coefficient. The circles represent the apparent diffusion coefficients obtained by taking into consideration the residual stress distributions produced in the welded joint. These values are found to be comparatively close to the values obtained for 2¼Cr-1Mo steel weld metal by Moreton et al [*9*] and to those obtained for α-iron by Johnson et al [*7*].

Correlation Between the Reduction of Hydrogen Concentration Through LTPWHT and Its Treating Conditions—Judging from the fact that the position where a transverse crack occurs corresponds to a point at which the hydrogen concentrations reach maximum value, it is very important from the standpoint of preventing the crack to make clear the correlation between the change of the highest hydrogen concentration during LTPWHT and its treating conditions.

Figure 22 shows the relation between the highest hydrogen concentration during LTPWHT, as seen in the hydrogen distribution presented in Fig. 21, and its treating conditions. The vertical axis indicates the ratio of the highest hydrogen concentration during LTPWHT, that is, C, to the hydrogen concentration C_0 just after the welding previously described. The horizontal axis indicates a parameter obtained by adding the parameter of hydrogen diffusion (τ), which is determined from the thermal history of the final pass of welds (also described previously), to the product $D_p t_p$ obtained by multiply-

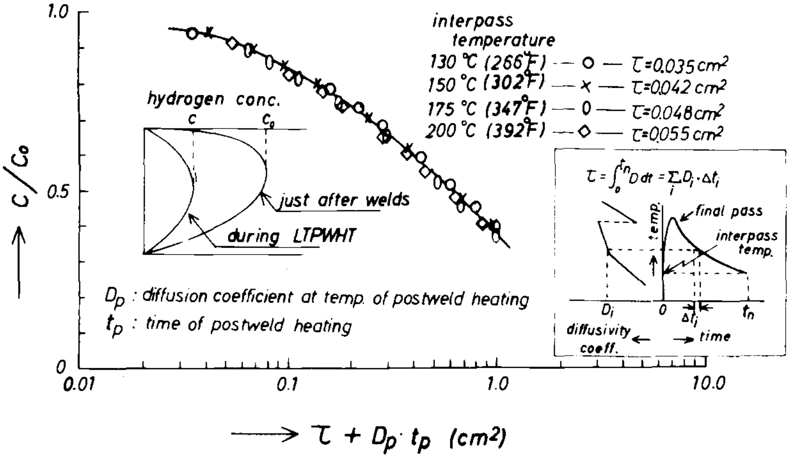

FIG. 22—*Influence of the distribution of the hydrogen concentrations just after welding on the relation between the change of the highest hydrogen concentration during LTPWHT and its treating conditions.*

ing the diffusion coefficient at the temperature of LTPWHT by its holding time.

Regarding the time when the final pass of welds is deposited as the commencement of the LTPWHT, Fig. 22 shows the influence of the distribution of the hydrogen concentrations just after welding upon the relation between C/C_0 and $(\tau + D_p \cdot t_p)$. The initial distribution of hydrogen concentration given for analyses was varied by changing the interpass temperature during welding.

It is seen from Fig. 22 that even if the distribution of the hydrogen concentrations just after welding is varied, the relation between C/C_0 and $(\tau + D_p \cdot t_p)$ can be expressed by almost only one curve.

Figure 23 presents the influence of the plate thickness on the relation between the change of the highest hydrogen concentration during LTPWHT and its treating conditions. The figure shows that at the early stage of the LTPWHT the change of the highest concentration of hydrogen is not influenced by the plate thickness. This is because a point at which the highest concentration of hydrogen appears comes just below the final bead of welds, and the hydrogen diffusion at that point is influenced mainly by the surface of the plate. It is also seen that as the LTPWHT proceeds, the point at which the distribution of the hydrogen concentrations reaches its maximum value comes inside, so that the influence of the plate thickness comes out gradually.

Moreover, judging from the condition of the LTPWHT for preventing the cracks that will be described later, its condition for preventing the cracks is within at most 1.5 cm^2 by the value of $(\tau + D_p \cdot t_p)$. Accordingly, its condi-

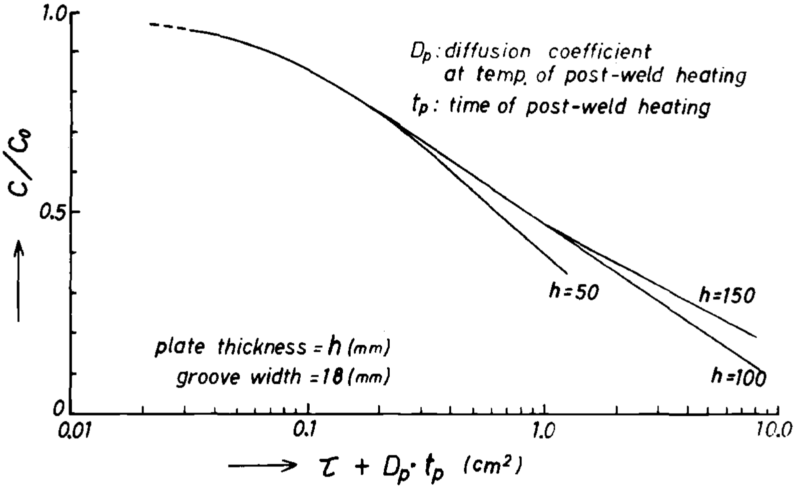

FIG. 23—*Influence of plate thickness on the relation between the reduction of the highest hydrogen concentration through LTPWHT and its treating conditions.*

tion where plate thickness is over 150 mm can be evaluated using the relation between C/C_0 and $(\tau + D_p \cdot t_p)$ for the 150-mm-thick plate presented here.

Figure 24 indicates the influence of the groove width on the relation between C/C_0 and $(\tau + D_p \cdot t_p)$. It is seen that the reduction of the hydrogen concentration is retarded with an increase in the groove width. This is because the gradient of the hydrogen concentration decreases in the direction transverse to the weld line with an increase in the groove width.

In consequence, by first substituting the critical hydrogen concentration under which the cracks do not occur, as will be described later, for the value C of the vertical axis in Fig. 24, and then substituting the hydrogen concentration just after welding, which has been mentioned previously, for the value C_0 in the same figure, the conditions of the LTPWHT for preventing the cracks can be determined from the value of the horizontal axis, that is, $(\tau + D_p \cdot t_p)$, depending on the plate thickness and groove width.

Critical Hydrogen Concentration under which Cracks Do Not Occur

In order to make clear the critical level to which the residual hydrogen concentration in weld zone has to be reduced to prevent the occurrence of the transverse cracks through LTPWHT, a cracking test using restraint test specimens was carried out with the testing parameters of the dimensions of the weld zone, preheat and interpass temperature during welding, and holding time of LTPWHT being changed as shown in Table 3. On the other hand, the heating temperature during LTPWHT was kept almost constant at

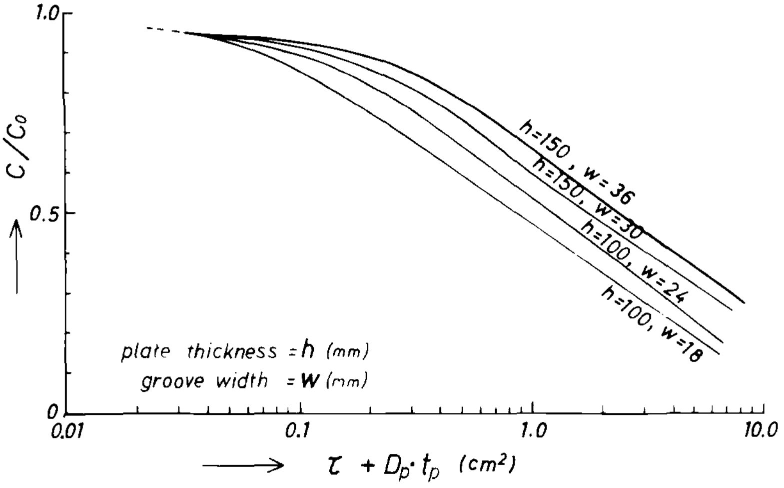

FIG. 24—*Influence of the groove width on the relation between the reduction of the highest hydrogen concentration through LTPWHT and its treating conditions.*

TABLE 3—*Conditions of cracking test.*

Plate Thickness, mm	Groove Angle, deg	Radius, mm	Interpass Temperature, °C	Temperature of LTPWHT, °C	Holding Time, h
55	8	8	130	180 to 200	1.5, 2.6, 3.2
100	7	8	130	180 to 205	2.5, 7.0
150	5.5	8	150	205	7.5

about 200°C (392°F). Other welding conditions were the same as those presented in Tables 1 and 2.

Next, the distribution of hydrogen concentrations at the time when the test specimen cooled to 100°C (212°F) after LTPWHT was calculated by the aforementioned computer program, which could evaluate hydrogen diffusion during LTPWHT. The thermal history was recorded throughout the treatment from after welding until the test specimen attained 100°C (212°F) after LTPWHT.

Figure 25 shows the results of the cracking test and the calculation of the distribution of the hydrogen concentrations. Broken and solid lines represent the distributions of hydrogen concentrations where transverse cracks are observed and are not observed, respectively. It is seen that the highest hydrogen concentration had to be reduced to less than 3.3 mL/100 g to prevent occurrence of the cracks.

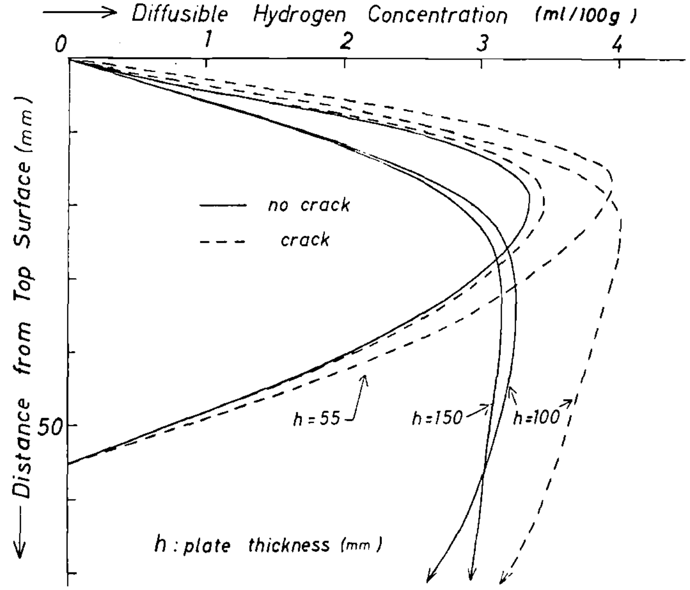

FIG. 25—*Both results of the cracking test and the calculation on the distribution of the hydrogen concentration.*

LTPWHT Conditions Required to Prevent the Occurrence of Transverse Cracks

Procedure for Determination of the LTPWHT Conditions to Prevent the Cracks—Judging from the aforementioned results, it is certain that the LTPWHT condition for preventing the cracks changes according to residual hydrogen concentration just after welding. Therefore its condition depends upon the parameters, such as dimensions of the weld zone, hydrogen level of the flux used, and other welding conditions.

A procedure for determining LTPWHT conditions that would prevent the cracks follows:

1. Determine the values of a plate thickness, an interpass temperature and a pass interval; then the diffusion parameter of hydrogen during welding (τ) can be evaluated by using Fig. 19.
2. Put its value of τ into the abscissa of Fig. 18; then the ratio of C_o to $C_{o,o}$ can be evaluated, where C_o and $C_{o,o}$ represent the residual hydrogen concentration just after welding right below the final pass of welds and the hydrogen concentration at the initial pass of welds immediately after its bead is deposited, respectively.
3. Put $C_{o,o}$ into $C_o/C_{o,o}$; then C_o can be determined. The amount of $C_{o,o}$ equals 4.74 mL/100 g where a conventional fused type of flux is used under

the heat input of 40 kJ/cm, as was described before. A method to measure its amount experimentally will be shown later.

4. Calculate C_{cr}/C_o, where C_{cr} is the critical hydrogen concentration for preventing the transverse cracks, namely, 3.3 mL/100 g.

5. Put C_{cr}/C_o into the ordinate of Fig. 24; the required condition for the residual hydrogen concentration just after welding, C_o, to decrease to C_{cr} can then be obtained in terms of $(\tau + D_p \cdot t_p)$ from the horizontal axis depending upon the plate thickness and groove width.

6. Subtract τ from $(\tau + D_p \cdot t_p)$; the preventing condition of the cracks through LTPWHT, namely, $D_p \cdot t_p$, can then be determined, where D_p and t_p are the diffusion coefficient of hydrogen at the temperature of LTPWHT and its holding time, respectively. (Using a temperature dependence of hydrogen diffusivity coefficient, an arbitrary combination of the temperature and holding time of LTPWHT to prevent the cracks can be selected.)

LTPWHT Condition Required to Prevent the Cracks—It is obvious that if a lower-hydrogen type of flux is used, the residual hydrogen concentration just after welding will decrease, so that the LTPWHT condition required to prevent the cracks will be mitigated. Let us now investigate the LTPWHT condition where the newly developed fused type of flux is being utilized.

In order to evaluate the LTPWHT condition when the flux is changed, the hydrogen concentration in the first bead just after its bead is deposited—namely, $C_{o,o}$—has only to be determined. Thus the value of $C_{o,o}$ when the lower-hydrogen type of flux was used was measured experimentally by the method indicated in Fig. 27.

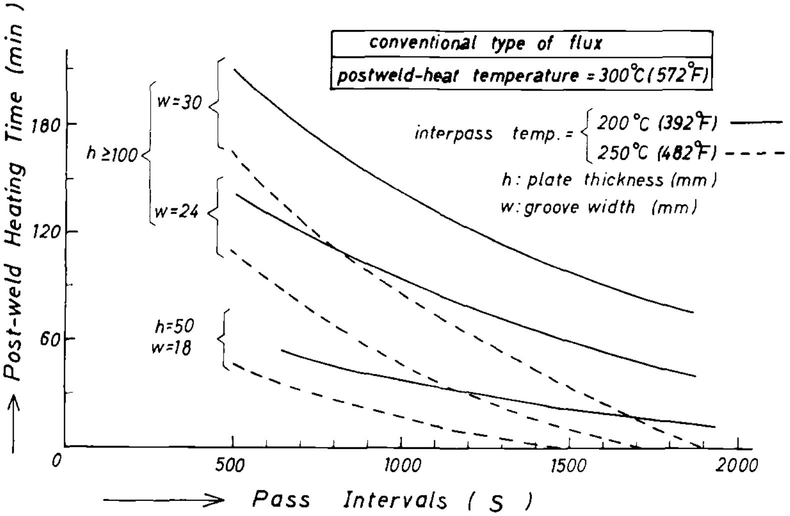

FIG. 26—*Preventing transverse cracks by LTPWHT where a conventional fused type of flux is used.*

The test specimens were first immersed into water just after one pass weld and then put into liquid nitrogen to make the test specimens separate easily. Each specimen fractured forcibly was, further, put into a glass vacuum bottle and kept at room temperature for about 20 days. The amount of hydrogen accumulated in the bottle was measured by a vacuum extraction system. Finally, its value was converted into $C_{o,o}$ by dividing it by the total weight of penetration and deposited metal. The welding conditions were the same as those listed in Table 2.

It was shown in Fig. 16 that, assuming $C_{o,o}$ was 4.74 mL/100 g when a conventional type of flux was used, the calculated distributions of hydrogen concentrations coincided with the experimental distributions. In order to check the validity of this method, the $C_{o,o}$-value where both a conventional type and a new type of flux were used was measured experimentally by applying the method.

As a result, the average value of $C_{o,o}$ measured 4.94 mL/100 g for a conventional type; this was very close to 4.74 mL/100 g. Therefore it is considered that this method has enough reliability to determine $C_{o,o}$-value. For a new type its value measured 3.13 mL/100 g, and was reduced by 34 percent compared with the case of a conventional one.

The preventing conditions of the transverse cracks through LTPWHT where a newly developed flux was used were obtained as shown in Fig. 28 by using the value of $C_{o,o}$, namely, 3.13 mL/100 g, and by applying the aforementioned procedure. Comparing its result with that shown in Fig. 26, we see clearly that by using a new type of flux in place of a conventional one the mitigation of about 100°C (212°F) concerning an interpass temperature during welding can be attained, and that the holding time of LTPWHT required for preventing the cracks can be greatly reduced.

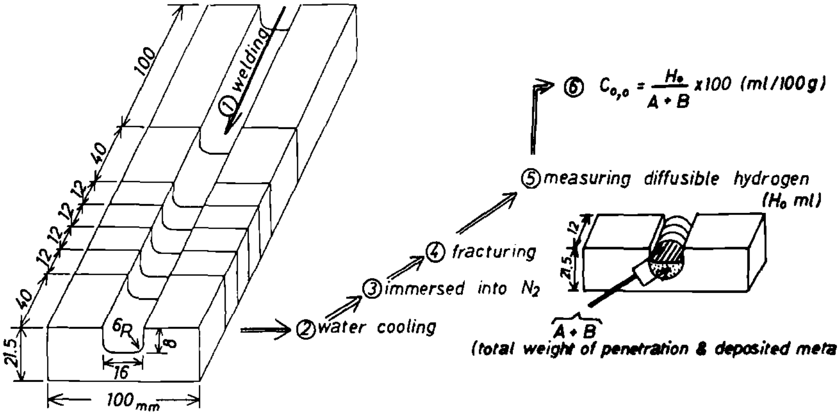

FIG. 27—*Procedure for measuring* $C_{o,o}$.

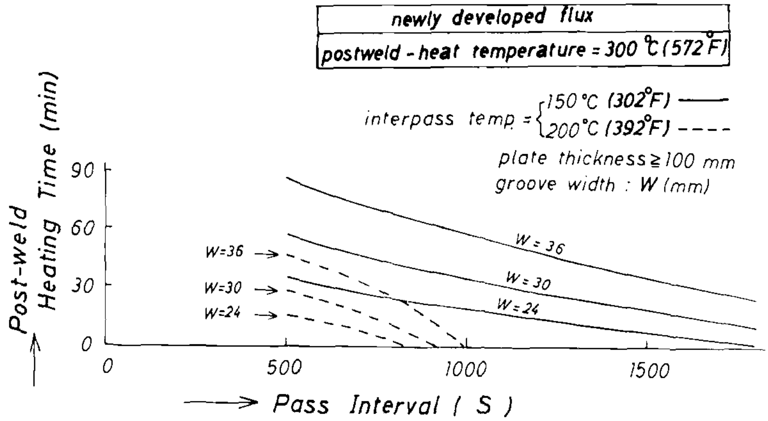

FIG. 28—*Preventing transverse cracks by LTPWHT where a newly developed lower-hydrogen flux is used.*

Application of LTPWHT to Heavy-Wall Pressure Vessels

To show the validity of this approach, we applied this method to a prototype of the forged rings of 3000 mm inner diameter and 250 mm thickness. Girth welding to join these shell courses was performed by the tandem submerged arc welding process with a combination of conventional flux and wire. LTPWHT at 300°C for 1 h followed in accordance with the results presented in Fig. 26. The welded region was sectioned for magnetic particle examination. No cracks were observed.

Also, a number of thick-wall pressure vessels have been made by utilizing LTPWHT instead of ISR—for example, hydrocracker reactors of 3900 mm inner diameter, 222 mm wall thickness, and a weight of 510 tons. All excess weld reinforcement was removed by grinding after LTPWHT; and UT inspection, magnetic particle examination, and radiographic inspections specified by the ASME Code were performed to determine if weld defects were present. None were found.

Conclusion

LTPWHT has been established as a successful method for preventing transverse cracks apt to occur in heavy-section butt weldments of 2¼Cr-1Mo steel and has made it possible for the conventional ISR to be omitted. It is hoped that various problems pertaining to the fabrication of a thick-wall pressure vessel, such as security of the strength and toughness of the material, prevention of the SR cracking besides hydrogen-induced weld cracking, smooth fabrication schedule, and reduction of energy consumption, can be solved by the use of this method.

References

[*1*] Fujii, T., "On the Prevention of Hydrogen-Induced Weld Cracking in Steel Weldments," IIW Document IX-876-74.

[*2*] Nishio, Y., Yoshida, Y., and Miura, Y., *Journal of the Japan Welding Society*, Vol. 44, No. 4, 1975, pp. 345–350.

[*3*] Caplan, J. S. and Landerman, E., WRC Bulletin 216, June 1976, pp. 1–23.

[*4*] Takahashi, E., Iwai, K., and Satoh, K., *Transactions of the Japan Welding Society*, Vol. 10, No. 1, April 1979, pp. 36–45.

[*5*] Uda, M. et al, "Vacuum Extraction System for Measuring Diffusible Hydrogen," Preprints of the National Meeting of Japan Welding Society, No. 14, Spring 1974, pp. 18–19.

[*6*] Takahashi, E. and Iwai, K., *Transactions of the Japan Welding Society*, Vol. 10, No. 1, April 1979, pp. 46–52.

[*7*] Johnson, E. W. and Hill, M. L., *Transactions of the Metallurgical Society of American Institute Metallurgical Engineer*, Vol. 218, Dec. 1960, pp. 1104–1112.

[*8*] Chew, B. and Fabling, F. T., *Metal Construction and British Welding Journal*, April 1972, pp. 132–134.

[*9*] Moreton, J., Coe, F. R., and Boniszewski, T., *Metal Construction and British Welding Journal*, June 1971, pp. 223–228.

[*10*] Sykes, C., Burton, H., and Gegg, C. C., *Journal of the Iron and Steel Institute*, Vol. 156, 1947, p. 155.

[*11*] Bockris, J. O'M., Beck, W., et al, *Acta Metallurgica*, Vol. 19, Nov. 1971, pp. 1209–1217.

L. E. Wagner[1]

Comparison of Peened versus Postweld Heat-Treated Chromium-Molybdenum Alloy Steel Weldments

---

REFERENCE: Wagner, L. E., "**Comparison of Peened versus Postweld Heat-Treated Chromium-Molybdenum Alloy Steel Weldments,**" *Application of 2¼Cr-1Mo Steel for Thick-Wall Pressure Vessels, ASTM STP 755,* G. S. Sangdahl and M. Semchyshen, Eds., American Society for Testing and Materials, 1982, pp. 451-466.

ABSTRACT: Shielded metal arc weldments were made using 2¼Cr-1Mo alloy steel electrodes (AWS 5.5 Class E9018-B3) and 1¼Cr-½Mo alloy steel plates (ASME SA387 Grade 11 Class 2). The properties of these 38-mm (1½-in.)-thick weldments are compared in two conditions: (*1*) peened (all beads except the first and last layers were peened for 0.5 min), and (*2*) postweld heat treated (PWHT) at 704°C (1300°F). Both all-welded and transverse weld properties are compared.

The hardness, yield strength and tensile strength (at both room and elevated temperature), and stress rupture strength for the peened weldments are higher than for the PWHT weldments. The creep rates for the peened weldments are lower than for the PWHT weldments.

In general, the ductility and stress corrosion properties for the PWHT weldments are better than for the peened weldments.

KEY WORDS: 2¼Cr-1Mo weld, 1¼Cr-½Mo base, peened, postweld heat treated, hardness, tensile, stress rupture, creep rate, stress corrosion

This investigation was made to determine the differences in properties between weldments that have been peened after welding with no subsequent heat treatment and weldments that have been postweld heat treated (PWHT).

Peening welds has, in general, been an aid in preventing weld cracks and in reducing shrinkage stresses and distortion. Peening is the application of hammer blows to cause the plastic flow of metal. The inward contraction of each bead as it cools is counteracted by the lateral spread of the weld bead when peened. "The effectiveness of peening has been amply demonstrated by

---

[1] Materials Engineer, Westinghouse Electric Corporation, Philadelphia, Pa. 19113.

many instances in which cracking was prevented, in thick joints having extremely high restraint, only by peening" [*1*].[2] Calamari et al [*2*] observed embrittlement of the weld metal when it was peened. They also observed that the embrittlement was eliminated by the heat of the subsequent covering weld deposit.

Pellini and Eschbacker [*3*] showed that a heavily peened weld surface layer may be a crack starter. Peening of an unsupported weld pass is also inadvisable as it is likely to tear. Therefore peening of the first layer (if unsupported) and the last layer is considered a dangerous practice [*1*].

If the weld is peened at a white heat, the metal will be so soft that the peening tool will sink deep into the weld and the grain size will not be changed. If peening is done at a dull red heat (slightly above the transition temperature), the grain size will be refined. Below a dull red heat, peening cold works the metal and, while increasing its strength, impairs the ductility. Cold work distorts the grains and causes the weld to become prone to cracking. Peening will be most effective if the weld is at a dull red heat. Normally, after the welder has completed a section of the weld, the weld is hot at the end but relatively cold at the starting point. If the peening is done by the operator, the starting point will probably be cold worked, the intermediate length grain will be refined, and the hot end will be at too high a temperature for grain refinement. If the weld is reheated to the proper temperature or if a helper follows the welder at the proper distance with the peening hammer, peening can be done at the correct temperature [*4*]. These procedures are not always practical.

"Peening can be employed to counteract transverse shrinkage. Depending on the circumstances, peening can be applied to remove all shrinkage, to remove as little as desired, or may be carried to a degree that accomplishes an expansion at the joint" [5].

Procedure

For this investigation 178 mm (7 in.) wide by 762 mm (30 in.) long 1¼Cr-½Mo alloy steel plates (ASME SA387 Grade 11 Class 2) were welded with 2¼Cr-1Mo alloy steel electrodes (AWS 5.5, Class E9018-B3) using the shielded metal arc welding process. A total of four weldments, 762 mm (30 in.) by 356 mm (14 in.) by 38 mm (1½ in.), were made. All weldments were made using a 232°C (450°F) preheat and interpass temperature.

All beads except those in the first and last layer were peened for approximately ½ min for Weldments 1 and 2. Each bead, which was approximately 203 mm (8 in.) long per electrode, was peened immediately after being deposited. A pneumatic chipping hammer with a 4.8 mm (3/16 in.) radius round nosed tool was used for peening. For the first five layers, 4-mm (5/32-in.)-diameter electrodes were used, and then 4.8-mm (3/16-in.)-diameter

---

[2] The italic numbers in brackets refer to the list of references appended to this paper.

electrodes were used for the remaining layers. These weldments were not postweld heat treated.

Weldments 3 and 4 were welded using the same size electrodes as above but without peening. These weldments were postweld heat treated at 704°C (1300°F) for 2 h.

All four weldments were acceptable to the radiographic requirements of the ASME Code, Section VIII, Division I.

Test Results and Discussion

The chemical analyses for all weldments were the same as all plates were from the same heat of steel and all electrodes were from the same lot.

A photomacrograph of a section of the peened weldment is shown in Fig. 1, and a photomacrograph of a section of the PWHT weldment is shown in Fig. 2. As both weldments had the same joint geometry and root gap before welding, it is obvious that the PWHT weldment contracted more than the peened weldment. No attempt was made to measure or control the amount of shrinkage. The photomacrographs show some grain refinement for the peened weldment compared with the PWHT weldment. This grain refinement is also seen in the photomicrographs (Figs. 3 and 4).

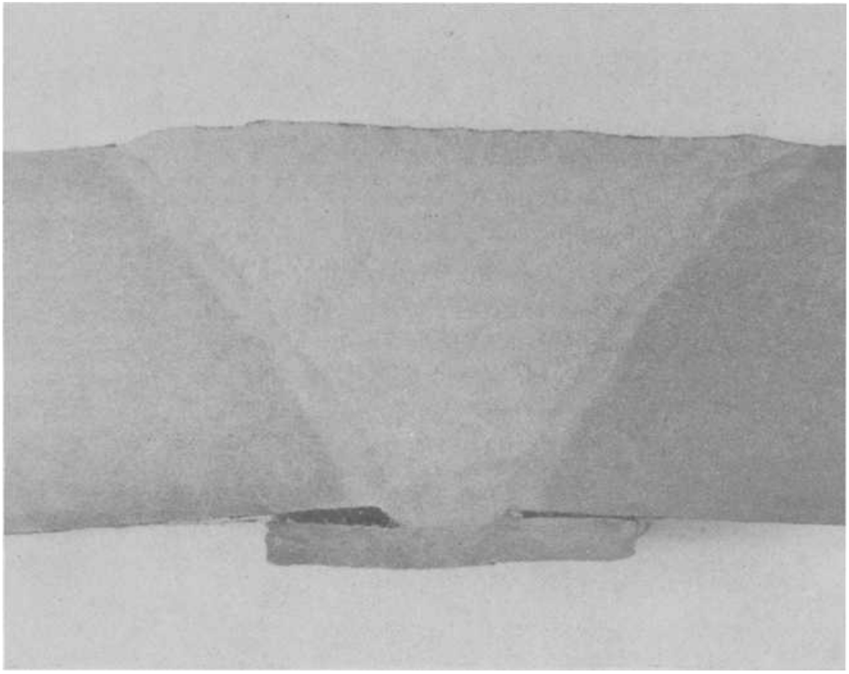

FIG. 1—*Photomacrograph of peened weld cross section (X1.3).*

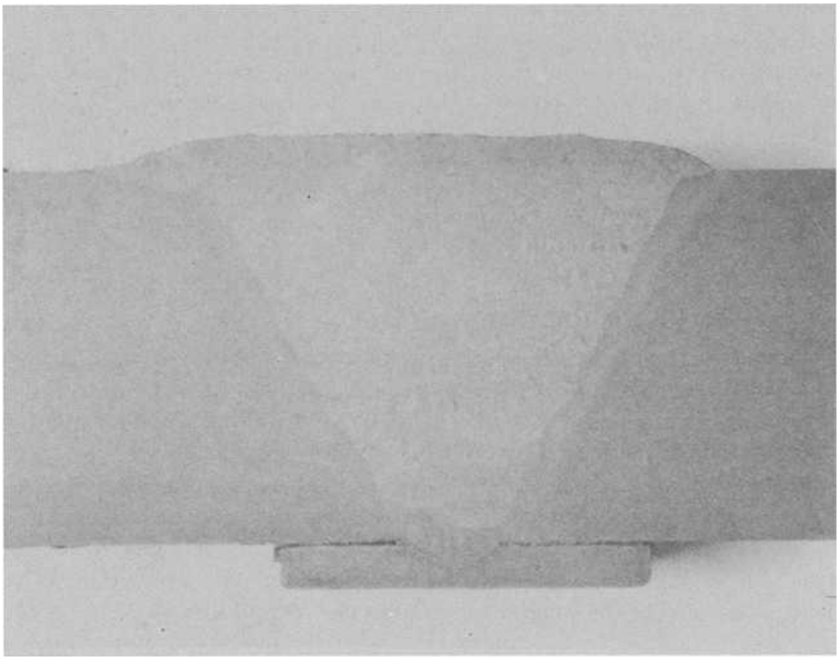

FIG. 2—*Photomacrograph of PWHT weld cross section (X1.3).*

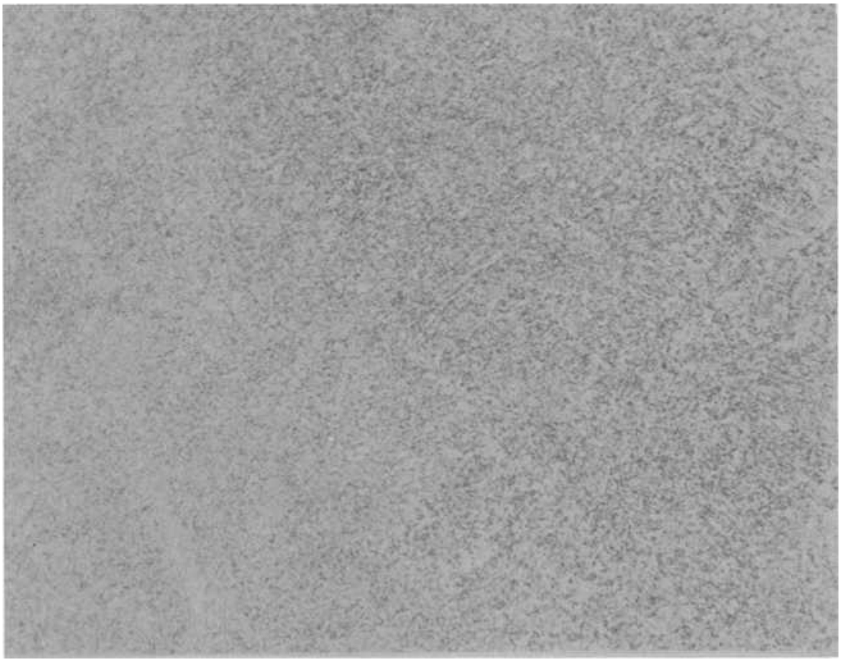

FIG. 3—*Photomicrograph of peened weld cross section (X100)*

FIG. 4—*Photomicrograph of PWHT weld cross section (X100).*

The lack of complete grain refinement is probably due to the method of peening, as stated in the introduction: "If the peening is done by the operator, the starting point will probably be cold worked, the intermediate length grain will be refined, and the hot end will be at too high a temperature for grain refinement".

The results of the 30-kg-load diamond pyramid hardness testing of Weldments 2 and 4 are shown in Table 1. As can be seen, the hardness is greater for the peened weldment in the weld metal, heat-affected zone (HAZ), and base metal.

Weldments 1 and 3 were used for tests for qualifying the procedure in accordance with ASME Code, Section IX. Both weldments met the requirements, which include reduced section tensile specimens and side bends. Weldments 1 and 3 were used to determine room temperature and elevated temperature tensile properties using 9-mm (0.357-in.)-diameter specimens. The results are shown in Tables 2 and 3, and are plotted in Figures 5 to 8. The transverse weld specimens were oriented so that the HAZ was located at the center of the specimen. However, all fractures occurred in the base metal beyond the HAZ.

As can be seen from the all-weld results, the peened specimens have higher strength and in most cases lower ductility than the PWHT specimens.

TABLE 1—*Diamond pyramid hardness (30 kg load).*

	Weldment 2 (Peened)	Weldment 4 (PWHT)
Base metal	164	157
Base metal	169	159
Base metal	167	158
Base metal	164	160
Base metal average	166	158
Heat-affected zone	271	199
Heat-affected zone	251	206
Heat-affected zone	245	222
Heat-affected zone	246	209
HAZ average	253	209
Weld	269	238
Weld	286	234
Weld average	277	236

TABLE 2—*Tensile properties (all-weld specimens).*

Weldment	Temperature, °C (°F)	0.2% Y.S., MPa (ksi)	U.T.S., MPa (ksi)	Elongation, %	Reduction of Area, %
1 (peened)	21 (70)	665 (96.5)	823 (119.6)	24.3	64.9
3 (PWHT)	21 (70)	566 (82.2)	692 (100.3)	25.4	71.9
1 (peened)	93 (200)	646 (93.7)	764 (110.8)	21.4	62.8
3 (PWHT)	93 (200)	523 (75.9)	632 (93.1)	24.3	71.9
1 (peened)	204 (400)	617 (89.5)	721 (104.5)	23.3	66.3
3 (PWHT)	204 (400)	492 (71.4)	597 (86.6)	22.1	72.4
1 (peened)	316 (600)	653 (94.7)	833 (120.8)	23.3	52.3
3 (PWHT)	316 (600)	475 (68.9)	571 (82.8)	19.3	70.1
1 (peened)	427 (800)	575 (83.3)	850 (123.0)	20.8	54.2
3 (PWHT)	427 (800)	425 (61.7)	565 (81.8)	21.4	68.1
1 (peened)	482 (900)	577 (83.7)	780 (113.0)	20.9	58.6
3 (PWHT)	482 (900)	446 (64.7)	516 (74.8)	21.4	72.2
1 (peened)	538 (1000)	521 (75.6)	694 (100.5)	20.2	62.8
3 (PWHT)	538 (1000)	396 (57.3)	571 (68.3)	19.8	75.3
1 (peened)	593 (1100)	263 (38.2)	545 (79.0)	18.6	69.3
3 (PWHT)	593 (1100)	300 (43.5)	396 (57.5)	21.4	52.3

The transweld tensile tests are actually tests of the base metal, as the fractures occurred in the base metal beyond the HAZ. The lower strengths of the PWHT weldments compared with the peened weldment (we are really testing normalized and tempered plate) indicate that the 704°C (1300°F) PWHT is too high. The suppliers temper this plate material at 621°C (1150°F) to 704°C (1300°F) for ¾ h per 25.4 mm (1 in.) of thickness.

Weldments 1 and 3 were used for transweld creep rupture testing oriented with an HAZ located in the notch of a plain bar—notch bar specimen.

TABLE 3—*Tensile properties (transweld specimens).*[a]

Weldment	Temperature, °C (°F)	0.2% Y.S., MPa (ksi)	U.T.S., MPa (ksi)	Elongation, %	Reduction of Area, %
1 (peened)	21 (70)	382 (55.3)	556 (80.6)	17.9	62.2
3 (PWHT)	21 (70)	339 (49.2)	540 (78.4)	18.3	63.2
1 (peened)	93 (200)	344 (50.0)	507 (73.6)	15.1	61.5
3 (PWHT)	93 (200)	276 (40.0)	498 (72.1)	22.0	66.2
1 (peened)	204 (400)	408 (59.3)	504 (73.0)	10.7	55.7
3 (PWHT)	204 (400)	292 (42.4)	460 (66.7)	16.9	62.2
1 (peened)	316 (600)	386 (56.0)	510 (74.0)	12.3	56.4
3 (PWHT)	316 (600)	310 (45.0)	475 (68.9)	15.1	57.2
1 (peened)	427 (800)	331 (48.0)	494 (71.6)	17.1	59.3
3 (PWHT)	427 (800)	298 (43.2)	463 (67.1)	15.3	57.8
1 (peened)	482 (900)	334 (48.5)	464 (67.3)	16.5	61.5
3 (PWHT)	482 (900)	254 (35.4)	417 (60.5)	22.6	74.7
1 (peened)	538 (1000)	304 (44.1)	416 (60.3)	17.5	68.7
3 (PWHT)	538 (1000)	277 (40.2)	388 (56.3)	22.6	79.6
1 (peened)	593 (1100)	254 (36.9)	354 (51.3)	25.0	78.8
3 (PWHT)	593 (1100)	229 (33.2)	323 (46.8)	24.3	78.8

[a] All fractures occurred in the base metal.

Weldments 2 and 4 were used for all-weld creep rupture testing with plain bar-notch bar specimens. All failures occurred in the plain bar area and were not tested further in the notch bar area. The creep rupture test results are shown in Table 4 and plotted in Figures 9 and 10. For the Larson Miller Parameter (LMP), t is time to rupture in hours. For the all-weld specimens, the peened weld [824 MPa (119.6 ksi) U.T.S.] had longer times to rupture and lower creep rates than the PWHT welds [691 MPa (100.3 ksi) U.T.S.]. This same variation with tensile strength was noted for 2¼Cr-1Mo alloy steel weld metal in a previous investigation [*6*]. Data from the investigation are shown for comparison in Figs. 9 and 10.

Table 4 indicates that most of the transweld creep-rupture specimens failed in the HAZ with low ductility. The occurrence of a ductility minimum is attributed to the formation of a carbide denuded zone near the grain boundaries [*7*]. During the creep process, carbides are precipitated on the grain boundaries diluting the matrix of the alloying elements. To balance the matrix chemistry, carbides from the matrix near the grain boundary dissolve. This process of carbide dissolving into the matrix and precipitating at the grain boundary continues, resulting in a very narrow zone adjacent to the grain boundaries that is essentially free of carbides. Since this denuded zone is soft, high localized deformation occurs here and overall ductility decreases. However, as the denuded zone increases in width, the localized strain decreases and ductility starts to recover [*6*].

Weldments 2 and 4 were used for stress-corrosion U-bend test specimens.

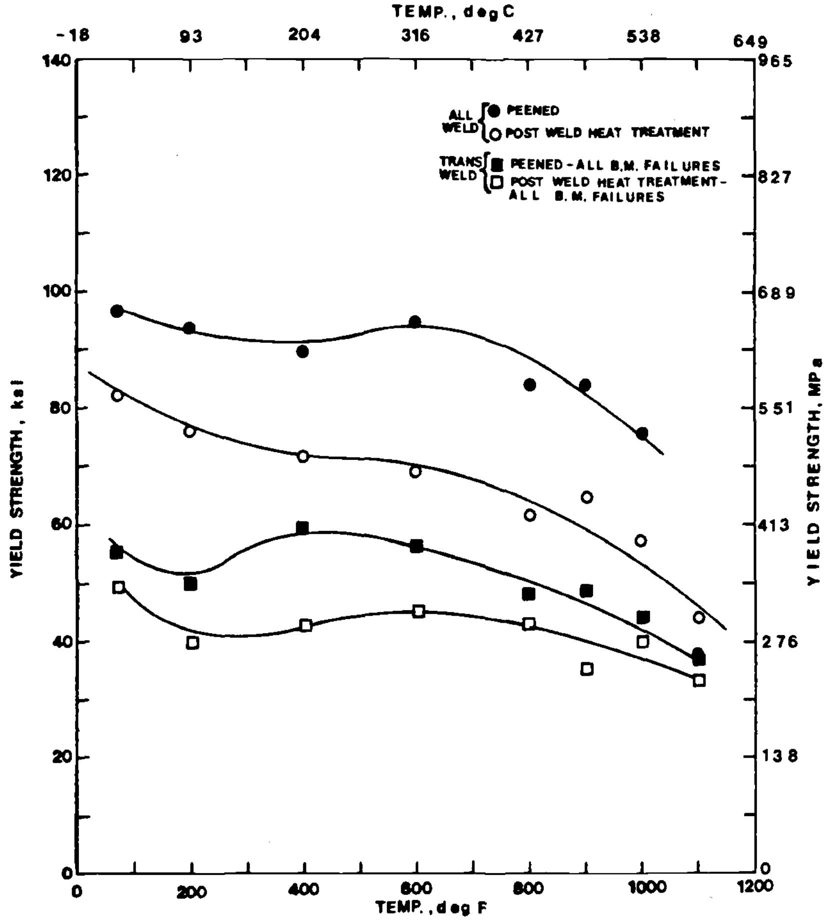

FIG. 5—*Yield strength versus temperature.*

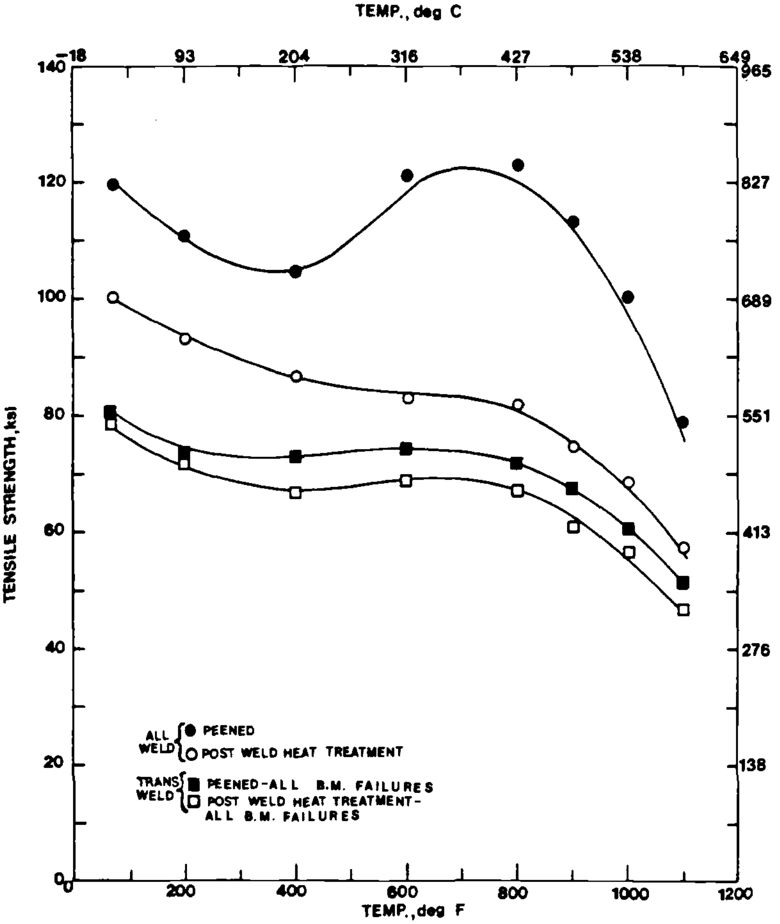

FIG. 6—*Tensile strength versus temperature.*

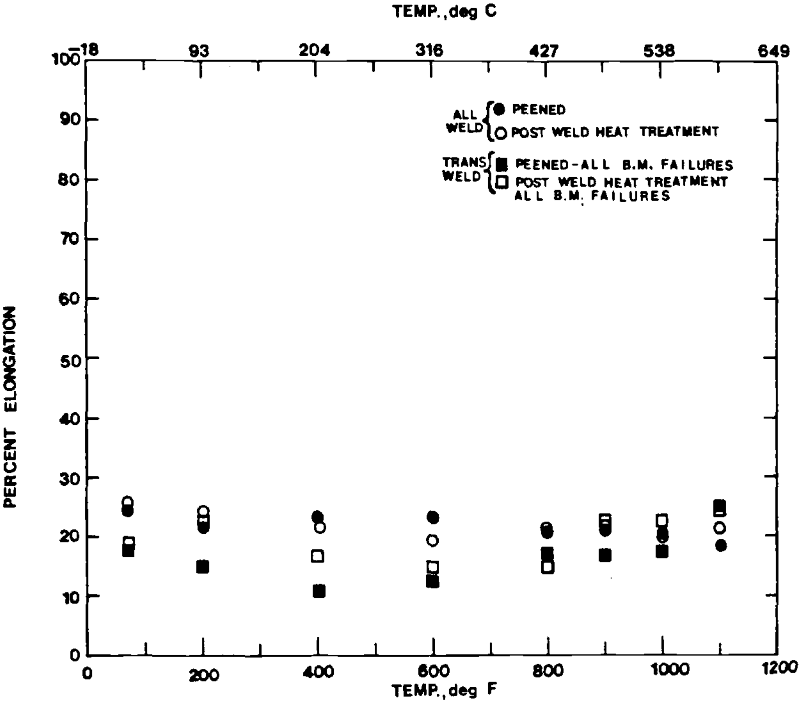

FIG. 7—*Percent elongation versus temperature.*

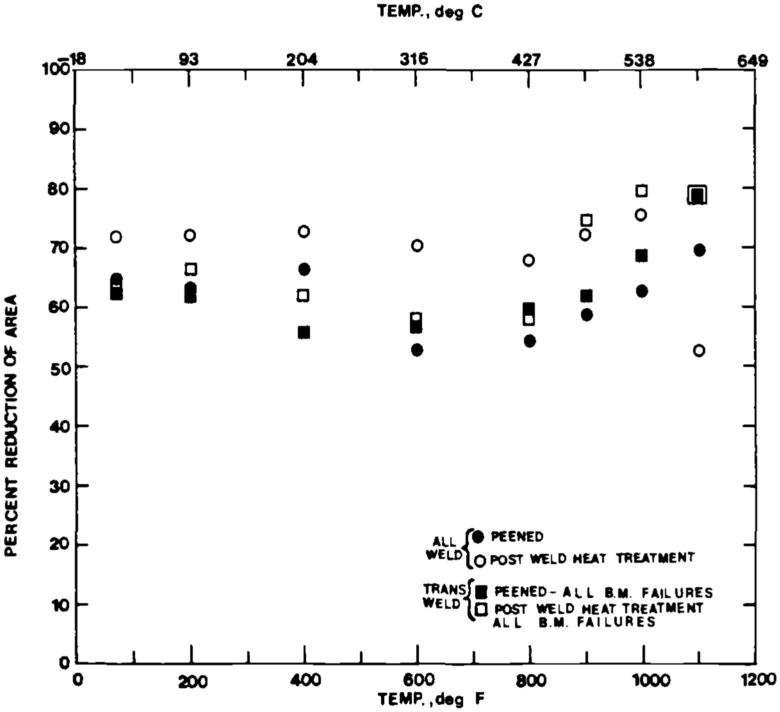

FIG. 8—*Percent reduction of area versus temperature.*

TABLE 4—*Creep rupture test results.*

Weldment	Specimen Type	Temperature, °C (°F)	Stress, MPa (ksi)	Rupture Time, h	Elongation, %	Reduction of Area, %	Minimum Creep Rate, %/h	Fracture Location
1-1 (peened)	transweld	538 (1000)	220 (32)	1015	2.0	7.7	5.50×10^{-4}	weld and HAZ
1-2 (peened)	transweld	538 (1000)	206 (30)	1142	4.1	13.0	6.22×10^{-4}	HAZ
1-3 (peened)	transweld	538 (1000)	200 (29)	1301	3.8	3.3	2.75×10^{-4}	HAZ
3-1 (PWHT)	transweld	538 (1000)	220 (32)	661	4.7	15.1	3.25×10^{-3}	HAZ
3-2 (PWHT)	transweld	538 (1000)	206 (30)	1098	2.7	9.8	1.39×10^{-3}	HAZ
3-3 (PWHT)	transweld	538 (1000)	193 (28)	617	19.9	83.6	1.50×10^{-3}	weld
2-1 (peened)	all-weld	538 (1000)	220 (32)	1594	22.0	74.5	5.42×10^{-4}	...
2-2 (peened)	all-weld	538 (1000)	214 (31)	3027	20.3	59.9	4.10×10^{-4}	...
2-3 (peened)	all-weld	538 (1000)	179 (26)	6098	20.2	54.0	2.50×10^{-4}	...
4-1 (PWHT)	all-weld	538 (1000)	276 (40)	128	20.8	74.6	...	...
4-2 (PWHT)	all-weld	538 (1000)	255 (37)	391	28.8	81.7	...	...
4-3 (PWHT)	all-weld	538 (1000)	220 (32)	1301	24.5	76.1	1.38×10^{-3}	...
4-4 (PWHT)	all-weld	538 (1000)	260 (30)	1916	25.2	74.3	1.00×10^{-3}	...
4-5 (PWHT)	all-weld	538 (1000)	172 (25)	4860	20.6	74.5	2.43×10^{-4}	...

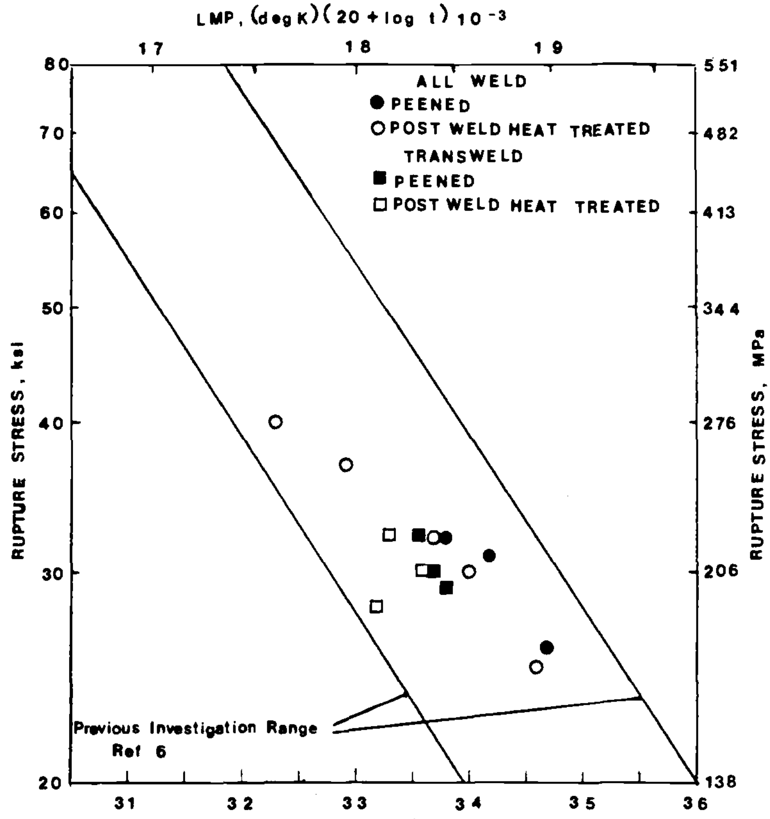

FIG. 9—*Rupture stress versus Larson-Miller parameter.*

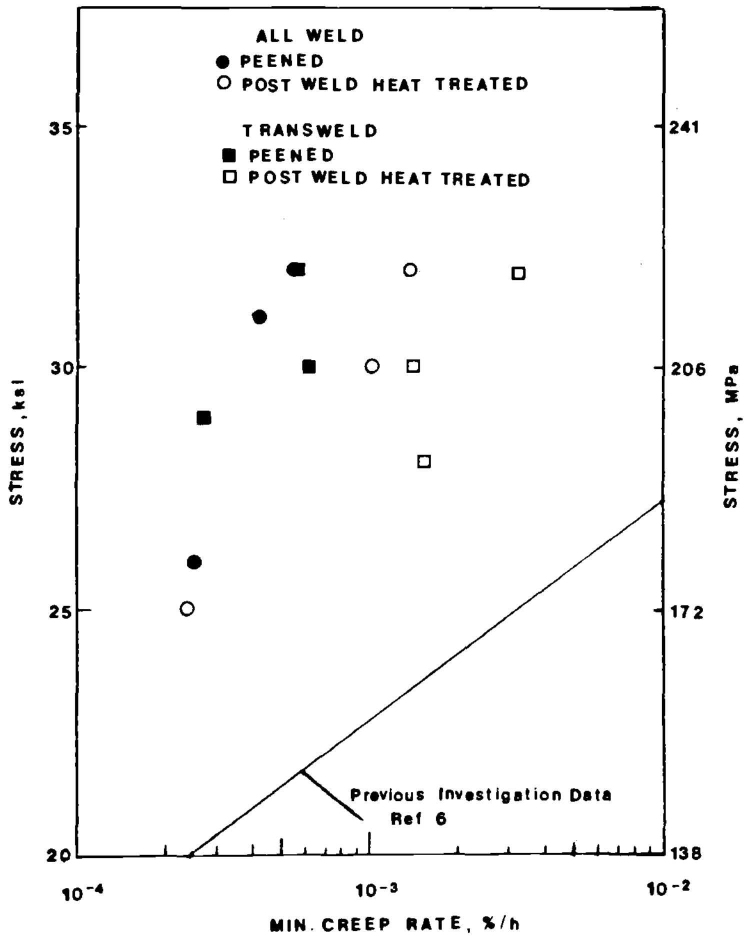

FIG. 10—*Stress versus minimum creep rate.*

The stress-corrosion specimens exposed to factory steam condensate at 77°C (170°F) all showed heavy rusting and pitting after exposure for 8492 h, with no difference between the peened and PWHT specimens. No cracks were detectable. The results of exposing U-bend test specimens to boiling 10 percent sodium hydroxide (NaOH) are shown in Table 5. In general, the peened specimens showed evidence of slightly greater attack compared with the PWHT specimens.

Conclusions

1. The hardness, yield strength and tensile strength (at both room and elevated temperature), and stress rupture strength for the peened weldments are higher than for the PWHT weldments. The creep rates for the peened weldments are lower than for the PWHT weldments.

TABLE 5—*Stress-corrosion bend test results (exposed to boiling 10 percent NaOH).*

		Condition of Specimen at			
Weldment	Specimen Location	120 h	2352 and 3192 h	4824 h	5640 h
2 (peened)	weld	...	...	small crack on bend	...
2 (peened)	weld	...	...	...	small crack on bend
4 (PWHT)	weld	...	discolored black	...	small crack on bend
4 (PWHT)	weld	...	discolored black	...	...
2 (peened)	base metal	...	...	...	...
2 (peened)	base metal	...	...	...	...
4 (PWHT)	base metal	...	...	...	...
4 (PWHT)	base metal	...	...	...	...
2 (peened)	HAZ	discolored black	discolored black	large crack on bend	...
2 (peened)	HAZ	discolored black	discolored black	...	small crack on bend
4 (PWHT)	HAZ	discolored black	discolored black	...	small crack on bend
4 (PWHT)	HAZ	discolored black	discolored black	...	small crack on bend

Notes:

(1) After 936 h all specimens were covered with thick white tenacious deposit which was removed for this inspection. This deposit was probably caused by the glass kettle used for this test. The kettle was changed to Teflon for the remainder of the testing.

(2) When cracks are noted, testing of cracked specimens is discontinued.

(3) After 4008 h all specimens were discolored black.

(4) After 8328 h there were no changes in the five specimens remaining on test.

2. In general, the ductility and stress-corrosion properties for the PWHT weldments are better than for the peened weldments.

Acknowledgments

Credit is due R. E. Clark for planning this investigation.

References

[*1*] Stout, R. D. and Doty, W. D., *Weldability of Steels*, Welding Research Council, 1971, p. 170.

[*2*] Calamari, P. D., Crum, F. J., and Place, G. W., "An Investigation on Peening," *Welding Journal, Research Supplement*, Vol. 32, 1953, pp. 387-S-402-S.

[*3*] Pellini, W. S. and Eschbacker, E. W., "Effects of Peening Last Pass of Welds," *Welding Journal, Research Supplement*, Vol. 33, 1954, pp. 71-S-76-S.

[*4*] Linert, G. E., *Welding Metallurgy*, Vol. I, American Welding Society, 1965, pp. 310-311.

[*5*] Linert, G. E., *Welding Metallurgy*, Vol. II, American Welding Society, 1965, p. 131.

[*6*] Wagner, L. E. and Seth, B. B. "Creep Rupture Behavior of 2¼Cr-1Mo Weld Metal," Metal Properties Council Symposium MPC-9, 1978, pp. 103-138.

[*7*] Swift, R. A., "The Mechanism of Creep Embrittlement in 2¼Cr-1Mo Steel," in *2¼Cr-1Mo Steel in Pressure Vessels and Piping*, American Society of Mechanical Engineers, New York, 1971.

Summary

Summary

T. E. Scott's keynote address notes the need to develop coal liquefaction as an alternative to crude oil as an energy source. He cites the pressure vessels and piping as a most critical area, with the following potential problems: (*1*) pressure vessel fabrication (sometimes in the field), (*2*) evaluation of thick-section material properties (particularly weld metal and heat-affected zone), (*3*) effect of high-temperature/high-pressure hydrogen service on material properties, (*4*) temper embrittlement, (*5*) need for improved nondestructive examination techniques, and (*6*) use of fracture mechanics for evaluation of fracture toughness and crack growth.

Evidence was given in several papers that 2¼Cr-1Mo steel for pressure vessel shells up to 51 cm (20 in.) thick can be produced with present technology. Plate, forgings, and castings have been produced in this thickness range.

A fundamental concern expressed in several papers was the need to develop a suitable microstructure throughout the section. For optimum strength and notch toughness, it was considered desirable to have a microstructure consisting of 100 percent bainite and free, or nearly free, polygonal ferrite.

A primary factor in achieving a suitable microstructure is the rate of cooling through the phase transformation range. In these thicknesses, normalizing or air cooling is too slow. Data show that a water quench with thorough agitation can produce cooling rates from −6.7 to −12.7°C/min (20 to 9°F/min) at the midthickness of sections from 30 to 51 cm (12 to 20 in.). Depending on the composition or hardenability of the 2¼Cr-1Mo steel, tests have shown that a microstructure free of ferrite can be achieved with cooling rates from −12.7 to 2.2°C (9 to 36°F/min). Thus some amount of ferrite can be expected for some heats of 2¼Cr-1Mo steel in section of 30 cm (12 in.) thick and over.

Various papers dealt with the metallography of quenched and tempered 2¼Cr-1Mo steel and with means of increasing the hardenability. Several alloy modifications have been found to be effective (namely, minor additions of manganese and nickel, or trace additions of titanium and boron). The hardenability has also been increased by the use of a higher austenitizing temperature.

Temper embrittlement is a form of high-temperature damage that can occur to 2¼Cr-1Mo steel. Several papers demonstrated that it can be controlled by restricting either the silicon or the phosphorus content to a very low level. Both methods have advantages and possible disadvantages, which need further evaluation.

Several papers dealt with the effect of hydrogen at high temperatures and pressures on the properties and performance of the steel. Some damaging effects have been noted, such as changes in microstructure and mechanical properties, particularly ductility. It can also increase the degree of temper embrittlement, can be damaging to the stainless weld overlay, and can significantly increase crack growth rates. Further study is warranted.

Some papers discussed fabrication procedures and welding methods aimed at increased efficiency and quality for very thick weldments. Fabrication of ultralarge pressure vessels in the shop or in the field is feasible.

Crack propagation behavior under these severe service conditions is being studied. Higher strength steels are more severely affected.

In conclusion, this symposium has presented a well-defined state of the art for design and construction of ultrathick pressure vessels for coal liquefaction and for petroleum refining processes subjected to similar conditions. Guidance has been provided for further research.

G. S. Sangdahl

Senior Metallurgical Consultant, Chicago Bridge & Iron Company, Oak Brook, Ill. 60521; symposium co-chairman and co-editor

M. Semchyshen

Vice-President, Metallurgical Development, Climax Molybdenum Company, Ann Arbor, Mich. 48106; symposium co-chairman and co-editor

Index